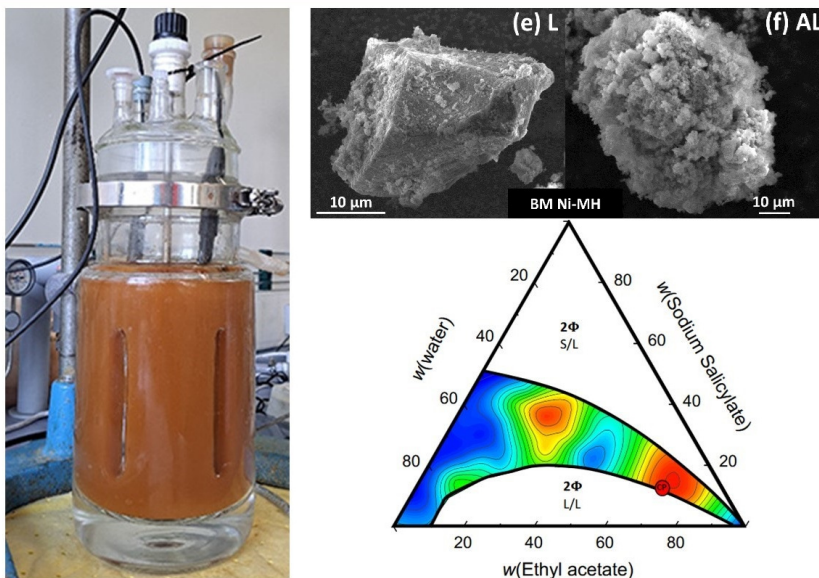


COMPTES RENDUS DE L'ACADÉMIE DES SCIENCES

Chimie



Volume 27, Special Issue S4, 2024

Special issue / Numéro spécial

GDR Prométhée – French Research Network on
Hydrometallurgical Processes for Primary and Secondary Resources

GDR Prométhée – Groupement de Recherche sur les Procédés
Hydrométallurgiques pour la Gestion Intégrée des Ressources
Primaires et Secondaires

Guest editors / Rédacteurs en chef invités

Laurent Cassayre, Hervé Muhr



ACADÉMIE
DES SCIENCES
INSTITUT DE FRANCE

Académie des sciences — Paris

ISSN: 1878-1543 (electronic)



Comptes Rendus

Chimie

Objective of the journal

Comptes Rendus Chimie is an international peer-reviewed electronic journal, covering all areas of chemistry.

It publishes special issues, original research articles, review articles, accounts, historical perspectives, pedagogical texts or conference proceedings, of unlimited length, in English or in French and in as flexible a format as necessary (figures, associated data, etc.).

Comptes Rendus Chimie has been published since 2020 with the centre Mersenne pour l'édition scientifique ouverte (Mersenne Center for open scientific publishing), according to a virtuous Diamond Open Access policy, free for authors (no author processing charges nor publishing fees) as well as for readers (immediate and permanent open access).

Editorial director: Antoine Triller.

Editors-in-chief: Pierre Braunstein.

Associate editors: Azzedine Bousseksou, Janine Cossy.

Advisory board: Rick D. Adams, Didier Astruc, Guy Bertrand, Bruno Chaudret, Avelino Corma, Patrick Couvreur, Stefanie Dehnen, Paul J. Dyson, Odile Eisenstein, Marc Fontecave, Pierre Grandclaude, Robert Guillaumont, Paul Knochel, Daniel Mansuy, Bernard Meunier, Armando J. L. Pombeiro, Michel Pouchard, Didier Roux, João Rocha, Clément Sanchez, Philippe Sautet, Jean-Pierre Sauvage, Patrice Simon, Pierre Sinaÿ.

Scientific secretary: Julien Desmarets.

About the journal

Comptes Rendus Chimie is published exclusively in electronic format.

All information on the journal, as well as the full text of all articles, is available on its website at: <https://comptes-rendus.academie-sciences.fr/chimie/>.

Author enquiries

For any inquiries about submitting a manuscript, please refer to the journal's website: <https://comptes-rendus.academie-sciences.fr/chimie/>.

Contact

Académie des sciences

23 quai de Conti

75006 Paris (France)

cr-chimie@academie-sciences.fr



The articles in this journal are published under the license
Creative Commons Attribution 4.0 International (CC-BY 4.0)
<https://creativecommons.org/licenses/by/4.0/deed.en>



Contents / Sommaire

Guest Editors	1-1
Laurent Cassayre, Hervé Muhr Special issue on hydrometallurgical processes for the integrated management of primary and secondary resources: Foreword	3-4
Nicolas M. Charpentier, Dong Xia, Jean-Christophe P. Gabriel Printed circuit board recycling: a focus on a novel, efficient and sustainable process for spent critical metals recovery	5-15
Agathe Hubau, Kathy Bru, Safiatou Idrissa Oumarou, Cécile Leycuras Lessons learned from the upscaling of an iron bio-oxidation process to improve uranium recovery	17-35
Clément Laskar, Amine Dakkoune, Carine Julcour, Florent Bourgeois, Béatrice Biscans, Laurent Cassayre Case-based analysis of mechanically-assisted leaching for hydrometallurgical extraction of critical metals from ores and wastes: application in chalcopyrite, ferronickel slag, and Ni-MH black mass	37-52
Emilie Régnier, Agathe Hubau, Solène Touzé, Sylvain Guignot, Daniel Meyer, Olivier Diat, Damien Bourgeois Copper leaching with aqueous foams for the processing of electronic waste	53-61
Jérôme Jacob, Douglas Pino-Herrera, Catherine Greffié, Guillaume Wille, Emmanuelle Plat Reprocessing of waste produced during acid mine drainage lime treatment by selective leaching	63-80
Mateus De Souza Buriti, Pierre Cézac, Lidia Casás Dissolution and precipitation of jarosite-type compounds: state of the art and future perspectives	81-109
Christian Manfoumbi, Kevin Roger, Martine Meireles Filtering the unfilterable: tuning the mesostructure of precipitating silica gels to improve the filterability of acidic lixiviation slurries	111-122
Virginie Nachbaur, Firas Ayadi, Béatrice Foulon, Malick Jean, Valérie Pralong, Samuel Jouen A sustainable solvothermal process extracting critical elements from Li-ion batteries	123-132
Lorena E. Ramirez Velazquez, Hervé Muhr Lithium recovery from secondary sources: A review in battery recycling with emphasis on chemical precipitation	133-141

Julie Réaux-Durain, Boushra Mortada, Murielle Bertrand, Jérôme Maynadié, Michaël Carboni, Daniel Meyer, Damien Bourgeois Back-extraction of major actinides from organic phase through precipitation	143-152
Fabrice Giusti, Elise Guerinoni, David Lemire, Marine Thimotée, Guilhem Arrachart, Sandrine Dourdain, Stéphane Pellet-Rostaing Solvent extraction of uranium from an acidic medium for the front-end of nuclear fuel cycle: from mechanisms understanding to innovative process design	153-183
Asmae El Maangar, Johannes Gramüeller, Verena Huber, Pierre Degot, Didier Touraud, Ruth Gschwind, Werner Kunz, Thomas Zemb Solubilisation–microstructure relationship of trivalent salts in hydrotropic ternary systems	185-202
Calogera Bertoloni, Vitalys Mba Ekomo, Benoît Villemejeanne, Charly Lemoine, Romain Duwald, Emmanuel Billy, Hakima Mendil-Jakani, Sophie Legeai Propylene glycol-based deep eutectic solvent as an alternative to Ethaline for electrometallurgy	203-214

GDR Prométhée - French Research Network on *Hydrometallurgical Processes for Primary and Secondary Resources*

Guest Editors



Laurent Cassayre

Laurent Cassayre is CNRS Research Director at the *Laboratoire de Génie Chimique* in Toulouse. He holds a PhD in Process Engineering from the University of Toulouse (2005) and an Habilitation to Supervise Research from the *Institut National Polytechnique de Toulouse* (2015). His areas of interest include pyrometallurgy (high-temperature electrochemical processes) and hydrometallurgical processes, with applications in metal recycling and recovery. His current scientific activities focus on the problems associated with the calculation of thermodynamic equilibria, and the contribution that this type of approach can make to the understanding, implementation, and optimisation of hydrometallurgical processes. He has been the director of the GDR PROMETHEE since 2022.



Hervé Muhr

Hervé Muhr is CNRS Research Director at the *Laboratoire Réactions et Génie des Procédés* in Nancy. He obtained his PhD in Chemical Engineering in 1993 and an Habilitation to Supervise Research from the *Institut National Polytechnique de Lorraine* in 2000. He is a specialist in precipitation and crystallization processes, which are major unit operations in hydrometallurgy. His current scientific activities focus on the recycling of Li-ion batteries and electronic cards for optimal metal recovery. He has been the deputy director of the GDR PROMETHEE since 2022.



Foreword

GDR Prométhée – French Research Network on *Hydrometallurgical Processes for Primary and Secondary Resources*

Special issue on hydrometallurgical processes for the integrated management of primary and secondary resources: Foreword

Laurent Cassayre[®] and Hervé Muhr

This special issue is the initiative of the Prométhée GDR, a national research group dedicated to the study of hydrometallurgical processes for the integrated management of primary and secondary resources. This GDR was created in January 2016 and renewed in 2021, and brings together around 150 research actors from 27 academic laboratories, as well as CEA, IFPEN and BRGM teams. It contributes to structure French research community on hydrometallurgical processes, for a better management of non-energy mineral resources, from mining to recycling. The CNRS, via its two institutes “Chemistry” and “Engineering”, is funding this GDR.

The community was invited to submit part of their work for this special issue of the journal *Comptes Rendus de l'Académie des Sciences*. Following a standard review process, 13 of these articles have been published, among which four review articles and nine research papers. They cover and combine a wide range of scientific fields, from chemical engineering, separation chemistry, electrochemistry, biometallurgy, physical chemistry or mechanochemistry, and address a various range of metal elements, such as noble metals, transition metals, lithium, rare earths, uranium and actinides. More specifically, this special issue starts with a presentation of a specific classification process for electronic wastes [1]. Then four articles are dedicated to leaching and bioleaching processes [2–5], three

articles deal with both leaching and precipitation operations [6–8], two focus on precipitation [9,10], two consider chemical aspects of solvent extraction [11,12] and a last paper is dedicated to electrometallurgy of noble metals in deep eutectic solvents [13].

We would like to thank all authors for their implication in this Special Issue, as well as the >30 reviewers who provided many valuable insights on these papers.

Laurent Cassayre
Laboratoire de Génie Chimique
Toulouse
France
laurent.cassayre@ensiacet.fr

Hervé Muhr
Laboratoire Réactions et Génie des Procédés
Nancy
France
herve.muhr@univ-lorraine.fr

References

- [1] N. M. Charpentier, D. Xia and J.-C. P. Gabriel, “Printed circuit board recycling: a focus on a novel, efficient and sustainable process for spent critical metals recovery”, *C. R. Chim.* **27** (2024), pp. 5–15.

- [2] A. Hubau, K. Bru, S. I. Oumarou and C. Leycuras, "Lessons learned from the upscaling of an iron bio-oxidation process to improve uranium recovery", *C. R. Chim.* **27** (2024), pp. 17–35.
- [3] C. Laskar, A. Dakkoune, C. Julcour, F. Bourgeois, B. Biscans and L. Cassayre, "Case-based analysis of mechanically-assisted leaching for hydrometallurgical extraction of critical metals from ores and wastes: application in chalcopyrite, ferronickel slag, and Ni-MH black mass", *C. R. Chim.* **27** (2024), pp. 37–52.
- [4] E. Régnier, A. Hubau, S. Touzé, S. Guignot, D. Meyer, O. Diat and D. Bourgeois, "Copper leaching with aqueous foams for the processing of electronic waste", *C. R. Chim.* **27** (2024), pp. 53–61.
- [5] J. Jacob, D. Pino-Herrera, C. Greffié, G. Wille and E. Plat, "Reprocessing of waste produced during acid mine drainage lime treatment by selective leaching", *C. R. Chim.* **27** (2024), pp. 63–80.
- [6] M. De Souza Buriti, P. Cézac and L. Casás, "Dissolution and precipitation of jarosite-type compounds: state of the art and future perspectives", *C. R. Chim.* **27** (2024), pp. 81–109.
- [7] C. Manfoumbi, K. Roger and M. Meireles, "Filtering the unfilterable: tuning the mesostructure of precipitating silica gels to improve the filterability of acidic lixiviation slurries", *C. R. Chim.* **27** (2024), pp. 111–122.
- [8] V. Nachbaur, F. Ayadi, B. Foulon, M. Jean, V. Pralong and S. Jouen, "A sustainable solvothermal process extracting critical elements from Li-ion batteries", *C. R. Chim.* **27** (2024), pp. 123–132.
- [9] L. E. Ramirez Velazquez and H. Muhr, "Lithium recovery from secondary sources: A review in battery recycling with emphasis on chemical precipitation", *C. R. Chim.* **27** (2024), pp. 133–141.
- [10] J. Réaux-Durain, B. Mortada, M. Bertrand, J. Maynadié, M. Carboni, D. Meyer and D. Bourgeois, "Back-extraction of major actinides from organic phase through precipitation", *C. R. Chim.* **27** (2024), pp. 143–152.
- [11] F. Giusti, E. Guerinoni, D. Lemire, M. Thimotée, G. Arrachart, S. Dourdain and S. Pellet-Rostaing, "Solvent extraction of uranium from an acidic medium for the front-end of nuclear fuel cycle: from mechanisms understanding to innovative process design", *C. R. Chim.* **27** (2024), pp. 153–183.
- [12] A. El Maangar, J. Gramüeller, V. Huber, P. Degot, D. Touraud, R. M. Gschwind, W. Kunz and T. Zemb, "Solubilisation–microstructure relationship of trivalent salts in hydrotropic ternary systems", *C. R. Chim.* **27** (2024), pp. 185–202.
- [13] C. Bertoloni, V. Mba Ekomo, B. Villemejeanne, C. Lemoine, R. Duwald, E. Billy, H. Mendil-Jakani and S. Legeai, "Propylene glycol-based deep eutectic solvent as an alternative to Ethaline for electrometallurgy", *C. R. Chim.* **27** (2024), pp. 203–214.



Review article

GDR Prométhée – French Research Network on *Hydrometallurgical Processes for Primary and Secondary Resources*

Printed circuit board recycling: a focus on a novel, efficient and sustainable process for spent critical metals recovery

Nicolas M. Charpentier^{✉,a}, Dong Xia^{✉,b} and Jean-Christophe P. Gabriel^{✉,*,a,b}

^a Université Paris-Saclay, CEA, CNRS, NIMBE, LICSEN, 91191, Gif-sur-Yvette, France

^b SCARCE Laboratory, Energy Research Institute @ NTU (ERI@N), Nanyang Technological University, 637553, Singapore

E-mail: jean-christophe.gabriel@cea.fr (J.-C. P. Gabriel)

Abstract. In this article, we present a novel and sustainable approach for recycling printed circuit boards (PCBs), potentially enabling the complete transformation of collected waste into reusable raw materials. Our methodology starts with the disassembly of PCBs for the extraction of all electronic components (ECs). These ECs are then subjected to a classification process using advanced sorting techniques, including machine vision and multi-energy X-ray transmission spectroscopy powered by artificial intelligence, which allows ECs with similar elemental composition to be accurately sorted together. This sorting approach can effectively enrich the target elements up to 10,000 times their original content, enabling their subsequent recovery through dedicated physico-hydrometallurgical processes. These tailored methods offer enhanced efficiency and improved environmental sustainability for recycling valuable and critical elements such as rare earth elements, tantalum, and platinum group metals. Notably, our approach not only demonstrates superior sustainability but also offers increased economic viability, making it a more financially profitable solution.

Keywords. Recycling, Waste PCBs, Machine vision, Multi-energy X-ray transmission.

Funding. National Research Foundation, Singapore, and National Environment Agency, Singapore under its Closing the Waste Loop R&D Initiative (Award No. USS-IF-2018-4) and Closing the Resource Loop Funding Initiative (Award No. CTRL-2023-1D-01), REVIWEEE project grant managed by the French National Research Agency (ANR) under the France 2030 program, Award No. ANR-22-PERE-0009.

Manuscript received 2 October 2023, revised 21 December 2023 and 24 January 2024, accepted 24 January 2024.

1. Introduction

1.1. Background on e-waste challenges

The proliferation of electronic devices is leading to the fastest growing issue of waste management. Con-

currently, this need is accompanied by an increasing demand for raw materials for their manufacturing, the extraction of which is also a source of environmental and societal concerns. Furthermore, many raw materials required for electronic device production are exploited only in specific regions of the world, challenging the supply independence of other countries. This is, for example, the case for

*Corresponding author

rare earth elements (REEs: neodymium, yttrium, lanthanum, dysprosium...) [1] or metals like tantalum, cobalt, or nickel, which are fundamental components of many electronic devices [2]. Such metals and materials have therefore been identified as critical raw materials [3].

Facing this dual environmental and strategic challenge, research is committed to developing new solutions for recycling elements found in electronic waste. However, traditional recycling methods fail to recover many such key elements due to their often too low and variable concentration in the overall mass of electronic waste to be processed and the complexity of the associated mixtures of chemical elements. Currently, only about a dozen elements, out of the more than sixty present in electronic waste, are being recycled (see Table 1). Moreover, these traditional recycling methods can potentially be polluting and hazardous because they rely on hydrometallurgical and pyrometallurgical processes [4,5]. Most of the current recyclers have recycling processes based on these technologies (see Table 1) [6,7]. The remaining elements are neither recycled nor valorized and mostly end up mixed and diluted in landfilled ashes (bottom and fly), although sometimes used as landfill fill (an application banned in some countries due to the potential leaching of toxic metals by rainwater).

Therefore, today, the primary obstacle to recycling these strategic elements is their low and variable concentrations in the waste stream to be treated. To solve this, it is essential to develop economically viable new strategies for electronic waste management that can simplify the composition and enrich the input materials, allowing us to access these elements and thus reduce the environmental impact of their production while enabling certain regions to access strategic metals that would otherwise be lost.

1.2. *Importance of sustainable resource recovery in e-waste management*

To achieve this, our analysis of the situation led us to modify the current PCB recycling strategy by combining: (i) a step for disassembling printed circuits, followed by (ii) an advanced component sorting enabling the recovery of targeted elements by the tailored process. The novelty of this approach lies in the technology used for sorting, which, for the first time,

allows it to be done based on the elemental composition of the objects to be separated, in order to enrich the outgoing streams with targeted elements [8]. Although various industrial methods already exist for the disassembly phase, which we recently reviewed [9], component sorting is still insufficient, as it is either too rudimentary (done manually), or when optically sorted lacks elemental composition knowledge to sort based on the elements of interest [10]; or too slow (3s per tantalum capacitor recovery using laser desoldering, optical recognition and robotic EC picking) [11]. Two main process families are opposed here: “look and pick” processes, which first evaluate the interesting components on printed circuit boards (PCBs) and then selectively disassemble them, focusing on valuable components, and the “disassemble and sort” strategy, which involves simultaneous disassembly of all components, followed by their sorting, taking into account the total value of the components. Although promising, this sorting strategy based solely on visual recognition quickly reaches its limits when visually similar components have different compositions. Moreover, these approaches are often either too slow or require too much robotic equipment, and hence capital expenditures, to be adopted by a wide majority of recyclers.

To address this problem, several methods for characterizing PCBs and components have been developed and described in the literature. For example, infrared spectroscopy, traditionally used to differentiate plastics, can be applied to the sorting of electronic components [12,13]. The use of Laser-Induced Breakdown Spectroscopy (LIBS) [14] has also been explored for sorting plastics from electronics, which are often contaminated with flame retardants [15,16]. These methods can be used to map PCBs and components, creating images in which each pixel represents a spectrum. These hyperspectral images (HSI) contain a large amount of information that can be exploited for component sorting from both spatial and spectral perspectives. However, these methods only allow the analysis of a thin layer at the surface of the component and do not represent the internal composition of materials often encapsulated in plastic, epoxy or ceramics.

To obtain elemental information on the internal composition of often heterogeneous objects, X-ray Transmission Spectroscopy (XRT) at few energy levels (2 to 5 energy bins) has been developed in various

Table 1. List of some existing recycling processes and elements they can recover, updated from Refs [6,7]

Company	Process	Elements recovered
Umicore	Pyrometallurgy, hydrometallurgy and electrochemistry	Fe, Al, Cu, Ag, Au, Pd, Pt, Ir, Rh, Ru, In, Se, Te, Pb, Sn, Sb, Bi
Noranda	Hydrometallurgy and electrochemistry	Fe, Pb, Zn, Cu, Ag, Au, Pd, Pt, Se, Te, Ni
Boliden	Pyrometallurgy	Cu, Ag, Au, Pd, Ni, Se, Zn, Pb, Sb, In, Cd
DOWA	Pyrometallurgy, hydrometallurgy and electrochemistry	Au, Ag, Cu, In, Pd, Pt, Sn, Pb, Sb, Bi, Se, Te
Aurubis	Hydrometallurgy and Pyrometallurgy	Cu, Pb, Sb, Bi, Te, Zn, Sn, Ni
Boliden's Rönnskär	Pyrometallurgy	Cu, Ag, Au, Pd, Ni, Se, Zn, Pb
Outotec	Pyrometallurgy	Zn, Cu, Au, Ag, In, Pb, Cd, Ge

fields, mainly in mining, allowing the differentiation of ores through the study of their atomic density [17,18], as well as in airport luggage scanners. However, this low energy resolution would not allow for the prerequisite capacity to differentiate between chemical elements that are present in PCBs. To address this issue, we present an original method for sorting electronic components that combines optical sorting and multi-energy XRT (MEXRT) relying on artificial intelligence (AI). These new-generation detectors, initially developed at CEA/LETI, have only been commercially available for a few years, under a CEA licensing agreement, from Detection Technologies. Other makers are now also providing such detectors. Indeed, thanks to the 128-level energy resolution of the MEXRT detector used, it is possible to differentiate components based on their elemental composition, hence simplifying the elemental mixture and enrich the final streams with the elements of interest.

This crucial step is highly significant because PCBs exhibit a complex, heterogeneous, and variable composition. Indeed, numerous studies have consistently demonstrated a substantial variation in the composition of different PCBs. Upon careful comparison of these studies, it becomes apparent that, for many elements, the standard deviation for their concentration average can be equal to or even exceed their average concentration (Table 2). Moreover, it should be noted that in some cases, certain element concentrations are not reported from the analysis, either because they were not present or possibly due to the inherent difficulty in quantifying them. Hence, it is worth mentioning that, in the majority of the

studies reviewed, refractory elements like Tantalum (Ta) [19], are often not analyzed/reported, the reason is unclear as it is not discussed in these articles. This table highlights the high variability in PCBs composition depending on their type and year of production. Indeed, in most recycling plants, PCBs are received without previous sorting. Therefore, the need for a versatile analytical tool capable of distinguishing and characterizing elements within PCB components is undeniable, as it could play a crucial role in advancing the field of e-waste recycling and critical metals recovery.

2. Advanced sorting technics

For the components to be sorted, they first need to be dismantled from the PCBs through a disassembly process. Various industrial or pre-industrial methods are already available for this disassembly, either chemical, by dissolving solder joints using acids, by solder fusion, or by simple mechanical means [1]. These methods all have advantages and drawbacks depending on what constraints are applied to the components, sometimes burning them, corroding them, or possibly breaking them. This is not totally neutral as these alterations can have an impact on the visual aspect of the ECs and therefore on the downstream optical-based sorting process steps and more specifically when it comes to recognizing the components [24]. In our studies, we mostly relied on oven-baking PCBs to melt the solder, followed by vigorous shaking to loosen the ECs and render them free from the bare board.

Table 2. Average and standard deviation of metals content in PCBs calculated from analytical values reported in twenty-three different studies [20–23]; full table and references are available in Supplementary Table S1

Metal content	Average	Standard Dev.
Cu (%)	22.26	9.46
Al (%)	3.67	3.32
Pb (%)	2.50	2.70
Zn (%)	2.51	3.58
Ni (%)	1.99	2.89
Fe (%)	6.41	10.42
Sn (%)	2.61	1.48
Sb (%)	0.06	0.01
Cr (%)	0.18	0.25
Na (%)	0.48	N/A
Ca (%)	3.05	3.30
Ba (%)	3.05	N/A*
Ag (ppm)	1170.95	1570.28
Au (ppm)	991.50	1210.19
Pt (ppm)	0.00	N/A*
Cd (ppm)	1183.00	N/A*
K (ppm)	180.00	N/A*
In (ppm)	500.00	N/A*
Mn (ppm)	4593.67	4836.90
Se (ppm)	21.00	N/A*
As (ppm)	11.00	N/A*
Mg (ppm)	750.00	353.55
Pd (ppm)	101.00	103.41
Co (ppm)	350.00	70.71
Ti (ppm)	400.00	N/A*
Ta (ppm)	200.00	400.00
REEs (ppm)	30.47	N/A*
Total Metals (%)	32.47	7.38

* N/A indicates that none or only one report of concentration has been found for this element in PCBs.

2.1. Physical sorting process

Although not always efficient as an elemental sorting method, physical methods are simple to use and can easily segregate some similar components [25],

and already allow for a simplification of the bin's elemental composition. Despite the diversity of electronic components, it is important to note that similarities can be observed among components of similar sizes. Therefore, the use of sieve sorting proves to be both easy and effective for removing large components, such as connectors or heat exchangers generally homogenous in terms of composition. Furthermore, this process also eliminates components that are too small for further processing or broken parts of components. This size-based sorting step also contributes to reducing the heterogeneity of the incoming stream by limiting the diversity of components to a few types in each size class, facilitating further sorting processes.

2.2. Presentation of the 10 kg/h sorting prototype

In order to then sort the different electronic components, we chose to convey them on a belt to take them in front of the different cameras, detectors and ejection mechanisms. The prototype has been previously described in detail, and a picture of it can be seen in Figure 1 [26]. In brief, it is composed of a white conveyor belt, measuring 10 cm wide and 2.5 m long, transporting the components under the optical camera and then into the MEXRT spectrometer for classification before they are ejected from the belt into the appropriate sorting bin by a pneumatic air propulsion system.

2.2.1. Machine vision-based optical sorting

The components are first subjected to optical sorting. This method utilizes a combination of a high-resolution camera and a convolutional neural network (CNN) specially trained on a dataset created from real components. This optical sorting allows for the precise identification of components by type, leveraging their appearance. With a camera capturing 75 images per second, component image acquisition occurs in real-time. These images are then sent to the computer for classification by the CNN. Optimization of image processing and the recognition algorithm enable the sorting of 60 components per second on a single line with an accuracy above 97%. While this method already separates certain components with relatively homogeneous compositions (CPU, cylindrical aluminum-based capacitors, or copper-rich induction coils), it suffers from a lack

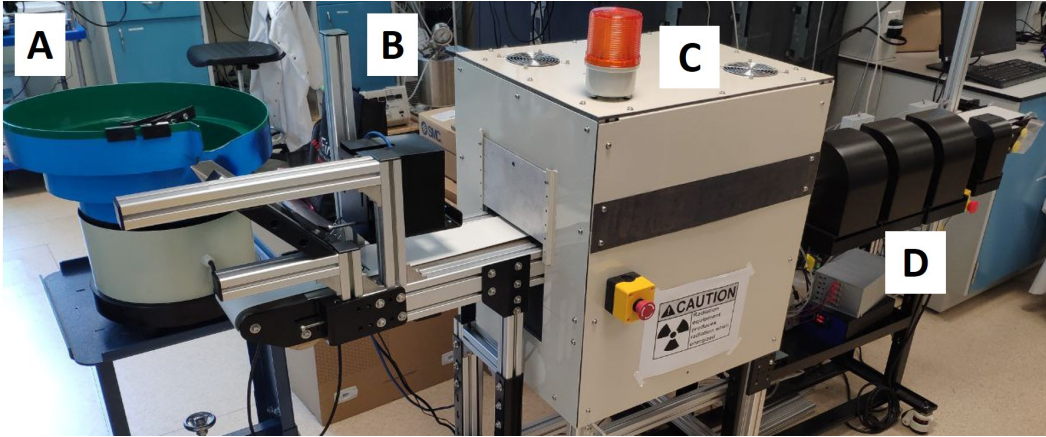


Figure 1. Picture of the 10 kg/h Electronic Components sorting prototype with (A) the bowl feeder; (B) the Optical camera/Light fixture; (C) the MEXRT housing and imaging system; and (D) Four sorting bins.

of information about the chemical composition of other components, such as resistors, other types of capacitors, or highly integrated electronic components, which are often visually similar but may contain a multitude of different elements.

2.2.2. Multi-energy X-ray transmission spectroscopy

To address this issue of elemental composition-based sorting, components that cannot be differentiated by optical sorting are then subjected to MEXRT sorting. When compared to X-ray Fluorescence (XRF), MEXRT has various advantages. First, since we are looking directly at the absorption of the direct beam, we have the largest possible signal-over-noise-ratio, whereas it is orders of magnitude smaller with XRF when using the same sampling time [27]. Second, we can easily perform an imaging of the devices by combining the 128-pixel 1D detector with the movement of the conveyor belt, which renders a 2D image of the passing ECs. Hence, MEXRT proves to be a rapid method for performing composition-based sorting by using their absorption spectra. Indeed, this method not only relies on studying the atomic density of the material, as a denser material absorbs more radiation at a constant thickness, but also has the ability to study the energy of absorbed radiation. Hence, it is possible to more precisely define the material's composition by studying the energy of the absorption k-edge of the elements it comprises. The k-edge corresponds to the binding energy of electrons in the k-shell of an atom, representing the minimum energy required for a photon to be

fully ejected from this shell. This phenomenon results in a sharp decrease in photon transmission at the corresponding energy, as these photons are absorbed by the electrons. Each chemical element has a unique structure, with binding energies of its core electrons that are specific to it, thus allowing for its identification. By comparing the local maxima of absorption spectra and referencing the theoretical values of these thresholds, it is thus possible to determine the elemental composition of a material from its transmission spectrum (Figure 2).

To achieve this, the components are moved on the conveyor belt at a constant speed of 15 cm/s between the X-ray source (VJ X-RAY (NY) LLC MODEL: IXS160BP200P107 equipped with a tungsten anode, working typically at 100 kV and 0.3 mA) and the detector (ME100, Detection Technologies under CEA license). X-rays penetrate the material, and their absorption represents the total radiation absorbed by the elements composing the material. The transmitted radiation is then detected on the other side of the component by the detector. Moreover, the detector used allows for multi-energy spectroscopy. It consists of a line of 128 pixels, with each pixel capable of detecting photons and their energy from 20 keV to 160 keV, with a precision of 1.1 keV (128 levels of energy). By stacking the acquisition lines, it is possible to reconstruct a hyperspectral image of the components, with each pixel representing the transmission spectrum of the material at that specific location. With a pixel size of 0.8 mm and an acquisition speed of 2 ms per line, the image of a 40 mm

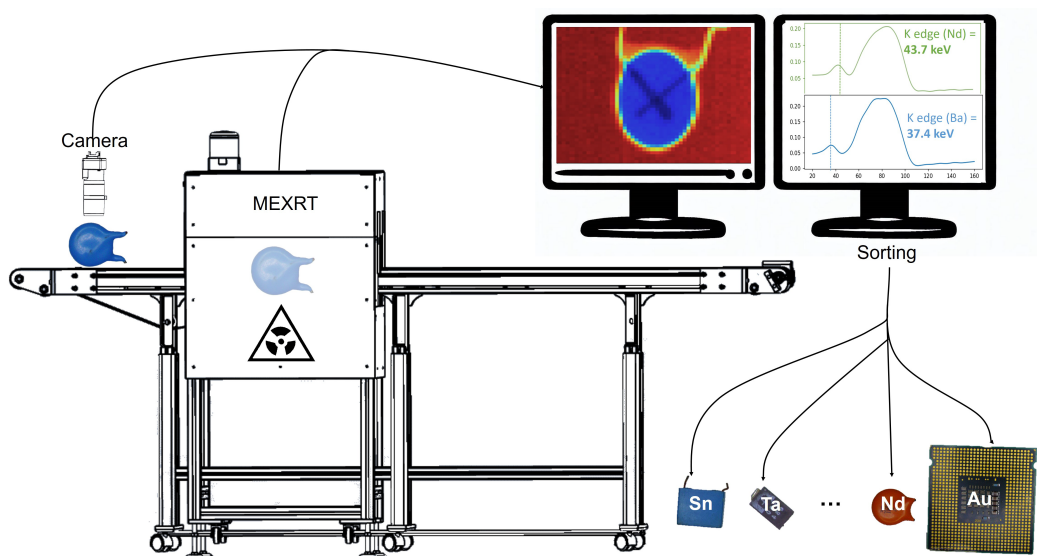


Figure 2. Schematic description of the dual optical/MEXRT based sorting process.

component can be obtained in 100 ms. Adding the processing time for these hyperspectral images, it is possible to sort up to 4 components per second using MEXRT spectroscopy (and per line of ECs on the conveyor belt). It should indeed be noted that our prototype currently works with a single line of ECs. Faster sorting rates could easily be obtained using multiple lines and an end-of-belt sorting mechanism.

3. Tailored extraction methods and advancements in hydrometallurgical processes

The extraction of electronic components with simplified and specific compositions from the electronic waste stream opens up new possibilities for recycling processes. This is especially relevant when dealing with spent critical metals that are not currently recovered and recycled. This is the case, for example, with the recycling of rare earth elements such as the highly-priced neodymium (Nd) found in ceramic capacitors (according to <https://strategicmetalsinvest.com/>, its trading price has varied from \$65,000 per metric ton in 2020 to \$265,000 at its peak in early 2022; it is currently traded around \$126,000/Mt). These capacitors use barium titanate (BaTiO_3) as a dielectric material, sometimes doped with rare earth elements to adjust its electronic properties. Nd in particular is used in these capacitors, either as a sole rare earth or together with others. From a market

share point of view, if Nd is mostly used in permanent magnets, it should be noted that in 2011 capacitors represented 12% of the overall Nd market [4]. PCBs from the urban mine therefore represent a very significant potential source of it. However, no efficient recycling strategy has been proposed nor implemented yet due to its too low concentration in the overall waste PCB supply due to the inaccessibility of a concentrated source of such capacitors. Thanks to the use of our dual optical/MEXRT sorting demonstrator, sorting bins containing almost solely ceramic capacitors containing Nd are now accessible. They can indeed be separated from other electronic components through optical sorting and from visually similar ceramic capacitors using MEXRT sorting with an accuracy of 100% [28]. Using this sorting process, the Nd concentration in the sorting bin containing Nd-containing ceramic capacitors can reach 15% by mass. One can then tailor a specific extraction method based on simple physical and hydrometallurgical processes [28]. In brief, the process begins with a physical beneficiation step involving the controlled fracturing of capacitors, facilitating the separation of their various components through density-based separation and subsequent magnetic sorting. Following this, the fractions rich in Nd are subjected to nitric acid leaching, selectively dissolving the Nd. Subsequently, Nd is precipitated via oxalic acid and ultimately undergoes calcination to yield Nd oxide

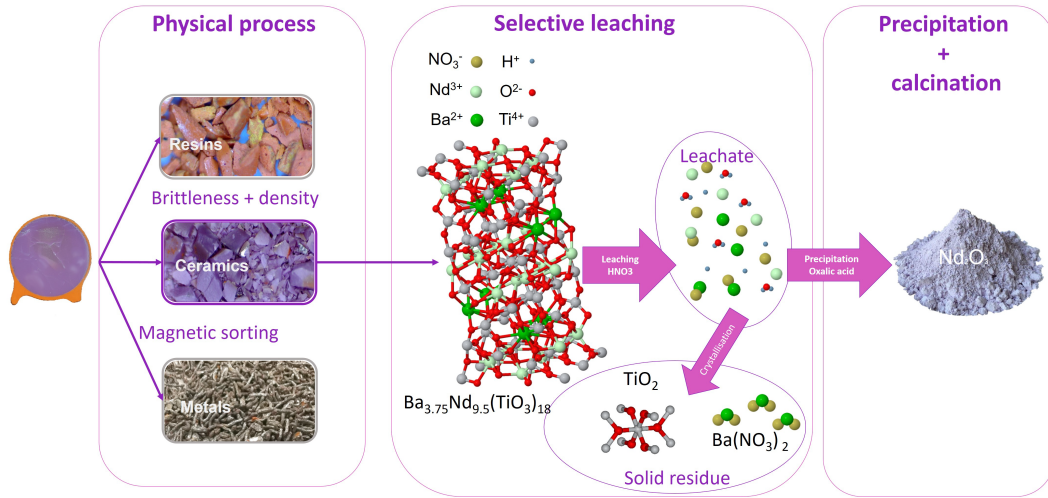


Figure 3. Neodymium (Nd) recovery process from Nd-based ceramic capacitors.

(Figure 3). This process, tailored for Nd extraction from ceramic capacitors, provides better control over the quantity and reuse of solvents used.

Overall, by combining this sorting with a suitable process for extracting Nd from these capacitors, we modelled that it is possible to establish an economically viable and sustainable recycling process. Indeed, this custom-developed process allows for the recycling of 91.1% of the Nd present in the capacitors into pure Nd oxide at 99.6% purity, and the extra capital expenditure associated with implementing this approach was modelled to be recovered within three to five years (based solely on the Nd recovery) [28]. By developing similar processes or utilizing existing ones for the recycling of other specific components/elements, this sorting method opens up prospects for more sustainable and efficient electronic waste recycling.

4. Large-scale validation and perspectives


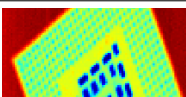

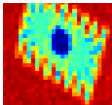

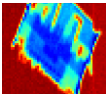

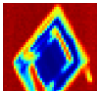

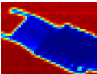

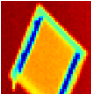

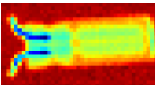

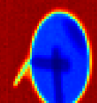

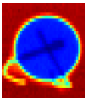

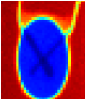

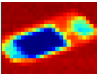

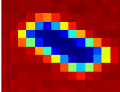
The process described in the previous sections based on sieving, optical and MEXRT sorting has then been studied on a larger scale for better evaluation. The performance of this sorting process can be evaluated in two ways: firstly, by its accuracy in sorting components based on a database of known components; secondly, the process's ability to enrich bins with targeted elements was assessed to study the process's relevance from this perspective.

4.1. Validation and key figures of the process

Optical sorting allows distinguishing eight types of component families with an accuracy of 97.4%. The use of MEXRT sorting then allows distinguishing other types of components and composition, within any given optical-sorting bin. This is mainly the case for ceramic capacitors, which for example can contain (i) rare earth elements but whose visual appearance provides no information about the composition, or (ii) Ta capacitors. By combining optical sorting and MEXRT, the total process can sort up to fourteen types of components with an average accuracy of 96.9% (Table 3). The global sorting process has been evaluated using a total of 442 ECs divided into different size categories and types (~50 ECs for each type).


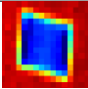

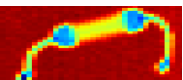
The speed of optical sorting reaches 60 components per second, while the acquisition and sorting speed by MEXRT is 4 components per second. The average mass of the studied components being 0.65 g, the average sorting speed of the prototype would be 9.36 kg/h if all the components were processed both optically and by MEXRT. Although slower than optical sorting, MEXRT sorting allows for more precise differentiation of other types of components. Due to its reduced speed compared to optical sorting, MEXRT sorting is reserved for a sub-fraction of components that cannot be sorted optically. This dichotomy thus accelerates the overall

Table 3. Electronic components with their respective MEXRT images, main elements and recognition precision

Components	Optical image	X-ray transmission image	Main elements or of interest	Accuracy Global process (optical + MEXRT)
CPU			Au, Cu	92%
IC chips			Au, Ni, Cu, Sn, Si	96%
Connectors			Au, Ni, Cu, Sn, Si	98%
Relays			Fe, Cu, Sn	100%
Inductors			Fe, Cu	100%
MPC			Fe, Cu, Ca, Sn, Al	100%
Al capacitors			Al, Ni, Sn	97%
Nd-based ceramic capacitors			Ba, Nd, Ti, Ni, Sn, Ag	100%
Ba-based ceramic capacitors			Ba, REEs, Ti, Ni, Sn, Ag	92%
Non Ba-based ceramic capacitors			Ca, Mn, Ni, Sn, Ag	90%
Ta-based capacitor			Ta, Ni, Mn, Ag, Co, Fe	100%
Ba-based MLCC			Ba, REEs, Ti, Ni, Sn, Ag	100%

(continued on next page)

Table 3. (continued)

Components	Optical image	X-ray transmission image	Main elements or of interest	Accuracy Global process (optical + MEXRT)
Non Ba-based MLCC			Ca, Mn, Ni, Sn, Ag	86%
Resistors			Ni, Cu, Sn	100%

Adapted with authorisation from [26].

sorting speed by minimizing the use of MEXRT sorting. Furthermore, it should be noted that this strategy appears reasonable as our current observation is that only 10% of the ECs requires a MEXRT sorting step. Since this step is roughly ten time slower, this indicates that a cascade sorting process for 100% of the ECs is achievable at industrial sorting rates requirements.

Compared to traditional sorting methods, this process combining optical sorting and MEXRT therefore represents a promising solution to meet the needs of electronic waste sorting in the recycling process. This method offers several significant advantages. Firstly, it provides access to a greater number of components, thus expanding the range of recyclable chemical elements. Furthermore, this method allows components to be sorted based on their elemental composition with increased precision. By combining the advantages of fast optical sorting and the capability of MEXRT sorting to differentiate elements, this process represents a major advancement in the field of electronic waste recycling, providing access to classified and chemically simplified components, and enriched in targeted critical elements, once sorted.

4.2. Large-scale sorting evaluation

The process's ability to sort components and concentrate elements of interest was proven on a larger scale on a mixture of 9.05 kg of waste PCBs [26]. The results of this study demonstrate a significant enrichment of target elements such as Au, Pd, Mn, Ta, or Nd in certain fractions. In particular, sorting CPUs allows for the enrichment of the final stream to a rate of 0.14 wt% in gold, while its concentration was

not even detectable in the initial stream (less than 0.1 ppm). Other components, for which recycling processes already exist, were also separated, such as Ta capacitors [24], aluminium electrolytic capacitors [29], Nd ceramic capacitors [28], or multilayer ceramic capacitors (MLCCs) [30]. Although recycling processes for some of these components already existed, a means of accessing them was lacking, and that is precisely what this sorting process now accomplishes and enables.

In addition to its role in enriching streams with certain targeted components and elements, this sorting process also reduces the chemical complexity of sorting bins. Indeed, after sorting, the fraction containing inductors exhibits a composition of 45.6 ± 2 wt% of iron, 38.5 ± 2 wt% of copper, and 20.82 ± 2 wt% of tin. This significant simplification of the composition of the streams greatly facilitates the recycling of various elements, making the streams less complex to process and the recovery rates higher. By eliminating the presence of undesirable elements and enriching the streams with targeted elements, the process contributes to creating more homogeneous streams, thus facilitating their subsequent treatment. Furthermore, the development of microfluidic platforms [31] fully integrated with on-line characterization methods, such as FTIR [32] and XRF [8], will ensure the cost effective and fast development of new hydrometallurgy processes, whether liquid–liquid [33–35], solid–liquid [36] or for the measurement of thermodynamic data such as components chemical activities, including for the solvent [30,32].

The larger-scale modeling of this sorting process has demonstrated its effectiveness and relevance for electronic component sorting on Nd-based ceramic

capacitors [28]. This process simplifies recycling and access to various elements present in electronic waste by reducing the complexity of the final streams. This approach opens up new prospects for more sustainable electronic waste management and the recycling of previously overlooked and therefore spent chemical elements.

4.3. Perspectives

This prototype enables a sorting speed of 10 kg/h of sorted components on a single line. Extrapolating this technology to an industrial scale enabling 50 components to be classified in parallel, the average sorting speed could reach 500 kg/h. In comparison, plastic sorting lines have a speed comprised between 100 kg/h and 1000 kg/h [37]. In 2020, France generated 849,097 metric tons of electronic waste [38], which translates into ~23,000 metric tons of electronic components (PCBs represent ~6 wt% by weight of global electronic waste [39]). With the sorting process presented here, all the electronic components discarded in France could be sorted in 46,000 hours using a 500 kg/h sorting speed. To achieve this task, six 500 kg/h capacity sorting lines would be sufficient to sort all the electronic components generated in France over one year. Extrapolated worldwide (52 Million Mt of waste from electric and electronic equipment), a minimum of ~725 machines would be needed (with the hypothesis of a 24 h-a-day 365-days-a-year running time). These results suggest considerable market potential for a large-scale usage and application in the field of e-waste recycling. However, collection rates and volumes of e-waste production can vary considerably geographically (from almost 50% at present in the best cases to zero in the worst). For these reasons, different types and sizes of treatment facilities may be needed, whether in the form of large centralized facilities or smaller facilities spread over an area, either in fixed or containerized form, allowing for a nomadic facility that can move to the waste. We are currently expanding our library of economically viable complete processes to as many chemical elements possible (targeting the critical ones first), as well as searching for a tool manufacturer to scale it up and bring it to the market. It should be noted that the output of the developed processes is not only the targeted metals but also allows for the recovery of all

the chemical elements in a composition that can be traded. This solution for EC recycling is a paradigm shift in the recycling industry and will require a process upgrade compared to current recycling methods, with the addition of two new upstream process steps (dismantling and sorting). While industrial tools for the first step are already available on the market, we are looking for industrial partners to commercialize this smart sorting tools. The many discussions we have had with recyclers have made it clear that they are eager to have access to this technology.

5. Conclusion

In conclusion, the described prototype and the associated processes, have been validated at a technological readiness level of 4 and they represent a significant advancement in the field of electronic waste recycling. The combination of physical sorting methods, optical characterization, and MEXRT supported by AI allows for the first time to precisely target elements of critical interest to enrich the sorting output streams. This sorting process provides access to strategic and critical elements that were previously lost during recycling processes due to their overall low concentration. Furthermore, this process enables a more environmentally friendly recovery of the targeted elements by tailoring specific process that limits energy and chemicals usage. Finally, this process has been modeled to be economically viable on an industrial scale, thereby opening the door to numerous new business opportunities in the field of electronic waste recycling.

Declaration of AI-assisted technologies in the writing process

During the preparation of this work the authors used “DeepL Write” in order to double-check for English spelling or grammatical errors or typos. After using this tool, the authors reviewed and edited the content as needed and take full responsibility for the content of the publication.

Declaration of interests

The authors do not work for, advise, own shares in, or receive funds from any organization that could benefit from this article, and have declared no affiliations other than their research organizations.

Funding

All authors acknowledge financial support from SCARCE project, which is supported by the National Research Foundation, Singapore, and the National Environment Agency, Singapore under its Closing the Waste Loop R&D Initiative (Award No. USS-IF-2018-4) and Closing the Resource Loop Funding Initiative (Award No. CTRL-2023-1D-01). NMC acknowledges financial support (salary) in 2023 by the REVIWEEE project grant managed by the French National Research Agency (ANR) under the France 2030 program, award No. ANR-22-PERE-0009.

Supplementary data

Supporting information for this article is available on the journal's website under <https://doi.org/10.5802/crchim.291> or from the author.

References

- [1] A. Gonzalez, L. Pantoja Munoz, H. Garelick, D. Purchase, *16th International Conference on Environmental Science and Technology, September 2019*, 2019, [Online]. Available: https://cest2019.gnest.org/sites/default/files/presentation_file_list/cest2019_00201_poster_paper.pdf, 4-5 pages.
- [2] J. A. Kinnaird, P. A. M. Nex, *Routledge Handbook of the Extractive Industries and Sustainable Development*, Routledge, 2022, 13-33 pages.
- [3] E. Commission, I. Directorate-General for Internal Market Entrepreneurship and SMEs, M. Grohol, C. Veeh, *Study on the Critical Raw Materials for the EU 2023—Final Report*, Publications Office of the European Union, 2023.
- [4] Z. Wu, W. Yuan, J. Li, X. Wang, L. Liu, J. Wang, *Front. Environ. Sci. Eng.*, 2017, **11**, article no. 8.
- [5] A. Iqbal, M. R. Jan, J. Shah, B. Rashid, *Environ. Sci. Pollut. Res.*, 2022, **29**, 88763-88778.
- [6] R. Aune, "Typical e-waste recycling processes by pyrometallurgy", Accessed: September 11, 2023. [Online]. Available: <https://www.futurelearn.com/info/courses/ewaste-and-battery-recycling-technology-design-challenges/0/steps/292808>.
- [7] J. Cui, L. Zhang, *J. Hazard. Mater.*, 2008, **158**, 228-256.
- [8] A. A. Maurice *et al.*, *Nano Select*, 2022, **3**, 425-436.
- [9] A. A. Maurice, K. N. Dinh, N. M. Charpentier, A. Brambilla, J. C. P. Gabriel, *Sustainability*, 2021, **13**, article no. 10357.
- [10] H. Ramon, J. R. Peeters, W. Sterkens, J. R. Duflou, K. Kellens, W. Dewulf, *Procedia CIRP*, 2020, **90**, 421-425.
- [11] A. E. Villarreal, A. K. Frías, F. G. Rendón, T. Flores, L. Ponce, G. Vázquez-Bautista, *Emerging Challenges for Experimental Mechanics in Energy and Environmental Applications, Proceedings of the 5th International Symposium on Experimental Mechanics and 9th Symposium on Optics in Industry (ISEM-SOI), 2015*, Conference Proceedings of the Society for Experimental Mechanics Series, Springer, Cham, 2017.
- [12] L. Rapolti *et al.*, *Minerals*, 2021, **11**, article no. 1292.
- [13] R. Laszlo, R. Holonec, R. Copindean, F. Dragan, *Proceedings of the 2019 8th International Conference on Modern Power Systems MPS 2019*, 2019, 8-11 pages.
- [14] Q. Zeng, J. B. Sirven, J. C. P. Gabriel, C. Y. Tay, J. M. Lee, *TrAC - Trends Anal. Chem.*, 2021, **140**, article no. 116280.
- [15] C. Jia, P. Das, I. Kim, Y.-J. Yoon, C. Y. Tay, J.-M. Lee, *J. Ind. Eng. Chem.*, 2022, **110**, 84-99.
- [16] D. Xia, A. Maurice, A. Leybros, J.-M. Lee, A. Grandjean, J.-C. P. Gabriel, *Chemosphere*, 2021, **263**, article no. 128282.
- [17] M. M. Veras *et al.*, *Miner. Eng.*, 2020, **147**, article no. 106151.
- [18] Y. Yeyu *et al.*, *J. Instrum.*, 2021, **16**, article no. P11041.
- [19] M. Nieberl, A. Hornung, M. Sajdak, A. J. Majewski, M. Ouadi, *Resour. Conserv. Recycl.*, 2023, **190**, article no. 106866.
- [20] M. Annamalai, K. Gurumurthy, *J. Air Waste Manage. Assoc.*, 2021, **71**, 315-327.
- [21] W. A. Bizzo, R. A. Figueiredo, V. F. De Andrade, *Materials (Basel)*, 2014, **7**, 4555-4566.
- [22] F. Cucchiella, I. D'Adamo, P. Rosa, S. Terzi, *J. Clean. Prod.*, 2016, **121**, 130-141.
- [23] A. Popović, V. Manojlović, B. Adnadjević, J. Petrović, Ž. Kamberović, M. Ranitović, *Processes*, 2022, **10**, article no. 1152.
- [24] B. Kopacek, *IFAC-PapersOnLine*, 2016, **49**, 190-195.
- [25] M. Kaya, *Energy Technology 2017*, Minerals, Metals and Materials Series, no. 9783319521916, Springer International Publishing, Cham, 2017, 433-451 pages.
- [26] N. M. Charpentier *et al.*, *Resour. Conserv. Recycl.*, 2023, **196**, article no. 107033.
- [27] L. Hamawy, "Development of an image reconstruction method based on the detected X-ray fluorescence for sample analysis [Développement d'une méthode de reconstruction d'image basée sur la détection de la fluorescence X pour l'analyse d'échantillon]", Theses, Université de Grenoble; Université Libanaise, 2014.
- [28] D. Xia, N. M. Charpentier, A. A. Maurice, A. Brambilla, Q. Yan, J. C. P. Gabriel, *Chem. Eng. J.*, 2022, **441**, article no. 135886.
- [29] J. Wang, Z. Xu, *J. Hazard. Mater.*, 2017, **326**, 1-9.
- [30] C. Penisson, A. Wilk, J. Theisen, V. Kokoric, B. Mizaikoff, J. C. P. Gabriel, *TechConnect Briefs 2018 - Advanced Materials*, 2018, 198-201 pages.
- [31] A. Maurice, J. Theisen, J.-C. P. Gabriel, *Curr. Opin. Colloid Interface Sci.*, 2020, **46**, 20-35.
- [32] V. Kokoric *et al.*, *Anal. Chem.*, 2018, **90**, 4445-4451.
- [33] J. Theisen, C. Penisson, J. Rey, T. Zemb, J. Duhamet, J.-C. P. Gabriel, *J. Membr. Sci.*, 2019, **586**, 318-325.
- [34] A. El Maangar, J. Theisen, C. Penisson, T. Zemb, J.-C. P. Gabriel, *Phys. Chem. Chem. Phys.*, 2020, **22**, 5449-5462.
- [35] F. Olivier, A. A. Maurice, D. Meyer, J. C. Gabriel, *C. R. Chim.*, 2022, **25**, 137-148.
- [36] F. L. Olivier, S. M. Chevrier, B. Keller, J. C. P. Gabriel, *Chem. Eng. J.*, 2023, **454**, article no. 140306.
- [37] J. Lim, Y. Ahn, H. Cho, J. Kim, *Process Saf. Environ. Prot.*, 2022, **165**, 420-430.
- [38] M. Jover, M. Borie, S. Moriceau, "Équipements électriques et électroniques : données 202 - Rapport annuel", 2021, 0-105 pages, [Online]. Available: <https://bibliothèque.ademe.fr/>.
- [39] S. Pinho, M. Ferreira, M. F. Almeida, *Resour. Conserv. Recycl.*, 2018, **132**, 71-76.

Research article

GDR Prométhée – French Research Network on *Hydrometallurgical Processes for Primary and Secondary Resources*

Lessons learned from the upscaling of an iron bio-oxidation process to improve uranium recovery

Agathe Hubau^{Ⓢ,a}, Kathy Bru^{Ⓢ,*,a}, Safiatou Idrissa Oumarou^b and Cécile Leycuras^c^a BRGM, F-45060 Orléans, France^b Somaïr, Arlit, Niger^c Orano Mining, CIME, 2, route de Lavaugrasse, 87250 Bessines sur Gartempe, France*E-mails:* a.hubau@brgm.fr (A. Hubau), k.bru@brgm.fr (K. Bru),
safiatou.idrissa-oumarou@orano.group (S. Idrissa Oumarou),
cecile.leycuras@orano.group (C. Leycuras)

Abstract. This study presents the various steps performed for the industrial implementation of a process dedicated to the bio-oxidation of the ferrous iron contained in the solution used to leach uranium with the objective of increasing its recovery. These steps included theoretical works, laboratory-scale tests on synthetic effluents and laboratory- and pilot-scale tests on industrial effluents at the mining site. The main results from each of these steps are presented as well as the challenges that have to be addressed for the integration of this process into the existing flowsheet. They allowed to get insights into the upscaling of a biotechnology at an industrial scale.

Keywords. Bio-oxidation, Ferrous iron, Ferric iron, Bioprocess, Uranium recovery, Industrial implementation.

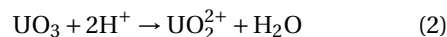
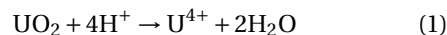
Funding. Project IronBiox ("Bioaugmentation en fer ferrique") funded by Orano Mining.

Manuscript received 5 July 2023, revised 4 March 2024, accepted 25 April 2024.

1. Introduction

Over 200 different minerals have been reported in the literature to host uranium, but only 20 of them are of economic importance (from which uraninite, coffinite, brannerite and orthobrannerite) [1]. Uranium is generally finely disseminated within the ore, in a tetravalent or hexavalent form, meaning that concentration steps to remove the gangue material is not possible since it would result in loss of uranium in tailings. The ore is then usually completely

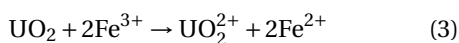
leached after crushing or grinding. In the leaching process, sulfuric acid is mainly used, and the dissolution equations from U(IV) and U(VI) are respectively listed in Equations (1) and (2).



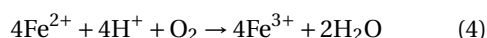
UO₃ dissolution (Equation (2)) occurs in dilute sulfuric acid while UO₂ dissolution (Equation (1)) requires an oxidizing reagent. The choice of the reagent depends on several factors such as the composition of the solid, the economy of the process and the availability of the reagents at the mining site. Ferric iron is

*Corresponding author

one of the cheapest oxidizing reagents and is therefore the principal oxidant of U(IV) in acid leaching circuits [2]. The dissolution reaction of tetravalent uranium with ferric iron leads to soluble hexavalent uranium, as described in Equation (3).



Iron can come directly from the ore since it can be present under different mineral phases or it can be added as chemicals. Ferric iron Fe^{3+} can then be regenerated from ferrous iron Fe^{2+} using an oxidant, MnO_2 being often used for such purpose [2], or using microorganisms, following Equation (4).



Bio-oxidation of iron uses chemolithotrophic microorganisms (various *Leptospirilli* and *Thiobacilli*), which take their energy exclusively from the oxidation of ferrous iron by oxygen, using dissolved CO_2 as the unique source of carbon, and need for their growth a high level of acidity in solution with pH values below 3. These microorganisms participate in the natural biogeochemical cycles related to sulfide metal deposits. Acidophilic bioleaching, i.e., catalysis of sulfur and ferrous iron oxidation by microorganisms, is a recognized industrial scale process used for the dissolution of Au, Cu, Ni or Co from concentrates, ores, and mining waste (see BIOX or KCC operations [3,4]). Through the oxidation of sulfides into sulfates and ferrous into ferric iron, microorganisms enhance metal dissolution. In the presence of a low sulfide content or in the absence of sulfides, bioleaching can still be used, the main action of the microorganisms being the bio-oxidation of ferrous iron (Equation (4)). Bioleaching presents the advantages of in situ generation of the leaching agent (ferric iron and protons), mild operating conditions in terms of pH (around 1–2) and temperature (20–50 °C), and low operating costs [5]. The main drawback is a longer residence time compared to chemical leaching [6]. The potential of bioleaching for the recovery of uranium from ores was recognized since the 1950s [7]. However, uranium was reported to inhibit microorganisms growth and activity, the toxic threshold concentration depending on the species and strains. This toxicity can be addressed using an indirect leaching approach in which the production of the acidic ferric iron solution and the leaching of the ore are separated in two-stage processes [7]. This

indirect approach is quite unusual for conventional bioleaching operations, where the minerals to leach often serve as a solid support for microorganisms. This means that the use of the indirect approach requires overcoming several scientific bottlenecks such as O_2 supply, attachment of the microorganisms on a solid support, and management of the precipitates.

This work aims to investigate the indirect bio-oxidation of ferrous iron into ferric iron on two case studies, the KATCO mine in Kazakhstan and the Somaïr mine in Niger, with the objective of increasing uranium recovery yields and kinetics. This paper summarizes the different steps undertaken to study the process and to perform its scale-up on the two case studies. It also provides insights into the main lessons learned in bringing a biotechnology process from laboratory to industrial scale.

2. Presentation of the case studies

The two case studies are mining sites predominantly owned by Orano Mining: the KATCO mining site (Kazakhstan), owned at 51% by Orano Mining and 49% by Kazatomprom; and the Somaïr mining site (Niger), owned at 63.34% by Orano Mining and 36.66% by SOPAMIN (Société du Patrimoine des MINes du Niger). Table 1 provides some general information about these two mining sites.

2.1. KATCO case study (Kazakhstan)

KATCO is the world's largest in situ uranium mine, accounting for 15% of Kazakhstan's annual uranium production and 7% of world production. At this site, a leaching solution containing dilute sulfuric acid is injected through wells into the uranium deposit. Uranium is dissolved as the leaching solution passes through the deposit and is pumped to the surface. Uranium is then extracted from the leachate with ion exchange resins, followed by steps of refining, concentration, and precipitation leading to the production of the so-called yellowcake. The raffinate is re-injected into the wells after acidification, continuing the closed circuit process.

An iron-oxidizing bioprocess was investigated in order to increase uranium recovery. To allow the adequate integration of this process into the current flowsheet (Figure 1), the following requirements were considered: a bio-oxidation kinetics of at least

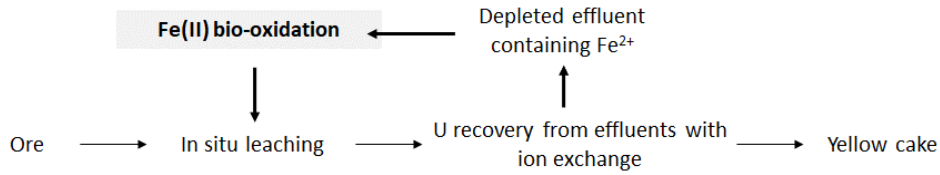


Figure 1. Uranium leaching flowsheet for the KATCO case study including the investigated bio-oxidation processes.

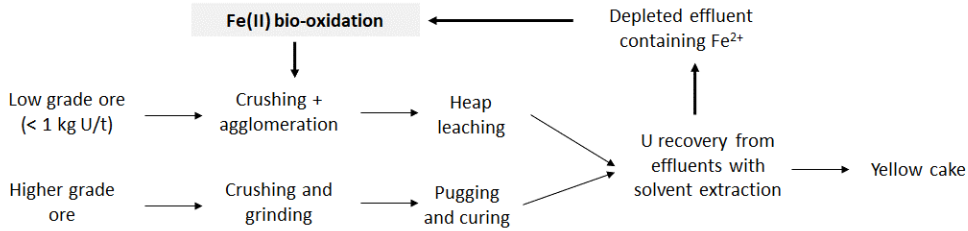


Figure 2. Uranium leaching flowsheet for the Somaïr case study including the investigated bio-oxidation processes.

Table 1. Case studies description (data from Orano Mining)

	KATCO	Somaïr
Average content of U	0.2 to 0.5 kg U/t ore	1.8 kg U/t ore
Annual production capacity	4000 t/year	2000 t/year
Starting production year	2006	1971
Total uranium production	46,000 t	>75,000 t
% of annual world production	7%	3.5%

1 g·L⁻¹·h⁻¹, since the ferrous iron concentration in the leaching solution reaches around 1 g·L⁻¹ after U recovery and the Hydraulic Residence Time (HRT) of the current flowsheet is 1 h, no addition of nutrients to enhance microbial growth, and no temperature regulation. The latter requirement is all the more important that the temperature at the KATCO mining site varies from -5 °C to 20 °C (data from Suzak city, 60 km away from the KATCO site).

2.2. Somaïr case study (Niger)

In Somaïr, the deposit is a horizontal sedimentary deposit at a depth of around 50 to 70 m. Extraction is performed from an open pit mine. The ore is then treated either by heap leaching or pugging-and-curing leaching, depending on its uranium grade (Figure 2). The static treatment (acid heap leaching)

is operated on the low- or very low-grade ore (<1 kg U/t ore). It consists in crushing the ore, agglomerating it with sulfuric acid and then stacking it in sealed areas to be dripped with an acid solution for several months. By percolating the ore, a leachate enriched in uranium is obtained. For the higher grade ore, a dynamic treatment (pugging and curing) is performed. In dynamic treatment, the ore is crushed and ground before undergoing a sulfuric acid and nitrate leaching for several hours. Uranium leachate is then recovered. After both leaching steps, solvent extraction is performed, followed by purification steps and precipitation. A concentrate of sodium uranate called yellowcake containing 75 wt% of uranium is produced.

In order to increase uranium recovery, MnO₂ is currently used as the oxidizing reagent for heap leaching on-site. The use of iron-oxidizing bacteria

	2013	2014	2015	2016	2017	2018	2019	2020	2021	2022
Preliminary studies										
- Definition of the Intellectual Property Rights and Literature review										
- Thermodynamic study										
- Development of heat balance models to evaluate the influence of the ambient temperature on the temperature within the bio-oxidation process										
Laboratory-scale tests on the KATCO case study										
- Investigation of the potential of the KCC consortium for bio-oxidation, performed on synthetic solution										
- Influence of ferrous iron bio-oxidation on uranium recovery										
Laboratory-scale tests on the Somaïr case study										
- Investigation of the potential of the KCC consortium for bio-oxidation, performed on synthetic solution										
- Prefeasibility study										
- Risk assessment										
Transfer of microorganisms on site										
On-site tests performed at the Somaïr mine										
- Laboratory-scale tests in shake flasks										
- Laboratory-scale tests in 6 L reactors										
- Pilot-scale tests in 30 L reactors, including the update of the prefeasibility study and of the risk assessment										
- Pilot-scale tests in a 700 L reactor, including the update of the prefeasibility study and of the risk assessment										

Figure 3. Schedule of the study related to bio-oxidation of ferrous iron to ferric iron to improve uranium recovery.

was investigated with the objective to reduce the consumption of MnO_2 (Figure 2). In particular, it was estimated that implementing bio-oxidation would allow to save more than 43% of MnO_2 , leading then to a reduction in the related operating costs of more than 547 k€/year [8]. As for the KATCO case study, the implementation of bio-oxidation should be performed without any nutrients addition nor temperature regulation, the temperature at the Somaïr mining site varying from 5 °C to 45 °C. Regarding the processing conditions, the ferrous iron concentration is much higher in Somaïr than in KATCO, reaching 10 to 20 g·L⁻¹, and the HRT is also higher with a value of 24 h. A bio-oxidation kinetics of 0.5 g·L⁻¹·h⁻¹ should thus be reached. Another important parameter to consider is the use of solvent extraction to recover U which may lead to traces of organic solvents in the depleted effluent containing Fe^{2+} as these traces may inhibit microbial activities [9].

3. Main steps of the study

The study of the potential of an iron-oxidizing bio-process for improving uranium recovery and of its on-site implementation started in 2013. This study was performed in close collaboration between Orano Mining and the BRGM (French Geological Survey), which has a great expertise in bioleaching processes [4]. Figure 3 presents the main steps of this

study. Firstly, theoretical studies were performed on both case studies in order to get valuable information on the process such as the theoretical increase in uranium recovery, the formation of precipitates, and the influence of the ambient temperature on the evolution of the temperature within the bioprocess. Experimental works were then performed using the KCC consortium, mainly composed of the genera *Leptospirillum*, *Acidithiobacillus* and *Sulfobacillus*, which are either iron or sulfur oxidizers or both. This consortium was chosen as it previously demonstrated high efficiency for sulfides bioleaching and ferrous iron bio-oxidation [10]. These first experimental works were performed with a focus on the KATCO case study as it presents a higher potential for the bio-oxidation process (details are given in the following paragraphs). In 2018, due to an Orano Mining internal decision, it was decided to perform the implementation of this innovative process on the Somaïr case study and to no longer work on the KATCO case study. All these steps are detailed in the following paragraphs.

3.1. Preliminary studies

The first objective of the preliminary studies was to define the intellectual property rights, by reviewing the commercial operations and the associated patents. The Total Patent database was used with

the following key words: “Iron oxidation AND ferrous iron AND bio”, “Iron III production AND bio”, “Ferrous iron oxidizing bacteria”, “Uranium leaching AND bio AND oxidation”. Several patents were found on the use of ferrous iron bio-oxidation, such as US4139456A 1979-02-13 [11] or US6043022A 2000-03-28 [12], but no patents were found on its application for uranium recovery. Moreover, no commercial operation related to such process was identified.

Another objective of the preliminary studies was to perform thermodynamic calculations in order to get valuable information, even if theoretical, on the bio-oxidation process. These calculations aim at (i) describing the various reaction equilibria affecting the dissolution of uranium when an acidic ferric iron solution is used, (ii) obtaining a quantitative description of the compositions of the solutions, in terms of dissolved species in particular, and (iii) predicting the formation of precipitates during the bio-oxidation of ferrous iron to ferric iron. Simulations were performed with the Phreeqc 7.3 software, which uses the *llnl* database developed for uranium speciation complexation equilibria. Simulation results confirmed the increase in U(IV) recovery by using acidic and oxidizing solutions and indicated that precipitates of iron hydroxides or jarosite (K, Na) may occur. These precipitates will have to be taken into account for the design of the pilot and the industrial processes since they can lead to clogging and then require the definition of a dedicated cleaning strategy.

The last objective of the preliminary studies was to evaluate the influence of the ambient temperature on the evolution of the temperature within the bio-process and to check if it is compatible with microbial activity. For the KATCO case study, the heat balance modeling was carried out following the methodology used by Talati and Stenstrom [13] and considering that the bio-oxidation is performed in a pond of 3000 m³ since this pond was used for the recovery of leachates. The equipment chosen for performing the bio-oxidation was a floating agitation system recently developed by Milton Roy Mixing and Air Liquide for wastewater treatment applications. This system allows both mixing and suspending solids in the solution as well as injecting gases into the solution. It was chosen as it was proven that it allows decreasing the costs of bioleaching processes when implemented in stirred tank reactors [14]. Results showed only small variations of the temperature in the pond regardless

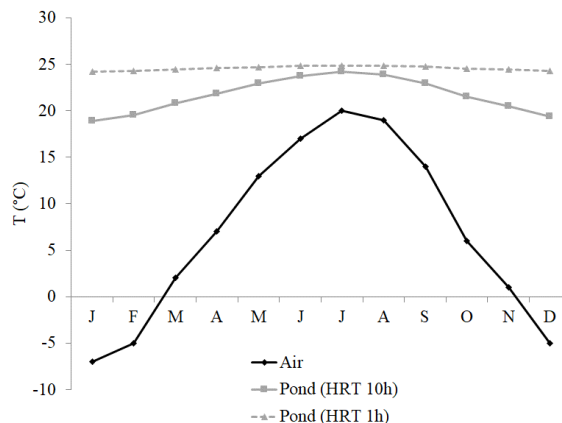


Figure 4. Air and pond temperatures simulated for the KATCO case study.

of the atmospheric conditions (from less than -5°C in January to 20°C in July), the pond temperature varying between 24.2°C and 24.8°C (Figure 4), and these temperatures are compatible with the growth and activity of mesophilic or moderate thermophilic microorganisms. This is due to the short HRT in the pond, which was 1 h. Indeed, a longer HRT in the pond would have led to a higher amplitude in the temperature evolution, as showed in Figure 4. This is because main thermal losses are linked to the aeration of the pond and surface convection.

A heat balance model was also developed and implemented for the case study of Somaïr. Similarly as for the KATCO case study, results showed that the temperature of the pond is very close to the temperature of the inlet effluent even if the HRT is 24 h. This is because the main parameter controlling the temperature of the pond considered in the Somaïr case study is the temperature of the inlet effluent with only a minor influence of the aeration of the pond.

3.2. Laboratory-scale tests at the BRGM and at Orano Mining's Innovation Center for Extractive Metallurgy (CIME)

3.2.1. Laboratory-scale tests on the KATCO case study

3.2.1.1. Objectives. The first experimental works were performed on the case study of KATCO since it presents a higher potential for the bio-oxidation process (considering the mineralogy of the deposit) and some operating conditions are more favorable for

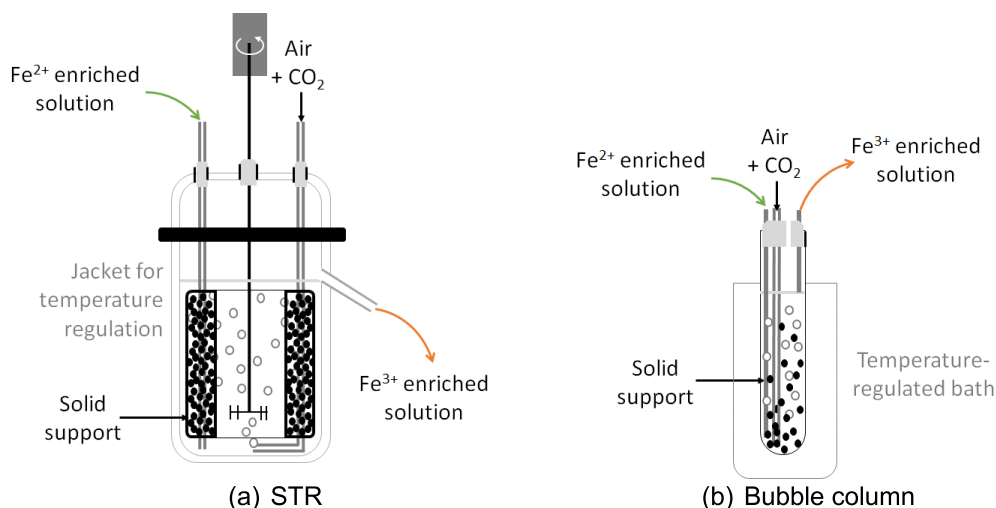


Figure 5. Schematic diagram of the experimental devices used to assess bio-oxidation kinetics with KCC consortium, (a) STR and (b) bubble column.

such a process compared to the case study of Somaïr. This is in particular the case of the lower Fe concentration, which reduces the process piloting issues associated with the formation of Fe-precipitates, and of the use of ion exchange resins instead of solvent extraction for uranium recovery, therefore avoiding the presence of traces of organic solvent which could inhibit the microorganisms.

The laboratory-scale tests were performed with a threefold objective:

- (1) To assess the feasibility of reaching and maintaining bio-oxidation rates with a well-known microbial consortium in continuous mode at a temperature of 20 °C.
- (2) To determine the influence of the HRT on bio-oxidation rates.
- (3) To demonstrate the increase of uranium recovery yield and rate in the presence of biogenic ferric iron.

3.2.1.2. Methods. Experiments were performed in two steps. First, 2 L stirred tank reactor (STR) experiments were performed at the BRGM laboratory on a synthetic solution with a composition in major elements similar to the KATCO effluent (Fe, Ca, Mg, Al, SO₄²⁻ and Cl).

As mentioned before, the KCC consortium was chosen for these tests. It is important to mention

that similar acidophilic microorganisms (same genera and species) were previously found in Kazakhstan [15–17]. One test was also performed in abiotic conditions in order to assess the influence of the biomass on the bio-oxidation of the ferrous iron. A solid support made with coal particles was introduced into the STR in a basket (Figure 5) in order to allow the biomass to create biofilms. Indeed, attached bacteria are often more efficient than planktonic cells due to higher resilience of biofilms towards potential inhibitions [18]. As O₂ and CO₂ supply are key parameters for the bio-oxidation of ferrous iron (Equation (4)), STRs were equipped with baffles and a Rushton turbine to ensure high mass transfers. The temperature was regulated to 25 °C as the preliminary study showed that this would be the operation temperature in KATCO. The reactor was first launched in batch mode to allow the fixation of the microorganisms on the solid support and then operated in continuous mode by progressively reducing the HRT. HRT is related to the liquid phase in all the works performed in this study since the solid support was kept within the reactor in order to allow the biomass to grow.

Secondly, tests coupling the ferrous iron bio-oxidation and the KATCO ore leaching were performed. A bubble column, considered as fluidized bed reactor, was considered for the bio-oxidation reactor. This choice was motivated by the small

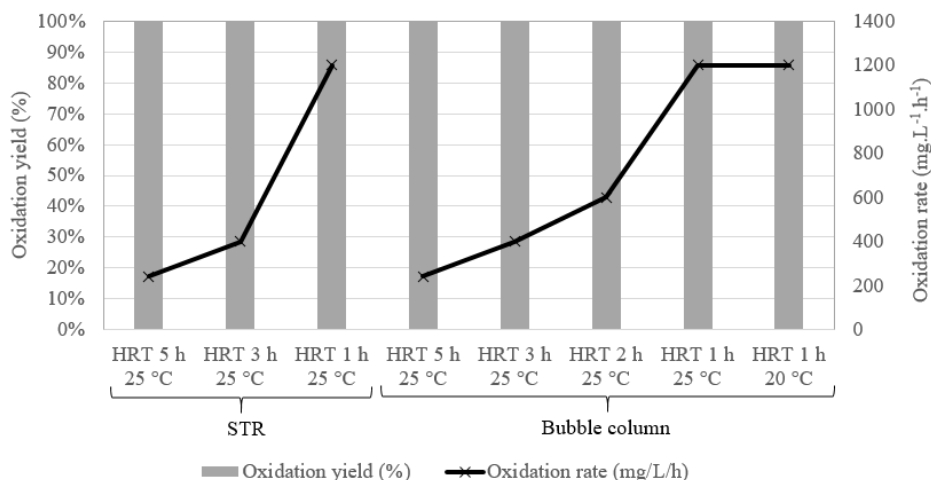


Figure 6. Bio-oxidation rates and yields in the STR experiments (left) and bubble column (right) with a KATCO synthetic effluent and for various operating conditions (from [19]).

volume of the bubble column which allows continuous coupling with the uranium leaching test since its input flow rate was $100 \text{ mL}\cdot\text{h}^{-1}$ (Figure 5). The bubble column was operated at 20°C with coal as solid support. The reactor was first launched in batch mode to allow fixation of the microorganisms on the solid support and then operated in continuous mode by progressively reducing the HRT. Bio-oxidation in bubble columns was optimized at the BRGM laboratory and then operated in close loop by Orano Mining in their laboratory. Tests were performed with a real effluent from KATCO. Uranium leaching was performed in columns, each column containing about ten kg of ore each. Fe^{3+} -enriched solution was injected at a flow rate of $100 \text{ mL}\cdot\text{h}^{-1}$ allowing an ascending volumetric flow rate per unit area of $4 \text{ L}\cdot\text{h}^{-1}\cdot\text{m}^{-2}$, close to the one used at the KATCO mine. Effluents were acidified to pH 1.6 with dilute sulfuric acid, before passing through anionic resins to recover uranium. Uranium-depleted solutions were then treated in the bio-oxidation column for ferrous iron oxidation.

Each reactor was monitored daily for pH, redox potential and temperature. Sampling was performed daily in the Fe^{3+} -enriched solution in order to analyze the total Fe concentrations—by Atomic Absorption Spectroscopy (AAS)—and the Fe^{2+} concentrations—by titration with Ce(IV) sulfate 0.001 M . Bacterial cells were also counted occasionally in the Fe^{3+} -enriched solution. In order to determine the dynamics of microbial populations,

DNA extraction followed by CE-SSCP (capillary electrophoresis with single-strand conformation polymorphism) was performed at the end of each test. Results related to the biomass are not given here due to confidentiality issues.

3.2.1.3. Results. STR experiments performed in abiotic conditions, i.e., without microorganisms, led to an oxidation rate of about $0.1 \text{ g}\cdot\text{L}^{-1}\cdot\text{h}^{-1}$, showing that the air oxidation of ferrous iron does not allow to reach industrial requirements (here set at $1 \text{ g}\cdot\text{L}^{-1}\cdot\text{h}^{-1}$). When using the KCC consortium, an oxidation rate of about $1.1 \text{ g}\cdot\text{L}^{-1}\cdot\text{h}^{-1}$ was obtained at a HRT of 1 h, confirming the potential of the biomass to perform the bio-oxidation of ferrous iron into ferric iron. It should be mentioned that this performance was obtained at 25°C , whereas the optimal temperature for the KCC consortium is $40\text{--}42^\circ\text{C}$ [10], confirming the robustness of this consortium (Figure 6, left). Similar results were obtained with the bubble column (Figure 6, right). It is then interesting to highlight that it was possible to adapt the biomass for oxidizing 100% of Fe^{2+} at a HRT of 1 h and at 20°C , as shown in Figure 6. Moreover, no washout of the biomass was observed, confirming that the use of a solid support enables the biomass to be maintained in the reactor even if the HRT was lower than its doubling time since, for example, the doubling time of *L. ferrophilum* is around 3.1 h [20–22]. During these tests, the clogging of the biomass support by a biofilm growth and/or by precipitates remained moderate.

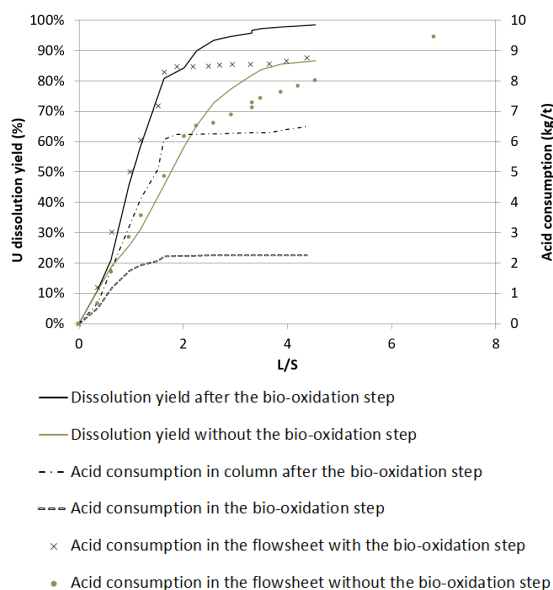


Figure 7. Uranium dissolution yields and acid consumption as a function of L/S ratio (from [19]).

A high reproducibility was observed between the results obtained with the STR and with the bubble column, confirming the robustness of the process. Moreover, the bio-oxidation rate showed only small variations when the oxidation yield reached its maximum value. For example, at a HRT of 3 h in the STR, the relative standard deviation of the bio-oxidation rate was 1.2% during 6 days, which corresponds to 48 HRT and 6 measurements of the kinetics. At a HRT of 1 h in the bubble column, the bio-oxidation rate varied by 2.4% during 14 days, which corresponds to 336 HRT and 10 measurements of the kinetics.

When the bio-oxidation of ferrous iron was coupled with uranium leaching, an increase in uranium recovery was observed compared to acid leaching only (Figure 7).

This was accompanied by a decrease in acid consumption of 0.6 kg/t ore, which represents a reduction of 6.4% in the total acid consumption. These tests were performed on a real effluent from the KATCO case study and therefore showed that the presence of traces of radioelements did not significantly affect the bio-oxidation performances.

3.2.2. Laboratory-scale tests on the Somaïr case study

3.2.2.1. Objectives. As mentioned previously, a change in the case study occurred in 2018 due to an Orano Mining internal decision and the Somaïr case study was chosen for the on-site implementation of the bio-oxidation of ferrous iron. Since the composition of the Somaïr effluent markedly differs from the KATCO one, in particular regarding the Fe^{2+} concentration with values up to $20 \text{ g}\cdot\text{L}^{-1}$, complementary laboratory-scale tests in bubble columns were performed in Orano Mining's Innovation Center for Extractive Metallurgy (CIME). The objectives of these tests were to assess the influence of the change in effluent composition on the bio-oxidation performances and to collect reliable data to design the pilot-scale experiments.

3.2.2.2. Methods. Tests were performed in a 5 L STR similar to the one described in Section 3.2.1.2 with a similar monitoring. A synthetic solution with a composition similar to that of the Somaïr effluent was used, in particular regarding the content in iron, nutrients (K, Mg, P, NH_4^+) and potential inhibitor elements (Al, NO_3^- , Cl^-). Continuous tests were performed at 30°C , the mean temperature of the effluent, and the pH was regulated at 1.2. The reactor was first launched in batch mode to allow the fixation of the microorganisms on the solid support and then operated in continuous mode by progressively reducing the HRT.

3.2.2.3. Results. Some of the results obtained during the experiments are given in Figure 8. As showed in Figure 8, it is possible to reach and maintain the bio-oxidation rate targeted for the Somaïr case study, which is around $500 \text{ mg}\cdot\text{L}^{-1}\cdot\text{h}^{-1}$. This bio-oxidation rate was obtained for a bio-oxidation yield lower than 100% and did not change regardless of the decrease in the HRT, which seems to indicate that the maximum oxidative performances of the biomass have been reached. Moreover, the solid support concentration seems to be a limiting factor since it was not possible to reach a bio-oxidation of $500 \text{ mg}\cdot\text{L}^{-1}\cdot\text{h}^{-1}$ with a solid support concentration of $40 \text{ g}\cdot\text{L}^{-1}$. Figure 8 also shows a decrease in the oxidation rate after several days of operation. This could be explained by the formation of iron precipitates, which clogged the solid support leading to a reduction in the bio-oxidation performances, since the biomass was fixed

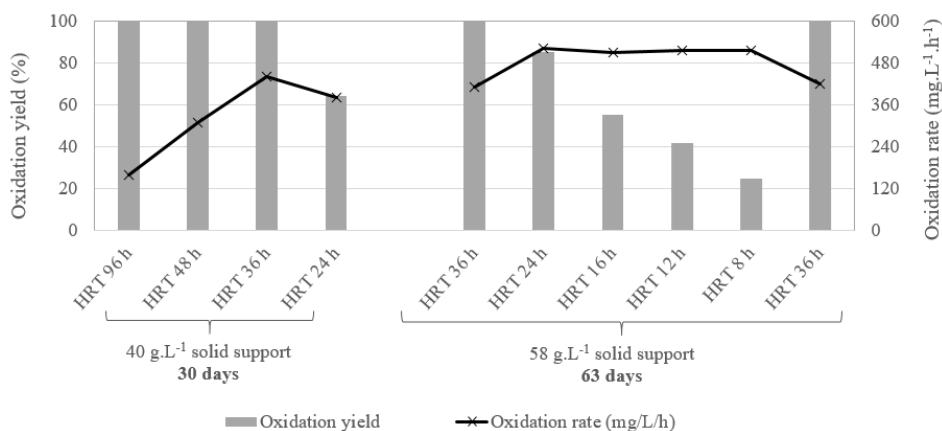


Figure 8. Bio-oxidation yield and rate during laboratory-scale tests with the synthetic effluent from the Somaïr case study.

on the solid support. This assumption was supported by the observation of a very large quantity of red-orange precipitates when the reactor was stopped and opened. This precipitate is most probably mainly composed of jarosite, which is the predominant precipitate detected in bioleaching systems, even at low pH [20]. A similar effect of the iron precipitates when coal particles are used as solid support for bio-oxidation was reported by Hubau et al. [20]. In particular, they demonstrated that jarosite formation clogged the solid support pores, inducing very low mass transfers and a reduced microbial activity. This clogging effect was somehow mitigated after some time when using a bubble column due to the attrition occurring within the fluidized bed which opened the coal pores, leading to a new increase in the bio-oxidation rate [20]. These phenomena, observed at microscopic scale, create high variations in kinetics at macroscopic scale and should then be considered carefully when designing a bioreactor. In particular, it seems that other solid supports could be more appropriate for the bio-oxidation of Fe^{2+} -rich effluents, such as woven nylon [23].

The results obtained with these works performed at laboratory scale on a synthetic effluent from the Somaïr case study confirmed the potential of the bio-oxidation to improve uranium recovery. A prefeasibility study and a design to cost analysis were performed based on these first results, including in particular the comparison of the two designs for the bioreactor which are the STR and the bubble column, the latter being similar to a fluidized reactor, with no

mechanical agitation. First estimations of the capital expenditures (CAPEX) and operational expenditures (OPEX) as well as a risk assessment were performed. In particular, results showed that CAPEX and OPEX are reduced by more than 30% and 40%, respectively, when using a fluidized reactor. The main drawback identified for such reactor is related to mass transfers, meaning that works will have to be performed on its design to optimize them. A planning for on-site implementation and up-scaling of the process was then defined.

3.3. On-site tests performed at the Somaïr mine

First of all, the transfer of microorganisms on-site followed Nagoya protocol on Access to Genetic Resources and the Fair and Equitable Sharing of Benefits Arising from their Utilization to the Convention on Biological Diversity. This protocol, adopted in 2010 and ratified by 137 parties, deals with the use of genetic resources, in order to share fairly and equitably the benefits and thus to contribute to the conservation and sustainable use of biodiversity.

Moreover, a dedicated training of the mining operators was conducted allowing them to efficiently monitor and operate bioprocesses. This training also included information related to the risks associated to handling the bio-oxidation solutions that would be produced, the main one being the acidity of the solutions. It should be mentioned that the mine operators already had several acid effluents to manage on-site and had therefore defined the appropriate



Figure 9. Photo of the laboratory developed at the Somaïr mine (@Orano Mining).

safety measures. In addition, a laboratory equipped for bioprocesses development and monitoring was implemented on-site (Figure 9). In particular, it included a microscope for cell counting with Thoma plates. These were a prerequisite for the transfer to the Somaïr mine of the process development, operation and up-scaling works.

A method for the continuous monitoring of the main operating parameters was established on-site and was used at each scale. The reactors were equipped with pH, redox potential, dissolved O_2 and temperature probes with continuous records (time step around 2h30). Total Fe concentrations were determined daily through AAS, while an empirical correlation was used to evaluate Fe^{2+} concentrations from redox potential values [24]. In order to determine the biomass concentration, Thoma cell counting was performed. Regarding the biomass attached to the solid, a detachment protocol based on the use of ultrasounds was established on-site (Thoma cell counting after detachment) but its execution remained limited due to difficulties in sampling the solid support.

3.3.1. Laboratory-scale tests in shake flasks

3.3.1.1. Objectives. The main objectives of the tests in shake flasks performed on-site were to adapt the microbial consortium to the industrial effluents and to define how the bio-oxidation process could be integrated in the current flowsheet. In particular, two integration options were investigated:

- In the first one (Figure 10), bio-oxidation is performed on the leachate from the heap leaching (called “production effluents”). In this case, uranium-enriched leachate is recirculated in the heap after its bio-oxidation in order to concentrate uranium in the leachate before its recovery in the solvent extraction unit. The main drawback of this option is the potential toxicity of uranium towards bio-oxidation microorganisms.
- In the second one (Figure 11), bio-oxidation is conducted on the raffinate, i.e., the uranium-depleted effluent after the solvent extraction unit. The advantage of this option is that radioelements concentration in the raffinate is very low. However, the raffinate may contain traces of organic solvents due to its treatment in the solvent extraction unit.

This step also aimed to check that all the equipment planned to be used in the pilot and industrial operations do not present any toxicity towards the microorganisms. Last but not least, this step aimed to produce the biomass that will be used to inoculate the 6 L bioreactors.

3.3.1.2. Methods. Subcultures were performed in 1 L bottles with a working volume of 250 mL, placed on a shaking table. The temperature was not regulated and could therefore vary from 17 °C to 43 °C in a 24-h period (evolution of temperature in the laboratory). In order to ensure a good adaptation of the microorganisms to the industrial effluents (both from the production effluent and the raffinate), they were first diluted at 50 vol% with the synthetic effluent and their content was gradually increased up to 100 vol%. The protocol used to subculture and scale up the process consisted in inoculating 10% of both solid and liquid phase. pH and redox potentials were measured on a daily basis.

3.3.1.3. Results. Results showed that the bio-oxidation rate strongly depended on the effluent composition, with values varying from $10 \text{ mg}\cdot\text{L}^{-1}\cdot\text{h}^{-1}$ to $120 \text{ mg}\cdot\text{L}^{-1}\cdot\text{h}^{-1}$. These results have to be considered carefully, since the tests were performed in batch mode with no control of some of the operating conditions, such as temperature and aeration, and with a monitoring carried out only once or twice a day, whereas Fe^{2+} was sometimes completely oxidized in few hours. It was therefore not possible

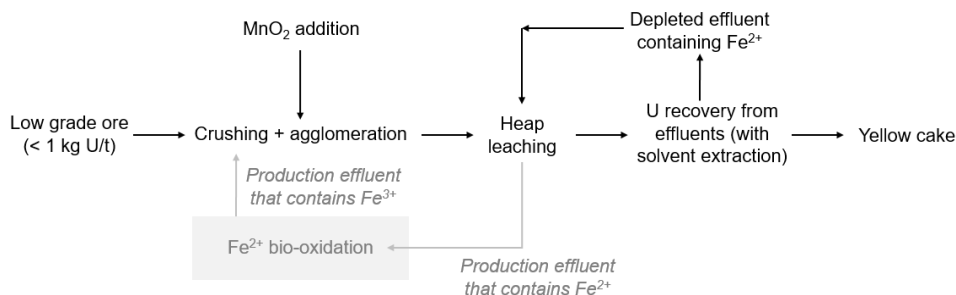


Figure 10. First bio-oxidation processing option for the Somaïr case study.

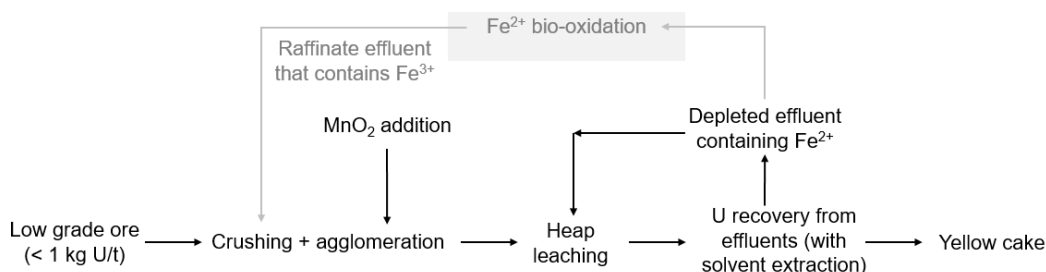


Figure 11. Second bio-oxidation processing option for the Somaïr case study.

to use the obtained values of the bio-oxidation rate to predict the performances of a continuous operation. However, these results gave interesting insights into the adaptation of the microorganisms to the two industrial effluents. In particular, it was observed that the use of uranium-enriched effluent led to far lower bio-oxidation rates compared to the ones obtained with the uranium-depleted effluent. Bio-oxidation should therefore be performed on the uranium-depleted effluent, which corresponds to the processing option presented in Figure 11 even if the effluent may contain traces of solvent. The influence of traces of solvent on bio-oxidation performances was investigated and results showed a detrimental effect, consistent with the study from Mazuelos et al. [9]. In order to limit this issue, it was recommended to add a decantation step before the bio-oxidation process and to pump the effluent from the bottom of the decantation system since the solvent will stay at the surface. Another solution could be to add a treatment step with activated charcoal since it is usually used to remove organic solvents but this treatment is quite expensive and complex to operate (in particular for the regeneration of the activated charcoal) at a remote industrial site.

3.3.2. Laboratory-scale tests in 6 L reactors

3.3.2.1. Objectives. The laboratory-scale tests performed in 6 L reactors had three objectives. The first one was to assess the ability of the microorganisms to oxidize industrial effluents at the targeted rate ($500 \text{ mg}\cdot\text{L}^{-1}\cdot\text{h}^{-1}$) and to test the influence of the operating conditions on the performances. The second one was to investigate the efficiency of woven polypropylene as solid support for biomass. This choice was motivated by previous works showing that bio-oxidation performances with woven polypropylene are not as affected by the formation of precipitates as when using coal particles [23]. The last objective was to produce enough biomass to inoculate larger-scale bioreactors.

3.3.2.2. Methods. Similarly to the laboratory-scale tests performed at the BRGM and at Orano Mining's CIME, two types of reactors were used: (i) a 5 L STR, similar to the one described in Section 3.2.1.2. Figure 5 was used from September 2019 to March 2020 and (ii) a 6 L bubble column was operated from April 2020 to March 2022. In both reactors, the input effluent was injected at the bottom of the reactor and overflowed from the top. Air was also injected at

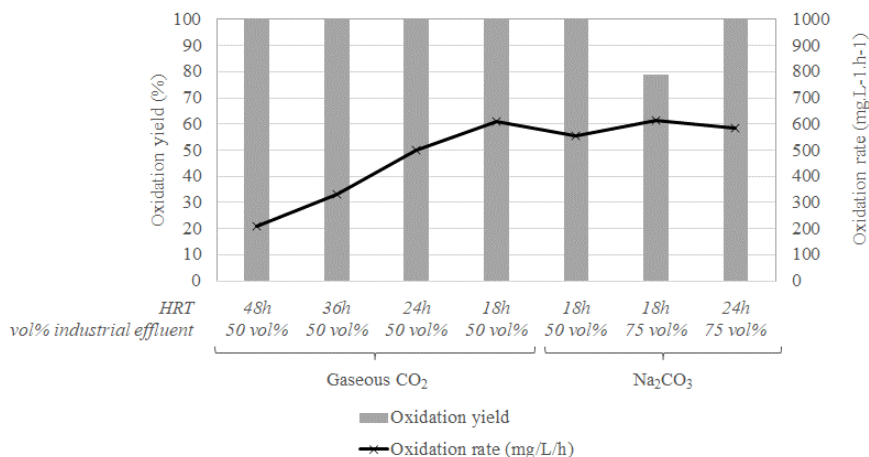


Figure 12. Bio-oxidation yields and rates in the 5 L STR operated on the Somaïr site.

the bottom through a fritted cylinder. For the supply of CO₂, gas bottles were mostly used but Na₂CO₃ was also considered as it is already used on-site for uranium production, which would then simplify the logistics at this remote site. Some tests were also performed without any enrichment of the air in CO₂. In the 5 L STR, the woven polypropylene was placed in the basket and was “crumpled” to reach the targeted solid support concentration. In the bubble column, the solid support was fixed in the middle of the column: woven polypropylene support was either crumpled in a basket or stretched across the height, i.e., in the same direction as the liquid and bubbles flow. The reactors were first launched in batch mode to allow fixation of the microorganisms on the solid support and then operated in continuous mode by progressively reducing the HRT. The tests were first conducted on an effluent made with 50 vol% of industrial effluent and 50 vol% of synthetic effluent, the content of industrial effluent being then increased to 75 vol% and to 100 vol% when the biomass was considered robust enough to be adapted to such effluent. In order to monitor the biomass, DNA extraction and CE-SSCP were performed on the solid phase from time to time. Results related to the biomass are not given here due to confidentiality issues.

3.3.2.3. Results. The first tests were performed in the 5 L STR with a temperature maintained at 40 °C. Results showed that it is possible to reach and maintain a Fe²⁺ bio-oxidation rate of at least 500 mg·L⁻¹·h⁻¹,

a bio-oxidation rate of about 600 mg·L⁻¹·h⁻¹ being even reached and maintained in some of the operating conditions investigated (Figure 12). As shown in Figure 12, the HRT was first reduced from 48 h to 18 h, each reduction performed after stabilizing the bio-oxidation yield at 100%. These good bio-oxidation performances obtained with the woven polypropylene showed that this material can be used as solid support for biomass.

The CO₂ supply was changed from gaseous CO₂ to Na₂CO₃ after 70 days of operation without affecting the performances. However, it affected the acid consumption by increasing the pH. H₂SO₄ addition was finely monitored to estimate the additional cost associated to the use of Na₂CO₃.

The concentration of industrial effluent was increased from 50 vol% to 75 vol% after about 85 days. A decrease in the bio-oxidation yield was observed with no change in the bio-oxidation rate. This can be due to a limited bio-oxidation capacity of the biomass with the amount of solid support used, since an increase in HRT allowed to reach again a bio-oxidation yield of 100%. Similar results were obtained with the 6 L bubble column.

After more than 60 days of operation, no precipitates were observed on the solid support. This confirmed the benefits of using woven polypropylene as solid support instead of coal particles which tend to be clogged quite easily (see Section 3.2.2). Moreover, it was observed that the mode of handling the solid support had a strong effect on the decrease

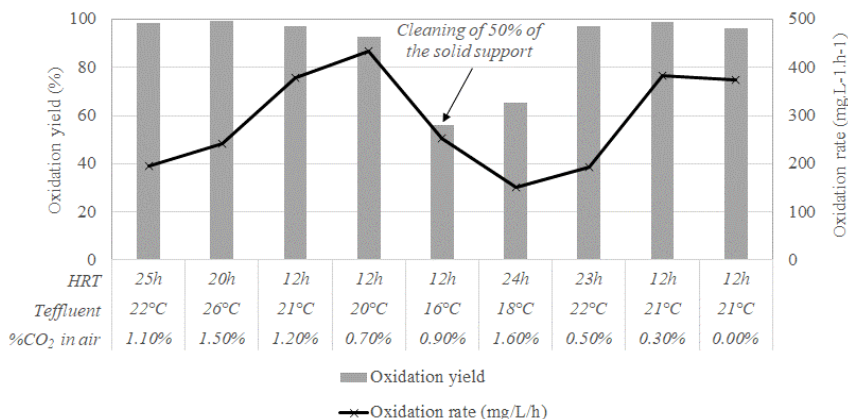


Figure 13. Bio-oxidation yields and rates in the 6 L bubble column operated on the Somaïr site (from December 2021 to March 2022).

in bio-oxidation performances due to the formation of precipitates: stretching the woven polypropylene across the height allowed to more than double the time of operation before a cleaning is required compared to crumpling the solid support in a central basket.

The potential of the biomass to bio-oxidize the Fe^{2+} contained in the industrial effluent without any dilution, i.e., with a concentration of 100 vol%, was tested in the 6 L bubble column. A bio-oxidation yield of 100% was obtained for a HRT of 25 h, which corresponds to a bio-oxidation rate of about $350 \text{ mg} \cdot \text{L}^{-1} \cdot \text{h}^{-1}$.

The 6 L bubble column reactor was also used to investigate the influence of temperature regulation and CO_2 enrichment of air on the bio-oxidation performances. Tests were performed from July 2021 to March 2022 on an industrial effluent concentrated at 50 vol%. Results obtained from December 2021 to March 2022 are given in Figure 13. The relative standard deviation of the bio-oxidation rates during each operating condition was low (less than 5%). These relative standard deviations were in the same order of magnitude than the ones observed during the laboratory-scale tests at the BRGM laboratory (Section 3.2.1) despite the higher difficulty in maintaining stable operating conditions on-site. It is therefore possible to compare the results obtained at different operating conditions. Good performances were obtained at temperatures far lower than 40 °C, which is really promising from an industrial perspective. Regarding the CO_2 partial pressure, a bio-oxidation

yield of almost 100% was obtained even when the air was not enriched in CO_2 . These results should be confirmed at a larger scale, especially since in the 6 L bubble column the air flow rate was in large excess to guarantee a good homogenization and mass transfers within the bioreactor, and biomass had time to colonize the solid support before the enrichment in CO_2 was turned off.

The 6 L bubble column was operated for several months (from April 2020 to November 2022). During this long period of operation, clogging of the solid support by precipitates was observed. Even if the quantity of precipitates was highly reduced compared to when using coal particles, it raised the issue of maintenance. A protocol based on partial cleaning of the solid support on a regular basis was therefore developed and validated.

Based on these results, 9 Key Performances Indicators (KPI) were defined in order to better evaluate and compare the performances of the bio-oxidation process at each step of the scale-up. They are therefore critical milestones to reach for the industrial implementation of this bioprocess. Some examples of KPIs considered here are the following: concentration of industrial effluent, bio-oxidation rate, frequency of maintenance of the solid support and time to reach the optimal performances again after a maintenance operation.

3.3.3. Pilot-scale tests in 30 L reactors

3.3.3.1. Objectives. The pilot-scale tests performed in 30 L reactors aimed to optimize the operating

parameters, in particular for the start and the restart of the bioreactor after a maintenance operation. They also aimed to produce enough biomass to inoculate the larger-scale bioreactor.

3.3.3.2. Methods. 3 bubble columns, similar to the 6 L bubble column (with woven polypropylene used as solid support and stretched across the height of the columns), were operated from August 2020 to November 2022. Air was initially enriched with gaseous CO₂ (1%) before switching to Na₂CO₃ supply. Temperature was set at 35 °C. The reactors were first launched in batch mode to allow fixation of the microorganisms on the solid support and then operated in continuous mode by progressively reducing the HRT. O₂ and CO₂ partial pressures were occasionally measured at the top of the reactors. In order to monitor the biomass, DNA extraction and CE-SSCP were performed on the solid phase from time to time.

3.3.3.3. Results. Similarly to the 6 L bubble column tests, the bio-oxidation performances were not affected when the temperature was no longer regulated and when the air was not enriched in CO₂. This result was observed when the industrial effluent was concentrated at 100 vol%. However, it was observed that a CO₂ enrichment of the air is requested when the operation is being started or during a batch mode operation in order to ensure an efficient microbial growth. It was also observed that a temperature of around 20 °C is a limiting factor in such phases.

The experiments performed with the 30 L reactors also allowed to determine the quantity of solid support required to maintain a biomass concentration allowing to reach the targeted bio-oxidation performances. The initial ratio of woven polypropylene, set to 40 m²·m⁻³, led to a bio-oxidation rate of about 350 mg·L⁻¹·h⁻¹ when the industrial effluent was used (i.e., concentration of 100 vol%). This ratio was progressively reduced to 9 m²·m⁻³ and results showed that this ratio still allowed reaching and maintaining a bio-oxidation rate of about 350 mg·L⁻¹·h⁻¹.

Moreover, this testing campaign demonstrated the importance of O₂ transfer. In particular, when a clogging of the fritted cylinder was observed, leading then to a reduction of the air flow rate, the bio-oxidation performances were strongly decreased. It was observed that the declogging of the fritted cylinder allowed reaching again the bio-oxidation performances within a short period, confirming the

robustness of the biomass. Finally, it should be mentioned that a bio-oxidation rate of about 300–350 mg·L⁻¹·h⁻¹ was obtained for more than 4 months of continuous operation of the bioreactors.

3.3.4. Pilot-scale tests in a 700 L reactor

3.3.4.1. Objectives. The 700 L bioreactor was operated in order to continue the scale-up of the bioprocess and in particular to define the operating protocol to inoculate a bioreactor with a scale factor higher than the usual one. Indeed, upscaling in bioprocesses is usually performed with a scale factor of 10 but here it was planned to go from 30 L to 700 L, i.e., a scale factor of 23. This step also aimed to define additional KPIs and to get more reliable data for the design of the industrial system.

3.3.4.2. Methods. A tank of 700 L was designed in which the industrial effluent was injected at the bottom of the reactor and overflowed from the top. An air diffuser tube bound in a spiral at the bottom of the reactor was used to inject air. Na₂CO₃ was used for the CO₂ supply, with a CO₂ content in the air of 0.4–0.6%. No regulation of temperature was used. Woven polypropylene was used as solid support and a dedicated system was designed in order to stretch it across the height of the tank. The volumetric ratio of solid support was the same as for the 30 L bioreactor in order to keep the same concentration of biomass. K_La (Volumetric Mass Transfer Coefficient) was determined for different air flow rates in order to ensure sufficient O₂ mass transfer by comparison to O₂ uptake rate and stoichiometry of the reaction.

This reactor was operated between April 2022 and November 2022. It was first launched in batch mode to allow fixation of the microorganisms on the solid support and then operated in continuous mode by progressively reducing the HRT. O₂ and CO₂ partial pressures were occasionally measured at the top of the reactor, as well as O₂ uptake rate (through dissolved O₂ probe).

3.3.4.3. Results. The batch phase and the first continuous steps went quite fine even if the inoculation ratio was low (3.5% for the solid support). In particular, a bio-oxidation yield of 80% was obtained with a HRT of 48 h, which corresponds to a bio-oxidation rate of 160 mg·L⁻¹·h⁻¹. The effluent was



Figure 14. Evolution of the colonization of one piece of the solid support (woven polypropylene) by the biomass (©Orano Mining).

then changed to another one produced on the mining site (details not communicated here due to confidentiality issues), which led to a strong decrease in bio-oxidation performances. This may be caused by the presence of elements which inhibit the microorganisms. However, it was not possible to validate this assumption since Orano Mining decided to stop the study.

Even if it was not possible to reach good bio-oxidation performances with this 700 L bioreactor, its piloting still allowed defining a protocol to observe the colonization of the solid support by the biomass, as showed in Figure 14. This protocol and the feedback of its use could be used in another case study as they bring insightful information on the colonization of the solid support by the biomass, which is a critical parameter for a successful scale-up of a bioprocess.

4. Discussion

These works carried out at different scales highlighted that the main critical parameters for the implementation of the process of bio-oxidation of ferrous iron to ferric iron are related to biomass and to mass transfers. Specific works were then performed both at the mining site and at the BRGM and CIME laboratories.

First of all, it is critical to understand the mechanisms related to biofilm formation and growth in order to reach good performances of the bioprocess. Due to limited access to characterization equipment at the Somaïr mine, the in-depth characterization works were performed at BRGM, on a 150 mL bubble column operated in continuous mode fed with a model solution (ferrous sulfate in a nutrient medium). The aim was to better understand the biofilm formation and its influence on the

bio-oxidation rate of the bioreactor. In particular, cryogenic scanning electron microscopy (Cryo-SEM) was used to observe the attachment of cells onto the solid support without prior preparation steps (the methodology is described in [20]). A comparison of biofilms between new and old woven polypropylenes (used as solid support for 1.5 month and 1.75 year respectively) was performed (Figure 15). These works showed that even though the woven polypropylene had large holes (around 400 μm , as used on-site), biofilms completely clogged the solid support, probably affecting the mass transfer. Thin sections were also observed with a scanning transmission electron microscopy (STEM) (the methodology was adapted from [25]). It enabled to see that the microorganisms did not seem to be directly in contact with the polypropylene, a layer of extracellular polymeric substances secreted by the bacteria being in-between. It was also observed that precipitates were included in the biofilms and that microorganisms did not seem to be located in the same areas than precipitates, as if their inclusion in the biofilm was not simultaneous. Monitoring of the biofilm growth was performed on-site with the development of specific methodologies. In particular, a methodology was developed in order to estimate the amount of biomass attached to the solid support, this methodology including a dedicated protocol for recovering the attached cells followed by counting in Thoma cells. A methodology was also developed to estimate the growth of the biofilms on the woven polypropylene used in the 700 L reactor. This methodology is based on taking pictures of several given pieces of the solid support, at the same distance and with the same light on a regular basis (see Figure 14).

Another important feature of the biomass is related to its inhibition by elements possibly found in

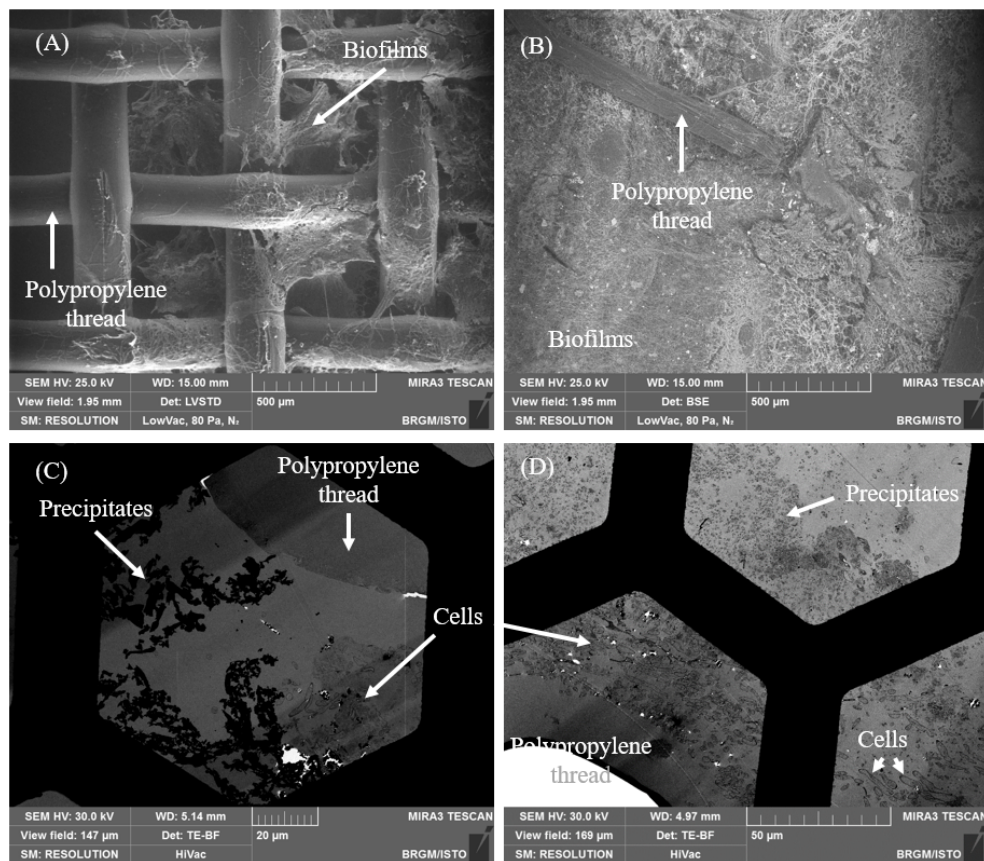


Figure 15. Cryo-SEM (A and B) and STEM (C and D) photographs of biofilms on woven polypropylene support (new support A and C; old support B and D).

the industrial effluents. Indeed, even if some potential inhibitory elements were identified before performing the tests, such as uranium in the production effluent (Figure 10) or traces of organic solvents in the raffinate (Figure 11), others elements may have an inhibitory effect on the metabolic activity of the bacteria. An ecotoxicity approach was then developed on-site. In this approach, detailed analysis of the effluents was combined to laboratory-scale tests in shake flasks. Such approach was implemented on a regular basis on the industrial effluent used for the tests since some variations in its chemical composition can be found.

Another key parameter of the performances of this bio-oxidation process is the formation of precipitates, as they play a significant role in the mass transfers. In this study, precipitates were produced even though pH was most of the time regulated to

1.2. These precipitates were not characterized due to the difficulty in collecting and analysing them, since they are associated to radioelements. However, some information could be obtained from Hubau et al. [20] who performed bio-oxidation tests in a similar context with SEM-EDS (Scanning Electron Microscope-Energy Dispersive Spectroscopy) characterization of the precipitates [20]. They showed that precipitates were a mixture of jarosite and ammoniojarosite, which are often reported in bioleaching systems. These precipitates came from ferric iron and sulfates together with cationic nutrients (K^+ , NH_4^+ , ...). Understanding the precipitation mechanisms is crucial to decrease their production allowing then improving mass transfers and optimizing maintenance of the bioreactors.

Last but not least, it is essential to optimize gas-liquid mass transfers all along the upscaling of

the process. Gas–liquid mass transfers were studied at each step of the on-site tests (except for the laboratory-scale tests in shake flasks) by analyzing gas composition in the outlet flow of the bioreactor, by measuring O_2 uptake rate during bio-oxidation and by estimating $k_L a$. It should be mentioned that there is a need to develop monitoring instruments dedicated to acidophilic bioleaching environments in order to optimize gas–liquid mass transfers. For example, it would have been very useful to measure the dissolved CO_2 content. However, the related probes available on the market are, to our knowledge, not adapted to this application.

5. Main lessons learned

Even if the study was stopped before industrial implementation of the investigated bioprocess, several lessons were learned from the tests performed at laboratory- and pilot-scale. This work also allowed identifying opportunities of process improvement.

In particular, the conception of the bioreactor (dimensions, stirring, air injection, mode of handling the solid support within the reactor) was shown to be a key parameter for the industrial implementation of the ferrous iron bio-oxidation. This is all the more important that some critical requirements are somehow antagonist. For example, it is required to avoid bacterial washout from the reactor in order to maintain high bio-oxidation performances so fluid turbulences should be limited to avoid biofilm detachment from the solid support. However, a good homogenization is a prerequisite to ensure high mass transfer, in particular for gas, and then high bio-oxidation performances. It is also essential to consider the management of precipitates when designing the bioreactor in order to maintain the performances over long periods of time and to limit the effects of the maintenance phase. Last but not least, the design of the bioreactor has a strong impact on the CAPEX and on the OPEX. For example, a Stirred Tank Reactor allows high mass transfer but leads to high CAPEX and OPEX. Using a pond with air diffusers (which could be considered as the industrial equivalent of the bubble column) has the advantages of low CAPEX and OPEX but may lead to hydrodynamic short circuits and then to low mass transfers.

Regarding the operating conditions, results showed that the microorganisms used in the bioprocess have a strong robustness, which is a really positive feature since it means that they can be adapted to changes in operating conditions without decreasing their performances, and that a brutal change in operating conditions (due to an unexpected issue for example) does not lead to a loss in biomass. In particular, regarding the effluent composition, it was observed that it is possible to adapt the biomass to high concentrations of elements by first diluting the effluent and progressively decreasing the dilution level. This parameter is easier to evaluate in continuous mode rather than in batch mode, as the change in effluent composition is less abrupt. Moreover, results showed that the temperature and the enrichment of air in CO_2 , which highly determines the biomass formation, are very important during batch phases such as the start-up or the restart after a maintenance operation. They are not so important during the bio-oxidation phase. These phases should then be carefully considered during the scale-up and later for the industrial exploitation of the process, as they are decisive for the on-site implementation, not only from a technical point of view but also from an economic point of view.

Results obtained in this study highlighted the need to have and to maintain shake flasks for checking the toxicity of any new effluent or material that will have to be placed within the bioreactors. These shake flasks could also be used to assess the composition of the effluent towards the biomass resistance in case of an unexpected change in the mine process.

Another lesson learned from this study is that it is essential to have a good knowledge of the biofilm properties. Monitoring the overall process parameters (oxidation yield, total Fe and Fe^{2+} concentrations, etc.) does not allow understanding the mechanisms related to the biofilms (such as formation, growth, clogging, detachment), which are nevertheless a pivotal point of this bioprocess. Changes in biomass at the microscopic scale may result in high variations of the behavior and performances of the whole process at macroscopic scale. Better understanding the biofilm properties often requires access to cutting-edge characterization equipment not available on the industrial sites, so strong collaboration with research laboratories should be encouraged.

Finally, the definition of Key Performance Indicators (KPIs) quite early in the implementation strategy was proven to be very effective to guide the planning of the experimental testwork for the upscaling of the bioprocess. They also constitutes the basis of an iterative approach for the update of the techno-economic feasibility of the process, considering the information obtained at the different development steps, allowing the identification of technical and economic hot spots as soon as they appear, which need then more research work for their optimization.

6. Conclusions

The development of the bio-oxidation of ferrous iron to improve uranium recovery was initiated with theoretical works and with laboratory-scale tests performed on synthetic effluent to evaluate its potential. From these first results, the main steps for its upscaling and its implementation on a mining site were defined. The main results from each of these steps are presented, discussed and put into perspective in order to support an iterative approach for the design of the bioreactor and for the update of the techno-economic feasibility of the process with the final objective to define the most appropriate operational technology and flowsheet.

Even if this study was stopped at the 700 L piloting stage due to an internal decision of Orano Mining, it still allowed improving process know-how and operational experience that could then be used for the industrial implementation of any bioprocess. In particular, several lessons can be learned and allow identifying opportunities to improve the investigated bioprocess and the approach used for its upscaling.

Declaration of interests

The authors do not work for, advise, own shares in, or receive funds from any organization that could benefit from this article, and have declared no affiliations other than their research organizations.

Funding

This study was performed under the project IronBiox (“Bioaugmentation en fer ferrique”) funded by Orano Mining.

Acknowledgments

The authors thank all the persons who have contributed to this project and in particular Mohamed Kariman, Allasane Issaka Oumarou and Moussa Sabiou from Somaïr; Dominique Morin, Yannick Ménard, Christopher Bryan, Jérôme Jacob, Catherine Jouliau, Pierre Gallé, Dominique Breeze and Patrick d’Hugues from BRGM; Jean-Luc Rey, Véronique Dutheil, Alexandre Michaut, Magali Celier and Pascal Nardoux from Orano Mining.

References

- [1] P. C. Burns, R. J. Finch, *Uranium: Mineralogy, Geochemistry and the Environment*, Reviews in Mineralogy, vol. 38, Mineralogical Society of America, De Gruyter, Golden, Colorado, 1999, 679 pages.
- [2] R. Venter, M. Boylett, *SAIMM Hydrometallurgy Conference, 24–26 February 2009, Johannesburg (South Africa)*, Southern African Institute of Mining and Metallurgy, Johannesburg, 2009, 445–456 pages.
- [3] P. C. van Aswegen, J. van Niekerk, W. Olivier, in *Biomining* (D. E. Rawlings, D. B. Johnson, eds.), Springer, Berlin, Heidelberg, 2007.
- [4] D. H. R. Morin, P. d’Hugues, in *Biomining* (D. E. Rawlings, D. B. Johnson, eds.), Springer, Berlin, Heidelberg, 2007.
- [5] D. H. R. Morin, in *Microbial Processing of Metal Sulfides* (E. R. Donati, W. Sand, eds.), Dordrecht, Springer, 2007.
- [6] A. B. Umanskii, A. M. Klyushnikov, *J. Radioanal. Nucl. Chem.*, 2013, **295**, 151–156.
- [7] A. H. Kaksonen, A. J. Lakaniemi, O. H. Tuovinen, *J. Cleaner Prod.*, 2020, **264**, article no. 121586.
- [8] Somaïr, 2021, Rapport Environnemental, Social et Sociétal, 48 p.
- [9] A. Mazuelos, N. Iglesias, F. Carranza, *Process Biochem.*, 1999, **35**, 425–431.
- [10] A. G. Guezennec, C. Jouliau, J. Jacob, A. Archane, D. Ibarra, R. de Buyer, F. Bodéan, P. D’Hugues, *Miner. Eng.*, 2017, **106**, 64–70.
- [11] US4139456A 1979-02-13 Process for oxidation treatment of Fe²⁺ in waste water (Dowa Mining, Japan).
- [12] US6043022A 2000-03-28 Apparatus and method for the generation and use of ferric ions (University of Michigan, United States).
- [13] S. N. Talati, M. K. Stenstrom, *J. Environ. Eng.*, 1990, **116**, 70–86.
- [14] A.-G. Guézennec, M. Delclaud, F. Savreux, J. Jacob, P. d’Hugues, *Hydrometallurgy*, 2014, **2014**, Victoria (Canada). 7 p.
- [15] K. Bosecker, G. Mengel-Jung, A. Schippers, in *Biohydrometallurgy: A Sustainable Technology in Evolution, Part 1* (M. Theodos, A. Hatzikioseyan, E. Remoundaki, eds.), University of Athens, Greece, 2004, 585–593.
- [16] V. Bishimbayev, K. Bishimbayev, I. Akmaral, *Int. J. Contemp. Appl. Sci.*, 2015, **2**, 80–85.
- [17] Z. K. Kanaeva, A. G. Bulaev, A. T. Kanaev, T. F. Kondrat’eva, *Mikrobiologiya*, 2015, **84**, 323–330.

- [18] D. G. Karamanev, L. N. Nikolov, *Biotechnol. Bioeng.*, 1988, **31**, 295-299.
- [19] C. Leycuras, D. Morin, Y. Menard, K. Bru, *Mines Carrières*, 2019, **273**, 63-72.
- [20] A. Hubau, M. Minier, A. Chagnes, C. Jouliau, C. Perez, A. G. Guezennec, *Hydrometallurgy*, 2018, **180**, 180-192.
- [21] H. Halfmeier, W. Schafer-Treffenfeldt, M. Ressus, *Appl. Microbiol. Biotechnol.*, 1993, **40**, 416-420.
- [22] N. J. Coram, D. E. Rawlings, *Appl. Environ. Microbiol.*, 2002, **68**, 838-845.
- [23] A. Hubau, "Design of a bioleaching process for the recovery of metals contained in spent Printed Circuit Boards", Phd thesis, Université Paris Sciences et Lettres, 2019 (in French).
- [24] G. Yue, L. Zhao, O. G. Olvera, E. Asselin, *Hydrometallurgy*, 2014, **147-148**, 196-209.
- [25] G. Wille, J. Hellal, P. Ollivier, A. Richard, A. Burel, L. Jolly, M. Crampon, C. Michel, *Microsc. Microanal.*, 2017, **23**, 1159-1172.



Research article

GDR Prométhée – French Research Network on *Hydrometallurgical Processes for Primary and Secondary Resources*

Case-based analysis of mechanically-assisted leaching for hydrometallurgical extraction of critical metals from ores and wastes: application in chalcopyrite, ferronickel slag, and Ni-MH black mass

Clément Laskar^{*,a}, Amine Dakkoune^{*,a}, Carine Julcour^{*,a}, Florent Bourgeois^{*,a},
Béatrice Biscans^{*,a} and Laurent Cassayre^{*,a}

^a Laboratoire de Génie Chimique (LGC), Université de Toulouse, CNRS UMR 5563,
INP, UPS, 4, Allée Emile Monso, 31400 Toulouse, France
E-mail: clement.laskar@gmail.com (C. Laskar)

Abstract. The overall performance of hydrometallurgical leaching operations can be limited by the presence of various types of insoluble layers coating the surface of the treated solids. The attrition-leaching process, which is carried out in a stirred reactor containing millimetric beads, can partially overcome this problem and increase the extraction yield by physically abrading the layers. Through a comparative analysis of three different systems, this work develops a constructive discussion of the attrition-leaching process. The systems of interest are (i) mineral carbonation of ferronickel slag, (ii) dissolution of a chalcopyrite concentrate in sulfuric media, and (iii) dissolution of spent Ni-MH battery black mass powder in sulfuric media. In the case of ferronickel slag and chalcopyrite, the reaction yields are improved by a factor of 10 with attrition-leaching compared to leaching only, while there is no yield improvement in the case of Ni-MH black mass batteries, highlighting that the layers observed on the grain surface do not interfere with the leaching reaction. Despite very different system chemistries and conditions, the particle size distribution is similar for the three materials, showing that particles' behavior is controlled by the attrition environment. This work offers a simple setup for investigating the potential improvements of the kinetics and yields of leaching reaction due to concomitant attrition. It also allows a fundamental study of the physico-chemical processes involved, by testing whether a leaching reaction is hindered by an *in situ* passivation at the surface of a material.

Keywords. Mechano-chemical processing, Leaching, Passivation layer, Aqueous mineral carbonation, Ferronickel slags, Chalcopyrite, Nickel metal Ni-MH hydride batteries.

Funding. French National Research Agency project BIOMEALIX (Grant No. ANR-18-CE07-003101), project Carmex (Grant No. ANR-08-PCO2-002), New Caledonian Energy Agency ACE (Grant No. CS17-3160-00), French Environment and Energy Management Agency ADEME (Grant No. 1894C0021).

Manuscript received 20 November 2023, revised 24 June 2024, accepted 26 June 2024.

*Corresponding author

1. Introduction

Recycling, decarbonization, and energy optimization are crucial concerns for both chemical engineering and environmental conservation. Waste generation can be reduced by recovering end-of-life products (e.g., battery recycling) more efficiently and valorizing industrial and mining by-products (e.g. slags, mine tailings). Circular hydrometallurgical processes are promising solutions for these concerns [1]. Optimizing reagents consumption while achieving higher yields and faster reaction kinetics is therefore essential. In such hydrometallurgical processes, various parameters affect the efficiency of the leaching reaction [2], including the type and concentration of the leaching agent (e.g. H_2SO_4 , HCl), temperature, particle size, the agitation and the solid to liquid ratio (S/S+L). During reactions occurring at the solid–fluid interface, passivating layers may form on material surface through dissolution/precipitation mechanisms. These layers severely limit reactivity and applicability by hindering the kinetics of dissolution of materials, as they hinder the diffusion of the liquid reactant (e.g. protons) towards the unreacted core [2].

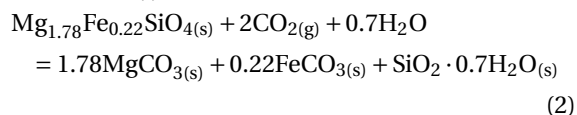
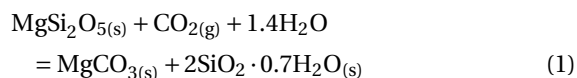
In this frame, mechano-chemical techniques play an important role in recovery of metals from wastes [3,4], as well as mineral carbonation [5], a very promising method for CO_2 storage and utilization due to its applicability to large-scale materials [6–10]. Mechanical activation of materials, achieved through attrition, amorphization and formation of new phases can, in particular, aid in increasing the reactive surface before or during leaching and enhance the dissolution rate [11].

Among the mechano-chemical processes, attrition-leaching is a promising option [12–15]. It consists in adding mm-sized beads directly in the leaching reactor, in order to intensify the leaching reaction, while improving kinetics and yield by particle grinding and *in situ* removal of leached layers. Attrition-leaching process shows synergy between two phenomena with very different timescales: attrition (time <second) and leaching of the material (time ~several hours). The attrition rate needs to be higher than the rate of passivation layer formation for an efficient depassivation on material surface. The leaching rate is related to the typical dissolution reaction time of the material, which is usually long for refractory materials. The main advantages of attrition-

leaching process are: attrition is a proven technology at large scale with slurry concentrations up to 40 wt% ($m_{\text{solid}}/m_{\text{solid}} + m_{\text{liquid}}$; S/S+L); broad feed particle size distribution, from μm to mm size range; operating at high temperature and pressure; scalability, from 4 L to 50 m^3 (e.g. IsaMill™ process [16]).

To investigate the applicability and efficiency of the attrition-leaching process, we have studied reactions of three different chemical systems where formation of layers on surface is observed during leaching (Figure 1): (i) mineral aqueous carbonation of ferronickel slag, an industrial waste produced by the primary nickel pyrometallurgical industry in New Caledonia, whose leaching is hindered by the formation of amorphous silica layers [13,14,17–20]; (ii) acid leaching of a chalcopyrite concentrate, one of the most abundant ores for copper primary production, in which Cu dissolution is inhibited by complex combined chemical and electronic phenomena [15,21,22]; (iii) dissolution of spent battery black mass powder, produced at industrial scale from nickel-metal hydride (Ni-MH) automotive batteries, whose particles exhibit a complex superposition of porous oxide layers [23], which are thought to inhibit the efficient dissolution of critical metals (Ni, Co, La, Ce) [24]. The disparity of three systems and its materials allows us to investigate the potential differences and similarities in their reactivity during the attrition-leaching process.

In these chemical systems, different types of layers can form on particles' surfaces (Figure 2). In the case of ferronickel slag, composed mainly of magnesium silicates (amorphous MgSi_2O_5 and ferrous forsterite, $\text{Mg}_{1.78}\text{Fe}_{0.22}\text{SiO}_4$, the Mg-rich endmember of the olivine solid solution series), an hydrated silica passivation layer ($\text{SiO}_2 \cdot x\text{H}_2\text{O}$) may form during the following carbonation reactions [18]:



Ferronickel slag is a promising material for mineral carbonation, as an industrial by-product [25]. However, due to the silicate layers, a dissolution plateau is reached without mechano-chemical activation, limiting the carbonation reaction [26,27].

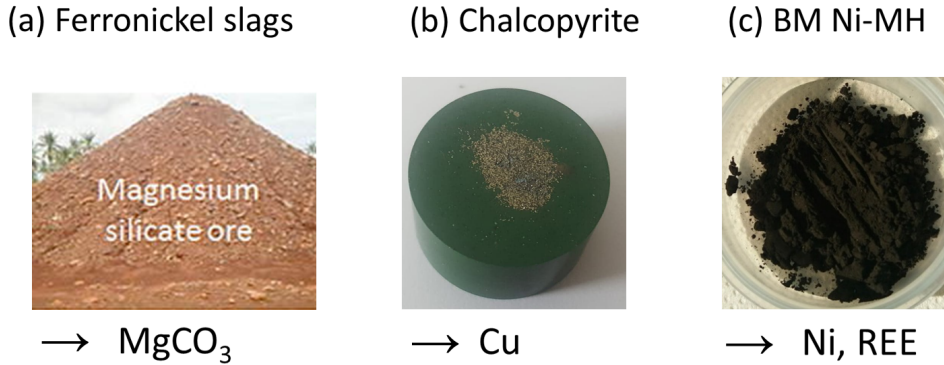


Figure 1. Systems used in this study: Ferronickel slag (a), chalcopyrite concentrate (b) and black mass of Ni-MH battery (c).

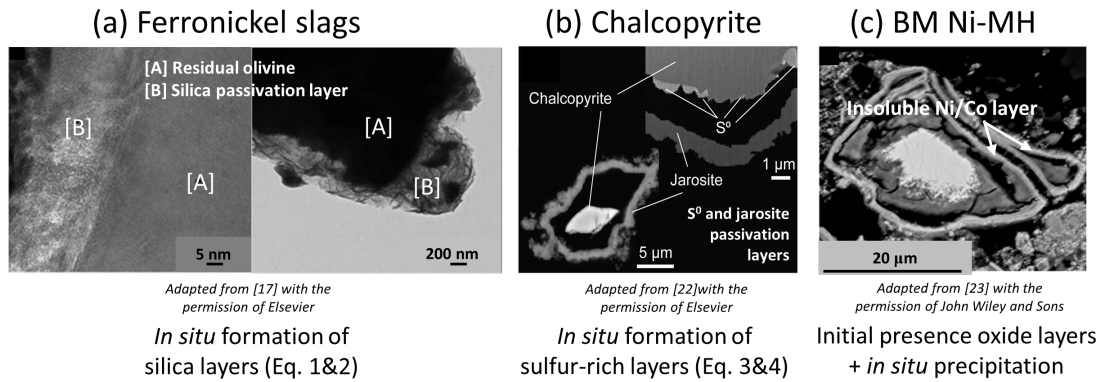
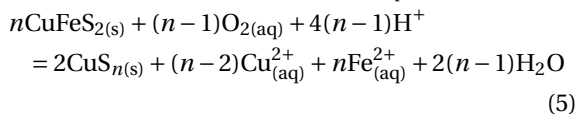
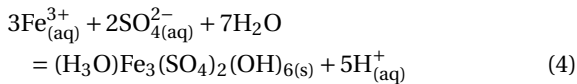
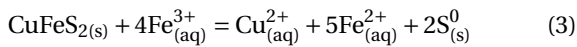


Figure 2. Respective phases and elements of interest and their chemical layers hindering the leaching reaction yields and kinetics: olivine grains ((Mg,Fe)₂SiO₄) with silica-rich (SiO₂) layers [17] (a); chalcopyrite grains (CuFeS₂) with sulfur (S⁰) and jarosite (KFe₃(SO₄)₂(OH)₆) layers [22] (b); and Ni/Co and REE (rare-earth elements) rich grains with Ni/Co insoluble layers [23] (c).

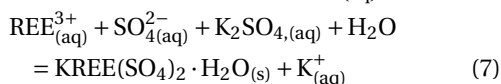
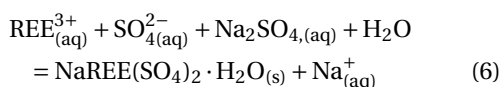
In the case of chalcopyrite (CuFeS₂), there is no consensus on the exact cause of passivation, and it is attributed to the *n*-type semiconducting nature of chalcopyrite [28], or formation of various sulfur-rich passivation layers [15]: elemental sulfur, S⁰ [29]; jarosite, KFe₃(SO₄)₂(OH)₆ [22]; copper polysulfide, CuS_{*n*} (*n* > 2; [30]), through the following reactions:



Mechano-chemical applications have been developed to optimize the chalcopyrite leaching step, which is very slow at moderate temperatures (~100 h at 75 °C; [31]): for example, by grinding the copper concentrate prior to leaching [32], or with a continuous flow between a leach tank reactor and a smaller stirred tank reactor (FLS[®] Rapid Oxidative Leach (ROL) process [33]).

In the case of black mass Ni-MH powder (BM Ni-MH), Zielinski [23] observed the presence of an insoluble Ni/Co oxide layer (62 at% Ni, 9 at% Co, <0.5 at% REE) on the surface of leached particles after 22 h in HCl solution of pH 3 at a temperature of 60 °C, while the leaching yield of Ni is not complete (<50%). This layer appears porous due to the hollow core structure

of the remaining particles after leaching. This raises a question about the effect of such layers on leaching efficiency, and whether attrition-leaching may enhance Ni dissolution. This limitation in dissolution of BM Ni-MH material for nickel has been frequently reported, with leaching yields remaining below 90% even after several hours at mildly acidic concentrations (<1 M HCl or H₂SO₄), as reported in a review by Cassayre [24]. In contrast, leaching yields of REE are rapid and high, reaching over 90% in just a few hours [24]. The limitation for REE leaching is the precipitation of these elements as double sulfate salts [24], as shown in the following reactions:



The potential limitation of Ni dissolution due to *in situ* precipitation of REE double sulfate salts has not been much investigated.

The implementation of mechano-chemical processes with mechanical activation prior to leaching has already been reported for these three systems: silicates carbonation (olivine, [34]; kimberlite and wollastonite, [35]; akermanite, [36]), copper ores leaching [32,33,37–41] and Ni-MH battery leaching [42]. However, only a few recent works have studied concomitant mechano-dissolution processes [12–15,18,20,33,36], calling further studies to identify and compare the governing mechanisms as well as the industrial feasibility for a variety of materials. Specifically, this study examines the case of BM Ni-MH dissolution, mechanically enhanced by attrition-leaching, for which leaching yields and kinetics may be improved owing to the presence of insoluble layers on the grain surface. The results obtained from the BM Ni-MH leaching experiments are compared to those obtained from previous studies with ferronickel slags [20] and chalcopyrite [15]. This comparison examines maximum dissolution yields, reaction kinetics, and physicochemical properties of the solid of these three materials, in order to provide a broader perspective of the synergistic effect of attrition-leaching and to highlight the potential of such process in materials passivation.

2. Materials and methods

2.1. Materials and chemicals

The composition of the materials used in this study is shown in Table 1.

- Ferronickel slags are a by-product of pyrometallurgical Ni extraction from New Caledonia's lateritic nickel ores (see [13] for more details). They are a mixture of ferrous forsterite (Fe_{0.22}Mg_{1.78}SiO₄) and an amorphous magnesium silicate phase (MgSi₂O₅).
- The chalcopyrite material was a flotation concentrate from the Aitik Mine in Sweden (see [15] for more details) which was homogenized and sampled using riffle splitters. This material was stored without any special precautions, which means that surface passivation due to air oxidation may have occurred. It consists of two major phases, chalcopyrite (CuFeS₂) and pyrite (FeS₂), and two minor phases, quartz (SiO₂) and molybdenite (MoS₂).
- Spent Ni-MH batteries were collected and treated by the SNAM Group and they consisted of a mixture of anodes, cathodes, and casing materials [43]. To obtain the resulting BM powder for use, these batteries were dismantled, thermolyzed in an oven and crushed by knife milling. BM was stored without any specific precautions until it was homogenized and sampled several years later using riffle splitters. It was then sieved to produce two different fractions: <100 µm and 100–500 µm. The material is a complex mixture of NiO, Ni and LaNi₅ particles. The presence of potassium (3–6 wt% K) is attributed to residual KOH electrolyte contained in the batteries.

Two types of beads were used as grinding media based on the chemistry of the aqueous solution, the operating conditions and the products to be valorized [44]: (i) glass beads (GlassBeads 1.5 type from Netzsch Group), with a density of 2.5 g/cm³, diameters between 1.2 and 1.6 mm and a chemical composition of 72.5 wt% SiO₂, 13 wt% Na₂O, 9 wt% CaO, and 4 wt% MgO; (ii) yttriated zirconia beads (Netzsch ZetaBeads Plus), with a density of 6.0 g/cm³ and a diameter of 1.0 mm. The glass beads were used for BM Ni-MH and chalcopyrite leaching to avoid

Table 1. Average chemical and mineralogical compositions of the materials

Ferronickel slag ^a											
Chemical composition (wt% as oxides)											
SiO ₂	MgO	Fe ₂ O ₃	Al ₂ O ₃	Cr ₂ O ₃	CaO	MnO					
52.6	31.2	12.4	2.7	1.1	0.7	0.2					
Phase distribution (wt%)											
Amorphous phase ^b		Mg _{1.78} Fe _{0.22} SiO ₄		FeCr ₂ O ₄		MgSiO ₃					
54–56		42–44		1.6		0.1–0.4					
Chalcopyrite ^c											
Elemental composition (wt%)											
Fe	Cu	Si	Al	K	Na	Zn	Mo	Ca	S _{SO₄}	S _{sulfide}	S ⁰
30.60	28.57	2.90 ±	0.83 ±	0.37 ±	0.21 ±	0.25 ±	0.17 ±	0.13 ±	0.21 ±	33.27	0.01 ±
± 0.17	± 0.23	0.20	0.05	0.02	0.02	0.01	0.01	0.01	0.01	± 0.32	0.01
Phase distribution (wt%)											
CuFeS ₂	FeS ₂	SiO ₂	MoS ₂	KAlSi ₃ O ₈	NaAlSi ₃ O ₈	Fe ₃ O ₄					
76.72	11.88	2.83	0.28	2.63	2.43	2.38					
BM Ni-MH											
Elemental composition (wt%)											
		Ni	La	K	Na	Co	Ce	Fe	Al		
<100 μm		45 ± 5 ^d	8.6 ± 1.8 ^d	5.2 ± 2.1 ^d	1.0	5.6	3.7	0.53	0.14		
100–500 μm		47	10.8	3.6	0.31	— ^f	— ^f	— ^f	— ^f		
Main phases ^e		Ni, NiO, CeO ₂ , graphite									
Minor phases ^e		Co ₃ La ₂ , La ₇ Ni ₁₆									

^aData taken from [20].^bAmorphous phase is mainly composed of amorphous MgSiO₅ [18].^cData taken from [15].^dUncertainties are derived from the standard deviation of a set of 5 samples, demonstrating the light inhomogeneity of this material due to the low amount used (0.2 g) for mineralization.^eAccording to [23].^f“—” means not measured.

breaking the glass reactor used to process these materials. The potential reactivity of the beads was also evaluated. Zirconia beads were used instead of glass beads in ferronickel slag experiments to avoid introducing an additional silica source in the reactor. Zirconia beads were also preferred to stainless steel beads to avoid corrosion of the beads and contamination of the solid products. Each system requires different attrition-leaching conditions, and notably the properties of the beads (nature, density, size, and

hardness) were adapted to the reactor used. This study focuses on the influence of attrition-leaching on the chemical reactions and potential passivation, without investigating the nature of the beads and the influence it can have on the reactions for each different system, which is beyond the scope of this study and would require additional experiments.

The chemicals used for chalcopyrite dissolution were sulfuric acid (95 wt%, VWR international) and hydrogen peroxide (30 wt%, VWR international). For

BM Ni-MH leaching, sulfuric acid was diluted in deionized water ($0.05 \mu\text{S}/\text{cm}$) to reach a concentration of 4.0 M. In the case of slag carbonation, the source of protons was the dissolution of CO_2 into water.

2.2. Experimental reactors and analytical protocols

Two different leaching reactors with a similar operating principle were used (Figure 3): (1) loading of water and the beads into the reactor vessel, start of stirring and setting the experimental conditions of pressure, temperature and possibly pH, redox potential (E_h) and CO_2 pressure; (2) loading of the material to be leached, marking the start of the reaction; (3) maintaining all conditions constant during the reaction time; (4) end of the reaction by stopping the stirring, cooling, emptying the reactor and separating the beads from the suspension by sieving. The different experimental configurations tested in this study were: leaching only—without beads (L), attrition by particle pre-grinding followed by leaching (A-L), and concomitant attrition and leaching, referred to as attrition-leaching (AL). The particle pre-grinding was carried out in the same reactor as the leaching, at similar loading and stirring rate (see below), but only with water and beads, for 24 h for ferromagnetic slag and 3 h for chalcopyrite materials, relative to the difference in material hardness.

The operating conditions of the three chemical systems used in this study are presented in Table 2. It should be noted that the glass reactor was designed for industrial level scalability. For chalcopyrite concentrate experiments, the suspension was 3.25 wt% by mass, and for BM Ni-MH experiments the suspension was 1–10 wt%. Various amounts (from 0.25 to 3 kg) of 1 mm glass beads were introduced in the reactor yielding a filling rate of 3–10 vol%. The reactor was equipped with a four-blade Teflon stirrer and a torque meter (MK2 ETH model, PM Instrumentation) to measure torque and rotational speed. No baffles were present in the reactor because the creation of a vortex was desired to increase the contact between the material and the beads. A cryostat (AC200, Thermofisher) was used to maintain a uniform temperature by circulating water through the double jacket. The mechanical stirrer was set at ~ 560 rpm during the experiments. A platinum temperature

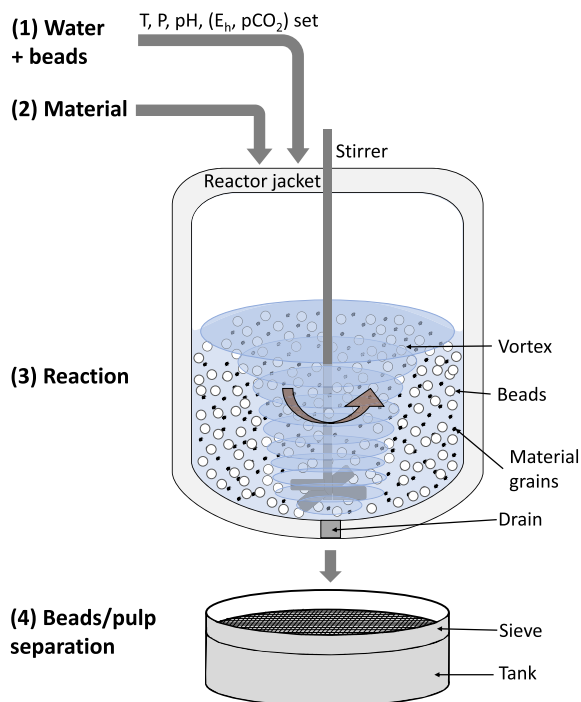


Figure 3. Schematic of an attrition-leaching (AL) experiment, showing the successive steps (1–4) of the experiment.

probe (Pt100 Duplex Probe, TC Direct) and a combined pH electrode (LL-Unitrode SC, Metrohm) were immersed in the solution to measure the temperature and pH, respectively, throughout the reaction. The combined pH electrode was protected by a thin SS grid to prevent the glass beads from damaging the probes. The pH was regulated using an automatic titrator (Titrand, Metrohm) by adding H_2SO_4 . The installation was connected to a computer which displayed and recorded the temperature, torque and stirring rate every minute. The acquisition and regulation of pH were carried out by the Tiamo software (at 0.1 Hz). The leaching rate for chalcopyrite and BM Ni-MH was measured by sample analysis of dissolved metal concentrations in the solution and by on-line monitoring of acid consumption. During a test run, the slurry was sampled with a 0.8 mm tube to prevent picking up beads. The sampled slurry was then filtered through a $0.25 \mu\text{m}$ syringe filter and the leachate samples obtained were analyzed by inductively coupled plasma-optical emission spectroscopy (ICP-OES; PerkinElmer Optima 8300) for the

Table 2. Operating parameters of the three chemical systems

System	Reactor material	V_{reactor} (L)	T (°C)	P (bar)	pH	E_h (mV vs SHE)	Stirring rate (rpm)	Beads material	Reference
Ferronickel slags	Stainless steel (peek liner)	0.3	150	10 (CO ₂)	5	—	500	Yttriated zirconia	[20]
Chalcopyrite	Glass	6	42	1	1.3	700	556	Glass	[15]
BM Ni-MH	Glass	6	40	1	1.0	—	560	Glass	This study

quantification of Cu, Ni, La, K and Na. The leaching yield $Y_{i(t)}^L$ (%) for the species at the time t of the experiment was obtained from the analysis of the liquid samples:

$$Y_{i(t)}^L (\%) = \frac{c_{m,i}(t) \cdot V_{\text{tot}}(t)}{m^0 \omega_i^0} \quad (8)$$

where $c_{m,i}(t)$ is the concentration of species i in the leachate sample at the time t , m^0 is the initial mass of the material, ω_i^0 is the mass fraction of species i in the starting material, and $V_{\text{tot}}(t)$ is expressed as:

$$V_{\text{tot}}(t) = V_{\text{H}_2\text{O}} + V_{\text{H}_2\text{SO}_4}(t) + V_{\text{H}_2\text{O}_2}(t) - \sum_{i=1}^{n(t)} V_{\text{sample},i} \quad (9)$$

where $V_{\text{H}_2\text{O}}$ is the initial volume of water added into the reactor, $V_{\text{H}_2\text{SO}_4}(t)$ is the volume of sulfuric acid added into the reactor at time t , $V_{\text{H}_2\text{O}_2}(t)$ is the volume of hydrogen peroxide added into the reactor at time t , $V_{\text{sample},i}$ is the volume of sample i and $n(t)$ is the number of samples at time t . Solid samples were also collected during the experiments for analysis. The beads were separated from the slurry at the end of each test run using an 850 μm RETSCH SS sieve. For BM Ni-MH experiments, 40 mL slurry samples were taken from the reactor during the experiment and the solid was then recovered in 2 different ways: (i) by solid filtration through a Büchner funnel with 0.2 μm filters (Whatman, mixed cellulose ester); (ii) by centrifugation (SIGMA Laboratory Centrifuges) at 6000 rpm for 5 min. In each case, the solid was then rinsed with 10 mL of deionized water to remove the residual leaching solution in the filter cake. Further details of the reactor and experimental protocol used for chalcopyrite experiments has been elaborated in Dakkoune [15]. In the carbonation experiments with ferronickel slags, leaching of Mg was followed indirectly by measuring the CO₂ consumption resulting from the rapid carbonation reaction between Mg^{2+} and aqueous HCO_3^- species. Further

details of the reactor and experimental protocol used has been elucidated in Dufourny [20].

A scanning electron microscope-field emission gun (SEM-FEG, JEOL JSM 7100F) equipped with an energy dispersive X-ray analyzer (EDX, Oxford ASDD X-Max detector) was used for particle observation, with an accelerating voltage of 10 kV and a working distance of 10 mm. The particle size distribution (PSD) was obtained by laser diffraction in wet dispersion mode using a Malvern Mastersizer 3000. Slurry samples were taken from the glass reactor in the same manner as liquid samples, but without filtration, and were diluted in deionized water to quench the reaction. For analysis of solids, we set the refractive index at 1.52, the absorption at 0.1 and the stirring rate at 1800 rpm. Five successive analyses were carried out for each sample.

The operating conditions used for these experiments are shown in Table 3. These conditions were chosen independently for each system to achieve sufficiently high reaction yields with leaching only mode. Temperature of 150 °C and CO₂ pressure of 10 bar used for carbonation of ferronickel slags were chosen to overcome the thermodynamic limitations of carbonation reaction [12]. Temperature of 42 °C for chalcopyrite leaching experiments was chosen to be compatible with bioleaching conditions [45]. Temperature for BM Ni-MH was set below the optimized temperature of 60 °C [46,47], to permit observation of potential effects of concomitant attrition and leaching on the reactions' kinetics and yields, as both increase with temperature.

3. Results and discussion

3.1. Yields and kinetics of reactions

As illustrated in Figure 4 and Table 3, the presence of beads in the reactor has a significant effect on the

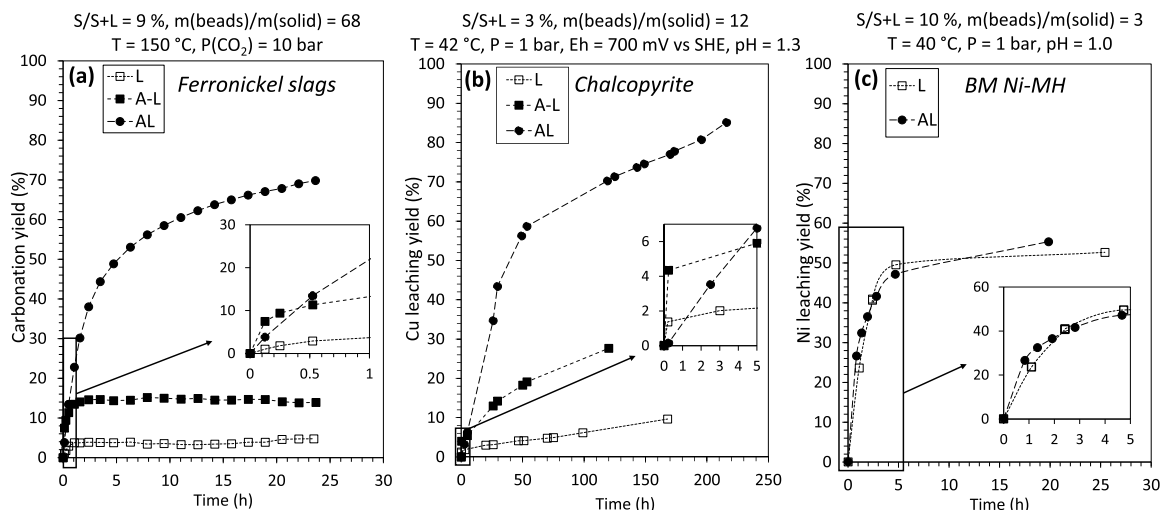


Figure 4. Reaction yields of reference (leaching only, L), two-step (attrition followed by leaching, A-L) and concomitant (attrition-leaching, AL) processes for ferronickel slag carbonation (a), chalcopyrite leaching (b) and BM Ni-MH leaching (c). Experimental data for ferronickel slag and chalcopyrite are taken from Dufourny [20] and Dakkoune [15], respectively.

Table 3. Summary of leaching experiments performed on ferronickel slags, chalcopyrite and BM Ni-MH

Material	Initial configuration				Final configuration		
	m_{solid} (g)	m_{beads} (g)	S/S + L initial (wt%)	Solid fraction (μm)	Time (h)	H^+ (mol)	H_2O_2 (mol)
<i>Ferronickel slag</i> ^a							
FS 1-L	8.0	—	9.1	<100	24	—	—
FS 1-A-L	8.1	—	9.4	<100	24	—	—
FS 1-AL	8.2	540	9.3	<100	24	—	—
<i>Chalcopyrite</i> ^b							
Ch-L	84	—	3.3	<200	96	0.1	0.08
Ch-A-L	84	—	3.3	<200	120	0.8	0.9
Ch-AL	84	1000	3.3	<200	216	1.2	1.5
<i>BM Ni-MH</i>							
BM2-L	306	—	10.0	<100	25	5.5	—
BM3-AL	298	1000	10.4	<100	20	5.8	—
BM4-L	30	—	1.2	<100	24	0.7	—
BM5-AL	30	1000	1.2	<100	22	0.7	—
BM6-AL	305	3000	9.7	<100	53	5.9	—
BM7-L	100	—	3.7	<100	20	1.8	—
BM8-AL	100	1000	3.8	<100	22	1.7	—
BM9-L	100	—	3.8	100–500	21	2.1	—
BM10-AL	100	1000	3.9	100–500	21	1.8	—

^aData taken from [20].

^bData taken from [15].

carbonation yield of ferronickel slags (Figure 4a) and on chalcopyrite dissolution (Figure 4b). However, this effect is negligible on Ni dissolution yield from BM Ni-MH (Figure 4c), where the Ni extraction yield is the same with the AL and L modes, reaching only ~50% after 20 h.

Several experimental conditions (size fraction, S/S+L ratio, amount of beads) have been investigated in BM Ni-MH leaching experiments, but the extraction yield always remained very similar, in the range 50–70% (Figure 5). Such yields are quite low compared to other Ni dissolution yields reported in literature at a similar pH of 1 (>80%; [24,46]). It is hypothesized that production (including thermal treatment) and storage conditions (long term storage in air) [23] may account for the yield variations of comparable BM Ni-MH materials due to the existence of Ni in two redox states and several phases (see Table 1), including a difficult-to-leach oxide phase [46].

Reaction kinetics are very different for the three systems used in our study. If we consider the reaction as a whole, in the case of ferronickel slags, the reaction stopped after ~2 h in L and A-L modes, while the yield increases and reaches a plateau after ~20 h in AL mode (Figure 4a). For chalcopyrite leaching, the kinetics are higher in the first 50 h of reaction for the AL mode, reaching a 60% Cu extraction yield. Furthermore, even if the yield continues to increase with time for the three modes, the highest dissolution rate is with the AL mode (Figure 4b). For BM Ni-MH leaching, as mentioned earlier, the kinetics are globally similar for L and AL modes and the dissolution rate starts to decrease after ~5 h.

If we consider the first instants of the reactions for the three materials (plotted in the inserts of Figure 4a–c), we can observe some similarities. During the initial moments of the reactions, AL mode exhibits a higher dissolution rate than L mode for all materials, including BM Ni-MH (Figure 4a–c). In the experiments with ferronickel slags and chalcopyrite, the kinetics of A-L mode are initially higher than that of AL mode (Figure 4a,b), due to preliminary grinding resulting in enhanced reactive surface area. After 20 min for carbonation and 5 h for Cu leaching, the AL mode leads to faster kinetics. As discussed in previous studies [15,20], the formation of passivation layers quickly limits the reaction in the A-L mode, while these layers are peeled off in AL mode. AL mode

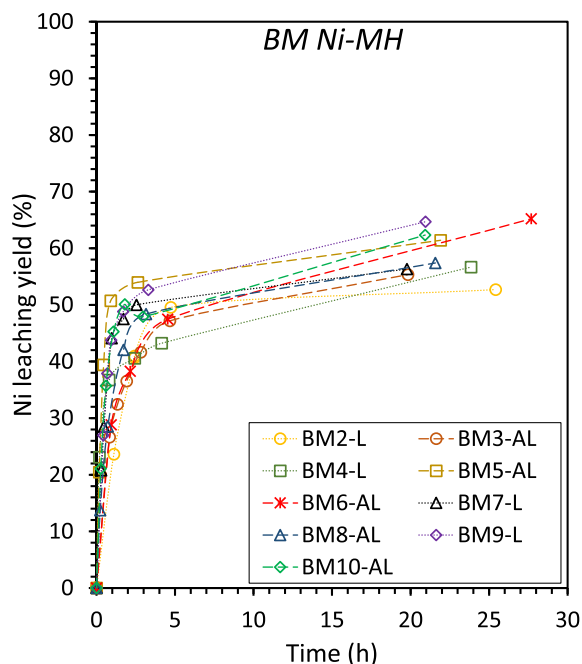


Figure 5. Leaching yields of Ni in aqueous H_2SO_4 solution at pH 1.0, $T = 40^\circ\text{C}$, $P = 1$ bar for BM Ni-MH leaching experiments, with different solid fractions (<100 and 100–500 μm), S/S+L ratios (1–10%), and amounts of beads (1–3 kg). Experimental conditions for each run are detailed in Table 3.

ability to depassivate particles during the reaction is the main advantage of *in situ* attrition compared to the mechanical activation implemented before the addition of the reactant in the A-L mode. It is important to note that each material presents its own characteristics, resulting in different choices of operating conditions (size fraction, S/S+L ratio, and amount of beads), as illustrated in Figure 4. Furthermore, parameters such as the ratio $m(\text{beads})/m(\text{solid})$ and S/S+L were investigated for the BM Ni-MH in this study, and the kinetics and yields (Table 3 and Figure 5) were similar.

Regarding leaching of BM Ni-MH, we analyzed the progression of acid consumption (thanks to 0.1 Hz monitoring) to better follow reaction kinetics during the initial 2-h period of leaching (see Figure 6). We assumed that acid consumption was proportional to the concentration of Ni in the aqueous phase,

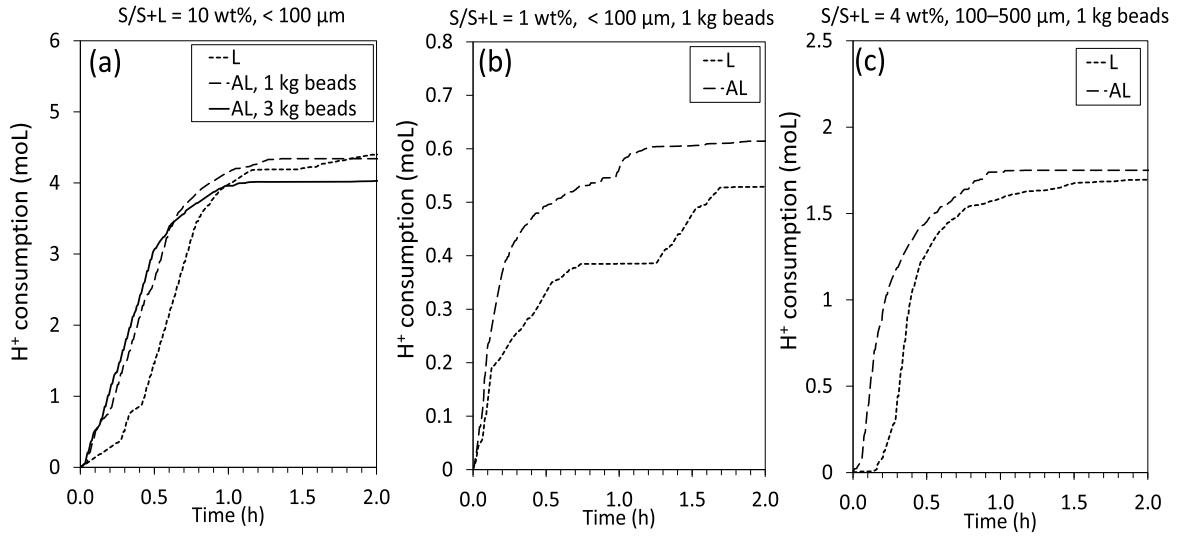
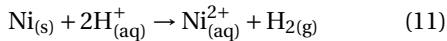
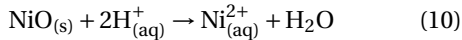


Figure 6. Acid consumption during the early stage of BM Ni-MH leaching experiments, with (L; leaching) and without beads (AL; attrition-leaching), for the size fraction $<100\ \mu\text{m}$ with $\text{S/S+L} = 10\ \text{wt\%}$ (a) and $\text{S/S+L} = 1\ \text{wt\%}$ (b) and for the size fraction $100\text{--}500\ \mu\text{m}$ with $\text{S/S+L} = 4\ \text{wt\%}$ (c).

as determined by the main dissolution reactions:



Based on data, it can be inferred that the dissolution reaction is faster with attrition-leaching than leaching only in the first hour, whatever the size fraction used (<100 or $100\text{--}500\ \mu\text{m}$, Figure 6b,c). Additionally, using a larger amount of beads (1 kg or 3 kg of beads, Figure 6a) did not show any impact.

3.2. Particle size distribution

Particle size was investigated for each system, based on the Malvern's PSD measurements and direct SEM observations of the particles recovered at the end of the experiments or sampled during the runs. For the three materials, SEM micrographs at the end of the experiments show that large grains ($>10\ \mu\text{m}$) are still present in the L mode experiments (Figure 7a,c,e), and the particles consisted of agglomerates ($5\text{--}50\ \mu\text{m}$) of very fine grains ($<100\ \text{nm}$) in the AL mode experiments (Figure 7b,d,f). The AL mode thus led to the formation of a large quantity of particles with a mean size below $1\ \mu\text{m}$, while the initial size was $\sim 50\ \mu\text{m}$.

As dissolution reactions are surface dependent, particle surface area distribution was estimated from the measured particle volume distribution (Figure 8a–c). The distributions were deconvoluted for similar reaction times (20–26 h) for the three materials by using a combination of 2 lognormal distributions $f_i(x)$ as shown below:

$$f(x) = \lambda f_1(x) + (1 - \lambda) f_2(x) \quad (12)$$

where $x = \text{Lognormal}(\mu_i, \sigma_i)$

where μ_i is the mean value and σ_i is the standard deviation of the i th lognormal distribution and λ is the proportion of the first distribution. The deconvolution with 2 lognormal distributions was deemed sufficient as it was clearly seen in most cases and it fitted rather well the particle surface area distributions at all selected reaction times for all three materials. As illustrated in Figure 8a–c, a significant size change occurred during the attrition-leaching process with the occurrence of a bimodal distribution for the three materials. The first mode (mode 1) corresponds to small agglomerates ($0.5\text{--}0.7\ \mu\text{m}$) that are likely due to the binding of smaller particles ($<100\ \text{nm}$), which is evidenced in the SEM pictures for the three materials (Figure 7b,d,f). The second mode (mode 2) corresponds to medium sized agglomerates ($\sim 1\text{--}10\ \mu\text{m}$). Initially, they include the original particles which are

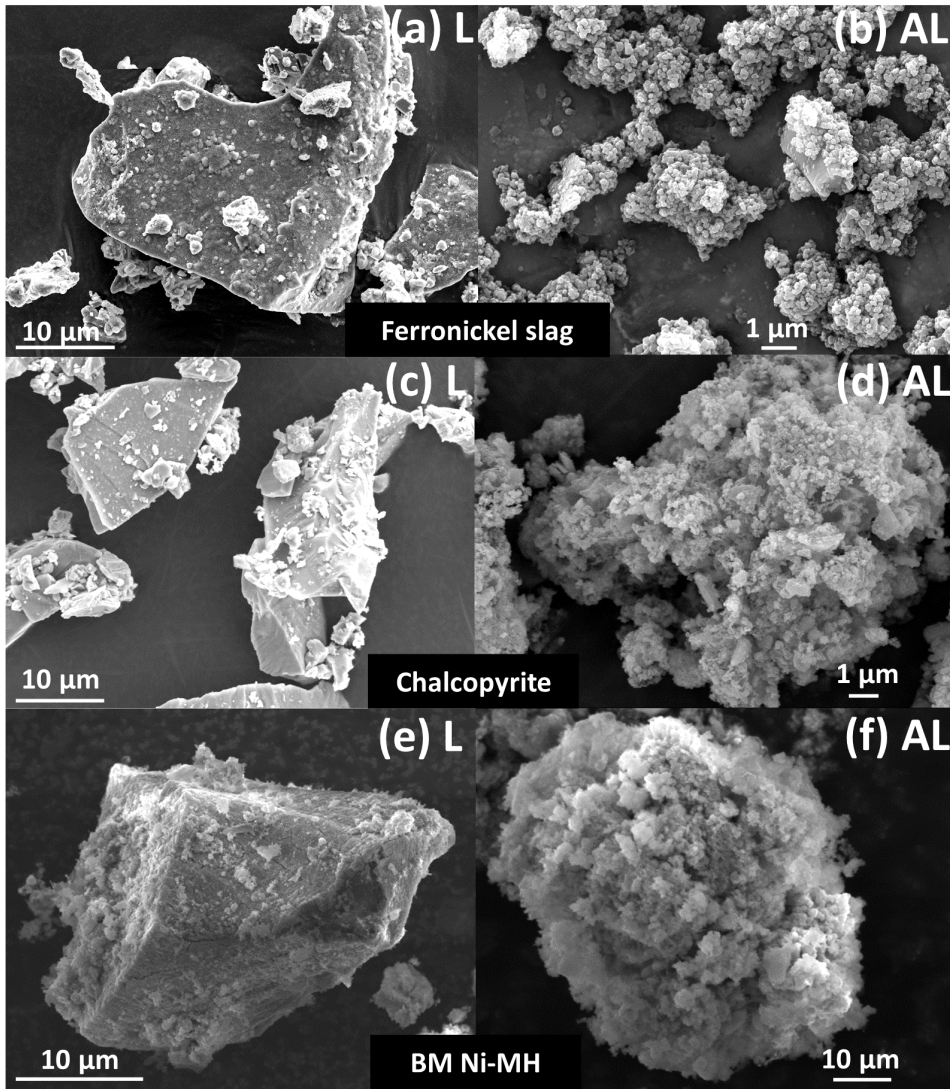


Figure 7. SEM micrographs of: ferronickel slag ($<100\ \mu\text{m}$) after leaching (a) and attrition-leaching (540 g of 1 mm beads) (b), at $150\ ^\circ\text{C}$, $P(\text{CO}_2) = 10\ \text{bar}$, $t = 24\ \text{h}$; raw chalcopyrite concentrate (c) and after 168 h of attrition-leaching (500 g of beads) (d) at $\text{pH} = 1.3$, $E_h = 700\ \text{mV vs SHE}$, $T = 42\ ^\circ\text{C}$, $t = 168\ \text{h}$; BM Ni-MH ($<100\ \mu\text{m}$) after leaching (e) and attrition-leaching (1 kg of beads) (f) at $\text{pH} = 1.0$, $T = 40\ ^\circ\text{C}$, $t = 24\ \text{h}$.

eventually subjected to abrasion and/or dissolution over time. In Figure 8b,c it can be seen that the proportion of the first mode compared to the second mode increases through time for chalcopyrite and BM Ni-MH materials. The particle size of the second mode also decreases through time, with a more pronounced effect for BM Ni-MH than for chalcopyrite. On the contrary, the proportion between these two

modes is quite constant for the experiments with ferronickel slags.

As schematized in Figure 9, our hypothesis to explain the formation of such similar agglomerates in each system is that a balance between the agglomeration of small particles and the breakage of large agglomerates is taking place. At the very beginning of the attrition-leaching process (between $t = 0\ \text{h}$ and

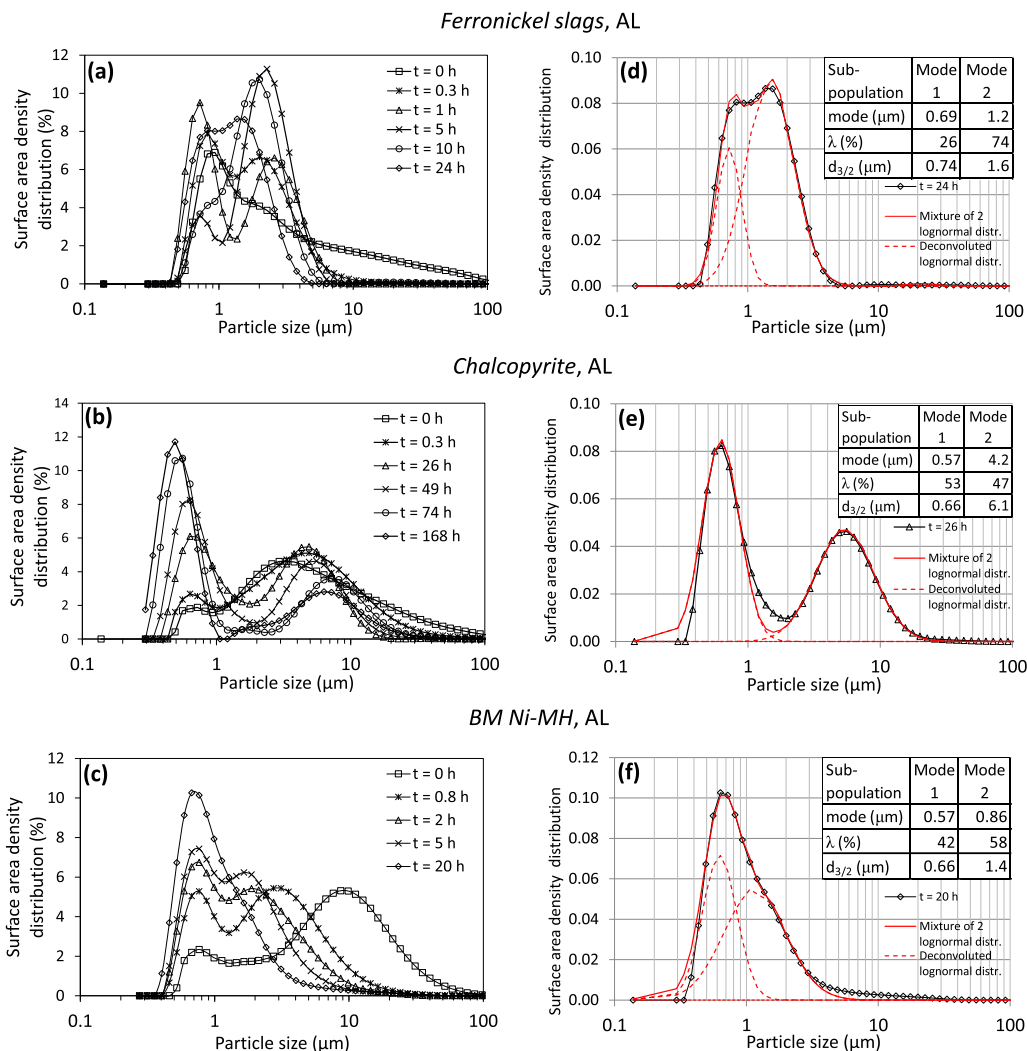


Figure 8. Surface area density distribution of particles sampled from the reactor at different reaction times during attrition-leaching (AL) of ferronickel slags (a), chalcopyrite (b) and BM Ni-MH (c), and their respective PSD surface deconvolution (d), (e) and (f), with corresponding distribution parameters, for similar reaction times (20–26 h).

$t = 0.3$ – 0.8 h), the particles larger than $10 \mu\text{m}$ are fragmented, leading to their disappearance, as can be seen in surface area density distribution of Figure 8a–c. It is worth noting that the first mode is very similar for the three materials, while the second mode differs significantly, highlighting a possible influence of the materials' nature on the breaking efficiency of the beads and on the cohesion of the nanometer-sized grains together to form more or less resistant agglomerates.

The following steps illustrate the successive and continuous synergistic mechanisms during the attrition-leaching process (Figure 9): (i) comminution increases the specific surface area; (ii) if a passivation layer forms, it is removed from the particle surface by attrition; (iii) re-agglomeration of the particles, leading to a decrease in the reactive surface and/or to diffusional effects; (iv) the re-agglomerated particles reach a size limit as they are partially fragmented by the beads.

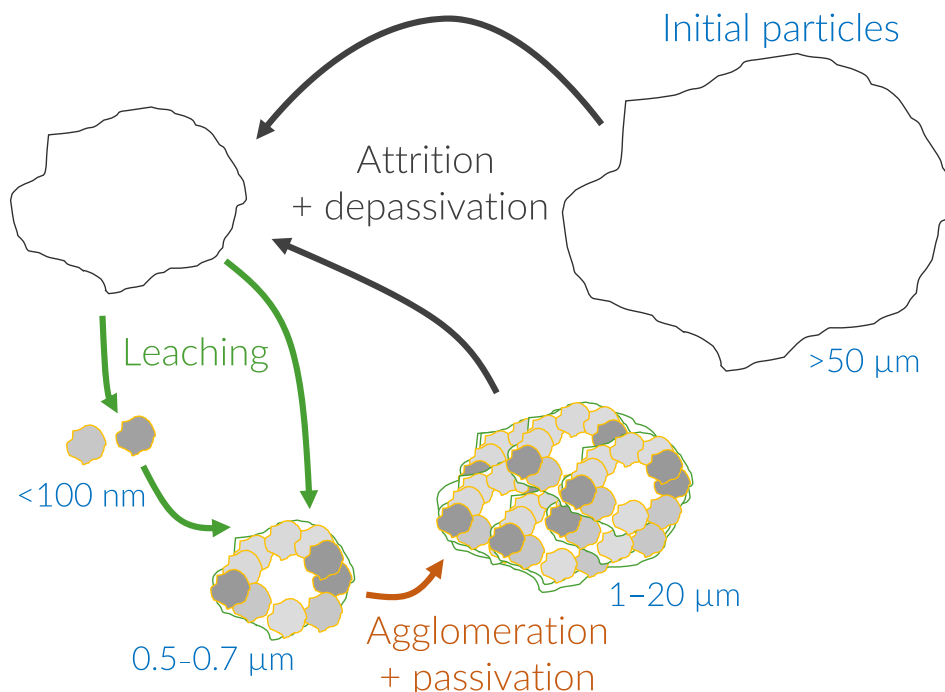


Figure 9. Scheme of concomitant particles' attrition and agglomeration to explain the particle size distribution and multi-scale aggregates.

3.3. A material-dependent synergy

Although the three processes considered in this work occur at different reaction timescales due to their chemical differences, the combination of leaching and attrition significantly enhances the extraction yields of both ferronickel slag carbonation and chalcopyrite leaching. Conversely, in the case of BM Ni-MH, no quantitative effect of attrition-leaching on the time-extraction yield of Ni was observed compared to leaching only (Figure 4 and Table 3). No particular effect of the amount of beads (1 or 3 kg of beads) or S/S+L ratio on the BM Ni-MH dissolution yield was observed either (Table 3). Nevertheless, similar attrition and particle breakage mechanism was observed for the three materials (Figure 8), as confirmed by the similarity of their PSD modes. The observed synergy in the attrition-leaching mode is a complex phenomenon likely caused by the continuous attrition of the reactive surface. An observation by transmission electron microscopy (TEM) of thin sections prepared with a focused ion beam (FIB) by Dufourny [20] showed that a potential source of the attrition-leaching synergy is the continuous de-

passivation of the reaction front. It was also found that the ratio of micropore to mesopore volume was 4 times lower for AL mode than for A-L and L modes, showing that the specific surface area also controls the kinetics and yields of the reaction.

In the case of BM Ni-MH material, we expected the porous insoluble layers to hinder the reaction rate. However, as attrition-leaching was only marginally beneficial to the dissolution of Ni in the initial moments of reaction due to particle grinding, our work showed that there was no passivation of BM grains, and thus the limitation in Ni leaching yield is due to other causes. The precipitation of potassium-REE double sulfate salts $\text{KREE}(\text{SO}_4)_2 \cdot \text{H}_2\text{O}_{(\text{s})}$ (see Equation (7)) may be responsible for Ni leaching inhibition. Such precipitation reaction takes place at high S/S+L ratios, when REE concentrations reach the solubility limit of the salts. As shown in Figure 10, we reached the REE solubility limit in some of our experiments, when the initial S/S+L was equal to 10 wt%, with a simultaneous decrease in La and K leaching yields in the fluid. The La extraction yields then remained below 40% after 5 hours of reaction, while La extraction yields were >70% with S/S+L

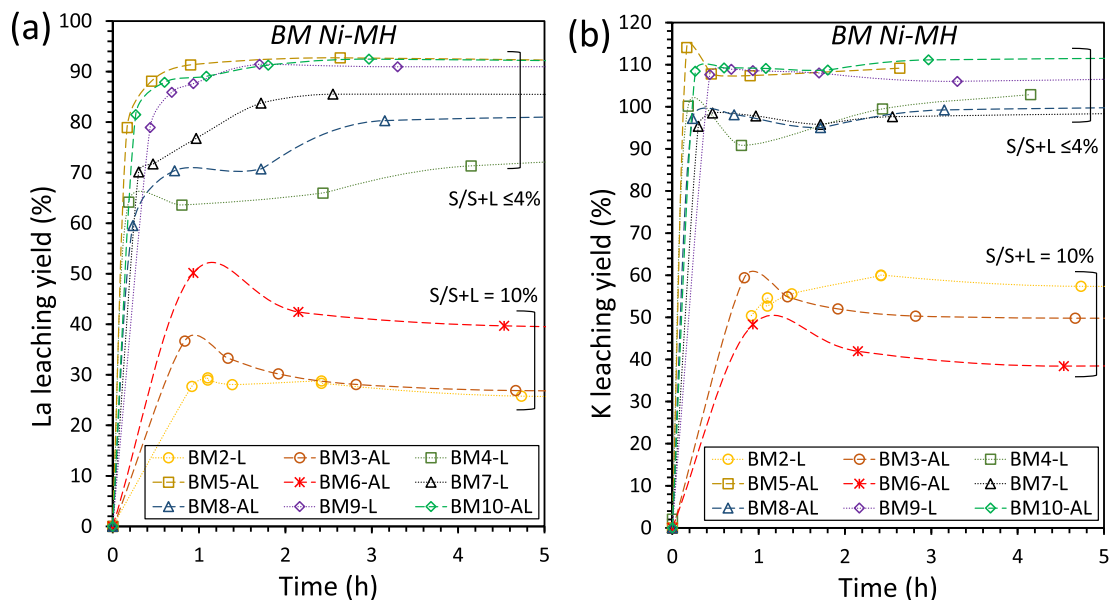


Figure 10. Leaching yields of La (a) and K (b) in aqueous H_2SO_4 solution at pH 1.0, $T = 40^\circ\text{C}$, $P = 1$ bar for BM Ni-MH leaching experiments. Experimental conditions for each run are detailed in Table 3. At $\text{S/S+L} = 10\%$ the double sulfate $\text{KREE}(\text{SO}_4)_2 \cdot \text{H}_2\text{O}_{(\text{s})}$ precipitates. K leaching yields above 100% are due to a light leak from the pH electrode (filled with KCl 3 M).

ratios of 4 wt% and 1 wt%. However, the precipitation of La did not interfere with the Ni dissolution yields as shown in experiments with S/S+L ratios of 10% (BM2-L, BM3-AL and BM6-AL) plotted in Figure 5, which have similar Ni dissolution yields than other experiments with S/S+L ratios lower than 4%. Furthermore, in the case of REE salts precipitation, the La extraction yields are similar for both AL and L modes with an S/S+L ratio of 10% (BM2-L and BM3-AL; Figure 10a). Since the presence of beads has no significant effect on the extraction yields of Ni, with and without REE salts precipitation, the limiting mechanisms are thus not related to diffusion through surface layers. Other hypotheses must be investigated to explain the limited Ni dissolution yield, which may be due to chemical limitations, such as limited dissolution of the different Ni phases in the black mass, specifically the nickel metal and the nickel oxide [23,46].

4. Conclusions and perspectives

Attrition-leaching is a simple and widely-applicable mechanochemical method for investigating leaching

reaction hindered by the formation of surface layers. In this study, the cases of three different materials were compared: ferronickel slags and chalcopyrite concentrates on one hand, using data from previous works, and BM Ni-MH on the other hand, based on a dedicated experimental study. The comparison shows that, at the very beginning of the reaction, the kinetics of the attrition-leaching process increases compared to leaching only, for all three materials. This is very likely due to the increase in reactive surface provoked by particles fragmentation. However, the subsequent influence of attrition on the yield depends directly on the material considered: in the case of ferronickel slag and chalcopyrite, a high gain is obtained with concomitant attrition, while in the case of BM Ni-MH there is no improvement.

Attrition-leaching appears to involve a synergistic mechanism that relies on the continuous abrasion of the surface layer. This layer can be a genuine passivation layer formed *in situ*, during the leaching reaction, due to the poor solubility of some secondary compounds, as in the case of ferronickel slag or chalcopyrite materials. It can also consist of an insoluble porous layer, as in the case of BM Ni-MH,

that does not control the leaching rate. The PSD analyses showed that, despite their very different leaching behavior, the three materials exhibited similar fragmentation effects, with comparable particle size distribution modes observed after sustained attrition. Furthermore, we showed that carrying out the leaching reactions in AL mode has a great potential to be studied further, including the potential mechano-chemical activation of refractory minerals, whose leaching may be inhibited by the formation of a passivation layer.

It is also important to note that attrition leaching experiments considered in this study were not optimized in terms of energy consumption. Indeed, the continuous energy-intensive agitation of the beads contained in the reactors lead to significant energy consumptions (e.g. 3.3 kWh/m³ for the glass reactor with 1 kg of glass beads). Therefore, if reaction times remain long, improvement of the system's efficiency and reduction of its energy consumption are required, for instance by utilizing a combination of short attrition-leaching steps and longer leaching only steps (e.g. [33]).

Acronyms

BM	Black mass
Ni-MH	Nickel-metal hydride
L	Leaching only
A-L	Attrition followed by leaching
AL	Attrition-leaching
S/S+L	Solid to liquid ratio
PSD	Particle size distribution

Declaration of interests

The authors do not work for, advise, own shares in, or receive funds from any organization that could benefit from this article, and have declared no affiliations other than their research organizations.

Funding

This work was funded by the French National Research Agency project BIOMECALIX (Grant No. ANR-18-CE07-003101), project Carmex (Grant No. ANR-08-PCO2-002), the New Caledonian Energy Agency

ACE (Grant No. CS17-3160-00) and the French Environment and Energy Management Agency ADEME (Grant No. 1894C0021).

Acknowledgments

We thank Boliden for the supply of chalcopyrite concentrate and we thank SNAM Group for the supply of black mass powder prepared from Ni-MH batteries. We also thank BRGM for collaboration with A.-G. Guezennec. The authors acknowledge the technical support at LGC Toulouse of M.-L. De Solan Bethmale, C. Rey-Rouch and A. Moreau for their contribution to chemical analyses and solid characterization. The contribution of J.-L. Labat, M. Riodel, L. Farhi, and Q. Ribière for the design and assembly of the experimental setup is gratefully acknowledged.

References

- [1] K. Binnemans, P. T. Jones, *J. Sustain. Metal.*, 2023, **9**, 1-25.
- [2] F. Faraji, A. Alizadeh, F. Rashchi, N. Mostoufi, *Rev. Chem. Eng.*, 2022, **38**, 113-148.
- [3] Q. Tan, J. Li, *Environ. Sci. Technol.*, 2015, **49**, 5849-5861.
- [4] O. S. Odebiyi, H. Du, B. Liu, S. Wang, *J. Sustain. Metal.*, 2022, **8**, 1393-1421.
- [5] J. Li, M. Hitch, *Miner. Eng.*, 2018, **128**, 69-83.
- [6] J. Pronost, G. Beaudoin, J. Tremblay, F. Larachi, J. Duchesne, R. Hébert, M. Constantin, *Environ. Sci. Technol.*, 2011, **45**, 9413-9420.
- [7] A. B. Ghacham, L.-C. Pasquier, E. Cecchi, J.-F. Blais, G. Mercier, *Environ. Sci. Pollut. Res.*, 2016, **23**, 17635-17646.
- [8] A. Ben Ghacham, L.-C. Pasquier, E. Cecchi, J.-F. Blais, G. Mercier, *J. Cleaner Prod.*, 2017, **166**, 869-878.
- [9] S. Ó. Snæbjörnsdóttir, B. Sigfússon, C. Marieni, D. Goldberg, S. R. Gislason, E. H. Oelkers, *Nat. Rev. Earth Environ.*, 2020, **1**, 90-102.
- [10] N. Thonemann, L. Zacharopoulos, F. Fromme, J. Nühlen, *J. Cleaner Prod.*, 2022, **332**, article no. 130067.
- [11] P. Baláz, M. Achimovičová, *Hydrometallurgy*, 2006, **84**, 60-68.
- [12] C. Julcour, F. Bourgeois, B. Bonfils, I. Benhamed, F. Guyot, F. Bodéan, C. Petiot, É. C. Gaucher, *Chem. Eng. J.*, 2015, **262**, 716-726.
- [13] C. Julcour, L. Cassayre, I. Benhamed, J. Diouani, F. Bourgeois, *Front. Chem. Eng.*, 2020, **2**, article no. 588579.
- [14] G. Rim, D. Wang, M. Rayson, G. Brent, A.-H. A. Park, *Indust. Eng. Chem. Res.*, 2020, **59**, 6517-6531.
- [15] A. Dakkoune, F. Bourgeois, A. Po, C. Joulain, A. Hubau, S. Touzé, C. Julcour, A.-G. Guezennec, L. Cassayre, *ACS Eng. Au*, 2023, **3**, 195-209.
- [16] G. S. Anderson, P. A. Bandarian, *Miner. Eng.*, 2019, **132**, 211-219.
- [17] F. Bodéan, F. Bourgeois, C. Petiot, T. Augé, B. Bonfils, C. Julcour-Lebigue, F. Guyot, A. Boukary, J. Tremosa, A. Lassin, E. C. Gaucher, P. Chiquet, *Miner. Eng.*, 2014, **59**, 52-63.

- [18] F. Bourgeois, P. Laniesse, M. Cyr, C. Julcour, *Front. Energy Res.*, 2020, **8**, article no. 113.
- [19] F. Gao, Z. Huang, H. Li, X. Li, K. Wang, M. F. Hamza, Y. Wei, T. Fujita, *J. Cleaner Prod.*, 2021, **303**, article no. 127049.
- [20] A. Dufourny, C. Julcour, J. Esvan, L. Cassayre, P. Laniesse, F. Bourgeois, *Front. Clim.*, 2022, **4**, article no. 946735.
- [21] A. Ghahremaninezhad, D. G. Dixon, E. Asselin, *Electrochim. Acta*, 2013, **87**, 97-112.
- [22] M. Kartal, F. Xia, D. Ralph, W. D. A. Rickard, F. Renard, W. Li, *Hydrometallurgy*, 2020, **191**, article no. 105192.
- [23] M. Zielinski, L. Cassayre, P. Destrac, N. Coppey, G. Garin, B. Biscans, *ChemSusChem*, 2020, **13**, 616-628.
- [24] L. Cassayre, B. Guzhov, M. Zielinski, B. Biscans, *Renew. Sustain. Energy Rev.*, 2022, **170**, article no. 112983.
- [25] F. Abdul, A. Iizuka, H.-J. Ho, K. Adachi, E. Shibata, *Environ. Sci. Pollut. Res.*, 2023, **30**, 78041-78074.
- [26] D. Daval, O. Sissmann, N. Menguy, G. D. Saldi, F. Guyot, I. Martinez, J. Corvisier, B. Garcia, I. Machouk, K. G. Knauss, R. Hellmann, *Chem. Geol.*, 2011, **284**, 193-209.
- [27] F. Farhang, T. K. Oliver, M. S. Rayson, G. F. Brent, T. S. Molloy, M. Stockenhuber, E. M. Kennedy, *J. CO₂ Util.*, 2019, **30**, 123-129.
- [28] G. M. O'Connor, J. J. Eksteen, *Miner. Eng.*, 2020, **154**, article no. 106401.
- [29] C. Lv, H. Wu, W. Lin, J. B. Illerup, A. P. Karcz, S. Ye, A. J. Damø, *Hydrometallurgy*, 2019, **188**, 22-30.
- [30] R. P. Hackl, D. B. Dreisinger, E. Peters, J. A. King, *Hydrometallurgy*, 1995, **39**, 25-48.
- [31] J. Li, N. Kawashima, K. Kaplun, V. J. Absolon, A. R. Gerson, *Geochim. Cosmochim. Acta*, 2010, **74**, 2881-2893.
- [32] Y. Li, B. Wang, Q. Xiao, C. Lartey, Q. Zhang, *Hydrometallurgy*, 2017, **173**, 149-155.
- [33] M. Mulligan, *J. South. Afr. Inst. Min. Metall.*, 2017, **117**, 741-747.
- [34] A. V. G. Chizmeshya, M. J. McKelvy, K. Squires, R. W. Carpenter, H. Bearat, *A Novel Approach to Mineral Carbonation: Enhancing Carbonation While Avoiding Mineral Pretreatment Process Cost*, Arizona State University, Tempe, AZ, 2007.
- [35] S. Chalouati, A. Yoosefdoost, Y. W. Chiang, R. M. Santos, *Int. J. Coal Geol.*, 2023, **277**, article no. 104332.
- [36] X. Ke, V. A. Baki, L. Skevi, *J. CO₂ Util.*, 2023, **68**, article no. 102367.
- [37] J. R. Cobble, C. E. Jordan, D. A. Rice, *Hydrometallurgical Production of Copper from Flotation Concentrates*, U.S. Department of the Interior, Bureau of Mines, 1993.
- [38] M. Minagawa, S. Hisatomi, T. Kato, G. Granata, C. Tokoro, *Adv. Powder Technol.*, 2018, **29**, 471-478.
- [39] G. Granata, K. Takahashi, T. Kato, C. Tokoro, *Miner. Eng.*, 2019, **131**, 280-285.
- [40] S.-T. Cao, X.-F. Zheng, Z.-Y. Nie, Y.-H. Zhou, H.-C. Liu, J.-H. Chen, H.-Y. Yang, J.-L. Xia, *Minerals*, 2020, **10**, article no. 788.
- [41] L. Mussapyrova, R. Nadirov, P. Baláž, M. Rajňák, R. Bureš, M. Baláž, *J. Mater. Res. Technol.*, 2021, **12**, 2011-2025.
- [42] A. Porvali, S. Ojanen, B. P. Wilson, R. Serna-Guerrero, M. Lundström, *J. Sustain. Metal.*, 2020, **6**, 78-90.
- [43] M. Zielinski, L. Cassayre, P. Floquet, M. Macouin, P. Destrac, N. Coppey, C. Foulet, B. Biscans, *Waste Manage.*, 2020, **118**, 677-687.
- [44] L. Cassayre, F. Bourgeois, C. Julcour-Lebigue, I. Benhamed, J. Diouani, K. Nahdi, *IMPC 2016: XXVIII International Mineral Processing Congress Proceedings*, Curran Associates, 2016, 1 pages.
- [45] A. Hubau, A.-G. Guezennec, C. Joulain, C. Falagán, D. Dew, K. A. Hudson-Edwards, *Hydrometallurgy*, 2020, **197**, article no. 105484.
- [46] M. Takano, S. Asano, M. Goto, *Hydrometallurgy*, 2022, **209**, article no. 105826.
- [47] A. M. A.-A. Otron, T. Millogo, L.-H. Tran, J.-F. Blais, *Environ. Technol.*, 2023, 1-13.



Research article

GDR Prométhée – French Research Network on *Hydrometallurgical Processes for Primary and Secondary Resources*

Copper leaching with aqueous foams for the processing of electronic waste

Emilie Régnier^a, Agathe Hubau^{*,b}, Solène Touzé^{*,b}, Sylvain Guignot^{*,b}, Daniel Meyer^a, Olivier Diat^{*,a} and Damien Bourgeois^{*,*,a}

^a Institut de Chimie Séparative de Marcoule, ICSM, CEA, CNRS, ENSCM, Univ Montpellier, BP 17171, Marcoule, 30207 Bagnols-sur-Cèze, France

^b BRGM, F-45060 Orléans, France

E-mail: damien.bourgeois@umontpellier.fr (D. Bourgeois)

Abstract. Aqueous foams have been used in various hydrometallurgical processes, and have recently emerged as an alternative technique for the leaching of metallic copper, using hydrochloric acid and O₂ from air as an oxidant. In the present study, we describe how this technique has been successfully applied to the leaching of copper from waste printed circuits boards (WPCBs). First of all, the use of HCl based foams was successfully applied to the leaching of sole copper, and the impact of the size of copper particles was studied. It was demonstrated that use of mixtures of fine and large particles give excellent results. Then, on ground WPCBs, a first classical leaching stage using aqueous HCl solution was performed in order to remove maximum quantity of reducible metals (aluminum, iron, zinc...). Then, almost quantitative copper leaching employing HCl based foam was performed. Copper is almost exclusively leached during this stage, and the complete mass balance in 5 major metals present in WPCBs (aluminum, iron, zinc, nickel and copper) is detailed. Kinetics of the copper leaching were greatly enhanced through addition of substoichiometric quantity of cupric ions at the beginning of the process, so that extensive grinding of the waste is not necessary.

Keywords. Foams, Copper, Leaching, Shredding.

Funding. ANR-17-CE08-0016 FOAMEX.

Manuscript received 14 December 2023, revised 1 March 2024, accepted 11 April 2024.

1. Introduction

Aqueous foams, which are composed of air bubbles separated by thin liquid films stabilized by surfactant molecules, have been widely used in hydrometallurgy for the concentration of various species: ions, colloids, ore particles, microorganisms [1–5]... At industrial scale, foams are often employed to separate mineral particles in froth flotation processes [6]. Their use has been extended to various extraction

processes such as deinking of aqueous solutions via flotation [7,8], and in the nuclear industry for extraction and concentration of uranium, in aggressive and strongly acidic environments [9,10]. All these examples take benefit of the peculiar features of liquid foams: These foams are mostly composed of gas, so that less than 10% of their volume fraction is water, even less than 5% in the case of dry foams. The resulting volume of aqueous phase to be treated is considerably reduced. However, to be effective in terms of extraction, the extraction must be carried out through the liquid gas interfaces developed in the

*Corresponding author

foam, and not by the transport of the liquid in the aqueous films, as this fraction must be minimized. The gas can be inert (N_2), simply air, containing O_2 , or also more reactive such as an O_3/O_2 mixture. The use of an oxidizing gas brings additional reactivity to the solutes in the aqueous phase. Foams also contain surface active agents, which have detergency properties and can remove impurities from a surface and/or activate it. The choice of the surfactant is key for the stability of the foams, as the lifetime of the foams strongly depends on coalescence of bubbles, facilitated by the drainage of liquid out of the films [11]. Coalescence events lead e.g. to the detachment of mineral particles from the interface and loss of the particles into the initial slurry during flotation processes. Leaching of ores using foams was proposed in the 70's [12], however with scarce applications so far to our knowledge. Recently, the possibility to use foam based on diluted aqueous hydrochloric or sulfuric acid solutions for the leaching of metallic copper or silver has been demonstrated [13]. The perspectives opened by these model studies drove our attention to the application of foams for the leaching of copper from electronic waste (e-waste).

The recovery of metals from e-waste, known as Urban mining [14–16], has drawn considerable attention during last decade. The high content in copper, much higher than in natural ores, has led to the set-up of pyrometallurgical and hydrometallurgical processes dedicated to copper recovery [17]. Latter processes always rely on a leaching stage, generally based on the use of a large amount of a concentrated aqueous solution. In the case of copper, it is well known that the sole action of H^+ in the acid is not sufficient to leach metallic copper, and that an oxidant is needed [18]. Metallic copper is thus generally leached using nitric acid, ferric sulphate in sulfuric acid, or a mixture of hydrochloric acid with hydrogen peroxide [19]. Electroleaching can also be implemented, either directly on adequate waste which are connected to the anode, or indirectly through the electrogeneration of a reactive intermediate such as chlorine in chloride media [20]. Latter two approaches require specific equipment. The use of O_2 as an oxidant suffers from slow gas–liquid transfer, so that the use of a hydrochloric acid solution stirred under air is not sufficient for copper leaching. Acceleration of gas–liquid transfer when employing a foam proved to be sufficient to observe significant leaching

of copper in the above mentioned study [13], which lets suggest that further process development is possible using air as oxidant. It is thus the purpose of this article to report our progress on the leaching of copper from e-waste with hydrochloric acid-based foams. Brij®S10 (polyoxyethylene(10) stearyl ether, $C_{18}H_{37}(OCH_2CH_2)_nOH$, $n \sim 10$) was employed to generate the foam, as it is a standard neutral surfactant readily available at industrial scale, which is known for its good foaming ability and stability in acidic media [21], and has been previously studied in our laboratory [22]. The present study resulted in a leaching strategy based on two stages, which enables efficient recovery of base metals, with most copper almost quantitatively leached during the second stage employing an acidic foam.

2. Materials and methods

Approximately 500 kg of waste printed circuits boards (WPCB) were provided by a waste recovery company operating in France. Concentrated nitric acid and concentrated hydrochloric acid were purchased from Carlo Erba reagents. Surfactant Brij®S10 (polyoxyethylene(10) stearyl ether, $C_{18}H_{37}(OCH_2CH_2)_nOH$, $n \sim 10$) was purchased from Sigma-Aldrich and used without further purification. Gas used was filtered air provided through a compressor.

2.1. Grinding of e-waste

Batteries and aluminum heat sinks were first manually disassembled from WPCB before the entire sample (485 kg) was shredded with an industrial cutting mill to a particle size of less than 30 mm. The sample was subsequently quartered with a rotary divider; one quarter (122 kg) of the sample was then shredded anew, with an industrial cutting mill equipped with a bottom sieve with perforation size of 10 mm. The –10 mm sample was further divided with a rifle splitter to obtain sub-sample masses of approximately 4 kg. Two of these fractions were gathered to form a sample of 7.4 kg, which was then shredded in its entirety in a lab knife mill (Retsch SM2000 with tungsten carbide grinding tools), fitted with a bottom sieve with perforation size of 2 mm. The weights of the disruptive materials and of the lost material amounted to less than 9 and 1% of the initial

Table 1. Average composition of ground WPCB particles according to their size

Particles size	Weight content ^a					
	Cu (%)	Fe (%)	Ni (%)	Pb (%)	Zn (%)	Co (mg/kg)
>2 mm	13.0	57.1	0.99	0.14	2.28	485
1–2 mm	15.2	11.2	0.43	1.06	1.89	78
500 μm –1 mm	25.2	8.3	0.50	1.74	1.95	551
250–500 μm	24.0	7.7	0.50	1.58	1.40	845
100–250 μm	18.8	9.8	0.40	1.50	1.40	818
63–100 μm	5.5	19.3	0.46	1.55	1.53	557
40–63 μm	2.7	15.2	0.32	1.00	1.07	240
<40 μm	2.5	9.3	0.35	1.53	1.33	162
Total	17.8	12.4	0.47	1.25	1.83	314
0–750 μm	15.9 (1.8)	14.8 (1.2)	0.38 (0.07)	1.3 (0.2)	1.8 (0.3)	392 (107)

Note: ^a The sum of contents in metals does not reach 100% as WPCB also contain organic polymers and inorganic (glass) fibers.

materials respectively. The former were added to the final ground sample to produce the same composition as the original WPCB materials. This sample was then dry-sieved up to 500 μm , and wet-sieved from 500 μm down to $-40 \mu\text{m}$.

2.2. Elemental analysis of WPCB samples

Samples of weights varying between 4 and 6 g were taken from each of the previously formed size fraction, and subjected to a hot, atmospheric leaching in aqua regia, at 200 °C during 2 h. After cooling, each leachate was filtered (filter porosity of 43 μm), and the resulting filtrate was diluted with weakly concentrated nitric acid (0.5 mol·L⁻¹). The concentrations of Fe, Cu, Ni, Zn, Pb and Co in the filtrates were measured by flame AAS (VARIAN 220 FS).

2.3. Leaching using foam

In a 250 mL two-neck round bottom flask, was introduced the solid (either Cu 40 μm powder, Cu wire, Cu 1 mm beads, or samples of ground WPCB detailed in Table 1) to be leached (ca. 500 mg, weighed with precision), followed by 10 mL of a 2 mM BrijS10 aqueous HCl solution of fixed concentration (see text for details). Air was bubbled during ca. 5 min using a fritted glass tube, at 5 mL/min flow, to grow the foam to approximatively 100 mL (a mark was put on

the outside of the flask). The flask was then connected to a Buchi rotavapor, and rotated at 100 rpm. At fixed time intervals, rotation was stopped and the system was left to settle over few min, an aliquot of the leaching aqueous solution was taken (ca. 200 μL using a glass Pasteur pipette) and centrifuged during 1 min at 6000 rpm, and 100 μL of resulting solution were taken and diluted into a 1.0% (w/w) HCl/HNO₃ with HNO₃/HCl = 9 (v/v) aqueous solution. Air was also regularly reinjected, approximatively once per h, to regenerate the foam as it progressively collapses. Concentrations of metals in the aliquots were determined by inductively coupled plasma atomic emission spectroscopy (ICP/AES, SPECTRO ARCOS ICP Spectrometer, AMETEK Materials Analysis). Given concentrations are calculated as the means of three replicates on three different wavelengths for each metal; relative standard deviations were determined and lie between 1 and 4%.

2.4. Pre-treatment of PCB particles

About 5 g of WPCB weighed with precision were put in contact with 60 mL (L/S ratio: 12 mL/g of solid) of an aqueous 3 M HCl solution in a glass vial. The resulting mixture was heated to 60 °C and stirred for 3 h at room temperature (20 °C \pm 2 °C). The resulting mixture was then filtered on a Büchner set-up equipped with a paper filter under vacuum. The resulting solid was used without further treatment for

subsequent leaching using foam, or stored in glass vials under N_2 atmosphere.

3. Results and discussion

3.1. Grinding of e-waste

The collected WPCB were first of all shredded and ground. In order to evaluate the optimal size for leaching stage, various fractions have been sieved and collected (Table 1).

The copper content is strongly dependent on the size of the particles. The large particles contain much more copper, which can be related to the fact that (i) copper is employed in coils of wires and printed circuits, and (ii) copper is a ductile metal, difficult to shred into tiny pieces. Thus, the leaching efficiency according to mean copper particle size rapidly appeared as a key point to study [23].

3.2. Set up of experimental device for foam leaching

The design of solid–liquid–gas reactors has been the subject of numerous chemical engineering studies, which will not be discussed here. In the frame of this study, several approaches have been envisioned to design a suitable tool for leaching experiments at the laboratory scale. First of all, a classical column was tested, but it rapidly appeared that it is complicated to have an homogeneous suspension of particles in the foam. Dense particles, and especially large copper particles, tend to fall to the bottom of the column and thus in the liquid employed to generate the foam. Light particles are rapidly expelled from the column at the front-end of the foam, and hydrophobic particles accumulate at the periphery of the column, with very poor contact with foam (see Figure S11). As it is important to have a homogeneous dispersion of the solid in the foam we turned to a rotating drum, which can be easily simulated with classical laboratory apparatus and glassware (Figure 1).

First set-up was based on a simple round bottom flask attached to a mechanical stirrer inclined with an about 30° angle, and placed on a wooden support that would limit friction during rotation. The set up was upgraded using a Buchi rotavapor, which limits friction and enables to heat the flask at a controlled temperature using a water bath if desired. A two-neck

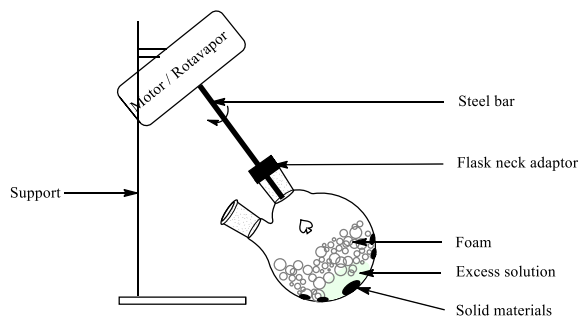


Figure 1. Schematic description of the experimental procedure employed for ground WPCB leaching using foams.

flask was employed to enable regular sampling of the reaction mixture, and if necessary gas injection to regenerate the collapsed foam. Leaching was performed at room temperature: in these conditions, foam remains stable over more than 1 h without further gas injection. Experiments at 40 °C were attempted in order to increase leaching rate, however, gas injection was necessary after 15 min as the foam collapsed more quickly, so that the effect of temperature has not been investigated. Such a laboratory set-up is seen as a rough model for rotating drum devices, which have been developed at large scale for leaching of various solids including e-waste, as well as other classical operations such as filtration. In our study we did not investigate the optimal volume of foam to employ, as a small volume of liquid may lead to very large volumes of foams, which could be an important drawback for further scaling-up or industrial application. Each leaching experiment was repeated at least three times, and the error bars displayed result from the mean results over these repetitions.

3.3. Leaching of pure metallic copper

The first studies on pure metallic copper led to mitigated results (Figure 2). First of all, as expected, small particles (copper powder, 40 μm average particle size) led to rapid dissolution. But larger particles (copper beads, 1 mm diameter) led to sluggish Cu leaching. Latter result could be explained by the fact that the beads sink and stay at the bottom of the rotating flask. On the other hand, the small metallic particles were well dispersed in the foam, facilitating the contact to liquid (HCl) and gas (O_2 in

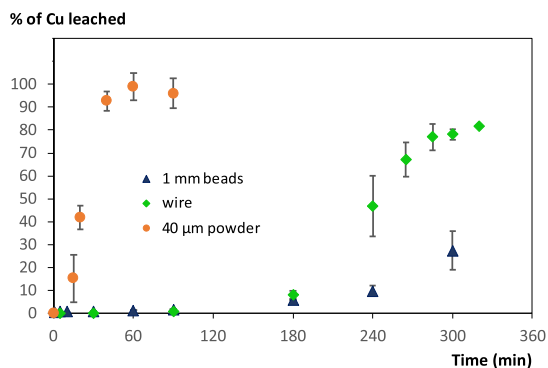


Figure 2. Evolution of Cu leaching using foams according to the Cu source (foam prepared using 3 M HCl and 2 mM Brij S10, 10 mL of liquid for 500 mg solid).

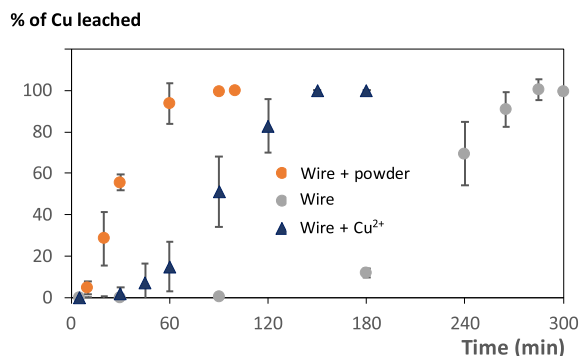


Figure 3. Evolution of Cu wire leaching using foams upon addition of 40 μm Cu powder or 10 wt% CuSO_4 (foam prepared using 3 M HCl and 2 mM Brij S10, 10 mL of liquid for 500 mg solid).

air) necessary for the reaction. However, results on Cu wire were quite disappointing, even if the wires did not sink in the solution and were well dispersed in the foam. These results will be discussed later in the paper. Similar experiment conducted in solution without surfactant and with continuous air bubbling (5 mL/min) led to 2 to 3 times lower Cu dissolution yield, even after 5 h. In parallel, experiments performed with the surfactant but without addition of air led to negligible dissolution. It is reasonable to assume that the use of foams enables a better transfer of gas into the liquid. As described before [13], two physical transfer reactions are important: (i) gas-liquid transfer of O_2 , and (ii) diffusion of dissolved O_2 and HCl in the liquid phase towards the surface of the solid. These issues are easily answered using liquid foams. The liquid fraction of foams was not properly controlled in our system, in comparison with previous work [13], only adjusted through regular bubbling in the foam to reach a ca. 10 fold volume of liquid initially employed. The concentration in surfactant (2 mM) was fixed to ensure sufficient stability of the foam: lower concentration led to progressive collapse of the foam, whereas higher amount did not increase foam stability.

The kinetic profile also rose our attention. The initial Cu dissolution rate is close to zero in the case of beads and wire, and appears to be low in the case of powder, as if an initiation step was necessary in the Cu dissolution mechanism. Furthermore, the sigmoidal profile observed suggests an autocatalytic

mechanism. Such an autocatalytic mechanism has been previously reported in ammonia solutions [24]. Depending on the oxygen (and ammonia) concentration, the autocatalytic term was found to be predominant. To our knowledge, no similar mechanism study on metallic copper has been performed in chloride media, although the oxidizing features of cupric chloride are well known, and have been employed for copper minerals [25] or even gold [26] leaching. In the present study, the occurrence of an autocatalytic mechanism and the impact of cupric ions were clearly proven by two key experiments (Figure 3): First of all, addition of a small quantity of Cu^{2+} ions (10% respective to totally Cu content) led to a decrease by a factor of 2 of the duration needed for complete Cu dissolution. More impressive was the gain in Cu dissolution observed when starting from a 1/1 mixture of wire and powder: The kinetics profile was very close to that observed with Cu powder alone (see Figure SI2). The remarkable increase in reaction kinetics can be interpreted from a chemical point of view by dissolution of Cu metal by Cu^{2+} ions present in solution rather than by dissolved O_2 and H^+ , as latter reaction involves 3 reagents (Cu, O_2 and H^+ ions). However, there is still a visible induction period, suggesting that the surface state of the Cu metal is also important. Physical activation of the Cu via e.g. Friction with the Cu particles can be envisioned. Latter parameter was not further investigated, as available reports in the literature suggest very complex mechanisms [27].

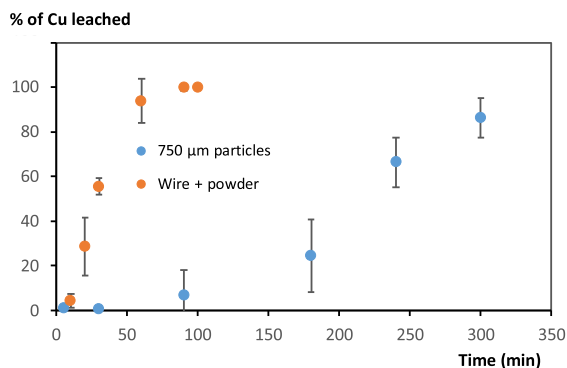


Figure 4. Evolution of Cu leaching from WPCB particles using foams, with comparison with a mixture of Cu wire and Cu 40 µm powder (foam prepared using 3 M HCl and 2 mM Brij S10, 10 mL of liquid for 500 mg solid).

Altogether, these results suggest that the presence of copper particles of various dimensions in the ground e-waste is a favorable factor for efficient copper leaching, and we turned to leaching experiments on a real sample of ground WPCB, of size lower than 750 µm, obtained after classical shredding and grinding operations of composition given in Table 1.

3.4. Leaching of copper from ground e-waste

Copper leaching from ground WPCB with foam using the experimental conditions described above led to rather poor results in comparison with previous results obtained on pure metallic copper (Figure 4). The dissolution of Cu is (i) incomplete and (ii) much slower than in the case of the mixture of Cu powder and Cu wire described in previous section (and even slower than in the case of Cu wire alone).

E-waste are composed of numerous metals, with most of them expected to be oxidized more easily than copper (Table 1). The leaching of metallic copper is based on an acidic oxidizing process, and in these conditions, other metals such as Zn, Fe, Ni, Al, etc... which are more reducible than Cu are expected to be also leached [28]. Consequently, it is reasonable to suppose that experiments led on ground WPCB did not give satisfactory results regarding Cu leaching, as these other metals were preferentially attacked, and Cu preserved. After 5 h reaction time, the solution was still very acidic (control using pH

Table 2. Leaching yield of Al, Fe and Cu upon treatment of ground WPCB with aqueous HCl of variable concentration during 5 h at room temperature (5 g of ground WPCB, size <750 µm, for 60 mL aqueous HCl solution)

Metal	HCl concentration (mol·L ⁻¹)			
	0.1	1	3	5
Cu	<1%	<1%	1%	3%
Fe	8%	15%	24%	22%
Al	5%	56%	92%	95%

paper) and simple calculation showed that protons were still in large excess: the limit in Cu leaching probably arises from kinetic limitations, but we did not continue the experiment over a longer period for practical reasons. Rather, a first treatment of ground WPCB was set in place. Attack of the solid with aqueous HCl in solution led to significant leaching of Al, and no leaching of Cu (Table 2). Leaching of other metals such as Fe, was moderate (Table 2). Al leaching kinetics were rapid (Figure SI3), but Fe leaching was much slower, and difficult to push to completion (Table SI1).

Such a pre-treatment of ground WPCB should thus improve the efficiency of Cu leaching with the foam as less acid should be consumed by metals more reducible than Cu such as Al. Also, the possibility to leach sequentially different metals using the same acid is appealing: It can be envisioned to leach reducible metals with HCl alone, then Cu with HCl and O₂ in the foam, leaving noble metals in the residue for further treatment (not discussed in this article). Thus, ground WPCB (size <750 µm) was processed in two stages: In a first stage, Al and some Fe were leached using a 3 M HCl solution (L/S ratio: 12 mL/g of solid). This operation does not leach significant Cu quantity (Table 2). In a second stage, the residue was further treated with an HCl based foam, and the Cu leaching is almost complete (Figure 5).

Although the Cu leaching yield is almost quantitative (97 ± 3%), the leaching rate remains low, and the improvement regarding the untreated WPCB sample appears marginal. Therefore, we decided to have a closer look at the impact of the fineness of the grinding. Two particle fractions obtained after sieving and rich in Cu were studied (Figure 6).

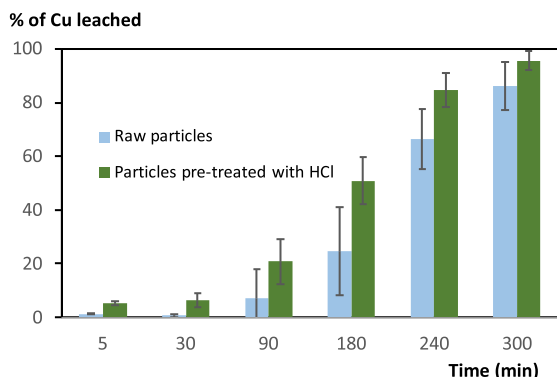


Figure 5. Influence of preliminary treatment of ground WPCB with aqueous HCl (60 mL of 3 M aqueous HCl solution for 5 g of ground PCB during 3 h at room temperature) on the outcome of Cu leaching using foam (foam prepared using 3 M HCl and 2 mM Brij S10, 10 mL of liquid for 500 mg solid).

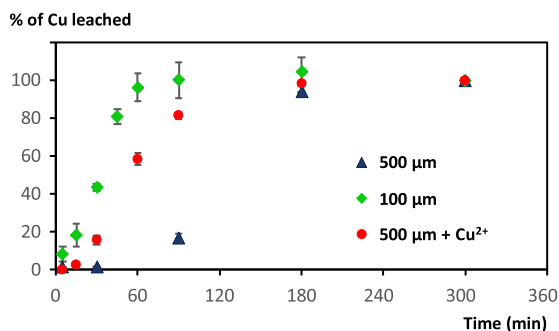


Figure 6. Rate of Cu leaching from WPCB particles using foams according to the particles size (foam prepared using 3 M HCl and 2 mM Brij S10, 10 mL of liquid for 500 mg solid).

As observed previously on metallic Cu alone, leaching is more rapid when mean particle size is smaller. Quantitative Cu leaching was observed on the 100–250 µm fraction after 2 h, whereas the reaction profile on the 500–1000 µm particles fraction is sluggish, and quite similar to the non-sieved (<750 µm) batch previously employed. Also, addition of 10% Cu²⁺ ions enabled to increase the leaching rate (Figure 6). There seems to be still a short induction time, shorter than that observed on Cu wire (Figure 3). This point was attributed to the fact that during the pre-treatment, the very fine Cu particles should be preferentially dissolved, as they are

more reactive. Altogether these results demonstrate that fine grinding of WPCB is not compulsory for efficient Cu recovery using foams. A minimum of grinding is necessary to achieve liberation of all Cu contained inside components, but excessive grinding is useless as leaching efficiency can be attained by initial addition of a small quantity of Cu²⁺ ions, which will be recovered afterwards. Also, in a continuous process, there should be always some Cu present in the leaching solution as Cu²⁺ ions. Furthermore, as stated beforehand, Cu is difficult to grind into very fine particles, and most Cu is contained in large particles: The 500–1000 µm fraction is the richest in Cu compared to other fractions. To our knowledge, the balance between cost in energy (not evaluated here) to lower the mean particle size, and Cu leaching efficiency has not been evaluated yet, whatever the leaching strategy.

3.5. Leaching of major metals from WPCB during the entire process

Based on these results, we examined the outcome of five major metals (Cu, Fe, Ni, Zn and Al) during the two-stage leaching sequence: first stage is a leaching in solution using a 3 M aqueous HCl solution (S/L ratio 1 L/83 g) during 5 h at room temperature, and second stage is a leaching in foam using again a 3 M aqueous HCl solution containing 2 mM Brij S10 (S/L ratio 1 L/50 g) during 5 h at room temperature. Repartition of these 5 metals between first leachate, second leachate and solid residue is given in Figure 7.

As expected, most Al is leached during the first stage. Remaining Al is found in the residue, probably as oxide incorporated in the glass fibers that reinforces the epoxy plastic support. Then, almost all the Cu is leached during the second stage, with a non-significant loss in the solid residue. The outcome of Fe, Zn and Ni is more intriguing as these metals are mostly leached during the second stage, although the acid quantity obtained in the first stage largely exceeds the amount required for complete dissolution. Passivation of metallic Zn with a resistant oxide surface can be invoked, but this argument may not stand for Fe, which passivation by oxide is inefficient. The subsequent isolation of copper from the foam leachate after foam collapse has not been investigated. A neutral surfactant employed, with a very low amount (2 mM, i.e. 1.4 g·L⁻¹).

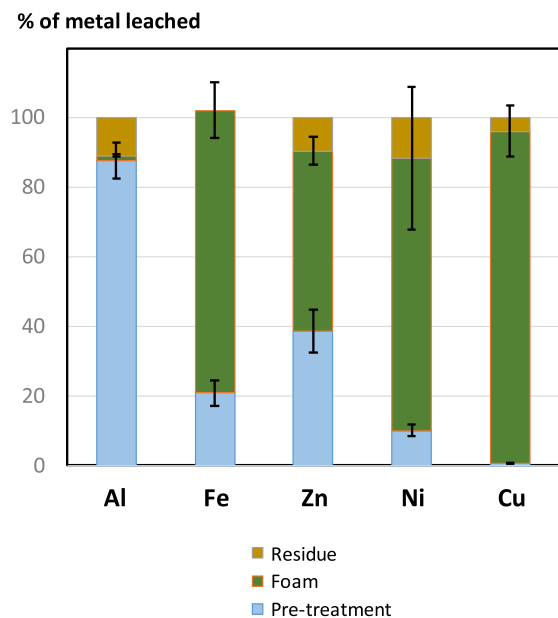


Figure 7. Repartition of major metals contained in ground WPCB according to the leaching stage and remaining solid residue (1st stage: 3 M HCl solution, S/L ratio 1 L/83 g, 5 h; 2nd stage: foam prepared using 3 M HCl and 2 mM Brij S10, S/L ratio 1 L/50 g).

Therefore, interferences with classical precipitation or electrodeposition processes are not anticipated. However, it is not clear whether these processes will be affected by easy foam formation, or if the final purity of copper will be altered. Finally, the reuse of the surfactant will require further dedicated studies.

4. Conclusion

Foams appear as an interesting alternative to classical aqueous solutions for the leaching of Cu from ground WPCB. By simply adding a small quantity of readily available surfactant Brij S10 (2 mM, i.e. ca. 1.4 g/L) into a dilute aqueous HCl solution, efficient Cu leaching was observed after injection of air into the solution and formation of the foam. The foam is stable over extended period and increases gas–liquid transfer, so that O₂ contained in air can act as Cu oxidant. This approach is different from classical use of foams in hydrometallurgy (particular and ionic flotation, foam fractionation). Foams are used as

a biphasic fluid medium to replace aqueous solutions employed for leaching, minimizing the amount of liquid employed. In continuation to our simple laboratory setup, our intention is to develop a pilot reactor (ca. 1 L scale), fully characterized in terms of gas–liquid transfer, with adequate gas injection and samplings systems. The efficiency of Cu leaching by the foam was improved by performing a first leaching in HCl solution (without surfactant), and a 2-stage strategy that enables complete Al removing, as well as part of Fe, Zn and Ni, was devised. The final leachate contains Cu in a concentration close to 10 g/L, and its processing using existing techniques such as precipitation can be easily envisioned. Furthermore, during this study we evidenced that Cu in e-waste accumulates in fraction of larger size during grinding, and that the average size of the fraction with the highest Cu content (500–1000 μm) is well suited to leaching with foams. Leaching is complete after 5 h, and the kinetics can be improved through addition of 10% Cu²⁺ ions to the leaching medium. Thus, extensive milling of the waste, which can be quite energy consuming, is not necessary. This study also revealed a particular behavior of Fe: although this metal was expected to be easily removed during first stage of leaching using dilute HCl aqueous solution without foam (i.e. without O₂ as an oxidant), it proved to be reluctant to dissolution. On the contrary, during the leaching of Cu with the foam, Fe was easily dissolved along with Cu. The mutual interactions between both metals during leaching with HCl/O₂ has not been studied to our knowledge. Detailed studies dedicated to the understanding of the mechanism of both Cu dissolution by HCl/O₂ in foam and relationship with Fe are underway and will be reported in due course.

Declaration of interests

The authors do not work for, advise, own shares in, or receive funds from any organization that could benefit from this article, and have declared no affiliations other than their research organizations.

Funding

We would like to acknowledge ANR-17-CE08-0016 FOAMEX.

Acknowledgements

We would also like to acknowledge C. Monteux, N. Pantoustier, P. Bauduin and P. Perrin for fruitful discussions, and B. Baus-Lagarde for assistance during the ICP-OES analyses.

Supplementary data

Supporting information for this article is available on the journal's website under <https://doi.org/10.5802/crchim.311> or from the author.

References

- [1] F. Sebba, *Nature*, 1959, **184**, 1062-1063.
- [2] N. W. Rice, F. Sebba, *J. Appl. Chem.*, 1965, **15**, 105-109.
- [3] R. Lemlich, *Ind. Eng. Chem.*, 1968, **60**, 16-29.
- [4] F. Doyle, *Int. J. Miner. Process.*, 2003, **72**, 387-399.
- [5] L. Chang, Y. Cao, G. Fan, C. Li, W. Peng, *RSC Adv.*, 2019, **9**, 20226-20239.
- [6] S. Farrokhpay, *Adv. Colloid Interface Sci.*, 2011, **166**, 1-7.
- [7] K. Theander, R. J. Pugh, *Colloids Surf. A: Physicochem. Eng. Asp.*, 2004, **240**, 111-130.
- [8] A. K. Nanda, L. Silveri, M. A. Mccool, "Method and apparatus for deinking", 1984 (GB19830010494 19830419). Accessed December 14, 2023, https://worldwide.espacenet.com/publicationDetails/biblio?FT=D&date=19841031&DB=EPODOC&locale=fr_EP&CC=ZA&NR=842186B&KC=B&ND=4.
- [9] D. A. White, J. M. Taylor, *Trans. Inst. Min. Metall. Sect. C*, 1989, **98**, C106-C110.
- [10] L. Stoica, D. Filip, Gh. Filip, A. Razvan, R. Radulescu, *J. Radioanal. Nucl. Chem.*, 1998, **229**, 139-142.
- [11] I. Cantat, S. Cohen-Addad, F. Elias *et al.* (eds.), *Foams: Structure and Dynamics*, Oxford Academic, Oxford, 2013, Online edition, accessed 14 May 2024.
- [12] R. Houot, *Int. J. Miner. Process.*, 1983, **10**, 183-204.
- [13] P. Trinh, A. Mikhailovskaya, M. Zhang *et al.*, *ACS Sustain. Chem. Eng.*, 2021, **9**, 14022-14028.
- [14] M. Simoni, E. P. Kuhn, L. S. Morf, R. Kuendig, F. Adam, *Waste Manag.*, 2015, **45**, 10-21.
- [15] Z. Sun, Y. Xiao, H. Agterhuis, J. Sietsma, Y. Yang, *J. Clean. Prod.*, 2016, **112**, 2977-2987.
- [16] X. Zeng, J. A. Mathews, J. Li, *Environ. Sci. Technol.*, 2018, **52**, 4835-4841.
- [17] M. Kaya, *Waste Manage.*, 2016, **57**, 64-90.
- [18] S. X. Shi, S. Q. Jiang, C. C. Nie, B. Li, H. H. Chang, X. N. Zhu, *Process. Saf. Environ. Prot.*, 2022, **166**, 123-132.
- [19] M. Jung, K. Yoo, R. D. Alorro, "Dismantling of electric and electronic components from waste printed circuit boards by hydrochloric acid leaching with stannic ions", Accessed December 14, 2023, https://www.jstage.jst.go.jp/article/matertrans/58/7/58_M2017096/_html/-char/en.
- [20] Y. F. Guimarães, I. D. Santos, A. J. B. Dutra, *Hydrometallurgy*, 2014, **149**, 63-70.
- [21] B. Petkova, S. Tcholakova, M. Cherkova *et al.*, *Adv. Colloid Interface Sci.*, 2020, **276**, article no. 102084.
- [22] J. Lamolinairie, B. Dollet, J. L. Bridot, P. Bauduin, O. Diat, L. Chiappisi, *Soft Matter*, 2022, **18**, 8733-8747.
- [23] Y. Yao, J. He, B. Yang, Y. Zhao, L. Zhu, *Powder Technol.*, 2023, **415**, article no. 118103.
- [24] F. Habashi, *Ber. Bunsengesell. Phys. Chem.*, 1963, **67**, 402-406.
- [25] M. Lundström, J. Aromaa, O. Forsén, O. Hyvärinen, M. H. Barker, *Hydrometallurgy*, 2005, **77**, 89-95.
- [26] M. Lampinen, S. Seisko, O. Forsström *et al.*, *Hydrometallurgy*, 2017, **169**, 103-111.
- [27] Y. J. Lee, T. T. Ly, T. Lee *et al.*, *Appl. Surf. Sci.*, 2021, **562**, article no. 150148.
- [28] F. Lambert, S. Gaydardzhiev, G. Léonard, G. Lewis, P. F. Bareel, D. Bastin, *Miner. Eng.*, 2015, **76**, 38-46.

Research article

GDR Prométhée - French Research Network on *Hydrometallurgical Processes for Primary and Secondary Resources*

Reprocessing of waste produced during acid mine drainage lime treatment by selective leaching

Jérôme Jacob^{✉,*}, Douglas Pino-Herrera[✉], Catherine Greffié^a, Guillaume Wille[✉],
and Emmanuelle Plat[✉]^a BRGM, F-45060 Orléans, FranceE-mail: j.jacob@brgm.fr (J. Jacob)

Abstract. Acid mine drainages (AMDs) are a major environmental problem, but they can also contain valuable metals. A typical treatment of AMDs consists in the neutralization and precipitation of metals by liming, which produces a sludge mainly composed of iron oxyhydroxides and gypsum. Depending on the AMD composition, the sludge can contain important concentrations of valuable metals. This research work aimed at studying acid leaching of copper and zinc present in the sludge with the final goal of developing a process to recover these metals. Tests were carried out using sludge from a former mining site in France. The first stage of this process involves a leaching stage to selectively dissolve Cu, Zn, and Cd using H₂SO₄. This process allows more than 80% of Cu and Zn as well as 98% of Cd in the sludge to be leached under optimal operating conditions, which are between 5% and 15% of solid content and between 150 and 200 g H₂SO₄·kg⁻¹ at room temperature. Using more acid marginally increases the dissolution rates but at the cost of much higher acid consumption linked to the dissolution of iron and therefore a loss of selectivity.

Keywords. Acid mine drainage, Lime, Sludge, Zinc, Copper, Recovery, Leaching.

Funding. Department for Mine Safety and Risk Prevention of BRGM: French Geological Survey.

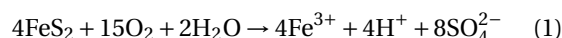
Manuscript received 6 November 2023, revised 10 April 2024 and 28 June 2024, accepted 18 July 2024.

1. Introduction

It is estimated that 19,300 km of rivers and 72,000 ha of lakes and aquatic reservoirs are severely affected by mining effluents worldwide [1]. In addition to the economic damage they cause, acid mine drainage (AMD) poses serious risks to human health. The contamination of surface water and sediments by mining sites therefore represents a major public health issue [2,3]. Like many other European countries, France has a long tradition of mining dating back to the Neolithic period [4]. In the 1980s, economic

constraints led to the end of mining in mainland France [5]. The map of mineral deposits in France lists 1400 sites that have produced ores [6].

When mining waste or mining structures (galeries, mine shafts, and open pits) containing sulfide minerals, such as pyrite (FeS₂) and pyrrhotite (Fe_(1-x)S with $x < 0.125$), come into contact with water and oxygen, an oxidation reaction can occur that will lead to the production of AMD according to Equation (1) in the case of pyrite.

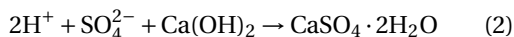


AMD can contain high concentrations of sulfate, Fe, Al, Mn, As, Cu, Zn, and other metals and metalloids.

*Corresponding author

Mine drainage can remain acidic for a very long time. For example, the Montana Department of Environmental Quality has validated a model which shows that acid drainage from the Golden Sunlight mine (USA) will continue to flow for thousands of years [7]. A recent study by Tabelin *et al.* [8] estimated that AMD generation in the relatively small tailings dam of a closed Au–Ag–Cu–Co–Zn mine in Hokkaido, Japan, will continue for at least 1000 years. One of the oldest documented mining regions in the world, the Rio Tinto region in Spain, has been experiencing AMD-related problems for around 5000 years [9].

If preventive measures such as handling plans, alkaline amendment, and covers are not implemented before the oxidation reactions begin, AMD production is difficult and even impossible to stop [10]. Besides their potential impacts on the environment, AMD can also contain valuable metals. In general, there is a positive correlation between the acidity of the treated effluent and the concentration of the metals in the water, particularly for Cu, Zn, Ni, and Mn, as explained by Plumlee *et al.* [11]. As the flows of AMD are difficult, if not impossible, to control permanently, they need to be treated for a long time. These systems represent a significant long-term cost to society, to which must be added the storage of solid waste resulting from these treatments that accumulates over time. Chemical neutralization involves mixing AMD with alkaline materials (such as limestone, magnesia, and lime) to precipitate most of the heavy metals. The AMD treatment by reaction with lime is described by Equation (2):



The increase in pH during lime treatment triggers the precipitation of divalent and trivalent metals present in the AMD in the form of metal oxy/hydroxides or sulfates, which are often poorly crystallized [12,13]. Lime treatment is the method of choice for mines as it is effective, easy to implement and operate, and can be tailored to site-specific geochemical properties of AMD [14]. It has been estimated that 90% of AMDs are treated by liming worldwide [15,16]. Although effective, this process generates bulky sludge composed largely of gypsum ($\text{CaSO}_4 \cdot 2\text{H}_2\text{O}$), which can be a source of secondary impacts if it is not stored under optimal conditions. For example, some heavy metals present in this sludge can be leached by rain water and released into the environment.

On one hand, these metals can be potentially harmful for human health and for the environment, but, on the other hand, they can also be economic and technologically valuable, particularly in the current context of energy transition, as they can attain significant concentrations in the sludge. For instance, analyses carried out on lime treatment sludge from seven mines in Canada show that some metals can be present at very high concentrations: up to 1.4% of copper and 22% of zinc [17,18]. There have been numerous studies focusing on the recovery of metals directly from AMD using specific processes [19,20], but very few authors have studied the recovery of metals in historical sludge dumps produced through conventional lime treatment of AMD [21,22].

The work of Macias *et al.* [18] is particularly noteworthy as well as the patent by Ziemkiewicz *et al.* [22] on the recovery of rare earth elements (REEs) from AMD, which includes liming of the AMD and subsequent treatment of the sludge although this process was designed specifically to recover REEs [23].

The recovery of valuable metals in AMD presents a significant challenge, as fluxes of these metals are often too low. Inline metal recovery is rarely economically viable due to both low water flow rates and/or low metal concentrations. Consequently, this research work aims to address the large-scale challenge posed by substantial sludge deposits that have accumulated over decades instead of developing a process for recovering metals directly from AMD or from the daily-produced sludge by lime treatment. By targeting these existing deposits, we propose a short treatment operation designed to recover valuable metals efficiently, offering a novel solution to a long-standing environmental and economic issue.

In particular, this study covers the selective leaching of metals from a specific AMD lime treatment sludge to recover Cu and Zn while decreasing the amount of Cd in the sludge. For this purpose, sludge from the lime treatment of AMD at a specific French site was characterized and the optimal acid leaching operating conditions (solid content, acid-to-solid ratio, temperature) were determined. Applying optimal conditions means maximizing the leaching yields of Cu, Zn (for economic viability), and Cd (for environmental concerns) while minimizing the leaching of Fe and Al.

The dissolution of Fe and Al consumes reagents without adding value, increasing the operational costs of the process. Moreover, high concentrations of Fe and Al in the leachate can impede the downstream recovery processes. Compared to a pregnant leach solution (PLS) without Fe and Al, the selective removal of these elements requires more reagents, potentially different ones, and additional treatment steps downstream. In particular, the solid/liquid separation of Al precipitates is challenging. Finally, the presence of Fe and Al in the PLS makes it more difficult to achieve the target purity of Cu and Zn products [24,25].

2. Materials and methods

2.1. Mine site and sludge deposit

The ore deposit from which the AMD is produced is a stockwork containing barite (BaSO_4), galena (PbS), sphalerite (ZnS), and chalcopyrite (CuFeS_2) in altered soda-dacitic lavas near the Devonian Brévenne rift. It was covered by Triassic sediments (clay and sandstone), which were mineralized in turn by hydrothermal fluids during their deposit. Then, primary sulfides were oxidized allowing the formation of secondary minerals of lead, zinc, and especially copper. The mine was active from 1414 to 1842 for the extraction of copper, and it is estimated that 15,000 t of Cu was produced during this period. From 1842 to 1877, 9000 t of pyrite was mined for sulfuric acid production in addition to the reprocessing of mining waste produced during previous copper extraction (BRGM, internal communication).

AMD has been flowing from water adits since unknown but ancient times. Its average characteristics and uncertainties (95% confidence intervals) calculated using 134 monthly samples from 1998 to 2012 are presented in Table 1. Metals were analysed by SGS company in accordance with standard NF EN ISO 11885 and sulfate are in accordance with standard NF T 90-40. The AMD contains significant amounts of sulfate, iron, and zinc, but also some aluminum and copper.

Lime treatment of AMD started in the middle of the 19th century and still continues as of 2024. All the sludge resulting from more than 150 years of lime treatment was stockpiled on site. The size of the sludge deposits was estimated with GIS software using data from the bibliography including maps

from different periods and settling pond cleaning reports as well as an elevation model and the depth of six sludge core samples drilled in 2002 (see Section 2.2.1). The total sludge volume is estimated at 77,000 m^3 or around 170,000 t according to the measure of sludge density in the laboratory ($2.2 \pm 0.4 \text{ t} \cdot \text{m}^{-3}$, $n = 3$).

2.1.1. Core sample characterization

An aerial view of the sludge dump is shown on Figure 1, including the position of six core samples drilled in order to obtain a general characterization of the sludge accumulated on the site.

The depth and number of analysis on each core sample are presented in Table 2. Sampling of core “C5” was planned but never actually drilled, and therefore, no results of this sample are available.

22 samples allowed the calculation of a robust average and a good estimate of the heterogeneity of this sludge deposit and not specifically the inductively coupled plasma atomic emission spectroscopy (ICP-AES). Carbonates were analyzed by volumetric determination of mineral carbon (NF EN ISO 10693). Mineralogy of the core sample was characterized by X-ray diffraction (XRD, SIEMENS type D5000), scanning electron microscope (SEM, JEOL 6100), and transmission electron microscopy (TEM) with energy dispersive spectroscopy (EDS) (Philips CM 120). Both SEM and TEM analyses were employed to characterize our samples due to the wide range of crystal sizes present. SEM was used to observe larger crystals such as gypsum crystals that were up to 20 μm in size. TEM was used to study nanometric-sized mineral phases and to investigate possible carrier phases for the metals Cu and Zn, including clean mineral phases as well as substituted or adsorbed metals.

2.2. Leaching tests

2.2.1. Characterization of sludge sample used in leaching tests

For the leaching tests, six samples of superficial AMD sludge of a total mass of 15 kg were collected from different points of the site in 2021. Sample preparation included drying in an oven at 40 °C for a period of 48 h to remove excess moisture, disaggregating using a mortar, sieving at 2 mm, and mixing and homogenization of the six samples.



Figure 1. Sludge dump and core sampling locations (C1–C7) on the mining site. For details of the core samples' depth and number of analyses, refer to Table 2.

Table 1. Chemical composition of AMD samples from 1998 to 2012 ($n = 134$)*

Flow rate ($\text{m}^3 \cdot \text{h}^{-1}$)	pH	Al ($\text{mg} \cdot \text{L}^{-1}$)	Cu ($\text{mg} \cdot \text{L}^{-1}$)	Fe ($\text{mg} \cdot \text{L}^{-1}$)	SO_4 ($\text{mg} \cdot \text{L}^{-1}$)	Zn ($\text{mg} \cdot \text{L}^{-1}$)
7.2	2.7 ± 0.1	50 ± 5	32 ± 7	260 ± 40	2300 ± 150	210 ± 20

* n indicates the number of samples analyzed from 1998 to 2012.

Table 2. Sludge depth on each core and number of chemical analyses

Core	Core depth (m)	Sludge depth (m)	Number of analyses
C1	8	6	6
C2	8	>8	3
C3	9	3	3
C4	6	4	2
C6	12	8	4
C7	10	8	4

Representative subsamples for characterization and leaching tests were then obtained using a riffle splitter. The density of the dried sludge was measured by water displacement. The chemical composition of the homogenized sample was determined by ALS laboratory by different in-house methods. Fusion decomposition was used for major elements such as Fe, Al, Si, and Ca, while Cu, Cd, and Zn were analyzed using a four-acid digestion method (HCl, HNO_3 , HF, and HClO_4). Both analyses were followed by ICP-AES and the loss on ignition test at 1000 °C. Sulfate was

determined from the difference between total sulfur (by Leco furnace and infrared spectroscopy) and sulfide (by Leco furnace and Na_2CO_3 leach). In selected experiments, metal contents of solid samples were measured before and after leaching using a portable X-ray fluorescence (pXRF) Niton XL3t 980 (Thermo Fisher) to perform mass balance calculation. Given the semi-quantitative nature of pXRF analysis, we implemented a stringent protocol to ensure that the data utilized in our study provided accurate elemental concentrations and enabled confident use in mass balance calculations. This protocol includes validation against standard samples, repeated measurements, and systematic verification of XRF spectra. They are inspired by the methods and principles presented by several authors including Touzé *et al.* [26], Lemièrre [27], and López-Núñez [28].

SEM images were collected on TESCAN Mira3 XMU (low vacuum field emission SEM) at BRGM, using a high voltage of 15 kV. EDS analyses were performed on an EDAX APEX system equipped with a 70 mm² silicon drift detector (SDD). Sample powders were dispersed on an aluminum stub covered with a double-coated carbon conductive tape and coated

with a 20 nm conductive carbon layer. TEM was conducted on JEOL ARM200CF (double C_s corrected cold FEG TEM/STEM) at the electron microscopy platform MACLE (CNRS Orleans). EDS analyses were obtained on a JEOL Centurio SDD detector. Images and analyses were performed at 200 kV.

2.2.2. Experimental setup

Three different experimental setups were used to study the leaching of Zn and Cu from the lime treatment sludge: 250 mL shake flasks, then 0.5 L stirred tank reactors (STRs), and finally 2 L STRs. The tests in 250 mL shake flasks were carried out only at low solid contents in order to avoid mass transfer and solubility limitations. Tests with higher solid contents necessitated the transition to STR, initially at 0.5 L and then at 2 L to ensure a good solid suspension. The progression to a larger volume was also driven by the need for sufficient sample quantities for accurate residue analysis via pXRF.

2.2.2.1. Tests in shake flask. For preliminary leaching tests, 250 mL shake flasks were used at low solid contents (<1.3% mass/mass). The working volume of these tests was fixed at 150 mL. Magnetic stirrers were added to the shake flasks, and agitation was carried out using a magnetic stirring table at 150 rpm (Supplementary Figure S1). Shake flasks were covered with Parafilm® to avoid excessive evaporation. For each experiment, the flasks were filled with 150 mL of deionized water and the specific amount of solid required. Then, the pH was decreased by adding H_2SO_4 to a value close to 3.0 ± 0.2 . Throughout the duration of each test, pH was maintained between 3.0 and 3.5 by adding a solution of sulfuric acid ($1 \text{ mol} \cdot \text{L}^{-1}$) dropwise when pH was higher than 3.5.

This value was chosen so that the solution would be as acidic as possible to leach a maximum of Cu and Zn without dissolving iron, as Fe^{3+} can begin to be significantly soluble below a pH of 3.0 [29]. Samples were taken to determine metal concentrations, and temperature, pH, conductivity, and redox potential (E_h) were measured directly in the reactors at the initial time and at approximately 0.25 h, 1 h, 2 h, 4 h, 6 h, and 24 h after the beginning of the experiment. For metal concentration measurements, about 2 mL of pulp was filtered at $0.45 \mu\text{m}$, diluted 10 times using 1% HNO_3 , and placed at 4°C . The total amount of solids passing through the filter was

considered negligible since particle size measurements of the sludge showed that only 0.82% of particles were smaller than $0.42 \mu\text{m}$. Metal concentrations (Al, Cd, Cu, Fe, and Zn) were then measured on the filtrate either by atomic absorption spectroscopy (SpectrAA 220FS, Varian) or using a 4210 microwave plasma atomic emission spectroscopy from Agilent Technologies.

2.2.2.2. Tests in STRs. Leaching experiments were also performed in two types of reactors with working volumes of 0.5 L (Supplementary Figure S1) and 2 L. The experimental setup was fully described by Guezennec *et al.* [30]. They were equipped with four baffles mounted 90° apart and extended down to the base of the vessel for pulp mixing. The 0.5 L reactor was equipped with an axial flow three-blade 45° impeller, whereas the 2 L reactor (Figure 2) had a dual impeller system (axial/axial) with the same characteristics (three-blade 45° axial flow). The agitation speed was fixed at 600 rpm for both systems. The temperature control system (LAUDA MC) circulated warm water (22°C , 40°C , or 60°C) in the reactor jacket to maintain constant operating temperatures. Experiments conducted above room temperature aimed to assess the potential for reducing iron solubility and thereby enhance the selectivity of the leaching process [31].

The experimental procedure was similar to that for shake flasks but used the required working volume of deionized water according to the reactor size (0.5 L or 2 L). However, no pH control was performed in STR tests. The total amount of sulfuric acid required for the experiment was added before the solid in the reactors. The goal was to maintain an initially high acidic environment during the early stages of the reaction. The monitoring of physicochemical parameters and leachate sampling and analyses were performed as described for shake-flask experiments (Section 2.2.2.1). At the end of some of the tests in 2 L reactors, the entire amount of pulp was filtered using glass microfiber Whatman® filter grade GF/A (cut-off $0.8 \mu\text{m}$).

2.2.3. Calculations

The solid content was calculated using Equation (3).

$$C_{\text{solid}} = \frac{m_{\text{dry solid}}}{m_{\text{pulp}}} \times 100\% \quad (3)$$



Figure 2. Photograph of the experimental setup using 2 L reactors.

where C_{solid} represents the percentage of the pulp that is solid material, $m_{\text{dry solid}}$ (kg) is the mass of the solid (the sludge) after drying and before leaching, and m_{pulp} (kg) is the total mass of the pulp mixture, including both the liquid and solid phases.

The acid-to-solid ratios were calculated according to Equation (4).

$$a_{\text{ratio}} = \frac{m_{\text{H}_2\text{SO}_4}}{m_{\text{dry solid}}} \quad (4)$$

where a_{ratio} ($\text{g}\cdot\text{kg}^{-1}$) is the acid-to-solid ratio, $m_{\text{H}_2\text{SO}_4}$ (g) is the total mass of sulfuric acid added to the pulp, and $m_{\text{dry solid}}$ (kg) is the mass of the sludge material after drying prior to the leaching process.

When solid analysis was not possible (for tests with solid contents lower than 1.3% m/m), leaching yields were calculated from analysis of the liquid phase as shown in Equation (5).

$$LY_{\text{liquid}} = \frac{C_{\text{M,liquid}} \cdot V_{\text{liquid}}}{C_{\text{M,solid,initial}} \cdot m_{\text{dry solid}}} \times 100\% \quad (5)$$

where LY_{liquid} (%) is the leaching yield of the metal calculated from the mass of the element of interest

dissolved in the liquid phase, $C_{\text{M,liquid}}$ ($\text{mg}\cdot\text{L}^{-1}$) is the concentration of metal (M) in the liquid phase after the leaching process and quantifies how much of the metal has been transferred into the solution, V_{liquid} (L) is the total volume of the liquid phase in the test, and $C_{\text{M,solid,initial}}$ ($\text{mg}\cdot\text{kg}^{-1}$) is the concentration of the metal (M) in the sludge before leaching.

When the compositions of the residual solid after leaching were analyzed (for tests with solid contents higher than 2.9% m/m), leaching yields were calculated both by Equation (5) and from the analyses of the solids according to Equation (6).

$$LY_{\text{solid}} = \frac{C_{\text{M,solid,initial}} \cdot m_{\text{dry solid}} - C_{\text{M,solid,final}} \cdot m_{\text{leached solid}}}{C_{\text{M,solid,initial}} \cdot m_{\text{dry solid}}} \times 100\% \quad (6)$$

where LY_{solid} (%) is the leaching yield of the metal calculated from the solid phase, $C_{\text{M,solid,final}}$ ($\text{mg}\cdot\text{kg}^{-1}$) is the concentration of the metal (M) in the solid after leaching, and $m_{\text{leached solid}}$ (kg) is the mass of the dry solid after leaching.

Mass balances for the targeted metals were performed, and the differences between the leaching yields calculated from solid and liquid phases were always less than 10%.

3. Results

3.1. Core sample characterization

The sludge is mainly composed of Ca, Fe, and SO_4 with significant amounts of Cu and Zn, with about 1% and 5% respectively of the total mass of the samples, as presented in Table 3. Other elements present in low amounts are Al and Si. It is important to highlight that there is also a non-negligible amount of Cd, a heavy metal potentially harmful for human health and the environment. Uncertainties calculated as 95% confidence intervals show that the concentration variabilities are generally low despite the fact that samples included come from different cores and several depths. This means that the sludge accumulated on the dump can be considered fairly homogeneous.

The main minerals identified by XRD were gypsum ($\text{CaSO}_4 \cdot 2\text{H}_2\text{O}$), quartz (SiO_2), an amorphous phase (probable ferrihydrite, possibly ferrihydrite ($\text{Fe}_{3-0.5}\text{y}(\text{OH})_y \cdot n\text{H}_2\text{O}$) as commonly observed in

Table 3. Average composition of sludge core samples and the sludge used in leaching tests

Compound (%)	Core samples ($n^* = 22$)	Sludge used in leaching tests
Al ₂ O ₃	$3.3 \pm 0.4^{**}$	3.5
CaO	24 ± 1	17
Cd	0.011 ± 0.003	0.010
CO ₃ ²⁻	0.7 ± 0.3	1.3
Cu	1.3 ± 0.2	1.1
Fe ₂ O ₃	17 ± 1	16
SiO ₂	3.5 ± 0.8	7
SO ₄ ²⁻	31.9 ± 0.6	26
Zn	5 ± 1	5
Mass loss at 105 °C	60 ± 2	26

*Number of samples analyzed. **Uncertainties correspond to 95% confidence intervals.

liming of AMD [17,32]), feldspar ((Ba,Ca,Na,K,NH₄)(Al,B,Si)₄O₈), illite ((K,H₃O)(Al,Mg,Fe)₂(Si,Al)₄O₁₀[(OH)₂,(H₂O)]), barite (BaSO₄), calcite (CaCO₃), lepidocrocite (γFeO(OH)), and jarosite (KFe₃(SO₄)₂(OH)₆). The identification of metal-bearing phases was made very difficult by the abundance of gypsum and the high proportion of the amorphous phase. A detailed study of these samples by EDS–SEM and XRD revealed the presence of Cu–Fe crystallites with a “desert rose” morphology (Figure 3), identified by XRD as delafossite (CuFeO₂) and ferriferous tabular crystallites with Zn. XRD diffractograms of a delafossite-rich sample and a lepidocrocite-rich sample are presented in Supplementary Figures S2 and S3. The only crystallized ferriferous phase identified in this specific sample is lepidocrocite. There are also some ferriferous aggregates with no trace of other metals and very abundant gypsum that contains no trace of metallic elements. No zinciferous mineral phase was clearly identified by XRD.

3.2. Leaching tests

3.2.1. Characterization of sludge sample used in leaching tests and residues

As can be observed in Table 3, the composition of the sludge used in the leaching tests is similar to that of the core samples. Indeed, the contents of Fe, Cd, Cu, and Zn in the sludge used for the leaching test fall within the 95% confidence intervals of those found in the core samples. The EDS–SEM mapping of sludge before leaching is presented in

Figure 4. This SEM map illustrates the elemental distribution within our sludge sample prior to leaching. Notably, Ca and S are closely linked, forming large and well-defined crystals indicative of gypsum. Conversely, the distribution of iron in the sample appears diffuse, with no identifiable crystalline form at this scale of observation. This suggests that the iron-bearing phases are very finely grained and/or pseudo-amorphous [29,33]. Sulfur’s lack of association with iron suggests the minimal presence of iron sulfate minerals, such as schwertmannite and jarosite, in this sample. In contrast, Zn shows a strong association with Fe, which may be representative of metal-substituted iron oxides or oxyhydroxides. Interestingly, some regions rich in iron show no corresponding zinc presence, pointing to a heterogeneous distribution of zinc within the iron matrix. Cu is likely also associated with iron; however, its concentration is too close to the quantification limit and the bremsstrahlung background to allow a meaningful interpretation other than indicating the absence of any Cu-rich minerals. Gypsum crystals are completely devoid of zinc, whereas traces of copper are present. The absence of distinct copper or zinc hotspots at this scale indicates that there are no specific copper or zinc minerals present or if they are, they exist in such low abundance that they are not detectable.

SEM mapping of residue after leaching (with an acid-to-solid ratio of 150 g·kg⁻¹ and with 0.7% of solid content) was also carried out. However, the concentrations of Zn and Cu after leaching

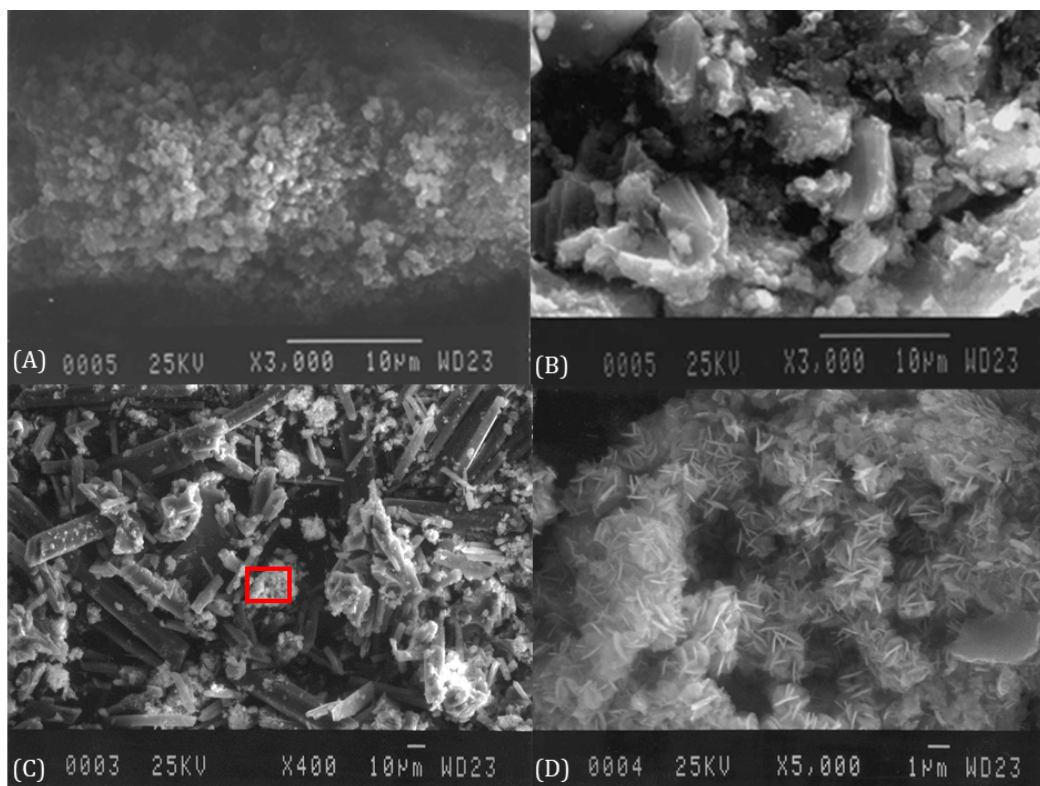


Figure 3. SEM microphotographs of (A) iron-rich aggregates, (B) tabular iron-rich zinciferous rods, (C) gypsum, and (D) delafossite, which is the focus of the red rectangle from (C).

are too close to the quantification limit and the bremsstrahlung background to allow a meaningful interpretation aside from the absence of Zn-rich minerals at this scale. These results are presented in Supplementary Material Figure S4.

The TEM images and EDS analyses of a gypsum crystal and iron-rich aggregates are shown in Figure 5 and Table 4. They confirm the virtual absence of Cu and Zn in gypsum and their strong association with iron. On the EDS analyses of the gypsum crystals observed in the TEM, the stronger association of Cu with gypsum is much less obvious (compared with the SEM map). At this much smaller scale, the crystal form of the ferriferous phases is also poorly defined, suggesting very fine-grained or pseudo-amorphous minerals.

3.2.2. Cu and Zn leaching behavior

Leaching tests of the sludge were performed first in shake flasks with low solid contents and with

manual pH control in order to obtain basic information about the leaching kinetics. Preliminary tests conducted at solid contents of 1.1% and 0.75% with pH levels of 5.4 and 4.0, respectively, indicated that a pH below 4.0 is necessary to achieve substantial dissolution of target metals Zn and Cu. At these conditions, leaching yields were 0% for Cu and 24% for Zn at pH 5.4 and 8% for Cu and 37% for Zn at pH 4.0. For this reason, it was decided to perform experiments correcting manually the pH to 3.0 when it was higher than 3.5.

Table 5 shows the operating conditions at which the leaching tests in shake flasks were performed and the resulting Cu and Zn leaching yields. Figure 6 shows the Zn and Cu concentrations as well as the pH changes in time as a function of the leaching time for both tests lasting 24 h (T1 and T3). The pH increased between the monitoring points at fixed time intervals as a result of the leaching reactions, and it was necessary to manually decrease it with diluted H_2SO_4 . In these experiments, the pH

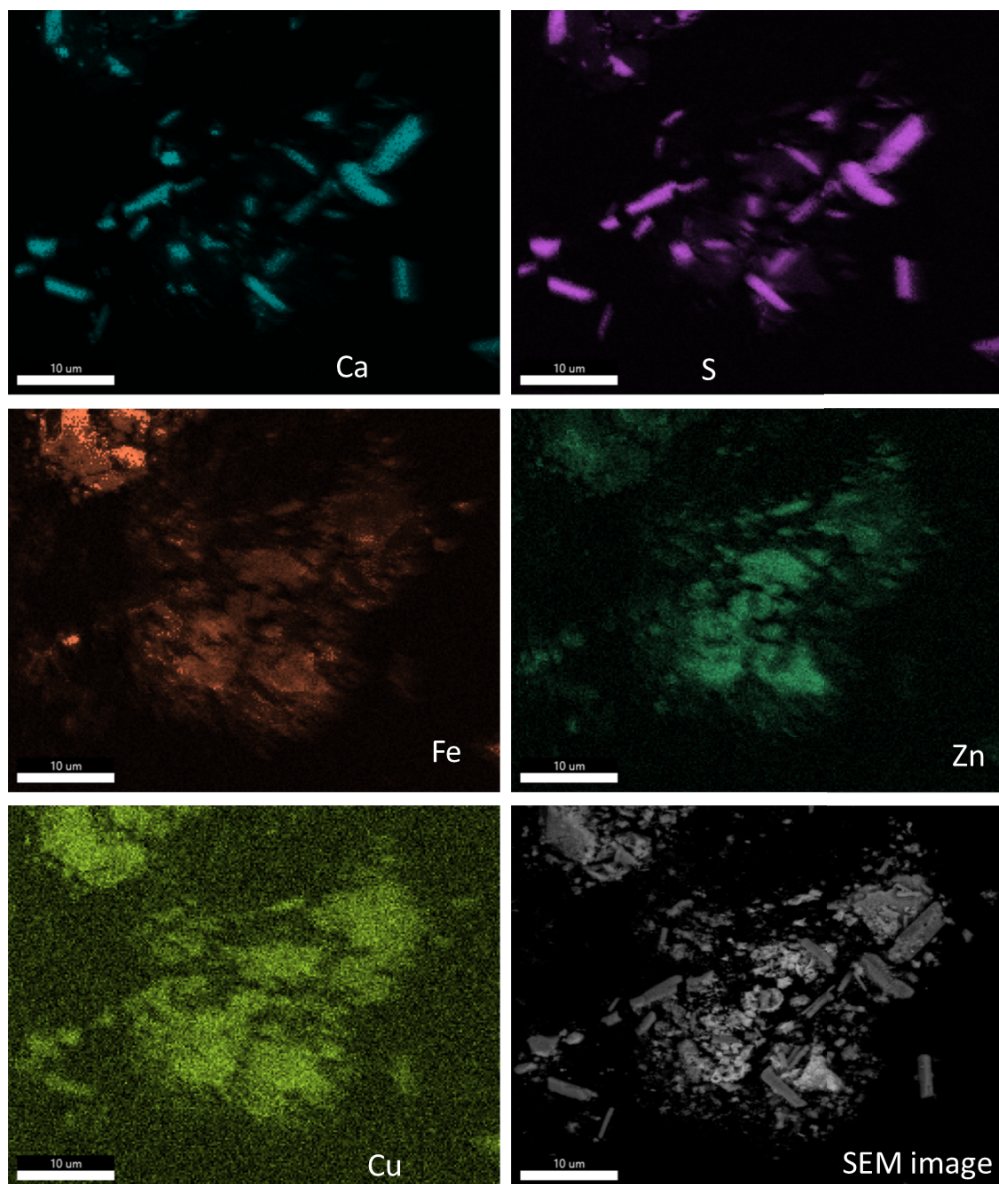


Figure 4. EDS–SEM mapping of sludge before leaching.

Table 4. TEM–EDS analysis of gypsum crystal and iron-rich aggregates

	Al (%)	Si (%)	S (%)	K (%)	Ca (%)	Fe (%)	Cu (%)	Zn (%)
(A) Whole area	n.d	n.d	46.59	n.d	52.52	0.3	0.1	0.49
(B) 28	8.37	3.77	5.33	0.17	0.91	60.50	7.40	13.56
(B) 29	7.77	9.37	2.38	0.98	1.30	61.17	5.63	11.40

varied from 2.7 to 4.2. It is important to note that the “final pH” shown in Table 5 is the value measured

at the last monitoring point without manual pH adjustment.

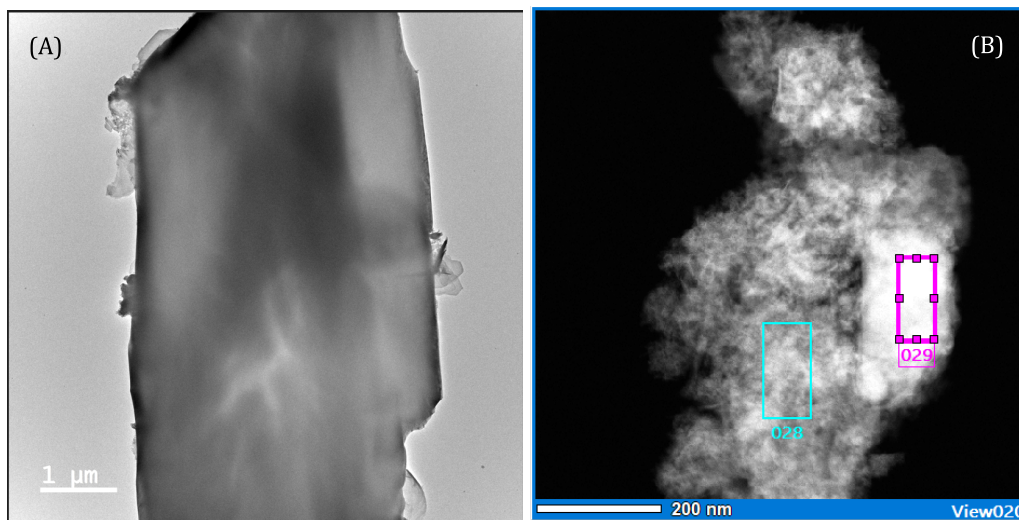


Figure 5. TEM microphotograph and location of semi-quantitative EDS analyses: (A) gypsum crystal and (B) iron-rich aggregates.

Table 5. Operating conditions and results of shake-flask leaching tests

	Leaching time (h)	Solid content (%)	Acid-to-solid ratio (g·kg ⁻¹)	Initial pH	Final pH	<i>LY</i> _{liquid} (%)	
						Zn	Cu
T1	24	0.68	106	2.7	3.6	75	66
T2	5.3	0.74	102	2.4	3.5	73	67
T3	24	0.79	118	3.4	3.6	75	70
T4	5.3	0.74	120	2.6	3.5	76	73
T5	5.3	0.73	125	3.2	3.5	77	71

The leaching curves follow a similar trend in both tests: (i) a very fast metal leaching during the first 0.25 h; (ii) a fast decrease in the leaching rate between 0.25 h and 4 h or 6 h; and (iii) a stabilization of the concentration at the end of the test. Moreover, it can be noted that for test T3, the concentrations of both Zn and Cu increase with time and reach a plateau around 310 mg·L⁻¹ and 60 mg·L⁻¹, respectively, after 4 h. However, it is not possible to say whether the concentration plateau was reached in test T1 since no samples between 6 h and 24 h were taken. Additionally, the final pH values of both tests are similar as well as the final leaching yields for both metals. Moreover, the pH curve shows that pH was manually decreased to slightly lower values in T3 than in T1 during the monitoring points between 2 h and 4 h. This resulted in a higher acid-to-solid ratio and a faster stabilization of the concentration of metals

after 6 h. These results imply that the chemical reaction can be completed after only 6 h when the pH is kept low (<3.5) since the beginning of the reaction. Extrapolating this idea, adding more acid at the beginning of the reaction, and thus decreasing the pH at early stages of the reaction, may help to reduce the leaching time. Therefore, for the tests using STRs, it was decided to add the total required amount of acid at the beginning instead of controlling the pH.

In order to verify the repeatability of the leaching tests, three leaching tests in 0.5 L STR were carried out under very similar operating conditions (shown in Table 6). The concentrations of Zn and Cu as well as the leachate pH are depicted in Figure 7. It is important to highlight that for these tests, the total amount of acid necessary to reach the required acid-to-solid ratio in each reactor was added at the beginning of the experiment. The leaching behavior

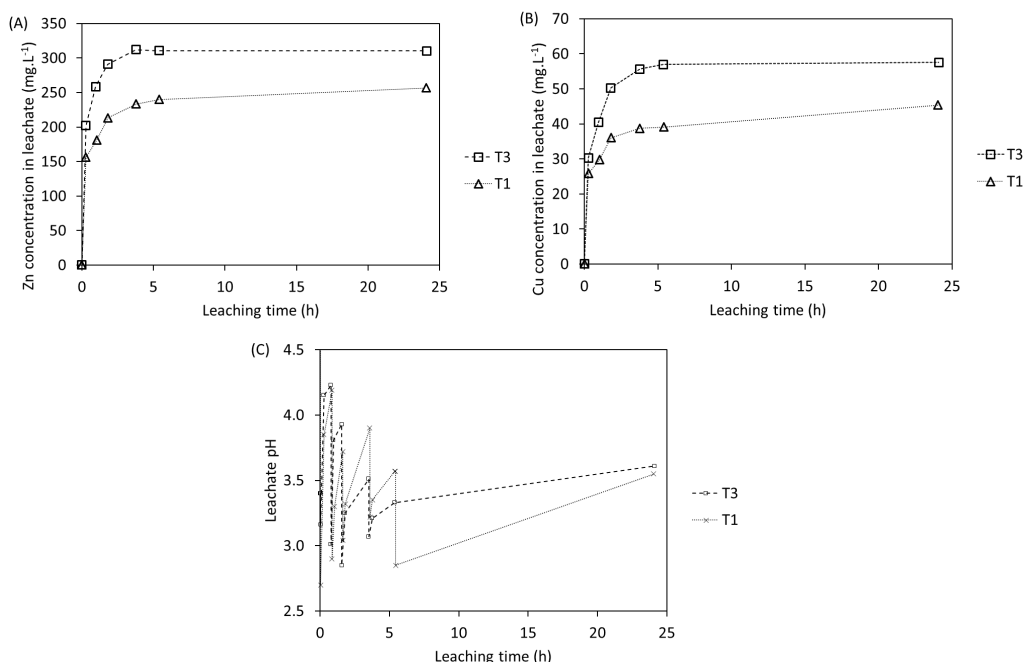


Figure 6. Concentrations of (A) Zn and (B) Cu and (C) leachate pH for tests with 24 h of duration in shake flasks.

of the metals follows the same trend as in the shake-flask tests previously presented, confirming that 6 h is sufficient to reach an equilibrium in Zn and Cu concentrations under the conditions of the test. One can note that the pH also follows a similar trend. The final pH depends not only on the acid-to-solid ratio used but also on the solid content. A notable pH difference was observed for R3 compared to R1 and R2. Although the acid-to-solid ratio for R3 ($153 \text{ g}\cdot\text{kg}^{-1}$) was slightly lower than that for R1 and R2 ($157 \text{ g}\cdot\text{kg}^{-1}$), this difference seems insufficient to fully explain the pH discrepancy. It is possible that minor variations in the initial conditions or inhomogeneities within the sludge samples influenced the pH results. The results show that even with slight variations in the acid-to-solid ratio, the relative uncertainties of the leaching yield are 2 and 3% for Zn and Cu, respectively.

3.2.3. Effect of acid-to-solid ratio on leaching time and efficiency

As shown in Table 5, several acid-to-solid ratios were tested in 250 mL shake-flask experiments. The results are depicted in Figure 8. One can note that higher acid-to-solid ratios resulted in faster leaching

rates during the first two hours. Moreover, the maximum leaching yield plateau is reached between 1 h and 2 h for both metals Zn and Cu, using an acid-to-solid ratio of $125 \text{ g}\cdot\text{kg}^{-1}$ (T5). However, regardless of the acid-to-solid ratio, we consistently observe incomplete dissolution (with a maximum leaching yield of approximately 77% for Zn and 75% for Cu) in these tests.

Experiments at different acid-to-solid ratios with low solid contents (between 0.6% and 1.3%) were carried out in 250 mL shake flasks, whereas 2 L reactors were used for higher acid-to-solid ratios with a solid ratio of 0.7% m/m at reaction times of 6 h and 24 h. The results are all depicted in Figure 9. They show that the leaching yield increased with acid-to-solid ratio up to about $250 \text{ g}\cdot\text{kg}^{-1}$ for both Zn and Cu, regardless of the experimental setup used. Further increases in the acid-to-solid ratio to $350 \text{ g}\cdot\text{kg}^{-1}$ and $450 \text{ g}\cdot\text{kg}^{-1}$ did not significantly increase the maximum leaching yield obtained, which was 90% for Cu and 84% for Zn.

The Fe leaching also increases with acid-to-solid ratio, and it becomes significant above $200 \text{ g}\cdot\text{kg}^{-1}$. This may be due to the dissolution of iron oxyhydroxides, such as ferrihydrite, caused by the low pH values

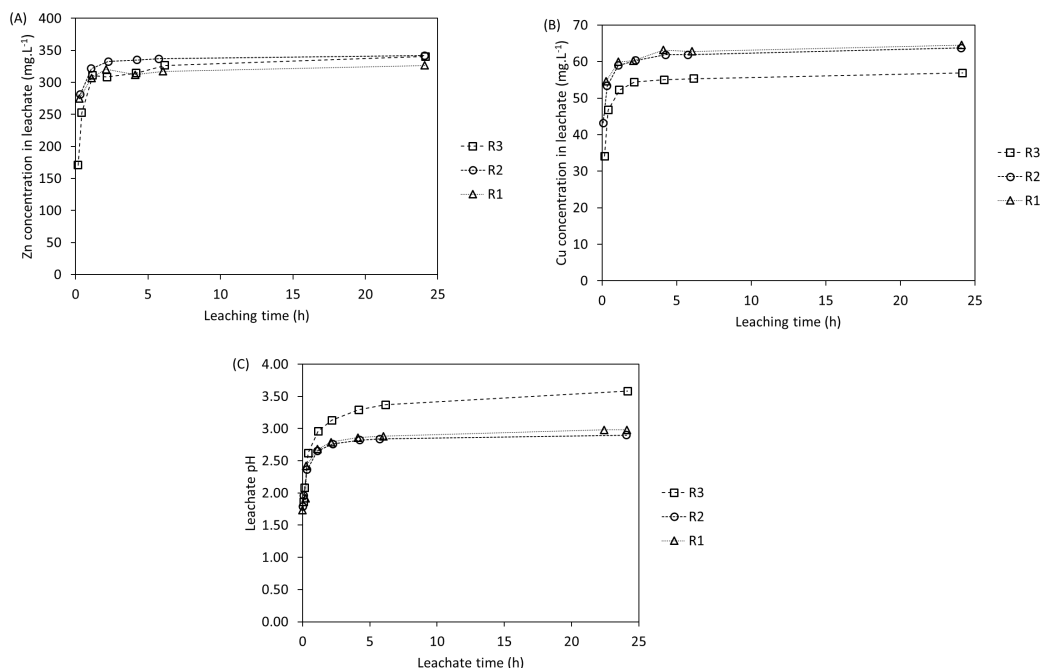


Figure 7. Concentrations of (A) Zn and (B) Cu and (C) leachate pH in 0.5 L STR tests.

Table 6. Operating conditions and results of 0.5 L STR leaching tests

	Solid content (%)	Acid-to-solid ratio ($\text{g}\cdot\text{kg}^{-1}$)	Initial pH	Final pH	Leaching yield (% liquid phase)	
					Zn	Cu
R1	0.72	157	1.7	3.0	78	80
R2	0.77	157	1.8	2.9	75	78
R3	0.70	153	1.9	3.6	79	74
Average					77	77
Std. deviation					2	3

(<3.0) obtained at the beginning of the experiments using high acid-to-solid ratios [29]. The initial pH (before solid addition) and the final pH at different acid-to-solid ratios in STRs for low solid contents (from 0.7% to 1.3% m/m) are presented in Supplementary Material Figure S5. One can note that the higher the acid-to-solid ratio, the lower the initial and final pH values. In the four reactors where Cd concentrations were measured, the leaching efficiency ranged from 96% to 100% for all acid-to-solid ratios tested (values of $200 \text{ g}\cdot\text{kg}^{-1}$ or higher as presented in Supplementary Material Table S1).

Experiments in 2 L reactors with a solid content of 2.9% at different acid-to-solid ratios with a reaction time of 24 h were performed to investigate the influence of acid-to-solid ratio on residue composition and on metal leaching yields compared to leaching tests at lower solid contents. Figure 10A shows the resulting leaching yields of these tests and Figure 10B shows the resulting Zn and Cu concentrations in the residues after leaching. An increase in acid-to-solid ratio from 200 to $450 \text{ g}\cdot\text{kg}^{-1}$ resulted in an increase in dissolution rates of Cu from 86% to 93% and Zn from 82% to 92%.

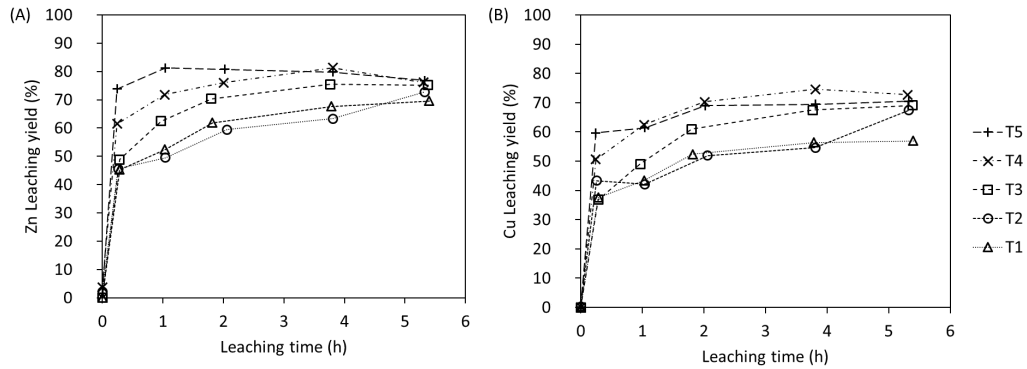


Figure 8. (A) Zn and (B) Cu leaching yields (LY_{liquid}) for tests in shake flasks.

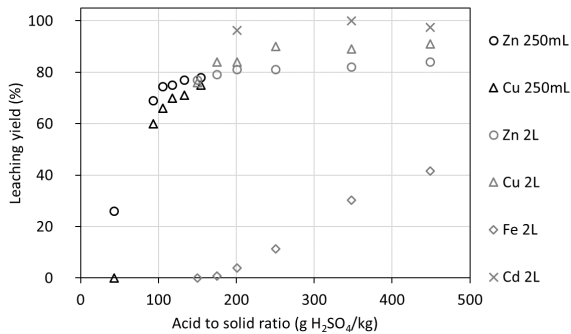


Figure 9. Metal leaching yields (LY_{liquid}) at different acid-to-solid ratios in shake-flask tests and STRs for low solid contents (from 0.7% to 1.3% m/m).

An augmentation of the acid-to-solid ratio to $650 \text{ g}\cdot\text{kg}^{-1}$ did not have a visible impact on the leaching yield of Cu and Zn compared to an acid-to-solid ratio of $450 \text{ g}\cdot\text{kg}^{-1}$. On the other hand, the Fe leaching yield increased significantly when the acid-to-solid ratio increased from $200 \text{ g}\cdot\text{kg}^{-1}$ to $450 \text{ g}\cdot\text{kg}^{-1}$ and, as for Zn and Cu, it remained almost unchanged with a further increase in this parameter to $650 \text{ g}\cdot\text{kg}^{-1}$. The content in the leaching residue was reduced from 5.2% to 0.78% for Zn and from 1.0% to 0.22% for Cu, using an acid-to-solid ratio of $200 \text{ g}\cdot\text{kg}^{-1}$. For the tests using an acid-to-solid ratio of $650 \text{ g}\cdot\text{kg}^{-1}$, the Zn content in the leaching residue was 0.31% while the Cu content was 0.08%. These results demonstrate the limited effect of increasing significantly the acid-to-solid ratio on Zn and Cu leaching efficiencies for values higher than $200 \text{ g}\cdot\text{kg}^{-1}$.

3.2.4. Effect of solid content on leaching yield

Another set of experiments was performed in which the acid-to-solid ratio was fixed at $200 \text{ g}\cdot\text{kg}^{-1}$ (Figure 11) to assess the influence of solid content on leaching yields. In this case, an increase in solid content from 2.9% to 4.5% appeared to enhance the leaching efficiency for both metals. Further increasing this value to about 8.6% did not significantly influence the leaching yield. However, with a solid content of 16%, a leaching efficiency decrease is observed. Moreover, the variations in the leaching efficiency of these metals were also reflected in the metal content in the leaching residue.

The results of these experiments suggest that the leaching efficiency of metals might have a positive correlation with the solid content up to 4.5%. However, further increases beyond 8.6% values could have a slightly negative effect on the leaching yields of Cu and Zn but a more substantial effect for Fe. Given the small variations observed and the limited number of data points (only two up to 4.5%) without replicates, these results should be interpreted with caution. Further statistical confirmation with replicates and more data points would be necessary to validate these findings.

Throughout the leaching experiments, the final calcium concentrations were consistently measured between 440 and $570 \text{ mg}\cdot\text{L}^{-1}$. These concentrations are close to or moderately lower than the Ca concentration of an aqueous solution in equilibrium with gypsum under standard conditions. Consequently, the dissolution rates of calcium were predominantly determined by the solid content, resulting in a wide

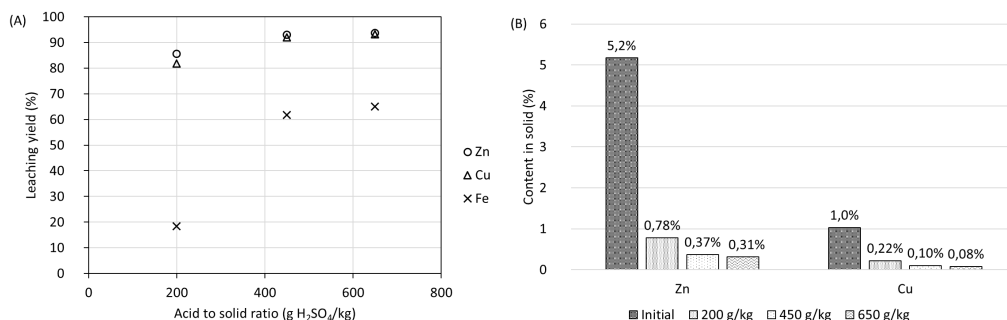


Figure 10. (A) Metal leaching yields (LY_{solid}) and (B) metal contents in solid residue at different acid-to-solid ratios with a solid content of 2.9% m/m.

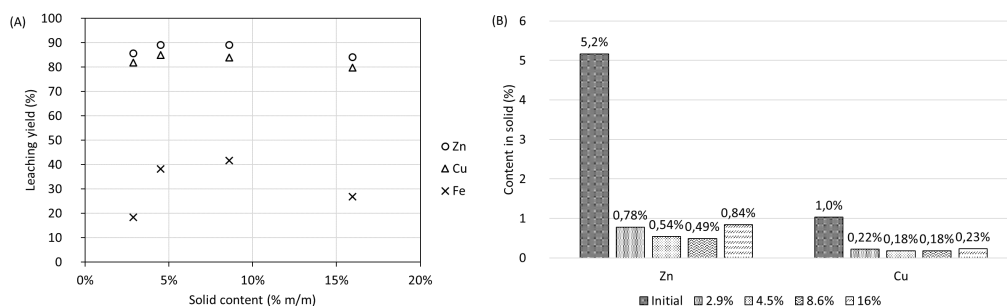


Figure 11. (A) Metal leaching yields (LY_{solid}) and (B) metal contents in solid residue at different solid contents at an acid-to-solid ratio of 200 g H₂SO₄·kg⁻¹.

range of leaching yields from 4% (at a solid content of 9.4%) to 64% (at a solid content of 0.7%) as presented in Supplementary Figure S6. There also appears to be a minor unknown phenomenon decreasing Ca concentration at lower pH.

3.2.5. Effect of temperature on leaching yield

The effect of temperature on metal leaching efficiency was also studied with an acid-to-solid ratio of 200 g·kg⁻¹, a solid content of 2.9%, and a reaction time of 24 h. Figure 12 shows the Zn and Cu leaching yields as well as the Fe concentration in the leachate at 22 °C, 40 °C, and 60 °C. One can observe that by increasing the temperature from 22 °C to 40 °C, it was possible to increase both Zn and Cu leaching yields by respectively 2 and 4 percentage points (pp) at these conditions. However, no significant enhancement of efficiency is observed if the temperature is further increased to 60 °C. It is interesting to observe that the Fe concentration in the leachate decreases considerably as the temperature increases.

It is known that Fe(III) can precipitate even at low pH values in the form of jarosite (KFe₃(SO₄)₂(OH)₆) or schwertmannite (Fe₈O₈(OH)₆(SO₄)·nH₂O) and that this phenomenon is favored by the increase in temperature [34].

4. Discussion

4.1. Implication of mineralogy on metal leaching behavior

A common result for all the leaching tests performed in this study is the presence of a concentration plateau for Zn and Cu at the end of the experiments, in general after 6 h, which corresponds to an incomplete leaching of these metals. The parametric study aimed at improving the leaching kinetics, which resulted in slightly higher leaching yields. However, it is clear that there is a limitation regarding the maximum leaching efficiency achieved at the conditions tested, which translates into an incomplete removal

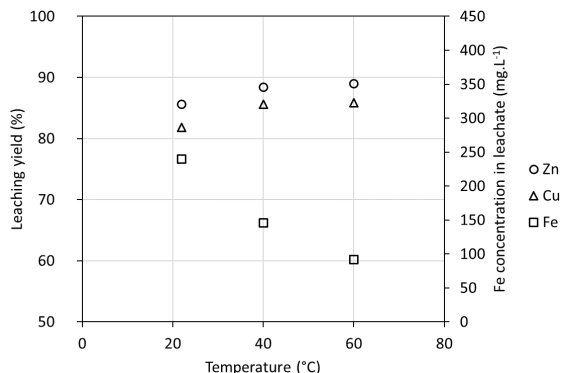


Figure 12. Metal leaching yields (LY_{solid}) at different temperatures using 200 g H_2SO_4 /kg and 2.9% m/m of solids after 24 h.

of Cu and Zn from the sludge. Nevertheless, introducing the entire acid quantity at the beginning of the reaction, rather than having a constant pH in the system, improved the leaching kinetics and yields for the same amount of acid. This implies that having a higher acidic environment at the early stages of the reaction is beneficial for metal leaching. Several hypotheses can explain these observations. Our first hypothesis is that a small proportion of Cu and Zn are embedded in the amorphous iron mineral. This is based on the limited evidence of Zn- and Cu-rich mineral phases in the sludge (excepting few delafossite crystals identified for Cu but which also contain Fe).

Figure 13 plots the correlations between Zn and Cu leaching yields and Fe leaching yields. A positive linear correlation was found for both Zn ($R^2 = 0.9161$) and Cu ($R^2 = 0.9025$) at 22 °C in 2 L reactors. Interestingly, for most experiments, the increases in metal leaching yields over 85% are observed for conditions involving high acid-to-solid ratios ($>250 \text{ g}\cdot\text{kg}^{-1}$) or moderate-to-high solid contents ($>2.9\%$). These conditions imply a very low pH (<1.7) at the beginning of the experiments, which caused the partial dissolution of Fe compounds.

The maximum leaching yield obtained in this study was 94% for Zn and 93% for Cu at a solid content of 2.9% and an acid-to-solid ratio of $650 \text{ g}\cdot\text{kg}^{-1}$. However, when acid-to-solid ratios are higher than $200 \text{ g}\cdot\text{kg}^{-1}$, the improvement in both Cu and Zn leaching efficiencies is limited since a significant part of the acid added reacts with iron oxyhydroxides such

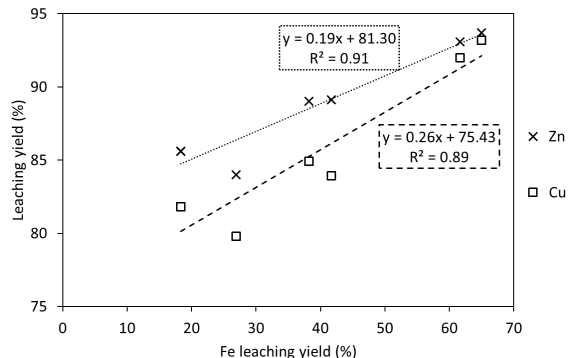
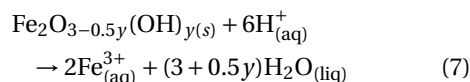


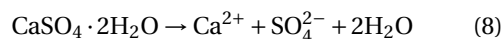
Figure 13. Correlation between targeted metal leaching yields and Fe leaching yields for experiments at 22 °C in 2 L reactors.

as the ferrihydrite according to Equation (7) [33]:



Here, $\log K = 8.46$ for two-line ferrihydrite and 10.12 for six-line ferrihydrite, both at standard conditions (25 °C and 1 bar). $\text{Fe}_2\text{O}_{3-0.5y}(\text{OH})_y$ is the formula proposed by Yu et al. [33] as ferrihydrite has not only variable chemical composition depending on the degree of hydration but also variable crystallinity.

Besides, lower initial pH values obtained at high acid-to-solid ratios can also increase the solubility of the gypsum present in significant quantities in the sludge. Gypsum dissolved according to Equation (8) with a solubility product in water (K_{sp}) of 2.58×10^{-5} [35]:

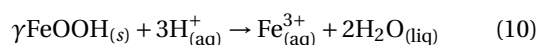


At pH lower than 1.9, the species HSO_4^- may become predominant over SO_4^{2-} [36]. Thus, the increase in sulfate concentration in the leachate caused by the gypsum dissolution may act as a buffer, according to Equation (9), with a pK_a of 1.9.



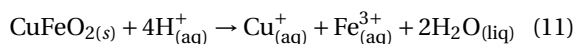
Therefore, at high acid-to-solid ratios and very low pH values, free protons are not only consumed in the leaching of Cu and Zn but also in other reactions involving the dissolution of other metals such as Fe and Ca. The increase in acid-to-solid ratios to values higher than about $200 \text{ g}\cdot\text{kg}^{-1}$ may decrease the selectivity of the process towards Zn and Cu recovery, and it can be even considered as an inefficient way of enhancing the leaching efficiencies of

the targeted metals. The limitation on metal dissolution despite the increase in acid-to-solid ratio could then be explained by the presence of non-soluble Cu and Zn minerals in sulfuric acidic media at the pH tested in this study. As previously detailed, the study of sludge mineralogy revealed the presence of Cu-Fe crystallites, identified as delafossite (CuFeO_2), as well as ferrihydrous tabular crystallites with Zn (probably $\gamma\text{FeO}(\text{OH})$). Therefore, the remaining Cu and Zn may be trapped in these less soluble Fe minerals present in the sludge. The dissolution reaction of lepidocrocite [29] is presented in Equation (10).



Here, $\log K = 1.4$ at standard conditions (25 °C and 1 bar). Indeed, by comparing the solubility products of the iron minerals in this study at standard conditions (similar to the conditions of experiments performed), it is possible to observe that there is a difference of about 2.9 orders of magnitude for the product, dissolved Fe^{3+} , between two-line ferrihydrite and lepidocrocite. The difference is even higher for the better crystallized six-line ferrihydrite. This implies a lower solubility of the lepidocrocite, which may potentially contain residual Zn and Cu at similar conditions of pH, solution composition, and ionic strength.

Due to the absence of specific literature detailing the acid leaching reaction of delafossite with sulfuric acid but knowing that in delafossite, iron is trivalent while copper is monovalent [37], we have proposed a plausible chemical reaction balanced stoichiometrically according to Equation (11).



In their investigation of copper smelter flue dust containing delafossite, Vitkova *et al.* [38] subjected the material to leaching with HNO_3 , adjusting the pH to 3.0. They found that approximately 60% of copper remained undissolved, and delafossite was present in all residue samples post-leaching. Complementing this, Khalid *et al.* [39] observed incomplete copper dissolution from delafossite-containing converter slag when using 1 M H_2SO_4 . These studies imply that delafossite exhibits limited solubility in acidic environments, thereby supporting the hypothesis of the presence of undissolved delafossite in our residues.

4.2. Implications in a potential industrial process for the valorization of sludge

The results of this study indicate the feasibility of selectively leaching Zn, Cu, and Cd from lime treatment sludge, particularly when compared to Fe, which is a predominant component of sludge. This is supported by the leaching tests in 2 L reactors at an acid-to-solid ratio of $175 \text{ g}\cdot\text{kg}^{-1}$, which demonstrated leaching yields of 84% for Cu and 79% for Zn and complete leaching of Cd while keeping the leaching yield for Fe below 1% as detailed in Figure 9.

The rise in temperature from 22 °C to 40 °C can also be a means to augment both Zn and Cu dissolution. It also decreases the Fe concentration in the leachate due to the precipitation of Fe oxyhydroxysulfates, which is favored at higher temperatures. Nonetheless, this would imply heating the reactors, which will influence the operating costs. Given the little gain regarding Zn and Cu leaching yields at 40 °C compared to ambient temperature, the implementation of heated reactors with temperature control might not be viable from an economic and environmental point of view. Nevertheless, this option should be further studied.

On the other hand, experiments show that it is possible that a high solid content in the reactor (16%) caused solid-liquid mass transfer limitations, which produced lower leaching yields than those found at lower solid contents. High solid contents can lead to increased viscosity and reduced mixing efficiency, hampering mass transfer between the solid phase and the leachate. This can limit the accessibility of the leachate to Cu and Zn minerals on the particles. Another factor that could explain this is the decreased ratio of surface area to volume: as the solid content increases, the available surface area for reaction per unit volume of the solution decreases, leading to lower reaction rates. An optimum solid content at which metal leaching is optimal should exist, probably between 5% and 15% m/m. In any case, more information is needed on this point to define whether the efficiency limitation at high solid contents is linked to the kinetics of the chemical reactions involved in mineral dissolution or is related to the hydrodynamic conditions of the reactor.

Nonetheless, at 16% solid content and an acid-to-solid ratio of $200 \text{ g}\cdot\text{kg}^{-1}$, the leachate contains $8.2 \text{ g}\cdot\text{L}^{-1}$ Zn, $1.5 \text{ g}\cdot\text{L}^{-1}$ Cu, and $1.7 \text{ g}\cdot\text{L}^{-1}$ Fe. These

concentrations of Cu and Zn are sufficient for an economically viable downstream metal recovery process to be envisaged [24,40]. Iron concentrations at this level are obviously an issue given the objective of selective leaching (as explained in Section 1), but as shown in Figure 9, a limited decrease in acid-to-solid ratio significantly decreases iron leaching. Nevertheless, the optimum operating conditions for leaching will have to be investigated in reactors fed in continuous mode.

5. Conclusion

Sludges produced from the lime treatment of AMD can sometimes represent a significant deposit of valuable metals. On the site presented in this study, the deposit of anthropogenic ore is estimated at 150 kt containing 1.3% Cu and 5.1% Zn. These contents of Cu and Zn are higher than those found in many deposits being mined today. The selective leaching process applied in this study allowed the leaching of more than 80% of Cu and Zn from the sludge under optimal operating conditions, which are defined between 5% m/m and 15% m/m of solid content with an acid-to-solid ratio between 150 and 200 g·kg⁻¹ at room temperature (22 °C). Using more acid marginally increases the dissolution rates at the cost of much higher acid consumption linked to the dissolution of iron and therefore a loss of selectivity. Increasing the temperature to 40 °C improves the dissolution of Cu and Zn and decreases that of Fe, but its potential economic impact has not yet been estimated. The results of this work will serve to further develop the process by adding selective precipitation and purification steps. Moreover, the data acquired during this study will be used to carry out a preliminary economic assessment, including operating expenses, capital expenses, and return on investment.

Declaration of interests

The authors do not work for, advise, own shares in, or receive funds from any organization that could benefit from this article, and have declared no affiliations other than their research organizations.

Funding

This work has been funded by the Department for Mine Safety and Risk Prevention of BRGM: French Geological Survey.

Acknowledgments

The authors would like to thank the former and current project team members: Maxime Vignon, Rachel Seillier, Rany Ajami, Benoit Henry, Jérémy Engevin, Camille Becquet, Mohamed Djemil, Stéphane Touzelet, and Marine Respaut. This project has benefited from the expertise and facilities of Platform MACLE-CVL, which was co-funded by the European Union and Centre-Val de Loire Region (FEDER).

Supplementary data

Supporting information for this article is available on the journal's website under <https://doi.org/10.5802/crchim.327> or from the author.

References

- [1] D. B. Johnson and K. B. Hallberg, *Sci. Total Environ.* **338** (2005), pp. 3–14.
- [2] Z. Li, Z. Ma, T. J. van der Kuijp, Z. Yuan and L. Huang, *Sci. Total Environ.* **468–469** (2014), pp. 843–853.
- [3] S. Farag, R. Das, W. H. J. Strosnider and R. T. Wilson, *J. Occup. Environ. Med.* **57** (2015), pp. 543–551.
- [4] D. Artignan, P. Baranger, P. Billaud, M. Lansiaart and B. Mazenc, *L'élaboration des Plans de Prévention des Risques Miniers. Guide méthodologique - Volet technique relatif à l'évaluation de l'aléa "pollution des sols et des eaux"*, BRGM: Orléans, 2008. BRGM/RP-55143-FR.
- [5] M. Castello and M. Bouchi-Lamontagne, *L'après-mine en France*, Editions BRGM: Rueil-Malmaison Orléans Paris, 2006.
- [6] S. Altmann, P. Conil, M. Bornuat, J. Marroncle, I. Salpeur and J. Feraud, *Les résidus miniers français, typologie et principaux impacts environnementaux potentiels*, BRGM: Orléans, 1997. BRGM/RR-39503-FR. Accessed: November 3, 2023. [Online]. http://pmb.brgm.fr/brgm/brgm_broogle_notice.php?id=43520.
- [7] United States. Bureau of Land Management, Montana. Department of Environmental Quality, Montana. Department of Natural Resources and Conservation, and United States. Army. Corps of Engineers, Eds, *Draft environmental impact statement Golden Sunlight Mine* :, US Department of the Interior, Bureau of Land Management, Butte District, 1997.

- [8] C. Tabelin, A. Sasaki, T. Igarashi, S. Tomiyama, M. Villacorte-Tabelin, M. Ito and N. Hiroyoshi, *MATEC Web of Conferences*, EDP Sciences: Les Ulis, 2019, p. 06003.
- [9] R. A. Davis Jr, A. T. Welty, J. Borrego, J. A. Morales, J. G. Pendon and J. G. Ryan, *Environ. Geol.* **39** (2000), pp. 1107–1116.
- [10] J. G. Skousen, P. F. Ziemkiewicz and L. M. McDonald, *Extr. Ind. Soc.* **6** (2019), pp. 241–249.
- [11] G. S. Plumlee, K. S. Smith, M. R. Montour, W. H. Ficklin and E. L. Mosier, *Environ. Geochem. Miner. Deposit. Rev. Economic Geol.* **6** (1999), pp. 373–432.
- [12] D. T. Chen, W. Y. Au, S. Ewijk, A. Roy and J. A. Stegemann, *J. Hazard. Mater.* **416** (2021), article no. 125676.
- [13] R. Anwar, M. Ahmed, P. Seats, Q. Huang and L.-S. Lin, *Rev. Environ. Sci. Biotechnol.* **20** (2021), pp. 679–695.
- [14] I. Moodley, C. M. Sheridan, U. Kappelmeyer and A. Akcil, *Miner. Eng.* **126** (2018), pp. 207–220.
- [15] J. Skousen, in *Acid Mine Drainage, Rock Drainage, and Acid Sulfate Soils: Causes, Assessment, Prediction, Prevention, and Remediation* (J. A. Jacobs, J. H. Lehr and S. M. Testa, eds.), Wiley: Hoboken, NJ, 2014, pp. 325–337.
- [16] J. Taylor, S. Pape and N. Murphy, in *Proceedings of the 5th Australian Workshop on Acid Drainage* (L. C. Bell and R. W. McLean, eds.), Australian Centre for Minerals Extension and Research: Fremantle, 2005, pp. 1–49. Accessed: November 3, 2023. [Online]. https://earthsystems.com.au/wp-content/uploads/2012/02/AMD_Treatment_Technologies_06.pdf.
- [17] B. C. Aubé and J. M. Zinck, in *Proceedings of the Sudbury '99 Mining and the Environment II, September 7–13* (D. Goldsack, N. Belzile, P. Yearwood and G. Hall, eds.), Centre in Mining and Mineral Exploration Research (CIMMER): Sudbury, ON, 1999, pp. 261–270.
- [18] F. Macías, R. Pérez-López, M. A. Caraballo, C. R. Cánovas and J. M. Nieto, *J. Clean. Prod.* **141** (2017), pp. 1057–1066.
- [19] D. K. Nordstrom, R. J. Howell, K. M. Campbell, C. N. Alpers, L. Sartz, M. Sillanpää and A. Häkkinen, in *Proceedings of 13th International Mine Water Association Congress* (C. Wolkersdofer, ed.), Lappeenranta University of Technology (LUT): Lappeenranta, 2017, pp. 1138–1146. Accessed: November 3, 2023. [Online]. <https://pubs.er.usgs.gov/publication/70190131>.
- [20] A. H. Kaksonen and J. A. Puhakka, *Eng. Life Sci.* **7** (2007), pp. 541–564.
- [21] F. Macías, M. A. Caraballo, J. M. Nieto, T. S. Rötting and C. Ayora, *J. Environ. Manage.* **104** (2012), pp. 93–100.
- [22] P. Ziemkiewicz, A. Noble and C. Vass, Systems and processes for recovery of high-grade rare earth concentrate from acid mine drainage, US patent, US10954582B2, 2021. Online at <https://patents.google.com/patent/US10954582B2/en>. Accessed: November 3, 2023. [Online].
- [23] B. Aubé and J. Zinck, *Proceedings, Brazil–Canada Seminar on Mine Rehabilitation–Technological Innovations*, Desktop Publishing: Florianópolis, 2003, pp. 89–105. Accessed: January 16, 2024. [Online]. <http://mineralis.cetem.gov.br:8080/bitstream/cetem/681/3/brazil-canada-seminar-on-mine-rehabilitation.pdf#page=89>.
- [24] M. L. Free, *Hydrometallurgy: Fundamentals and Applications*, Springer Nature: Cham, 2021.
- [25] M. Nicol, *Hydrometallurgy: Practice*, Elsevier: Amsterdam, 2022.
- [26] S. Touzé, V. Laperche, A. Hubau and P. Moreau, *Waste Manag.* **146** (2022), pp. 66–76.
- [27] B. Lemiére, *J. Geochem. Explor.* **188** (2018), pp. 350–363.
- [28] R. López-Núñez, *Appl. Sci.* **12** (2022), article no. 6944.
- [29] R. M. Cornell and U. Schwertmann, *The Iron Oxides: Structure, Properties, Reactions, Occurrences, and Uses*, 2nd, completely rev. and extended edition, Wiley-VCH: Weinheim, 2003.
- [30] A.-G. Guezennec, C. Joulain, C. Delort, F. Bodénan, S. Hedrich and P. D’hugues, *Hydrometallurgy* **180** (2018), pp. 277–286.
- [31] X. Liu and F. J. Millero, *Mar. Chem.* **77** (2002), pp. 43–54.
- [32] A. J. Martin, S. Fawcett, E. Kulczycki, D. Loomer, T. Al and A. Rollo, *Application of high-resolution microscopy methods to the analysis of fine-grained and amorphous treatment sludges*. Online at <https://open.library.ubc.ca/soa/cIRcle/collections/59368/items/1.0107744>. [Online]. Accessed: March 11, 2024.
- [33] J.-Y. Yu, M. Park and J. Kim, *Geochem. J.* **36** (2002), pp. 119–132.
- [34] J. E. Dutrizac, *Metall. Trans. B* **14** (1983), pp. 531–539.
- [35] A. C. Bennett and F. Adams, *Soil Sci. Soc. Am. J.* **36** (1972), pp. 288–291.
- [36] W. Stumm and J. J. Morgan, *Aquatic Chemistry: Chemical Equilibria and Rates in Natural Waters*, Wiley: Hoboken, NJ, 1996.
- [37] C. Delorme and F. Bertaut, *J. Phys. Radium* **14** (1953), pp. 129–130.
- [38] M. Vítková, V. Ettler, J. Hyks, T. Astrup and B. Křibek, *Appl. Geochem.* **26** (2011), S263–S266.
- [39] M. K. Khalid, J. Hamuyuni, V. Agarwal, J. Pihlasalo, M. Haapalainen and M. Lundström, *J. Clean. Prod.* **215** (2019), pp. 1005–1013.
- [40] W. Qin, W. Li, Z. Lan and G. Qiu, *Miner. Eng.* **20** (2007), pp. 694–700.

Review article

GDR Prométhée – French Research Network on *Hydrometallurgical Processes for Primary and Secondary Resources*

Dissolution and precipitation of jarosite-type compounds: state of the art and future perspectives

Mateus De Souza Buriti ^a, Pierre Cézac ^{*,a} and Lidia Casas ^{*,a}^a Université de Pau et des Pays de l'Adour, E2S UPPA, LaTEP, Rue Jules Ferry BP 7511
64 075 PAU Cedex, Pau, FranceE-mails: mdsburiti@univ-pau.fr (M. De Souza Buriti), pierre.cezac@univ-pau.fr
(P. Cézac), lidia.casas@univ-pau.fr (L. Casas)

Abstract. Jarosite-type compounds are complex-structured minerals that are widely distributed in natural environments, utilized in industrial processes, or formed as byproducts of these processes. Consequently, a comprehensive understanding of the kinetics and thermodynamics of jarosite precipitation and dissolution is important for the effective control and management of this mineral. However, literature data is lacking or inconsistent regarding these phenomena. The availability of accurate and reliable data is of utmost importance for the development and improvement of robust hydrometallurgical processes and for regulating the environmental impact of this mineral. In light of this importance, this work aims to review the most important studies published up to 2023 related to obtaining data on jarosite dissolution and precipitation. Therefore, this article contributes to a detailed analysis of the current state of the art and outlines future prospects for research on this secondary mineral.

Keywords. Jarosite, Kinetics, Thermodynamics, Environment, Industrial processes.

Manuscript received 14 December 2023, revised 26 April 2024 and 25 May 2024, accepted 27 May 2024.

1. Introduction

Jarosite-type compounds are minerals belonging to the alunite–jarosite group presenting an ideally general formula $[A_\alpha B_\beta (CO_4)_\gamma (OH)_\delta]$. Several types of jarosites can form depending on the ions occupying the **A**-, **B**-, and **C**-sites in the mineral structure. **A**-sites are commonly occupied by monovalent (K^+ , Na^+ , Ag^+ , Tl^+ , NH_4^+ , Rb^+ , H_3O^+), divalent (Cu^{2+} , Hg^{2+} , Ca^{2+} , Sr^{2+} , Ba^{2+} , Pb^{2+}), trivalent or quadrivalent (Ga^{3+} , Cr^{3+} , Th^{4+} , U^{4+}) cations. The **B**-site can be occupied by smaller cations with octahedral coordination (Fe^{3+} and Al^{3+}), or minor ions such as V^{3+} ,

Fe^{2+} , Cu^{2+} , Zn^{2+} , Mg^{2+} . Finally, the **C**-site can be occupied by S^{6+} , Cr^{6+} , As^{5+} or P^{5+} [1–6]. Ion stoichiometry (α , β , γ , δ) will be directly related to the valency of the ions present in the **A**-, **B**-, and **C**-sites.

The most important and common jarosite-type mineral found in terrestrial environments is K-jarosite $[KFe_3(SO_4)_2(OH)_6]$. The structure of jarosite is based on linear tetrahedral–octahedral–tetrahedral (T–O–T) sheets, made up from slightly distorted FeO_6 octahedra and SO_4 tetrahedra [5,7]. Authors affirm that K-jarosite structure generally contains ferric ion vacancies and “additional water” in the form of hydronium. Therefore, the chemical formula is more correctly written as $H_3O_{1-x}K_xFe_{3-y}[(OH)_{6-3y}(H_2O)_{3y}(SO_4)_2]$ [3,4,7–9].

According to Alpers et al. [4], any attempt to define the thermodynamic properties of minerals in the

*Corresponding author

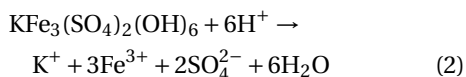
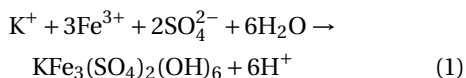
alunite–jarosite group must consider issues related to the non-stoichiometry of their structures. Indeed, the values of the $(\text{Al} + \text{Fe})/\text{SO}_4$ ratio can vary considerably from the ideal stoichiometry of 3/2 (3 moles of Fe^{3+} to 2 moles of sulfate), as observed in the work of Härtig *et al.* [8], with ratios ranging from 2.20/2 to 2.52/2, as well as in the research of Ripmeester *et al.* [9], with a ratio of 2.33/2.

1.1. *Jarosite in the environmental context*

Jarosite-type compounds are largely found in the terrestrial ecosystem as ferric sulfate salt that often forms in acidic and oxidizing environments enriched in sulfate. Different studies have shown its presence in:

- Acid sulfate soils formed from pyrite sediments [10–13];
- Acid sulfate waters [14];
- Acid rock drainage (ARD) or acid mine drainage (AMD) [4,15–23];
- Weathering residues from sulfide ore deposits [24];
- Alteration of coal from pyritic coal beds [25];
- Clay layers and beds [26,27];
- Proximity to volcanic fissures [28–30];
- Oceanic fumaroles [31,32] and hot springs [33];
- Hydrothermal environments [34,35], sometimes associated with basalt [36];
- Hypersaline lakes, such as those in Australia and Antarctica [26,29,37–42].

The formation of jarosite and the release of H^+ are often attributed to the oxidation of sulfur-bearing minerals such as pyrite (FeS_2), which alters groundwater and effluent environments [43,44]. Ideally, the formation (1) and dissolving (2) equations for K-jarosite are expressed below:



On the other hand, the dissolution of jarosite in AMD occurs when the acid production exceeds the buffering capacity of the surrounding rock or soil. The pH values in pyritic mine waste and acid lakes typically range from pH 1.5 to 3 [45], leading to the release of

heavy metals present in the jarosite structure. Therefore, it is essential to understand the formation of jarosite and its dissolution, as well as their impact on soil and water chemistry, in order to effectively manage soils containing sulfur-bearing minerals [46].

Furthermore, the early 2000s brought the discovery, in situ and from orbiting spacecraft, of jarosite on Martian soil [47–55]. This observation indicates that oxidizing and acidic fluids were present when jarosite was formed [48,56,57], and consequently, suggests the possibility of water existence on Martian soil. Other evidence has shown that hematite found on Mars has also been formed from jarosite [36,58,59].

1.2. *Jarosite in the hydrometallurgical industrial context*

Since the 1960s, the hydrometallurgical industry has been widely using the precipitation of jarosite compounds in industrial processes for separation of zinc from iron [60]. The production of zinc generates a large amount of jarosite-type compounds, which represents a potential environmental problem, since the jarosite scavenger property allows the presence of toxic elements in the iron residues. On the other hand, these residues may present economic value with the recovery of critical and valuable metals from zinc production waste. The study of jarosite leaching conditions constitutes, therefore, an attractive research area to reduce environmental issues and produce new resources [61].

Due to the presence of jarosite in industrial processes, it is of great importance to manage its residues, as its formation and dissolution mechanisms can alter the chemical environmental of rivers and groundwater by releasing the retained acidity, sulfate, hazardous elements, and secondary mineral waste depending on the conditions. Therefore, understanding the immobilization property of jarosite-type compounds is useful in forming stable minerals to reduce their spread in soils and aquifers and to help manage waste materials from mining tailings.

Therefore, having in mind the wide range of applications, rigorously understanding and evaluating jarosite dissolution and stability is important to predict the effect of long-term jarosite behavior on soil, water, and industrial processes, as well as to effectively manage hazardous waste to create

potential remediation strategies, diminish environmental impact and improve hydrometallurgical processes to create economic profit [43,44,46,62–67].

With that aim, the collection and critical assessment of thermodynamic and kinetic data for jarosite dissolution and precipitation processes are necessary. Therefore, numerous scientists and research groups have made efforts to elucidate the behavior of jarosite-type compounds under different conditions over the past decades. Regardless, the results described in the literature concerning the solubility and kinetics of this compound are highly variable [46,68]. Consequently, this review dedicates the following sections to shedding light on the works conducted up to this date and explaining the potential sources of disagreement among them.

1.3. Jarosite stability and transformations

Ferric phases undergo transformations into alternative phases upon removal from their stability zones. Jarosite-type compounds, for instance, are documented to go through a transformation resulting in the different phases, as illustrated in Figure 1.

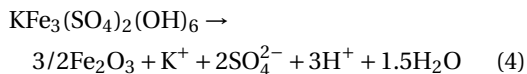
It is established that jarosite can easily decompose when removed from its stability zone, transforming into phases of iron oxide or iron (III) oxyhydroxide [5,35]. These transformations can also result in the release of acidity. Jarosite is considered a retained acidity (RA) resource in these environments, a form of acidity potentially released through the hydrolysis of poorly soluble and poorly crystalline Al^{3+} or Fe^{3+} minerals [46,65,66,69]. According to Stoffregen [70], under surface conditions, jarosite tends to transform into goethite through the following reaction when exposed to diluted water with a higher pH:



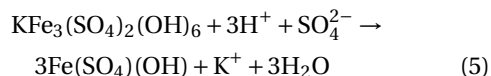
However, this reaction can be complicated by the formation of metastable phases such as schwertmannite and ferrihydrite [71]. Ferrihydrite is a well-known hydrated iron oxide with chemical formula $5\text{Fe}_2\text{O}_3 \cdot 9\text{H}_2\text{O}$ [72], where the hydration level can vary depending on how much water is present within the molecular arrangement [73,74]. Schwertmannite is an oxyhydroxysulfate with chemical formula $\text{Fe}_8\text{O}_8(\text{OH})_{8-2x}(\text{SO}_4)_x \cdot n\text{H}_2\text{O}$ where $1 \leq x \leq 1.75$.

Above the transition temperatures from goethite to hematite, i.e., at 373.15 K, the transformation

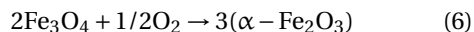
reaction of jarosite becomes:



The only compound that has appeared in addition to the previous equation is the formation of $\text{Fe}(\text{SO}_4)(\text{OH})$, which does not exist naturally but has already been reported by Posnjak and Merwin [75] in the study of the $\text{Fe}_2\text{O}_3\text{--H}_2\text{O--SO}_3$ system at temperatures higher than 373.15 K:



The anhydrous forms of iron oxide can also exhibit different polymorphs, meaning the same chemical structure but different crystalline systems. The most well-known forms are hematite ($\alpha\text{-Fe}_2\text{O}_3$) and maghemite ($\gamma\text{-Fe}_2\text{O}_3$). Hematite can be formed from magnetite through the following equation:



Like iron oxides, anhydrous iron oxyhydroxides (FeOOH) can exhibit several polymorphs. Goethite ($\alpha\text{-FeOOH}$) is the most well-known compound, but there is also akaganeite ($\beta\text{-FeOOH}$) and lepidocrocite ($\gamma\text{-FeOOH}$). Redox-pH potential diagrams have been constructed showing the jarosite–hematite boundary between pH 2 and 4, and jarosite–goethite between pH 2 and 3 [76].

Bigham *et al.* [77] analyzed ochreous sediments as well as their associated solutions from twenty-eight AMD sites ranging from 279 to 300 K. The results revealed a change in solid composition depending on the pH of the mixture. Precipitates formed above pH 6.5 were mainly composed of ferrihydrite or a mixture of ferrihydrite and goethite. In contrast, precipitates with pH between 2.8 and 4.5 were mainly composed of schwertmannite, with traces of goethite and/or jarosite. Solutions with intermediate pH (between 4.5 and 6.5) produced a mixture of ferrihydrite and schwertmannite. Only the solution at pH 2.6 contained a considerable amount of jarosite. Bigham and his colleagues also developed a revised model for mineral speciation at 298 K and redox potential ranging, according to the pH, from -237 to 947 mV ($\text{pH} > 6.5$), 118 to 1065 mV ($2.8 < \text{pH} < 4.5$), 0 to 1000 mV ($4.5 < \text{pH} < 6.5$) and 592 to 1184 mV ($\text{pH} < 2.6$).

The continuation of this paper is organized as follows: Section 2 presents thermodynamic studies of

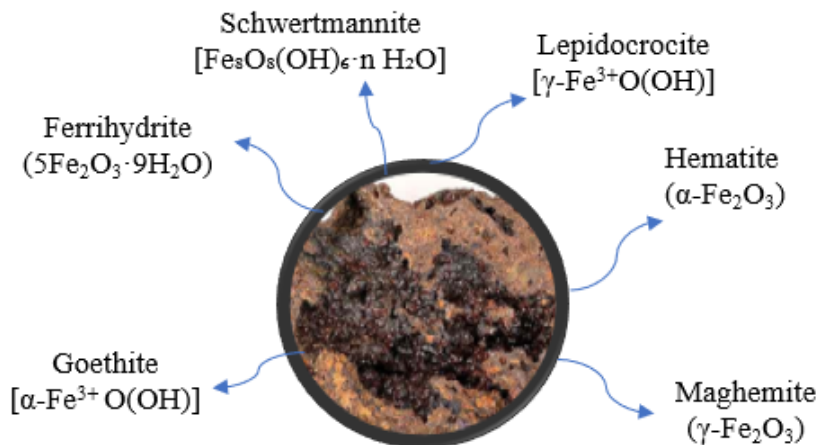


Figure 1. Transformations of jarosite compounds into different ferric phases.

jarosite, including those using dissolution, precipitation, and calorimetry. Section 3 discusses the kinetic dissolution studies within the environmental and industrial contexts. Section 4 focuses on the kinetic studies of jarosite-type compound precipitation at high and low temperatures, both with and without the presence of microorganisms. Finally, Section 5 highlights the most relevant methods used in the literature to characterize jarosite phases.

2. Thermodynamic studies of jarosite

Several studies have focused extensively on the study of the crystallography and structure of jarosite compounds [78,79]. The investigations into the structure of jarosite date back to the mid-20th century. Initially, Parker [80] examined alunite minerals containing potassium or sodium. Concurrently, Brophy *et al.* [81] studied K-jarosite and K-alunite. Kubisz [82] dedicated his research to the study of potassium and hydronium substitution in jarosite, demonstrating the existence of H_3O -jarosite.

However, Brophy and Sheridan [2] were the first to investigate the substitution of $\text{K-Na-H}_3\text{O}^+$ mixture in the jarosite structure under terrestrial surface temperature and pressure conditions. Additionally, in their study, they asserted that hydronium substitution by potassium in the jarosite structure is facilitated by an increase in temperature, in line with several studies conducted in the 1950s on the composition of natural and synthetic jarosites.

Furthermore, Ross *et al.* [83] showed that H_3O -jarosite can form in the absence of alkalis.

Since the studies on the structure and composition of jarosites, researchers have frequently noted the variability of the solubility product data. Some authors have delved into dissolution and/or precipitation phenomena to obtain thermodynamic data [4,7,68,70,84–86], while others have reinterpreted these results by introducing additional thermodynamic data for equilibrium calculations, proposing new values [22,24,87–90].

Nevertheless, the most cited paper and reliable data used nowadays still is Baron and Palmer [68] who studied the thermochemistry and solubility of synthetic K-Jarosite dissolution at different pH and near room temperatures using a stirred batch reactor and were the first to carry out a calorimetric study of K-Jarosite. This study formed a basis for other similar investigations, like the thermodynamic study by Smith *et al.* [7] who calculated the solubility product constant (K_{sp}), the ion activity product (IAP) and saturation indices (SI). However, more recently, Lemire *et al.* [90] from the OECD Nuclear Energy Agency published a book on the chemical thermodynamics of iron re-evaluating the results obtained by Baron and Palmer [68], which will be discussed later in Section 2.1.

Other authors, like Drouet and Navrotsky [76], worked with the calorimetric study of Na-jarosite, while Majzlan *et al.* [91] studied thermodynamic properties of H_3O -jarosite. Other authors studied

the thermodynamics of jarosite such as Jamieson *et al.* [17], Navrotsky *et al.* [19], Casas *et al.* [92], and Forray *et al.* [93].

Hence, Section 2 is divided into two main parts. Section 2.1 presents studies using dissolution and precipitation processes to obtain thermodynamic data, while Section 2.2 focuses on thermodynamic data obtained through calorimetry studies.

2.1. *Thermodynamic studies through dissolution and precipitation*

Table 1 presents the thermodynamic solubility constants, mostly at 298.15 K, reported in the literature, which vary considerably from one study to another. For example, for K-jarosite, the logarithm of the equilibrium constant ranges from -7.12 to -12.51 , a difference of five orders of magnitude. These discrepancies are primarily explained by variations in the methodologies used, which will be described in this section.

Brown [84] investigated the precipitation of K-jarosite at 298.15 K and 0.1 MPa over a six-month period. He used K_2SO_4 , hydrated $FeSO_4$, and dissolved $Fe_2(SO_4)_3$ in known concentrations of H_2SO_4 . Subsequently, he employed a reverse approach (dissolution) using 0.5 g of jarosite in 0.005 M H_2SO_4 solution for six months. Brown considered the potential presence of additional compounds after precipitation and dissolution experiments. Consequently, X-ray diffraction (XRD) analysis was employed to address this question. However, all the X-ray diffraction patterns could only be identified as jarosite lines. Through the calculations of the free energy of formation, he demonstrated that equilibrium was practically reached by both methods with a slight difference in free energy of formation (-3276 ± 84 and -3192 ± 25 kJ/mol for precipitation and dissolution, respectively). Additionally, he calculated redox potential (E_h), pH, and plotted the activity logarithm diagram for the jarosite–goethite–pyrite system, highlighting the equilibrium of these minerals under ambient conditions.

The Gibbs free energies found by Brown [84] were initially recalculated (-3302 ± 84 and -3300 ± 25 kJ/mol for precipitation and dissolution, respectively) by Zotov *et al.* [87], who identified an arithmetic error in the calculations. Then, they used different thermodynamic data from Naumov *et al.* [96].

Furthermore, Zotov *et al.* [87] conducted precipitation experiments using a natural water sample and found the Gibbs free energy to be -3305.7 kJ/mol. Subsequently, Van Breemen [88] also revised Brown's [84] values using other thermodynamic data from Robie and Walbaum [97] and found the Gibbs free energy to be equal to -3299 kJ/mol.

Vlek and colleagues [85] determined the solubility product of jarosite using the chelation method. Given that the solubility of Fe (III) compounds was low under their conditions, solubility measurements to detect the presence of iron were limited to highly acidic solutions. They developed a new method involving the use of EDTA as a chelating agent to increase the concentrations of Fe (III) from a natural jarosite sample, taken from a sulfate-acidic soil, in suspension. In this way, dissolution was studied, yielding a Gibbs free energy of -3310.4 kJ/mol and a logarithm of the solubility product constant ($\log K_{sp}$) of -9.86 . They acknowledged that the results obtained in their study could be subject to various errors resulting from pH measurements, iron concentrations, as well as incorrect estimations of constants and ionic strength. Moreover, they did not mention the use of XRD to identify the remaining solids after the experiments. Baron and Palmer [68] subsequently recalculated their Gibbs free energy with different free energies for the ions and found a value of -3331.4 kJ/mol.

Kashkay *et al.* [86] conducted three precipitation experiments from supersaturated solutions of K-jarosite, Na-jarosite, and Pb-jarosite over a 15-month period at room temperature. Additionally, they performed precipitations at 373.15 K. The Gibbs free energy for K-jarosite was -3299.7 ± 4 kJ/mol at 298.15 K and -3184 kJ/mol at 373.15 K. The solubility found at 298.15 K was greater for Na-jarosite than for K-jarosite.

In his thesis, Nordström [21] studied hydrogeochemical and microbiological parameters influencing the chemical speciation of heavy metals in AMD effluents in Northern California. His calculations revealed that the samples were in a state of supersaturation with respect to jarosite.

Hladky and Slansky [89] investigated the stability of minerals in the alunite–jarosite group in aqueous solutions at room temperature and pressure. Stability domains concerning pH were investigated for K-jarosite, Na-jarosite, and Pb-jarosite using Gibbs free

Table 1. Solubility constants of jarosites found in the literature at 298.15 K

Authors	Jarosite-type	Method	$\log K_{sp}$	$\Delta_f G^\circ_{298.15}$ (kJ/mol)
Brown [84]	K	Prec. and Diss.	−9.65	−3276 and −3192
Zotov et al. [87]	K	Precipitation	−9.47	−3305.70
Van Breemen [88]	K	Dissolution recalculated	−9.46	−3299.00
Vlek et al. [85]	K	Dissolution	−9.86	−3331.40
Kashkay et al. [86]	K	Precipitation	−9.32	−3299.67
Lindsay [94]	K		−12.51	
Hladky and Slansky [89]	K	Calculated	−9.08	
Bladh [24]	K	Dissolution	−7.12	−3287.60
Chapman et al. [22]	K	Dissolution	−9.21	
Alpers et al. [4]	K	Precipitation	−9.35	−3300.25
Stoffregen [70]	K	Precipitation	−8.8	−3416.3 ^a
Öborn and Berggren [95]	K	Dissolution	−9.42 to −9.41	
Baron and Palmer [68]	K	Dissolution	−11.0	−3309.8
Smith et al. [7]	K	Dissolution	−11.3	
Lemire et al. [90]	K	Recalculated	−9.8	
Kashkay et al. [86]	Na	Precipitation	−8.93	−3256.70
Hladky and Slansky [89]	Na	Calculated	−5.10	
Bladh [24]	Na	Dissolution	−3.60	
Chapman et al. [22]	Na	Dissolution	−5.28	
Alpers et al. [4]	Na	Precipitation	−7.18	
Öborn and Berggren [95]	Na	Dissolution	−9.39 to −9.31	
Hladky and Slansky [89]	Pb	Calculated	−7.89	
Chapman et al. [22]	Pb	Dissolution	−16.28	
Bladh [24]	H ₃ O	Dissolution	−3.57	
Alpers et al. [4]	H ₃ O	Precipitation	−6.04	

^a Values of $\Delta_f G^\circ$ at 473.15 K and 10 MPa.

energy values. It was revealed that pH constitutes the main control factor for the stability of minerals in the alunite group under the studied conditions.

Bladh [24] simulated the chemical erosion of felsic rocks to study the formation of goethite, jarosite and alunite. He recalculated the thermodynamic data previously obtained by Brown [84], Zotov et al. [87], Vlek et al. [85], and Van Breemen [88]. According to Bladh, the ambiguities present in those studies arose from the varied data regarding the free energies of ions that were utilized in the calculation. He calculated the solubility product ($\log K_{sp}$) to be −7.12, while that of Na-jarosite was −3.60, and H₃O-jarosite was −3.57.

The Gibbs free energy determined by Bladh [24] for K-jarosite (−3287.60 kJ/mol, recalculated by Baron and Palmer [68]) from Posnjak and Merwin [75] and Kashkay et al. [86] data is inconsistent with Alpers et al. [4] data. However, values reported by Zotov et al. [87] and Vlek et al. [85] are closer. Despite this, Kashkay et al. [86] were the only ones to provide a set of data for all three substitution ions (K–Na–H₃O) in the A-site of jarosite at that time.

Chapman et al. [22] studied two AMD samples to understand the processes controlling the transfer and attenuation of heavy metals. They highlighted the variation in jarosite solubility thermodynamic data, making it difficult to select the necessary

thermodynamic parameters (K_{sp}) to predict the saturation state of a mixture. They claimed that this variation is probably due to the use of different $\Delta_f G^\circ$ values. They utilized X-ray powder diffraction to identify the solids. However, the results were limited to identifying the mineral phases since most of the precipitates were amorphous.

Several values for the of Fe^{3+} have already been reported. For example, Chapman and colleagues [22] chose to use the data used by Naumov *et al.* [96], Kashkay *et al.* [86], and Zotov [87] because they considered them coherent with each other. The results obtained by Nordström *et al.* [21] regarding the solubility product varied three to five orders of magnitude below than those found by Chapman *et al.* [22].

Alpers *et al.* [4] studied precipitates from AMD solutions in California, USA. In their experiments, seven samples with initial pH between 0.8 and 1.4 were kept for 11 to 13 years at a temperature of 295 ± 3 K. At the time of sampling, they were undersaturated with respect to jarosite. The oxidation of ferrous iron during storage led to saturation and precipitation of the ore. These minerals were characterized by solid analysis techniques such as XRD, scanning electron microscopy (SEM)-energy dispersive X-ray spectroscopy (EDS), and thermogravimetric analysis. The crystals had a diameter between 5 and 10 μm and a rhombohedral shape. The authors state that the well-crystallized nature indicated that the AMD had reached a thermodynamic equilibrium with jarosite. The relationship between crystallinity and equilibrium will be further addressed in Section 4.3.

Thus, Alpers *et al.* [4] recommended using a $\Delta_f G^\circ$ value of 3293.5 ± 2.1 kJ/mol for a solid with composition $K_{0.77}Na_{0.03}(H_3O)_{0.20}Fe_3(SO_4)_2(OH)_6$. The average $\log K_{sp}$ of -9.35 showed good agreement with previous results from Chapman *et al.* [22]. Alpers and colleagues highlighted the need to determine the solubility of jarosite for more varied compositions to quantify the influence on solubility of substitution in the A-site (K, Na, H_3O). Despite the lack of data, they observed that the K- H_3O substitution approaches the ideal substitution compared to Na-K and Na- H_3O substitutions. Alpers *et al.* [4] estimated that additional experimental work was needed to accurately determine the solubility and free energy of formation of jarosite.

Stoffregen [70] studied the stability relationships between jarosite and Na-jarosite at temperatures

ranging from 423.15 to 523.15 K through hydrothermal experiments lasting 1 to 11 weeks. X-ray powder diffraction was used to identify phases present in the products after the experiments. Experimental study of jarosite at high temperatures has advantages: (i) there are only three stable phases at temperatures above 423.15 K, compared to seven phases reported at 298.15 K by Posnjak and Merwin [75], (ii) reaction rates are higher, and (iii) hydronium substitution, which is common in natural jarosites and complicates the determination of terminal member properties, is negligible [4].

The Gibbs free energies were calculated by Stoffregen [70] at 473.15 K and 10 MPa, as presented in Table 1. Furthermore, they suggested that jarosite and Na-jarosite form nearly ideal minerals (A-site substituted only for K or Na) at 473.15 K, and there is complete miscibility between the two types of jarosite at 298.15 K.

Öborn and Berggren [95] studied two types of jarosite (K- and Na-jarosite) from sulfide sedimentary deposits in the Baltic Sea. The jarosites were characterized by XRD after dissolution, and the solubility product was determined from the dissolution of samples that reached equilibrium at different time intervals (from 6 h to 8 days). The solubility constants corresponded to -9.41 to -9.42 . Additionally, Bigham *et al.* [77] reported solubility values for K-jarosite in a range from -9.21 (Kashkay *et al.* [86]; Chapman *et al.* [22]) to -12.51 (Lindsay [94]).

Today, the results obtained by Baron and Palmer [68] are most commonly used to predict the dissolution/precipitation of jarosite. Indeed, their work enabled the calculation of Gibbs free energies, enthalpy, entropy, and heat capacity. They were the first researchers to conduct a calorimetric study of the free energy of formation. Dissolution experiments of synthetic K-jarosite were conducted at different pH values (1.5–3.0) and temperatures close to room temperature (277.15–308.15 K) using a batch reactor. Two methodological approaches were considered for dissolution: first, the temperature at 298.15 K was kept constant while the pH varied from 1.5 to 3; second, the temperature varied from 277.15 to 308.15 K with a constant pH of 2. The composition (chemical formula) of jarosite was quasi-ideal, and the solids remained in the reactor for up to six months. XRD analyses were not conducted to characterize the reaction product solids in

detail. Their study served as the basis for subsequent similar studies.

They observed that equilibrium was reached after 40 to 125 days of dissolution at pH 2 and 298.15 K, with an initial concentration of 0.2 g of jarosite/L of solution. The results obtained by Baron and Palmer [68] were closer to those of Alpers *et al.* [4], but one to two orders of magnitude higher compared to the results of Kashkay *et al.* [86] and Chapman *et al.* [22]. K_{sp} decreases as the temperature increases, ranging from -11.06 at 277.15 K to -11.68 at 308.15 K, indicating a negative enthalpy [68]. In other words, the addition of heat does not favor the reaction. However, this dependence in this temperature range is not linear, implying a variation in the enthalpy of reaction as the temperature changes.

According to Baron and Palmer [68], several reasons explain the divergences from previous studies:

- (a) Inconsistency of thermodynamic data and variations in the values used for the calculation of free energies and ion activities;
- (b) Substitution of ions in the jarosite structure;
- (c) Variations introduced by different experimental methodologies;
- (d) Analytical uncertainties.

Arslan and Arslan [60] conducted a review of the stability regions between jarosite and goethite at 298.15 and 368.15 K. They observed that the stability region of jarosite not only shifts toward a more acidic and oxidizing zone as the temperature increases but also becomes more restricted. However, they emphasized that, in addition to these thermodynamic considerations, the reaction kinetics play a significant role in the precipitation of iron compounds.

The work of Baron and Palmer [68] was considered the starting point for more complex structures containing mixtures of Fe^{3+} and Al^{3+} in **B**-sites, as well as the substitution of S^{6+} and Cr^{6+} in **C**-sites. Baron and Palmer [98] also studied the dissolution of analog jarosite with Cr substitution in the sulfur site. These studies were further pursued based on calorimetric investigations.

Thermodynamics was also studied by Smith *et al.* [7], aiming to monitor the ion release during dissolution and to characterize the newly formed solid phases. They calculated the equilibrium constant (K_{sp}) and solid saturation ratios (Ω) at pH 2 and 8 and room temperature (293.15 K). The results

are close to those of Baron and Palmer [68], with $\log K_{sp}$ equal to -11.30 . According to these authors, positive saturation ratios for hematite and goethite indicate the likely appearance of these minerals after a prolonged dissolution period. They utilized XRD analysis to identify the solids remaining after dissolution.

The study conducted by Smith and colleagues [7] was significant as it was the first to examine the dissolution of jarosite and the formation of new phases at pH 8, where Fe^{3+} reprecipitates. This is likely responsible for preventing the continuation of jarosite dissolution and reinforces the incongruence of jarosite dissolution already observed by Baron and Palmer [68]. This incongruence (non-stoichiometry of the solid) is due to the strong stability of the FeO_6 octahedron compared to the weak stability of $\text{KFe}(\text{OH})_4$.

Smith *et al.* [99] also investigated the dissolution of Pb-jarosite $[(\text{H}_3\text{O})_{0.74}\text{Pb}_{0.13}\text{Fe}_{2.92}(\text{SO}_4)_2(\text{OH})_{5.76}]$ and arsenic-substituted Pb-jarosite $[(\text{H}_3\text{O})_{0.68}\text{Pb}_{0.32}\text{Fe}_{2.86}(\text{SO}_4)_{1.69}(\text{AsO}_4)_{0.31}(\text{OH})_{5.59}]$ at pH 2 and 8. The $\log K_{sp}$ results showed a decrease (-9.35 to -10.65) compared to the standard jarosite structure. Their study demonstrated that, since jarosite dissolution is non-stoichiometric under the conditions studied, it is important to step back from diagrams such as Stoffregen [70] since the solid stability limits assume that the dissolution reaction occurs congruently (stoichiometrically).

Casas *et al.* [92] studied solubility through the precipitation of Na-jarosite and the speciation of an $\text{Fe}(\text{III})$ – Na – H_2SO_4 – H_2O system at 343.15 K. They reported a lack of information on Na-jarosite solubility. Solubility data available in the literature up to that point had been obtained at room temperature or above 363.15 K. There was no information in the range 333.15–353.15 K, corresponding to the temperature range in which thermophilic microorganisms are active. The synthesis was carried out in reactors using a mixture of NaOH and $\text{FeH}(\text{SO}_4)_2$. Different mixtures of sulfuric acid and ferric iron were prepared and left to reach equilibrium for 45 days in a rotary oven at 343.15 K. The formation of Na-jarosite was observed at pH above 1.72 with the presence of goethite in the mixture after XRD analysis of the remaining solids. In contrast, for pH below 1.42, Na-jarosite was pure. Research by Casas and colleagues highlighted the dependence of ionic balance on

bisulfates and sulfate complexes such as $\text{FeH}(\text{SO}_4)_2$, FeHSO_4^{2+} , FeSO_4^+ , HSO_4^- , and H^+ . The concentrations of these species are strongly influenced by acidity and temperature. The equilibrium constant found for Na-jarosite at 343.15 K was 16.5 ± 0.3 .

As mentioned earlier in this section, Lemire *et al.* [90] re-evaluated the $\log K_{\text{sp}}$ value at 298.15 K, revising from -11.0 to -9.8 . According to them, uncertainties in the stoichiometry, particle size, crystallinity variation, and the incongruence of dissolution (as reinforced by Smith *et al.* [7]) render the estimations provided by Baron and Palmer [68] merely speculative.

This detailed section illustrates that estimating the solubility of jarosite-type compounds is a complex task that has been attempted by numerous scientists over the past 50 years. The biggest challenges in estimating this constant are related to the variety of substitutions within the mineral, the variability of experimental methodologies employed, and discrepancies in the thermodynamic data regarding the free energy of ions. Despite the revaluation of Lemire *et al.* [90], who considered the calculated solubility product constant found by Baron and Palmer as speculative, their study has remained the most widely utilized since due to its detailed methodology and well-explained results. The techniques utilized by Baron and Palmer [68], including the precipitation methodology to obtain the solids used in the dissolution experiments, continue to be employed. The principal trends were also confirmed by Smith *et al.* [7] and were further corroborated by calorimetric studies described in Section 2.2 which affirmed that Baron and Palmer [68] had achieved equilibrium.

2.2. Thermodynamic studies through calorimetry

Drouet and Navrotsky [76] conducted a calorimetric study to obtain formation enthalpies through dissolution calorimetry in molten mixtures at high temperatures. In contrast to Stoffregen [70], who used estimations, the data were obtained directly. However, the results of Stoffregen [70] are not consistent with the equation

$$\Delta_f G^\circ = \Delta_f H^\circ - T \Delta_f S^\circ \quad (7)$$

On the other hand, Drouet and Navrotsky [76] also determined the heat capacity using Differential

Scanning Calorimetry (DSC), and it appears to agree with the results obtained by Stoffregen [70]. The recommended values for Gibbs free energy (-3318 kJ/mol) from calorimetric data are similar to the findings in previous studies, indicating that the redox/pH potential diagrams no longer need adjustments and that equilibrium was achieved in Baron and Palmer's study [68].

Subsequently, Drouet *et al.* [100] conducted calorimetric studies to determine the enthalpy of jarosite containing chromate (CrO_4). Furthermore, Drouet *et al.* [101] also investigated solid mixtures between Na-jarosite and Na-alunite. From these studies, they determined the enthalpy of formation and were able to recommend values for Gibbs free energy and entropy.

Similar to Drouet and colleagues, Majzlan *et al.* [91] focused on the thermodynamic properties of H_3O -jarosite and obtained data on enthalpy, heat capacity, and entropy. Then, Majzlan *et al.* [102] continued their research on different jarosite-type compounds (K, Na, Rb, and NH_4), reporting their heat capacities and entropies. They calculated entropies from experimentally measured C_p data using an adiabatic calorimeter, unlike Stoffregen [70] who extrapolated data from experiments at high temperatures. Majzlan and collaborators considered their data more reliable. According to them, the significant variations found in the values of thermodynamic properties of jarosite indicated that the study of these properties would need to be addressed more reliably in future work. Additionally, with the data on enthalpy and entropy, it would be possible to calculate phase diagrams for the phase equilibria of this complex and challenging mineralogical group.

Forray *et al.* [103] studied the formation of yavapaiite $\text{KFe}(\text{SO}_4)_2$ resulting from the heating of K-jarosite at temperatures above 673.15 K to better understand the decomposition of this mineral. Then, in 2010, Forray and colleagues [93] synthesized, characterized, and studied the thermodynamics of Pb-jarosite, providing the enthalpy of formation of the compound and enabling the calculation of Pb-Fe- SO_4 - H_2O diagrams as well as the estimation of the equilibrium constant ($\log K_{\text{sp}}$ ranging from -24.3 to -26.2). Furthermore, Forray *et al.* [104] continued their work on the synthesis and thermodynamics of Pb-As, Pb-Cu, and Pb-Zn jarosite mixtures, resulting in the following $\log K_{\text{sp}}$ values: -13.94 ± 1.89 ; $-4.38 \pm$

1.81; -3.75 ± 1.80 , respectively. They concluded that the transformations and dissolution reactions of arsenic-containing jarosites are much more complex.

3. Kinetic studies of jarosite dissolution processes

The most used tool to model dissolution and precipitation processes in the geochemistry field is thermodynamics. Nonetheless, not every mineral can attain equilibrium in a rapid way, especially when using conditions at low temperatures and neutral pH. These minerals presenting slow reaction rates often keep geochemical processes from reaching equilibrium and this makes geochemical kinetics another essential tool for modeling these situations [105]. Therefore, elucidating the behavior of jarosite dissolution and precipitation can aid in the development of robust models which describe the geochemical cycling of these elements in the environment and in hydrometallurgical processes.

The importance of studying the dissolution kinetics of jarosite compounds gained academic significance after the 1990s. Kinetic data have been found and modeled by several authors. The results generally converge in the same direction; however, differences appear mainly due to the various parameters used in the studies. Three main models have been used to mathematically represent the process and the effects of variables: the derivative kinetic model (DVKM), the Noyes–Whitney kinetic model (NWKM), and the shrinking core kinetic model (SCKM).

The DVKM entails obtaining initial rate constants derived through the fitting of initial kinetic data to a second-order polynomial equation and calculating the slope, considering the beginning of the curve as time zero.

While the NWKM describes dissolution as a diffusion process, proportional to the difference between the solute's saturation concentration in the solvent (solubility) and the solute's concentration in the solution. This concentration gradient-based approach is inspired by Fick's law and has influenced several diffusion-based dissolution models [106]. This equation is widely used in the study of dissolution in the pharmaceutical field.

The SCKM, initially developed by Yagi and Kunii [107] is described by Levenspiel [108]. It considers mass transfer mechanisms in the studies of

the dissolution reaction of a solid in a fluid. In this model, particle size decreases over time, and particles eventually disappear as the reaction progresses. During dissolution, two main steps are observed: (i) the induction period, where the reaction front is forming and the concentration increases very slowly, and (ii) the progressive period, where the reaction front is already established and the concentrations increase faster until reaching equilibrium.

In this section, the studies will be divided into two categories: those intended for the study in environmental settings (Section 3.1) and those in the hydrometallurgical industry conditions (Section 3.2). Additionally, Section 3.3 discusses the nature of the jarosite-type compound samples used in the thermodynamic studies of Section 2 and in the kinetic studies of Sections 3.1 and 3.2, whether they are natural or synthetic and how this distinction may influence the outcomes.

3.1. Kinetics of jarosite environmental dissolution

Many researchers started studying jarosite dissolution rates with different conditions and methodologies. The first robust study of the dissolution kinetics of jarosite was conducted by Baron and Palmer [68], focusing on the release of ions in an acidic environmental medium. They used the Noyes–Whitney model to fit the data from dissolution at pH 2 and 298.15 K, resulting in a first-order kinetics and a kinetic constant K equal to $7.9 \pm 0.5 \times 10^{-7} \text{ s}^{-1}$. As discussed earlier, in the thermodynamic part studied by these authors, their study served as a basis for subsequent research.

Gasharova *et al.* [45] investigated the surface behavior of jarosite using Atomic Force Microscopy (AFM) at pH 5.5. The goal was to directly observe morphological changes on the surfaces of jarosite depending on interactions with different aqueous solutions, to study the mechanisms of dissolution and to compare dissolution rates of jarosites containing K^+ and H_3O^+ . The kinetic rates found for each jarosite compound were two orders of magnitude higher than those of Baron and Palmer [68] using the DVKM model, -6.84 and -6.35 for K^+ and H_3O^+ , respectively.

The dissolution rates of K-jarosite were also studied by Smith *et al.* [7] to simulate conditions

similar to ARD/AMD sites and remediated sites, using pH values of 2 and 8 at 293.15 K. They noticed that Baron and Palmer [68] had studied dissolutions at low temperatures but without characterizing the solids produced at the end of the reaction. Even without investigating temperature and agitation, they suggested that the dissolution was controlled by mass transfer.

In Figure 2, equilibrium was reached by both Baron and Palmer *et al.* [68] and Smith *et al.* [7] with the same acid medium (HCl), same pH (2) and initial concentration (0.2 g/L), and similar temperatures (293.15 and 298.15 K, respectively). However, the time required to reach this quasi-equilibrium was approximately 80 days for Smith *et al.* [7] and 40 days for Baron and Palmer [68]. The concentrations at the end of dissolution were similar for iron (Fe), potassium (K), and sulfate (SO_4^{2-}), 0.390, 0.204, and 0.330 mmol/L, respectively, for Smith *et al.* [7] compared to 0.434, 0.178, and 0.332 mmol/L for Baron and Palmer [68]. However, the dissolution curves indicate a significantly faster attainment of equilibrium for the earlier study. The kinetic data ($\log r$) turned out to be -8.51 for Baron and Palmer [68] and -8.80 for Smith *et al.* [7]. This difference can be partially attributed to the 5 K temperature difference between the experiments.

Welch *et al.* [43] used higher pH values (3 and 4) to simulate ARD conditions in Australia using a natural sample. According to their observations, equilibrium was not reached after 12 days. Jarosite continued to dissolve for the rest of the year, though at a slower rate. Figure 3 shows dissolution kinetic curves at pH 3. Figure 3(a) shows kinetic data utilizing HCl, which promotes the release of elements in larger quantities, while H_2SO_4 (Figure 3b) produces a less pronounced release.

Elwood Madden *et al.* [109], Pritchett *et al.* [110], and Legett *et al.* [111] simulated conditions closely resembling those found on Mars with different pH, temperatures, and salinities for the dissolution of K-jarosite, and Zahai *et al.* [112] for Na-jarosite.

Elwood Madden *et al.* [109] studied the effect of pH (1 to 10) and temperature (277.15 to 323.15 K) on the initial kinetic rates of K-jarosite dissolution. Their objective was also to investigate morphologies and reaction products. Linear regression on rates found from experiments resulted in a value of $E_a = 79$ kJ/mol, applying the Arrhenius equation.

Moreover, a Type V behavior was found where the lowest rate is at pH 3.5, but the rate increases either by increasing a_{H^+} (pH < 3.5) or increasing a_{OH^-} (pH > 3.5). A general trend of the Elwood-Madden *et al.* data [109] can be observed in Figure 4.

Kendall *et al.* [44] used the same conditions as Smith *et al.* [7] but added a third scenario in which a sudden input of fresh water (ultrapure water) was considered, using As-jarosite to compare with K-jarosite dissolution in a sulfuric acid medium. They observed a faster release of K^+ during the first two hours, followed by a decrease in speed. Regarding Fe^{3+} , its release proved faster after the first day, exceeding the potassium concentration. Despite the effect observed by Welch *et al.* [43], where dissolution kinetics are faster for chloride environments than for sulfuric environments, Kendall *et al.* [44] reached equilibrium in 14 days of experimentation, much faster than Baron and Palmer [68] or Smith *et al.* [7], challenging the accuracy or reliability of the results obtained by Kendall and collaborators.

Similar to Baron and Palmer [68], the dissolution rate studies mentioned above used batch reactors that do not take reactive transport into account, a critical aspect in environmental geochemistry [46,113]. Therefore, more recent research in this field has studied the dissolution process in continuous flow reactors to consider the effect of liquid flowing.

Dixon *et al.* [42] studied the dissolution rates of jarosite in circulation reactors, showing that dissolution rates are not affected by the flow rate, but they did not explore the relationship with pH. Meanwhile, Qian *et al.* [114] studied the dissolution of natural jarosite under quiescent solution conditions using non-stirred batch reactors and column leaching experiments. They reported slower dissolution rates than those observed using dissolution methods in stirred reactors.

However, the use of gravity-driven column leaching experiments, while more realistic, did not allow control over mass transport conditions within the column. Noticing this lack of information, Trueman *et al.* [46] investigated the dissolution of jarosite in a circulation reactor with a constant flow rate and at various pH levels.

All these studies provided useful insights under a range of different conditions such as pH, tem-

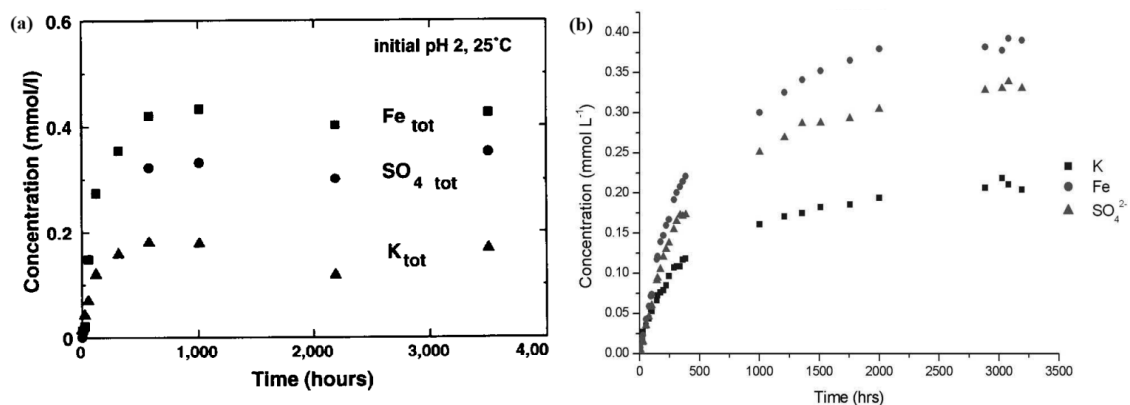


Figure 2. Dissolution curves of K-jarosite for (a) Baron and Palmer [68] and (b) Smith et al. [7] (Figures reprinted with permission from Elsevier).

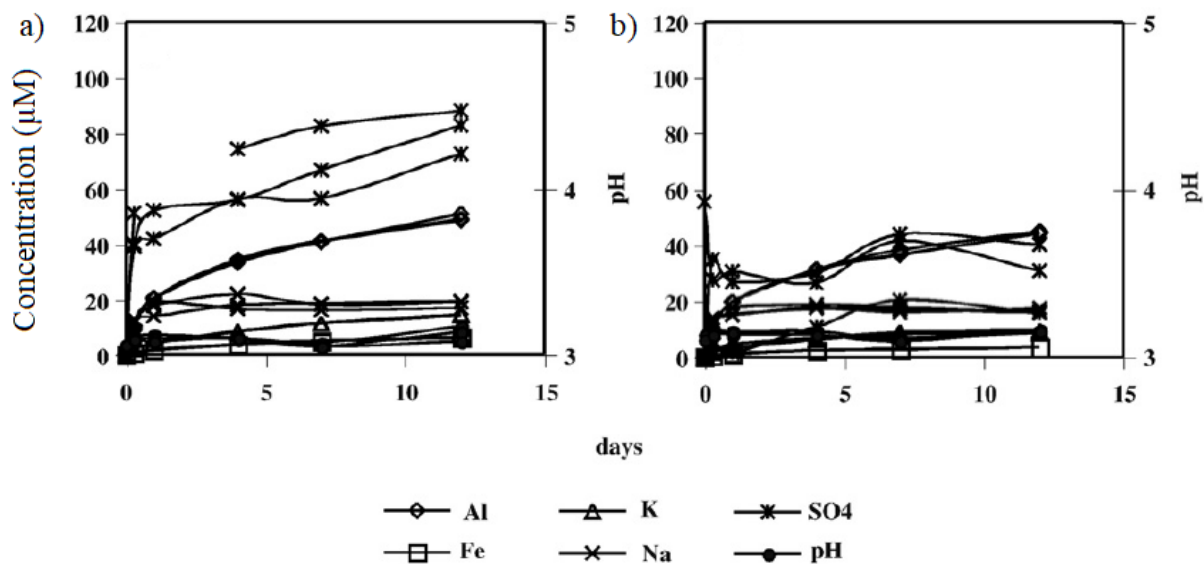


Figure 3. Dissolution curves of K-jarosite according to Welch et al. [43] at pH 3 using (a) HCl and (b) H_2SO_4 (Figures reprinted with permission from Elsevier).

perature, and salinity. However, varying orders of magnitude were found for the dissolution rate because of differing experimental conditions or mineral samples.

As an example, Figure 4 illustrates the variation in dissolution rate values of K-jarosite with pH for reactions in batch reactors at room temperature (293.15–298.15 K).

Figure 4 shows the variation in rate even for similar conditions of pH and temperature, the most

important parameters for jarosite dissolution. These variations are likely due to the nature of jarosite (natural or synthetic), its structure and ion substitution, differing solid/liquid ratios, stirring speeds, and the duration of dissolution monitoring (several authors, such as Elwood Madden et al. [109] or Kendall et al. [44], have used only the first two hours, which increases the rate for potassium ions). In Table 2, the different studies in batch reactors (or AFM study, used by Gasharova et al. [45]) are gathered along with

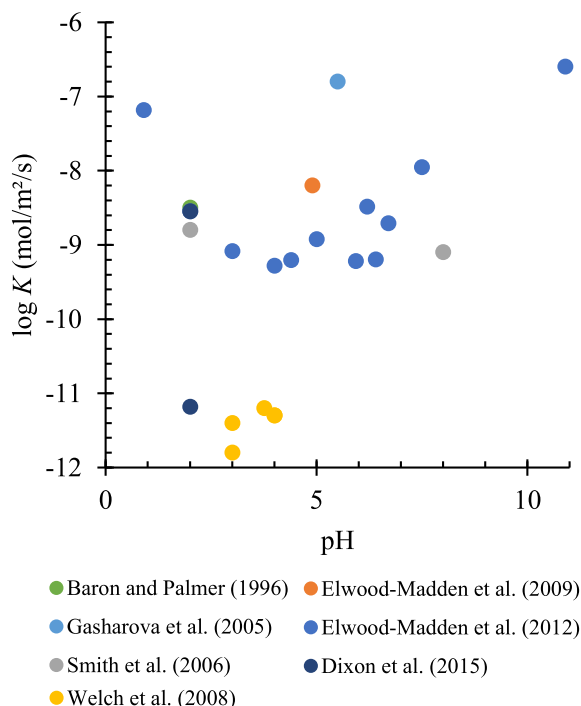


Figure 4. Variation of the dissolution rate ($\text{mol/m}^2/\text{s}$) of K-jarosite with pH at room temperature (293.15–298.15 K).

their main parameters and results.

3.2. Kinetics of jarosite industrial dissolution

Numerous efforts have been made to examine the impacts of chemical composition, temperature, pH, and particle size on dissolution rates in various reactive industrial environments. Due to the growing interest in the recovery of strategic metals from industrial residues containing Zn, as well as other high-value metals such as Pb, Cu, Ag, Cd, Co [61,116], several leaching agents have been used as promising alternatives to recovery processes. Meanwhile, others authors have focused on avoiding the release of toxic metals in industrially precipitated jarosite.

The shrinking core kinetic model (SCKM) has been widely utilized over the past thirty years to describe the decomposition kinetics of jarosite-type compounds by evaluating decomposition conditions in order to prevent environmental issues and recover high-value metals such as silver. Primarily, researchers have used an alkaline medium as lixiviant

in numerous studies regarding jarosites containing silver [117–124], prompting many studies in alkaline environments ($\text{NaOH}/\text{Ca}(\text{OH})_2$). In these dissolutions, jarosite decomposition typically occurs between 323.15 and 363.15 K, and silver is leached with or without cyanide. Other studies have also examined the release of minerals such as rubidium [125], arsenic [126–128], chromium [129,130] mercury [131], and thallium [67]. However, in recent years, attention has also been given to the use of various acids as a decomposition medium, as evidenced in Table 3 where conditions are displayed, as well as the activation energies and reaction order for both the induction and progressive periods.

3.2.1. Dissolution through alkaline medium

One of the first team to study this dissolution was Roca et al. [117], who utilized NaOH and $\text{Ca}(\text{OH})_2$ as basic medium, temperatures ranging from 298.15 to 333.15 K, and NaCN concentrations from 5 to 30 mM. Subsequently, Patiño et al. [119] investigated the cyanidation–decomposition of Pb-jarosite containing silver, also using both alkaline media because this type of jarosite is commonly found in Nature and industrial processes.

Later, Patiño et al. [120] examined the decomposition of silver-containing Na-jarosite with cyanidation. They obtained activation energies of 96 kJ/mol for the NaOH medium and 39.6 kJ/mol for the $\text{Ca}(\text{OH})_2$ medium. Additionally, they found that the addition of salts such as NaCl or Na_2SO_4 increased the reaction rate for the experimental conditions used.

Cruells et al. [122] studied the decomposition of silver-containing K-jarosite using the same media. They obtained activation energies of 86 kJ/mol for the NaOH medium and 36 kJ/mol for the $\text{Ca}(\text{OH})_2$ medium. When coupling with cyanidation (CN^-), the activation energy decreased to 43 kJ/mol for NaOH and increased to 80 kJ/mol with $\text{Ca}(\text{OH})_2$.

Salinas et al. [123] investigated alkaline (NaOH) decomposition coupled with cyanidation of NH_4 -jarosites containing silver. When only NaOH was utilized, the activation energy rose to 77 kJ/mol, while coupling with CN^- reduced the energy to 46 kJ/mol.

Patiño et al. [121] studied silver-containing NH_4 -jarosite using $\text{Ca}(\text{OH})_2$. They found an activation energy of 70 kJ/mol using only the base and 29 kJ/mol

Table 2. Kinetic data ($\log r$) of jarosite dissolution

$a_{\text{H}_2\text{O}}$	Initial pH	T (K)	Solution	$\log r^a$	Authors	Element
K-jarosite						
1	1.97	296.15	H ₂ SO ₄	−11.18	Dixon et al. [42]	K ⁺
1	1.97	296.15	H ₂ SO ₄	−11.19	Dixon et al. [42]	Fe ³⁺
1	8	296.15	Tris	−7.95 (0.13)	Kendall et al. [44]	K ⁺
1	6	296.15	Water	−9.20 (0.05)	Kendall et al. [44]	K ⁺
1	2	296.15	H ₂ SO ₄	−9.10 (0.00)	Kendall et al. [44]	Fe ³⁺
1	2	296.15	H ₂ SO ₄	−8.42 (0.03)	Kendall et al. [44]	K ⁺
0.75	N.D.	273.15	NaCl	−9.94(0.09)	Pritchett et al. [110]	K ⁺
0.35	N.D.	273.15	CaCl ₂	−11.51(0.05)	Pritchett et al. [110]	K ⁺
0.75	N.D.	263.15	NaCl	−11.55(0.00)	Pritchett et al. [110]	K ⁺
1	6.4	280.15	Water	−9.71 (0.16)	Elwood Madden et al. [109]	K ⁺
1	6.8	296.15	Water	−9.2 (0.05)	Elwood Madden et al. [109]	K ⁺
1	5.9	313.15	Water	−8.59 (0.03)	Elwood Madden et al. [109]	K ⁺
1	6.4	323.15	Water	−7.15 (0.08)	Elwood Madden et al. [109]	K ⁺
1	0.9	296.15	H ₂ SO ₄	−7.18 (0.06)	Elwood Madden et al. [109]	K ⁺
1	2	296.15	H ₂ SO ₄	−8.54 (0.06)	Elwood Madden et al. [109]	K ⁺
1	3	296.15	H ₂ SO ₄	−9.08 (0.05)	Elwood Madden et al. [109]	K ⁺
1	4	296.15	H ₂ SO ₄	−9.28 (0.02)	Elwood Madden et al. [109]	K ⁺
1	5.9	296.15	NaOH	−9.22 (0.18)	Elwood Madden et al. [109]	K ⁺
1	6.4	296.15	NaOH	−9.20 (0.10)	Elwood Madden et al. [109]	K ⁺
1	7.1	296.15	NaOH	−8.92 (0.05)	Elwood Madden et al. [109]	K ⁺
1	9.6	296.15	NaOH	−8.71 (0.09)	Elwood Madden et al. [109]	K ⁺
1	10.9	296.15	NaOH	−6.60 (0.07)	Elwood Madden et al. [109]	K ⁺
1	6.3	296.15	MES	−8.49 (0.07)	Elwood Madden et al. [109]	K ⁺
1	7.9	296.15	MES	−7.95 (0.13)	Elwood Madden et al. [109]	K ⁺
1	4.3	296.15	Water	−9.1 (0.4)	Elwood Madden et al. [115]	K ⁺
1	4.9	296.15	Water	−8.2 (0.5)	Elwood Madden et al. [115]	K ⁺
1	2	293.15	HClO ₄	−8.8	Smith et al. [7]	K ⁺
1	8	293.15	Ca(OH) ₂	−9.1	Smith et al. [7]	K ⁺
1	3.76	298.15	Water	−11.2 (0.1)	Welch et al. [43]	K ⁺
1	4	298.15	HCl	−11.3 (0.9)	Welch et al. [43]	K ⁺
1	3	298.15	HCl	−11.4 (0.4)	Welch et al. [43]	K ⁺
1	4	298.15	H ₂ SO ₄	−11.3 (0.5)	Welch et al. [43]	K ⁺
1	3	298.15	H ₂ SO ₄	−11.8 (0.3)	Welch et al. [43]	K ⁺
1	5.5	298.15	Water	−6.8 (0.4)	Gasharova et al. [45]	K ⁺
1	2	298.15	HClO ₄	−8.5 (0.03)	Baron and Palmer [68]	K ⁺
Na-jarosite						
N.D.	5.7	277.15	Water	−9.29(0.20)	Zahrai et al. [112]	Na ⁺
N.D.	8.1	295.15	Water	−8.85(0.06)	Zahrai et al. [112]	Na ⁺

(continued on next page)

Table 2. (continued)

$a_{\text{H}_2\text{O}}$	Initial pH	T (K)	Solution	$\log r^a$	Authors	Element
N.D.	1	295.15	H ₂ SO ₄	−6.98(0.06)	Zahrai et al. [112]	Na ⁺
N.D.	2	295.15	H ₂ SO ₄	−6.85(0.35)	Zahrai et al. [112]	Na ⁺
N.D.	8	295.15	Tris+HCl	−7.22(0.16)	Zahrai et al. [112]	Na ⁺
N.D.	10	295.15	Tris	−6.93(0.06)	Zahrai et al. [112]	Na ⁺
N.D.	5.7	323.15	Water	−7.89(0.35)	Zahrai et al. [112]	Na ⁺
0.75	N.D.	273.15	CaCl ₂	−10.58(0.38)	Pritchett et al. [110]	Na ⁺
0.35	N.D.	273.15	CaCl ₂	−11.19(0.17)	Pritchett et al. [110]	Na ⁺

^aThe values in parentheses represent the standard deviation among repeated experiments.

Buffers: Tris (Tris(Hydroxymethyl)aminomethane) and MES (2-(*N*-morpholino)ethanesulfonic acid).

adding CN[−]. The decomposition rates were higher than those of jarosites produced during the zinc hydrometallurgical process. Roca et al. [118] used the same type of jarosite as Patiño et al. [121] and studied its decomposition in a cyanide and alkaline environment using NaOH instead of Ca(OH)₂. The activation energy for the induction period was higher than for the progressive conversion period. The activation energies for the progressive period were 60 kJ/mol without cyanide and 52 kJ/mol with cyanide. They confirmed a trend of reduced activation energy using cyanidation, as already observed by Salinas et al. [123].

González-Ibarra et al. [135] investigated the kinetic decomposition of an industrial jarosite using both NaOH and Ca(OH)₂ as well as cyanidation. They succeeded in increasing silver recovery by coupling alkalinity with cyanidation. When using NaOH, kinetics were controlled by the chemical reaction stage, while using Ca(OH)₂, diffusion through a passivation layer of CaCO₃ played a crucial role, and the activation energies were 40.42 and 21.72 kJ/mol, respectively.

Islas et al. [136] studied the leaching of silver in jarosites using non-cyanide complexing agents such as thiosulfate (S₂O₃^{2−}) and thiocyanate (SCN[−]), as they are less harmful to human health. The proposed overall kinetic equations allow optimizing jarosite leaching using these complexing agents as alternatives to cyanide.

Reyes et al. [132] studied the reactivity of Na-jarosites containing arsenic. They found activation energies of 57.11 kJ/mol for NaOH and 48.61 kJ/mol

for Ca(OH)₂. Flores et al. [126] investigated the decomposition of K-jarosites containing arsenic using NaOH and Ca(OH)₂ media, with activation energies of 60.3 kJ/mol and 74.4 kJ/mol, respectively. This difference in activation energy between K- and Na-jarosite may be related to the fact that K-jarosite is more stable during dissolution than Na-jarosite.

Patiño et al. [127,133] examined the decomposition of Na-As-jarosite in NaOH and Ca(OH)₂ media, the former through a design of experiments approach and the latter using only the SCKM.

The first study reported the presence of unreacted As-jarosite and the formation of halos of Fe(OH)₃ particles with adsorbed AsO₄. Temperature and OH[−] concentration, as well as their combination, were the most influential parameters on the kinetics. The second study found activation energies of 60.3 kJ/mol and 74.4 kJ/mol for NaOH and Ca(OH)₂ media, respectively. This corroborates the claim that activation energies are lower with NaOH than with Ca(OH)₂, indicating easier dissolution when NaOH is used.

Méndez et al. [128] studied NH₄-K-jarosite containing arsenic, and Flores et al. [137] investigated the decomposition of arsenic-containing NH₄-Na-jarosite, both using NaOH medium. The controlling mechanism was the chemical reaction, and there was the formation of Fe(OH)₃ with adsorbed arsenate. Flores and collaborators emphasized that using this type of jarosite is an alternative to arsenic removal from water because, even after decomposition, arsenic is retained in the residual solid.

Pérez-Labra et al. [125] synthesized rubidium

Table 3. Literature using the shrinking core kinetic model to describe the dissolution of jarosite-type compounds

Authors using a basic medium	Jarosite type	Leaching medium	<i>T</i> (K)	<i>E</i> _{a,pro} (kJ/mol)	<i>n</i> _{pro}	<i>E</i> _{a,ind} (kJ/mol)	<i>n</i> _{ind}
Roca et al. [117]	[Ag _{0.78} (H ₃ O) _{0.22}]Fe ₃ (SO ₄) ₂ (OH) ₆	NaOH Ca(OH) ₂	323.15 323.15	42.00 42.00	0.50 0.00	71.00 71.00	0.50 0.00
Patiño et al. [119]	Pb _{0.32} Ag _{0.011} (H ₃ O) _{0.35}]Fe ₃ (SO ₄) ₂ (OH) ₆	NaOH Ca(OH) ₂	323.15 323.15	53.00 47.00	1.00 0.00	N.D. N.D.	N.D. N.D.
Patiño et al. [120]	[Na _{0.675} Ag _{0.005} (H ₃ O) _{0.32}]Fe ₃ (SO ₄) ₂ (OH) ₆	NaOH Ca(OH) ₂	308.15 308.15	96.00 47.00	0.40 0.50	84.00 84.00	0.90 0.70
Cruells et al. [122]	[K _{0.91} Ag _{0.007} (H ₃ O) _{0.83}]Fe ₃ (SO ₄) ₂ (OH) ₆	NaOH Ca(OH) ₂	303.15 303.15	43.00 80.00	0.60 0.50	86.00 36.00	0.70 0.20
Salinas et al. [123]	[Ag _{0.001} Na _{0.07} K _{0.02} Pb _{0.007} (NH ₄) _{0.59} (H ₃ O) _{0.31}]Fe ₃ (SO ₄) ₂ (OH) ₆	NaOH NaOH/NaCN	308.15 308.15	77.00 46.00	1.10 0.80	88.00 154.00	1.40 3.20
Patiño et al. [121]	[(NH ₄) _{0.71} Ag _{0.040} (H ₃ O) _{0.24}]Fe _{2.85} (SO ₄) ₂ (OH) _{5.50}	Ca(OH) ₂ Ca(OH) ₂ /NaCN	308.15 308.15	70.00 29.00	0.40 0.65	N.D. N.D.	N.D. N.D.
Roca et al. [118]	[(NH ₄) _{0.71} Ag _{0.040} (H ₃ O) _{0.25}]Fe _{2.85} (SO ₄) ₂ (OH) _{5.50}	NaOH NaOH/NaCN	303.15/323.15	60.00 52.00	0.60 0.00	80.00 54.00	0.75 0.50
Reyes et al. [132]	[Na _{0.87} (H ₃ O) _{0.13}]Fe _{2.5} (SO ₄) _{1.95} (AsO ₄) _{0.05} [(OH) _{4.45} (H ₂ O) _{1.55}]	NaOH Ca(OH) ₂	303.15 303.15	57.10 48.60	0.70 1.51	120.40 79.40	1.00 0/1
Perez-Labra et al. [125]	Rb _{0.9432} Fe ₃ (SO ₄) _{2.1245} (OH) ₆	Ca(OH) ₂	298.15	98.70	0.43	N.D.	N.D.
Flores et al. [126]	[K _{0.75} (H ₃ O) _{0.25}]Fe _{1.84} (SO ₄) _{1.82} (AsO ₄) _{0.18} [(OH) _{2.34} (H ₂ O) _{3.66}]	NaOH Ca(OH) ₂	60.30 74.40	60.30 74.40	1.86 1.14	84.70 88.30	2.65 0.24
Patiño et al. [127]	[Na _{0.87} (H ₃ O) _{0.13}]Fe _{2.50} (SO ₄) _{1.95} (AsO ₄) _{0.05} [(OH) _{4.45} (H ₂ O) _{1.55}]	NaOH Ca(OH) ₂	303.15 303.15	57.11 48.22	0.746/0 1.56	118.11 73.50	1.06 1.03
Patiño et al. [133]	KFe ₃ (SO ₄) _{1.82} (AsO ₄) _{0.18} (OH) _{5.82}	NaOH Ca(OH) ₂	303.15 303.15	60.30 74.40	1.86 1.15	84.60 88.20	0.23/2.65 0.24/0
Méndez et al. [128]	[(NH ₄) _{0.23} K _{0.77}]Fe _{2.47} (SO ₄) _{1.69} (AsO ₄) _{0.31} [(OH) _{4.01} (H ₂ O) _{1.59}]	NaOH	N.D.	N.D.	N.D.	N.D.	N.D.
Islas et al. [134]	Tl _{0.86} (H ₃ O) _{0.25} Fe _{3.11} (SO ₄) _{2.11} [(OH) _{6.11} (H ₂ O) _{0.44}]	NaOH	N.D.	N.D.	N.D.	N.D.	N.D.
Mireles et al. [129]	[K _{0.86} (H ₃ O) _{0.14}]Fe _{2.67} [(SO ₄) _{1.23} (CrO ₄) _{0.77}][(OH) _{5.01} (H ₂ O) _{0.99}]	Ca(OH) ₂		51.56	1.99	63.75	0.67

(continued on next page)

Table 3. (continued)

Authors using a basic medium	Jarosite type	Leaching medium	T (K)	$E_{a,pro}$ (kJ/mol)	η_{pro}	$E_{a,ind}$ (kJ/mol)	η_{ind}
González-Ibarra et al. [135]	AgFe ₃ (SO ₄) ₂ (OH) ₆	NaOH Ca(OH) ₂	303.15 303.15	40.42 21.72	N.D. N.D.	N.D. N.D.	N.D. N.D.
Reyes et al. [130]	[K. (H ₃ O)]Fe ₃ [(SO ₄) _{2-x} (CrO ₄) _x](OH) ₆ (H ₂ O) _n]	NaOH	303.15	75.70	1.10	82.70	1.10
Ordóñez et al. [131]	Hg _{0.39} (H ₃ O) _{0.22} Fe _{2.71} (SO ₄) _{2.17} [(OH) _{4.79} (H ₂ O) _{2.09}]	NaOH	303.15	56.90	0.99/0	81.70	0.52/1.48
	Tl _{0.86} (H ₃ O) _{0.14} Fe _{3.11} (SO ₄) _{2.11} (OH) _{6.11} (H ₂ O) _{0.44}	NaOH	303.15	91.90	1.10	101.60	1.10
	Hg _{0.39} (H ₃ O) _{0.22} Fe _{2.71} (SO ₄) _{2.17} (OH) _{4.79} (H ₂ O) _{2.09}	NaOH	303.15	56.90	0.99	81.70	1.48
Islas et al. [67]	Pb _{0.48} (H ₃ O) _{0.04} Fe _{2.97} (SO ₄) _{1.93} (OH) _{6.05} (H ₂ O) _{0.6}	NaOH	303.15	85.20	0.74	66.40	1.19
	Pb _{0.39} (H ₃ O) _{0.22} Fe _{2.89} (S _{0.92} As _{0.08} O ₄) ₂ (OH) _{5.51} (H ₂ O) _{0.49}	NaOH	303.15	66.10	0.99	96.90	2.40
Islas et al. [136]	(Na _{0.96} Ag _{0.04})Fe _{2.82} (SO ₄) _{2.01} (OH) _{5.36} (H ₂ O) _{0.86}	NaOH/CN ⁻	303.15	46.30	0.61	69.80	0.66
		NaOH/S ₂ O ₃ ²⁻	303.15	53.30	0.51	70.10	0.51
		NaOH/SCN ⁻	303.15	45.10	0.60	71.50	0.59
Flores et al. [137]	[(NH ₄) _{0.72} Na _{0.06} (H ₃ O) _{0.21}]Fe ₃ (2.52)(SO ₄) _{1.85} (AsO ₄) _{0.15} [(OH) _{4.41} (H ₂ O) _{1.59}]	NaOH/CN	303.15	51.60	0.94	65.00	1.22
Authors using an acidic medium	Jarosite type	Leaching medium	T (K)	$E_{a,pro}$ (kJ/mol)	η_{pro}	$E_{a,ind}$ (kJ/mol)	η_{ind}
Calla-Choque [138]	Ag/Cu	Thiourea	N.D.	N.D.	N.D.	N.D.	N.D.
Reyes et al. [130]	[K. (H ₃ O)]Fe ₃ [(SO ₄) _{2-x} (CrO ₄) _x](OH) ₆ (H ₂ O) _n]	HCl	303.15/323.15	68.03	1.2	109.4	1.05/0.47
Reyes et al. [61]	[(M. H ₃ O)]Fe ₃ [(S _{1-x} As _x O ₄) ₂](OH) ₆ (H ₂ O) _n]	H ₂ SO ₄	303.15/323.15	77.9	1.2	66.8	1
	Tl _{0.86} (H ₃ O) _{0.14} Fe _{3.11} (SO ₄) _{2.11} (OH) _{6.11} (H ₂ O) _{0.44}	H ₂ SO ₄	303.15	58.4	1.07	55.9	0.9
	Hg _{0.39} (H ₃ O) _{0.22} Fe _{2.71} (SO ₄) _{2.17} (OH) _{4.79} (H ₂ O) _{2.09}	H ₂ SO ₄	303.15	83.5	0.98	61.2	0.98
Islas et al. [67]	Pb _{0.48} (H ₃ O) _{0.04} Fe _{2.97} (SO ₄) _{1.93} (OH) _{6.05} (H ₂ O) _{0.6}	H ₂ SO ₄	303.15	63.3	1.01	55.9	1.1
	Pb _{0.39} (H ₃ O) _{0.22} Fe _{2.89} (S _{0.92} As _{0.08} O ₄) ₂ (OH) _{5.51} (H ₂ O) _{0.49}	H ₂ SO ₄	303.15	77.3	1.05	35.1	0.99
Calla-Choque and Lapidus [124]	Ag	Thiourea et Oxalate	N.D.	N.D.	N.D.	N.D.	N.D.
Calla-Choque and Lapidus [139]	NaFe ₃ (SO ₄) ₂ (OH) ₆ , Ag	Thiourea et Oxalate	303.15	44	N.D.	N.D.	N.D.
Nolasco et al. [140]	[Na _{0.70} (H ₃ O) _{0.30}][Fe _{2.95} Cu _{0.042}](SO ₄) _{2.25} [(OH) _{5.46} (H ₂ O) _{0.54}]	H ₂ SO ₄	323.15	57.9	1.1	N.D.	N.D.

jarosite and studied its decomposition in an alkaline solution containing five different concentrations of Ca(OH)_2 . The obtained solid residues incorporated calcium and formed goethite. The kinetic analysis could be modeled by the SCKM with the chemical reaction control stage, with an activation energy of 98.70 kJ/mol.

Islas *et al.* [134] studied the dissolution of thallium jarosite using NaOH, leading to the formation of an amorphous solid around the particle, likely containing hydroxide and thallium. The decomposition of this type of jarosite seems to be described by a constant particle size model, controlled by the chemical reaction.

Mireles *et al.* [129] analyzed the decomposition kinetics of chromium-containing jarosite in a Ca(OH)_2 medium. Experimental data show that the reaction follows the SCKM with chemical reaction control. The activation energy was 63.75 kJ/mol for the induction period and 51.56 kJ/mol for the progressive period, and the reaction results in the formation of Fe(OH)_3 residues.

Ordoñez *et al.* [131] dedicated their study to the decomposition of mercury jarosite in a NaOH medium. The activation energy was 81.70 kJ/mol for the induction period and 56.90 kJ/mol for the progressive period.

This section illustrates that the dissolution of various types of jarosite has been extensively studied, mainly utilizing NaOH and Ca(OH)_2 as basic mediums. A trend was observed where reactions occurring in NaOH medium were less energy-dependent compared to those in Ca(OH)_2 medium. Cyanidation was also employed to enhance the dissolution rate in basic medium. Moreover, other complexing agents (such as $\text{SCN}^-/\text{S}_2\text{O}_3^{2-}$) were studied as alternatives to CN^- . Passivation layers and the formation of other mineral phases were identified depending on the basic medium and conditions employed. The SCKM revealed that the induction period exhibits a higher dependency on temperature (high E_a) than the progressive period.

3.2.2. Dissolution through acidic medium

More recently, acid dissolution has also attracted attention, given that jarosite is an acidic compound and requires a large amount of base for its dissolution process in a basic environment. Calla Choque *et al.* [138] were the first researchers to apply the

SCKM to the acid decomposition of jarosite, coupling leaching with thiourea as a complexing agent to study the effect of different cations (Cu^{2+} , Fe^{3+} , Zn^{2+} , Fe^{2+}) in this system for silver recovery. They reported that acid decomposition would be an interesting alternative as jarosites are naturally acidic, meaning that process costs would be reduced.

Subsequently, Reyes *et al.* [130] studied the dissolution rates of K–Cr(VI)-jarosite in acidic (HCl) and basic (NaOH) environments to investigate the mobility of chromium under more extreme conditions (mostly at $\text{pH} < 1$ and $T > 303.15$ K). They suggested studying reactions at an intermediate pH ($2 \leq \text{pH} \leq 10$) because unreacted solids remain, and calculations must consider equilibrium.

While Reyes *et al.* [61] studied the dissolution kinetics of Na–As-, K–As-, and NH_4 –As-jarosites in sulfuric acid to determine the factors influencing the recovery of high-value metals by varying pH, temperature, particle size, and substitution at A- and C-sites of jarosite-type compounds. Sulfuric acid was chosen due to its lower cost and better compatibility with other reducing agents. Similar to their previous research, Reyes and collaborators used more extreme conditions to calculate condition parameters (mostly $\text{pH} < 1$ and $T > 303.15$ K) to obtain the final model. For $\text{pH} < 1$, they reported that the decomposition process follows the SCKM controlled by the chemical reaction stage. The authors demonstrated that, for the acidity levels used, ion substitution does not influence the dissolution rate.

Islas *et al.* [67] studied the dissolution of several jarosites containing potentially hazardous elements (Pb, As, Tl, Cr) in different conditions using the SCKM in basic (NaOH) and acidic (H_2SO_4) media. They demonstrated that the kinetics-controlling step is the chemical reaction at extreme pH levels ($\text{pH} < 1$), and mass transfer in the liquid phase when pH deviates towards less extreme values ($1 < \text{pH} < 1.68$).

Calla-Choque and Lapidus [139] undertook a study to analyze the effects of pH, temperature, and solid/liquid ratio on silver recovery from jarosite, employing complexing agents such as thiourea and oxalate. Their research highlights the use of oxalate in stabilizing thiourea within an acidic environment. The decomposition of jarosite releases powerful oxidants, mainly iron, inducing chemical instability and thiourea oxidation. Results showed improved recovery with a temperature increase from

323.15 to 333.15 K, pH reduction, and adjusting the solid/liquid ratio. In addition, when oxalate was used, thiourea degradation was minimized, consequently decreasing the temperature required for jarosite dissolution.

Calla-Choque and Lapidus [124] studied the dissolution rate with a non-homogeneous particle size system, unlike the approach in Reyes *et al.* [61], which used specific particle sizes, in the presence of oxalate and thiourea at different pH and temperatures. They modified the SCKM to account for particle size variation. According to Gbor and Jia [141], particle size distribution is of fundamental importance when evaluating kinetics with the SCKM. However, it is often disregarded, leading to erroneous conclusions about the control regime of the process.

Nolasco *et al.* [140] conducted jarosite dissolution in acidic conditions and investigated how the incorporation of divalent cations, such as Cu^{2+} and Fe^{2+} , into jarosite structure affects the reaction rate. The SKCM was able to satisfactorily describe the leaching behavior of Na-jarosite containing copper under acidic conditions. According to authors, the nature of the central atom bonding (Fe–OH) within the jarosite structure plays an important role in acid dissolution. They suggested that the complete replacement of B-site by other trivalent cations could likely alter the dissolution rate.

Studies on dissolution rates in acidic medium are relatively recent in the literature but have reached a higher level of scientific maturity, partly due to the groundwork laid by studies conducted in basic mediums. Temperature, pH, particle size, ion substitution into jarosite structure, utilization of complexing agents, and use of different acids are the main parameters investigated. These studies reveal certain trends, such as the chemical kinetic control of the progressive period when extreme pH levels (<1.5) and temperatures (>323 K) are employed. However, further experiments are required to elucidate the behavior of the SCKM under conditions of less acidic pH (>1.5) and ambient temperature (~295 K) during the experiments.

3.3. Natural and synthetic jarosites

Based on the kinetic studies previously presented in this section, it is noteworthy that the nature of the jarosite-type compound can impact the results. For

this reason, this additional subsection on the dissolution kinetics presents some kinetic studies that synthesized jarosite-type compounds and the methodology used to achieve this synthesis. The use of synthesized methodologies allows other scientists to replicate the experiments and compare them with new dissolution conditions, for example. On the other hand, some authors have preferred the use of natural jarosite samples to replicate processes as they occur in the environment. However, natural jarosite often contains different amounts of other species that will influence the concentration of elements in aqueous solution. Additionally, the effect of the temporal alteration of rocks and minerals can also reduce the dissolution rate of this mineral.

3.3.1. Synthetic jarosites

The article by Driscoll and Leinze [142] is one of the most frequently used as a guideline for the synthesis of different types of jarosites within the scope of their work at the United States Geological Survey (USGS). Their method is based on the synthesis of K-jarosite as proposed by Baron and Palmer [68]. They mix 17.2 g of hydrated ferric sulfate ($\text{Fe}_2(\text{SO}_4)_3 \cdot n\text{H}_2\text{O}$) and 5.6 g of potassium hydroxide (KOH) dissolved in 100 ml of 18 M Ω -cm ultrapure water. The solution is prepared on a hot plate at 368.15 K with stirring. Moderate boiling is maintained for 4 h; then, the solution is removed from the hot plate, and after decantation, the liquid phase is rinsed with deionized water. The washings are discarded, and the remaining solid is placed in a drying oven at 383.15 K for 24 h. After drying, the substance is recovered, in the form of a yellow-brown precipitate. Smith *et al.* [7], Elwood Madden *et al.* [109], Zahrai *et al.* [112], Pritchett *et al.* [110], Kendall *et al.* [44], and Dixon *et al.* [42] have used the method validated by Driscoll and Leinze [142].

As explained by Baron and Palmer [68], synthetic jarosite exhibits a potassium deficiency due to the substitution by hydronium ions (H_3O^+) in the alkali ion position. Various factors control this hydronium substitution, including pH and the activity of K^+ . To minimize this substitution and synthesize a product with a composition close to the ideal, it is necessary to add an excess amount of KOH, thereby increasing the activity of K^+ and simultaneously reducing the concentration of H^+ .

Other authors have employed different methods for the production of K-jarosite. Gasharova *et al.* [45] based their synthesis on the one suggested by Fairchild *et al.* [143], in which crystallization at 423.15 K and 0.5 MPa occurs from an aqueous solution of K_2SO_4 and $\text{Fe}_2(\text{SO}_4)_3$ in 1 N sulfuric acid. Jones *et al.* [144] synthesized jarosite according to the method of Dutrizac *et al.* [145], Dutrizac and Jambor [27], and Crabbe *et al.* [146], dissolving 6.4 g $\text{Fe}_2(\text{SO}_4)_3 \cdot n\text{H}_2\text{O}$ and 24 g HNO_3 in 800 g deionized water, then adding 0.8 ml H_2SO_4 and heating at 363.15 K for 24 h. Brand *et al.* [147] used 1.74 g of $\text{Fe}_2(\text{SO}_4)_3 \cdot 9\text{H}_2\text{O}$ and 0.70 g of K_2SO_4 diluted in deionized water, reacting at 368.15 K for 5 h, then filtering through a syringe filter, obtaining a calculated composition of $\text{K}_{0.9}(\text{H}_3\text{O})_{0.1}\text{Fe}_{2.39}(\text{SO}_4)_2\text{OH}_{4.17}(\text{H}_2\text{O})_{1.83}$. Reyes *et al.* [61] synthesized K-jarosite using the method of Patiño [127], which was based on that of Dutrizac *et al.* [148] for Na-jarosite. In this method, 1 L solution was used containing 0.3 mol/L of $\text{Fe}_2(\text{SO}_4)_3 \cdot n\text{H}_2\text{O}$, 0.01 mol/L of H_2SO_4 , 0.027 mol/L of $\text{Na}_2\text{HAsO}_4 \cdot 7\text{H}_2\text{O}$, and 0.2 mol/L of Z_2SO_4 , where Z represents monovalent alkaline species Na^+ , K^+ , NH_4^+ . Jarosite was formed by dissolving the reagents, adjusting the pH with H_2SO_4 or MgCO_3 , then heating a 2 L reactor for 24 h at 370 K. At the end of the reaction, slurries were filtered, washed in hot water and dried at 383 K.

3.3.2. Natural jarosites

Welch *et al.* [43] used natural jarosite samples [$\text{K}(\text{H}_3\text{O})\text{Fe}_3(\text{SO}_4)_2(\text{OH})_6$] from a degraded acidic sulfate soils site on the north coast of New South Wales, Australia, in order to determine experimentally the dissolution kinetics. Similarly, Qian *et al.* [114] and Trueman *et al.* [46] also used natural jarosite. Calla-Choque and Lapidus [124] used jarosite from a zinc leaching plant in Mexico.

It was evident that Welch and colleagues' jarosite dissolved very slowly compared to synthetically prepared material in the study by Smith *et al.* [7]. Indeed, the solids presented different morphologies: euhedral [45] for natural jarosite or anhedral [7] for synthesized jarosite. The reactivity differences between synthetic mineral and naturally weathered samples have been documented for sulfates [149,150] and silicate minerals [151–153], as indicated by Welch *et al.* [43].

According to White and Brantley [153], when studying silicate dissolution, the time dependency of silicate weathering can be discussed in intrinsic terms, as the surface area increases with the duration of weathering, accumulation of leached layers, and secondary precipitates. Alternatively, it can be discussed in extrinsic terms, as low permeability, high mineral/fluid ratios and increased solute concentrations, produce weathering reactions close to thermodynamic equilibrium under field conditions compared to highly unsaturated conditions during experimental reaction. These factors could explain the differences between dissolution rates of natural and synthesized samples.

4. Precipitation kinetics of jarosite-type compounds

4.1. Studies in abiotic environments at high temperatures

The precipitation of jarosite is of significant industrial interest due to the adoption of the industrial process known as the "Jarosite Process". This process is employed for controlling hydrometallurgical impurities, primarily in zinc production. During its course, ferric iron precipitates in the form of jarosite, and zinc can be recovered. These processes are known to occur at elevated temperatures exceeding 363.15 K [27].

Dutrizac is one of the authors who has extensively researched the effects of conditions on the precipitation of various jarosite-compounds types in hydrometallurgical processes and their behavior in the presence of other elements in different reaction environments.

Dutrizac and Kaiman [154] initially worked on the synthesis of rubidium and thallium jarosite. Subsequently, Dutrizac *et al.* [145] investigated the conditions affecting the formation of Pb-jarosite, while Dutrizac [155] studied their formation in hydrochloric acid. Dutrizac and Dinardo [156] examined the coprecipitation of copper and zinc with Pb-jarosite.

Dutrizac and collaborators have also studied the behavior of several elements during the precipitation of jarosite compounds, including: selenate [157], mercury [158], cesium and lithium [159], silver [160], arsenic at 370.15 K from sulfate and

hydrochloric acid medium [161] as well as at 423.15 K [148], cadmium [162], thiocyanate and cyanate [163], gallium [164], lanthanides [165], vanadium [166], rare earth elements [167], thallium (III) [168], chromium (III) [169,170], germanium and tin [171], alkaline-earth elements (beryllium and radium) [172], halides (fluoride, chloride, bromide, and iodide) [173], scandium, yttrium, and uranium [174], selenium (VI) and selenium (IV) [175].

Among Dutrizac's most important findings, in his study of the effects of alkaline precipitation of Na-jarosite, he demonstrates that alkali substitution in the jarosite structure and solid formation yields increase with an increase in alkali concentration in the precipitation solution. According to the author, seeding and ionic strength had little influence on the yield since for a 24 h reaction the iron-precipitated % remained almost constant. The author established that the stability of different precipitated jarosite types follows the order: $K > NH_4^+ > Na$. Agitation proved to be partially important in this process, meaning that it has a positive influence as it is necessary to keep the solids in suspension. However, additional agitation does not have a significant effect, which in general leads to conclude that the process is probably limited by the surface reaction rather than diffusion [62].

Limpo *et al.* [176] studied the influence of acidity, Fe^{3+} concentration, ammonia concentration, and seeding on the precipitation rate of Fe^{3+} as NH_4 -jarosite from solutions containing sulfuric acid at temperatures between 363.15 and 373.15 K. These authors observed that the control step was crystal growth, and the nucleation rate was proportional to the surface area of the solids introduced into the system, the ammonia concentration, and the concentration of the $Fe_2(OH)_4^{2+}$ complex produced in the solution. This study demonstrated that the acidity of the solution had a significant, inversely proportional influence on the precipitation rate due to competition between hydrogen ions and ammonium ions to be adsorbed on the jarosite surface. Furthermore, pH appeared to regulate the concentration of the complex, making it a crucial element to ensure the success of the iron precipitation.

The study of seeding at different temperatures was then undertaken and showed positive effects on precipitation rate. Teixeira and Tavares [177] conducted batch experiments to study the effect of seeding on the initial precipitation rate of NH_4 -jarosite, noticing

a linear increase with the growing quantity of seeds. This trend proved valid for both high and low concentrations of Fe^{3+} , NH_4^+ , and Mn^{2+} .

Dutrizac [178] investigated the effect of seeding on the precipitation of NH_4 -jarosite and Na-jarosite, connecting it to other factors such as pH, temperature, and concentrations of ferric sulfate. The experiments were conducted with a solution containing 0.30 M $Fe(SO_4)_{1.5}$, 0.30 M Na_2SO_4 , a pH of 1.5, a temperature of 371.15 K, and agitation at 500 rpm, lasting around 8 h. His conclusions indicated that seeding promotes precipitation, where the initial rate increases linearly in the presence of seeds (from 0 to 100 g/L). The presence of seeds also broadens the jarosite precipitation range to lower pH and temperatures, thereby eliminating the induction time.

Among the discoveries he made, he determined that the activation energy of Na-jarosite in the presence of seeds was equal to 106 kJ/mol. The increase in temperature (from 353.15 to 373.15 K) and pH (from 1.10 to 2.00) favors precipitation. In order to calculate the initial kinetic rate, he fitted the data to a second-order polynomial and calculated the slope using the derivative kinetic method (DVKM) as explained in Section 3.

Dutrizac [178] also compiled apparent activation energy data published by different authors [179–181] up to that year, demonstrating the variety of results for different types of jarosite but always at high temperatures and using restricted temperature ranges.

Dutrizac [182] examined the factors influencing the precipitation of K-jarosite in a hydrochloric and sulfate medium. Subsequently, Dutrizac [183] compared the precipitation rates of NH_4 -jarosite and Na-jarosite in a ferric sulfate medium (0.30 M $Fe(SO_4)_{1.5}$ /sulfuric acid) at a temperature between 343.15 and 373.15 K. The results showed an activation energy of 87 kJ/mol and indicated a faster precipitation of NH_4 -jarosite compared to Na-jarosite.

In the hydrometallurgical industry, significant efforts have been made to study the precipitation of jarosite at high temperatures in abiotic environments (>363.15 K), given that the majority of microorganisms are not capable of thriving at such high temperatures. However, the development of hydrometallurgy for the recovery of high-value metals has

led to the creation of new processes operating at more moderate temperatures due to the use of a biotic medium. In this way, additional research has emerged to consider lower temperatures as can be seen in the next section.

4.2. *Studies in biotic environments at low temperatures*

Investigations aiming to understand the formation of jarosite under biotic environments and low temperatures, as well as the rate at which this reaction takes place, are necessary. Its precipitation can compromise the performance of recovering high-value metals. Additionally, understanding precipitation is very important since it can lead to the formation of diffusion barriers on mineral surfaces, impacting dissolution rate, reducing the concentration of ferric iron, hindering ore attack, and potentially trapping high-value metals, such as silver.

In this regard, researchers have dedicated their work to study the control of mineral formation, including jarosite, in the presence of microorganisms. The experimental results obtained in sulfate-rich bioleaching systems, studied by Toro [184], suggest the formation of jarosite at a 303.15 K in environments rich in *Acidithiobacillus* bacteria. In these systems, jarosite precipitation exhibits very favorable and non-selective kinetics regarding pH. This is attributable to the high concentration of iron (III), which promotes the formation of precipitation intermediates of this phase, as well as the presence of bacterial cells serving as surface for crystalline growth.

Wang et al. [185] synthesized schwertmannite and jarosite from solutions containing ferrous iron sulfate, inoculated with *Acidithiobacillus ferrooxidans*. Schwertmannite transformed into $\text{H}_3\text{O}-\text{NH}_4$ -jarosite when the reaction time increased from 19 to 40 days, and the reaction temperature from 309.15 to 318.15 K, in acidic medium at pH 2.

Wang et al. [186] synthesized NH_4 -jarosite in the presence of microorganisms (*A. ferrooxidans* between 295.15 and 309.15 K, *Sulfolobus metallicus* at 318.15 K, and *Acidithiobacillus caldus* and *Sulfobacillus* spp. at 338.15 K) at temperatures ranging from 295.15 to 338.15 K and ferrous sulfate oxidation in pH ranging from 2 to 3, with varying concentrations of NH_4^+ . Schwertmannite served as a

solid precursor for jarosite formation. An increase in ammonium concentration favored the formation of jarosite rather than schwertmannite.

Egal et al. [187] investigated arsenic trapping during Fe^{2+} oxidation in a medium containing *Acidithiobacillus ferrooxidans*. They found that the type of bacteria used favored the formation of tooeleite ore rather than schwertmannite, while jarosite formed without the need for bacteria at the end of the experiments (after 15 days).

Recently, process studies involving the oxidation of iron by archaea at 343.15 K in continuous reactor were undertaken by Kaksonen [188] as well as Kaksonen [189] in a two-stage airlift bioreactor, aiming to assess the performance of these reactors and their ability to separate the jarosite produced during the reaction.

4.3. *Studies in abiotic environments at low temperatures*

Despite the advancement of research in jarosite precipitation at low temperatures under biotic conditions, little data was found to understand jarosite precipitation at low temperatures without the influence of microorganisms. Consequently, new studies under these conditions have been initiated in the last few years.

Bigham et al. [190] characterized ferric iron precipitates in batch experiments conducted at temperatures ranging from 295.15 to 313.15 K, using ferric sulfate and mineral salts in sulfuric acid. The goal of these experiments was to simulate bioleaching solutions in an oxidizing environment containing K^+ , Mg^{2+} , Ca^{2+} , NO_3^- , and PO_4^{3-} . The duration of the experiments was 10 days. They observed a decrease in Fe^{3+} concentration in the solution as the experiment temperature increased. The phases formed were primarily composed of H_3O -jarosite. However, a phase similar to Maus salt ($\text{K}_5\text{Fe}_3(\text{SO}_4)_6(\text{OH})_{2.8}\text{H}_2\text{O}$) was identified at temperatures below 298.15 K. When potassium was replaced by hydronium in Maus salt, metavoltine was produced [191]. The proportion of poorly crystallized or non-crystallized crystals decreased with increasing temperature.

According to Sasaki and Konno [192] and Wang [186], synthesis conditions play a crucial role in the structure and morphology of jarosite samples. They observed a tendency for the formation of more

individual particles at higher temperatures. Some particles exhibited needle-shaped surface characteristics, which could be attributed to metavoltine formation.

However, based on the observation of surface morphology, these characteristics also resemble previous descriptions of schwertmannite $[\text{Fe}_8\text{O}_8(\text{OH})_6(\text{SO}_4)]$ [185,186,193]. The presence of schwertmannite is not observed in the diffractograms because this mineral is poorly crystallized, and its characteristic peaks are broad and masked by the sharper jarosite peaks. Similarly, the background noise in the diffractograms is directly proportional to the amount of poorly crystallized materials, including potentially schwertmannite.

As part of the study on jarosite formation under ambient-like conditions, Kim *et al.* [194] investigated the effects of the presence of oxyanions (AsO_4^- , SeO_3^- , SeO_4^- , MoO_4^- , CrO_4^-) in a solution of ferric sulfate (III) and potassium hydroxide, varying concentrations and aging times (1 h to 40 days). They utilized techniques such as XRD, SEM, and chemical analysis, to follow the precipitation chemical reaction. Initially, an amorphous phase formed for all samples. As the aging time increased, K-jarosite and oxyanions-containing jarosite began to precipitate at room temperature, with varying precipitation rates and levels of crystallinity. As stated before in Section 2.1, crystallinity increases over time as equilibrium is achieved.

In jarosite samples with low precipitation rates and low crystallinity, the amorphous phase contained high concentrations of oxyanions, likely due to the rapid precipitation of the amorphous phase of iron oxyanions. The results demonstrated that jarosite coprecipitation could play a more significant role in controlling the behavior of CrO_4^- than AsO_4^- in the context of acid drainage from mining operations. Oxyanions-containing jarosites exhibited oxyanion concentrations similar to those in the starting solution, suggesting that amorphous phases dissolve and recrystallize in equilibrium with the liquid phase over the aging period.

These studies conducted at low temperatures and in the absence of microorganisms show that the parameters employed during precipitation experiments have an impact not only on the crystallinity and surface characteristics of particles, but also on the formation of additional mineral phases. It indi-

cates the importance of solid analysis to understand the phenomenon and highlights the challenge in characterizing ferric iron phases. Further research is warranted to evaluate the kinetics of jarosite formation and improve the comprehension of its formation reaction.

5. Characterization of the solid phases of jarosite

Solid analyses are crucial in evaluating jarosite-type compounds, given the diversity of jarosites that can exist both in Nature and in industrial processes. This variety leads to complex solid structures, different morphologies, and surfaces. The inherent complexity of these variations makes the identification of these compounds challenging.

Among the commonly employed methods for the identification and assessment of jarosites, scanning electron microscopy (SEM) and X-ray diffraction (XRD) appear indispensable.

The study of the dissolution and precipitation of jarosite-type compounds has resulted in different X-ray diffractograms and varied SEM images. As an example, in Figure 5, two completely different jarosite morphologies are presented.

In Figure 5(a), jarosite exhibits an irregular and globular shape with various grain sizes, most measuring between 1 and 5 μm . Some grains show cleaved sides, which may be signs of mechanical abrasion resulting from agitation during synthesis [7]. Similar particle morphologies for synthetic jarosite have been reported elsewhere [194]. On the other hand, in Figure 5(b), using a natural sample, Welch *et al.* [43] observed a relatively euhedral shape for jarosite, with a grain size ranging from 0.5 to 5 μm . Qian *et al.* [114] also used euhedral Na-jarosite, indicating a highly crystalline phase, similar to Gasharova *et al.* [45].

According to Sasaki and Konno [192], particle morphology is also influenced by cations in the A-site. K-jarosite exhibits a round shape, while NH_4 -jarosite manifests as an agglomeration of pseudo cubic particles. The anhedral and euhedral natures of different samples can lead to varying dissolution rates. Another example illustrating these differences concerns the evolution of the morphology of jarosites synthesized by Reyes *et al.* [130] as the amount of

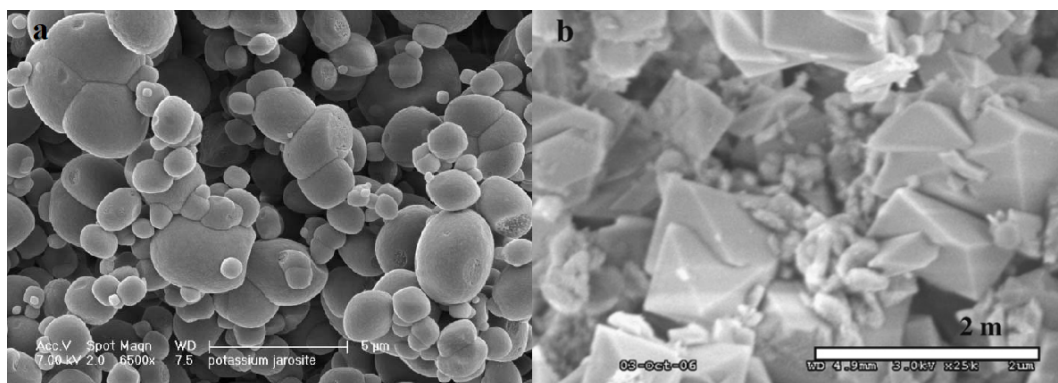


Figure 5. SEM of synthetic anhedral jarosite (a) by Smith *et al.* [7] and natural euhedral jarosite (b) by Welch *et al.* [43] (Figures reprinted with permission from Elsevier).

chromium in the structure increases. The morphology evolves from Figure 6a/b to Figure 6c/d.

Due to these differences, the use of solid analyses is essential to understand the morphologies and structures of this type of mineral, as well as to assess how they may influence the thermodynamic and kinetic data of precipitation/dissolution of these solids.

6. Conclusion and perspectives

The bibliographic review presented in this article traces the evolution of the existing research on jarosite dissolution and precipitation, initially aimed at understanding the structure of jarosite and its presence in the environment. Subsequently, these studies focused on acquiring thermodynamic and kinetic data related to the formation and dissolution of jarosite compounds.

The entirety of this literature review highlights a marked diversity in existing results. Among these, significant divergences and gaps have been identified:

- A major issue arising from these published data is the difficulty in obtaining thermodynamic and kinetic data due to the time required to reach equilibrium under the conditions used. To circumvent long-duration experiments, a trend has emerged favoring studies under more extreme conditions (high temperature and low pH) that promote faster dissolution or precipitation.
- When less favorable reaction conditions were employed, shortcuts such as using the first few hours of the reaction were employed to describe the kinetics. This time lapse, varying according to the application and conditions, proves insufficient to predict the behavior of jarosite compound kinetics. This is due to both reactions (dissolution and precipitation) requiring extended times, leading to solution evolution, and the transformation of solids in terms of structure and morphology.
- The transformations undergone can result sometimes in poorly crystalline solids with different morphologies, which can influence the data obtained. Therefore, the use of solid analysis methods is crucial for a correct understanding of the results and for comparison with previous findings.
- The disparity in kinetic data highlights that using different precipitation methodologies in order to produce jarosite solids for dissolution studies could introduce errors, as the solids may vary, and complicate the comparison between studies.
- The diversity of jarosite structures observed in the environment and in industry also places constraints on comparisons between experiments, as ions incorporated into their structure can alter kinetics and thermodynamic properties.
- Comparing these results is further complicated by the choice of thermodynamic and

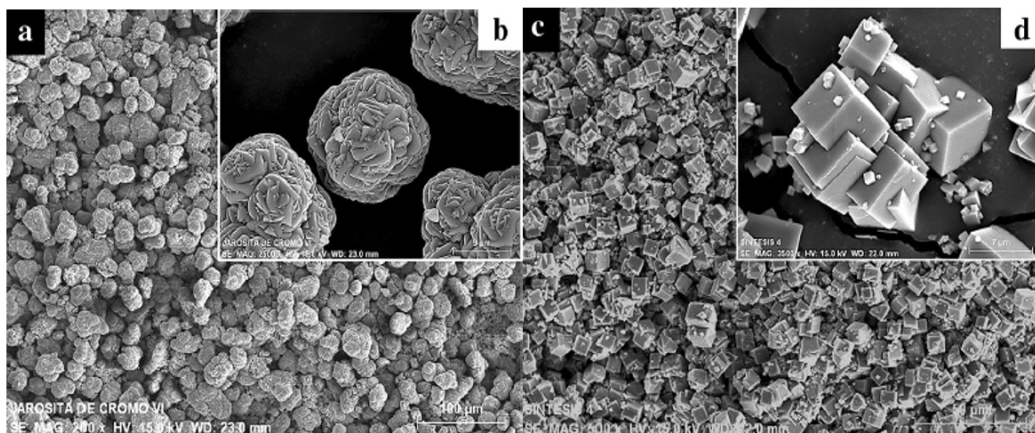


Figure 6. Cr-jarosites synthesized with increasing amounts of chromium by Reyes et al. [130] (Figures reprinted from open access article).

kinetic models, along with their inherent limitations in accurately characterizing the intricate reactive mechanisms of jarosite compounds.

However, where difficulties persist, opportunities to discover mechanisms, characterize behaviors, improve existing data, and resolve contradictions emerge.

- The challenge for further kinetic studies of jarosite lies primarily in understanding the dissolution and precipitation reaction mechanisms at temperatures closer to room temperature, conditions under which most jarosites form in the environment and where some industrial processes take place.
- The studies must take into account the evolution of precipitated and dissolved solids over time.
- It seems fundamental to understand how the precipitation methodology can influence the synthesized solid and how morphology can play a significant role in dissolution.
- The use of different models to describe both phenomena (dissolution/precipitation) is important. The use of models that connect the thermodynamic and the kinetic aspects, such as the Transition State Theory, widely used by geochemists, would be of great value to facilitate the control of the kinetics using the thermodynamics of solutions.

Declaration of interests

The authors do not work for, advise, own shares in, or receive funds from any organization that could benefit from this article, and have declared no affiliations other than their research organizations.

References

- [1] J. Kubisz, *Polska Akad. Nauk., Prace Geol.* **22** (1964), pp. 1–93.
- [2] G. P. Brophy and M. F. Sheridan, *Am. Mineral.* **50** (1965), pp. 1595–1607.
- [3] J. Kubisz, *Miner. Pol.* **1** (1970), pp. 47–57.
- [4] C. N. Alpers, R. O. Rye, D. K. Nordstrom and J. W. Ball, *Sci. Géol. Bull.* **42** (1989), pp. 281–298.
- [5] R. E. Stoffregen, C. N. Alpers and J. L. Jambor, *Rev. Miner. Geochem.* **40** (2000), pp. 453–479.
- [6] N. Eftekhari, M. Kargar, F. R. Zamin, N. Rastakhiz and Z. Manafi, *Ann. Chim.: Sci. Matériaux* **44** (2020), pp. 43–52.
- [7] A. M. Smith, K. A. Hudson-Edwards, W. E. Dubbin and K. Wright, *Geochim. Cosmochim. Acta* **70** (2006), pp. 608–621.
- [8] C. Härtig, P. Brand and K. Bohmhammel, *Z. Anorg. Allg. Chem.* **508** (1984), pp. 159–164.
- [9] J. A. Ripmeester, C. I. Ratcliffe, J. E. Dutrizac and J. L. Jambor, *Can. Mineral.* **22** (1986), pp. 773–784.
- [10] U. Schwertmann, *Naturwiss* **48** (1961), pp. 159–160.
- [11] C. Bloomfield and J. K. Coulter, *Adv. Agron.* **25** (1973), pp. 265–326.
- [12] M. J. Dudas, *Soil Sci. Soc. Am. J.* **48** (1984), pp. 1451–1452.
- [13] H. Hyashi, *Nendo Kagaku* **34** (1994), pp. 118–124.
- [14] B. B. Bowen and K. C. Benison, *Appl. Geochem.* **24** (2009), pp. 268–284.
- [15] H. Zänker, H. Moll, W. Richter, V. Brendler, C. Hennig, T. Reich, A. Kluge and G. Huttig, *Appl. Geochem.* **17** (2002), pp. 633–648.

- [16] W. B. Gagliano, M. R. Brill, J. M. Bigham, F. S. Jones and S. J. Traina, *Geochim. Cosmochim. Acta* **68** (2004), pp. 2119–2128.
- [17] H. E. Jamieson, C. Robinson, C. N. Alpers, D. K. Nordstrom, A. Poustovetov and H. A. Lowers, *Can. Mineral.* **43** (2005), pp. 1225–1242.
- [18] E. Murad and P. Rojik, *Clay Mineral.* **40** (2005), pp. 427–440.
- [19] A. Navrotsky, F. L. Forray, C. Drouet, S. Kumpulainen, L. Carlson and M.-L. Räsänen, *Appl. Geochem.* **22** (2007), pp. 760–777.
- [20] R. A. Koski, L. Munk, A. L. Foster, W. C. Shanks and L. L. Stillings, *Appl. Geochem.* **23** (2008), pp. 227–254.
- [21] D. K. Nordstrom, *Hydrogeochemical and microbiological factors affecting the heavy metal chemistry of an acid mine drainage system*, Phd dissertation, Stanford University, 1977.
- [22] B. M. Chapman, D. R. Jones and R. F. Jung, *Geochim. Cosmochim. Acta* **47** (1983), pp. 1957–1973.
- [23] K. A. Hudson-Edwards, C. Schell and M. G. Macklin, *Appl. Geochem.* **14** (1999), pp. 55–70.
- [24] K. W. Bladh, *Econ. Geol.* **77** (1982), pp. 176–184.
- [25] P. J. Sullivan and A. A. Sobek, *Mineral. Environ.* **4** (1982), pp. 9–17.
- [26] C. N. Alpers, R. O. Rye, D. K. Nordstrom, L. D. White and B.-S. King, *Chem. Geol.* **96** (1992), pp. 203–226.
- [27] J. E. Dutrizac and J. L. Jambor, *Rev. Mineral. Geochem.* **40** (2000), pp. 405–452.
- [28] J. H. Johnston, *Geochim. Cosmochim. Acta* **41** (1977), pp. 539–544.
- [29] D. R. Zimbelman, R. O. Rye and G. N. Breit, *Chem. Geol.* **215** (2005), pp. 37–60.
- [30] P. Schiffman, R. Zierenberg, N. Marks, J. L. Bishop and M. Darby Dyar, *Geology* **34** (2006), pp. 921–924.
- [31] P. Fullignati, A. Sbrana, W. Luperini and V. Greco, *J. Volcanol. Geotherm. Res.* **115** (2002), pp. 397–410.
- [32] J. J. Papike, J. M. Karner and C. K. Shearer, *Geochim. Cosmochim. Acta* **70** (2006), pp. 1309–1321.
- [33] R. I. Tkachenko and A. V. Zotov, in *Hydrothermal Mineral-Forming Solutions in the Areas of Active Volcanism*, 1st edition (S. I. Naboko, ed.), Amerind Publishing Co.: New Delhi, 1982, pp. 126–131.
- [34] W. J. Keith, L. Calk and R. P. Ashley, *USGS Shorter Contributions to Mineralogy and Petrology*, Geological Survey Professional Paper, 1124-C, U.S. Geological Survey, 1979, pp. C1–C5.
- [35] R. E. Stoffregen and R. Rye, *Abstr. Pap. Am. Chem. Soc.* **204** (1992), article no. 86GEOC.
- [36] D. C. Golden, D. W. Ming, R. V. Morris and T. G. Graff, *Mars. Am. Mineral.* **93** (2008), pp. 1201–1214.
- [37] D. T. Long, N. E. Fegan, J. D. McKee, W. B. Lyons, M. E. Hines and P. G. Macumber, *Chem. Geol.* **96** (1992), pp. 183–202.
- [38] F. Risacher, H. Alonso and C. Salazar, *Chem. Geol.* **187** (2002), pp. 39–57.
- [39] K. C. Benison and D. A. Laclair, *Astrobiology* **3** (2003), pp. 609–618.
- [40] K. C. Benison, B. B. Bowen, F. Oboh-Ikuenobe, E. A. Jag-niecki, D. A. Laclair, S. L. Story, M. R. Mormile and B. Y. Hong, *J. Sediment. Res.* **77** (2007), pp. 366–388.
- [41] B. B. Bowen and K. C. Benison, *Appl. Geochem.* **24** (2009), pp. 268–284.
- [42] E. M. Dixon, A. S. Madden, E. M. Hausrath and M. E. Elwood Madden, *J. Geophys. Res.: Planets* **120** (2015), pp. 625–642.
- [43] S. A. Welch, D. Kirste, A. G. Christy, F. R. Beavis and S. G. Beavis, *Chem. Geol.* **254** (2008), pp. 73–86.
- [44] M. R. Kendall, A. S. Madden, M. E. Elwood Madden and Q. Hu, *Geochim. Cosmochim. Acta* **112** (2013), pp. 192–207.
- [45] B. Gasharova, J. Göttlicher and U. Becker, *Chem. Geol.* **215** (2005), pp. 499–516.
- [46] A. M. Trueman, M. J. Mclaughlin, L. M. Mosley and R. W. Fitzpatrick, *Chem. Geol.* **543** (2020), article no. 119606.
- [47] P. R. Christensen, M. B. Wyatt, T. D. Glotch, et al., *Science* **306** (2004), pp. 1733–1739.
- [48] M. E. Elwood Madden, R. J. Bodnar and J. D. Rimstidt, *Nature* **431** (2004), pp. 821–823.
- [49] G. Klingelhofer, R. V. Morris, B. Bernhardt, et al., *Science* **306** (2004), pp. 1740–1745.
- [50] S. W. Squyres, R. E. Arvidson, D. Bollen, et al., *J. Geophys. Res.: Planets* **111** (2006), article no. E12S12.
- [51] R. V. Morris and G. Klingelhofer, in *The Martian Surface: Composition, Mineralogy, and Physical Properties*, III edition (J. F. Bell, ed.), Cambridge Planetary Science, Cambridge University Press, 2008, pp. 339–365.
- [52] T. D. Glotch and P. R. Christensen, *J. Geophys. Res.* **110** (2005), article no. E090006.
- [53] T. D. Glotch and J. L. Bandfield, *J. Geophys. Res.: Planets* **111** (2006), article no. E12S06.
- [54] W. H. Farrand, T. D. Glotch, J. W. Rice, J. A. Hurowitz and G. A. Swayze, *Icarus* **204** (2009), pp. 478–488.
- [55] L. H. Roach, J. F. Mustard, G. Swayze, R. E. Milliken, J. L. Bishop, S. L. Murchie and K. Lichtenberg, *Icarus* **206** (2010), pp. 253–268.
- [56] J. P. Bibring, Y. Langevin, J. F. Mustard, et al., *Science* **312** (2006), pp. 400–404.
- [57] J. P. Bibring, R. E. Arvidson, A. Gendrin, et al., *Science* **317** (2007), pp. 1206–1210.
- [58] S. W. Squyres and A. H. Knoll, *Earth Planet. Sci. Lett.* **240** (2005), pp. 1–10.
- [59] A. S. Madden, V. E. Hamilton, M. E. Elwood Madden, P. R. Larson and M. A. Miller, *Earth Planet. Sci. Lett.* **298** (2010), pp. 377–384.
- [60] C. Arslan and F. Arslan, *Turkish J. Eng. Environ. Sci.* **27** (2003), pp. 45–52.
- [61] I. A. Reyes, F. Patiño, M. U. Flores, T. Pandiyan, R. Cruz, E. J. Gutierrez, M. Reyes and V. H. Flores, *Hydrometallurgy* **167** (2017), pp. 16–29.
- [62] J. E. Dutrizac, *Metall. Trans. B* **14** (1983), pp. 531–539.
- [63] J. M. Bigham and D. K. Nordstrom, in *Sulfate Minerals: Crystallography, Geochemistry, and Environmental Significance* (C. N. Alpers, J. L. Jambor and D. K. Nordstrom, eds.), Reviews in Mineralogy and Geochemistry, Mineralogical Society of America, Washington, DC, The Geochemical Society: St. Louis, Missouri, 2000, pp. 351–403.

- [64] M. O. Figueiredo and T. P. Silva, *Int. J. Environ. Res. Pub. Health* **8** (2011), pp. 1575–1582.
- [65] C. L. Vithana, L. A. Sullivan, R. T. Bush and E. D. Burton, *Soil Res.* **51** (2013), pp. 203–214.
- [66] C. L. Vithana, L. A. Sullivan, R. T. Bush and E. D. Burton, *Appl. Geochem.* **51** (2014), pp. 130–138.
- [67] H. Islas, M. U. Flores, I. A. Reyes, et al., *J. Hazard. Mater.* **386** (2020), article no. 121664.
- [68] D. Baron and C. D. Palmer, *Geochim. Cosmochim. Acta* **60** (1996), pp. 185–195.
- [69] L. Sullivan, N. Ward, N. Toppler and G. Lancaster, *National acid sulfate soils guidance: National acid sulfate soils identification and laboratory methods manual*, 2018. Department of Agriculture and Water Resources, Canberra, ACT. CC BY 4.0.
- [70] R. E. Stoffregen, *Geochim. Cosmochim. Acta* **57** (1993), pp. 2417–2429.
- [71] D. K. Nordstrom, in *Acid Sulfate Weathering* (J. A. Kittrick, D. S. Fanning and L. R. Hossner, eds.), SSSA Special Publication (Soil Science Society of America), No. 10, Wiley, 1982, pp. 37–56. Chapter 3.
- [72] M. Fleischer, G. Y. Chao and A. Kato, *Am. Mineral.* **60** (1975), pp. 485–489.
- [73] H. Chappell, W. Thom, D. Bowron, N. Faria, P. Hasnip and J. Powell, *Phys. Rev. Mater.* **1** (2017), article no. 036002.
- [74] M. Sassi and K. Rosso, *ACS Earth Space Chem.* **3** (2018), pp. 70–78.
- [75] E. Posnjak and H. E. Merwin, *J. Am. Chem. Soc.* **44** (1922), pp. 1965–1964.
- [76] C. Drouet and A. Navrotsky, *Geochim. Cosmochim. Acta* **67** (2003), pp. 2063–2076.
- [77] J. M. Bigham, U. Schwertmann, S. J. Traina, R. L. Winland and M. Wolf, *Geochim. Cosmochim. Acta* **60** (1996), pp. 2111–2121.
- [78] S. B. Hendricks, *Am. Mineral.* **22** (1937), pp. 773–784.
- [79] S. Menchetti and C. Sabelli, *Neues Jahrb. Mineral. Monatsh.* **9** (1976), pp. 406–417.
- [80] R. L. Parker, *Am. Mineral.* **47** (1962), pp. 127–136.
- [81] G. P. Brophy, E. S. Scott and R. A. Snellgrove, *Am. Mineral.* **47** (1962), pp. 112–126.
- [82] J. Kubisz, *Bull. Acad. Pol. Sci., Ser. Sci. Chim. Géol. Et géogr.* **VIII** (1960), pp. 95–99.
- [83] G. J. Ross, K. C. Ivanson and N. M. Miles, in *Acid Sulfate Weathering* (J. A. Kittrick, D. S. Fanning and L. R. Hossner, eds.), SSSA Special Publication (Soil Science Society of America), No. 10, Wiley, 1982, pp. 77–94. Chapter 5.
- [84] J. B. Brown, *Can. Mineral.* **10** (1970), pp. 696–702.
- [85] P. L. G. Vlek, T. J. M. Blom, J. Beek and W. L. Lindsay, *Soil Sci. Soc. Am. J.* **38** (1974), pp. 429–432.
- [86] C. M. Kashkay, Y. B. Borovskaya and M. A. Badazade, *Geochem. Intl* **12** (1975), pp. 115–121.
- [87] A. V. Zotov, G. D. Mironova and V. L. Rusinov, *Geochem. Intl.* **5** (1973), pp. 577–582.
- [88] N. Van Breemen, in *Proceedings of the 1972 (Wageningen, Netherlands) International Acid Sulphate Soils Symposium* (H. Dost, ed.), Int. Land Reclamation Inst. Publication 18: Wageningen, 1973, pp. 66–139.
- [89] G. Hladky and E. Slansky, *Bull. Mineral.* **104** (1981), pp. 468–477.
- [90] R. J. Lemire, U. Berner, C. Musikas, D. A. Palmer, P. Taylor and O. Tochiyama, *Chemical Thermodynamics*, OECD Nuclear Energy Agency Data Bank, OECD Publications: Paris, 2013.
- [91] J. Majzlan, R. Stevens, J. Boerio-Goates, B. F. Woodfield, A. Navrotsky, P. C. Bruns, M. K. Crawford and T. G. Amos, *Phys. Chem. Mineral.* **31** (2004), pp. 518–531.
- [92] J. M. Casas, C. Paipa, T. Godoy and T. Vargas, *J. Geochem. Explor.* **97** (2007), pp. 111–119.
- [93] F. L. Forray, A. M. L. Smith, C. Drouet, A. Navrotsky, K. Wright, K. A. Hudson-Edwards and W. E. Dubbin, *Geochim. Cosmochim. Acta* **74** (2010), pp. 215–224.
- [94] W. L. Lindsay, *Chemical Equilibria in Soils*, John Wiley and Sons, 1979.
- [95] I. Öborn and D. Berggren, *Geoderma* **66** (1995), pp. 213–225.
- [96] G. B. Naumov, I. L. Ryzhenko and I. L. Khodakovskiy, in *Handbook of Thermodynamic Data* (I. Barnes and V. Speltz, eds.), NTIS publication: Washington DC, 1971. PB-226, 722.
- [97] R. A. Robie and D. R. Walbaum, *Geological Survey Bulletin* 1259, U.S. Government Printing Office: Washington, 1968, p. 256.
- [98] D. Baron and C. D. Palmer, *Geochim. Cosmochim. Acta* **66** (2002), pp. 2841–2853.
- [99] A. M. L. Smith, W. E. Dubbin, K. Wright and K. A. Hudson-Edwards, *Chem. Geol.* **229** (2006), pp. 344–361.
- [100] C. Drouet, D. Baron and A. Navrotsky, *Am. Mineral.* **88** (2003), pp. 1949–1954.
- [101] C. Drouet, K. L. Pass, S. Draucker and A. Navrotsky, *Geochim. Cosmochim. Acta* **68** (2004), pp. 2197–2205.
- [102] J. Majzlan, P. Glasnák, R. A. Fisher, M. A. White, M. B. Johnson, B. Woodfield and J. Boerio-Goates, *Phys. Chem. Mineral.* **37** (2010), pp. 635–651.
- [103] F. L. Forray, C. Drouet and A. Navrotsky, *Geochim. Cosmochim. Acta* **69** (2005), pp. 2133–2140.
- [104] F. L. Forray, A. M. L. Smith, A. Navrotsky, K. Wright, K. A. Hudson-Edwards and W. E. Dubbin, *Geochim. Cosmochim. Acta* **127** (2014), pp. 107–119.
- [105] J. D. Rimstidt, S. L. Brantley and A. Olsen, *Geochim. Cosmochim. Acta* **99** (2012), pp. 159–178.
- [106] R. J. Seager, A. J. Acevedo, F. Spill and M. H. Zaman, *Sci. Rep.* **8** (2018), article no. 7711.
- [107] S. Yagi and D. Kunii, *Fifth Symposium (International) on Combustion*, Reinhold: New York, 1955, pp. 231–244.
- [108] O. Levenspiel, *Engenharia das Reações Químicas*, 3rd edition, Edgard Blücher LTDA: São Paulo, 2000, p. 584.
- [109] M. E. Elwood Madden, A. S. Madden, J. D. Rimstidt, S. Zhai, M. R. Kendall and M. A. Miller, *Geochim. Cosmochim. Acta* **91** (2012), pp. 306–321.
- [110] B. N. Pritchett, M. E. Elwood Madden and A. S. Madden, *Earth Planet. Sci. Lett.* **357–358** (2012), pp. 327–336.
- [111] C. Legett Iv, B. N. Pritchett, A. S. Elwood Madden, C. M. Phillips-Lander and M. E. Elwood Madden, *Icarus* **301** (2018), pp. 189–195.
- [112] S. K. Zahrai, M. E. Elwood Madden, A. S. Madden and J. D. Rimstidt, *Icarus* **223** (2013), pp. 438–443.
- [113] C. I. Steefel, D. J. Depaolo and P. C. Lichtner, *Earth Planet. Sci. Lett.* **240** (2005), pp. 539–558.

- [114] G. Qian, R. Fan, M. C. Short, R. C. Schumann, J. Li, Y. Li, R. S. C. Smart and A. R. Gerson, *Chem. Geol.* **504** (2019), pp. 14–27.
- [115] M. E. Elwood Madden, A. E. Madden and J. D. Rimstidt, *Geology* **37** (2009), pp. 635–638.
- [116] E. Abkhoshk, E. Jorjani, M. S. Al-Harashsheh, F. Rashchi and M. Naazeri, *Hydrometallurgy* **149** (2014), pp. 153–167.
- [117] A. Roca, F. Patiño, J. Viñals and C. Núñez, *Hydrometallurgy* **33** (1993), pp. 341–357.
- [118] A. Roca, M. Cruells, F. Patiño, I. Rivera and M. Plata, *Hydrometallurgy* **81** (2006), pp. 15–23.
- [119] F. Patiño, J. Viñals, A. Roca and C. Núñez, *Hydrometallurgy* **34** (1994), pp. 279–291.
- [120] F. Patiño, E. Salinas, M. Cruells and A. Roca, *Hydrometallurgy* **49** (1998), pp. 323–336.
- [121] F. Patiño, M. Cruells, A. Roca, E. Salinas and M. Pérez, *Hydrometallurgy* **70** (2003), pp. 153–161.
- [122] M. Cruells, A. Roca, F. Patiño, E. Salinas and I. Rivera, *Hydrometallurgy* **55** (2000), pp. 153–163.
- [123] E. Salinas, A. Roca, M. Cruells, F. Patiño and D. A. Córdoba, *Hydrometallurgy* **60** (2001), pp. 237–246.
- [124] D. Calla-Choque and G. T. Lapidus, *Hydrometallurgy* **200** (2021), article no. 105565.
- [125] M. Perez-Labra, A. Romero-Serrano, E. Salinas-Rodriguez, E. Avila-Davila and M. Reyes-Perez, *Metall. Mater. Trans. B Process Metall. Mater. Process. Sci.* **43B** (2012), pp. 773–779.
- [126] M. U. Flores, F. Patiño, I. A. Reyes, I. Rivera, M. Reyes and J. C. Juárez, *J. Braz. Chem. Soc.* **23** (2012), pp. 1018–1023.
- [127] F. Patiño, I. A. Reyes, M. U. Flores, T. Pandiyan, A. Roca, M. Reyes and J. Hernández, *Hydrometallurgy* **137** (2013), pp. 115–125.
- [128] J. E. Méndez, M. U. Flores, P. Francisco, M. Reyes, J. C. Juárez, I. A. Reyes and E. G. Palacios, *Eur. Metall. Conf., GDMB I* (2015), pp. 523–536.
- [129] I. Mireles et al., *J. Braz. Chem. Soc.* **26** (2016), pp. 1014–1025.
- [130] I. A. Reyes, I. Mireles, F. Patiño, T. Pandiyan, M. U. Flores, E. G. Palacios, E. J. Gutiérrez and M. Reyes, *Geochem. Trans.* **17** (2016), article no. 3.
- [131] S. Ordoñez, M. U. Flores, F. Patiño, I. A. Reyes, H. Islas, M. Reyes, E. Mendez and E. G. Palacios, *Int. J. Chem. Kinet.* **49** (2017), pp. 798–809.
- [132] I. A. Reyes, F. Patiño, I. Riviera, M. U. Flores, M. Reyes and J. Hernández, *J. Braz. Chem. Soc.* **22** (2011), pp. 2260–2267.
- [133] F. Patiño, M. U. Flores, I. A. Reyes, M. Reyes, J. Hernández, I. Rivera and J. Juárez, *Geochem. Trans.* **14** (2013), article no. 2.
- [134] H. Islas, F. Patiño, A. Roca, I. A. Reyes, M. U. Flores, E. G. Palacios and M. Reyes, *24th International Conference on Metallurgy and Materials. June 3rd–5th 2015, Brno, Czech Republic, EU*, 2015.
- [135] A. A. González-Ibarra, F. Nava-Alonso, A. Uribe-Salas and E. N. Castillo-Ventureño, *Can. Metall. Q.* **55** (2016), pp. 448–454.
- [136] H. Islas et al., *Miner. Eng.* **174** (2021), article no. 107250.
- [137] V. H. Flores, A. Patiño, M. U. Flores, I. A. Reyes, M. Reyes and H. Islas, *Metals* **12** (2022), article no. 584.
- [138] D. Calla-Choque, F. Nava-Alonso and J. C. Fuentes-Aceituno, *J. Hazard. Mater.* **317** (2016), pp. 440–448.
- [139] D. Calla-Choque and G. T. Lapidus, *Hydrometallurgy* **192** (2020), article no. 105289.
- [140] M. C. Nolasco, L. F. Flores, E. J. Gutiérrez, J. Aguilar, E. G. Palacios, M. U. Flores, I. Rodríguez and I. A. Reyes, *Hydrometallurgy* **212** (2022), article no. 105907.
- [141] P. K. Gbor and C. Q. Jia, *Chem. Eng. Sci.* **59** (2004), pp. 1979–1987.
- [142] R. L. Driscoll and R. W. Leinz, *Methods For Synthesis of Some Jarosites: U. S. Geological Survey, Techniques and Methods 05-D1*, U.S. Geological Survey: Reston, Virginia, 2005, p. 5.
- [143] J. G. Fairchild, *Am. Mineral.* **18** (1933), pp. 543–547.
- [144] F. Jones, *Minerals* **7** (2017), article no. 90.
- [145] J. E. Dutrizac, O. Dinardo and S. Kaiman, *Hydrometallurgy* **5** (1980), pp. 305–324.
- [146] H. Crabbe, N. Fernandez and F. Jones, *J. Crystall. Growth* **416** (2015), pp. 28–33.
- [147] H. E. A. Brand, N. V. Y. Scarlett and I. E. Grey, *J. Appl. Crystall.* **45** (2012), pp. 535–545.
- [148] J. E. Dutrizac, J. L. Jambor and T. T. Chen, *Can. Metall. Q.* **26** (1987), pp. 103–115.
- [149] N. Y. Uchameyshvili, S. D. Malinin and N. I. Khitarov, *Geochem. Int.* **10** (1966), pp. 951–963.
- [150] V. G. Strübel, *Neues Jahr. Miner. Monatsh.* **7/8** (1967), pp. 223–234.
- [151] W. H. Casey, J. F. Banfield, H. R. Westrich and L. McLaughlin, *Chem. Geol.* **105** (1993), pp. 1–15.
- [152] M. A. Velbel, *Am. Mineral.* **78** (1993), pp. 405–414.
- [153] A. F. White and S. L. Brantley, *Chem. Geol.* **202** (2003), pp. 479–506.
- [154] J. E. Dutrizac and S. Kaiman, *Can. Mineral.* **14** (1976), pp. 151–158.
- [155] J. E. Dutrizac, *Hydrometallurgy* **26** (1991), pp. 327–346.
- [156] J. E. Dutrizac and O. Dinardo, *Hydrometallurgy* **11** (1983), pp. 61–78.
- [157] J. E. Dutrizac, O. Dinardo and S. Kaiman, *Hydrometallurgy* **6** (1981), pp. 327–337.
- [158] J. E. Dutrizac and T. T. Chen, *Can. Mineral.* **19** (1981), pp. 559–569.
- [159] J. E. Dutrizac and J. L. Jambor, *Hydrometallurgy* **17** (1987), pp. 251–265.
- [160] J. E. Dutrizac and J. L. Jambor, *Trans. Inst. Min. Metall., C: Mineral Proc. Extractive Metall.* **96** (1987), pp. 206–218.
- [161] J. E. Dutrizac and J. L. Jambor, *Can. Metall. Q.* **26** (1987), pp. 91–101.
- [162] J. E. Dutrizac, D. J. Hardy and T. T. Chen, *Hydrometallurgy* **41** (1996), pp. 269–285.
- [163] J. E. Dutrizac and D. J. Hardy, *Hydrometallurgy* **45** (1997), pp. 83–95.
- [164] J. E. Dutrizac and T. T. Chen, *Can. Metall. Q.* **39** (2000), pp. 1–14.
- [165] J. E. Dutrizac, *Electrometallurgy and Environmental Hydrometallurgy* (C. Young, A. Alfantazi, C. Anderson, A. James, D. Dreisinger and B. Harris, eds.), The Miner-

- als Metals and Materials Society: Warrendale, PA, 2003, pp. 1755–1771.
- [166] J. E. Dutrizac and T. T. Chen, *Can. Metall. Q.* **42** (2003), pp. 187–197.
- [167] J. E. Dutrizac, *Hydrometallurgy* **73** (2004), pp. 11–30.
- [168] J. E. Dutrizac, T. T. Chen and S. Beauchemin, *Hydrometallurgy* **79** (2005), pp. 138–153.
- [169] J. E. Dutrizac, *Proceedings of the Global Symposium on Recycling, Waste Treatment and Clean Technology (RE-WAS '04)* (I. Gaballah, B. Mishra, R. Solozabal and M. Tanaka, eds.), The Minerals, Metals and Materials Society: Madrid, 2004, pp. 1049–1060.
- [170] J. E. Dutrizac and T. T. Chen, *Can. Metall. Q.* **45** (2006), pp. 249–260.
- [171] J. E. Dutrizac and T. T. Chen, *Proceedings – European Metallurgical Conference, EMC 2007*, GDMB Medienverlag: Dusseldorf, 2007, pp. 1077–1098.
- [172] J. E. Dutrizac and T. T. Chen, *Can. Metall. Q.* **47** (2008), pp. 387–401.
- [173] J. E. Dutrizac and T. T. Chen, *5th European Metallurgical Conference. Proceeding-European Metallurgical Conference, EMC*, GDMB Medienverlag: Innsbruck, 2009, pp. 977–1000.
- [174] J. E. Dutrizac and T. T. Chen, *Hydrometallurgy* **98** (2009), pp. 128–135.
- [175] J. E. Dutrizac and T. T. Chen, *World of Metallurgy – ERZMETALL* **65** (2012), pp. 297–305.
- [176] G. C. Limpo, *Revista de Metal. (COM)* **12** (1976), pp. 123–135.
- [177] L. A. Teixeira and L. Y. Tavares, in *Iron Control in Hydrometallurgy* (J. E. Dutrizac and A. J. Monhemius, eds.), Ellis Horwood: Chichester, 1986, pp. 431–453.
- [178] J. E. Dutrizac, *Hydrometallurgy* **42** (1996), pp. 293–312.
- [179] Q. Wang, R. Ma and Z. Tan, in *Zinc '85* (K. Tozawa, ed.), Mining and Metallurgical Institute of Japan: Tokyo, 1975, pp. 675–690.
- [180] E. V. Margulis, L. S. Getskin and N. A. Zapuskalova, *Russ. J. Inorg. Chem.* **22** (1977), pp. 1362–1365.
- [181] H. Kubo, M. Kawahara and Y. Shirane, *Nippon Kogyo Kaishi* **98** (1982), pp. 1257–1261.
- [182] J. E. Dutrizac, *Metall. Mater. Trans. B* **39B** (2008), pp. 771–783.
- [183] J. E. Dutrizac, *Can. Metall. Q.* **49** (2010), pp. 121–130.
- [184] L. Toro, B. Paponett and C. Cantalini, *Hydrometallurgy* **20** (1988), pp. 1–9.
- [185] H. Wang, J. M. Bigham and O. H. Tuovinen, *Mater. Sci. Eng. C* **26** (2006), pp. 588–592.
- [186] H. Wang, J. M. Bigham, F. S. Jones and O. H. Tuovinen, *Geochim. Cosmochim. Acta* **71** (2007), pp. 155–164.
- [187] M. Egal, C. Casiot, G. Morin, M. Parmentier, O. Bruneel, S. Lebrun and F. Elbaz-Poulichet, *Chem. Geol.* **265** (2009), pp. 432–441.
- [188] A. H. Kaksonen, C. Morris, F. Hilario, et al., *Hydrometallurgy* **150** (2014), pp. 227–235.
- [189] A. H. Kaksonen, C. Morris, J. Wylie, J. Li, K. Usher, F. Hilario and C. A. Du Plessis, *Hydrometallurgy* **168** (2016), pp. 40–48.
- [190] J. M. Bigham, S. F. Jones, B. Ozkaya, E. Sahinkaya, J. A. Puhakka and O. H. Tuovine, *Int. J. Miner. Process.* **94** (2010), pp. 121–128.
- [191] F. Scordari, F. Vurro and S. Menchetti, *Tschermaks Mineral. Petrogr. Mitt.* **22** (1975), pp. 88–97.
- [192] K. Sasaki and H. Konno, *Can. Mineral.* **38** (2000), pp. 45–66.
- [193] J. M. Bigham, L. Carlson and E. Murad, *Mineral. Mag.* **58** (1994), pp. 641–648.
- [194] Y. Kim, *J. Hazard. Mater.* **353** (2018), pp. 118–126.



Research article

GDR Prométhée – French Research Network on *Hydrometallurgical Processes for Primary and Secondary Resources*

Filtering the unfilterable: tuning the mesostructure of precipitating silica gels to improve the filterability of acidic lixiviation slurries

Christian Manfoumbi ^a, Kevin Roger ^{*,*,a} and Martine Meireles ^{*,*,a}

^a Laboratoire de Génie Chimique, Université de Toulouse, CNRS, INPT, UPS, Toulouse, 31432, France

E-mails: kevin.roger@cnrs.fr (K. Roger), martine.meireles-masbernard@cnrs.fr (M. Meireles)

Abstract. Silica precipitation is a ubiquitous but deleterious phenomenon occurring in many hydrometallurgical processes. Indeed, silicon is often released during the dissolution of minerals under acidic leaching conditions. Eventually, it precipitates into a hard-to-filter silica gel, which has prompted some efforts to hinder silica precipitation through pretreatment or extra dilution. However, these approaches are usually either mineral-specific or costly. Here, we propose a disruptive strategy based on controlling the gel's mesostructure and therefore its filterability. We designed an alternative precipitation pathway consisting of adding extra silicate ions but at basic pH. Using small-angle X-ray scattering, we show that this pathway transforms the network of polymeric silica ("polymer gel") obtained under highly acidic leaching conditions into a network of dense silica particles ("particle gel"). This structural compaction at the mesoscopic length scale cascades to the macroscale and leads to a drastic improvement in filterability by two orders of magnitude. Furthermore, we demonstrate that this method is generic by applying it successfully to both a model and real ore systems.

Keywords. Lixiviation, Silica, Precipitation, Mesostructure, Filterability.

Funding. ERAMET Research, French State and Région Occitanie (CPER IMATECBIO grant).

Manuscript received 15 December 2023, revised 31 May 2024 and 4 September 2024, accepted 27 September 2024.

1. Introduction

Rare earth elements (REEs) play a critical role in the global economy due to their numerous applications. They are notably used in electronic and steel industries, as well as permanent magnets, lasers, and batteries. The ongoing development of cleaner energy

sources and transportation especially contributes to the sharp increase in REE industrial uses [1–3]. This rising demand is still mostly met by increasing the extraction from natural minerals [3,4] despite ongoing efforts in recycling REE, for instance in electronic equipment. Less known and rarer, niobium (Nb) is also a key strategic element for future technologies, and its demand is anticipated to increase by 700% in the next 25 years [1] with about 10% of the market concerning high-purity Nb [5]. Strikingly, about

*Corresponding authors

99% of Nb produced worldwide is extracted from pyrochlore-type materials, which are refractory rocks that also contain REEs.

In this context, the Mabounié (Gabon) deposit discovered in 1986 is an interesting example of a niobium-rich deposit that requires innovative extraction strategies [6]. Indeed, hydrometallurgy is more suited than pyrometallurgy to extract both Nb and REE, but the known fluoride acid route to perform the liquid–liquid extraction is environmentally problematic. This situation stimulated the development of an innovative hydrometallurgical process for the leaching of niobium- and REE-bearing pyrochlore ores and the subsequent separation of Nb from REE [5,7–9]. The upstream part of this process produces a raw Nb concentrate through three main steps. First, refractory pyrochlores bearing Nb, REEs, U, and Ta are decomposed by making the non-magnetic ore react with concentrated sulfuric acid (96% H_2SO_4), yielding a paste that is then further roasted at 250–300 °C. Second, this roasted paste, also named calcinated powder to differentiate it from the untreated ore, is leached with water so that Nb, REE, and other elements from different mineral phases are solubilized in the aqueous phase. As the paste contains a high amount of sulfuric acid, this leaching step occurs at extremely acidic pH. Third, Nb and Ta are selectively thermoprecipitated from REE and U. In the downstream part, the raw Nb concentrate is purified.

However, the optimization of this complex process faced a ubiquitous problem in many hydrometallurgy processes, which is the formation of unfilterable silica gels. For instance, silica gel formation has been reported in hydrometallurgical processes for the extraction of rare earth from eudialyte mineral [2,10–12] or from bauxite residue [10, 13]. In hydrometallurgy, the occurrence of silica precipitation and the formation of gelatinous solutions or cakes is a serious drawback for the liquid/solid separation step with deleterious consequences on extraction processes and filterability. Apart from the problematic issue of clogging, the precipitate may blind ore particles from dissolution and reduce leaching kinetics. For instance, in the context of leaching calcium aluminate slags with aqueous HCl, for Al extraction, Tsaousi *et al.* state that avoiding SiO_2 gelation is key to designing robust leaching processes [14].

To facilitate the decomposition of mineral phases before leaching in water solution, pretreatments by reaction with mild to high acid concentration solutions as well as thermal steps are often implemented. However, these strategies are restricted to certain ore types and are typically ineffective for pyrochlore ores. Although silica is initially present in ores, its low solubility in aqueous solutions in both its amorphous and crystalline solid states precludes its involvement in the formation of unfilterable silica gels. Rather, silica gels form *in situ* during the leaching step due to the release of silicon traces when dissolving certain minerals, leading to their subsequent precipitation as silica. Furthermore, at the high ionic strength of the leaching solution, colloidal metastability is compromised due to charge screening, which leads to aggregation and thus gelation [15,16]. Gelation, a rheological transition, stems from a structural transition, which is the formation of a three-dimensional percolated network. Silica gels display a multiscale structure that notably depends on pH, a key parameter controlling its solubility and reactivity [16]. The mesostructure that corresponds to supramolecular and colloidal length scales (1–100 nm) is especially relevant to filtration [17].

In this article, we investigate strategies to avoid clogging during the filtration step that follows the acidic leaching of the ore. We first evaluate the extraction yield of the different elements over time. We notably highlight the existence of a characteristic time for the extraction of valuable elements and unveil silicon extraction from dissolved mineral phases and its precipitation as silicates in solution. We then discuss simple parametric approaches to hinder this silica precipitation, such as decreasing the extraction time or increasing the relative amount of leaching solution. We show that although these approaches are efficient, they are costly, polluting, and fragile. We then pivot to a different strategy that consists in rather mastering the mesostructure of the forming silica gel since this mesostructure underlies the overall filterability of the slurry. We present a pathway consisting of deliberately adding more silicates, but at a basic pH, before shifting back to acidic conditions to maintain the solubility of valuable elements prior to filtration. We show that this pathway indeed associates with a drastic densification of the mesostructure, yielding a particle-like instead of a polymer-like gel.

2. Results

2.1. *Extracting valuable elements through leaching: release and precipitation of silicon into a clogging gel*

The acidic leaching of an ore like that from the Mabounié deposit consists of dissolving minerals to solubilize in solution the elements of interest, here rare earth, niobium, and tantalum. This operation is performed at a given liquid/calcinated ratio (L/C), always expressed in this article at the initial time since most of the solid quickly dissolves. We characterized the calcinated powder by X-ray diffraction, which shows it contains essentially mikasaite, rhomboclase, koninckite (REE- and Nb-bearing phases), crandallite, quartz, baryte, and anhydrite. Comparison with the residue after 4 h of leaching shows the disappearance of rare-earth- and niobium-bearing phases (mikasaite, rhomboclase, koninckite) during the leaching and the appearance of sulfate phases. Therefore, while some of the ore is dissolved through the leaching step, allowing the release in solution of elements of interest, the rest of it remains as solids that must be filtered. Yet, filtration is often hindered by the formation of a clogging gel. To elucidate the nature of this gel, it is useful to monitor extraction over time through an elemental analysis by inductively coupled plasma (ICP). Figure 1A displays the extracted percentage of each major mineral element in the supernatant, obtained by centrifugation of the leached solution, measured by ICP at different times of leaching. We first observe a sharp increase in the concentration of all elements, indicating that some minerals dissolve and thus release elements in solution. This correlates to the rapid dissolution of the calcinated ore, with 77% of its mass dissolved in solution after 30 min. An asymptotic value is quickly reached within 1 h for all elements, with typical values of 70% for niobium and 60% for tantalum. However, there is a strong exception to this generic behavior in the case of silicon. Indeed, following the increase in concentration, a strong decrease is observed, indicating that silicon is somehow removed from the solution. This indicates the precipitation of the dissolved silicon into a new solid phase. It is worth noting that this reprecipitating amount is only a very small fraction of the total silicon content in the ore. QEMSCAN analyses indicate that silicon is mostly contained in quartz, which does not dissolve

during leaching. They also suggest the formation of amorphous silica in small amounts. Thermodynamically, silicon could not be simultaneously extracted from quartz and then reprecipitated in the same solution as silicates. It must then originate from mineral phases that dissolve during the leaching step in which silicon can be present as traces, consistently with the small percentages of extracted silica during leaching.

2.2. *Precipitation of silica at acidic pH: filterability of slurries*

Since the formation of the silica gel is detrimental to filtration, the simplest approach is to avoid or delay its formation, which corresponds to tuning, respectively, thermodynamics or kinetics of silica precipitation. Experimentally, the most straightforward way to play on both is to increase the amount of the leaching solution compared to the ore, which corresponds to increasing the liquid/calcinated ratio (L/C). Silicon extraction and precipitation can then be measured over time by sampling the reactor followed by an ICP analysis. Figure 2A displays the kinetics of silicon leaching and precipitation over time for three liquid/solid ratios of respectively 2, 4, and 8. Qualitatively, the same behavior is observed for all L/C ratios and mirrors the one observed for $L/C = 1$ displayed in Figure 1A. First, the silica concentration increases as silicon is released from the dissolved mineral phases bearing it as traces, before decreasing at longer times as it precipitates as amorphous silica in solution. However, the extent of this non-monotonic variation decreases sharply upon increasing the L/C ratio and thus increasing the dilution of the ore in the leaching solution. At the highest ratio of 8, the decrease is very mild and occurs over several hours, which is generally too long regarding operating conditions. In that case, silica is nearly at its solubility and the excess precipitates very slowly due to a low supersaturation. Therefore, the extent of precipitation is efficiently tuned by the L/C ratio.

We then investigated the filterability of the corresponding slurries by performing a dead-end filtration at constant pressure. We chose L/C ratios of 4, 6, and 8 to echo the change in the extent of silica precipitation evidenced in Figure 1A. We plot the time-to-volume ratio (t/V) as a function of filtrate volume (V) and observe a linear variation for all data. This

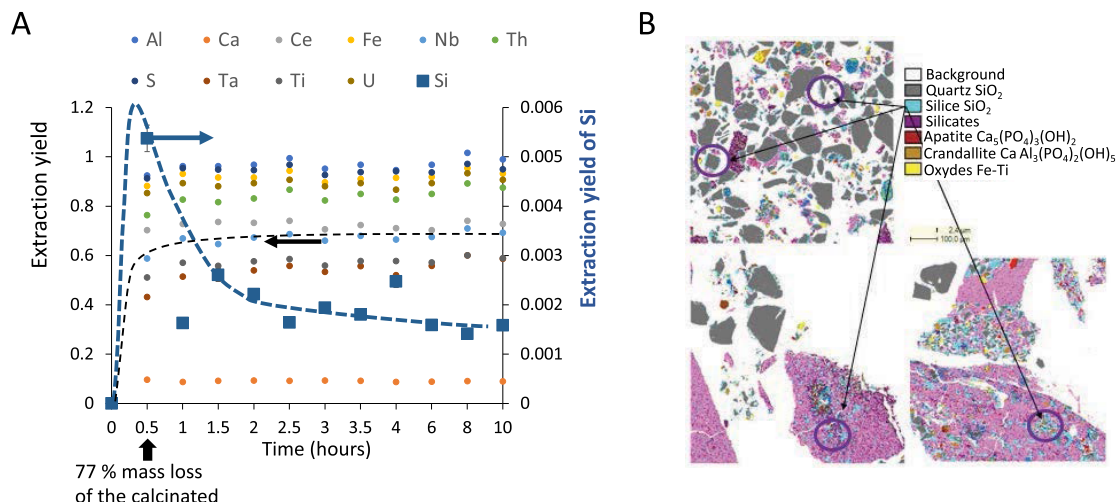


Figure 1. (A) Extraction monitoring of each element in solution over time, quantified by ICP and performed at $L/C = 1$. Reaching a value of 1 means that the whole amount of the element initially present in the calcinated ore was extracted in solution. All elements reach an asymptotic value of the extraction yield (left Y-axis) within 1 h except silicon, which displays a non-monotonic behavior and much lower extraction yields (right Y-axis). Note that after 30 min, 77% of the calcinated mass is dissolved in solution. (B) QEMSCAN field maps from residue samples collected after 0.5 h (top left), 1.5 h (down left), and 24 h (down right) leaching time. Images are field maps from 1×1 mm thin polished sections with false color composite images with different assigned mineral phases shown in the legend panel. Quartz and silica are two phases that are difficult to distinguish, but SiO₂ is identified on pixels for which the Si content is lower than that expected for quartz. These pixels are found either at the edge of quartz grains (map 0.5 h) or in small isolated grains in the sulfate matrix (anhydrite).

is consistent with the standard Darcy's filtration law. Indeed, neglecting the filter cloth resistance and assuming cake incompressibility, we obtain

$$\frac{t}{V(t)} = \frac{\mu \alpha M}{A^2 \Delta P} V(t), \quad (1)$$

where μ is the viscosity of the fluid phase, M is the mass of solids deposited on the cloth per unit of filtrate volume, A is the filter cloth area, ΔP is the difference of applied pressure, and α is the specific resistance of the cake. For each experiment, M was calculated from the ratio of the mass of solid deposited to the total volume of the filtrate, and the specific resistance of cake was thus calculated from the above equation. Increasing L/C leads to a decrease in the specific resistance, which means that the filterability is improved. We also see for $L/C = 4$ that the time at which filtration is performed can also play a significant role in filterability, which is related to the extent of silica precipitation. There, the longer the time, the

higher the specific resistance and thus the less filterable the slurry. Dilution or reducing contact time to limit precipitation or dissolution could thus be two strategies to overcome the deleterious effect of silica released during the extraction of valuable elements. Both strategies go hand in hand with a low degree of supersaturation and thus limited precipitation. However, none of them are applicable in practice. Indeed, to maximize the extraction of valuable species, the extraction time has to be of at least an hour and the time before filtration cannot be decreased too much. Furthermore, using large values of L/C ratios means a strong increase in acidic effluents, which is detrimental from both environmental and economic standpoints. Overall, the strategy is to work at the highest possible L/C and lowest time to extract sufficient valuable elements but avoid extended silica precipitation. However, this parametric approach is highly sensitive to any composition change in the ore and seems too fragile to design a robust process.

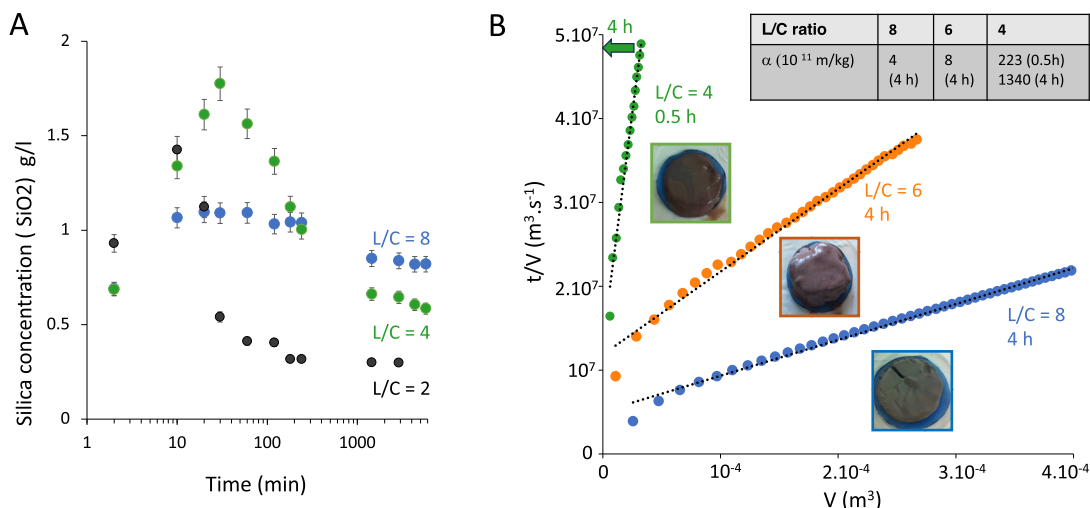


Figure 2. (A) Kinetics of silicon leaching and precipitation for three liquid-to-calcinated ratios L/C . The silica concentration is determined by the molybdenum blue assay in the supernatant of the leached slurry. Initially, silicon is extracted from dissolving mineral phases in solution and eventually precipitates as silica, which explains the non-monotonic variation of the silicon concentration in solution over time. The larger the L/C ratio, the smaller the extent of precipitation. (B) Filtration kinetics for slurries obtained after 0.5 h or 4 h of leaching for three L/C ratios. The linear variation of t/V with V allows us to calculate the specific resistance to filtration, α (kg/m³), according to Equation (1). The higher the resistance, the less filterable the slurry.

2.3. Precipitation of silicate solutions at acidic pH: filterability

Since avoiding silica precipitation is not an acceptable option, we turned to a different strategy consisting of mastering the mesostructure of the silica gel, which determines its filterability [17]. However, investigating silica precipitation in slurries obtained from the leaching of the real ore is challenging as the system displays a complex composition. Yet, it is possible as the first approach to start instead from silicate solutions as the source of Si and study the precipitation under given physicochemical conditions. Experiments were conducted under the same highly acidic pH and temperature conditions as for leaching the ore and filtered with the same protocol. This precipitation protocol is therefore quite different from usual synthesis methods that operate at much lower ionic strength. For instance, colloidal silica is typically prepared at a pH of 10, yielding smooth and dense particles and moderate ionic strength, ensuring colloidal stability through ionic repulsions. Therefore, we expect to obtain quite

different structures at very low pH and high ionic strength, which can be investigated in detail in this simpler model system with small-angle X-ray scattering (SAXS).

2.3.1. Precipitation of silicates at acidic pH: macro- and mesostructures

The SAXS is a powerful technique to probe mesostructures and was deployed on aliquots sampled over time as silica precipitates. After 60 min, we observe the formation of silica nanoparticles with a finite size evidenced at low q values by the Guinier regime of the scattered intensity (grey curve, Figure 3B). However, at high values and thus small distances, we do not observe the Porod law, which states that for well-defined interfaces, the scattered intensity should decrease as q^{-4} as is typically observed for colloidal silica prepared under basic conditions [17]. Instead, the scattered intensity decreases as q^{-2} , which can notably correspond to polymeric (so-called fractal) networks. Therefore, the acidic conditions under which silica precipitates drastically impact its resulting mesostructure.

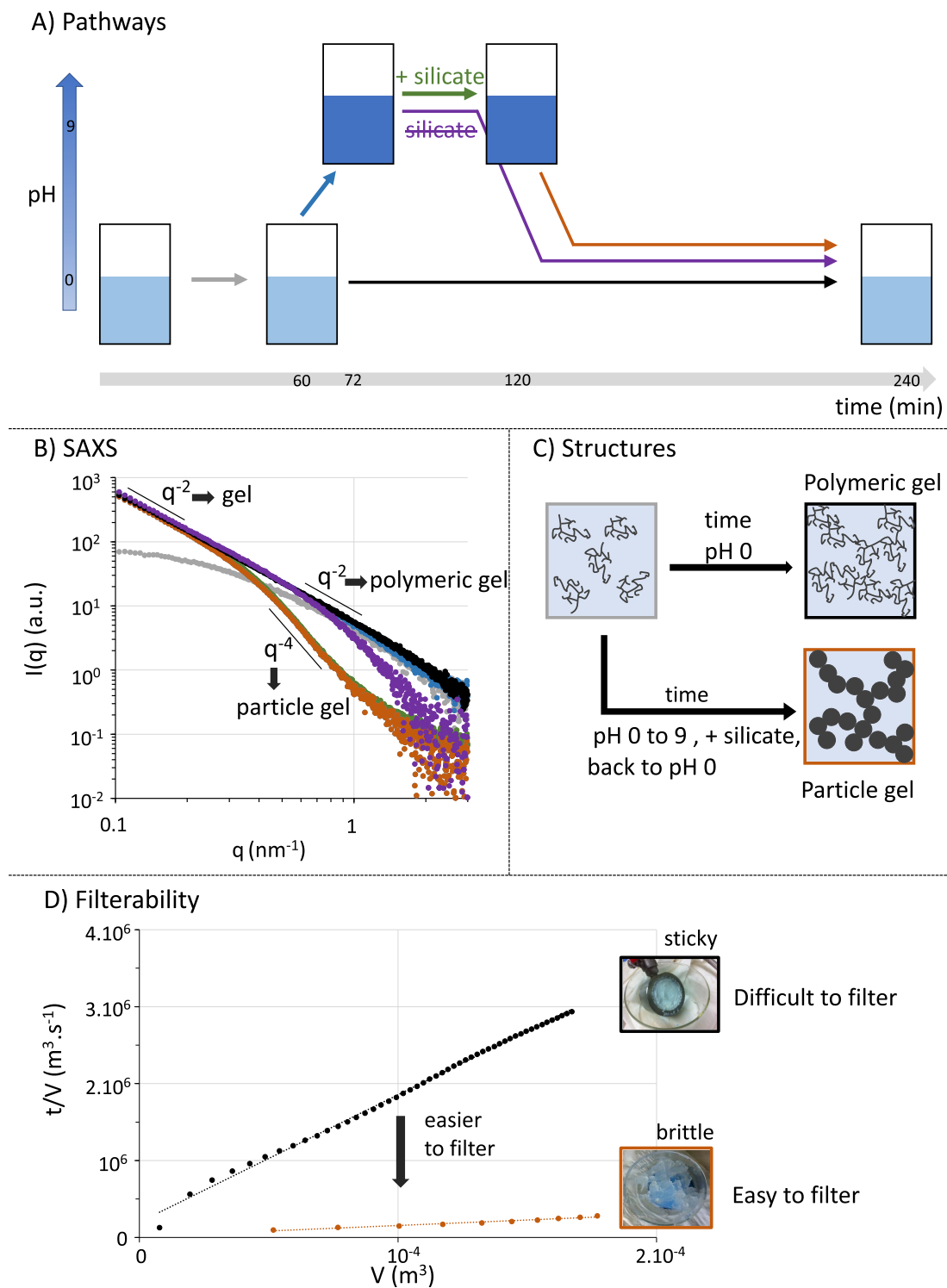


Figure 3. (A) Different silica precipitation paths in a hydrometallurgical process. The conventional method is to remain at pH 0. The alternative methods tested are to increase pH to 9 and then add or not silicates, before switching back to pH 0. Note that each step is associated with a color code throughout the figure.

Figure 3. (cont.) (B) After each step, a SAXS spectrum is acquired. Over time, a network forms in solution as visualized by the increase in small wave vector intensity q , which eventually leads to a structure factor decaying as q^{-2} (grey to black curves). The extension of this slope down to larger wave vectors and thus smaller distances indicates that the whole structure can be seen as a polymeric silica gel. Increasing pH to 9 does not change this structure (blue curve). However, adding silicate leads to the compaction of the mesostructure at small distances, and the Porod law in q^{-4} is recovered (green curve). This structure is maintained when switching back pH to 0 (orange curve). In contrast, when only the pH cycle is performed without adding silicates, the structure changes only to a smaller extent (purple curve). Note that scattering intensities are not on an absolute scale as the sampling is not achievable at a controlled silica concentration. They were thus scaled by arbitrary factors to highlight similarities and differences. (C) Schemes of the mesostructures obtained depending on the pH cycle used. (D) Filterability of the two different gels obtained (pH = 0 or pH cycle and silicate addition). The sticky gel obtained at pH 0 is strongly clogging while the brittle gel obtained through the pH cycle and silicate addition is much easier to filter. Small length scales thus dictate the filterability, and compacting them is a profitable process modification.

At longer times, the q^{-2} power law extends to lower q values, which highlights an increase in particle size and ultimately the formation of a percolated network that leads rheologically to gelation (black curve, Figure 3B). Interestingly, it means that the silica gel obtained here is structurally a multiscale polymeric network (“polymer gel”), rather than a network of dense colloidal particles (“particle gel”).

2.3.2. *Changing the precipitation pathway by adding silicate ions at basic pH*

Following these results, we tried to change the mesostructure by tuning pH during silica precipitation. For this purpose, we increased the pH during precipitation (blue arrow and curve in Figure 3). The resulting SAXS curve at 72 min overlapped with the one obtained after the precipitation of silica under acidic conditions after 240 min, evidencing that the overall mesostructure was not modified but that gelation proceeded faster. The pH was then returned to its original acidic value to dissolve anew the elements of interest (purple arrow and curve in Figure 3). The resulting SAXS data indicates an increase in the exponent of the power law at high q values, which indicates slight densification of the network. To amplify this modification, we devised an alternative pathway in which silicate is deliberately added at basic pH (green arrow) before returning to acidic pH (orange arrow). Strikingly, the two resulting spectra overlap indicating that the mesostructure is then unchanged by the pH variation. Furthermore, the power law then follows the Porod law indicating that silica/water

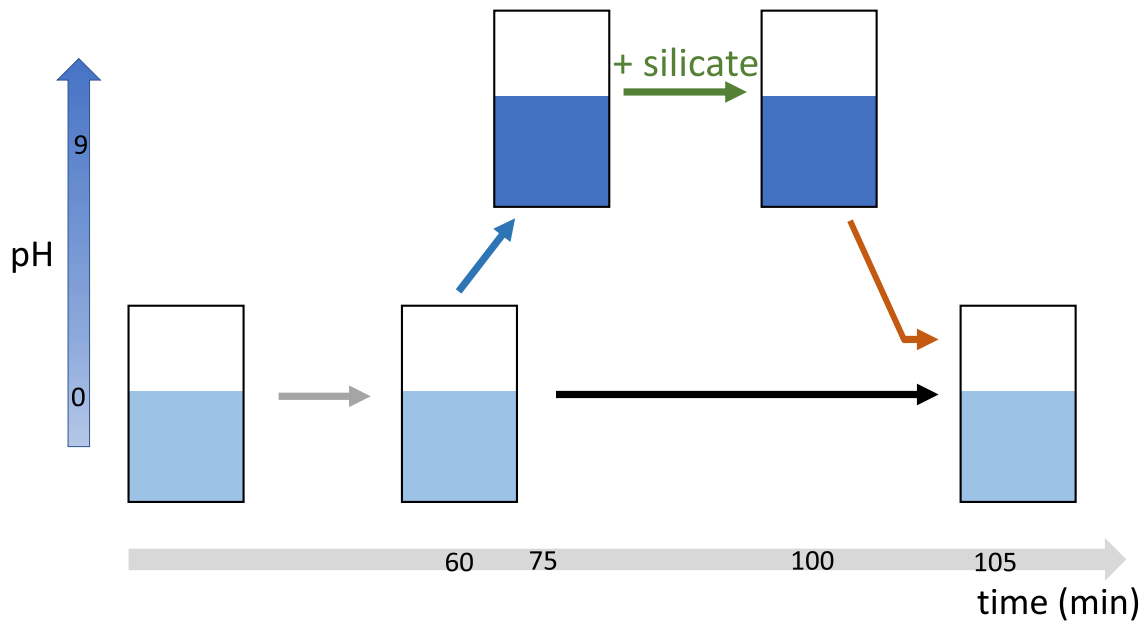
interfaces are now well defined and that the network is denser. Adding silicates at basic pH thus allows for drastically modifying the mesostructure, and can be described as a consolidation of the existing polymeric network, yielding a particle gel. This change in mesostructure cascades to the macroscale, as shown in Figure 3D, which demonstrates that it leads to a drastic improvement in the gel’s filterability. Thus, our counterintuitive strategy, which consists of deliberately adding at the right pH the problematic species in the process, silica, is a powerful means to solve the practical problem of filterability.

2.3.3. *Applying the mesostructure shaping strategy to real ore extraction*

To verify the feasibility of this strategy in the real system, we applied the same procedure to the ore (see Figure 4A). We first checked that the pH cycle did not compromise extraction yields, as the precipitation of some dissolved elements (Nb, REE, etc.) at basic pH was in fact fully reversible when returning to the initial acidic pH. Figure 4B displays a decrease in specific resistance by two orders of magnitude when tuning silica precipitation through this pH cycle with a consolidation step, similarly to the model system previously presented.

In practice, the pulp thus becomes filterable. It is interesting to stress that the overall procedure leads to a final liquid/solid ratio of 4 and thus would indeed correspond to non-filterable conditions (see Figure 2B). We did not optimize this ratio, but it could be further reduced if more concentrated sodium

A) Pathways



B) Filterability

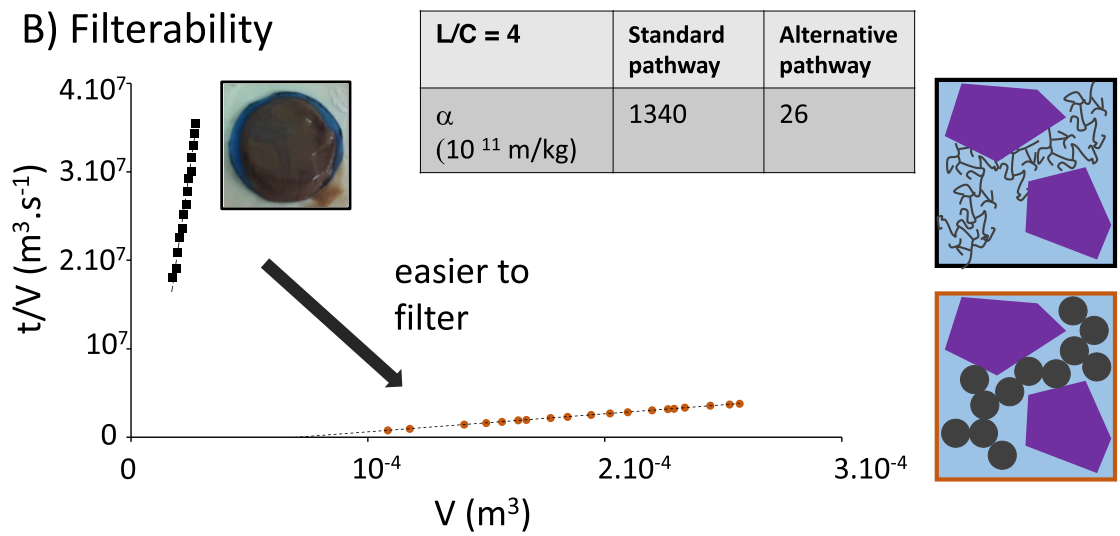


Figure 4. (A) Conventional and alternative precipitation pathways performed on the real ore. In the alternative pathway, silicates are added at basic pH before shifting back the pH to high acidic values. (B) Resulting filterability profiles for both gels were obtained throughout the two pathways. The strong collapse of the specific resistance when performing the silicate addition at the basic pH pathway indicates a tremendous improvement in the filterability. Note that the final liquid/solid ratio is 4. The scheme proposed is the same as in Figure 3 but includes insoluble mineral grains (purple) in addition to the forming silica networks.

hydroxide and silicate solutions are used. Overall, this method is thus more advantageous than the dilution strategy tested and presented in Figure 2B, where a ratio of 8 would lead to comparable results but would require a much larger volume and thus decreased profitability. We are confident that this difference could be further increased through optimization, whereas the dilution pathway is bounded by silicate solubility, an equilibrium parameter.

3. Conclusion

In hydrometallurgy, the occurrence of silica precipitation is as ubiquitous as it is deleterious for the design and operation of leaching and downstream stages of the process. Indeed, the resulting gel formation drastically hinders filterability. Although some pretreatment steps have been proposed to restrain silica precipitation through converting silica-bearing mineral phases into an insoluble form, the so-called digestion steps, they are not universal and typically do not apply to the pyrochlore ores we use in this study. Another simpler way is to increase the liquid/solid ratio during extraction by leaching, a dilution step, which eventually leads to operating under conditions where silicates remain solubilized. However, they may eventually precipitate later, which then hugely impacts the overall profitability.

Overall, it is challenging to fight thermodynamics when designing an efficient process. In this work, we shifted our stance to accepting silica precipitation into a gel but rather proposed that by carefully tuning the structure of the gel in the 1–100 nm range, it could be made filterable. Inspired by syntheses of filterable silica performed at basic pH, our idea was to deliberately add the problematic species rather than to remove it by using a pH shift. This may seem counterintuitive, but this addition, when performed at basic pH, leads to a compaction at the smallest length scales of the gel. Indeed, we then transition from a multiscale polymeric network (“polymer gel”) to a network of dense colloidal particles (“particle gel”). This mesostructure change is readily observed in SAXS as a change from a q^{-2} to a q^{-4} power law, which is typically observed for smooth objects such as silica at basic pH [17].

We have demonstrated that this strategy, devised on a model system, can be successfully implemented

in the extraction of real ores. It is worth stressing that this strategy is generic and not very sensitive to the exact ore used as silica precipitation is mostly controlled by the pH value. Overall, rather than avoiding silica precipitation, we have controlled it at the relevant length scale for filterability, which paves the way for disruptive process modifications in hydrometallurgical processes involving silica precipitation and filtration steps.

4. Materials and methods

4.1. Leaching of calcinated powder

Calcinated powder was provided by ERAMET. It originates from the Mabounié upstream hydrometallurgical process that combines consecutive sulfation and roasting of pristine ore, mostly aimed at converting the pyrochlore mineralogical phase containing the value elements into metallic sulfates to facilitate their leaching. The conditions used to obtain the calcinated powder are described by Beltrami and co-workers in several publications [5,8,9]. The mass composition in terms of the main chemical elements in calcinated powder is given in Table 1.

Leaching of the calcinated powder was performed in an insulated glass reactor equipped with a three-blade impeller, a pH electrode, and a thermometer equipped with a Pt100 probe. Deionized water was used throughout all the experiments. First, the reactor was filled with 500 ml of deionized water. Then a given mass of calcinated solid particles was introduced. This given mass defines the liquid-to-solid ratio: a liquid-to-solid ratio equal to 1 was obtained by mixing 500 g of calcine powder with 500 ml of water. Right after the calcinated powder addition, the mixture was continuously agitated at 400 rpm. The leaching experiments were conducted at a temperature of 90 °C and for contact times between 30 and 1500 min, starting from the time of powder addition. To ensure the solubilization of valuable elements such as niobium and tantalum from metallic sulfates, leaching has to be performed below pH 2. This condition is easily met without any acid addition thanks to the initial acidity of the calcinated powder. For liquid-to-solid ratios (L/C) ranging from 1 to 4, the solution acidity is equivalent to 1 mol/l H^+ in the leaching solution just after the addition of calcinated powder.

Table 1. Mass composition of the different main elements in the calcinated powder

Element	Al	Ca	Ce	Fe	Nb	P	S	Si	Ti
Mass percentage	4	1.5	0.4	10.8	1.1	2.3	17.3	4.4	1.3

In the first series of experiments, the chemical compositions of both solid and liquid phases were monitored over time from 0.5 h to 24 h. First, slurries were collected from the reactor at the end of the experiment and diluted by a factor 2 with deionized water before its centrifugation at 3000 g for 15 min. The yielded sediment was washed twice with 5 mL of deionized water per gram of solid and subsequently dried at 80 °C for 48 h. The resulting powder was analyzed by both X-ray diffraction and scanning electron microscopy (QEMSCAN). Diffraction patterns were obtained using a PANalytical X'Pert Pro diffractometer (Cu K radiation, 1.5406 Å) and identified with the HighScore Software. SEM-QEMSCAN analyses were carried out using an FER Quanta 650 F SEM platform. Separately, the liquid phase obtained after centrifugation was analyzed by inductively coupled plasma atomic emission spectrometry for the compounds with low atomic weight (Al, Ca, Fe, P, S, Si, Ti) and by inductively coupled plasma atomic mass spectrometry for the compounds with high atomic weight (Ce, Nb, Ta, Th, U).

In the second series of experiments, we focused on the kinetics of silica dissolution/precipitation for liquid-to-solid (L/C) ratios of 2, 4, and 8. The same leaching protocol as described above was carried out, but this time, aliquots of slurries were sampled from the reactor at different contact times from a few minutes to several hours. The collected aliquots were diluted by a factor 2 by adding deionized water and then filtered (0.45 µm cutoff) to remove undissolved particles. The filtrates were analyzed by adapting a silicomolybdic acid spectrophotometric method, which is predominantly used for environmental or industrial waters, in order to measure the concentration of silica precursors in the liquid phase at different contact times [18–21].

4.2. Filtration of slurries

Filtration experiments were conducted with a laboratory filtration cell (Choquet, France) and filter cloths from Sefar Fyltis (France). The volume of the

cell was 102 cm³ and the filtration area was 38.5 cm². The hydraulic resistance of filter cloths was a hundred times less than the hydraulic resistance of the cakes formed during the filtration experiments, so the resistance of the medium was neglected. The cell was fed with the slurry collected from the leaching reactor and circulating from a guard reservoir maintained at a constant pressure by a regulated air supply. Filtration tests were undertaken just after the slurry reached room temperature and operated at a constant operating fluid pressure of 700 kPa and a temperature of 25 °C. During the filtration, solid particles present in the slurry accumulate on the filter to form a cake. The experiment was terminated when the cake filled the entire space of the cell or when fluid permeation out of the cell was no longer observed. After the filtration, the wet cake was recovered and the mass of solids in the cake was measured by thermogravimetric analysis (Mettler Toledo, Viroflay, France). This mass included the contribution of both solid particles and salts formed during leaching. The mass of salts was determined by measuring the conductivity of a dry pellet redispersed in Milli-Q water. The mass of solid particles in the cake was therefore estimated from the difference between the mass of solids and salt mass. Because we were interested in the permeability of the filtration cakes, we gravimetrically determined the flow rate by recording the mass of fluid permeating out of the cell on an electronic balance at regular time intervals. The cake-specific resistances were directly determined from the variation of the permeating volume V with filtration time t . Filtration experiments were repeated three times to check the reproducibility of the filtration data.

4.3. Precipitation of silicate solutions

Precipitation experiments were carried at $T = 90$ °C by quickly injecting 100 mL of a sodium silicate solution ($\text{pH} = 11$, $[\text{SiO}_2] = 130$ g/L, density 1.39 g/mL) in a reactor filled with 900 mL of an acidic solution (sulfuric acid medium at $[\text{H}^+] = 1$ mol/L).

The initial silicate concentration is thus of 13 g/L. During precipitation, samples are collected and “quenched” at pH 2 with a soda solution at 1 mol/L to stop the reaction as described in the literature by Iler and Alexander. The arrested samples are analyzed by SAXS on the Xeuss 2.0 platform available in-house.

The alternative pathway consists of increasing pH after 1 h, from pH 0 to 9 by adding 250 mL of a 8 mol/L sodium hydroxide solution at 20.8 mL/min. A consolidation step is then performed by slowly injecting 166 mL of a sodium silicate solution (70 g/L), at 4 mL/min, while maintaining pH at a set value of 9 by adding 40 mL of a sulfuric solution (1 mol/L). After this consolidation step, the pH was decreased back to 0 by adding 100 mL of a sulfuric acid solution at 8 mol/L.

4.4. Monosilicic acid concentration in solution using molybdenum blue methods and ultraviolet–visible light spectroscopy

To titrate the amount of monosilicic acid in the solution, we used a spectroscopic method proposed by Nagul *et al.* that uses the molybdenum blue reaction [20]. While ICP measures the whole silicon content in solution, this method is more specific to monomeric silica. This method was calibrated using a standardized silica stock solution (99.9% Si(OH)₄ monomer, VWR). The monitoring was performed at 800 nm, which corresponds to the absorption by the blue silicomolybdate complex.

4.5. Small-angle X-ray scattering

SAXS experiments were performed on a Xeuss 2.0 laboratory instrument from Xenocs. Samples were injected in disposable quartz capillaries (1.5 mm inner diameter). Azimuthal averaging was performed after mask subtraction, yielding one-dimensional spectra after normalization by transmissions. Since the sampling is heterogeneous, we did not display intensities on absolute scales but rather scaled them by arbitrary factors to highlight scaling laws over the q range.

Declaration of interests

The authors do not work for, advise, own shares in, or receive funds from any organization that could

benefit from this article, and have declared no affiliations other than their research organizations.

Acknowledgments

ERAMET Research is thanked for its financial support of the PhD grant to CM. Simon Blancher and Céline Rodriguez are acknowledged for performing the mineral characterization. Dominique Mannoni and Amandine Chabaneix are acknowledged for performing the ICP characterization. Bruno Courtaud, Philippe Ribagnac, and Denis Beltrami are acknowledged for stimulating discussions on this topic. The research federation FERMAT (Université de Toulouse, France) is acknowledged for providing access to the Xeuss 2.0 SAXS instrument (Xenocs) through the CPER IMATECBIO grant with support from Pierre Roblin.

References

- [1] E. Alonso, A. M. Sherman, T. J. Wallington, M. P. Everson, F. R. Field, R. Roth, R. E. Kirchain, *Environ. Sci. Technol.*, 2012, **46**, 3406–3414.
- [2] P. Davris, S. Stopic, E. Balomenos, D. Panias, I. Paspaliaris, B. Friedrich, *Miner. Eng.*, 2017, **108**, 115–122.
- [3] K. Binnemans, P. T. Jones, B. Blanpain, T. Van Gerven, Y. Yang, A. Walton, M. Buchert, *J. Cleaner Product.*, 2013, **51**, 1–22.
- [4] Q. Tan, J. Li, X. Zeng, *Crit. Rev. Environ. Sci. Technol.*, 2015, **45**, 749–776.
- [5] P. Ribagnac, G. Deblonde, S. Blancher *et al.*, *Separation and Purification Technology*, 2017, **189**, 1–10.
- [6] S. Belair, V. Weigel, *COM 2014—Conference of Metallurgists Proceedings*, Canadian Institute of Mining, Metallurgy and Petroleum, Wesmont, 2014, 978–1 pages.
- [7] V. W. Donati, B. Courtaud, *Proceedings of the 7th International Symposium on Hydrometallurgy 2014 (Hydro 2014)*, June 22–25, 2014, Victoria, British Columbia, Canada, vol. 2, 2014, 763–764 pages.
- [8] D. Beltrami, G. J.-P. Deblonde, S. Bélair, V. Weigel, *Hydrometallurgy*, 2015, **157**, 356–362.
- [9] G. J.-P. Deblonde, V. Weigel, Q. Bellier, R. Houdard, F. Delval-lée, S. Bélair, D. Beltrami, *Separat. Purif. Technol.*, 2016, **162**, 180–187.
- [10] R. M. Rivera, B. Ulenaers, G. Ounoughene, K. Binnemans, T. Van Gerven, *Miner. Eng.*, 2018, **119**, 82–92.
- [11] D. Voßenkaul, A. Birich, N. Müller, N. Stoltz, B. Friedrich, *J. Sustain. Metal.*, 2017, **3**, 79–89.
- [12] A. Balinski, O. Wiche, N. Kelly, M. A. Reuter, C. Scharf, *Hydrometallurgy*, 2020, **194**, article no. 105345.
- [13] C. R. Borra, J. Mermans, B. Blanpain, Y. Pontikes, K. Binnemans, T. Van Gerven, *Miner. Eng.*, 2016, **92**, 151–159.
- [14] G. M. Tsaousi, A. Toli, A. Bempelou, D. Kotsanis, M. Vafeias, E. Balomenos, D. Panias, *Sustainability*, 2023, **15**, 15462–15475.

- [15] G. B. Alexander, *J. Am. Chem. Soc.*, 1954, **76**, 2094-2096.
- [16] R. Iler, *The Chemistry of Silica: Solubility, Polymerization, Colloid and Surface Properties, and Biochemistry*, Wiley Interscience, New York, 1979.
- [17] D. M. Ragueh, M. Meireles, B. Cabane, J. Gummel, *Separat. Purif. Technol.*, 2015, **156**, 2-11.
- [18] G. B. Alexander, *J. Am. Chem. Soc.*, 1953, **75**, 5655-5657.
- [19] T. Coradin, D. Eglin, J. Livage, *Spectroscopy*, 2004, **18**, article no. 356207.
- [20] E. A. Nagul, I. D. McKelvie, P. Worsfold, S. D. Kolev, *Anal. Chim. Acta*, 2015, **890**, 60-82.
- [21] V. W. Truesdale, C. J. Smith, *Analyst*, 1976, **101**, 19-31.

Research article

GDR Prométhée – French Research Network on *Hydrometallurgical Processes for Primary and Secondary Resources*

A sustainable solvothermal process extracting critical elements from Li-ion batteries

Virginie Nachbaur^{*,a}, Firas Ayadi^a, Béatrice Foulon^a, Malick Jean^a, Valérie Pralong^{*,b} and Samuel Jouen^{*,a}^a GPM, Normandie Univ, UNIROUEN, INSA Rouen, CNRS, 76000 Rouen, France^b CRISMAT, Univ. Caen, ENSICAEN, CNRS, 14050 Caen, FranceE-mails: virginie.nachbaur@univ-rouen.fr (V. Nachbaur),
samuel.jouen@univ-rouen.fr (S. Jouen)

Abstract. A solvothermal process was developed for extracting cobalt, nickel, lithium and manganese from LiCoO_2 (LCO) or $\text{Ni}_{(1-x-y)}\text{Mn}_x\text{Co}_y\text{O}_2$ (NMC) cathode active materials, without using any acid or base, neither high temperature. The solvent used, ethylene glycol, is a mild reducing agent and does not pose any unacceptable environmental risk. Structural characterization of the recovered products showed that cobalt and nickel are together in a metallic state (Co or Ni-Co alloy), lithium and manganese are in the form of carbonates easily separable due to their different solubilities in water. Magnetic separation was used to isolate Ni-Co alloy from MnCO_3 . The purities of the recovered products depend on the quantities of LCO powder processed and fall within the range of 90.5–97% for lithium carbonate and 96.7–99.9% for cobalt. In the case of NMC, the purities of Li_2CO_3 , MnCO_3 and $\text{Ni}_x\text{Co}_{(1-x)}$ are respectively 94.4%, 95.2% and 91%. The process demonstrated its effectiveness when treating NMC-type black mass extracted from a mobile phone battery.

Keywords. Li-ion batteries, Solvothermal, Polyol, Critical elements, Recycling.**Funding.** ESP (Energy and Propulsion Systems) Carnot Institute, European Union and the Normandy region (FEDER/FSE 2014-2020) and CNRS (French National Center for Scientific Research).

Manuscript received 30 September 2023, revised 7 February 2024, accepted 14 March 2024.

1. Introduction

Mineral resources play an essential role in the technologies associated with energy transition. These resources contain elements designated as critical by many countries. In particular, the growing deployment of electric vehicles requires considering the use of certain elements as a geopolitical issue. This is particularly the case for elements present in lithium-ion batteries (LiB) such as cobalt, lithium,

nickel, manganese, or graphite, whose increasing demand has revealed interdependencies and vulnerabilities [1]. In response to the urgency of the situation, the European Union is seeking to reduce its dependence while initiating a more environmentally friendly cycle by proposing a revision of the old Battery Directive [2]. The newly proposed directive [3] sets very ambitious recycling rate targets which must increase, between 2027 and 2031, from 90 to 95% for Co and Ni, and from 50 to 80% for Li, but also establishes, for the first time, requirements for recycled content in new batteries. These recycled contents

*Corresponding authors

must reach, by 2036, 26% for Co, 15% for Ni and 12% for Li. Recycling is, therefore, a strategic aspect since, by 2027, it is estimated that around 50,000 tons of used batteries will need to be processed in Europe, allowing for the recovery of 25,000 to 30,000 tons of metals of interest. Currently, recycling rates struggle to increase (less than 1% of Li is actually recycled globally), as recycling faces many barriers that hinder its development. Among these, the consumption of energy and chemicals is a significant factor in the cost of operations. This is particularly the case for pyrometallurgical and hydrometallurgical methods which are used at the industrial level to recycle elements such as cobalt, lithium, nickel, copper or manganese [4–6]. Pyrometallurgy, although it remains a frequently used process for the extraction of high-value metals such as cobalt and nickel, suffers from several drawbacks such as high operating temperature, production of toxic gases, high energy costs and the limited number of materials recovered (Li and Al are lost in the slag). Although hydrometallurgy (dissolution in acidic media in the presence of a reducing agent) is the preferred process for LiB recycling [7,8] due to high purity and recovery rate of metals, this process suffers from high consumption of quite aggressive media, unavoidably leading to the production of acidic effluents, and from the use of expensive extractants [9]. In order not to add acid, interesting studies have been carried out using subcritical water and an addition of chlorinated polyvinyl chloride (CPVC) or polyvinylidene fluoride (PVDF) [10,11]. The acid formed during the degradation of CPVC at 290 °C or PVDF at 350 °C (HCl or HF) induces the leaching of the valuable metals. Furthermore, several researches have been conducted using organic acids, ionic liquids (ILs) and deep eutectic-solvents (DESs), with the promise of a green approach [11–14]. However, despite a great deal of research in these areas, it has proved impossible to transpose the studies carried out on a laboratory scale to an industrial scale. Among the probable causes of this failure, the excessive viscosity of these solvents, their difficulty in being recycled, their limited chemical stability and their prohibitive prices are frequently mentioned [15].

The so-called polyol process has been used for the synthesis of finely divided metal particles from their oxides, hydroxides, or salts in polyalcohols [16–18]. The polyol (e.g., ethylene glycol, diethylene glycol) acts as both solvent and reducing agent. This method

can also be performed in a solvothermal way, which is a treatment performed in a closed reactor, above the boiling temperature of the solvent. In this case, a reduction of metal oxides is also observed, leading to the obtaining of several morphologies of the nanoparticles related to the concentration of the precursor [19]. Although ethylene glycol is often used as a component in mixtures (associated to a hydrogen bond acceptor) in DESs [20] or to a mild organic acid in an eco-friendly leaching system [21,22], it has never been used alone to extract metals for recycling purposes.

Ethylene glycol (EG) is a major industrial organic compound used in the production of polyester fibers and films, antifreeze, coolant, and numerous other applications. This solvent presents favorable features like low toxicity and noncorrosiveness, and it is environmentally benign and readily biodegradable [23].

In this study, a new original approach with a low environmental footprint was developed to recycle lithium-ion batteries cathodes [24]. This process is based on a solvothermal treatment of the cathode material in the presence of EG and carbonate ions and without any acid. Performed at low temperature (225 °C), the process converts the phase present in the cathode compound into several products easily separable. Ni and Co ions are reduced to the zero valent state, together in an alloy. Manganese cations and lithium cations combine with carbonate ions to form manganese carbonate and lithium carbonate. The resulting powder (which is a mixture of Ni–Co alloy, lithium carbonate and manganese carbonate) may be separated from the solvent by centrifugation, and the several solid compounds isolated, thanks to their solubilities, by a succession of washings and magnetic separation. In this work, the characterization of the recovered compounds was performed, their purities were determined, and the recovery rates by elements were calculated. As some of the Li^+ cations remain in EG after treatment, our research aims at showing that this solvent can be reused several times with the same efficiency, and that this reuse allows to recover all Li^+ cations coming from the previous steps. The combination of solvent and source of carbonate ions was first ascertained in the case of LCO in terms of recovery rate and purity of the recovered powders. The possibility of reusing the solvent in order to reduce the environmental impact of the process was then assessed.

Subsequently, the process was investigated both on NMC 111 cathode powder and on a black mass (BM) containing NMC cathode active material.

2. Materials and methods

2.1. Materials

The cathode powders (LiCoO_2 : LCO or $\text{LiCo}_{0.33}\text{Ni}_{0.33}\text{Mn}_{0.33}\text{O}_2$: NMC 111) were either obtained from MSE Supplies or synthesized through the ceramic route. X-ray diffraction (XRD) characterizations and chemical analyses of these powders are presented in Supporting Information Figures S1 and S2. The black mass (BM) was obtained from mobile phone batteries (Xiaomi model BN44), by discharging, opening in a glovebox, shredding in a cutting mill (Retsch SM 300), and sieving in a vibratory sieve shaker (Fritsch Analysette 3 Spartan) using a 100 μm grid size. XRD characterization of the sieved BM and inductively coupled plasma (ICP) analysis are shown in Supporting Information Figure S3. As graphite peaks are observed (ICDD file No. 65-6212), one can conclude that sieving was not efficient to remove graphite present in the BM. In fact, other separation techniques exist or are currently being developed to extract graphite from black mass before any processing, such as froth flotation [25,26]. Furthermore, ICP and Energy-dispersive X-ray spectroscopy (EDX) analysis (Supporting Information Figure S4) indicate that the cathode active material is a NMC-type.

The process is performed in a Teflon-lined bomb provided by Parr Instruments (4744 model, 45 mL) or by Top Industrie (2148 5000, 500 mL or 2148 4000, 1 L), depending on the amount of solvent used. The solvent used is ethylene glycol (Merck 99%) in the presence of carbonate ions (e.g. potassium carbonate Alfa Aesar 99.0% min), with an amount corresponding to $1.2\times$ the stoichiometric amount of carbonate ions necessary to form Li_2CO_3 from Li^+ cations contained in the cathode powder. A pressure calculation based on the saturation vapor pressure of ethylene glycol and the air pressure at 225 °C, indicates that in the 45 mL reactor using 30 mL of ethylene glycol, the pressure is expected to be 3.9 bars (i.e. an overpressure of 2.9 bars). Table 1 summarises the operating conditions for the treatments performed in this study.

Table 1. Conditions applied for the treatments of LCO and NMC cathode powders and for BM

Sample name	Mass of powder treated (g)	EG volume (mL)
LCO1	1.5	v-EG 30
LCO2	15	v-EG 300
LCO3	30	v-EG 600
LCO4	15	r-EG 300
NMC	1.5	v-EG 30
BM Xiaomi	2	v-EG 30

v-EG: virgin ethylene glycol; r-EG: reused ethylene glycol.

2.2. Experimental procedure

After introducing the cathode powder or the black mass, the reactor was filled with ethylene glycol in which potassium carbonate was previously dissolved. The reactor was then closed and heated to 225 °C for 10 h in an oven. This choice of experimental conditions comes from the conditions usually applied during polyol reduction treatments of metal oxides under solvothermal conditions (temperature higher than the boiling point of the solvent). After cooling, the reaction mixture comprises of both powder and liquid, and several steps of centrifugation, rinsing and magnetic separation (if needed) were carried out. These steps are illustrated in Figures 1a and b for the LCO and NMC cathode powder treatments, respectively. For LCO (Figure 1a), the solvent was first separated from the powder by centrifugation and stored for possible reuse. Then, the extracted powder was rinsed with distilled cold water while undergoing ultrasound dispersion, and separated again from water by a second step of centrifugation (P2). The rinse water was evaporated in an oven to recover a white powder (P1).

For NMC (Figure 1b), a subsequent step was added, in which the rinsed black powder was magnetically separated to isolate magnetic and non-magnetic fractions, each of which was dried. Magnetic separation was performed by mixing, under ultrasonic dispersion, the powder to be separated with water or ethanol in a beaker, and by approaching a $\text{Nd}_2\text{Fe}_{14}\text{B}$ magnet close to the side of the beaker, which attracts magnetic part of the powder (this op-

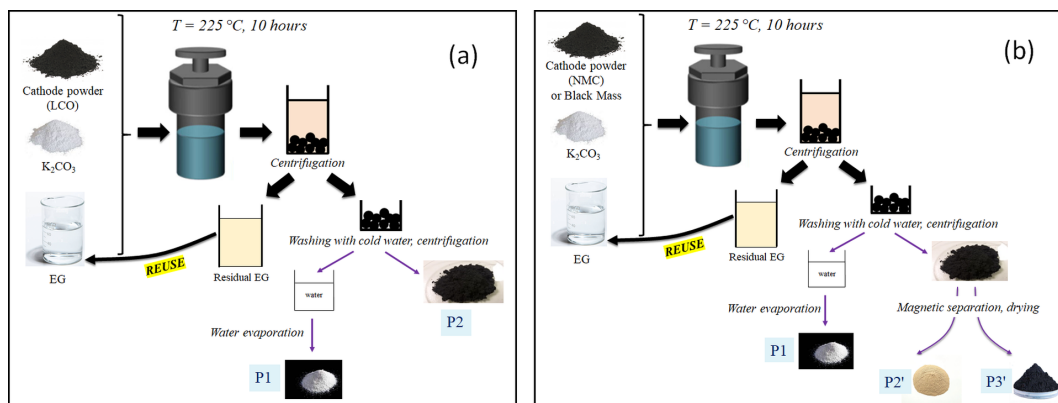


Figure 1. Summary diagram of the different stages of the solvothermal process for LCO cathode powder (a) and for NMC cathode powder and Black Mass (b).

eration was repeated twice). The fraction that was not attracted to the magnet was a beige powder (P2'), while the fraction that was attracted to the magnet was a black powder (P3').

2.3. Characterization methods

The crystallinity and purity of the obtained materials were characterized using an Empyrean diffractometer (PANalytical) or a D8 diffractometer (Bruker AXS), using Co $K\alpha$ radiations. The intensity was measured with a 2θ step of 0.01° . Phase identification was done using DIFFRAC.EVA (Bruker AXS). Powders were observed by Scanning Electron Microscopy (SEM) equipped with an Energy-dispersive X-ray spectroscopy (EDX) detector (Zeiss 1530). Infrared spectroscopy analyses were performed with a Shimadzu IR affinity-1 spectrometer. ATR spectra of liquid samples were obtained using a Glad-iATR instrument equipped with a monolithic diamond by accumulating 32 scans in the spectral range from $[4000-400] \text{ cm}^{-1}$ with a resolution of 4 cm^{-1} . Elemental quantification was performed by Crealins (Lyon, France) using inductively coupled plasma-atomic emission spectrometry (ICP-AES) iCAP 6500 Duo (Thermo Scientific) after acidic dissolution of the samples in the presence of sulfuric acid/nitric acid mixtures in an open environment at $220-240^\circ C$. The relative error on the mass % of the elements is 5%.

3. Results and discussion

3.1. Application of the process to LCO material

3.1.1. Use of virgin ethylene glycol

For this first experiment (LCO1), XRD analysis and Scanning Electron Microscopy results of P1 and P2 are presented in Figure 2. P1 powder (Figure 2a) consists of grains of few tens of micrometers and contains only one phase of lithium carbonate (monoclinic, ICDD file No. 22-1141). P2 powder (Figure 2b) contains particles of a few hundreds of nanometers which are formed through the aggregation of smaller particles. Phase analysis shows that two phases are present: a face-centered cubic (fcc) phase and a hexagonal close-packed (hcp) corresponding to metallic cobalt (ICDD files No. 15-0806 and 89-4308 respectively). This morphology and the coexistence of both phases is classically observed in the case of synthesis of cobalt nanoparticles by polyol way from cobalt salts [17,27].

Chemical analysis of the residual EG, after separation from the solid by centrifugation, shows that it contains dissolved lithium, with an amount corresponding to approximately 30 wt% of the initial lithium present in the LCO compound.

At this stage, the mechanism involved in the process can be explained as follows: $LiCoO_2$ phase is destroyed by the joint action of EG which reduces Co^{2+} cations to Co^0 , and carbonate ions which extract lithium cations to form lithium carbonate, according to (1)

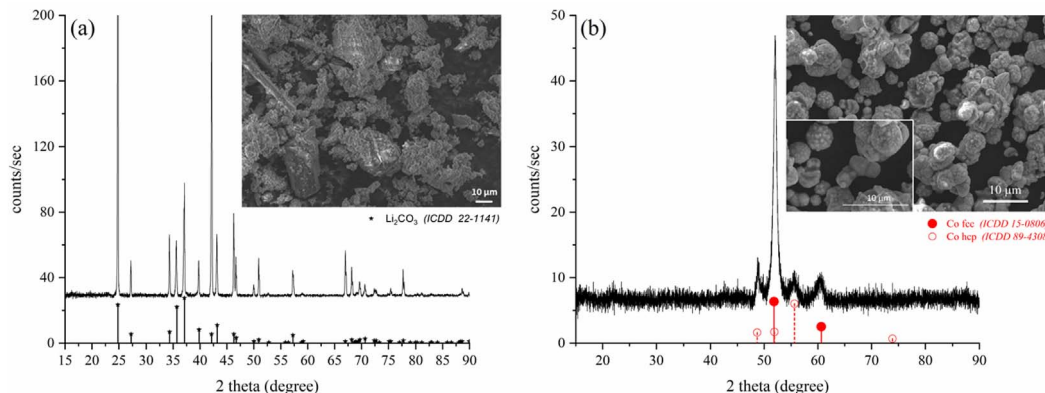
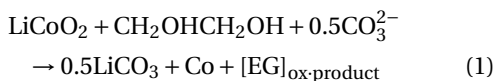


Figure 2. XRD patterns and SEM micrographs of P1 (a) and P2 (b) obtained after treating LCO compound.



where $[\text{EG}]_{\text{ox-product}}$ represents the possible oxidation products of EG as it will be discussed in Section 3.1.2.

The reduction is performed without any dissolution of cobalt cations, as cobalt was not detected in the residual EG. Lithium carbonate is partially soluble in EG, its solubility has been evaluated, under our solvothermal experimental conditions, to be approximately 3 g/L. After separation of the residual EG by centrifugation, the solid contains $\text{Co}_{(s)}$ and $\text{Li}_2\text{CO}_{3(s)}$. Li_2CO_3 is soluble in water, especially cold water (13.1 g/L at 20 °C and 15.2 g/L at 0 °C [24]), so it dissolves in water during the rinsing, while Co remains as a powder (P2). Lithium carbonate can be recovered by evaporating water, this is P1.

Recovery rates for lithium and cobalt are calculated according to Equations (2) and (3) where $m_{\text{LCO treated}}$ is the mass of LCO treated (1.5, 15 or 30 g), m_{P1} and m_{P2} are the recovered mass of P1 and P2 powders, %mass(Li) is the Li content in P1 and %mass(Co) is the Co content in P2, these two values being determined by ICP analysis. The values 7.4% and 62.1% are the content of respectively Li and Co in the initial cathode powder obtained by ICP analysis (Supporting Information Figure S1).

$$\text{Li recovery rate} = \frac{\% \text{mass (Li)} \times m_{\text{P1}}}{7.4\% \times m_{\text{LCO treated}}} \times 100 \quad (2)$$

$$\text{Co recovery rate} = \frac{\% \text{mass (Co)} \times m_{\text{P2}}}{62.1\% \times m_{\text{LCO treated}}} \times 100 \quad (3)$$

Recovery rates of Co and Li (respectively 84.1% and 40%), and purities of Co and Li_2CO_3 (respectively

96.7% and 90.5%) are indicated in Table 2 for this first experiment. Concerning the recovery rate of lithium in the form of carbonate powder, it should be remembered that part of this carbonate is dissolved in EG (around 30%). This part will be recovered during subsequent solvent reuse (see Section 3.1.2). These values, especially for the recovery rate of lithium, are quite low, if one examines the new directive concerning battery recycling [3]. This value of around 70% is below the threshold to be reached for lithium (80%).

As this first experiment was performed on a small amount of powder (1.5 g), unavoidable materials losses during the several steps (centrifugation, drying) have a strong influence on the recovery rates. The impact of these losses on the recovery rate is minimized by increasing the quantity of powder treated. The recycling process was performed on higher amounts of powder (15 g and 30 g, samples LCO2 and LCO3), with the same steps as described previously. As for the first experiment, a powder of Co was isolated, and a powder of Li_2CO_3 was recovered after evaporating the rinsing water. As it can be seen in Table 2, values of recovery rates and purity are greatly improved. The recovery rate of lithium in Li_2CO_3 form is between 55.9 and 69.7% with a purity between 95.2 and 97.1%. The recovery rate of cobalt is between 98.1 and 99.1%, i.e. identical for LCO2 and LCO3 taking into account measurement uncertainties, and with a purity of 99.9%.

3.1.2. Ethylene glycol reuse

In order to save EG and to recover more lithium, the solvent was reused (up to 4 times, but the result of only 1 time is shown here, sample LCO4). The

Table 2. Recovery rates of Li, Co, Ni and Mn and purity of P1, P2, P2' and P3' powders, calculated from ICP-AES analyses of the different powders extracted

Sample	LCO cathode			
	Recovery rate (%)		Purity (%)	
	Li ^a	Co	Li ₂ CO ₃	Co metal
LCO1	40.0	84.1	90.5	96.7
LCO2	69.7	99.1	95.2	99.9
LCO3	55.9	98.1	97.1	99.9
LCO4	101.3 ^b	99.3	95.4	99.9

Sample	NMC 111 cathode			
	Recovery rate (%)			
	Li ^a	Co	Ni	Mn
NMC	24	79	80.5	72

				Purity (%)		
				Li ₂ CO ₃	Ni _x Co _{1-x} alloy	MnCO ₃
				94.4	91	95.2

^aConsidering only P1 powder, without lithium dissolved in EG, ^bup to 100% due to the presence of Li ions in EG coming from the previous treatment.

phases obtained are the same that in Section 3.1.1, and the values of recovery rates and purities are indicated in Table 2. In this case, the recovery rate of lithium (calculated by comparing with the lithium amount present in 15 g of LCO treated) is higher than 100% because Li⁺ cations present in the solvent (and coming from a previous treatment of LCO) have precipitated as carbonate during the second treatment as saturation was reached more easily for this salt. This experiment also shows that EG is not degraded during the process, and that it remains efficient as a reducer for possible reuse.

In order to confirm the integrity of the ethylene glycol, infrared spectrometry was carried out on the solvent after extraction of the solid phase by centrifugation. Figure 3 shows the infrared spectra of virgin ethylene glycol, of the solvent after extraction of samples LCO1 and LCO4, and of a solvent after three successive reuses. The spectrum of the ethylene glycol presents absorption bands which correspond perfectly to what is expected [28]. After treatment, the solvent spectra still show all the absorption bands characteristic of ethylene glycol. Additional absorption bands appear at 1595, 1355 and 1125 cm⁻¹, whose intensities increase with the number of times the solvent is reused. The two bands located at 1595, 1355 cm⁻¹ could be attributed to asymmetric and symmetric elongation vibrations of the COO⁻ group in a glycolate (CH₂OHCOO⁻), or glyoxylate (CHOCO⁻), both of which are oxidation

products of ethylene glycol [29–31]. Doubt remains as to the attribution of the weak absorption band at 1125 cm⁻¹, whose wavenumber is slightly higher than already observed for these two compounds [29]. These results confirm that the reduction of Co(III) to cobalt metal during treatment does indeed involve a redox mechanism with ethylene glycol. The exact nature of the ethylene glycol oxidation product(s) remains to be confirmed. In addition, the solvent being in very large excess compared with the cathode compound (EG/LCO molar ratio = 36/1 in the case of LCO1, LCO2 and LCO3), it can be reused several times before being significantly oxidized.

3.2. Application of the process to NMC material

The process applied to NMC 111 powder, and following the scheme of Figure 1b, leads to the obtaining of 3 fractions of powder named P1, P2' and P3'. XRD analysis and Scanning Electron Microscopy results of these 3 powders are presented in Figure 4. As in the treatment of LCO, P1 (Figure 4a) only contains Li₂CO₃, with the same morphology that was previously observed (grains of few tens of micrometers). P2' powder (Figure 4c) consists in octahedral-shaped grains of around 10 micrometers and contains MnCO₃ as a single phase (rhombohedral, ICDD file No. 44-1472). P3' powder (Figure 4b) mainly contains spherical particles with heterogeneous sizes between few hundreds of nanometers and several

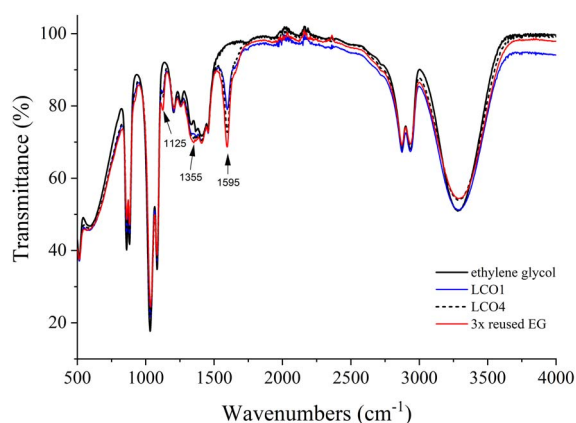


Figure 3. Infrared spectra of virgin ethylene glycol, EG after treatment and extraction of samples LCO1 and LCO4, and of EG after three successive reuses in the process.

micrometers, which are formed through the aggregation of smaller grains. Some octahedral grains are also observed. Concerning P3' powder, the XRD structural characterization shows the presence of diffraction peaks whose positions are between those of cobalt (ICDD file No. 15-0806) and nickel (ICDD files No. 87-0712), indicating the presence of a single-phase Ni–Co alloy. No hcp structure was identified, as usually observed while forming Ni–Co alloys by polyol way [17]. Peaks of MnCO_3 with a low intensity were also observed in P3' due to an incomplete magnetic separation, which explains the observation of octahedral-shaped grains in the SEM picture (Figure 4b).

The mechanism explained in Section 3.1.1 can be completed as follows for the treatment of NMC. After extraction of Li_2CO_3 by its dissolution in water, the remaining powder contains MnCO_3 (which is insoluble in water [32]) and the Ni–Co alloy. As the alloy is ferromagnetic, it is attracted by permanent magnet, whereas MnCO_3 is not.

Recovery rates of Co, Ni, Mn and Li are reported in Table 2 (respectively 79%, 80.5%, 72% and 24%). The value for cobalt is of a similar magnitude as when treating an equivalent quantity of LCO (84.1%). The purity of lithium carbonate (94.4%) is also comparable to what was obtained for LCO (90.5%). The low recovery rate for lithium means that Li^+ cations remain in EG, due to the precipitation of MnCO_3 .

These results show that, in EG, manganese carbonate precipitates preferentially and that it is therefore necessary to increase the amount of carbonate ions in order to improve the lithium recovery rate. The purity in the Ni–Co alloy (91%) is lower than for metallic cobalt in LCO, which can be explained by the presence of MnCO_3 in the alloy. The magnetic separation, which was performed by a very simple method, is the reason of this low value. The purity could be considerably increased by using more suitable techniques adapted for magnetically separating powders, such as high-gradient magnetic separator (HGMS) which creates strong magnetic forces developed in association with the intense fields delivered by a superconducting magnet [33,34].

3.3. Application of the process to a black mass

Despite the presence of graphite in addition to the active cathode material, the recycling treatment was applied to this BM to ensure that the graphite did not affect the process. It should be noted that in this case, magnetic separation was not carried out, which leads to the isolation of only two fractions instead of three. The first fraction is obtained after centrifugation and rinsing with water, and should contain the Ni–Co alloy and manganese carbonate (mixture of P2' and P3') if we refer to the Figure 1b. The second fraction is recovered by evaporating the rinsing water (P1) and should contain lithium carbonate. XRD characterization of these two fractions is shown in Figure 5.

As expected, the powder fraction (P2' + P3') contains the alloy and MnCO_3 , but it also contains graphite, which obviously was not affected by the process (Figure 5a). Concerning the powder P1, it contains Li_2CO_3 , but this phase is not the main one (Figure 5b). Another phase, identified as Li_3PO_4 (ICDD file No. 25-1030) is present with a higher content by regarding its diffraction peak intensities. But the main phase (by intensity) is a third compound, identified as LiF (ICDD file No. 45-1460). The formation of these two phases could be due to the presence of PVDF and/or the electrolyte in the BM before the treatment, although we did not identify these two compounds by the techniques we used. Concerning PVDF, its degradation seems unlikely at the temperature applied in the present study. Indeed, PVDF undergoes thermal decomposition only in the range 400–500 °C under atmospheric pressure [35], and

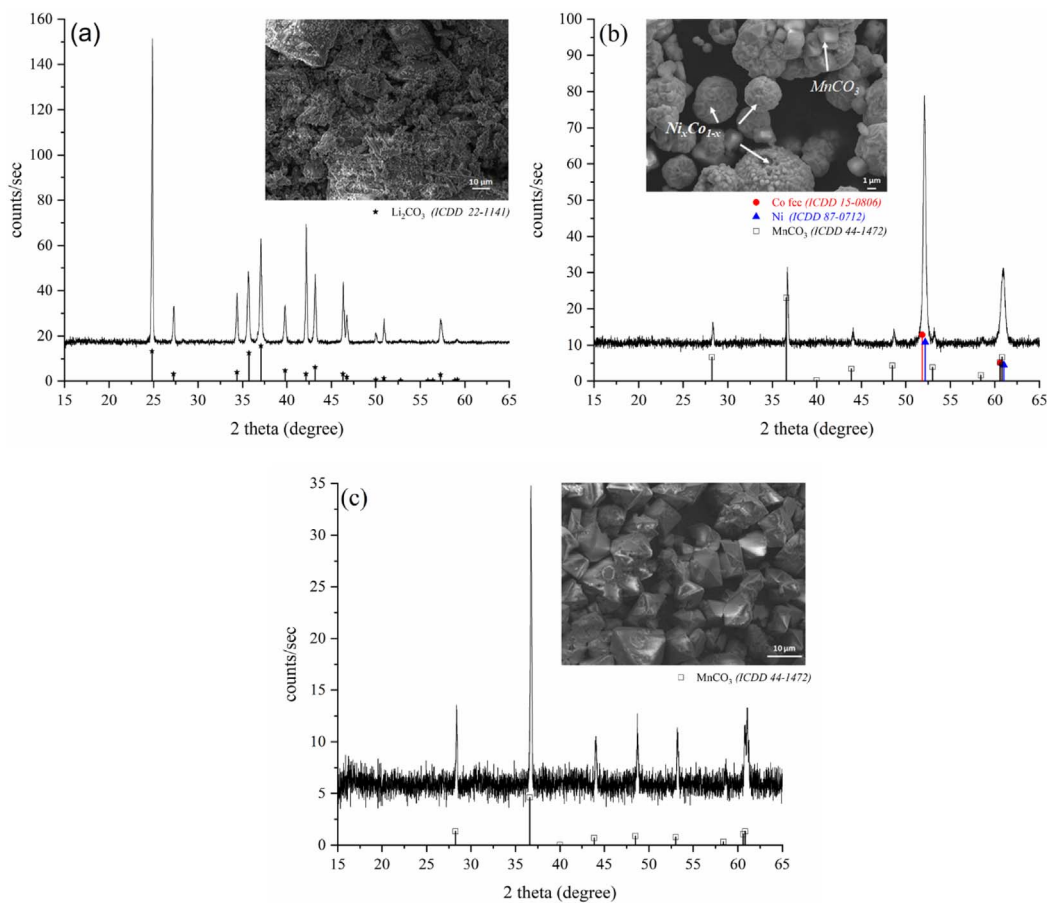


Figure 4. XRD patterns and SEM micrographs of P1 (a), P3' (b) and P2' (c) after treating NMC 111 compound. A small amount of MnCO_3 is present in P3' due to an incomplete magnetic separation.

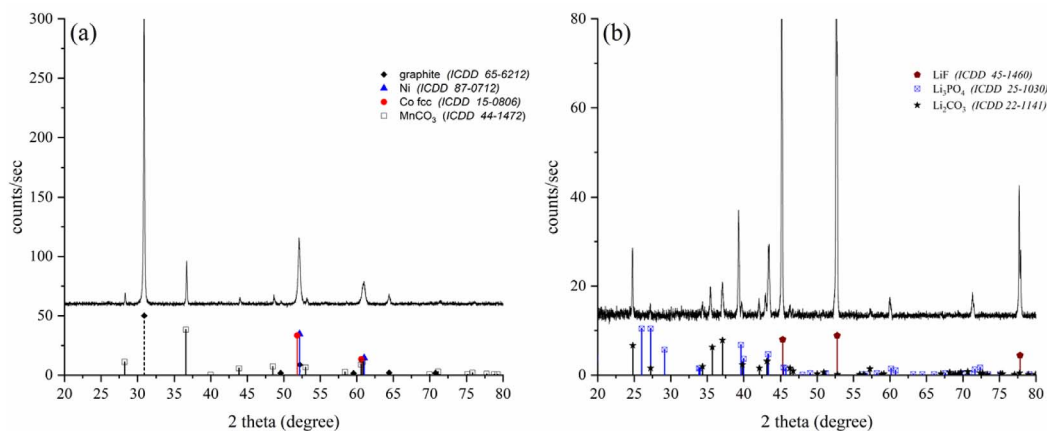


Figure 5. XRD patterns of the mixture P2' + P3' (a), and P1 (b) after treating the BM extracted from a Xiaomi battery.

under supercritical conditions in water it decomposes only above 290 °C [11]. Furthermore, it was shown that the PVDF present on cathodes was not degraded when treated in ethylene glycol at a temperature close to its boiling point (197 °C) [36]. A recent study shows that the conversion of LiPF_6 into LiF and Li_3PO_4 is possible by water extraction using a hydrothermal way [37]. In this study, the authors show that the interest of treating LiPF_6 lies in the fact that this compound is an environmental pollutant, and that producing LiF and Li_3PO_4 is economically profitable. The possibility that the process developed in the present study could be another way of treating LiPF_6 needs to be supported by additional characterisation, particularly spectroscopic, in order to clearly highlight the presence of the electrolyte before treatment.

4. Conclusions

A new method for recycling lithium-ion battery cathodes has been developed. This method enables the extraction and the separation of valuable elements (cobalt, nickel, lithium, manganese) without the need for high temperatures or the consumption of acids or bases. The solvent used, with low environmental impact, is reusable. Its continuous reuse allows for the accumulation of lithium as lithium carbonate, which partially dissolves during treatment, until EG becomes saturated, thereby increasing the lithium recovery rate.

Furthermore, it has been shown that recovery rates, especially for cobalt, are significantly improved when processing large quantities of active cathode materials. A magnetic separation step is necessary when the processed material contains cobalt, nickel, and manganese simultaneously. This step strongly influences the purities of the Ni-Co alloy and manganese carbonate collected after treatment. The use of more efficient magnetic separation devices than the one used in this study could greatly enhance these purities.

The application of this treatment to NMC-type black mass from a battery has demonstrated that the presence of graphite does not affect this process. Additionally, it has been shown that the recovered powder also contains LiF . Further investigations need to

be conducted to determine if this compound originates from the decomposition of LiPF_6 present in the electrolyte.

Declaration of interests

The authors do not work for, advise, own shares in, or receive funds from any organization that could benefit from this article, and have declared no affiliations other than their research organizations.

Funding

The authors would like to thank the ESP (Energy and Propulsion Systems) Carnot Institute for their financial support in the context of the NeoBATT project. This work was additionally supported by the European Union and the Normandy region as part of the operational program FEDER/FSE 2014-2020 through the RECYLION project, and by the CNRS (French National Center for Scientific Research) in the frame of the prematuration CARY-ION project.

Supplementary data

Supporting information for this article is available on the journal's website under <https://doi.org/10.5802/crchim.306> or from the author.

References

- [1] R. Danino-Perraud, *The Recycling of Lithium-ion Batteries: A Strategic Pillar for the European Battery Alliance*, Etudes de l'Ifri, Ifri, 2020.
- [2] Regulation (EU) 2023/1542 of the European Parliament and of the Council of 12 July 2023 concerning batteries and waste batteries, <https://eur-lex.europa.eu/eli/reg/2023/1542/oj>.
- [3] Directive 2006/66/CE of the European Parliament and of the Council of 6 September 2006 on batteries and accumulators and waste batteries and accumulators, <https://eur-lex.europa.eu/legal-content/EN/TXT/?uri=celex%3A32006L0066>.
- [4] G. Harper, R. Sommerville, E. Kendrick, L. Driscoll, P. Slater, R. Stolkin, A. Walton, P. Christensen, O. Heidrich, S. Lambert, A. Abbott, K. Ryder, L. Gaines, P. Anderson, *Nature*, 2019, **575**, 75-86.
- [5] E. Fan, L. Li, Z. Wang, J. Lin, Y. Huang, Y. Yao, R. Chen, F. Wu, *Chem. Rev.*, 2020, **120**, 7020-7063.
- [6] R. E. Ciez, J. F. Whitacre, *Nat. Sustain.*, 2019, **2**, 148-156.
- [7] D. A. Ferreira, L. M. Z. Prados, D. Majuste, M. B. Mansur, *J. Power Sources*, 2009, **187**, 238-246.

- [8] L. P. He, S. Y. Sun, X. F. Song, J. G. Yu, *Waste Manage.*, 2017, **64**, 171-181.
- [9] S. Wang, Z. Zhang, Z. Lu, Z. Xu, *Green Chem.*, 2020, **22**, 4473-4482.
- [10] T. Nshizirungu, M. Rana, Y. T. Jo, J.-H. Park, *J. Hazard. Mater.*, 2021, **414**, article no. 125575.
- [11] T. Nshizirungu, M. Rana, M. I. H. Khan, Y. T. Jo, S.-J. Park, J.-H. Park, *J. Environ. Chem. Eng.*, 2023, **11**, article no. 109160.
- [12] M. K. Tran, M. T. F. Rodrigues, K. Kato, G. Babu, P. M. Ajayan, *Nat. Energy*, 2019, **4**, 339-345.
- [13] N. Peeters, K. Binnemans, S. Riaño, *Green Chem.*, 2020, **22**, 4210-4221.
- [14] C. Padwal, H. D. Pham, S. Jadhav, T. T. Do, J. Nerkar, L. T. M. Hoang, A. Kumar Nanjundan, S. G. Mundree, D. P. Dubal, *Adv. Energy Sustainability Res.*, 2022, **3**, article no. 2100133.
- [15] K. Binnemans, P. T. Jones, *J. Sustain. Metall.*, 2023, **9**, 423-438.
- [16] F. Fievet, J. P. Lagier, *Solid State Ion.*, 1989, **32/33**, 198-205.
- [17] P. Toneguzzo, G. Viau, O. Acher, F. Guillet, E. Bruneton, F. Fievet-Vincent, F. Fievet, *J. Mater. Sci.*, 2000, **35**, 3767-3784.
- [18] F. Fievet, S. Ammar-Merah, R. Brayner, F. Chau, M. Giraud, F. Mammeri, J. Peron, J. Y. Piquemal, L. Sicard, G. Viau, *Chem. Soc. Rev.*, 2018, **47**, 5187-5233.
- [19] M. Jean, V. Nachbaur, J.-M. Le Breton, *J. Alloys Compd.*, 2012, **513**, 425-429.
- [20] D. Yetim, L. Svecova, J. C. Leprêtre, *ChemistryOpen*, 2024, **13**, article no. e202300061.
- [21] G. Zeng, J. Yao, C. Liu, X. Luo, H. Ji, X. Mi, C. Deng, *ACS Sustainable Chem. Eng.*, 2021, **9**, 16133-16142.
- [22] S. Rose, P. Xu, H. Gao, M. Li, X. Yu, Z. Chen, *Adv. Energy Sustainability Res.*, 2021, **2**, article no. 2100040.
- [23] C. A. Staples, J. B. Williams, G. R. Craig, K. M. Roberts, *Chemosphere*, 2001, **43**, 377-383.
- [24] F. Ayadi, V. Nachbaur, V. Pralong, "Process of extraction of lithium from a material comprising lithium and at least another metal", WO 2021/148403 A1 (29/07/2021).
- [25] R. Zhan, Z. Oldenburg, L. Pan, *Sustain. Mater. Technol.*, 2018, **17**, article no. e00062.
- [26] A. Vanderbruggen, J. Sygusch, M. Rudolph, R. Serna-Guerrero, *Colloids Surf. A*, 2021, **626**, article no. 127111.
- [27] C. W. Kim, H. G. Cha, Y. H. Kim, A. P. Jadhav, E. S. Ji, D. I. Kang, Y. S. Kang, *J. Phys. Chem. C*, 2009, **113**, 5081-5086.
- [28] H. Ghaedi, P. Kalhor, M. Zhao, P. T. Clough, E. J. Anthony, P. S. Fennell, *Front. Environ. Sci. Eng.*, 2022, **16**.
- [29] S.-C. Chang, Y. Ho, M. J. Weaver, *J. Am. Chem. Soc.*, 1991, **113**, 9506-9513.
- [30] L. Wang, H. Meng, P. K. Shen, C. Bianchini, F. Vizza, Z. Wei, *Phys. Chem. Chem. Phys.*, 2011, **13**, 2667-2673.
- [31] H. Wang, B. Jiang, T.-T. Zhao, K. Jiang, Y.-Y. Yang, J. Zhang, Z. Xie, W.-B. Cai, *ACS Catal.*, 2017, **7**, 2033-2041.
- [32] W. Haynes (ed.), *CRC Handbook of Chemistry and Physics*, 95th ed., CRC Press, Boca Raton, FL, 2014-2015.
- [33] J. Svoboda, *Magnetic Techniques for the Treatment of Materials*, Kluwer Academic Publisher, Springer, Dordrecht, 2004.
- [34] T. Fujita, *Powder Technology Handbook*, CRC Press, Boca Raton, FL, 2019, 461 pages.
- [35] J. E. Marshall, A. Zhenova, S. Roberts, T. Petchey, P. Zhu, C. E. J. Dancer, C. R. McElroy, E. Kendrick, V. Goodship, *Polymers*, 2021, **13**, article no. 1354.
- [36] Y. Bai, N. Muralidharan, J. Li, R. Essehli, I. Belharouak, *ChemSusChem*, 2020, **13**, 5664-5670.
- [37] H. Du, Y. Kang, C. Li, Y. Zhao, Y. Tian, J. Lu, Z. Chen, N. Gao, Z. Li, J. Wozny, T. Li, L. Wang, N. Tavajohi, F. Kang, B. Li, *Carbon Neutralization*, 2023, **2**, 416-424.

Review article

GDR Prométhée – French Research Network on *Hydrometallurgical Processes for Primary and Secondary Resources*

Lithium recovery from secondary sources: A review in battery recycling with emphasis on chemical precipitation

Lorena E. Ramirez Velazquez ^{*,a} and Hervé Muhr ^{*,a}

^a Université de Lorraine, Laboratoire Réactions et Génie des Procédés (LRGP) UMR 7274 CNRS, 1 rue Grandville BP20451, 54001 Nancy, France

E-mails: lorena.ramirez@univ-lorraine.fr (L. E. Ramirez Velazquez),
herve.muhr@univ-lorraine.fr (H. Muhr)

Abstract. The growing demand and rising prices of lithium have been driven by the expanding market of electrical vehicles and electronic devices. Therefore, the recovery of lithium from Li-ion batteries has gained enormous relevance. This document provides an overview of lithium's role in the battery industry in the ongoing energy transition. It also explores the various processes used over the years to extract valuable metals from spent lithium-ion Batteries and provides an up-to-date review of the current recycling methodologies applied to batteries. This work particularly emphasizes the hydrometallurgical process involving the chemical precipitation of lithium carbonate. Indeed it is the most sought-after form in the lithium value chain. This route had demonstrated good recovery yields as well as high purity levels. This method stands out from other recycling methods since it is environmentally friendly, consumes little energy, and does not require a large number of chemical reagents. This work encourages further exploration and refinement of hydrometallurgical practices to make recycled lithium a viable source for the battery supply chain.

Keywords. Precipitation, Lithium carbonate, Hydrometallurgy, Recycling, Lithium-ion batteries.

Manuscript received 29 September 2023, revised 23 January 2024 and 23 April 2024, accepted 15 May 2024.

1. Introduction

Lithium is a non-substitutable element of Li-ion batteries (LIBs) whose technology is indispensable in electromobility and energy transition. The worldwide usage for LIBs nowadays is about 700 GWh and is expected to increase in the next decade to around 4.7 TWh. The lithium demand for LIBs represents 60–66% of the market and is anticipated to rise to 95% by 2030. To satisfy this demand, around

120 to 150 new battery factories should be built around the globe [1]. Currently, the main supply of lithium are primary sources from Australia and Latin America. Primary sources include ores (pegmatite and granite) and salted waters such as continental and geothermal brines, volcano sediments, and sea water. Lithium content tends to be higher in mineral ore deposits compared to salted waters. However, access to these deposits is expensive since they must be mined from hard rock formations. Lithium extraction from continental brines is extremely energy-intensive, as the evaporation process

*Corresponding authors

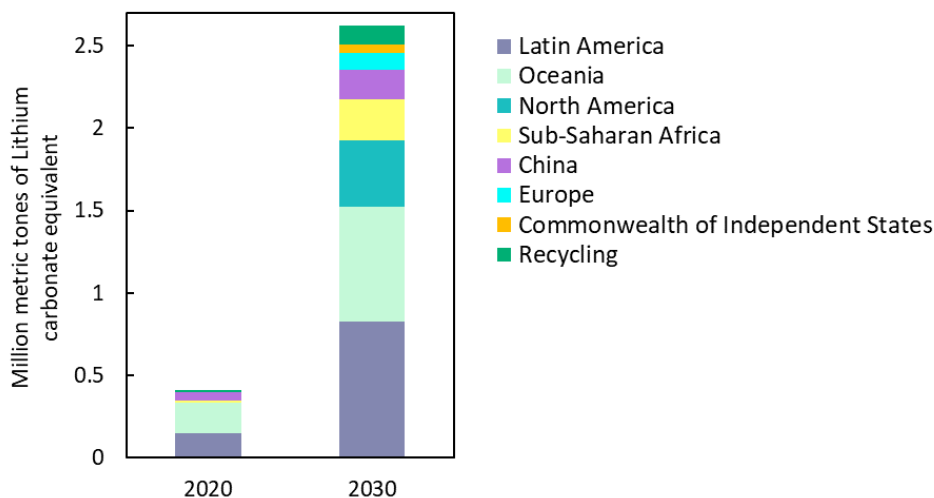


Figure 1. Global lithium product by source in million metric tons lithium carbonate equivalent. Data extracted from [1].

in ponds can take up to 24 months. Additionally, the water consumption stands at 800 m³ per ton of lithium carbonate. Geothermal brines represent just 3% of the global lithium reservoirs with no significant commercial plans to exploit these reserves. Today, lithium extraction from seawater remains in the research phase mainly because researchers are exploring various methods to elevate lithium concentration in seawater, which typically ranges from 0.1 to 0.2 ppm [2].

Nowadays, world powers like eastern and western Europe, Russia, and some independent state members of the Commonwealth are developing projects to recover lithium by their own means and sources in order to gain lithium supply independence. Figure 1 illustrates the forecast of lithium production by country in comparison with lithium recovery from secondary sources. It shows that recycling represents a small fraction when compared with the larger volume of lithium obtained from primary sources. At present, only 5% of discarded batteries are recycled [3].

Nevertheless, while there is a slight improvement in the projected growth of lithium recycling from 2020 to 2030, it is still far from being able to compete with primary sources. Indeed the recycling industry faces numerous challenges, primarily related to waste management, engineering and commercialization. One of the technical difficul-

ties lies in the design of LIBs. Batteries come in different sizes, forms, and chemistries, making the battery disassembly and materials separation extremely challenging. Therefore, scaling up pilot tests presents an arduous task, mainly because of the lack of regulation and standardization for the recovered materials [4]. Given the huge potential of battery recycling, ongoing advancements in recycling technologies are essential. This article aims to provide an overview of existing methods in metal recycling, including direct physical methods, pyrometallurgy, bio- and hydrometallurgy, with a specific focus on chemical precipitation.

2. Types of Li-ion batteries

LIBs are built with an anode, a cathode, an organic electrolyte, and a separator. The electrochemical properties of these batteries make them unique in the mobility market, characterized by their high specific and high-density energy. In addition, they can operate between 500 and 1000 cycles of charge-discharge, reaching at least 80% of their initial charge. On the other hand, LIBs require high-safety protocols during their handling to prevent overcharge and instability. At high temperatures and voltage, degradation may occur, and the potential fire hazard always exists [7]. Various cathode chemistries include commercial lithium cobalt oxide (LCO), lithium iron

Table 1. Features of commercial Li-ion batteries [5,6]

Composition	LiCoO ₂	LiFePO ₄	LiMn ₂ O ₄	LiAl _x Co _y Ni _x yO ₂	LiCo _x Mn _y Ni _x yO ₂
Material price/\$(kWh ⁻¹)	88	32	26	39	40–50
Battery price/\$(kWh ⁻¹)	357	222	251	199	145–230
Annual global demand for cathode materials in 2022 (kt)	23.1	58.5	9.0	20.1	259.9

phosphate (LFO), lithium manganese oxide (LMO), lithium nickel cobalt aluminum oxide (NCA), and nickel manganese cobalt (NCM). Depending on their composition, different recycling methods are preferred. For instance, LCO, NCA, and NCM can be treated with hydrometallurgical, pyrometallurgical, and direct pathways, while LFP and LMO are usually directly recycled [5]. Table 1 provides an outlook for the battery market, showing the interaction between global demand, materials and battery prices. Notably, lithium and cobalt, recognized as critical raw materials, influence battery manufacturing costs.

3. Pre-treatment methods for spent Li-ion batteries

Typically, LIBs retain some residual energy inside and for that reason a 10 wt% NaCl solution is used to discharge them. For this, the battery is submerged entirely into the electrolytic solution, inducing a controlled short-circuit. Thus, the risk of explosion and the emission of toxic gases are prevented. Other discharge approaches include electronic techniques and the use of conductive liquids. Nevertheless, the NaCl solution has proved the best compromise between cost and efficiency [8,9]. Once the battery is discharged, it undergoes separation and dismantling methods with the aim of separating the different materials according to their composition [9]. The choice of pre-treatment methods, whether mechanical, solvent-based, or involving calcination, depends on factors such as size, composition, and metal extraction processes. Pre-treatment methods can also be combined as needed.

Mechanical pre-treatment methods include crushing, sieving, particle size separation, flotation, gravity, and magnetic separation. Particle size separation aims to separate the minerals according to their particle size distribution after crushing

and sieving. The studies with a commercial granulator showed that electrode materials have a cutoff diameter of less than 0.5 mm, copper pieces around 1–6 mm, and plastics greater than 6 mm [10]. The flotation method uses a chemical agent which follows the principles of hydrophilicity and hydrophobicity. This agent is able to trap hydrophobic metals inside bubbles of a foam and these will float to the surface while the hydrophilic ones will remain in the mixture [10]. During magnetic separation, steel pieces are recovered with almost 100% efficiency. Finally, gravity separation aims to separate different materials according to their density, for example, plastic, composites, and aluminum foils [10].

The solvent pre-treatment makes use of solutions and solvents to isolate active materials from the foils usually composed of copper or aluminum. This process essentially functions by dissolving the binder allowing to pull out the active materials [9].

The calcination pre-treatment aims to separate carbon and other organic material from the battery. The temperature range is 150 to 500 °C [9].

4. Methods of lithium extraction from spent Li-ion batteries

There are three main methods of recovering metals from LIBs: the bio- and hydrometallurgical, pyrometallurgical and direct recycling (Figure 2). These methods can also be combined or integrated for a more efficient metal recovery.

Hydrometallurgy relies in extraction, purification, and recovery. Selective separation technologies are chosen according to the properties of products and impurities, requiring a leaching step [12]. While this method has low energy requirements and minimal gas emissions, wastewater treatment is essential [11]. In the bio-hydrometallurgy, bioleaching involves an interaction between microorganisms and metals for dissolution and then extraction.

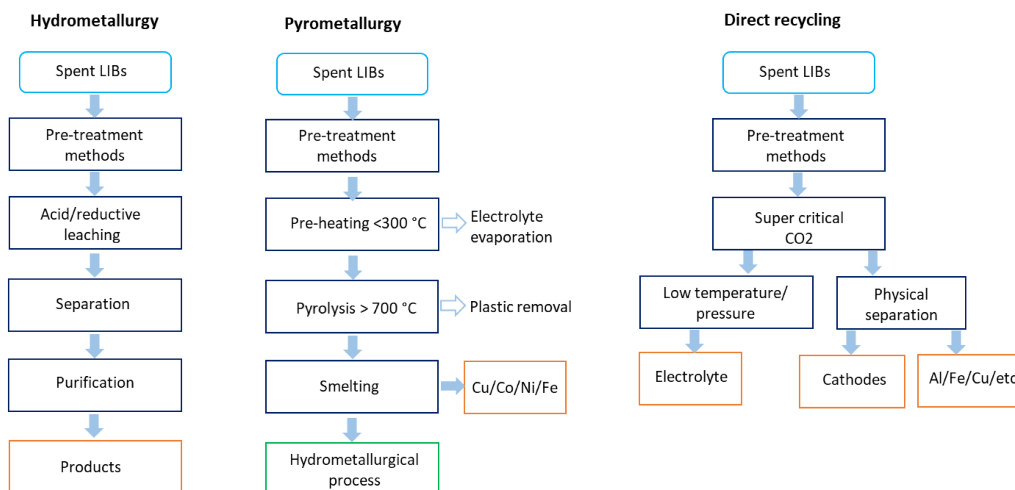


Figure 2. Methods of lithium extraction from spent lithium-ion batteries. Data extracted from [11].

Bio-hydrometallurgy offers innovative contributions for a greener process [13].

The pyrometallurgical method involves the incineration and smelting of LIBs in a plasma arc furnace at temperatures above 700 °C. Metals such as copper, cobalt, iron, and nickel are recovered in the form of alloys, while plastics and all organic compounds are incinerated. Aluminum, manganese, silicon, calcium, lithium, and traces of iron are found in the slag, requiring a hydrometallurgical process for metal recovery [11,14,15] (Figure 2). Although a simple operation, it requires costly equipment, excessive energy and is polluting [12].

Lately there has been a growing exploration of the direct physical recycling process. This method begins with a mechanical pretreatment method leading to individual cells. Then, these cells undergo treatment using supercritical CO₂, enabling the extraction and treatment of electrolytes. After reducing temperature and pressure, CO₂ can be separated from the electrolytes. Finally, the cathode material can be reused (Figure 2). This method has demonstrated several advantages, including low energy consumption, a high recovery rate and it is environmentally friendly. Nevertheless, it has high operational and equipment requirements. Additionally, not all materials can be successfully recovered through this process [11], similar to the pyrometallurgical method which requires a hydrometallurgical method in order to recover metals effectively.

5. Hydrometallurgy

This section will provide a deep description of the hydrometallurgical process which is commonly combined with the pyrometallurgical process. This technique primarily involves two steps: leaching and purification. This method has a great worldwide industrial potential and is the predominant approach to extract lithium. Hydrometallurgy is more suitable in recycling lithium when LIBs have a single chemical composition [16].

5.1. Leaching process

The objective of leaching is to obtain metal ions in an aqueous solution from the cathodes of the spent LIBs. The mechanism involves the following steps: initially, the reagent diffuses and adheres to the material's surface [17]. Then, an oxidoreduction reaction on the surface, results in the formation of highly soluble species. Reaction products detach from the surface and disperse (Figure 3). Choosing the right leaching agent is crucial to achieve high efficiency in the material dissolution. High selectivity towards the target metal is desired as well as the regeneration ability of the leaching agent. Leaching agents can be acids (inorganic or organic) or alkaline solutions. Acid leaching is the most common method since it can dissolve the cathode materials effectively. The most commonly used acids for leaching are hydrochloric acid, nitric acid, and sulfuric

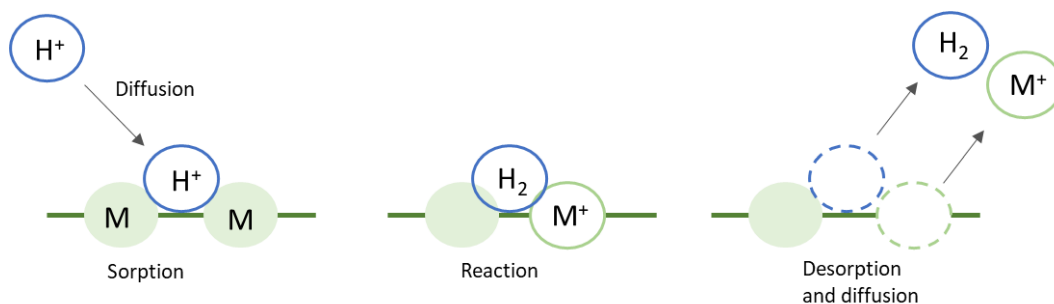


Figure 3. Mechanism of the leaching process of cathode materials from Li-ion batteries. Extracted from [17].

acid [8]. Sulfuric acid shows a non-oxidizing nature in contrast to HCl and HNO_3 . When HCl or HNO_3 reacts with cathode materials, production of NO_x or Cl_2 gases is observed. Cl_2 is hazardous for the environment as well as SO_x and NO_x . As a result, HCl is avoided because of its high cost and corrosive properties. Inorganic acids have demonstrated high efficiency for lithium and cobalt with rates of 98 and 95%, respectively [16].

Table 2 shows various leaching agents reported in the literature, along with their corresponding leaching rates. The data indicate a consistent approximate yield of 99% for lithium, while the yield can vary from 70 to 90% for cobalt.

The use of organic acids has been also explored, such as oxalic acid and citric acid among others. Organic acids exhibit notable characteristics such as their propensity for easy degradation, recyclability, and eco-friendliness. On the other hand, they are more expensive than the inorganic acids and their leaching rates are slower. As a result, the industry has not yet employed organic acids for the recovery of metals in spent LIBs [8].

Alkaline leaching is a well-known method in metal extraction, involving the interaction between hydroxide ions and metals. Sodium hydroxide and ammonium species are the most common leaching agents. Sodium hydroxide can dissolve the aluminum efficiently and it is slightly corrosive. Ammonia is used mainly in spent LIBs containing copper, cobalt, nickel, and zinc. Normally, for cathode leaching, a solution containing ammonium sulfite, ammonia, ammonium carbonate and deionized water is prepared. During the leaching process, ammonium carbonate acts as a buffer and ammonium sulfite serves as a

reductant. Afterwards, ammonium sulfite converts nickel and cobalt from their insoluble high oxidation states of to their soluble lower oxidation states [8].

5.2. Purification process

The purification process aims to separate valuable metals from the spent LIB solution after the leaching process. This leaching solution includes elements such as iron, aluminum, copper, manganese, nickel, cobalt, and lithium. This process could include solvent extraction, electrochemical extraction, and chemical precipitation. To enhance metal recovery, these techniques usually are used in combination [8]. For example, the use of solvent extraction combined with chemical precipitation allows the selective separation of copper, nickel, and lithium through chemical precipitation, while cobalt and manganese are efficiently separated using solvent extraction.

5.2.1. Solvent extraction

Solvent extraction uses a two-phase system to separate lithium from the leached cathode material, resulting in an efficient method since it demonstrates to be highly selective for metal ions. This technique relies on relative solubility to separate ions from polar and non-polar liquid. Nonpolar extractants are mainly used to separate valuable metals such as cobalt, nickel, magnesium, and lithium. Common extractants include di-(2-ethylhexyl) phosphoric acid (D2EHPA), diethylhexyl phosphoric acid (DEHPA), bis-(2,4,4-tri-methyl-pentyl) phosphonic acid (Cyanex 272), trioctylamine (TOA), and 2-ethylhexyl phosphonic acid mono-2-ethylhexyl ester (PC-88A). In some cases, a mixture of two or more

Table 2. Research results for the highest leaching rates of spent Li-ion batteries in inorganic acids

Cathode materials	Leaching agent	T (°C)	S/L ratio (g/L)	Time (min)	Leaching rate (%)	Ref.
LCO	2 M H_2SO_4 + 10 vol% H_2O_2	70	30	60	Co 98.5 Li 99.8	[18]
LCO	2 M H_2SO_4 + 5 vol% H_2O_2	80	50	60	Co ~ 99 Li ~ 99	[19]
LCO	1 M HNO_3 + 1.7 vol% H_2O_2	75	10	30	Co ~ 99 Li ~ 99	[20]
LCO	0.7 M H_3PO_4 + 4 vol% H_2O_2				Co ~ 99.7 Li ~ 99.9	[21]
LCO	2 M H_2SO_4 + 5 vol% H_2O_2	75	100	60	Co ~ 70 Li ~ 99.1	[22]

extractants is employed to enhance selectivity [8,9]. Table 3 displays a compilation of solvent extraction processes conducted over recent years, employing various spent materials. The extraction efficiency and purity of Li_2CO_3 vary depending on the spent material and the extractant employed.

5.2.2. Electrochemical extraction

Electrochemical deposition had demonstrated to be an effective method since it can separate the metals from a solution based on the potential difference between the electrodes. For example, Chu et al. [28] built a system using aluminum foil as cathode, the active material from the spent LIB as anode, and sulfuric acid as the electrolyte. Through electrolysis, a successful separation between the aluminum foil and the active material is achieved. The process can be explained as follows: copper enters the electrolyte as impurity and is electrodeposited on the cathode, while nickel, cobalt, and manganese remain undissolved. The aluminum foil remains insoluble within the solution [16]. This method proved to have an extraction efficiency for lithium ranging between 75–95% and the capability to extract other metals beyond Li_2CO_3 . The recycled lithium exhibited a high purity level of 99%.

Other electrochemical methods extract lithium using a lithium-selective transmissive membrane where spent LIBs are placed in a system using a Li-ion-conductive ceramic solid electrolyte. When active material is placed in water, lithium in the charged cathode does not dissolve while the lithium

in the anode dissolves in the water forming lithium hydroxide [9].

5.2.3. Chemical precipitation

Chemical precipitation is the most commonly used method for separating lithium from solutions after leaching the spent LIB cathodes. This method uses the pH-dependent difference of solubility in the active material to extract valuable metals. Chemical precipitation is used to remove ionic constituents from water by the addition of counterions to reduce solubility. Most metal are precipitated as hydroxides, sulfides, and carbonates [28]. Chemical precipitation generally involves simultaneous and rapid occurrence of nucleation, crystal growth, and other mechanisms, such as Ostwald ripening and agglomeration [29]. The main reactants include NaOH , Na_3PO_4 and Na_2CO_3 among others. They are used to precipitate valuable metals ions followed by lithium recovery, mainly in the form of Li_2CO_3 or Li_3PO_4 (Table 4). Li_2CO_3 is the most sought-after form of lithium as it consistently yields the highest purity levels.

5.3. Lithium precipitation in the form of Li_2CO_3

Carbonate precipitation is normally used in water treatment to reduce calcium hardness but nowadays it is a great option for lithium recovery from spent LIBs. It has been demonstrated that carbonate is able to decrease the solubility of some metals, while increasing that of others. The effect depends on the target metal and the pH at which the treatment is carried out [18,51]. Lithium carbonate exhibits

Table 3. Research of solvent extraction process of spent Li-ion batteries (LIBs) in the literature [10]

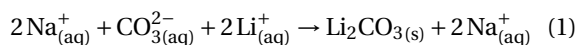
Spent materials	Residue	Efficiency (%)	Purity (%)	Extractants	REF
LIB scraps	Li ₂ CO ₃	80	>98	DEHPA Cyanex 272	[23]
LiCoO ₂	Li ₂ SO ₄ solution	Leaching 100	>99.5	PC-88A	[24]
LiNi _{0.5} Co _{0.2} Mn _{0.3} O ₂	Li ₂ CO ₃	Leaching 94	-	Cyanex 272	[25]
LIB scraps	Li ₂ CO ₃	72	99.7	DEHPA Cyanex 272	[26]
LiCoO ₂	Li ₂ CO ₃	86	74.2	Cyphos II-101	[27]

Table 4. Research of precipitation processes of spent Li-ion batteries (LIBs) in the literature

Spent materials	Residue	Efficiency (%)	Purity (wt%)	REF
LiCoO ₂	Li ₂ SO ₄	90	-	[30]
LIB scraps	LiF	50	>99	[31]
Cathode materials	Li ₂ CO ₃	80	96.97	[32]
Cathode materials	Li ₂ CO ₃	71	-	[33]
Mixed cathode materials	Li ₂ CO ₃	80	-	[34]
LiNi _{0.3} Co _{0.3} Mn _{0.3} O ₂	Li ₂ CO ₃	Leaching 99.7	-	[35]
Cathode materials	Li ₃ PO ₄	89	-	[36]
LiNi _{0.3} Co _{0.3} Mn _{0.3} O ₂	Li ₂ CO ₃	98	99.9	[37]
LiFePO ₄	Li ₃ PO ₄	82.6	96.5	[38]
Cathode material and graphite	Li ₂ CO ₃	Leaching 99.9	99.4	[39]
LiFePO ₄	Li ₂ CO ₃	95.1	99.95	[40]
Cathode materials	Li ₂ CO ₃	>90	99.93	[41]
Cathode materials	Li ₃ PO ₄	85.6	-	[42]
Anode	Li ₂ CO ₃	Leaching 100	>99	[43]
LiNi _{0.3} Co _{0.3} Mn _{0.3} O ₂	Li ₂ CO ₃	Leaching 99	-	[44]
LiNi _{0.5} Co _{0.2} Mn _{0.3} O ₂	Li ₂ CO ₃	76	>99.5	[45]
LiFePO ₄	Li ₂ CO ₃	99.4	-	[46]
Cathode	Li ₂ CO ₃	38	>98.48	[47]
LiFePO ₄	Li ₂ CO ₃	80	-	[48]
LiNi _{0.5} Co _{0.2} Mn _{0.3} O ₂	Li ₂ CO ₃	91.2	99	[49]
LiNi _x Co _{1-x-y} Mn _y O ₂	Li ₃ PO ₄	Leaching 99.1	-	[50]

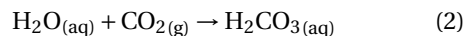
inverse solubility, thus the higher the temperature, the lower the residual content of dissolved lithium and therefore the higher the quantity of precipitated lithium carbonate [28,52] (Figure 4).

In the recycling industry, Li₂CO₃ is precipitated after a saturated solution of sodium carbonate is added into the mixture resulting from the leaching process. The precipitation reaction can be described as follows:



In this reaction, lithium ions in the solution react with sodium carbonate, resulting in the formation of lithium carbonate along with sodium ions.

The precipitation of Li₂CO₃ using carbon dioxide represents a promising and sustainable approach for lithium recovery. The carbonation process begins with the dissolution of CO₂ in water:



For precipitation to occur, the pH of the system should be alkaline, at least 8 and optimally higher

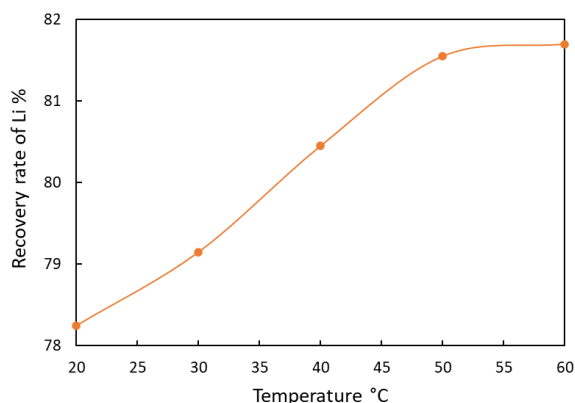
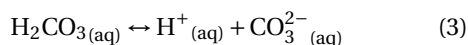
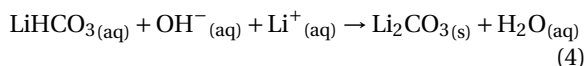


Figure 4. Evolution of the lithium recovery rate as a function of temperature. Data extracted from [34].

than 10. This is mainly because the dominant species in the system shifts to CO_3^{2-} at pH above 10, as indicated in the following reaction:



Lithium and bicarbonate ions coexist in the system. By maintaining an alkaline pH, lithium precipitation occurs, as shown in the next equation:



Different studies had explored this pathway (Table 4). For example, Han et al. [53] obtained a Li_2CO_3 precipitate after a leaching process of Li_2SO_4 using CO_2 gas in an alkaline solution. After analyzing different samples performed at various operational parameters, it was found that temperature and pH play a key role in the process. A substantial concentration of CO_3^{2-} ions within the system is critical to achieve a state of supersaturation, which enables the processes of nucleation and crystal growth. This study reveals a lithium recovery rate between 41.6 and 45.5% at an operational temperature of 50 °C. Matsumoto et al. [54] managed to precipitate lithium in the form of Li_2CO_3 by injecting CO_2 microbubbles where it was demonstrated that bubble size influences the particle size of the precipitate. The effect of supersaturation and temperature in the precipitation process were noted as well. In the study of Ramirez et al. [52], a Li_2CO_3 precipitation was carried out using a NaOH solution and injecting a gas flow of CO_2 followed by

a CO_2 purification to increase lithium purity, resulting in a lithium recovery yield of 48.3% and purity of 99.9%. Carbonate precipitation was demonstrated to be the safest, most economical, and most efficient method compared to the other methods discussed previously. However, the primary drawback lies in the low lithium concentration remaining in the solution after leaching [8,9]. Hence, the implementation of additional techniques, such as membrane technologies, should be considered. Nevertheless, it is important to acknowledge that this would increase operational complexity and costs.

6. Conclusion

Nowadays, lithium recycling is becoming an economic, environmental, and governmental issue due to the growing demand of e-mobility and electronic devices. For that reason, finding novel routes in the development of greener and low-cost processes is indispensable in the recycling of Li-ion batteries (LIBs). The recycling industry has encountered numerous drawbacks and challenges in the extraction of valuable metals from LIBs. Because of this, secondary sources of lithium are currently considered as unreliable for its integration into the lithium supply chain. However, promising progress has been made in the past years with regards to recycling LIBs. Different treatments and processes are being explored and, among the methods studied, hydrometallurgy involving carbonate precipitation has proved to be the most affordable and eco-friendly approach for lithium extraction. Additionally, using CO_2 not only produces a precipitate with superior purity but also plays a significant role in enhancing the sustainability of the process. Although this method offers several advantages, it is crucial to combine chemical precipitation with other techniques to enhance metal recovery yields. Further research should focus on improving and integrating hydrometallurgy with other technologies to advance the production of the next-generation batteries from recycled lithium.

Declaration of interests

The authors do not work for, advise, own shares in, or receive funds from any organization that could benefit from this article, and have declared no affiliations other than their research organizations.

References

- [1] M. Azevedo, M. Baczyńska, K. Hoffman, A. Krauze, *Lithium Mining: How New Production Technologies Could Fuel the Global EV Revolution*, McKinsey & Company, New York, NY, 2022, Retrieved June 1, 2023, from <https://www.mckinsey.com/industries/metals-and-mining/our-insights/lithium-mining-how-new-production-technologies-could-fuel-the-global-ev-revolution>.
- [2] S. Yang, F. Zhang, H. Ding, P. He, H. Zhou, *Joule*, 2, 1648-1651.
- [3] Cas Science Team. Lithium-Ion Battery Recycling, 2022, <https://www.cas.org/resources/cas-insights/sustainability/lithium-ion-battery-recycling> (10/06/2023).
- [4] K. M. Winslow, S. J. Laux, T. G. Townsend, *Resour. Conserv. Recycl.*, 2018, **129**, 263-277.
- [5] Z. J. Baum, R. E. Bird, X. Yu, J. Ma, *ACS Energy Lett.*, 2022, **7**, 712-719.
- [6] IEA, *Global EV Outlook 2023*, IEA, Paris, 2023, <https://www.iea.org/reports/global-ev-outlook-2023>, License: CC BY 4.0.
- [7] Y. Zhao, O. Pohl, A. I. Bhatt, G. E. Collis, P. J. Mahon, T. Rüther, A. F. Hollenkamp, *Sustain. Chem.*, 2021, **2**, 167-205.
- [8] Y. Yao, M. Zhu, Z. Zhao, B. Tong, Y. Fan, Z. Hua, *ACS Sustain. Chem. Eng.*, 2018, **6**, 13611-13627.
- [9] H. Bae, Y. Kim, *Mater. Adv.*, 2021, **2**, 3234-3250.
- [10] S. Sun, C. Jin, W. He, G. Li, H. Zhu, J. Huang, *Sci. Total Environ.*, 2021, **776**, article no. 145913.
- [11] L.-F. Zhou, D. Yang, T. Du, H. Gong, W.-B. Luo, *Front. Chem.*, 2020, **8**, article no. 578044.
- [12] C. Baumann, *Projet de Recherche et Développement*, ENSIC, Nancy, 2021.
- [13] W.-Q. Zhuang, J. P. Fitts, C. M. Ajo-Franklin, S. Maes, L. Alvarez-Cohen, T. Hennebel, *Curr. Opin. Biotechnol.*, 2015, **33**, 327-335.
- [14] W.-Q. Zhuang, J. P. Fitts, C. M. Ajo-Franklin, S. Maes, L. Alvarez-Cohen, T. Hennebel, *Curr. Opin. Biotechnol.*, 2015, **33**, 327-335.
- [15] O. Dolotko, N. Gehrke, T. Malliaridou, R. Sieweck, L. Herrmann, B. Hunzinger, M. Knapp, H. Ehrenberg, *Commun. Chem.*, 2023, **6**, article no. 49.
- [16] X. Duan, W. Zhu, Z. Ruan, M. Xie, J. Chen, X. Ren, *Energies*, 2022, **15**, article no. 1611.
- [17] A. Chagnes, *Technique d'ingénieur, Métallurgie Extractive*, ENSIC, Nancy, 2023, [Seminar presentation].
- [18] W. S. Chen, H. J. Ho, *Trans. Tech. Publ.*, 2018, **775**, 419-426.
- [19] L. Sun, K. Qiu, *J. Hazard. Mater.*, 2011, **194**, 378-384.
- [20] C. K. Lee, K.-I. Rhee, *Hydrometallurgy*, 2003, **68**, 5-10.
- [21] G. P. Nayaka, K. V. Pai, J. Manjanna, S. J. Keny, *Waste Manag.*, 2016, **51**, 234-238.
- [22] M. K. Jha, A. Kumari, A. K. Jha, V. Kumar, J. Hait, B. D. Pandey, *Waste Manag.*, 2013, **33**, 1890-1897.
- [23] G. Granata, E. Moscardini, F. Pagnanelli, F. Trabucco, L. Toro, *J. Power Sources*, 2012, **206**, 393-401.
- [24] L.-P. He, S.-Y. Sun, Y.-Y. Mu, X.-F. Song, J.-G. Yu, *ACS Sustain. Chem. Eng.*, 2017, **5**, 714-721.
- [25] W.-S. Chen, H.-J. Ho, *Metals*, 2018, **8**, article no. 321.
- [26] T. A. Atia, G. Elia, R. Hahn, P. Altimari, F. Pagnanelli, *J. Energy Chem.*, 2019, **35**, 220-227.
- [27] L. Xu, C. Chen, M.-L. Fu, *Hydrometallurgy*, 2020, **197**, article no. 105439.
- [28] W. Chu, Y. Zhang, L. Chen, K. Wu, Y. Huang, Y. Jia, *Sep. Purif. Technol.*, 2021, **269**, article no. 118704.
- [29] L. K. Wang, D. A. Vaccari, Y. Li, N. K. Shammass, in *Physicochemical Treatment Processes. Handbook of Environmental Engineering* (L. K. Wang, Y.-T. Hung, N. K. Shammass, eds.), vol. 3, Humana Press, Totowa, NJ, 2005, 141-197.
- [30] P. H. Karpinski, J. S. Wey, in *Handbook of Industrial Crystallization* (A. S. Myerson, ed.), Butterworth-Heinemann, Oxford, 2nd ed., 2002, 141-160.
- [31] S. Aktas, D. J. Fray, O. Burheim, J. Fenstad, E. Açma, *Miner. Process. Extr. Metall.*, 2006, **115**, 95-100.
- [32] J. F. Paulino, N. G. Busnardo, J. C. Afonso, *J. Hazardous Mater.*, 2008, **150**, 843-849.
- [33] R.-C. Wang, Y.-C. Lin, S.-H. Wu, *Hydrometallurgy*, 2009, **99**, 194-201.
- [34] S. Zhu, W. He, G. Li, X. Zhou, X. Zhang, J. Huang, *Trans. Nonferrous Metals Soc. China*, 2012, **22**, 2274-2281.
- [35] H. Zou, E. Gratz, D. Apelian, Y. Wang, *Green Chem.*, 2013, **15**, 1183-1191.
- [36] X. Zhang, H. Cao, Y. Xie, P. Ning, H. An, H. You, F. Nawaz, *Sep. Purif. Technol.*, 2015, **150**, 186-195.
- [37] X. Chen, T. Zhou, J. Kong, H. Fang, Y. Chen, *Sep. Purif. Technol.*, 2015, **141**, 76-83.
- [38] W. Gao, X. Zhang, X. Zheng, X. Lin, H. Cao, Y. Zhang, Z. Sun, *Environ. Sci. Technol.*, 2017, **51**, 1662-1669.
- [39] Y. Yang, X. Zheng, H. Cao, C. Zhao, X. Lin, P. Ning, Y. Zhang, W. Jin, Z. Sun, *ACS Sustain. Chem. Eng.*, 2017, **5**, 9972-9980.
- [40] S. Natarajan, A. B. Boricha, H. C. Bajaj, *Waste Manag.*, 2018, **77**, 455-465.
- [41] Y. Yang, X. Meng, H. Cao, X. Lin, C. Liu, Y. Sun, Y. Zhang, Z. Sun, *Green Chem.*, 2018, **20**, 3121-3133.
- [42] W. Gao, J. Song, H. Cao, X. Lin, X. Zhang, X. Zheng, Y. Zhang, Z. Sun, *J. Cleaner Prod.*, 2018, **178**, 833-845.
- [43] S. Tao, J. Li, L. Wang, L. Hu, H. Zhou, *Ionics*, 2019, **25**, 5643-5653.
- [44] Y. Yang, S. Song, S. Lei, W. Sun, H. Hou, F. Jiang, X. Ji, W. Zhao, Y. Hu, *Waste Manag.*, 2019, **85**, 529-537.
- [45] R. Sattar, S. Ilyas, H. N. Bhatti, A. Ghaffar, *Sep. Purif. Technol.*, 2019, **209**, 725-733.
- [46] Q. Li, K. Y. Fung, L. Xu, C. Wibowo, K. M. Ng, *Ind. Eng. Chem. Res.*, 2019, **58**, 3118-3130.
- [47] L. Li, Y. Bian, X. Zhang, Y. Yao, Q. Xue, E. Fan, F. Wu, R. Chen, *Waste Manag.*, 2019, **85**, 437-444.
- [48] C.-H. Jo, S.-T. Myung, *J. Power Sources*, 2019, **426**, 259-265.
- [49] P. Yadav, C. J. Jie, S. Tan, M. Srinivasan, *J. Hazardous Mater.*, 2020, **399**, article no. 123068.
- [50] W. Lv, Z. Wang, X. Zheng, H. Cao, M. He, Y. Zhang, H. Yu, Z. Sun, *ACS Sustain. Chem. Eng.*, 2020, **8**, 5165-5174.
- [51] W. Lv, Z. Wang, H. Cao, Y. Sun, Y. Zhang, Z. Sun, *ACS Sustain. Chem. Eng.*, 2018, **6**, 1504-1521.
- [52] L. R. Velázquez, L. Palos, M. L. P. Mostefa, H. Muhr, *J. Cryst. Growth*, 2024, **631**, article no. 127625.
- [53] B. Han, R. A. U. Haq, M. Louhi-Kultanen, *Hydrometallurgy*, 2020, **195**, article no. 105386.
- [54] M. Matsumoto, Y. Morita, M. Yoshinaga, S. Hirose, K. Onoe, *J. Chem. Eng. Japan*, 2009, **42**, s242-s248.

Research article

GDR Prométhée – French Research Network on *Hydrometallurgical Processes for Primary and Secondary Resources*

Back-extraction of major actinides from organic phase through precipitation

Julie Réaux-Durain ^a, Boushra Mortada ^a, Murielle Bertrand ^{a,b}, Jérôme Maynadié ^a,
Michaël Carboni ^a, Daniel Meyer ^a and Damien Bourgeois ^{a,*}^a ICSM, CEA, CNRS, ENCSM, University of Montpellier, Marcoule, France^b CEA, DES, ISEC, DMRC, BP 17171, 30207 Bagnols-sur-Cèze Cedex, FranceE-mail: damien.bourgeois@umontpellier.fr (D. Bourgeois)

Abstract. Recycling waste nuclear fuel through the production of mixed oxide (MOx) fuel allows for sustainable management of natural nuclear resources. With the aim of reducing the number of steps required for recycling U and Pu, the possibility of precipitating them directly from the organic phase (also referred to as precipitation stripping) using oxalic acid, is investigated herein. For practical reasons, proof-of-concept studies were performed using U(VI) and Th(IV), with the latter serving as a first model for Pu(IV). The results obtained show that, by controlling the concentrations of oxalic and nitric acids in the precipitation medium, total precipitation of Th and partial precipitation of U from the organic phase are attained. The actinides are precipitated in the form of oxalates, with the complete absence of impurities. Furthermore, the precipitates obtained can then be totally separated through washing with water, as proven by X-ray diffraction (XRD) and energy-dispersive X-ray (EDX) analyses. This allows control over the U:Th mass ratio in the final product. This work demonstrates the effectiveness of precipitation stripping using oxalic acid for the stripping of Th and U present in the organic phase, eliminating the need for reducing agents classically employed in the PUREX process.

Keywords. Solvent extraction, Stripping, Precipitation, Uranium, Thorium, Oxalic acid, Tributylphosphate.

Manuscript received 4 December 2023, revised 7 May 2024, accepted 22 May 2024.

1. Introduction

The operation of the reactors of the French nuclear power plants is based on a fuel composed of natural uranium oxide, enriched in isotope 235, and for some reactors, of a mixture of uranium and plutonium oxides, known as MOx (Mixed Oxide) fuel. The production of MOx fuel enables recycling both uranium and plutonium present in waste nuclear fuel,

and thus a sustainable management of natural nuclear resources [1].

The treatment of spent nuclear fuel is currently carried out in France following the PUREX (Plutonium, Uranium, Reduction, Extraction) process [2]. This consists in dissolving the spent nuclear fuel in nitric acid HNO₃, followed by the separation of uranium(VI) and plutonium(IV) from the aqueous medium through liquid–liquid extraction using tributylphosphate (TBP) as an extracting molecule [2,3]. Afterwards, two back-extraction (stripping) steps toward aqueous phases are performed to separate U from Pu, with the stripping of Pu relying on the

*Corresponding author

reduction of Pu(IV) to Pu(III). Pu(III) is then precipitated from the aqueous phase using oxalic acid ($C_2O_4H_2$). U(VI) is precipitated into uranium(VI) oxalate using the same technique. The solids obtained are then calcined so as to form the corresponding oxides, mixed (in controlled proportions) to form MOx and shaped into pellets to be used as fuel for the nuclear reactors. Inspired by the PUREX process, the COEXTM process was developed by the CEA (*Commissariat à l'Energie Atomique et aux Energies Alternatives*) with the aim of decreasing the number of steps during uranium and plutonium recycling, in addition to preventing the generation of pure-plutonium effluents, which may be used in non-civil applications [4,5]. Similar to the PUREX process, the COEXTM process involves in the first two steps the dissolution of waste nuclear fuel in nitric acid followed by extraction of both uranium and plutonium through liquid–liquid extraction using also TBP. The back-extraction step towards the aqueous phase has been optimized in the COEXTM process, so as to generate, in addition to an aqueous flux containing only uranium, another one containing both uranium and plutonium (U:Pu < 20%) [1]. Once uranium and plutonium from the mixed aqueous flux have been purified from minor impurities by liquid–liquid extraction, this flux can be directly used for the production of MOx fuel. This is accomplished through the oxalic coprecipitation of uranium(IV) and plutonium(III) from the aqueous phase [6], followed by a calcination step, which results in the formation of a mixed oxide (U,Pu)O₂ powder. Whether in the PUREX or COEXTM processes, oxalic acid (co)precipitation is carried out in aqueous medium, after a back-extraction step of Pu involving Pu(III). Thus, even though these two recycling methods are efficient in the production of MOx, they still involve numerous steps, especially due to the need to proceed to Pu(IV) reduction into Pu(III). The latter reduction is usually performed using U(IV) generated using hydrazine as a reducing agent, a carcinogenic substance.

Back-extraction of metallic elements from an organic phase through precipitation, also known as precipitation stripping, has been reported in the literature [7–11]. This process combines both the concentration of metal ions in the aqueous phase (stripping) and precipitation stages when bringing the metal-containing organic solution into contact with the aqueous solution containing the precipitating

agent. Most of these examples rely on oxalic acid use, and have been applied to the separation and purification of heavy metals and lanthanides. The process results in the formation of metal oxalate precipitates in the aqueous ($C_2O_4H_2$) phase, from which they can be collected by filtration. The extraction of plutonium (IV) from a plutonium-containing calcium fluoride slag issued from the production of plutonium metal was realized through direct oxalic precipitation from the organic phase [12]. Plutonium was first extracted in an organic solution containing TBP at 20% (v/v) in kerosene. The plutonium-charged organic phase was then put in contact with an aqueous solution of 0.25 mol/L $C_2O_4H_2$ in HNO_3 (1.5 to 3.0 mol/L). After 30 min of stirring, plutonium was precipitated in the aqueous phase in the form of a wet cake of plutonium oxalate [12]. Later on a process for recovering/separating plutonium(IV) from a mixture of plutonium(IV) and uranium(VI) or americium(III) was reported in the literature, through oxalic precipitation from an organic phase of TBP at 15–30% (v/v) in *n*-dodecane [13]. This resulted in the precipitation of plutonium in the form of plutonium oxalate in the aqueous phase, whereas uranium(VI) and americium(III) remained mainly concentrated in the organic solution.

To our knowledge, the oxalic coprecipitation of uranium and plutonium from the organic phase has not yet been reported in the literature. Therefore, with the aim of reprocessing uranium and plutonium issued from spent nuclear fuel through the production of MOx, we have studied the possibility of coprecipitating both actinides directly from the organic phase using oxalic acid as a precipitating agent through precipitation stripping. This approach aims to reduce the number of steps required for recycling U and Pu compared to the PUREX and COEXTM processes, by avoiding the back-extraction into the aqueous phase through reduction of Pu(IV) into Pu(III). The key points presented in this study are (1) the efficiency of the precipitation of both actinide(IV) and actinide(VI), and (2) the possibility of controlling the ratio of both metals in the precipitate obtained. The latter objective was motivated by the need to develop non-proliferating spent fuel reprocessing sequences, which avoid isolation of pure plutonium, as detailed in one of our previous studies [14]. This proof-of-concept study was carried out using thorium(IV) as a substitute for plutonium(IV).

The solids obtained were characterized to assess the mechanism of precipitation and their suitability for use in the further reprocessing sequence. The presence of an unwanted by-product was evidenced in the case of uranium(VI) precipitation stripping, and the experimental conditions were optimized to inhibit its occurrence.

2. Experimental section

All the reagents were used as received and without any further modification. Uranyl nitrate hexahydrate $\text{UO}_2(\text{NO}_3)_2 \cdot 6\text{H}_2\text{O}$ and $\text{Th}(\text{NO}_3)_4 \cdot 5\text{H}_2\text{O}$ were supplied by the CEA. Tri-*n*-butylphosphate (TBP, 97% pure), *n*-dodecane (<99% pure) and oxalic acid dihydrate were purchased from Sigma aldrich/Merck. Powder XRD (PXRD) patterns were obtained on a Bruker D8 Advance diffractometer, using $\text{CuK}\alpha$ radiation ($\lambda = 1.5418 \text{ \AA}$). Scanning electron microscopy (SEM) images were acquired using a FEI Quanta 200 environmental scanning electron microscope, the morphology of the samples was recorded with a secondary electron (SE) detector, whereas a backscattered electron detector (BSED) was used to detect the presence of the different elements constituting the precipitates through energy dispersive X-ray (EDX) analyses. Fourier transform infrared (FT-IR) spectroscopy analyses were performed on a IR-FT100 spectrometer from Perkin Elmer, equipped with an MIR source, a DTGS detector and an attenuated total reflectance (ATR) measurement mode. Analyses were carried out by placing a drop of the liquid or a pinch of the solid on the surface of the diamond analyzer. Thermo-gravimetric and thermodifferential analyses coupled with mass spectrometry (TGA-TDA-MS) were carried out on a SETSYS EVO 16 machine supplied by Setaram and coupled with a Hiden QGA300 mass spectrometer for gas analysis.

2.1. Liquid–liquid extraction: obtaining an organic phase highly charged in actinides

The general liquid–liquid extraction protocol involved an aqueous solution of $\text{UO}_2(\text{NO}_3)_2 \cdot 6\text{H}_2\text{O}$ (0.326 M) or a mixture of $\text{UO}_2(\text{NO}_3)_2 \cdot 6\text{H}_2\text{O}$ (0.326 M) and $\text{Th}(\text{NO}_3)_4 \cdot 5\text{H}_2\text{O}$ (0.18 M) in HNO_3 6 M. An organic solution of TBP (1 M) in *n*-dodecane was prepared and pre-equilibrated with 6 M HNO_3 by mixing the two solutions in an ampoule, shaken manually

for 10 min. Afterward, both phases were separated (A:O volume ratio equal to 5:1), and the aqueous phase was discarded. The organic solution of TBP and the aqueous solution containing U(VI) and Th(IV) were introduced into an Eppendorf tube and shaken in an Eppendorf Thermomixer at 20 °C and 100 rpm during 10 min. At the end of the extraction step, the organic solution, loaded in actinides, was separated from the aqueous phase. The former was stored for use in organic-phase oxalic precipitation.

2.2. Precipitation stripping of uranium and thorium

An aqueous $\text{C}_2\text{O}_4\text{H}_2$ solution in HNO_3 (see details in the Results and discussion section for the concentrations of $\text{C}_2\text{O}_4\text{H}_2$ and HNO_3 , volume 500 μL) was introduced into a 5 mL glass vial equipped with a magnetic stirrer. This was followed by the addition of the organic solution recovered from liquid–liquid extraction in a dropwise manner (500 μL) while stirring at 500 rpm at 20 ± 2 °C. Stirring was maintained for 1–2 h (see the Results and discussion section for the precise stirring time for the different experiments), after which the mixture was centrifuged, and the aqueous and organic phases, in addition to the solid precipitate, were collected. The liquid phases were stored in Eppendorf tubes for further ICP analyses (see below). The solid precipitate was washed with *n*-dodecane, then with *n*-heptane, and then dried at 40 °C for a few hours. The precipitation yield was determined from the mass balance after analysis of both remaining liquid aqueous and organic phases.

2.3. Quantification of uranium and thorium in solutions

Quantification of metals in solution was performed using inductively coupled plasma atomic-emission spectrometry (ICP-AES) with a Spectro Acros apparatus from Ametek. Aqueous phases were directly analyzed, using an aliquot directly diluted in a matrix solution consisting of 1% aqueous HNO_3 and 1% aqueous HCl, with a minimum HNO_3 :HCl volume ratio of 9:1. In order to determine the concentration of the actinides remaining in the organic phase after precipitation, these were back-extracted by a solution of HNO_3 0.01 M (A:O volume ratio equal to 100:1). The organic and aqueous solutions were introduced

into an Eppendorf tube and shaken at 20 °C and 1000 rpm for 10 min. The aqueous phase was then recovered and diluted in a matrix solution consisting of 1% aqueous HNO₃ and 1% aqueous HCl with a HNO₃:HCl volume ratio of 9:1.

3. Results and discussion

The experimental studies were conducted on an organic phase designed in order to mimic the extraction phase obtained during the first stage of the PUREX process [1]. In the PUREX process, after spent fuel dissolution in nitric acid, uranium(VI) and plutonium(IV) are extracted during a multistage counter-current extraction process, leading to a ca. 100 g/L load in U(VI). In the present study, we employed as organic phase a 1 M TBP solution in *n*-dodecane, which was loaded with uranium(VI) and thorium(IV) (as a substitute for plutonium(IV)) after a one-stage liquid–liquid extraction of a synthetic 6 M HNO₃ aqueous phase, prepared from U(VI) and Th(IV) nitrate salts. The load in U(VI) in the synthetic aqueous phase was close to saturation (0.326 M UO₂(NO₃)₂·6H₂O), in order to approach the targeted 100 g/L U(VI) concentration in the organic phase. The Th(IV) concentration in the synthetic aqueous phase (0.18 M Th(NO₃)₄·5H₂O) was chosen in order to reach a U:Th ratio of about 9:1 in the organic phase after liquid–liquid extraction, a value close to what is expected to occur (for Pu(IV)) when waste MOx fuel is recycled). Concentrations of U(VI) and Th(IV) in the organic phase were therefore 0.28 mol/L and 33 mmol/L respectively, i.e., 66 and 7.6 g respectively.

From a general point of view, actinides(IV) and actinides(VI) are well extracted into TBP-based organic solvents, contrary to actinides(III) (and actinides(V)) [1]. As a consequence, during the PUREX process, efficient stripping of plutonium is performed after reduction of Pu(IV) into Pu(III), which is considered inextractible, with distribution coefficients of about 10⁻². This step is required to get complete decontamination of organic phase from plutonium. Use of a low concentration HNO₃ aqueous solution leads to complete stripping only when a high aqueous-to-organic phase volume ratio is employed. This leads to complete stripping of U(VI) also, as exploited for the quantification of both U and Th in organic phases employing an aqueous-to-organic phase volume ratio equal to 100. Using a phase

volume ratio equal to 1, with a 0.1 M HNO₃ aqueous solution, stripping of Th(IV) is incomplete (ca. 90%) and 35% U(VI) is stripped as well. Complete actinide(IV) stripping was therefore approached using oxalic acid. As oxalic acid is not soluble in the organic phase, the stripping of U and Th from the organic phase via precipitation was performed by putting in contact the organic phase with an aqueous C₂O₄H₂ solution. The latter was prepared by dissolving oxalic acid dihydrate in a dilute HNO₃ solution or in water.

The coprecipitation of U and Th was carried out through dropwise addition of the actinide solution into the aqueous C₂O₄H₂ solution, using a volume ratio of the precursor solutions equal to one. All experiments were conducted at room temperature in a controlled environment (20 ± 2 °C), and temperature effect was not studied. In a first set of experiments, the concentration of C₂O₄H₂ in the initial aqueous solution was varied between 0 and 0.214 M, while fixing that of HNO₃ at 0.1 M (in anticipation of work with Pu(IV) which readily forms hydroxides unless in very acidic media). In these experiments, the quantity of C₂O₄H₂ was maintained lower than the quantity required for the total precipitation of both actinides present in the organic solvent (i.e., the sum of the molar amount of U(VI) and twice the molar amount of Th(IV)), in order to observe selectivity between U and Th precipitation. It was rapidly established that Th precipitates preferentially, even in the presence of U. Based on analysis of both aqueous and organic phases, at [C₂O₄H₂] < 0.114 M, thorium was totally precipitated (Table 1), whereas no traces of uranium were detected in the precipitate. When the amount of C₂O₄H₂ required for complete Th(IV) precipitation (0.07 M expressed in concentration, twice the amount of Th(IV)) was reached, U(VI) precipitation was not observed, and U(VI) was simply stripped into the aqueous phase. At 0.085 M C₂O₄H₂ concentration, about 37% of U(VI) were stripped from the organic phase, with no U(VI) detected in the precipitate. Only at [C₂O₄H₂] ≥ 0.114 M did uranium start precipitating, with the precipitation yield increasing as expected with the increase in C₂O₄H₂ concentration until it reached 46% at 0.214 M. Th was always found in the precipitate (as long as sufficient C₂O₄H₂ was added), but even at high C₂O₄H₂ concentration, U(VI) was distributed between the 3 phases, with non-negligible amount in the aqueous phase. The change in order of addition (i.e., addition of aqueous

Table 1. Variation of the mass percentage of uranium and thorium in the solid precipitate and organic phase as a function of the concentration of $C_2O_4H_2$ after organic-phase precipitation

[$C_2O_4H_2$]	0 M		0.057 M		0.085 M		0.114 M		0.142 M		0.214 M	
	U	Th	U	Th	U	Th	U	Th	U	Th	U	Th
Organic	65%	9%	68%	N.D.	63%	N.D.	56%	N.D.	51%	N.D.	37%	N.D.
Solid			0%	84%	0%	99%	13%	99%	23%	99%	46%	99%
(U:Th) _s			0		0		1.1		1.9		3.9	

Notes: $[HNO_3]$ is fixed at 0.1 M, and the complement to 100% represents the fraction of the considered element in the aqueous phase.

phase into organic solution) did not change the outcome of the reaction. The U(VI) precipitation was also found to have no kinetic limitation since rapid precipitation was observed, with no evolution after 30 min. The latter observation also revealed that it is difficult to decipher the detailed mechanism of precipitation stripping, i.e., to make the difference between direct precipitation in the organic phase after extraction of $C_2O_4H_2$ into the organic phase, or stripping of metal cations into the aqueous phase followed by precipitation with oxalic acid in the aqueous phase. As oxalic acid is poorly soluble in organic media, it can be suspected however that the precipitation occurs in the aqueous phase, or at least at the interface between both phases.

PXRD analysis of the solids obtained (Figure 1) revealed the precipitation of thorium in the form of thorium oxalate hexahydrate $(Th(C_2O_4)_2 \cdot 6H_2O)$ in all cases. At the concentration at which uranium starts precipitating (i.e., when $[C_2O_4H_2] \geq 0.114$ M), in addition to the peaks corresponding to $Th(C_2O_4)_2 \cdot 6H_2O$, peaks between 8 and 9° (2θ) started to appear, which surprisingly do not correspond to uranyl oxalate trihydrate $(UO_2(C_2O_4) \cdot 3H_2O)$. It is also important to note that the intensities of these peaks increased with increasing concentrations of $C_2O_4H_2$. Furthermore, these peaks could not be identified based on the ICDD (International Center for Crystal Data) and, thus correspond to an unknown phase. The expected peaks for uranyl oxalate were not detected in the diffractogram (Figure 1).

With the aim of determining the nature of the elements constituting the precipitates resulting from the organic-phase precipitation at different $C_2O_4H_2$ concentrations, EDX analyses were carried out. In addition to Th, U, C, and O, the spectra obtained revealed the presence of phosphorus in the powder

obtained for $[C_2O_4H_2] \geq 0.114$ M, whereas no phosphorus was detected at lower concentrations for which only Th was precipitated. These results may indicate that uranium, phosphorus and oxalate precipitate simultaneously. Furthermore, as TBP is the only source of phosphorus in the precipitation medium, it can be assumed that the uranium solid obtained probably contains TBP. Solids composed of uranium(VI) and analogs of TBP, including trimethylphosphate (TMP) and triisobutylphosphate, have already been reported in the literature [15,16]. Furthermore, Rahman *et al.* reported the formation of a TBP-containing solid during the precipitation stripping of U(VI) from TBP/kerosene by NH_4OH [10]. The presence of TBP in the solid was confirmed through complementary experiments that involved carrying out the precipitation of only uranium under the same precipitation stripping conditions (in terms of $C_2O_4H_2$ and HNO_3 concentrations). The results obtained are presented in the supporting information along with further characterization of the uranium precipitate. These analyses proved the presence of oxalate, nitrate or nitric acid, and uranium in the solid, but could not allow determination of its precise composition. Thus, the mixed-composite uranium solid will be referred to as U-TBP-Ox in the following.

When a phosphorus-containing uranium compound is calcined, a uranium phosphate is expected. Such a product is incompatible with the objectives of this work, which aims at obtaining precursors of actinide dioxides for MOx fuel. Uranium phosphates are minerals known for their relatively high chemical stability [17], once formed, and their transformation into uranium oxide is not possible. It is therefore essential to obtain only actinide oxalates at the end of the precipitation from the organic phase, so as not to

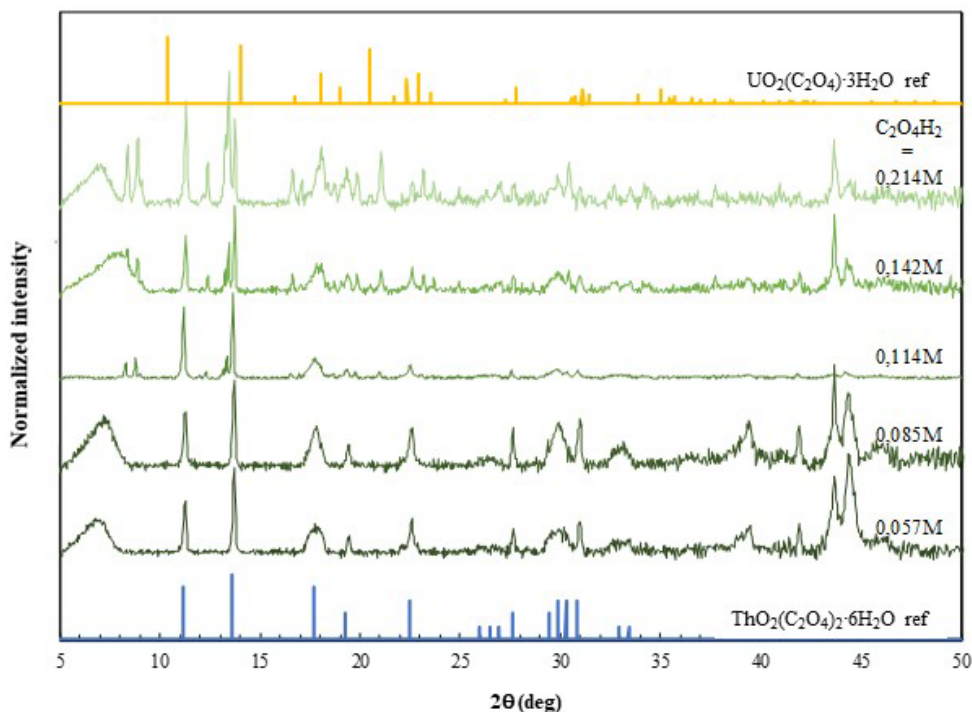


Figure 1. PXRD patterns of the precipitates obtained from organic-phase precipitation of uranium and thorium at variable $\text{C}_2\text{O}_4\text{H}_2$ concentrations and a fixed HNO_3 concentration of 0.1 M. Reference diffractograms of $\text{UO}_2(\text{C}_2\text{O}_4) \cdot 3\text{H}_2\text{O}$ and $\text{Th}(\text{C}_2\text{O}_4)_2 \cdot 6\text{H}_2\text{O}$ correspond to JCPDS No. 01-073-7325 and No. 00-022-1485, respectively.

introduce any phosphate impurities during the step of conversion into oxide by calcination, which could be difficult to remove [18].

Neither the mode of addition (organic into aqueous or vice versa) nor the stirring speed affected the nature of the precipitate obtained. Therefore, attempts towards precipitating uranyl oxalate from the organic phase without the precipitation of U-TBP-Ox were mainly focused on varying the concentration of $\text{C}_2\text{O}_4\text{H}_2$ and HNO_3 in the precipitation medium. To this end, a new set of experiments was carried out by increasing the HNO_3 concentration in the precipitation medium to 2 M (compared to 0.1 M in the previous set of experiments), whereas the oxalic acid concentration was varied between 0.08 and 0.24 M. The results obtained showed that thorium still totally precipitates at all $\text{C}_2\text{O}_4\text{H}_2$ concentrations, whereas uranium partially precipitates for $[\text{C}_2\text{O}_4\text{H}_2] \geq 0.2$ M (Table 2). It is important to note that, compared to the previous set of experiments (realized at a lower HNO_3 concentration), the precipitation yield of

uranium decreased, probably as U(VI) is more stabilized in the organic phase. This can be related to the fact that increasing aqueous HNO_3 concentration leads to an increase in the distribution ratio of U(VI) between an aqueous nitrate phase and a 30% TBP in *n*-dodecane organic phase. Consequently, the maximum U(VI):Th(IV) mass ratio reached 1.8, compared to 3.3 at lower HNO_3 concentrations. However, compared to the previous set of experiments realized at $[\text{HNO}_3] = 0.1$ M, in addition to the formation of $\text{Th}(\text{C}_2\text{O}_4)_2 \cdot 6\text{H}_2\text{O}$, XRD analyses revealed the formation of $\text{UO}_2(\text{C}_2\text{O}_4) \cdot 3\text{H}_2\text{O}$ at $[\text{HNO}_3] = 2$ M, with the intensity of the peaks corresponding to U-TBP-Ox being relatively low and decreasing with the increase in $\text{C}_2\text{O}_4\text{H}_2$ concentration (Figure 2). This indicates that increasing the concentrations of both $\text{C}_2\text{O}_4\text{H}_2$ and HNO_3 in the precipitation medium favors the precipitation of uranyl oxalate compared to U-TBP-Ox.

Therefore, with the aim of precipitating uranyl oxalate while limiting the precipitation of the

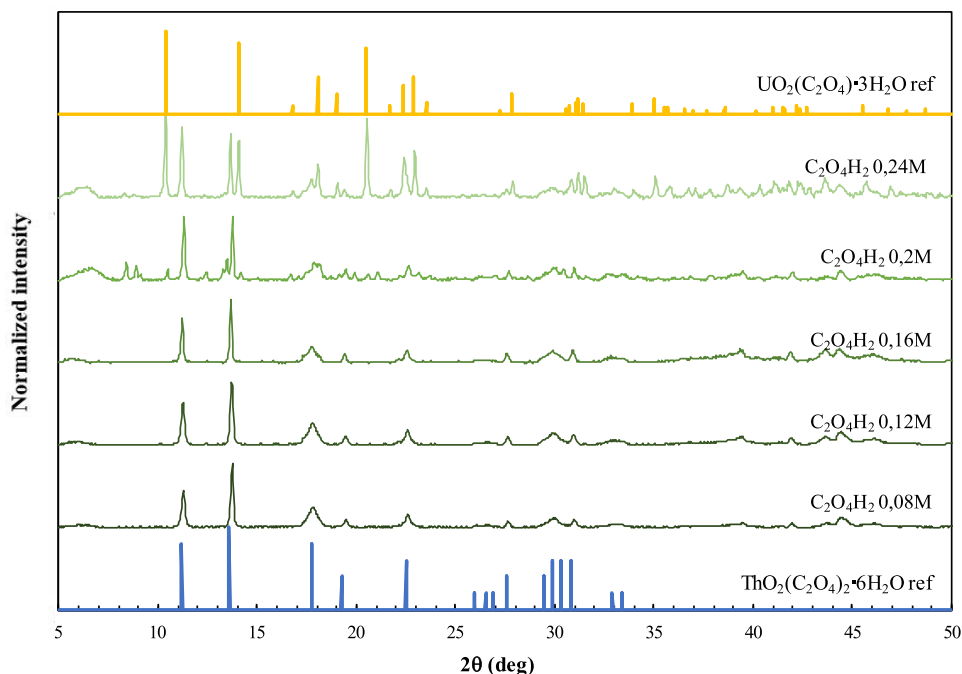


Figure 2. PXRD patterns of the precipitates obtained from organic-phase precipitation of uranium and thorium at variable $C_2O_4H_2$ concentrations and a fixed HNO_3 concentration of 2 M.

Table 2. Variation of the mass percentage of uranium and thorium in the solid precipitate and organic phase as a function of the concentration of $C_2O_4H_2$ after organic-phase precipitation

[$C_2O_4H_2$]	0.08 M		0.12 M		0.16 M		0.2 M		0.24 M	
	U	Th	U	Th	U	Th	U	Th	U	Th
Organic	81%	N.D.	78%	N.D.	74%	N.D.	61%	N.D.	51%	N.D.
Solid	0%	99%	0%	99%	5%	99%	24%	99%	33%	99%
(U:Th) _s	0		0		0.4		1.8		2.5	

Notes: [HNO_3] is fixed at 2 M, and the complement to 100% represents the fraction of the considered element in the aqueous phase.

U-TBP-Ox impurity, additional experiments were carried out while further increasing both $C_2O_4H_2$ and HNO_3 concentrations to 0.3 and 4 M, respectively. The XRD pattern of the precipitate formed is shown in Figure 3 (top). The results obtained show the precipitation of both uranium and thorium in the form of oxalates, with the complete absence of the U-TBP-Ox impurity, which was also confirmed by EDX analysis, which revealed the complete absence of phosphorus. Moreover, increasing the concentration of $C_2O_4H_2$ and HNO_3 increased the

precipitation yield of uranium to 95%, with Th still being totally precipitated and the U-TBP-Ox impurity not detected.

The control of the U:Th mass ratio during the precipitation experiment seems to be the result of a higher solubility of uranyl oxalate ($\text{Log}K_s = -8.5$ [19]) compared to thorium oxalate ($\text{Log}K_s = -24$ [20]). As the latter compound is more stable, it is reasonable to suppose that its precipitation occurs more quickly. Furthermore, uranyl oxalate is expected to be slightly soluble in water at 20 °C, with a

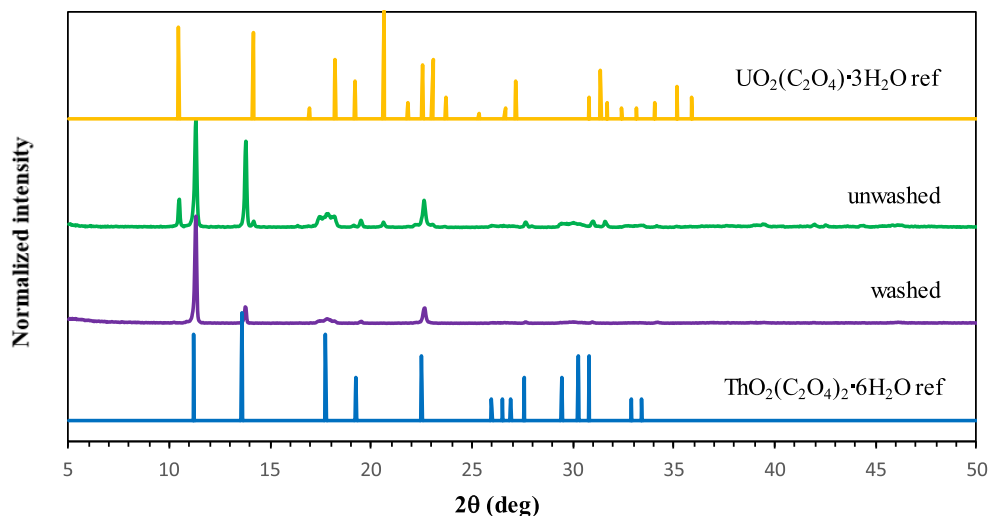


Figure 3. PXRD patterns of the precipitate obtained from organic-phase precipitation of uranium and thorium under optimized conditions ($[\text{C}_2\text{O}_4\text{H}_2] = 0.3 \text{ M}$ and $[\text{HNO}_3] = 4 \text{ M}$) after washing with dodecane (top) and washing with water (bottom).

solubility of about 23 mg/L (0.05 mmol/L, corresponding to 13 mg/L uranium). On the contrary, thorium oxalate has a very low solubility, in the nanomolar range. Thus, a post-synthetic treatment of the precipitate was proposed in order to remove uranyl oxalate from thorium oxalate through washing: the precipitate was washed with distilled water. The elimination of uranyl oxalate could be observed by the color of the precipitate which changed from pale yellow to white after the second wash, as uranyl oxalate is characterized by its pale yellow color. Moreover, ICP analysis performed on the supernatant revealed the presence of uranium (no traces of thorium) after the first and second wash. XRD analysis (Figure 4) performed on the precipitate revealed the presence of only $\text{Th}(\text{C}_2\text{O}_4)_2 \cdot 6\text{H}_2\text{O}$ with no traces of $\text{UO}_2(\text{C}_2\text{O}_4) \cdot 3\text{H}_2\text{O}$.

Therefore, following the oxalate precipitation from the organic phase, the uranium- and thorium-based precipitates can be separated through washing with water, and the U:Th ratio in the solid material can be further adjusted with Th always remaining in the solid. This allows a perfect control of the oxalate mixture composition before calcination. Uranium can be recovered from the remaining phases, and recovered through precipitation after addition of further $\text{C}_2\text{O}_4\text{H}_2$. The proposed approach thus enables

rapid recovery of Th(IV) from the U:Th mixture in the organic phase, either as such, or in the presence of a controlled amount of U(VI). Such studies pave the way towards the reprocessing of U(VI)/Pu(IV) phases, in order to enable multirecycling of Pu(IV) into MOx fuel.

These results suggest that uranium and thorium precipitate separately and do not coprecipitate to form a single material. Based on SEM analyses, the precipitate obtained exhibits a platelet shape (Figure 4). Moreover, EDX analysis reveals that U and Th are not systematically colocalized: some microdomains are Th-rich, whereas some others are U-rich (Figure 4). Altogether, whether the precipitation occurs in organic or aqueous phase, or at the interface, Th(IV) precipitates first as thorium oxalate, followed by U(VI) as uranyl oxalate as soon as acid content of the aqueous phase is sufficient. The U:Th ratio is monitored through either adjustment of the $\text{C}_2\text{O}_4\text{H}_2$ concentration, or after precipitation via selective leaching of uranyl oxalate.

4. Conclusion

During this study, we established the possibility of recovering Th(IV) by precipitation stripping using oxalic acid $\text{C}_2\text{O}_4\text{H}_2$, in the presence of a controlled

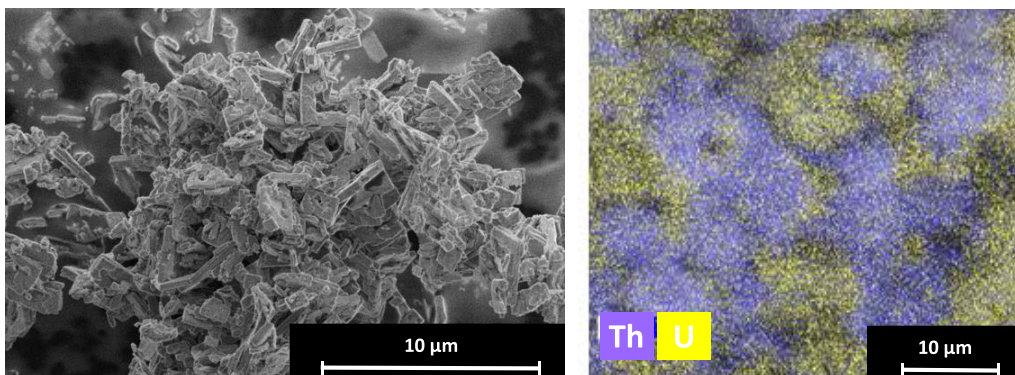


Figure 4. SEM analysis of the precipitate obtained from organic-phase precipitation of uranium and thorium under optimized conditions ($[\text{C}_2\text{O}_4\text{H}_2] = 0.3 \text{ M}$ and $[\text{HNO}_3] = 4 \text{ M}$): SE mode (left) and EDX-based elemental mapping of Th and U (right).

amount of U(VI), from an organic phase mimicking that which arises from the classical PUREX process. Th(IV) is quantitatively stripped as long as sufficient $\text{C}_2\text{O}_4\text{H}_2$ is introduced, whereas U(VI) only partially precipitates unless excess $\text{C}_2\text{O}_4\text{H}_2$ is employed. Furthermore, the results obtained show that clean precipitation of U and Th from the organic phase in the form of pure actinide oxalates was attained by controlling the concentrations of $\text{C}_2\text{O}_4\text{H}_2$ and HNO_3 in the precipitation medium. The U:Th ratio in the final solid is controlled by the amount of $\text{C}_2\text{O}_4\text{H}_2$ employed, and can be further adjusted through washing with water as $\text{UO}_2(\text{C}_2\text{O}_4) \cdot 3\text{H}_2\text{O}$ is more soluble in water than $\text{Th}(\text{C}_2\text{O}_4)_2 \cdot 6\text{H}_2\text{O}$. Compared to the PUREX process currently employed at industrial scale to recover U and Pu from waste nuclear fuel for the further production of MOx, precipitation stripping seems to be highly promising, as it allows the stripping of actinide(IV) without the aid of a reducing agent. Furthermore, this work opens the door for the application of precipitation stripping using other organic ligands as precipitating agents, which may lead to various morphologies of the uranium- and thorium-based precipitates and, eventually, to better control over the calcination and pelletization steps.

Declaration of interests

The authors do not work for, advise, own shares in, or receive funds from any organization that could benefit from this article, and have declared no affiliations other than their research organizations.

Supplementary data

Supporting information for this article is available on the journal's website under <https://doi.org/10.5802/crchim.320> or from the author.

References

- [1] E. Abonneau, P. Baron, C. Berthon *et al.*, *Treatment and Recycling of Spent Nuclear Fuel Actinide Partitioning—Application to Waste Management*, CEA and Editions du Moniteur, France, 2008.
- [2] E. R. Bertelsen, M. R. Antonio, M. P. Jensen, J. C. Shafer, *Solvent Extr. Ion Exch.*, 2021, **40**, 64–85.
- [3] J. Durain, D. Bourgeois, M. Bertrand, D. Meyer, *Solvent Extr. Ion Exch.*, 2019, **37**, 328–346.
- [4] B. Arab-Chapelet, S. Grandjean, G. Nowogrocki, F. Abraham, *J. Alloys Compd.*, 2007, **444–445**, 387–390.
- [5] S. Grandjean, A. Beres, C. Maillard, J. Rousselle, “Method for coprecipitation of actinides in different oxidation states and method for preparation of mixed compounds of actinides”, US2005288542 (A1), December 29, 2005. https://worldwide.espacenet.com/publicationDetails/biblio?FT=D&date=20051229&DB=EPODOC&locale=fr_EP&CC=US&NR=2005288542A1&KC=A1&ND=4 (accessed 2023-12-04).
- [6] D. Parmentier, M. Bertrand, E. Plasari, P. Baron, *Cryst. Struct. Theory Appl.*, 2013, **2**, 75–87.
- [7] S. Zielinski, M. Buca, M. Famulski, *Hydrometallurgy*, 1998, **48**, 253–263.
- [8] Y. Konishi, Y. Noda, S. Asai, *Ind. Eng. Chem. Res.*, 1998, **37**, 2093–2098.
- [9] Y. Konishi, Y. Noda, *Ind. Eng. Chem. Res.*, 2001, **40**, 1793–1797.
- [10] T. Palden, M. Regadio, B. Onghena, K. Binnemans, *ACS Sustainable Chem. Eng.*, 2019, **7**, 4239–4246.
- [11] K. Shah, K. Gupta, B. Sengupta, *J. Environ. Chem. Eng.*, 2017, **5**, 5260–5269.

- [12] F. Foxton, "Improvements in or relating to the recovery of plutonium from solutions containing it", GB783601A, September 25, 1957. <https://patents.google.com/patent/GB783601A/en> (accessed 2023-12-04).
- [13] L. H. J. M. Baetsle, P. P. M. H. D. Regge, D. J. G. Huys, S. Nemoto, "Procédé de Séparation Ou de Récupération de Plutonium et Plutonium Ainsi Obtenu", EP0251399A1, January 7, 1988. <https://patents.google.com/patent/EP0251399A1/fr> (accessed 2023-12-04).
- [14] J. Durain, D. Bourgeois, M. Bertrand, D. Meyer, *Molecules*, 2021, **26**, article no. 6234.
- [15] J. Diwu, T. Albrecht-Schmitt, in *Structural Chemistry of Transuranium Phosphonates* (A. Clearfield, K. Demadis, eds.), Royal Society of Chemistry, Cambridge, 2011, Chapter 19, 607-631.
- [16] G. Agostini, G. Giacometti, D. A. Clemente, M. Vicentini, *Inorg. Chim. Acta*, 1982, **62**, 237-240.
- [17] D. Gorman-Lewis, P. C. Burns, J. B. Fein, *J. Chem. Thermodyn.*, 2008, **40**, 335-352.
- [18] P. M. Smith, G. K. Schweitzer, S. McLain, *Metall. Mater. Trans. B*, 2002, **33**, 146-147.
- [19] F. Abraham, B. Arab-Chapelet, M. Rivenet, C. Tamain, S. Grandjean, *Coord. Chem. Rev.*, 2014, **266-267**, 28-68.
- [20] T. Kobayashi, Y. Sasaki, I. Takagi, H. Moriyama, *J. Nucl. Sci. Technol.*, 2009, **46**, 1085-1090.

Review article

GDR Prométhée – French Research Network on *Hydrometallurgical Processes for Primary and Secondary Resources*

Solvent extraction of uranium from an acidic medium for the front-end of nuclear fuel cycle: from mechanisms understanding to innovative process design

Fabrice Giusti^{✉,*}, Elise Guerinoni^{✉,a}, David Lemire^{✉,a}, Marine Thimotée^a, Guilhem Arrachart^{✉,*}, Sandrine Dourdain^{✉,a} and Stéphane Pellet-Rostaing^{✉,a}^a ICSM, Univ Montpellier, CEA, CNRS, ENSCM, Marcoule, France

E-mails: fabrice.giusti@cea.fr (F. Giusti), guilhem.arrachart@cea.fr (G. Arrachart)

Abstract. Despite the fact that methods for uranium extraction from an acidic medium (sulfuric, phosphoric or nitric) are relatively robust processes, the search for more efficient systems in terms of extraction efficiency and selectivity with respect to competitor ions remains relevant. To address this challenge, researchers have developed a wide range of new extracting molecular agents that allow efficient and selective liquid–liquid extraction of the target metal. After delivering a synoptic reminder of the former hydrometallurgical processes on which dogmas have been based, we present an exhaustive report of the structures that have been designed, synthesized and evaluated as useful hydrometallurgical tools for the extraction of uranium focused on the front-end of the nuclear fuel cycle. Moreover, peculiar emphasis has been given to theoretical aspects related to parameters, such as amphiphilic properties, which influence the extraction mechanism involved in each system, be it mono- or multifunctional ligand. Concluding remarks were afforded as consistent milestones of a prospective and promising route for the next hydrometallurgy including the influence of the stereochemistry.

Keywords. Uranium, Nuclear fuel cycle, Solvent extraction, Extractants synthesis, Chiral ligand, Mechanism.

Manuscript received 30 September 2023, revised 20 December 2023, accepted 24 January 2024.

1. Introduction

The nuclear fuel cycle includes the front-end steps (mining and milling, conversion, enrichment, and fuel fabrication) that prepare uranium for use in nuclear reactors and the back-end steps that manage spent nuclear fuel (reprocessing and reuse and disposal). Uranium is, in fact, the most widely used

raw material as UOX fuel in nuclear fission power plants, sometimes with Plutonium (MOX fuel). Uranium is relatively abundant in the earth's crust and can be found in various geological deposits (proterozoic unconformity, sandstones, metasomatite, granite-related, carbonates, etc.) [1], rivers and seawater. It can be extracted in a variety of forms and environments, ranging from very low grade to very high grade ores, as well as from mines with a different primary product such as copper or gold. Uranium

*Corresponding authors

resources are divided into conventional and unconventional resources. Conventional resources are defined as resources (pitchblende, uranite) from which uranium is recoverable as a primary product, co-product or significant by-product. Unconventional resources are those from which uranium can only be recovered as a minor by-product. This is particularly the case for low-grade deposits such as phosphate rock or phosphorite, which is mined primarily to produce phosphorus pentoxide for fertilizer production, as well as non-ferrous ores, carbonatite, black shale, rare earth elements (REE) deposits, lignite, and even very low levels of uranium, such as in seawater.

Historically, uranium has been produced primarily by open pit and underground mining techniques and then processed by conventional uranium milling, leaching and separation from the leach solutions by solvent extraction or ion exchange. Uranium can thus be recovered from the ore using dynamic or heap leaching processes, in which the preliminary crushed ore is either mixed with oxidizing acid or base solutions in a tank, or placed on an engineered barrier sprayed with acid or base. Other mining methods include in situ leaching (ISL), which involves the extraction of uranium from the deposit using an acid or alkaline solution directly injected into the confined underground zone, followed by chemical treatment to purify it. Sulfuric acid is the most common acid used in the leaching process because uranium sulfate salt is readily soluble in the hexavalent state. An oxidizing agent (sodium chlorate or manganese dioxide) is usually required because most of ores contain tetravalent uranium, which is poorly soluble in the acidic leach solutions. The resulting leach solutions consist of complex acid sulfate solutions containing a wide variety of ions in addition to uranium, including aluminum, calcium, iron, magnesium, molybdenum, vanadium, etc., depending on the composition of the ore being treated. It is therefore necessary to implement a stage for the separation of the uranium present in a sulfuric acid phase. However, uranium can also be found in a phosphoric acid phase if it comes from wet-process phosphoric acid (WPA) or in a nitric acid phase if it comes from the final purification before conversion and enrichment steps.

As a result, uranium can be present in different acidic environments (sulfuric, phosphoric or nitric,

etc.), which requires different conditions for its extraction and recovery involving specific extractants.

Despite the efficiency of the current systems, but due to some drawbacks, the search for more efficient and selective systems for uranium extraction and recovery with respect to competing ions is still relevant.

Through this review, we present the research carried out to understand and capture the mechanisms involved in the classical processes, but also the search for new systems.

2. Molecular systems for the extraction of uranium from conventional ores

The marketable uranium product, Yellowcake, can be obtained through various processes, depending on the origin of the ore from which it is produced. Uranium ores are categorized into two types: primary or conventional ores, which are the richest, and secondary ores, from which uranium is sometimes extracted as a by-product. The primary source of uranium production is obtained from conventional ores, achieved through the utilization of sulfuric acid leach liquors. The ore extracted from mine, whose fragments measure some centimeters or more in diameter, is crushed and ground to the consistency of fine sand. Since most of the conventional ores currently processed contain around 0.02% to 0.2% recoverable uranium, it is necessary to process 500 to 5000 kg of ore for each every kilogram of uranium recovered. Most uranium ore processing plants use wet milling, and the resulting sludge is directed to a leaching circuit, where sulfuric acid is added. Acid consumption does not depend on the uranium content of the ore, but on the constituents of the gangue. Thus total acid consumption can range from 10 kg H_2SO_4 per tonne of ore to over 100 kg/tonne. Leaching times vary from a few hours to more than 24. For some ores, leaching times can be considerably reduced by heating the pulp in tanks at temperatures of between 40 °C to 60 °C. However, these processes require purification of the leach liquor to effectively separate uranium from competing elements such as iron (Fe), molybdenum (Mo), zirconium (Zr), and others. Uranium is then selectively extracted from the leach solutions by solvent extraction or ion exchange. The uranium industry was the first hydrometallurgical industry to make extensive use of both processes. In the solvent

extraction process, the active agent is generally an organic molecule diluted in a petroleum fraction such as kerosene, which can selectively extract uranium ions by forming an organic complex that is insoluble in water. The organic phase is separated from the aqueous phase by continuous mixing and settling techniques. The uranium is then re-extracted from the organic complex by contacting it with a solution of inorganic salt, such as sodium chloride or ammonium sulfate. Thus, the marketable uranium product Yellowcake is precipitated from the re-extraction solution by adding ammonia, soda, magnesium hydroxide or hydrogen peroxide, and the resulting solid product is dried and packaged for shipment to a refining facility.

Since current industrial processes predominantly use solvent extraction to reach higher level of purification, this liquid–liquid extraction process consists in contacting the leachate with an immiscible organic solvent, a diluent loaded in lipophilic ligand. Through various interactions (ionic, electrostatic, polar) with the metal cation at the interface, liposoluble metal-ligand complexes are obtained that are then spontaneously transferred from the aqueous leachate to the organic phase. Recovery of the pure metal is then achieved during the back-extraction or stripping step. Depending on the nature of the metal, its release from the solvent can be induced by contact with an aqueous phase that may contain either acid-base or water-soluble ligand before the recovering step by precipitation or electrowinning. The effectiveness of the stripping process is driven by the concentration of the stripping reagent (H^+ , HO^- , etc.) that must be modulated according to the type (neutral or ionizable) of the liposoluble extractant.

Industrial uranium extraction began in 1955 with the development of the DiAlkyl Phosphoric acid EXtraction (DAPEX) process, which utilized di-2-ethylhexylphosphoric acid (HDEHP) as the extractant. This pioneering solvent extraction process was developed and marketed for uranium VI. However, owing to its limited selectivity when it came to competing metals, especially iron, it has been replaced in 1957 by the amine extraction (AMEX) process, which used a mixture of secondary and tertiary amines (in particular Alamine 336, mainly composed of tertiary amines) or more recently pure trialkylamine such as trioctylamine [2].

3. Historical of AMEX and DAPEX processes in sulfuric acid

AMEX and DAPEX processes were actually concomitantly developed at the Oak Ridge National Laboratory (ORNL) during the 50's. First ideas were about the designs of long alkyl chain polyamines but this concept was quickly dropped for the benefits of alkylamines and phosphorous derivatives [3]. Hence, numerous structures such as linear or branched di- or trialkylamines, trialkylphosphines oxide, mono-, di- or triesters of phosphinic, phosphonic or phosphoric acid were considered for uranium extraction. However, only a few of them exhibited the required properties allowing efficient large-scale processing, namely AMEX and DAPEX, discussed below.

3.1. The DAPEX process

The development of the DAPEX process at the ORNL relied on previous results reported by other laboratories where affinity of organophosphorus compounds towards uranium was extensively studied. More specifically, in 1949, it was fortuitously found that the hydrolysis products (mono- and dibutylphosphate) of the tri-*n*-butyl phosphate (TBP) showed higher affinity than that of the parent compound towards uranium in nitric media. Ensuing works allowed to set a first uranium extraction process based on long-chain monoalkylphosphoric acid at the pilot plant scale in 1954. A year earlier, dibutylphosphate was claimed as a potential ligand for uranium extraction from seawater [4].

Consequently, at the ORNL, emphasis was put on the development of a method involving the use of promising phosphate-based ligands. HDEHP was quickly identified as a good candidate as it was a cheap commercially available compound with very low water solubility [4].

Nevertheless, considering that neutral phosphorus derivatives such as phosphine oxides could provide efficient and applicable extraction properties, investigations were also carried out with a series of symmetrical trialkylphosphine oxide (TAPO) in the same laboratory [3].

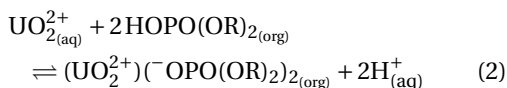
Extraction properties of HDEHP towards uranium contained in sulfuric acid leachates were assessed with regards to (i) ions (sulfate, uranium and other metals) and ligand concentrations, (ii) pH of the

leachate, (iii) nature of the diluent, (iv) temperature, (v) chemical structure of the phase modifier, (vi) volumetric phase ratio (A:O) of aqueous phase volume (A) to organic phase volume (O), (vii) required stripping conditions and (viii) up-scaling feasibility [4,5].

HDEHP is an ionizable acidic extractant that allows the transfer of metal by cationic exchange, that is, n protons are released in aqueous phase by the extractant while m metal cations are trapped in the organic phase. Because this exchange verifies electroneutrality, n and m are correlated as follows:

$$n = k \cdot m \quad (1)$$

where k is the cationic charge of the metal. HDEHP was known to auto-associate depending on its concentration and the nature of the diluent. It has been reported to form dimeric species in hexane, in the 0.025–2.1 mol·L⁻¹ concentration range and larger species at higher concentration [6]. However, before that the properties of HDEHP could be properly established, this transfer was assumed to obey the equilibrium described as follow:



Considering that in the concerned range of concentration, activities could be approximated by concentrations, the equilibrium constant was:

$$K_{\text{ex}} = \frac{\left[(\text{UO}_2^{2+})(^- \text{OPO}(\text{OR})_{2(\text{org})})_{2(\text{org})} \right]_{\text{eq}} \cdot [\text{H}^+]_{(\text{aq})}^2}{\left[\text{UO}_2^{2+} \right]_{\text{eq}} \cdot \left[\text{HOPO}(\text{OR})_{2(\text{org})} \right]_{\text{eq}}^2} \quad (3)$$

Finally, the distribution coefficient of uranium, which is the ratio at equilibrium of transferred uranium concentration to that of the metal remaining in aqueous phase, could be expressed as:

$$D_{\text{U}} = \frac{\left[(\text{UO}_2^{2+})(^- \text{OPO}(\text{OR})_{2(\text{org})})_{2(\text{org})} \right]_{\text{eq}}}{\left[\text{UO}_2^{2+} \right]_{\text{eq}}} \quad (4)$$

Experiments performed with various type of diluents (halohydrocarbons, ethers, plain hydrocarbons, aromatics and fatty alcohols) keeping all other parameters fixed (see above), showed that the best extraction (e.g. highest $D_{\text{U}} \sim 135$ at 298 K) was obtained in kerosene.

Although fatty alcohols were found to drastically impair the extraction of uranium, it was shown that

the organic phase supplemented with v:v 2% 2-ethylhexan-1-ol as a phase modifier (whose essential role is discussed in later section) could maintain a good level of uranium extraction ($D_{\text{U}} \sim 30$) without being subjected to the third phase formation (see AMEX process) occurring in pure kerosene during the stripping step. Thus, while operating with leachates partially miming (pH = 1, sulfate concentration range from 0.2 to 0.5 mol·L⁻¹, 4×10^{-3} mol·L⁻¹ uranium) those recovered with ores processing, first optimal system for uranium extraction could be defined as HDEHP solubilized at 0.1 mol·L⁻¹ in 98:2 v:v kerosene:2-ethylhexan-1-ol mixture. The best uranium extraction performance could be achieved with this mixture at 1:1 A:O at 298 K in short contact time (~ 2 min).

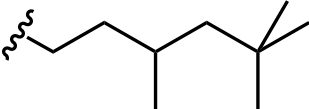
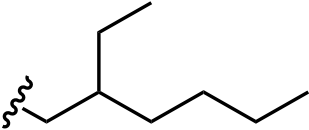
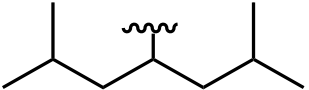
Efficiency and selectivity of the uranium extraction enabled by numerous other dialkylphosphates were evaluated for this system and this was an unexpected opportunity to preliminary investigate the structure-activity relationship (SAR) of the phosphoric diester ligand (Table 1).

Actually, ores leach liquors contain, in addition to uranium, many other elements present in higher or even much higher concentrations than those of uranium. Therefore, beside the affinity of the ligand could be lower for those elements than for the uranium, most of them might represent a cumbersome powerful competitor impairing the extraction process.

For instance, with tests performed according to the conditions previously established for U (VI) and with a 10⁻² mol·L⁻¹ single metal-containing solution, significant extractions were observed for thorium (IV), titanium (IV), iron (III), molybdenum (VI), Vanadium (IV) and cerium (IV) with $D_{\text{M}} = 26$ (Th = Ti), 16, 6, 1.8, 1.1 (V = Ce), respectively. These results also underlined the benefit brought by the fast U extraction equilibrium that should allow to circumvent the huge co-extraction of ferric cations that could take place in real condition at contact time longer than 2 min ($D_{\text{Fe}} \sim 250$ at $t = 7.5$ h with HDEHP). However, the iron extraction could be drastically lowered in the presence of reducing agents that converted ferric ions in ferrous one.

Stripping could be achieved at high mineral acid concentrations as well as in basic condition with 10% sodium carbonate, which was preferred because of its cheap and fast implementation. Moreover,

Table 1. D_U obtained for a series of dialkyl phosphoric esters at two concentrations of sulfate in the aqueous phase with $[U^{VI}] = 4 \times 10^{-3} \text{ mol}\cdot\text{L}^{-1}$

Dialkyl phosphoric ester $O \leftarrow P(OR)_2OH$	Formula of R	D_U ($0.5 \text{ mol}\cdot\text{L}^{-1} \text{ SO}_4^{2-}$)	D_U ($1.5 \text{ mol}\cdot\text{L}^{-1} \text{ SO}_4^{2-}$)
Dioctyl hydrogen phosphate	$n\text{-C}_8\text{H}_{17}\text{-}$	450	57
Bis(3,5,5-trimethylhexyl) hydrogen phosphate		260	41
Bis(2-ethylhexyl) hydrogen phosphate (HDEHP)		135	20
Bis(2,6-dimethylheptan-4-yl) hydrogen phosphate		10	2

Organic phase was $0.1 \text{ mol}\cdot\text{L}^{-1}$ extractant in w:v 98:2 kerosene:ol, contact time was 2 min. with A:O = 1:1. Data extracted from Blake et al. [5].

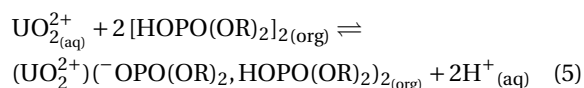
the uranium carbonate complex is water-soluble whereas those of competitors mostly precipitate, allowing thus to remove co-extracted contaminants from the recovered uranium. Nonetheless, as mentioned above, the main issue was the formation of the third phase that resulted from insolubility of HDEHP sodium salt in both phases and that could be addressed by supplying the kerosene with 2% 2-ethylhexan-1-ol. Once again, SAR could be explored for phase modifier and ligand. A significant impact of both the branching and the length of the alkyl chain was typically demonstrated but without place for some comprehensive explanations (see Table 2).

In a last stage, synthetic leachate liquors containing U, Fe and Al were processed on a pilot scale to allow the recovery (after acidic hydrolysis of carbonate salts and precipitation with ammonia and finally after calcination) of 98% U under its 78–84% pure U_3O_8 form.

Subsequent works focused on the use of neutral organophosphorus compounds as phase modifiers. At variance with fatty alcohol, few amount of trialkylphosphates, dialkylphosphonates or TAPO were found to increase the D_U by several orders of magnitude when compared to each respective D_U (ranging

from 0 to 5.9 for various TAPO tested at $0.3 \text{ mol}\cdot\text{L}^{-1}$ in kerosene, for instance) and to improve the selectivity towards U. TBP, dibutyl butylphosphonate (DBBP) and tributylphosphine oxide (TBPO) provided the strongest synergies (see Table 3).

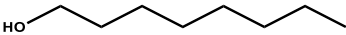
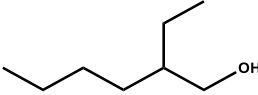
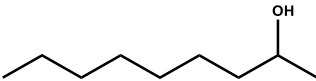
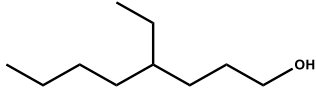
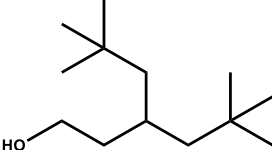
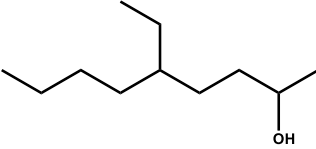
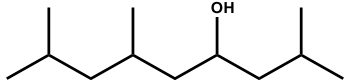
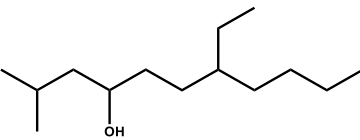
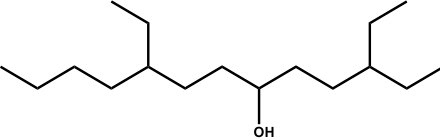
This synergy was explained by Blake et al. [7] after considering the revisited mechanism of U extraction mediated by HDEHP where the ligand forms dimers in the organic diluent. At low levels (maximum organic uranium concentration four times lower than that of HDEHP) [6] of extraction the associated equilibrium became:



And at a high level of extraction, (minimum organic uranium concentration more than four times higher than that of HDEHP) [6] polymers responding to formula as $(\text{UO}_2)_n(\text{R}_2\text{PO}_4)_{2n+2}\text{H}_2$ were formed in the organic phase. In the presence of a neutral extractant like TAPO, this did not happen as the neutral extractant played its role of solubilizing agent to lead to $(\text{UO}_2(\text{R}_2\text{PO}_4)_4\text{H}_2)(\text{R}_3\text{PO})$.

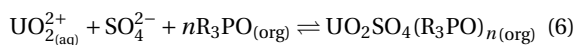
Indeed, neutral extractants do proceed via solvation of ionic species and absolutely not by ionic exchange. In this case, the metal is transferred to the

Table 2. Structures of various alcohols tested as phase modifiers and their respective amount needed in the diluent to prevent the formation of third phase during the stripping

Alcohol	Formula	w:v% needed as phase modifier
<i>n</i> -Octan-1-ol		0.9
2-Ethylhexanol		1
<i>n</i> -Octan-2-ol		1
4-Ethyl-octan-1-ol		0.9
3-Neopentyl-5,5-dimethyl hexanol		1.5
5-Ethyl-nonan-2-ol		2.5
2,6,8-Trimethylnonan-4-ol		7.5
7-Ethyl-2-methylundecan-4-ol		7.5
3,9-Diethyl-tridecan-6-ol		>12

Organic phase was 0.1 mol·L⁻¹ HDEHP in kerosene modified by various w:v percentages of phase modifier. Aqueous phase was 10% Na₂CO₃ and contact were performed at A:O = 1:1. Data extracted from Blake et al. [4].

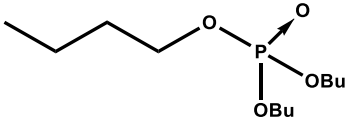
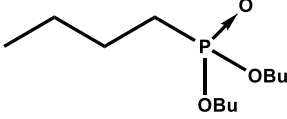
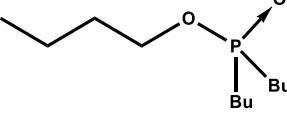
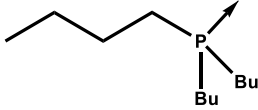
organic phase with its counterions, water and acids. The equilibrium of this transfer may be described as:



This points out the complexity of the involved synergy mechanism.

Although the processing of sulfuric leach liquors by DAPLEX was formerly applied at large scale and remains nowadays topic for studies [8–10], it has

Table 3. Values of D_U obtained with DEHPH at $0.1 \text{ mol}\cdot\text{L}^{-1}$ in kerosene modified by few w:v% of neutral organophosphorus compounds

Phase modifier	Formula	w:v% needed as phase modifier	Synergic D_U
Tri(<i>n</i> -butyl)phosphite	$\text{P}(\text{OBu})_3$	7	700
Tri(<i>n</i> -butyl)phosphate (TBP)		2.2	800
Dibutyl butylphosphonate		1.4	3000
Butyl dibutylphosphinate		0.9	2500
Tributylphosphine oxide		1.1	7000

Aqueous phase was $0.5 \text{ mol}\cdot\text{L}^{-1} \text{SO}_4^{2-}$, $0.004 \text{ mol}\cdot\text{L}^{-1} \text{U (VI)}$, pH = 1. Time contact was 10 min with 1:1 O:A at 298 K. Data extracted from Blake et al. [5].

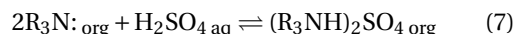
been progressively abandoned for the more selective AMEX process [10].

3.2. The AMEX process

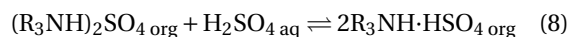
As mentioned above, the development of the AMEX process took place in the early 50's at the ORNL to be set at large scale at the end of the same decade [2]. Conditions were optimized according to similar approach as that followed for the DAPEX development. Tests were performed on several hundred of various primary, secondary, tertiary amines and tetraalkylammoniums (see some examples in Figure 1). The ligands were selected in respect of their solubility in the organic diluent (before and after contact with acidic leach liquors), their low ability to form a third phase and their extraction properties.

Considering solubility and phase behavior, it was found that, once protonated, only trialkylamines showed acceptable solubility in the diluent. More precisely, branched trialkylammoniums were found to be soluble in kerosene whereas linear one became soluble after supplying the diluent with 3–5%

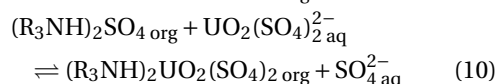
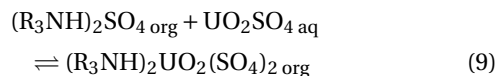
tridecanol as a phase modifier. In sulfuric acid, this protonation could be described as follows:



With enough acid, a further protonation might occur:



Uranium was transferred in the organic phase either by complexation of a neutral uranyl sulfate (Equation (9)) or by anion exchange (Equation (10)):



Efficiency of the extraction was shown to tightly depend on the concentration of aqueous sulfate (too high sulfate concentration led to uranium release), cationic competitors (molybdenum, vanadium, iron, etc.), free amine sulfate, pH of the leachate (too low pH led to ammonium salt hydrolysis) and the temperature (extraction decreased by 20 to 30% for 10 °C temperature rise), while D_U was not affected by the

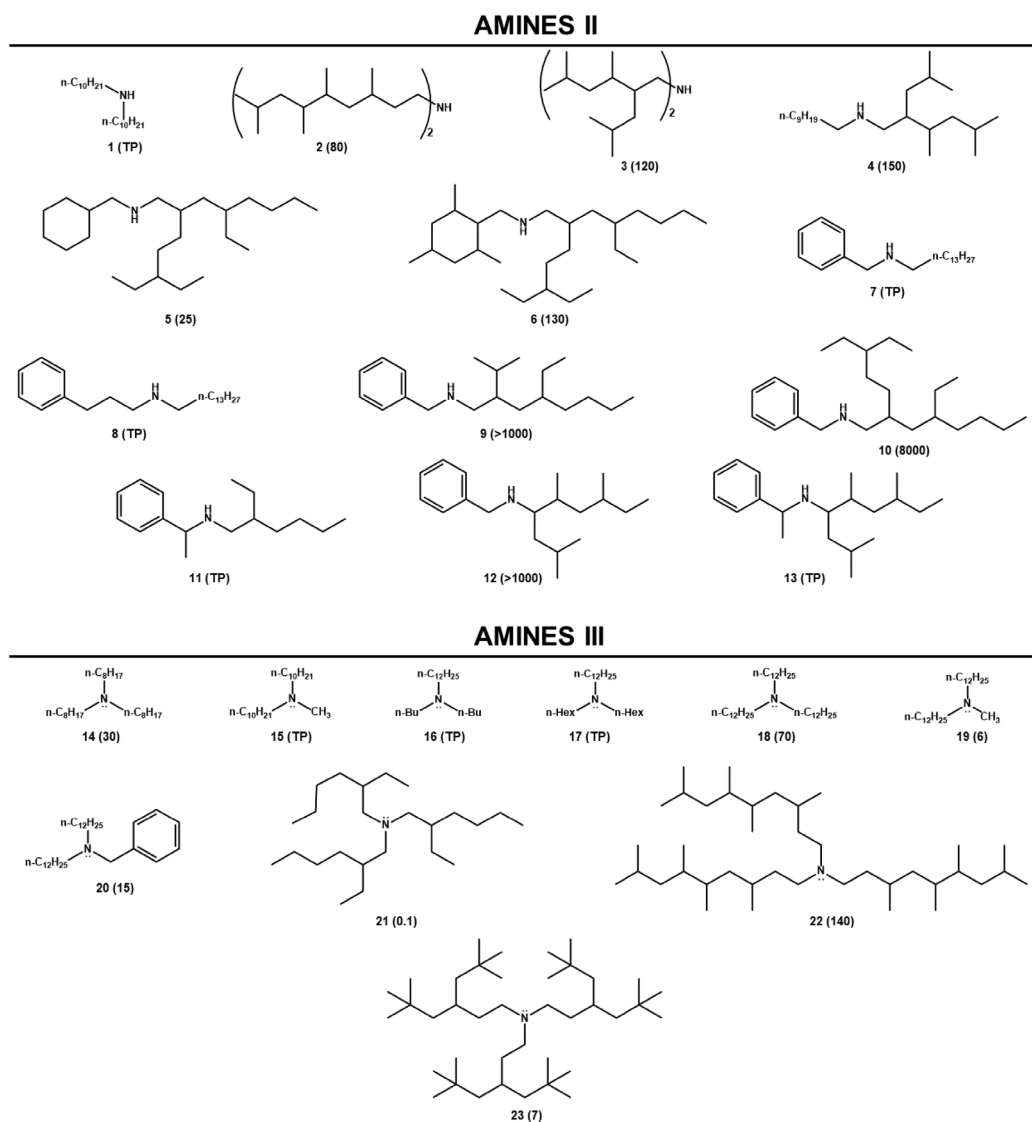


Figure 1. some structures (and related D_U) of amines II and amines III that were formerly assessed in the AMEX context. Conditions were $0.1 \text{ mol}\cdot\text{L}^{-1} \text{ SO}_4^{2-}$, pH 1, $4 \times 10^{-3} \text{ mol}\cdot\text{L}^{-1} \text{ U(VI)}$, phase ratio 1:1; $0.1 \text{ mol}\cdot\text{L}^{-1}$ amine in kerosene. TP stands for third phase formation. **Amine II:** *N,N*-di(decyl)amine (1), bis(3,5,6,8-tetramethylnonyl)amine (2), bis(2-isobutyl-3,5-dimethylhexyl)amine (3), *N*-(2-isobutyl-3,5-dimethylhexyl)decan-1-amine (4), *N*-(cyclohexylmethyl)-4-ethyl-2-(3-ethylpentyl)octan-1-amine (5), 4-ethyl-2-(3-ethylpentyl)-*N*-((2,4,6-trimethylcyclohexyl)methyl)octan-1-amine (6), *N*-benzyltetradecan-1-amine (7), *N*-(3-phenylpropyl)tetradecan-1-amine (8), *N*-benzyl-4-ethyl-2-isopropyloctan-1-amine (9), *N*-benzyl-4-ethyl-2-(3-ethylpentyl)octan-1-amine (10), 2-ethyl-*N*-(1-phenylethyl)hexan-1-amine (11), *N*-benzyl-2,5,7-trimethylnonan-4-amine (12), 2,5,7-trimethyl-*N*-(1-phenylethyl)nonan-4-amine (13). **Amine III:** trioctylamine (14), *N*-decyl-*N*-methyldecan-1-amine (15), *N,N*-dibutyl-dodecan-1-amine (16), *N,N*-dihexyl-dodecan-1-amine (17), tridodecylamine (18), *N*-dodecyl-*N*-methyl-dodecan-1-amine (19), *N*-benzyl-*N*-dodecyl-dodecan-1-amine (20), tris(2-ethylhexyl)amine (21), tris(3,5,6,8-tetramethylnonyl)amine (22), tris(5,5-dimethyl-3-neopentylhexyl)amine (23). Data extracted from Coleman et al. [2].

uranium concentration. Uranium:amine stoichiometry in the transferred complexes could be determined as 1:6 with linear to moderately branched secondary amines and as 1:4–5 with symmetrical trialkylamines (1:4.7 for tri-*n*-octylamine, for instance) or highly branched secondary amines. A mass law could be applied [2] showing that D_U evolved proportionately to the activity of the uncomplexed amine according to:

$$D_U = K_{\text{ex}} (a_{\text{R}_3\text{Norg}} - n \cdot a_{\text{Uorg}}) \quad (11)$$

where n varied between 4 and 6 according to the amine. The first power of this relationship suggested that the activity of the amine salt was nearly constant regardless of the initial amine concentration. Assumptions concerning the formation of homogeneous aggregates were readily discarded after analysis of the organic phase by light scattering as only partial and heterogeneous aggregation was evidenced [2].

Again, dependence of D_U on the structure of amines, could not be established with accuracy because the extracting properties were claimed to be driven by solvent effects subsequently to comparative studies carried out in kerosene, benzene and chloroform (partially shown in this paper) that were not fully understood. Indeed, if extraction was certainly mainly ruled by steric hindrance, basicity and lipophilicity, the observed effects seemed to result from a complex combination of these parameters. Moreover, it is interesting to note that while the authors had tried to characterize the colloidal properties of the system, they did not report some theories establishing the link between chemical structure and supramolecular assembly behavior. However, ignoring the supramolecular phenomena and considering the D_U values measured in the same solvent, namely kerosene (Figure 1), it was obvious that extraction was enhanced with a longer alkyl chain in the symmetrical linear trialkylamine series. It became more difficult to give proper explanations in the case of their dissymmetric isomers. In the branched trialkylamine series, the presence of an ethyl group on position 2 (tris(2-ethylhexyl)amine **22**) generated a drastic decrease of D_U while the highest level of extraction was reached with the branched trialkylamine **22** carrying methyl groups on positions 3, 5, 6 and 8. Comparison with the D_U obtained for a trialkylamine

bearing two bulky neopentyl groups on the same position leads to postulate that steric hindrance affects the process according to the position and the nature of the branching. *N*-benzyl secondary amine were the best extractants. For instance, the *N*-benzyl-4-ethyl-2-(3-ethylpentyl)octan-1-amine (**10**) showed exceptional efficiency in standard conditions ($D_U = 8000$) and was still extractant at very low pH ($D_U = 1$ with $[\text{H}_2\text{SO}_4] = 3 \text{ mol}\cdot\text{L}^{-1}$), finally, any attempt of rationalization based on the theoretical basicity of the tested amines should be a failure.

Selectivity of extraction could also be tuned according to the amines structure and the diluent. Some of the more promising and commercially available secondary and tertiary amines were successfully used in the AMEX process developed at large scale. For instance 90% of the uranium contained in the leach liquor could be extracted in countercurrent extraction equipment.

Stripping was easily achieved by displacement of uranyl with either chloride or nitrate ions, or alternatively by simple hydrolysis of the ammonium salt. The precipitated uranium oxide was recovered as predominant component presenting a few percent of contamination.

The main co-extracted competitors are molybdenum (VI), vanadium (V) and zirconium. At the time it was already known that vanadium (V) and molybdenum (VI) formed polymeric species incorporated in the organic phase. This further but not trivial detail is discussed below.

4. Current issues and progress in the AMEX process

Nowadays, the principle of the AMEX process is still the same but the composition of the system has been lightly revisited as it consists in a mixture of trialkylamines diluted in kerosene with 3% tridecanol. The mixture of trialkylamines, namely Alamine 336, is composed of trioctylamine (TOA), trinonylamine and tridecylamine.

Despite its widespread application and economic efficiency, the AMEX process also has drawbacks that warrant consideration: (i) the uranium separation factor is not optimal when compared to competing elements like Zr, Fe, Mo, and V, which are co-extracted [11,12], (ii) it requires the use of a volatile phase modifier to prevent the formation of a third

phase (organic phase splitting) [2], (iii) the amine extractants undergo degradation due to a radical reaction catalyzed by the co-extracted vanadium in the presence of the phase modifier [13], (iv) industrial facilities require significant quantities of organic diluent, typically kerosene, for solvent extraction carried out in mixer-settlers. Additionally to the resulting dysfunction, these issues have a high economical impact and must be addressed. For instance, the Somaïr plant in Niger maintains an inventory of approximately 900 m³ of solvent, with 75% replacement annually due to issues such as cruds formation, organic entrainment, and solvent evaporation. Moreover, in the same plant, a 50% loss of TOA due to chemical decomposition was noted over a year of activity [14]. Also, the selectivity with respect to molybdenum(VI) is not optimal which results in a decrease of the uranium extraction efficiency and of the loading capacity of the amine [15].

The degradation of tertiary amines by acidic hydrolysis and oxidation by nitrate [16] or radical reaction in the presence of vanadium(V) [13] is one of the main drawback of such systems.

The amines degradation phenomenon has been thoroughly studied by Chagnes and his co-workers [13,14,17–19]. It results in the appearance of growing concentration of dialkylamines and in the decrease of uranium extraction efficiency. First, they tried to provide a concrete solution with an applicability at large scale and showed by computer modeling that the flow-sheet of the AMEX process could be advantageously modified and optimized in order to delay the periodic replacement of the degraded TOA [17]. All their subsequent works allowed to clarify the mechanism of the TOA degradation, which involved transferred vanadium (V) and/or chromium (VI), the phase modifier (tridecanol) and the diluent (be it kerosene, TPH or *n*-dodecane).

Oxidation of vanadium (IV) to vanadium (V) should be the root of the problem since V^{IV} is not extracted in sulfuric media whereas V^V is extracted. Chagnes et al. properly monitored the already known conversion (see Coleman et al. [2]), after incorporation in 95:5 w:v *n*-dodecane:tridecanol mixture, of monomeric V^V to a polymeric species by ⁵¹V nuclear magnetic resonance (NMR) and Fourier Transform-Infrared (FT-IR) spectroscopies [14]. The first step is the formation of the transferable vanadium.sulfate complex VO₂SO₄⁻ taking place in the aqueous phase.

The sulfate complex is then transferred by anion exchange into the organic phase where it is not expected to form polynuclear species. However, the formation of decavanadate (HV₁₀O₂₈⁵⁻) was verified and assumed to result from the colloidal properties of the organic phase. Actually, trialkylammoniums form reverse-micelles in oily diluents and can incorporate further components other than the targeted metal such as water, salts and acids. Because the intrinsic properties (dielectric constant, ionic strength, etc.) of the yielded aqueous core might be significantly different from these of the sulfuric acid leach liquor, some redox reactions that were forbidden in usual aqueous media were instead allowed in reverse-assemblies.

Mechanism and kinetic of the degradation were investigated by UV-visible spectroscopy monitoring of the V^{IV} appearance in the aqueous phase (absorption of V^{IV} at $\lambda = 760$ nm) and degradation by-products contained in the organic phase were identified by Gas Chromatography coupled to Mass Spectrometer (GC-MS) [13]. Indeed, when the oxidation occurred, the V^{IV} yielded after reduction of the V^V was immediately released in the aqueous phase, signaling the beginning of the phenomenon that was found to evolve slowly. Its rate depended on the concentration of both V^V and sulfuric acid in the aqueous phase, and of TOA and solubilized dioxygen concentrations in the organic phase. Against all expectations, the kinetic of oxidation depended only poorly on the concentration of tridecanol whereas this latter was typically involved in the process. Actually, decavanadate and/or V^V·O₂ complex generated radical oxidative species that reacted first with tridecanol to yield tridecanal and then with TOA to produce mainly dioctylamine, octanal and (*E*)-*N,N*-dioctyloct-1-en-1-amine (Figure 2A). The role of phase modifier was more specifically studied in the context of another works undertaken by the same team [18]. A series of either commercially available or synthesized alcohols were tested as phase modifier regarding the impact on the kinetic of TOA degradation. Although SAR could not be established with accuracy, it was shown that the kinetic of degradation became slower even extremely slower in the presence of a long branched alkyl chain alcohol (Figure 2B).

Therefore, to optimize the AMEX process and enhance its efficiency, it is essential to gain a deeper insight into the mechanisms of this solvent extraction

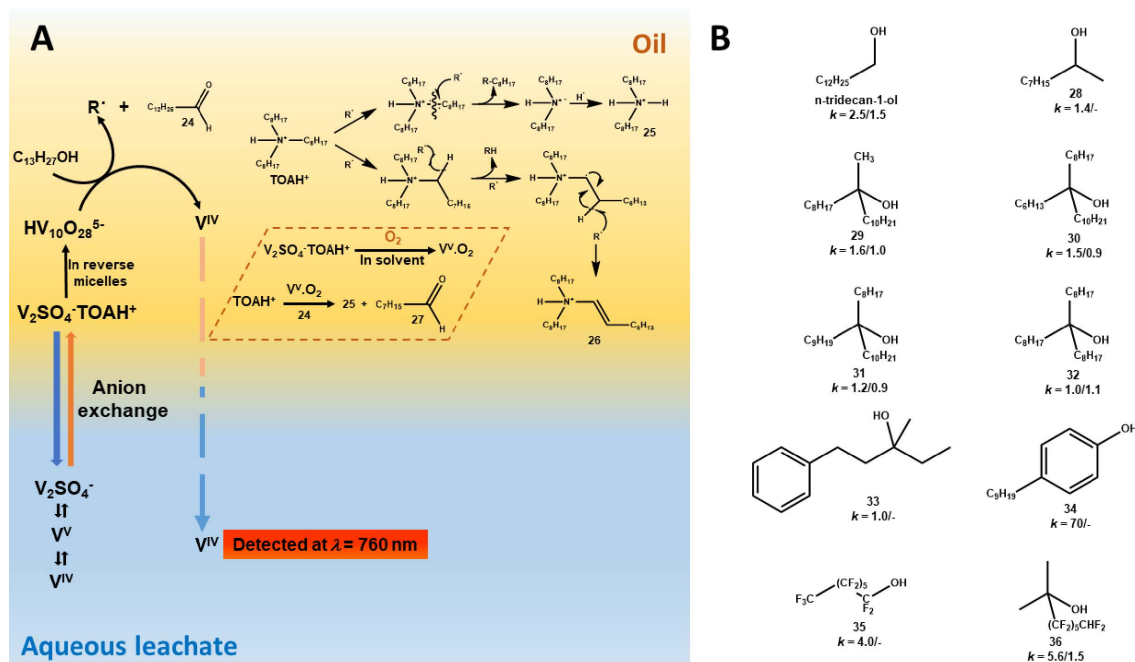


Figure 2. (A) Schematic representation of the two mechanisms of extractant degradation reported to occur in the AMEX process by Chagnes et al. [13,14]. Main degradation by-products are tetradecanal (24), dioctylammonium (25), (E)-N,N-dioctyl-1-en-1-aminium (26) and octanal (27). (B) Structures of phase modifier assessed by Chagnes et al. [18] with related values of the degradation kinetic constant k observed before/after degassing of the organic phase by nitrogen bubbling. Values are factors of 10^{-7} and k is expressed in s^{-1} . Tested alcohols were tridecan-1-ol, nonan-2-ol (28), 9-methylnonadecan-9-ol (29), 9-hexylnonadecan-9-ol (30), 10-octylicosan-10-ol (31), 9-octylheptadecan-9-ol (32), 3-methyl-1-phenylpentan-3-ol (33), 4-nonylphenol (34), 1,1,2,2,3,3,4,4,5,5,6,6,7,7,7-pentadecafluoroheptan-1-ol (35), 3,3,4,4,5,5,6,6,7,7,8,8-dodecafluoro-2-methyloctan-2-ol (36).

process and to focus on optimizing the composition of extractants employed. This process uses extractant mixtures consisting of a range of secondary and tertiary amines. While numerous studies have investigated the extraction capabilities of these secondary and tertiary amines, there has been a conspicuous lack of research dedicated to comprehending their inherent properties. Notably, most of these studies has addressed their aggregation characteristics, which are a consequence of their amphiphilic nature.

In the context of uranyl extraction in sulfuric acid solutions using tertiary amine extractants, an in-depth examination of the microstructure of uranyl complexes was conducted through a combination of Extended X-ray Absorption Fine Structure (EXAFS) analysis and Molecular Dynamics (MD) simulations [20]. The TOA extractant was used as a reference for tertiary amines. The MD simulations and classical

fitting methods yielded consistent results, revealing an unprecedented structure in the organic phase: the uranyl complex consists of three sulfate anions coordinated to the uranyl cation through U–O bonds in its first coordination shell (Figure 3a).

Further analysis of the EXAFS spectra demonstrated that uranyl trisulfate complexes exhibit dynamic behavior, transitioning between a configuration in which all three sulfate ions are bidentate and another configuration where two sulfate ions are bidentate, and one is monodentate. The MD simulations corroborated these findings, providing evidence that the configuration with three bidentate sulfate anions is energetically more favorable than the alternative arrangement with two bidentate and one monodentate sulfate ions (Figure 3b). Behind this sulfate coordination aspect, the distribution of exchangeable hydrogen bonds observed through MD

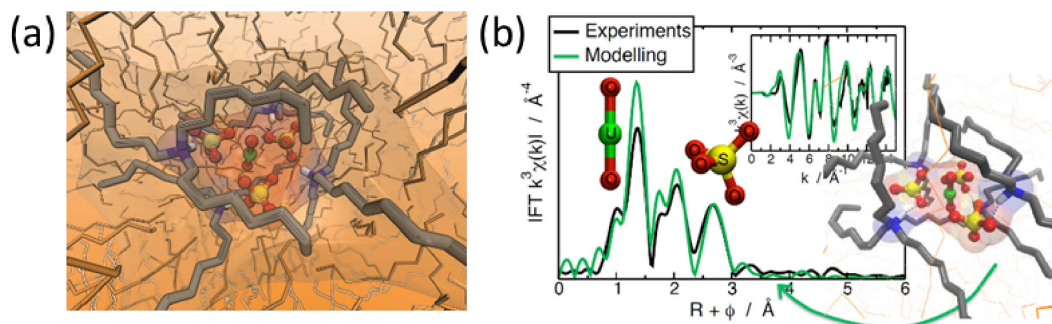


Figure 3. (a) Snapshots issued from MD simulations performed in *n*-dodecane presenting the complex $\text{UO}_2(\text{SO}_4)_3(\text{TOA})_4$ with 3 SO_4^{2-} in the bidentate coordination. The uranium atom is colored in green. (b) k^3 -weighted Fourier transformed EXAFS spectra of U-SO₄-TOA complex. Insert: corresponding k^3 -weighted EXAFS spectra [20]. Reproduced from Ref. [20] with permission from the Royal Society of Chemistry.

simulations also revealed a significant interplay between the inner- and outer-sphere environments of the uranyl complex.

The effect of alkyl chain configuration on the phase stability and the aggregation properties of tertiary amines has further been investigated [21]. The results showed that tertiary amines with longer or slightly branched alkyl chains exhibit enhanced phase stability and maintain their effectiveness in extracting uranium (Figure 4a).

Through a combination of techniques such as small-angle scattering to determine nanostructures in the organic phase and measurements of oil–water surface tension, it has been revealed that these effects on extraction and phase stability are linked to the presence of reverse aggregates characterized by smaller polar core volumes and reduced co-extraction of water. When the alkyl chains exhibit more pronounced branching, they prevent the formation of a swollen reverse aggregates, thereby hindering efficient extraction. This suggests that the arrangement and packing of the alkyl chains directly influence the efficiency of the solvent extraction system.

Taking such a structural approach into account, this study has not only demonstrated that smaller aggregates effectively prevent the formation of a third phase but also elucidated how reduced attractive interactions among these aggregates play a pivotal role in achieving this outcome.

An in-depth thermodynamic analysis, based on the “ienaic” approach, also provided a comprehen-

sive rationale for this phenomenon [22]. It highlighted the significant impact of the alkyl chains on the curvature free energy of the aggregates (Figure 4b). Notably, this curvature free energy emerges as a primary inhibitory factor affecting the transfer free energy of uranium, primarily due to the significant entropic contributions arising from the branching and packing of the extractants.

It is worth noting that this study was conducted using commercially available tertiary amines. However, for a more nuanced understanding, we synthesized a family of branched TOA isomers with different degrees of branching in terms of length, number, and location. Interesting complementary conclusions could be established. This work will be reported elsewhere [23].

An eco-friendly solvent extraction process has been innovatively developed for uranium extraction using diluent-free tri- and tetraalkylammonium-based extractants. A series of ammonium mixtures were systematically tested in absence of diluent to evaluate the influence of ammonium cations and anions on extraction efficiency, viscosity and phase separation [24].

Tetraalkylammoniums were readily accessible as they were commercially available as chloride (Cl^-) or bis(trifluoromethanesulfonyl)imide ($\text{N}(\text{Tf})_2^-$) salts of *N*-methyltriocylammonium and Aliquat 336 mixture (Figure 5a). Trialkylammonium-based ionic liquids (ILs) required synthesis. They were easily obtained by neutralizing the TOA diluted in ethanol with stoichiometric ($n = 0.5$ in Equation (12)) or half

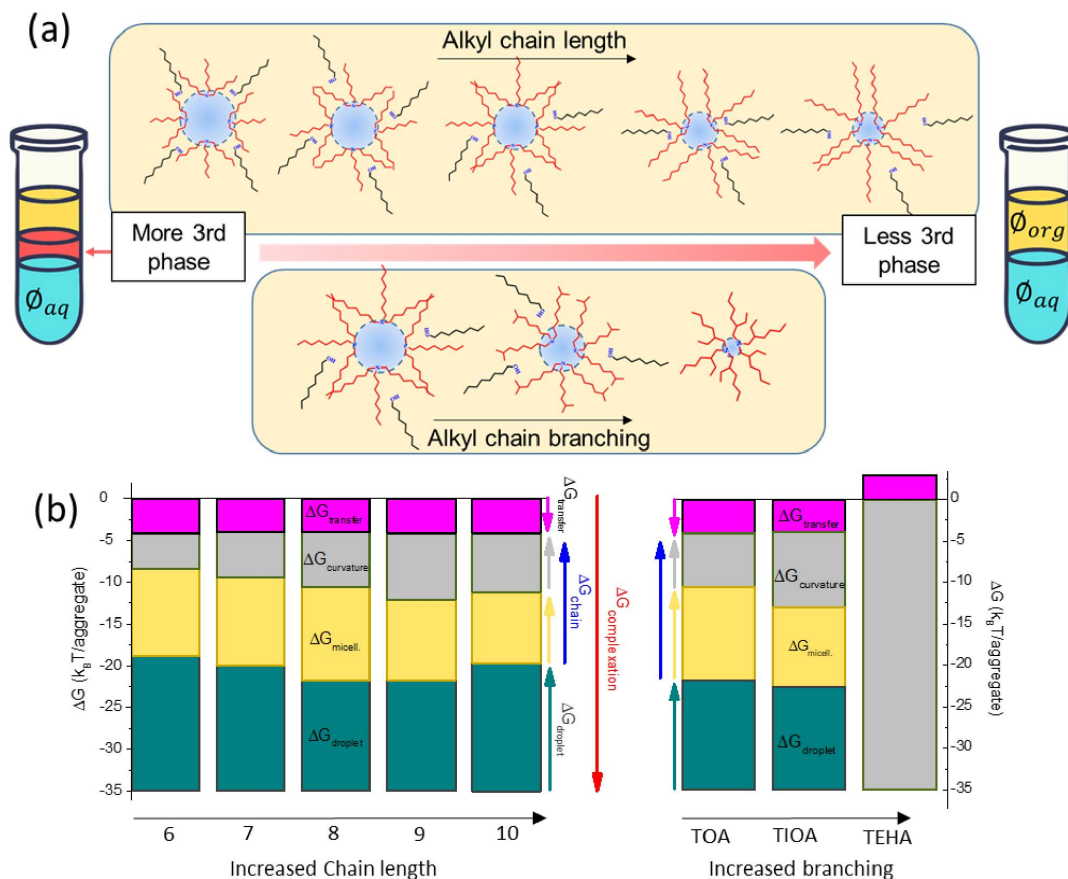
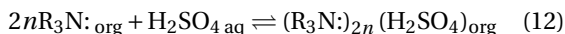
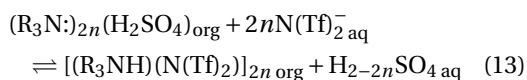


Figure 4. (a) Illustration of effect of tertiary amines alkyl chain length and branching on organic phase organization and stability [21]. (b) Main thermodynamic contributions to the uranium transfer energy plotted as a function of alkyl chains length and branching [22].

amount ($n = 1$ in Equation (12)) of sulfuric acid.



Extensive evaporation and drying under reduce pressure led to the expected sulfated IL. The complete protonation of the tertiary amines could be accurately by 1H NMR spectroscopy. Metathesis, performed by contacting an aqueous solution of an anion Y^- with IL Am^+X^- , followed by centrifugation and extensive washing allowed the quantitative displacement of anion X^- by anion Y^- (Equation (13)).



Numerous binary mixtures of each IL were yielded and their properties were tuned according to the molar ratio of each partner, the nature and the molar

ratio of each counterion ($N(Tf)_2^-$, Cl^- , HSO_4^- , SO_4^{2-}) (Figure 5a).

These systems have proven to be exceptionally effective and straightforward to implement, as they employ the same chemical components as those employed in the AMEX process. As presented in Figure 5b, distribution ratios of uranium obtained with some of these ammoniums salts and mixtures allow either comparable or much higher extraction than the classical TOA extractant (taken as reference for the AMEX process). Uranium extraction increases with sulfates concentrations, which is consistent with the recognized extraction mechanisms for such systems [20]. An interesting synergistic behavior with the molar ratio of one ammonium to another was further investigated as it could be advantageously considered to adjust physicochemical properties of

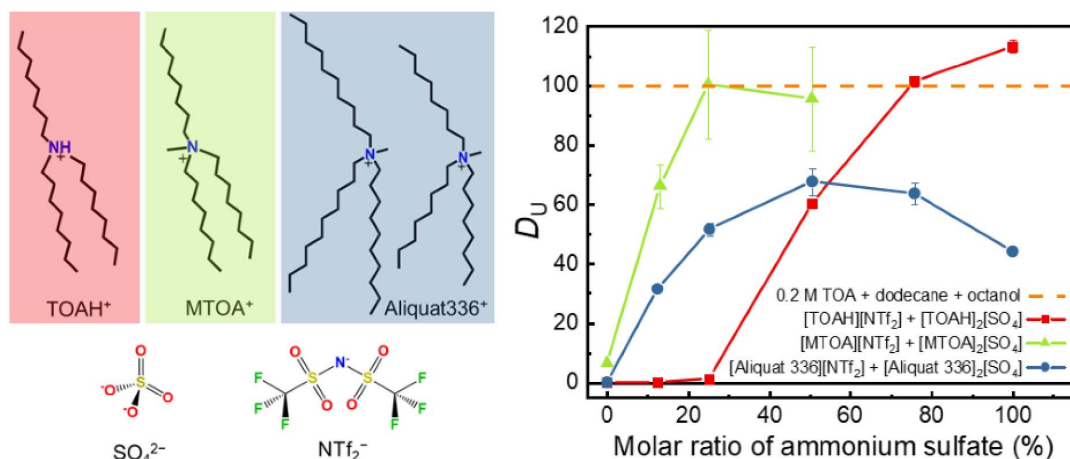


Figure 5. (a) Structure of the tested cations and anions. (b) Distribution ratios of Uranium obtained for mixte ammoniums plotted as a function of the molar ratio of the sulfate anion. The initial aqueous solution (pH = 1) contains 0.1 mol·L⁻¹ sulfuric acid, 1 mol·L⁻¹ ammonium sulfate, 250 mg·L⁻¹ U(VI). It was contacted to the organic phase with an aqueous to organic volume ratio A:O = 2:1 [24].

the final solvent (as viscosity or density) [25]. Furthermore, it has been established that adopting such alternatives not only serves to avoid the formation of a third phase and subsequent extractant degradation but also leads to a remarkable reduction in solvent evaporation losses. To provide a comprehensive evaluation of their sustainability, a comparative life cycle assessment (LCA) was carried out between this novel system and the conventional solvent [24]. The results indicate that the new system is 18 times less environmentally impactful.

Beyond focusing on the improvement of some historical and well established processes that still need optimization, developing new methods and/or new tools is certainly the more innovative and attractive alternative intended by organic chemists. This point is discussed in the following section.

5. Development of new ligands working in sulfuric media

The development of new, more efficient extractants than those currently used in the AMEX and DAPEX processes is an important issue for the uranium mining industry. Knowing that these processes are based on trialkylated tertiary amines for AMEX and organophosphorus compounds (HDEHP and tri-*n*-butylphosphate (TBP)) for DAPEX, various studies have investigated the possibility of combining amine

or amido to organophosphorus functional group to offer bifunctional extractants. These molecules are designed to have at least two distinct functional groups that enable them to selectively bind and extract uranium from a complex mixture in order to improve the efficiency and selectivity.

Organophosphorus compounds are very widely used in the context of separation chemistry in hydrometallurgy. The classification of organophosphorus extractants can vary based on different criteria, such as their structural features, chemical properties, or extraction mechanisms [26].

The coordination strength of the organophosphorus extractant can be enhanced with an increase in their basicity. This can be achieved by varying the oxidation state of phosphorus. Phosphines [R₃P], for instance, are generally more basic than phosphine oxides [R₃P(O)] due to the presence of an electron pair on the phosphorus atom in phosphines. The number of O atoms linked to the P atom plays also a role in the basicity of the phosphine oxides (R₃P(O)). Indeed, these compounds with one substituted oxygen atom are more basic than phosphinates [(R'O)P(O)R₂], phosphonates [(R'O)₂P(O)R], and finally phosphates [(R'O)₃P(O)]. The nature of the substituents (R) attached to the P atom can significantly influence the basicity of the compound. By introducing electron-donating groups or electron-withdrawing groups on the alkyl

groups attached to phosphorus, the overall electronic environment can be altered and consequently, the basicity of the compound. Bulkier substituents can decrease the basicity due to steric hindrance effects. In addition, they are usually categorized into neutral ($R' = \text{organic moiety}$) and acidic compounds ($R' = \text{H}$ or $R' = \text{H}$ and organic moiety).

Taking into account the versatility of organophosphorous compound, their combination with amine allowed proposing various α -amino-functionalized organophosphorus compounds with a strong potential for the extraction of lanthanides and actinides including uranium [27,28].

One of the first systems based on the use of α -amino-functionalized organophosphorus extractant described in the literature was proposed by Jagodić and Grdenić with the use of *N*-substituted monoesters of α -aminophosphonic acid (ethyl and octyl mono-esters of α -anilinobenzylphosphonic acid) (see Table 4 entry #1) as complexing agents for the extraction of various metal including uranium from sulfuric acid solutions [29]. Interestingly, it turned out that this category of extractant exhibits a different behaviour depending on the degree of oxidation of uranium. Uranium (IV) is extracted at lower sulfuric acid concentration while uranium (VI) is extracted over a wide concentration range (0.25 to 4.5 mol·L⁻¹ H₂SO₄).

An advantage of α -aminophosphonate-, phosphinate-, and phosphine oxide-based extractants is that they can be easily synthesized through Kabachnik–Fields, Mannich and Pudovik pathway [30–32].

The Kabachnik–Fields reaction is mainly used since it allows obtaining α -amino-functionalized organophosphorus derivatives in a single step by a three-component condensation reaction involving a carbonyl (aldehyde or ketone), an amine (primary or secondary amine) and a phosphoryl compound (phosphite, phosphinate, or phosphine oxide) [33].

According to this approach, Leydier et al. proposed different amino phosphine oxide type extractants for the extraction and recovery of uranium from sulfuric acid [34]. The condensation of an aldehyde, a dialkylamine, a dialkylphosphite or a dialkylphosphine oxide in the presence of *para*-toluene sulfonic acid in catalytic quantity in toluene leads to aminophosphine oxide (Figure 6). Among all the extractants synthesized, an interest was

demonstrated for the (1-(bis(2-ethylhexyl)amino)-4,6,6-trimethylheptan-2-yl)diethylphosphine oxide ($R_1 = R_2 = \text{Octyl}$; $R_3 = 2,4,4\text{-triMethylPentyl}$; $R_4 = 2\text{-EthylHexyl}$) (see Table 4 entry #2). Indeed under the conditions of the study this extractant shows extraction performance for uranium much higher with much greater selectivity than HDEHP or TOA used as a reference system.

More recently, Liao and coworkers showed that neutral aminophosphonate extractants exhibit high extraction ability towards high-valence metal ions such as U(IV). Indeed, bis(2-ethylhexyl) ((2-ethylhexyl)amino)methylphosphonate also called Cextrant 230 (see Table 4 entry #3) can form a $\text{UO}_2\text{SO}_4 \cdot 2[\text{Cextrant 230}]$ complex in which phosphoryl oxygen atom are involved in the coordination of UO_2^{2+} and the extraction of U(VI) is an exothermic process [35]. It has been shown that the extraction capacity can be influenced with steric hindrance and that the Cextrant 230, which has a relatively low steric hindrance, shows a strong affinity for high valence uranium.

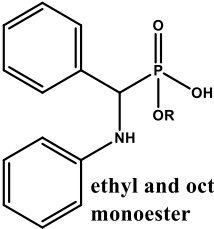
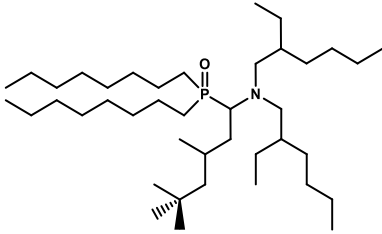
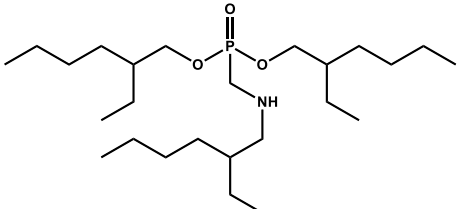
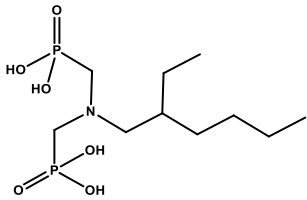
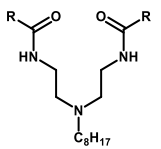
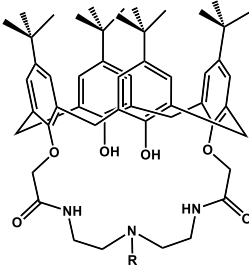
Usually the amino phosphorylated-based extractants are functionalized by long alkyl chains that can increase their lipophilicity in order to facilitate the separation between the aqueous feed phase and the organic phase. Recently, Moilanen and coworkers proposed water-soluble aminobis(phosphonate) ligands (see Table 4 entry #4) as precipitating agents for REEs, Th, and U allowing a selective separation [36].

Beyond organophosphorous extractant compounds, extractants with amino or amido moieties have been also investigated for the extraction and recovery of uranium from sulfuric leachates. The carbonyl oxygen atoms of the amide groups and the nitrogen atom of the amino groups allow to bind lanthanide and actinide ions.

Iminodiamides which combine amides and amine functionalities have been proposed for this purpose (see Table 4 entry #5) [37]. The chelating behaviour of the iminodiamides was evaluated through complementary analysis (FT-IR, NMR, Mass spectroscopy) and molecular modelling (DFT calculation) and the extraction performances showed the potential of this system for the extraction of uranium at low concentration in sulfuric acid.

In the same way, it could be demonstrated that iminodiamides could be attached on calixarene platform leading calix[4]azacrowns (see Table 4 entry

Table 4. Extractant and related extraction condition for the extraction of uranium from sulfuric acid solution

Entry	Extractant structure	Extraction condition	Reference
#1	 <p>ethyl and octyl α-anilinobenzylphosphonic acid monoester</p>	<p>Sn (II), UO₂ (II), VO (II), Sb(III), Bi(III), Ce(III), Ti(III), Fe(III), Ce(IV), Zr(IV), Sn(IV), Th(IV), Ti(IV), U(IV)</p> <p>Neutral and H₂SO₄ \geq 1 mol·L⁻¹</p>	[29]
#2		<p>U(VI), Fe(III), Mo(VI), Ce(III), La(III), Gd(III), Yb(III), Nd(III), Ti(IV), Zr(IV)</p> <p>H₂SO₄ 1 mol·L⁻¹ + Li₂SO₄ 1 mol·L⁻¹</p>	[34]
#3	 <p>bis(2-ethylhexyl)((2-ethylhexyl)amino)methylphosphonate (Cextrant 230)</p>	<p>Th(IV), U(VI), RE(III), Fe(III) and Al(III)</p> <p>Leach solution of ion-adsorption rare earth (RE) ores by aluminum sulfate</p> <p>H₂SO₄ \leq 1 mol·L⁻¹</p>	[35]
#4		<p>Separation by precipitation of thorium, uranium, and scandium from RE</p>	[36]
#5	 <p>R = heptyl or 2-heptyl</p>	<p>U(VI)</p> <p>Mo(VI), Zr(IV), Ti(IV), La(III), Ce(III) and Fe(III) 0.1 mol·L⁻¹</p> <p>H₂SO₄</p>	[37]
#6	 <p>R = Octyl or Ethylhexyl</p>	<p>U(VI)</p> <p>Mo(VI), Zr(IV), Ti(IV), La(III), Ce(III) and Fe(III) 0.1 mol·L⁻¹</p> <p>H₂SO₄</p>	[38]

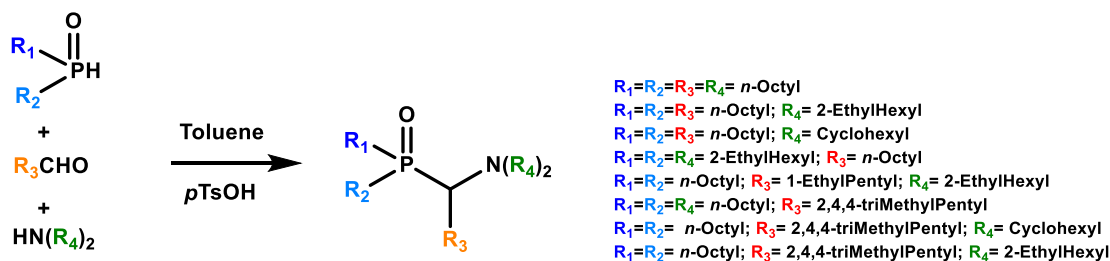


Figure 6. Kabachnik–Fields pathway for the synthesis of aminophosphine oxide extractant studied for the extraction and recovery of uranium from sulfuric acid [34].

#6) [38]. Such macrocycle is able to selectively extract uranium at low sulfuric acid concentration but in a different way in comparison to the “free” iminodi- amide. Indeed, the stoichiometry of complexation is different with the demonstration of complex 1:1 for the iminodiamide-functionalized calixarene while it was found to be 2:1 for the iminodiamide. Also, a lower efficiency can be noticed when the iminodi- amide is tethered on calixarene.

6. Molecular systems for the extraction of uranium from unconventional ores

Wet process phosphoric acid is a potential source of uranium as significant concentrations of uranium ranging from 20 to 200 mg·L⁻¹ can be found in phosphate rock. It represents an alternative resource for uranium production as large quantities of phosphate rock are processed annually to produce phosphoric acid [39–44].

Several hydrometallurgical processes such as precipitation [45,46], membrane separation [47–49], and liquid–liquid extraction [50,51] have been investigated to remove or recover uranium from the WPA.

Among these processes, liquid–liquid extraction has emerged as the benchmark technology for the industrial recovery of uranium from phosphoric acid [44].

Three processes have reached commercial status between the late 1970s and 2000 with varying degrees of success:

- (i) The URPPOS process (uranium from industrial phosphoric acid), developed at the ORNL, using a synergistic combination of HDEHP and trioctyl phosphine oxide (TOPO) as extractants for the recovery of

uranium(VI) from 4–6 mol·L⁻¹ phosphoric acid solution [52].

- (ii) The OctylPhenyl Acid Phosphate (OPAP) process, also from ORNL but using a mixture of mono- and dioctylphenylphosphoric acid as the extractant for the recovery of uranium(IV) from WPA [53].
- (iii) The OctylPyroPhosphoric Acid (OPPA) process, developed by Dow for the recovery of uranium(IV) by using octylpyrophosphoric acid as the extractant [53].

In each of these processes, organophosphorus extractants are used, as shown in Figure 7.

In the case of the URPPOS process, a mixture of a cationic exchanger HDEHP with a solvating agent TOPO is used in the following proportions 0.5 mol·L⁻¹ HDEHP + 0.125 mol·L⁻¹ TOPO in aliphatic diluents. Indeed, Hurst et al. [52] have shown that a synergistic effect is observed for a HDEHP/TOPO ratio of 4/1 with a significant increase in the uranium extraction compared to extractants used independently.

A number of studies have been carried out in order to gain a better understanding of the mechanisms involved in this synergistic extraction. Among the various mechanisms proposed to predict and gain insights into synergism in solvent extraction, studies with a molecular approach were usually proposed, explaining the extraction of species by the mechanism of addition, substitution, and solvation [55–59]. The possibility of pre-organizing a mixture of extractant molecules has further been explored on the system HDEHP/TOPO [60]. This concept encompasses scenarios such as synergistic aggregation of the extractants, promoting molecular interactions between extractant molecules and to enhancing the

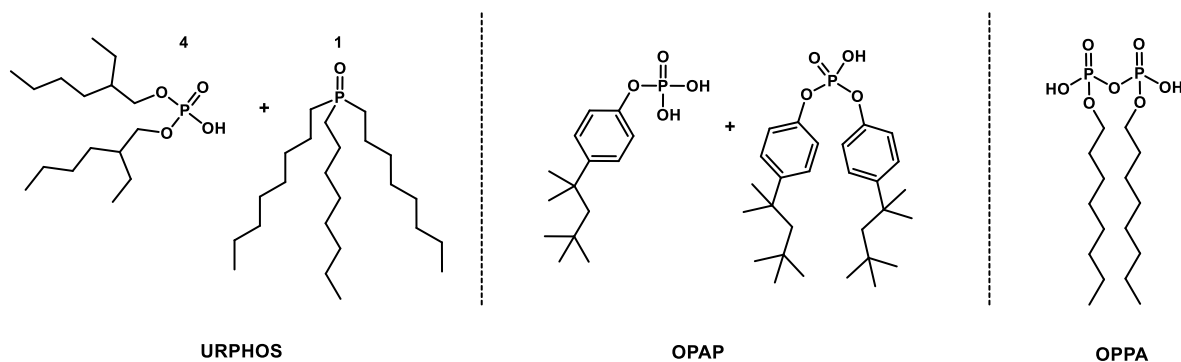


Figure 7. Chemical structure of extractant involved in URPHOS [52], OPAP [53] and OPPA [54] processes.

solubilization into the reverse micelles. To examine this hypothesis, the aggregates formed by the extractant molecules were characterized with neutron and X-ray scattering, but also thermodynamically in order to determine the critical aggregation concentration (CAC) for each ratio of the mixture (Figure 8). This unprecedented study revealed that lower CAC, which can be related to favored micellar energy, is concomitant with the synergistic extraction of uranium.

Conducted in the absence of any cations, this innovative study further demonstrated that there is no discernible preorganization of the extractants, suggesting that the synergistic aggregation observed in the presence of cations is a result of the chelation mechanism [61]. Finally, the synergistic extraction of uranium by HDEHP/TOPO was shown to be controlled by an entropic effect (offering more configurations to extract), by a favored extractant association (in presence of acid and cations), and by the curvature energy of the aggregates, this latter depending on both the extractant alkyl chains geometry (packing parameter) and the diluent penetration in the apolar shell of the aggregates [62]. These results were further confirmed on another extractant mixture thanks to a complete thermodynamic balance performed with the so-called inelastic approach [63,64].

7. Research on new extractants for uranium extraction from phosphoric acid medium

In spite of the accomplishments in uranium recovery from WPA (4–6 mol·L⁻¹ phosphoric acid solution), the three processes commercialized exhibit significant potential for enhancement, prompting further

research. The primary shortcomings of these developed methods are classically an inadequate selectivity and limited capacity.

Efforts have been dedicated to enhancements, particularly through the exploration of novel extractant systems surpassing the efficiency of URPHOS. The initial approach involved combining extractants in different ways: (i) mixing cation exchangers with TOPO [59,65–67], (ii) integrating solvating agents with HDEHP [68–70], or (iii) new synergy system [71–76].

However, the use of mixtures is limited by the need to control the composition during the extraction phase, particularly when recycling the extraction phase. To overcome this challenge, the search for multifunctional molecules has become a priority with a particular focus on autosynergistic molecules.

Such autosynergistic molecules refer to bifunctional extractants that incorporate both a cationic exchanger and a solvating agent within their structure.

For this purpose, the combination of phosphine oxide and phosphoric acid groups has been proposed (Figure 9).

One of the first examples studied was proposed by Warshawsky et al. using a *O*-methyl-di-hexyl-phosphine oxide *O'*-hexyl-2-ethyl phosphoric acid however a third-phase formation occurs during the extraction (Figure 9a) [75]. In a comparable approach, molecules that contain a phosphoric acid group, similar to HDEHP, and a phosphine oxide group, similar to TOPO, have been described (Figure 9b) [77].

A number of different extractants were synthesized on the basis of a reaction scheme

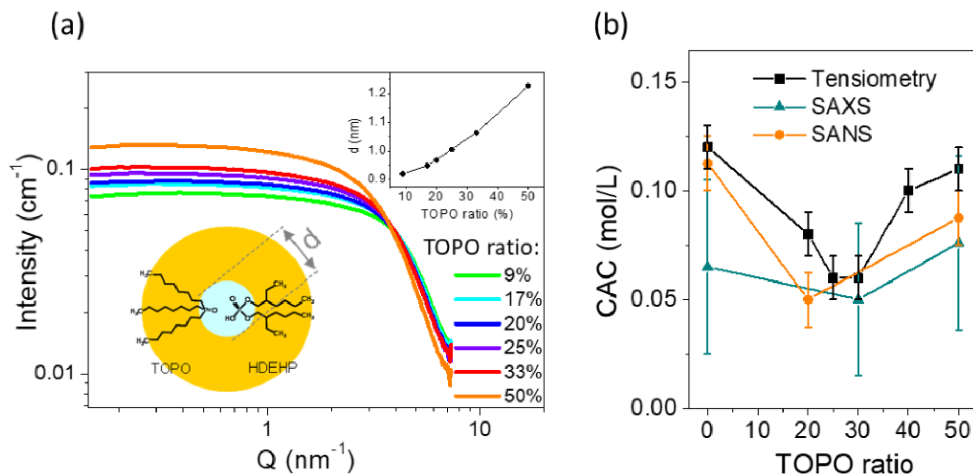


Figure 8. (a) SAXS data showing the aggregation of the extractant molecule. The top inset shows the deduced aggregate diameter. (b) CAC as a function of TOPO ratio determined from tensiometry, SAXS and SANS [60].

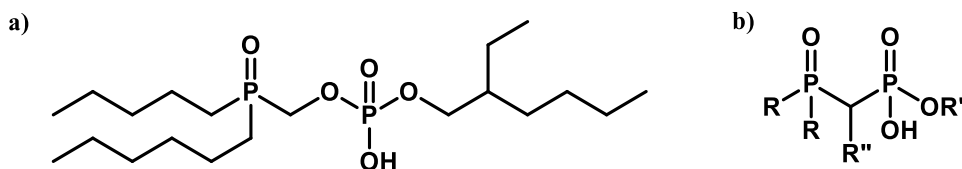


Figure 9. Bifunctional molecule bearing a phosphine oxide and phosphoric acid groups [75,77].

(Figure 10) involving di-*n*-octylphosphine oxide or di(2-ethylhexyl)phosphine oxide obtained from di-*n*-butylphosphite using the appropriate (alkyl)magnesium bromide. The introduction of an alcohol group, which is then substituted in a chloride derivative, allows an Arbuzov reaction to be carried out with a suitable trialkyl phosphite (P(OR')₃). The resulting (dialkylphosphoryl)-methyl-(dialkylphosphonate) can then be treated to become monosaponified or alkylated.

These “autosynergistic” molecules show an increased extraction efficiency for U(VI) compared to Fe(III) from concentrated phosphoric acid solutions (5 mol·L⁻¹). This efficiency exceeds that obtained by using two molecules in a synergistic ratio. Furthermore, the selective extraction of uranium from phosphoric acid proves to be superior to the HDEHP/TOPO system, even in the presence of numerous impurities. With such an extractant it is possible to achieve a distribution ratio for U(VI) that is more than 10 times higher than the one achieved with the HDEHP/TOPO system. This superiority has

been confirmed by investigations on an authentic industrial phosphoric acid solution.

The exploration of bifunctional molecules, involving the innovative combination of a neutral donor and an acidic extractant, that achieve the selective extraction of uranium from phosphoric acid has been extended to other molecule families. A novel family of bifunctional molecules has been successfully synthesized and extensively examined for their capability to extract U(VI) from phosphoric solutions. This approach is built upon amidophosphonic acid [78] and amino-phosphonate functional groups [79].

The reaction scheme depicted in Figure 11 illustrates the straightforward synthesis of these bifunctional molecules, starting with the amidation of *N,N*-dialkylamine with halogeno-acylchloride followed by an Arbuzov reaction with triethylphosphite to lead to the *N,N*-dialkylcarbamoylalkylphosphonate. The complete or partial hydrolysis of phosphonate respectively performed with bromotrimethylsilane or sodium hydroxide results in phosphonic acids or monophosphonate molecules. The possibility

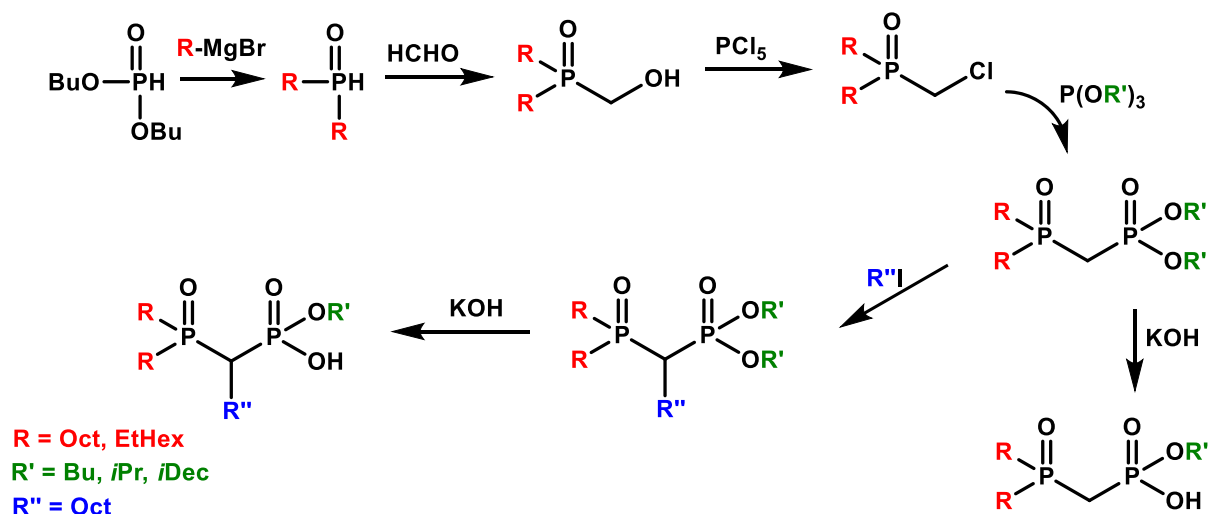


Figure 10. General synthesis of bifunctional molecules bearing a combination of phosphine oxide and phosphoric acid groups [77].

of introducing an alkyl group on the methylenic bridge was also considered before the hydrolysis step. Many structures have been synthesized according to this approach and then subjected for the extraction and recovery of uranium from phosphoric acid.

Taking a structure-activity perspective, a specific ligand named butyl-1-[*N,N*-bis(2-ethylhexyl) carbamoyl]nonyl phosphonic acid (DEHCNPB) has been subject to in-depth study due to its remarkable performance in selectively extracting and quantitatively recovering uranium [79,80]. These results stand in contrast to those of the URPHOS reference system. Indeed, the extraction efficiency reaches levels up to 90 times greater, and the selectivity is amplified by 150 times compared to the synergistic HDEHP/TOPO reference system. Importantly, this enhanced performance is achieved without any occurrence of third-phase formation during both the extraction and back-extraction processes which is totally reached by using ammonium carbonate.

Currently, this extractant appears to be most effective for the selective extraction and recovery of U(VI) from industrial phosphoric acid solution.

Further advancement includes the design of a comprehensive flow sheet and the ongoing development of a solvent extraction process using DEHCNPB as the central molecule [81].

As with the URPHOS reference system, mechanistic studies at the molecular and supramolecular scale were investigated for the DEHCNPB [79,80,82].

Slope methods and electrospray ionization mass spectroscopy (ESI-MS) analysis revealed the presence of complexes with four DEHCNPB [82]. Density functional theory (DFT) coupled to IR studies showed moreover that DEHCNPB molecules solely interact through their phosphonate groups by forming hydrogen bond, while the amide group does not participate to the association. The carbonyl group seems to participate primarily by forming hydrogen bond in the outer coordination sphere. Even if such an outer-sphere bond is not as strong as an uranium-oxygen bond, it was supposed to stabilize the uranyl complex and to favor the extraction of uranyl species. These effects combined with the favorable aggregation properties of the system was associated to the very high extraction efficiency of DEHCNPB toward U(VI).

Classical MD coupled with experimental data from Small-Angle Neutron Scattering (SANS) and Small-Angle X-ray Scattering (SAXS) techniques were further employed to elucidate the aggregation behavior of the bifunctional extractant DEHCNPB [83].

It showed that in the absence of uranium, the organic phase primarily consists of dimers and trimers held together by hydrogen bonds formed through the phosphonate groups, without any water molecules.

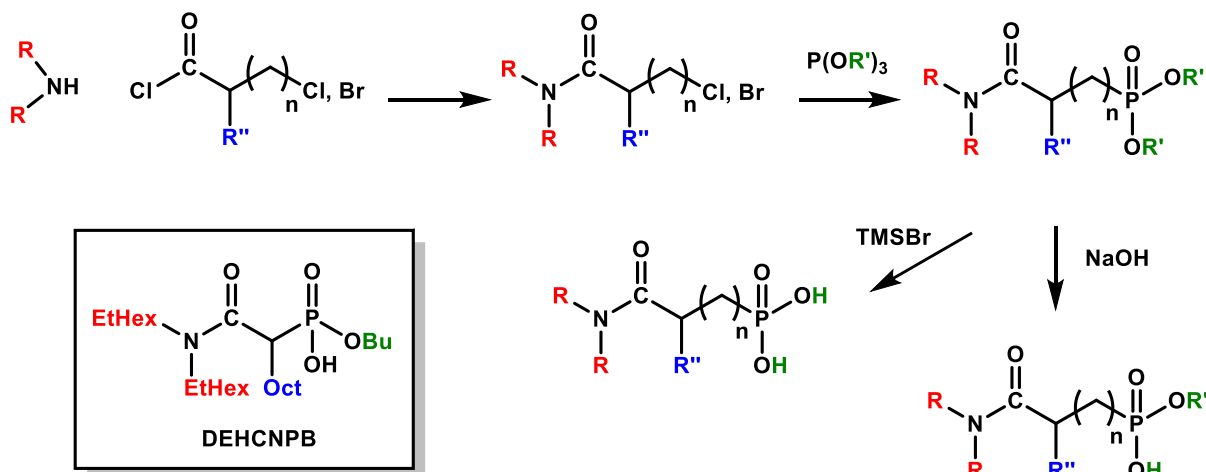


Figure 11. General synthesis of bifunctional molecules bearing a combination of amido and phosphoric acid groups and structure of butyl-1-[N,N-bis(2-ethylhexyl)carbamoyl]nonyl phosphonic acid (DEHCNPB) [78,79].

However, in the presence of uranium, it is observed that two to three extractant molecules directly coordinate with the uranyl cation through their phosphonate groups. Notably, uranyl remains partially hydrated in this organic solution, with the amide groups of the extractants forming hydrogen bonds with the water molecules bound to uranyl.

These intricate hydrogen bond networks surrounding the metallic cation serve to stabilize the complexes and facilitate the extraction process. These findings underline the significance of considering weak interactions to understand extraction processes and highlight how molecular simulations play a pivotal role in providing crucial insights into the intricate chemistry of organic phases characterized by a multitude of species.

8. Molecular systems for the purification of uranium in nitric acid

Uranium refining and conversion, which transforms yellow cake into different types of enriched uranium (uranium dioxide (UO₂), natural metallic uranium (U), etc.), is one of the most important steps in the nuclear fuel cycle, as it enables the purity levels required for use in nuclear reactors to be achieved. Uranium purification process consists of three sub-processes: dissolution, solvent extraction, solvent regeneration. The yellow cake is first dissolved in

nitric acid to produce a feed solution of metal nitrates. Uranium is then selectively extracted from this acidic feed with TBP diluted in kerosene or another suitable hydrocarbon mixture. Finally, uranium is stripped from the TBP extract in low acidified water to produce a highly purified uranyl nitrate, UO₂(NO₃)₂ [84,85].

Today, TBP extraction technology and processes are used worldwide for the purification of uranium from nitric acid feed solution. The success of TBP solvent extraction over other uranium purification processes is due to the fact that TBP (i) is highly selective for uranium and provides excellent decontamination from most impurities, (ii) is relatively stable to degradation under conditions normally used for uranium purification, (iii) has physicochemical properties tailored to the process in terms of density, viscosity, corrosion, etc [86].

In addition, TBP is one of the most versatile extractants, used at various stages of the nuclear fuel cycle, most notably in the Plutonium Uranium Reduction Extraction (PUREX) process for reprocessing spent nuclear fuel. In the context of this back-end of the nuclear fuel cycle, despite the performance of TBP, some drawbacks such as: (i) the co-extraction of neptunium and technetium, (ii) the difficulty of performing the back-extraction stage, with a necessary addition of U(IV) and hydrazine to assure the change in the oxidation state of the Pu(IV) to Pu(III), and

(iii) the significant degradation of the TBP through radiolysis and the water-solubility of the corresponding degradation products, led researchers to develop alternative extraction agents. Then, several research groups have carried out in-depth studies on uranium extraction with TBP [87–90].

If alternatives to TBP have been proposed in the context of the PUREX process, some are also proposed for the upstream part of the cycle [51]. Naturally, several organophosphorus derivatives have been proposed, such as HDEHP [91,92], TOPO [93], OPAP [94], mono-2-ethylhexyl (2-ethylhexyl)phosphonate (PC88A) [95], cyanex compounds [96–98], but it is the nitrogen-based extractants that have shown the most significant results. Among them, amides and diamides [99,100] and in particular monoamides have a high potential [101–104]. Symmetrical and non-symmetrical monoamides with linear or branched chains have been studied. Some of them are grouped in Table 5 [105–109]. The results of these studies show that depending on the alkyl group on the monoamides, the performance and selectivity of uranium extraction with respect to other cations can be modulated.

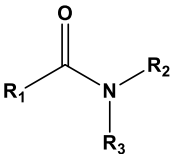
Another approach is the design of multifunctional molecules; various multifunctional compounds have shown promising properties (Table 6). For example, the combination of sulfur and nitrogen functions with amidosulfoxide structures [110] as well as the combination of phosphorus and nitrogen functions with iminomethylenediphosphonic acids [111] or aminophosphonic acid and aminophosphonate extractant [112] were suggested for the extraction and purification of uranium from dilute or concentrated nitric acid solutions. Recognizing the potential of this approach, the multifunctional ligands proposed for the extraction of uranium from the phosphoric medium such as amidophosphonates showed interest for the purification of uranium from the nitric medium. The importance of the presence of a biposphonate moiety rather than a monophosphonate moiety was demonstrated for high extraction efficiency and selectivity. In addition, the bifunctional extractant was found to improve the uranium loading capacity by a factor of about 1.3 compared to TBP and to have a slightly lower solubility in the aqueous phase. As with TBP, uranium extraction is favoured in high nitric acid concentrations, suggesting that back-extraction at low acidity is also possible [113].

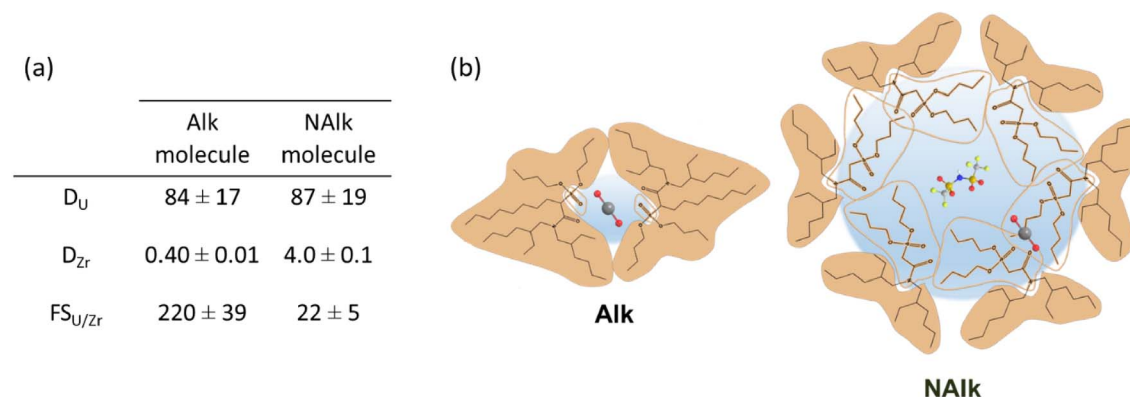
The extraction mechanisms of two bifunctional extractants, differing only by the grafting of an alkyl chain between their two functions, were studied at molecular and supramolecular scales to investigate the origin of their very different separation factors for uranium and zirconium (Figure 12a) [114]. This investigation aimed to uncover the reasons behind their significantly different separation factors when it comes to uranium and zirconium. By scrutinizing the complex structure through spectroscopic analyses, including FTIR, ESI-MS, and EXAFS, it was established that the alkylation process does not alter the chelation mechanism for uranium and zirconium. The stoichiometries of the formed complexes remained identical for both extractants, resulting in the formation of $\text{UO}_2\text{L}_2(\text{NO}_3)_2$ complexes and zirconium polynuclear complexes upon extraction into the organic phase. Consequently, the investigation shifted its focus to discerning the origins of selectivity by examining the supramolecular self-assembly behavior of these two bifunctional molecules.

SAXS and SANS showed that the most significant separation factors between uranium (U) and zirconium (Zr) are achieved when smaller aggregates are present (Figure 12b). Consequently, this study strongly suggests that the selectivity is governed by the supramolecular self-assembly of the two extractant molecules. In the case of the non-alkylated molecule, its larger packing parameter leads to the formation of larger aggregates, akin to reverse micelles. These larger aggregates have the ability to extract additional polar species into their polar core through a solubilization effect, which, in turn, reduces the separation factor between uranium and zirconium.

Here it has been demonstrated *de novo* that the efficiency and the selectivity of a liquid–liquid extraction process may rely on a complex combination of various parameters, among which the colloidal properties of the extraction system are certainly one of the main contributors. However, ability to self-assemble is itself driven by a peculiar combination of the lipophilic-hydrophilic balance of the ligand, the composition of the aqueous phase, the solvophobic effect and the geometry of the ligand [63,115–117]. As the geometry of the ligand is tightly linked to its stereochemistry, one interesting open insight was to investigate the SAR between stereochemistry and complexation properties at supramolecular scale. This aspect is discussed below.

Table 5. General formula of *N,N*-dialkylamides used for uranium extraction from nitric acid medium

Name			Reference
<i>N,N</i> -di-2-ethylhexylacetamide	$R_1 = \text{CH}_3$	$R_2 = R_3 = (\text{C}_4\text{H}_9)(\text{C}_2\text{H}_5)\text{CHCH}_2$	[105]
<i>N,N</i> -di-2-ethylhexylpropionamide	$R_1 = \text{CH}_3\text{CH}_2$	$R_2 = R_3 = (\text{C}_4\text{H}_9)(\text{C}_2\text{H}_5)\text{CHCH}_2$	[105]
<i>N,N</i> -di-2-ethylhexylbutyramide (DEHBA)	$R_1 = \text{CH}_3\text{CH}_2\text{CH}_2$	$R_2 = R_3 = (\text{C}_4\text{H}_9)(\text{C}_2\text{H}_5)\text{CHCH}_2$	[105]
<i>N,N</i> -di-2-ethylhexylisobutyramide (DEHiBA)	$R_1 = (\text{CH}_3)_2\text{CH}$	$R_2 = R_3 = (\text{C}_4\text{H}_9)(\text{C}_2\text{H}_5)\text{CHCH}_2$	[105–108]
<i>N,N</i> -di-2-ethylhexylpivalamide	$R_1 = (\text{CH}_3)_3\text{C}$	$R_2 = R_3 = (\text{C}_4\text{H}_9)(\text{C}_2\text{H}_5)\text{CHCH}_2$	[105]
<i>N,N</i> -dihexyloctanamide	$R_1 = \text{C}_8\text{H}_{17}$	$R_2 = R_3 = \text{C}_6\text{H}_{13}$	[108]
<i>N</i> -methyl- <i>N</i> -octyl-2-ethylhexanamide	$R_1 = (\text{C}_4\text{H}_9)(\text{C}_2\text{H}_5)\text{CHCH}_2$	$R_2 = \text{C}_8\text{H}_{17}$ $R_3 = \text{CH}_3$	[109]

**Figure 12.** (a) U/Zr distribution coefficients and corresponding separation factors for the alkylated and non-alkylated extractants (Alk and NAlk) diluted at $0.5 \text{ mol}\cdot\text{L}^{-1}$ in dodecane after contact with an aqueous phase: $[\text{HNO}_3] = 4 \text{ mol}\cdot\text{L}^{-1}$ $[\text{U}] = [\text{Zr}] = 10 \text{ mmol}\cdot\text{L}^{-1}$. (b) Schematic illustration of the aggregates formed with Alk and NAlk extractants according to their polar and apolar part distribution [114].

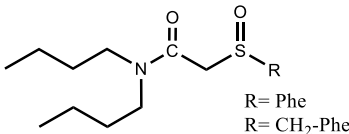
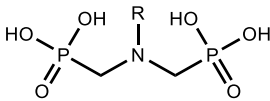
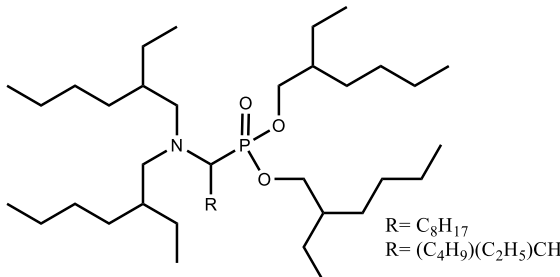
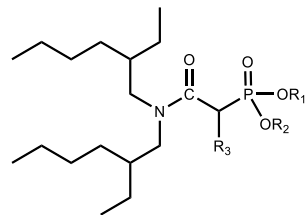
9. The influence of the ligands stereochemistry on the liquid–liquid extraction process

9.1. A foreword about significance of the stereoisomerism in the context of hydrometallurgy

By observing carefully all the ligands structures presented in previous sections (see entries 3 and 4

Table 4, for instance) or in the cited literature, the questioning about how extraction may be affected by the stereochemistry of the ligand is perfectly understandable. Indeed, branched alkyl chains and unsymmetrically substituted methylene bridges bring chirality and the possibility for isomery of position. Therefore, some studies have been carried out to demonstrate the effect of the diastereoisomerism

Table 6. General formula of multifunctional molecules used for uranium extraction from nitric acid medium

Entry	Extractant structure	Extraction condition	Reference
#1	 <p>R = Phe R = CH₂-Phe</p>	[extractant] = 0.5 mol·L ⁻¹ [U] = 10 ⁻¹⁰ mol·L ⁻¹ ; [HNO ₃] = 0.5–9.5 mol·L ⁻¹	[110]
#2	 <p>R = C₁₆H₃₃ R = C₁₀H₂₁</p>	[extractant] = 0.03–0.3 mol·L ⁻¹ [U] = 0.015 mol·L ⁻¹ ; pH = 2	[111]
#3	 <p>R = C₈H₁₇ R = (C₄H₉)(C₂H₅)CH</p>	[extractant] = 0.1 mol·L ⁻¹ [U ^{VI} = Fe ^{III} = Mo ^{VI} = Ce ^{III} = La ^{III} = Gd ^{III} = Yb ^{III} = Nd ^{III} = Ti ^{IV} = Zr ^{IV} = Th ^{IV}] = 250 mg·L ⁻¹ ; [HNO ₃] = 2 mol·L ⁻¹	[112]
#4	 <p>R₁ = R₂ = C₄H₉; R₃ = H R₁ = R₂ = C₄H₉; R₃ = C₈H₁₇ R₁ = H; R₂ = C₄H₉; R₃ = C₈H₁₇</p>	[extractant] = 0.2 mol·L ⁻¹ [U ^{VI} = Fe ^{III} = Mo ^{VI} = V ^{III} = Zr ^{IV} = Th ^{IV}] = 1 × 10 ⁻³ mol·L ⁻¹ ; [HNO ₃] = 4 mol·L ⁻¹	[113]

and/or the regioisomerism on the solvent exchange process. Nevertheless, as ambitious and challenging as they were, these studies have only been sparsely reported during the last four decades.

Pionnering works that concerned the use of two diastereoisomers (cis-syn-cis- and cis-anti-cis-isomers) of dicyclohexano-18-crown-6 ether (Figure 13A) in the context of uranium extraction [118] and reprocessing [119], were achieved during the 80's and the 90's by different teams. It was found that the cis-syn-cis-diastereoisomer had typical higher affinity for uranium than that of its cis-anti-cis-diastereoisomer. This was explained by the different orientation of the lone pairs of the oxygen atoms in both isomers as reported by Wang et al. [118], and a decade later, Dietz et al. [120] considered rather the difference of free energy reorganization needed for each complexed isomer. A year

later, Tsukube et al. reported that the selectivity towards Ag (I) of a series of tridentate pyridine podans (Figure 13B) could be easily adjusted by tuning the chirality of these derivatives [121]. Short explanations were only given at the molecular scale. Finally, a major step forward was done with the works of Wilden and Weßling who showed that diastereoisomerism of some chiral diglycolamide (DGA) derivatives (Figure 13C) could significantly affect the organization of the ligand and its interaction with other partners than the metal cation (lanthanide or actinide), on the inner- and the outer-sphere of coordination [122,123].

Beside the influence of the DGAs chirality, the effect induced on the liquid–liquid extraction (LLE) process by their regioisomerism was also highlighted by Stamberg et al. who assessed the intra-lanthanide selectivity of several DGAs

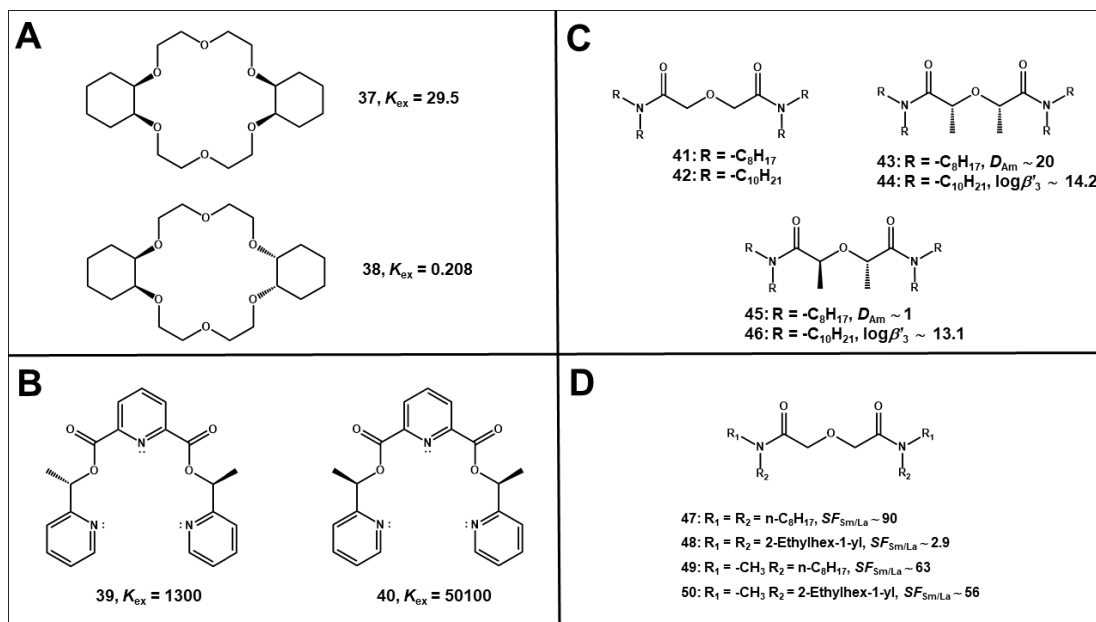


Figure 13. (A) Structure of the cis-syn-cis- (**37**) and cis-anti-cis- (**38**) isomers of dicyclohexano-18-crown-6 ether and respective uranium extraction equilibrium constant K_{ex} [118]. (B) Structure of two diastereoisomers of a chiral podand and respective silver extraction equilibrium constant K_{ex} [121]. (C) Structure of some achiral and chiral DGAs. *N,N,N',N'*-tetraoctyldiglycolamide (TODGA) **41** and *N,N,N',N'*-tetradecyldiglycolamide (TDDGA) **42** are achiral whereas their respective bis-*C*-methylated derivatives TODGA-Me₂ and mTDDGA can be distinguished in cis- (or meso) (**43** and **45**) and (**44** and **46**) trans-isomers. Americium coefficient distribution D_{Am} were obtained with extraction of 10^{-5} mol·L⁻¹ of Am in 4.3 mol·L⁻¹ HNO₃ performed at 298 K, with 0.1 mol·L⁻¹ ligand in TPH [122]. Stability constants $\log \beta'_n$ for the complexation of Cm (III) was measured in 2-propanol with 5 vol% H₂O and 10^{-2} mol·L⁻¹ HClO₄ [123]. (D) Structure of various DGAs and associated samarium to lanthanum factor separation ($SF_{Sm/Ln} = D_{Sm}/D_{Ln}$) determined by extraction of 5×10^{-4} mol·L⁻¹ of lanthanides in 3 mol·L⁻¹ HCl with 0.1 mol·L⁻¹ ligand in Isopar L with 30 vol% Exxal 13 at 298 K [124].

derivatives (Figure 13D) whose nitrogen substituents were either linear or branched alkyl chains [124]. Although it was not the main goal of these researches that focused more generally on the effect of chains length and the position of the branching, conclusions about regioisomerism could be established by comparing the results yielded by some of those DGAs derivatives that carried regiomers of a same alkyl chains (*n*-octyl, 2-ethylhexyl for instance). Explanations were given at the scale of the aggregate. Sterical hindrance and the interfacial properties varying according to the considered compound were claimed as the main parameters affecting differently the process. In the same way, the studies undertook with linear and branched trialkylamines by our team

in the AMEX context (see Section 4) comes to sustain these conclusions.

To summarize, some ensuing questions would be: if both diastereoisomerism and regioisomerism affect the process, which one is predominant? How? Why? What are the challenges afforded by chirality in the context of the fuel cycle?

The answer to the last question seems obvious if one considers that some current and extensive work aims to replace advantageously the TBP at the down-stream of the cycle by other ligands with more complex structures (see Section 8), thus potentially chiral as it is the case of the *N,N*-di(2-ethylhex-1-yl)butyramide (DEHBA) (Table 5) claimed as promising candidate.

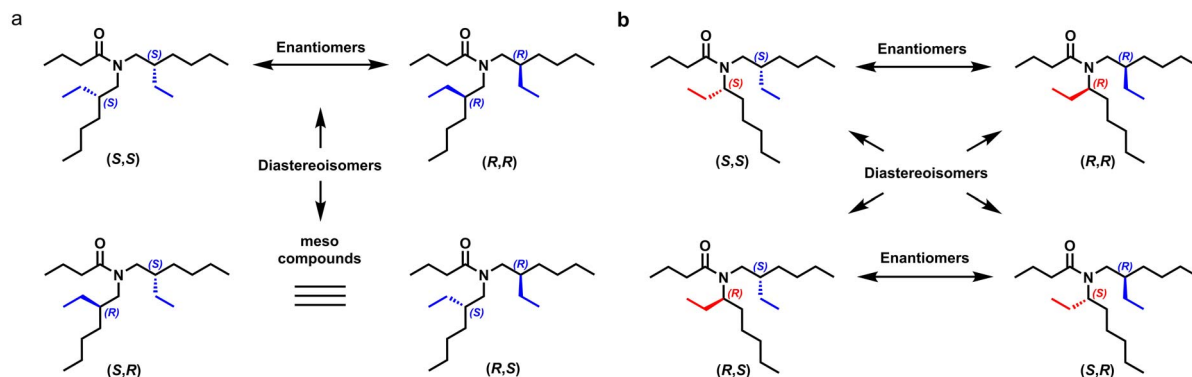


Figure 14. Structure of the stereoisomers of DEHBA (a) and EHOBA (b) [125,126].

Thus, in order to address the aforementioned resulting concerns, a partnership was established some years ago between the CEA Marcoule Atalante and the ICSM. Our first results and conclusions are briefly reported in the following section.

9.2. Impact of the stereochemistry of the DEHBA on the plutonium (IV) extraction [125]

The aims of this work was to: (i) clarify if the diastereoisomers and the regioisomers of the DEHBA presented marked differences of extraction properties towards uranium and plutonium, (ii) understand and explain the mechanism involved.

DEHBA is a ternary monoamide carrying two chiral centers and presenting three stereoisomers, which are the *(R,R)*-DEHBA, its enantiomer *(S,S)*-DEHBA and the achiral meso *(R,S)*- or *(S,R)*-DEHBA (Figure 14).

This molecule is commonly obtained as an achiral mixture via a Schotten–Baumann reaction starting from butyryl chloride and commercially available diastereomeric mixture of bis(2-ethylhexylamine). The first part of the project consisted of the development of diastereopure *(S,S)*- and *(R,S)*-forms of both the DEHBA and one of its regioisomer, namely the *N*-(2-ethylhexyl)-*N*-(octan-3-yl)butyramide, (EHOBA) [125,127]. The interest in providing EHOBA was to access to a DEHBA isomer for which one ethyl side chain was closer to the complexing amide function. Therefore, if there was one, the impact of chirality was expected to be more pronounced for the EHOBA. The synthesis of the diastereopure forms of the monoamides consisted to react activated butyric acid with the diastereopure forms of the

N,N-dialkylamine. These latter were obtained after a multi-steps synthesis. The diastereopure bis(2-ethylhexylamine) was yielded after reaction of the enantiopure 2-ethylhexylamine with enantiopure 3-(bromomethyl)heptane. Both synthons were derived from one of the two enantiomers of 2-ethylhexanoic acid resolved by diastereoselective recrystallization. The diastereopure *N*-(2-ethylhexyl)octan-3-amine was obtained after reaction of the enantiopure 2-ethylhexylamine with the racemic 3-bromooctane, followed by resolution of both yielded diastereoisomers on a chromatography column (Figure 15).

Each diastereoisomers mixture and the diastereopure form of DEHBA and EHOBA were evaluated in the context of U and Pu extraction in nitric media. It was found that the stereochemistry of DEHBA did not affect U extraction (not shown), whereas it impacted the extraction of Pu (Figure 16A).

Effect on Pu extraction was shown to be more significant for the EHOBA extractant as the branching is closer (α position) to the complexing site. In both cases, this stereochemical effect could be related to the formation of different inner or outer-sphere complexes (Figure 16B), which are demoted or promoted by steric hindrance.

To summarize, ligands stereochemistry which intervenes at different level in the solvent exchange process should be one of the major concerns to be clarified and addressed for a better understanding of the process. Moreover, once mastered, this key-parameter should allow to finely adjust the process. This last statement paved the way for further fundamental studies aiming to verify the impact of the

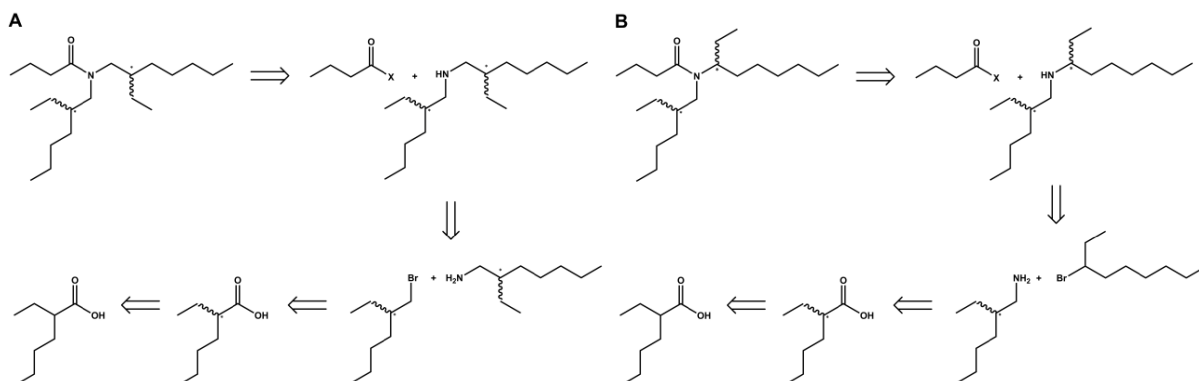


Figure 15. Retrosynthetic scheme of the synthesis of unresolved and diastereopure DEHBA (A) and EHOBA (B). Butanoyl-X may be a butanoyl halide or a reactive ester of butanoic acid. Unresolved form of EHOBA is obtained from the diastereoisomers mixture of *N*-(2-ethylhexyl)octan-3-amine, itself yielded by condensation of racemic 2-ethylhexylamine with racemic 3-bromooctane [125–128].

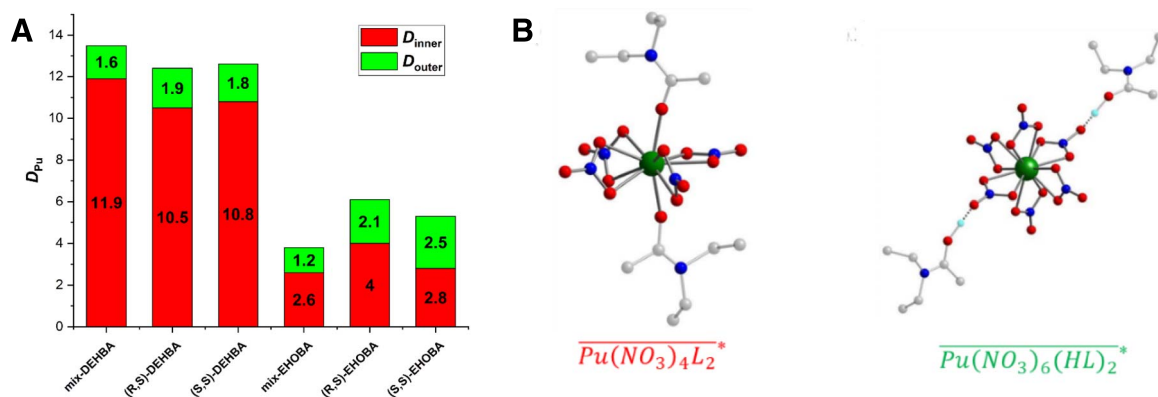


Figure 16. (A) D_{Pu} obtained after extraction of a Pu solution ($[Pu^{IV}]_{aq,ini} = 2.23 \times 10^{-2} \text{ mol}\cdot\text{L}^{-1}$, $[HNO_3]_{aq,ini} = 4 \text{ mol}\cdot\text{L}^{-1}$) by the various achiral mixtures (mix) or diastereopure monoamides ([Lig-and] = $1.2 \text{ mol}\cdot\text{L}^{-1}$) in hydrogenated tetrapropylene (TPH) at 298 K with 1:1 A:O. The proportion of each type of complex (inner- or outer-sphere) involved in the extraction mechanism was determined UV-vis spectroscopy (not shown). (B) Density functional theory (DFT) model of Pu monoamide inner- (left) and outer-sphere complex. For simplification, the simulation was achieved with the *N,N*-diethylpropanamide. Pu:ligand:nitrate stoichiometry was also given for each type of complex [125] (source: Figures 4b and 3 from Ref. [125] under licence CC BY-NC-ND).

stereochemistry of branched ligands, be it commonly used at large scale in hydrometallurgic process (HDEHP for instance) or at lab scale (monoamides, amino- and amidophosphonates). These works are currently under development at the ICSM.

10. Conclusion

As the uranium industry has expanded, research efforts have focused on optimizing techniques, es-

pecially leaching and liquid/liquid extraction in order to improve both the yield and selectivity toward the targeted uranium as well as the environmental footprint. Future challenges include recovering uranium from more complex resources, which may often be of lower grade and at greater depth than the deposits currently being processed. Thus, research has focused on the improvement of the recovering of uranium from conventional and unconventional resources, including sulfuric, phosphoric and nitric

acid, as well as low-grade ores and seawater. The uranium industry aims to develop this wide variety of mining and processing techniques because uranium ores are extremely diverse. For that, processing operations must be designed to take into account the specific composition and mineralogical characteristics of the ore to be treated. Extraction mechanisms of any given extraction operation should be investigated to comprehensively understand and quantify such variability. This understanding is essential for the selection of a combination of unit operations that can economically and environmentally accommodate this variability.

With the common goal of improving and understanding uranium extraction processes, this review aimed to put in regards the various extractant synthesis strategies and the mechanistic studies of uranium extraction in sulfuric, phosphoric and nitric media. As evidenced by the literature, these investigations are fundamental and should encompass a comprehensive characterization that includes both molecular and supramolecular descriptions of the organic phase structure. The alkyl chains of the synthesized and examined extractants, along with those of the diluent, were for instance modified to investigate their impact on the organic phase structure, uranium extraction efficiency, and on the third-phase formation. A study of a system in the absence of diluent was also described, considering the analogy of such a system to ionic liquid media.

Overall, this review shows that synthesizing and studying new extractants for uranium extraction remains essential for improving the efficiency, selectivity, and sustainability of nuclear fuel production while minimizing its environmental impact. These efforts are critical to the continued growth and advancement of nuclear energy technologies.

Abbreviations

AMEX:	amine extraction	D_U :	uranium distribution coefficient
DAPEX:	dialkylphosphoric acid extraction	EHOBa:	<i>N</i> -(2-ethylhexyl)- <i>N</i> -(octan-3-yl)butyramide
DBBP:	dibutyl butylphosphonate	ESI-MS :	electrospray ionization mass spectroscopy
DEHBA:	<i>N,N</i> -di(2-ethylhex-1-yl)butyramide	EXAFS:	extended X-ray absorption fine structure analysis
DEHCNPB:	butyl-1-[<i>N,N</i> -bis(2-ethylhexyl)carbamoyl]nonyl phosphonic acid	FT-IR:	Fourier-transform infrared spectroscopy
DGA:	diglycolamide	HDEHP:	di-2-ethylhexylphosphoric acid
		ILs:	ionic liquids
		ISL:	in situ leaching
		K_{ex} :	exchange equilibrium constant
		LCA:	life cycle assessment
		LLE:	liquid-liquid extraction
		MD:	molecular dynamics
		MS:	mass spectroscopy
		MOX:	mixture of oxides
		NMR:	nuclear magnetic resonance spectroscopy
		ORNL:	Oak-Ridge National Laboratory
		OPAP:	octyl phenyl acid phosphate
		OPPA:	octyl pyro phosphoric acid
		PC88A:	mono-2-ethylhexyl (2-ethylhexyl)phosphonate
		PUREX:	Plutonium Uranium Reduction EXtraction
		REE:	rare earth element
		SAR:	structure-activity relationship
		SANS:	Small-Angle Neutron Scattering
		SAXS:	Small-Angle X-ray Scattering
		TAPO:	trialkylphosphine oxide
		TBP:	tributylphosphate
		TBPO:	tributylphosphine oxide
		mTDDGA:	2,2'-oxybis(<i>N,N</i> -didecylpropanamide)
		TDDGA:	<i>N,N,N',N'</i> -tetradecyldiglycolamide
		TOA:	trioctylamine
		TODGA:	<i>N,N,N',N'</i> -tetraoctyldiglycolamide
		TODGA-Me2:	2,2'-oxybis(<i>N,N</i> -dioctylpropanamide)
		TOPO:	trioctylphosphine oxide
		TPH:	hydrogenated tetrapropylene
		UOX:	uranium oxide
		URPHOS:	uranium from industrial phosphoric acid
		WPA:	wet-process phosphoric acid

Declaration of interests

The authors do not work for, advise, own shares in, or receive funds from any organization that could benefit from this article, and have declared no affiliations other than their research organizations.

Acknowledgements

The authors acknowledge the GDR PROMETHEE, the NEEDS program as well as the CEA for their support. They also thank Tamir Sukhbaatar, Alexandre Artese, Zijun Lu, Nicolas Felines, Julien Rey, Mohamedine Wehbie, Olivia Pecheur, Raphael Turgis, Antoine Leydier, Beatrice Baus-Lagarde, Thomas Dumas, Cécile Marie, Manuel Miguirditchian, Thomas Zemb, Jean-Francois Dufrêche, Magali Duvail for their fruitful discussions and contributions on the subject of uranium extraction. The authors are also grateful to the Editors Elsevier, American Chemical Society, Taylor & Francis, Royal Society of Chemistry and Wiley for their applied copyright policy allowing free reproduction and/or modification of all original figures (sometimes only for authors of the original articles, please check those publishers' policies).

References

- [1] Nuclear Energy Agency; International Atomic Energy Agency, *Uranium 2020: Resources, Production and Demand*, Uranium; NEA 7551, OECD, 2021.
- [2] C. F. Coleman, K. B. Brown, J. G. Moore, D. J. Crouse, *Ind. Eng. Chem.*, 1958, **50**, 1756-1762.
- [3] C. A. Blake, K. B. Brown, C. F. Coleman, *Solvent Extraction of Uranium (and Vanadium) from Acid Liquors with Trialkylphosphine Oxides*, ORNL-1964; Oak Ridge National Lab. (ORNL), Oak Ridge, TN, 1955.
- [4] C. A. Blake, K. B. Brown, C. F. Coleman, *The Extraction and Recovery of Uranium (and Vanadium) From Acidic Liquors With Di(2-Ethylhexyl) Phosphoric Acid and Some Other Organophosphorus Acids*, ORNL-1903; Oak Ridge National Lab. (ORNL), Oak Ridge, TN, 1955.
- [5] C. A. Blake, D. J. Crouse, C. F. Coleman, K. B. Brown, A. D. Kelmers, *Further Studies of the Dialkylphosphoric Acid Extraction (DAPEX) Process for Uranium*, ORNL-2172; Oak Ridge National Lab. (ORNL), Oak Ridge, TN, 1956, 1-127 pages.
- [6] C. F. Baes, R. A. Zingaro, C. F. Coleman, *J. Phys. Chem.*, 1958, **62**, 129-136.
- [7] C. Blake, C. Baes, K. Brown, *Ind. Eng. Chem.*, 1958, **50**, 1763-1767.
- [8] C. Balaguer, C. Sorel, L. Hung, D. Hartmann, M. Marbet, N. Syna, *Procedia Chem.*, 2012, **7**, 139-145.
- [9] K. Kiegiel, A. Abramowska, P. Bieluszka, G. Zakrzewska-Kołodziej, S. Wołkiewicz, *J. Radioanal. Nucl. Chem.*, 2017, **311**, 589-598.
- [10] C. A. Nizinski, A. B. Hanson, B. C. Fullmer, N. J. Mecham, T. Tasdizen, L. W. McDonald, *Miner. Eng.*, 2020, **156**, article no. 106457.
- [11] T. Sato, H. Watanabe, *Sep. Sci. Technol.*, 1982, **17**, 625-634.
- [12] T. Sato, H. Watanabe, H. Suzuki, *Solvent Extr. Ion Exch.*, 1986, **4**, 987-998.
- [13] A. Chagnes, C. Fosse, B. Courtaud, J. Thiry, G. Cote, *Hydrometallurgy*, 2011, **105**, 328-333.
- [14] A. Chagnes, M.-N. Rager, B. Courtaud, J. Thiry, G. Cote, *Hydrometallurgy*, 2010, **104**, 20-24.
- [15] J. P. McDonald, P. L. Mattison, J. M. W. Mackenzie, *J. South Afr. Instit. Min. Metall.*, 1981, **81**, 303-308.
- [16] B. M. Munyungano, *J. South Afr. Instit. Min. Metall.*, 2007, **107**, 415-417.
- [17] A. Chagnes, B. Courtaud, J. Thiry, G. Cote, *J. Chem. Technol. Biotechnol.*, 2009, **84**, 1899-1907.
- [18] A. Chagnes, B. Courtaud, J. Thiry, J. Bayardon, S. Jugé, G. Cote, *Solvent Extr. Ion Exch.*, 2012, **30**, 67-76.
- [19] A. Chagnes, G. Cote, *Metals*, 2018, **8**, article no. 57.
- [20] T. Sukhbaatar, M. Duvail, T. Dumas, S. Dourdain, G. Arrachart, P. L. Solari, P. Guilbaud, S. Pellet-Rostaing, *Chem. Commun.*, 2019, **55**, 7583-7586.
- [21] Z. Lu, S. Dourdain, B. Demé, J.-F. Dufrêche, T. Zemb, S. Pellet-Rostaing, *J. Mol. Liq.*, 2022, **349**, article no. 118409.
- [22] Z. Lu, S. Dourdain, J.-F. Dufrêche, B. Demé, T. Zemb, S. Pellet-Rostaing, *J. Mol. Liq.*, 2022, **349**, article no. 118487.
- [23] E. Guerinoni, "Mécanismes moléculaires et supramoléculaires d'extraction de l'uranium par des amines tertiaires et des ammoniums quaternaires", Phd thesis, Montpellier UM2, ED 459, 2023.
- [24] E. Guerinoni, S. Dourdain, L. Zijun, G. Fabrice, G. Arrachart, J. Couturier, D. Hartmann, S. Pellet-Rostaing, *Hydrometallurgy*, 2024, **224**, article no. 106257.
- [25] E. Guerinoni, S. Dourdain, T. Dumas, G. Arrachart, F. Giusti, Z. Lu, P.-L. Solari, S. Pellet-Rostaing, *Separations*, 2023, **10**, article no. 509.
- [26] D. S. Flett, *J. Organomet. Chem.*, 2005, **690**, 2426-2438.
- [27] S. Kuang, Z. Zhang, Y. Li, G. Wu, H. Wei, W. Liao, *Hydrometallurgy*, 2017, **167**, 107-114.
- [28] E. Kukkonen, E. J. Virtanen, J. O. Moilanen, *Molecules*, 2022, **27**, article no. 3465.
- [29] V. Jagodić, D. Grdenić, *J. Inorg. Nucl. Chem.*, 1964, **26**, 1103-1109.
- [30] E. K. Fields, *J. Am. Chem. Soc.*, 1952, **74**, 1528-1531.
- [31] K. Moedritzer, R. R. Irani, *J. Org. Chem.*, 1966, **31**, 1603-1607.
- [32] A. N. Pudovk, *Dokl. Akad. Nauk SSSR*, 1950, **73**, 499-502.
- [33] G. Keglevich, E. Bálint, *Molecules*, 2012, **17**, 12821-12835.
- [34] S. Pellet-Rostaing, A. Leydier, G. Arrachart, R. Turgis, V. Dubois, "Compounds with Phosphine Oxide and Amine Functions as Ligands for Uranium(VI) Extraction from Aqueous Solutions of Sulfuric Acid", 2016, FR3034417 (A1) / WO2016156591 (A1).
- [35] X. Yang, Z. Zhang, S. Kuang, H. Wei, Y. Li, G. Wu, A. Geng, Y. Li, W. Liao, *Hydrometallurgy*, 2020, **194**, article no. 105343.
- [36] E. J. Virtanen, S. Perämäki, K. Helttunen, A. Väisänen, J. O. Moilanen, *ACS Omega*, 2021, **6**, 23977-23987.

- [37] M. Wehbie, G. Arrachart, T. Sukhbaatar, X. F. L. Goff, I. Karamé, S. Pellet-Rostaing, *Hydrometallurgy*, 2021, **200**, article no. 105550.
- [38] M. Wehbie, G. Arrachart, X. F. Le Goff, I. Karamé, S. Pellet-Rostaing, *Dalton Trans.*, 2018, **47**, 14594-14603.
- [39] G. Steiner, B. Geissler, N. Haneklaus, *Environ. Sci. Technol.*, 2020, **54**, 1287-1289.
- [40] A. Haneklaus, Y. Sun, R. Bol, B. Lottermoser, E. Schnug, *Environ. Sci. Technol.*, 2017, **51**, 753-754.
- [41] M. Walters, T. Baroody, W. Berry, *Technologies for Uranium Recovery from Phosphoric Acid*, AIChE Central Florida Section, Clearwater Convention, 2008.
- [42] C. Gupta, H. Singh, *Uranium Resource Processing: Secondary Resources*, Springer, Berlin, Heidelberg, 2003.
- [43] A. Boitsov, G. Capus, F. J. Dahlkamp, S. Kidd, G. Klassen, J. M. McMurray, H. Miyada, R. Shani, W. N. Szymski, D. H. Underhill, I. Vera, *Analysis of Uranium Supply to 2050*, International Atomic Energy Agency, Vienna, 2001, <https://www.iaea.org/publications/6115/analysis-of-uranium-supply-to-2050>.
- [44] A. Davister, M. G. Lyaudet, B. Schneider, Y. Volkman, I. Ezahr, T. Botella, A. Tolic, *The Recovery of Uranium from Phosphoric Acid*, IAEA-TECDOC 533; International Atomic Energy Agency, Vienna, 1989, https://www-pub.iaea.org/MTCD/Publications/PDF/te_0533.pdf.
- [45] N. Kabay, M. Demircioğlu, S. Yaylı, E. Günay, M. Yüksel, M. Sağlam, M. Streat, *Ind. Eng. Chem. Res.*, 1998, **37**, 1983-1990.
- [46] K. Weterings, J. Janssen, *Hydrometallurgy*, 1985, **15**, 173-190.
- [47] G. Mouysset, J. Molinier, M. Lenzi, *Hydrometallurgy*, 1983, **11**, 165-179.
- [48] N. T. El-Hazek, M. S. El Sayed, *J. Radioanal. Nucl. Chem.*, 2003, **257**, 347-352.
- [49] S. K. Singh, S. K. Misra, S. C. Tripathi, D. K. Singh, *Desalination*, 2010, **250**, 19-25.
- [50] D. Beltrami, G. Cote, H. Mokhtari, B. Courtaud, B. A. Moyer, A. Chagnes, *Chem. Rev.*, 2014, **114**, 12002-12023.
- [51] J. R. Kumar, J.-S. Kim, J.-Y. Lee, H.-S. Yoon, *Sep. Purif. Rev.*, 2011, **40**, 77-125.
- [52] F. J. Hurst, D. J. Crouse, K. B. Brown, *Ind. Eng. Chem. Proc. Des. Dev.*, 1972, **11**, 122-128.
- [53] F. J. Hurst, D. J. Crouse, *Ind. Eng. Chem. Proc. Des. Dev.*, 1974, **13**, 286-291.
- [54] W. L. MacCready, J. A. Wethington Jr, F. J. Hurst, *Nuclear Technol.*, 1981, **53**, 344-353.
- [55] D. Dyrssen, L. Kuča, S. E. Hansen, N. E. Levitin, G. Westin, *Acta Chem. Scand.*, 1960, **14**, 1945-1956.
- [56] C. F. Baes, *Nucl. Sci. Eng.*, 1963, **16**, 405-412.
- [57] S. Girgin, N. Acarkan, A. A. Sirkeci, *J. Radioanal. Nucl. Chem.*, 2002, **251**, 263-271.
- [58] D. Beltrami, G. Cote, H. Mokhtari, B. Courtaud, A. Chagnes, *Hydrometallurgy*, 2012, **129-130**, 118-125.
- [59] D. Beltrami, A. Chagnes, M. Haddad, A. Varnek, H. Mokhtari, B. Courtaud, G. Cote, *Hydrometallurgy*, 2013, **140**, 28-33.
- [60] S. Dourdain, I. Hofmeister, O. Pecheur, J.-F. Dufrêche, R. Turgis, A. Leydier, J. Jestin, F. Testard, S. Pellet-Rostaing, T. Zemb, *Langmuir*, 2012, **28**, 11319-11328.
- [61] O. Pecheur, S. Dourdain, D. Guillaumont, J. Rey, P. Guilbaud, L. Berthon, M. C. Charbonnel, S. Pellet-Rostaing, F. Testard, *J. Phys. Chem. B*, 2016, **120**, 2814-2823.
- [62] J. Rey, S. Dourdain, L. Berthon, J. Jestin, S. Pellet-Rostaing, T. Zemb, *Langmuir*, 2015, **31**, 7006-7015.
- [63] J. Rey, M. Bley, J.-F. Dufrêche, S. Gourdin, S. Pellet-Rostaing, T. Zemb, S. Dourdain, *Langmuir*, 2017, **33**, 13168-13179.
- [64] M. Špadina, S. Dourdain, J. Rey, K. Bohinc, S. Pellet-Rostaing, J.-F. Dufrêche, T. Zemb, *Solvent Extr. Ion Exch.*, 2022, **40**, 106-139.
- [65] D. Beltrami, A. Chagnes, M. Haddad, H. Laureano, H. Mokhtari, B. Courtaud, S. Jugé, G. Cote, *Sep. Sci. Technol.*, 2013, **48**, 480-486.
- [66] S. K. Singh, S. C. Tripathi, D. K. Singh, *Sep. Sci. Technol.*, 2010, **45**, 824-831.
- [67] M. Krea, H. Khalaf, *Hydrometallurgy*, 2000, **58**, 215-225.
- [68] D. K. Singh, M. Anitha, K. K. Yadav, M. K. Kotekar, R. Vijayalakshmi, H. Singh, *Desalin. Water Treat.*, 2012, **38**, 292-300.
- [69] A. A. Abdel-Khalek, M. M. Ali, A. E. M. Hussein, A. F. Abdel-Magied, *J. Radioanal. Nucl. Chem.*, 2011, **288**, 1-7.
- [70] F. Bunuş, I. Miu, R. Dumitrescu, *Hydrometallurgy*, 1994, **35**, 375-389.
- [71] S. K. Singh, P. S. Dhami, A. Dakshinamoorthy, M. Sunderanan, *Sep. Sci. Technol.*, 2009, **44**, 491-505.
- [72] H. Singh, S. L. Mishra, R. Vijayalakshmi, *Hydrometallurgy*, 2004, **73**, 63-70.
- [73] H. Singh, S. L. Mishra, M. Anitha, A. B. Giriwalker, R. Vijayalakshmi, M. K. Kotekar, *Hydrometallurgy*, 2003, **70**, 197-203.
- [74] G. Lyaudet, P. Du Penhoat, A. Textoris, *Ind. Minerale Mines Carrieres Tech.*, 1989, **71**, 168-179.
- [75] A. Warshawsky, N. Kahana, R. Arad-Yellin, *Hydrometallurgy*, 1989, **23**, 91-104.
- [76] R. Fitoussi, C. Musikas, *Sep. Sci. Technol.*, 1980, **15**, 845-860.
- [77] A. Leydier, G. Arrachart, R. Turgis, G. Bernier, C. Marie, M. Miguiditchian, S. Pellet-Rostaing, *Hydrometallurgy*, 2017, **171**, 262-266.
- [78] R. Turgis, A. Leydier, G. Arrachart, F. Burdet, S. Dourdain, G. Bernier, M. Miguiditchian, S. Pellet-Rostaing, *Solvent Extr. Ion Exch.*, 2014, **32**, 478-491.
- [79] R. Turgis, A. Leydier, G. Arrachart, F. Burdet, S. Dourdain, G. Bernier, M. Miguiditchian, S. Pellet-Rostaing, *Solvent Extr. Ion Exch.*, 2014, **32**, 685-702.
- [80] R. Turgis, A. Leydier, G. Arrachart, F. Burdet, S. Dourdain, G. Bernier, M. Miguiditchian, S. Pellet-Rostaing, *Procedia Eng.*, 2016, **138**, 258-266.
- [81] M. Miguiditchian, G. Bernier, V. Pacary, C. Balaguer, C. Sorel, R. Berlemont, B. Fries, M. Bertrand, B. Camès, A. Leydier, R. Turgis, G. Arrachart, S. Pellet-Rostaing, H. Mokhtari, *Solvent Extr. Ion Exch.*, 2016, **34**, 274-289.
- [82] O. Pecheur, D. Guillaumont, S. Dourdain, L. Berthon, R. Turgis, C. Fillaux, G. Arrachart, F. Testard, *Solvent Extr. Ion Exch.*, 2016, **34**, 260-273.
- [83] D. Moreno Martinez, E. Acher, M. Vatin, S. Dourdain, D. Guillaumont, P. Guilbaud, *J. Phys. Chem. B*, 2021, **125**, 10759-10771.
- [84] A. Boulaia, J. A. Vercellone, P. S. Bull, P. P. M. H. De Regge, A. Abrao, A. W. Ashbrook, J. P. Didyk, L. Chao, C.-E. Zhu, N. M. T. El-Hazek, L. Rigo, R. Faron, B. Becker, E. Leyser, E. L. Wehner, T. Sondermann, V. K. Kansal, A. G. Gharib, J. Ka-

- mali, A. M. A. Abdul Fatah, T. Mochiji, I. S. Chang, M. Shabir, A. G. M. Jackson, A. A. Poneis, A. J. A. Roux, T. E. Scholtz, D. E. Tiltmann, C. J. H. Venter, H. I. Lindholm, B. Ipekoglu, P. A. Bleasdale, V. Y. Labaton, H. Page, R. Todd, R. K. Webster, A. Tolic, S. Ajuria, J. L. Rojas, M. Ugajin, *Advances in Uranium Refining and Conversion*, IAEA-TECDOC 420; International Atomic Energy Agency, Vienna, 1987, https://www-pub.iaea.org/MTCD/Publications/PDF/te_420_web.pdf.
- [85] R. J. Ring, G. M. Ritcey, M. Roche, S. Ajuria, D. C. Seidel, K. D. Hester, G. Lyaudet, E. Mueller-Kahle, X. Gao, Y.-R. Zhong, D.-C. Xia, J.-J. Fan, *Uranium Extraction Technology*, Technical Reports Series 359, International Atomic Energy Agency, Vienna, 1993, https://www-pub.iaea.org/MTCD/Publications/PDF/trs359_web.pdf.
- [86] L. L. Burger, *The Chemistry of Tributyl Phosphate: A Review*, Technical Report 533, Hanford Atomic Products Operation, Washington, 1955.
- [87] Y. Shigetomi, T. Kojima, H. Kamba, *J. Nucl. Sci. Technol.*, 1983, **20**, 140-144.
- [88] Z.-M. Zhou, Y.-X. Sun, S.-N. Yu, H.-F. Du, *J. Radioanal. Nucl. Chem.*, 1996, **214**, 369-379.
- [89] J. Stas, A. Dahboub, H. Shlewit, *Period. Polytech. Chem. Eng.*, 2005, **49**, 3-18.
- [90] M. Alibrahim, H. Shlewit, *Period. Polytech. Chem. Eng.*, 2007, **51**, 57-60.
- [91] C.-T. Huang, T.-C. Huang, *Solvent Extr. Ion Exch.*, 1987, **5**, 611-631.
- [92] T. C. Huang, C. T. Huang, *Ind. Eng. Chem. Res.*, 1988, **27**, 1675-1680.
- [93] D. M. Petković, M. M. Kopećni, A. A. Mltrović, *Solvent Extr. Ion Exch.*, 1992, **10**, 685-696.
- [94] S. S. V. Ramakumar, O. V. Singh, S. N. Tandon, *J. Radioanal. Nucl. Chem.*, 1987, **118**, 283-289.
- [95] S. Biswas, P. N. Pathak, D. K. Singh, S. B. Roy, V. K. Manchanda, *J. Radioanal. Nucl. Chem.*, 2010, **284**, 13-19.
- [96] S. K. Sahu, M. L. P. Reddy, T. R. Ramamohan, V. Chakravorty, *Radiochim. Acta*, 2000, **88**, 33-38.
- [97] S. D. Dogmane, R. K. Singh, D. D. Bajpai, J. N. Mathur, *J. Radioanal. Nucl. Chem.*, 2002, **253**, 477-482.
- [98] M. Karve, C. Gaur, *J. Radioanal. Nucl. Chem.*, 2007, **273**, 405-409.
- [99] V. K. Manchanda, P. N. Pathak, *Sep. Purif. Technol.*, 2004, **35**, 85-103.
- [100] Y. Wang, G. Sun, D. Xie, B. Bao, W. Cao, *J. Radioanal. Nucl. Chem.*, 1996, **214**, 67-76.
- [101] G. Sun, B. Bao, C. Liu, *J. Radioanal. Nucl. Chem.*, 1997, **218**, 101-102.
- [102] J. S. Preston, A. C. Dupree, *Solvent Extr. Ion Exch.*, 1995, **13**, 391-413.
- [103] K. McCann, J. A. Drader, J. C. Braley, *Sep. Purif. Rev.*, 2018, **47**, 49-65.
- [104] M. Miguiditchian, P. Baron, I. Bisel, B. Dinh, C. Sorel, J. Bertin, "Procédé de Purification de l'uranium d'un Concentré d'uranium Naturel", 2009, FR 2954354 (A1)/WO2011076739 (A1).
- [105] P. N. Pathak, L. B. Kumbhare, V. K. Manchanda, *Solvent Extr. Ion Exch.*, 2001, **19**, 105-126.
- [106] F. Rodrigues, G. Ferru, L. Berthon, N. Boubals, P. Guilbaud, C. Sorel, O. Diat, P. Bauduin, J. P. Simonin, J. P. Morel, N. Morel-Desrosiers, M. C. Charbonnel, *Mol. Phys.*, 2014, **112**, 1362-1374.
- [107] P. N. Pathak, R. Veeraraghavan, D. R. Prabhu, G. R. Mahajan, V. K. Manchanda, *Sep. Sci. Technol.*, 1999, **34**, 2601-2614.
- [108] P. N. Pathak, A. S. Kanekar, D. R. Prabhu, V. K. Manchanda, *Solvent Extr. Ion Exch.*, 2009, **27**, 683-694.
- [109] A. Paquet, O. Diat, L. Berthon, P. Guilbaud, *J. Mol. Liq.*, 2019, **277**, 22-35.
- [110] J. S. Gamare, K. V. Chetty, S. K. Mukerjee, S. Kannan, *Anal. Sci.*, 2009, **25**, 1167-1170.
- [111] M. Bouhoun Ali, A. Y. Badjah Hadj Ahmed, M. Attou, A. Elias, M. A. Didi, *J. Appl. Sci.*, 2011, **11**, 284-291.
- [112] S. Pellet-Rostaing, G. Arrachart, A. Leydier, R. Turgis, S. Chapron, "Use of Bifunctional Compounds with Phosphonic Acid/Phosphonate and Amino Functions for Extracting Uranium (VI) from Aqueous Nitric Acid Solutions", 2017, FR3072824 (A).
- [113] A. Artese, S. Dourdain, N. Felines, G. Arrachart, N. Boubals, P. Guilbaud, S. Pellet-Rostaing, *Solvent Extr. Ion Exch.*, 2020, **38**, 703-718.
- [114] A. Artese, S. Dourdain, N. Boubals, T. Dumas, P. L. Solari, D. Menut, L. Berthon, P. Guilbaud, S. Pellet-Rostaing, *Solvent Extr. Ion Exch.*, 2022, **40**, 431-453.
- [115] J. Rey, S. Dourdain, J.-F. Dufreche, L. Berthon, J. M. Muller, S. Pellet-Rostaing, T. Zemb, *Langmuir*, 2016, **32**, 13095-13105.
- [116] G. Ferru, L. Berthon, C. Sorel, O. Diat, P. Bauduin, J.-P. Simonin, *Procedia Chem.*, 2012, **7**, 27-32.
- [117] G. Ferru, D. Gomes Rodrigues, L. Berthon, O. Diat, P. Bauduin, P. Guilbaud, *Angew. Chem. Int. Ed.*, 2014, **53**, 5346-5350.
- [118] W.-J. Wang, Q. Sun, B. Chen, *J. Radioanal. Nucl. Chem.*, 1986, **98**, 11-16.
- [119] M. Lemaire, A. Guy, R. Chomel, J. Foos, *J. Chem. Soc., Chem. Commun.*, 1991, 1152-1154.
- [120] M. L. Dietz, A. H. Bond, R. Chiarizia, V. J. Huber, A. W. Herlinger, B. P. Hay, *Chem. Commun.*, 1999, 1177-1178.
- [121] H. Tsukube, T. Yamada, S. Shinoda, *Ind. Eng. Chem. Res.*, 2000, **39**, 3412-3418.
- [122] A. Wilden, P. M. Kowalski, L. Klauf, B. Kraus, F. Kreft, G. Modolo, Y. Li, J. Rothe, K. Dardenne, A. Geist, A. Leoncini, J. Huskens, W. Verboom, *Chem. Eur. J.*, 2019, **25**, 5507-5513.
- [123] P. Weßling, M. Trumm, T. Sittel, A. Geist, P. J. Panak, *Radiochim. Acta*, 2022, **110**, 291-300.
- [124] D. Stamberg, M. R. Healy, V. S. Bryantsev, C. Albiesser, Y. Karslyan, B. Reinhart, A. Paulenova, M. Foster, I. Popovs, K. Lyon, B. A. Moyer, S. Jansone-Popova, *Inorg. Chem.*, 2020, **59**, 17620-17630.
- [125] D. Lemire, T. Dumas, C. Marie, F. Giusti, G. Arrachart, S. Dourdain, S. Pellet-Rostaing, *Eur. J. Inorg. Chem.*, 2023, **26**, article no. e202300461.
- [126] D. Lemire, "Effet de La Régio- et Stéréoisomérisation Sur Les Mécanismes d'extraction U/Pu Par Des Monoamides Énantio-purs", Phd thesis, Montpellier UM2, ED 459, 2023.
- [127] N. Felines, G. Arrachart, F. Giusti, A. Beillard, C. Marie, S. Pellet-Rostaing, *New J. Chem.*, 2021, **45**, 12798-12801.
- [128] N. Felines, "Ligands Optiquement Purs Pour l'extraction d'actinides", Phd thesis, Montpellier ENSCM, ED 459, 2020, <http://www.theses.fr/2020ENCM0007/document>.



Research article

GDR Prométhée – French Research Network on *Hydrometallurgical Processes for Primary and Secondary Resources*

Solubilisation–microstructure relationship of trivalent salts in hydrotropic ternary systems

Asmae El Maangar^a, Johannes Gramüeller^b, Verena Huber^c, Pierre Degot^c,
Didier Touraud^{*,c}, Ruth Gschwind^b, Werner Kunz^{*,c} and Thomas Zemb^{*,a}

^a ICSM, Univ. Montpellier, CEA, CNRS, ENSCM, Marcoule, France

^b Institute of Organic Chemistry, Faculty of Chemistry and Pharmacy, University of Regensburg, D-93040 Regensburg, Germany

^c Institute of Physical and Theoretical Chemistry, Faculty of Chemistry and Pharmacy, University of Regensburg, D-93040 Regensburg, Germany

E-mail: thomas.zemb@icsm.fr (T. Zemb)

Abstract. We show here that there are four different regimes of pronounced mesoscopic structuring in the monophasic region of the water/sodium salicylate/ethyl acetate ternary phase diagram. Surprisingly, the solubility of various lanthanides is highest in these regimes containing pre-nucleation clusters and not in the complexation regime. All four local maxima of solubility are characterised by their scattering and explained in terms of the driving forces behind the structuring and as a function of the added ions. The position of the critical point was determined by regions where critical opalescence is maximal. After centrifugation, the points located at the boundary of the diphasic zone separate into two immiscible fluids of equal volumes.

While the highest solubility of metal ions is found in the region of critical fluctuations, a still high solubility combined with a significant selectivity was found in the region of the pre-nucleation clusters. This new and previously unknown feature can also be explained and may pave the way for a new, green procedure of selective rare-earth metal recovery.

Keywords. Separation chemistry, Critical fluctuations, Sodium salicylate, Lanthanides, Pre-Ouzo effect, Hydrotropes.

Funding. CNRS through the International Research Project “NISI” program, Fonds der Chemischen Industrie.

Manuscript received 23 October 2023, revised 23 April 2024, accepted 8 April 2024.

1. Introduction

Ternary systems comprising a short-chain amphiphilic molecule called “hydrotrope” and two immiscible fluids are considered as powerful solubilisation media avoiding the use of surfactants [1–3]. Hydrotropes are small, usually water-soluble,

organic molecules [4]. They comprise hydrophilic and hydrophobic moieties, with the hydrophobic moiety being too small to induce micelle formation [5]. Typical examples include neutral compounds such as short-chain alcohols like ethanol, but also charged molecules, usually anionic compounds composed of an aromatic ring with an additional sulfate, sulfonate, or carboxylate group. Typical examples of hydrotropes are sodium salicylate

*Corresponding author

(NaSal), which is widely used in the pharmaceutical and body care industry, sodium xylene sulfonate (SXS), sodium cumene sulfonate (SCS) or sodium toluene sulfonate (NaTS). The existence of well-defined mesoscale inhomogeneities in macroscopically transparent solutions was shown to be often responsible for such unexpected solubilisation capacity. Such mesoscale inhomogeneity phenomena of oil-rich and water-rich domains are comparable to the microdomains observed in the classical water/oil/surfactant ternary systems (direct, bi-continuous, and reverse microemulsions) [1,3,6,7], and therefore we call the corresponding systems surfactant-free microemulsions (SFME).

The concept of hydrotropy, defined by Neuberg in 1916 [8,9], outlines the capability of short-chain amphiphilic molecules to solubilise hydrophobic compounds in a hydrophilic solvent. In SFME showing the compartmentation of hydrophilic and hydrophobic domains, the hydrotrope accumulates mostly at the interface between water-rich and oil-rich domains. The interface between the oil-rich and water-rich domains is usually considered as a kind of highly flexible film in dynamic exchange with the surrounding medium [3,10].

In contrast to surfactants, the amphiphilic character of hydrotropes is usually considered to be insufficiently pronounced to promote micellisation or self-aggregation of the hydrotrope itself in water [11]. However, they are able to form loose or ill-defined aggregates at higher concentrations (~ 1 M) than those that would be necessary for surfactants (10^{-2} – 10^{-3} M). Sometimes the loose aggregation only happens when a hydrophobic solute is present. The solute is solubilised in binary or ternary solvents as isolated molecules, and it is not clear until now how aggregation enhances solubilisation [12]. Shimizu *et al.* described theoretically this hydrotropic solubilisation using an approach derived from pure statistical thermodynamics. They considered hydrotropic solubilisation to be the result of a subtle balance between hydrotrope–hydrotrope interaction and solute–hydrotrope interaction. In other studies, the authors argued that strong hydrotrope–hydrotrope interactions, resulting in a pre-structuring of the hydrotrope in H_2O , diminish the solubilisation efficiency of solutes [13,14]. However, the opposite was also found [7]. This solubilisation efficiency could also come from an entropic effect in the bulk of the

solvent by preferential adsorption as recently shown by Spadian *et al.* [15]. As we will see in the following, things are even more complex.

Various examples of solubilisation with anionic hydrotropes are described in the literature: Theneskumar *et al.* have solubilised a highly hydrophobic compound, lauric acid, in water using different hydrotropes such as SCS, SXS and NaTS [16]. A high amount of hydrotrope (over 0.5 mol/L) was necessary to enhance the solubility of lauric acid by a factor of 6 at room temperature. The same hydrotropes also enhance the solubility of the water-insoluble hydroxyacetophenones [17]. NaSal was used to increase the solubility of salicylic acid in water [18] and is widely used in the pharmaceutical industry as hydrotrope [19–21].

From the phase diagram consisting of water, NaSal, and ethyl acetate (EA), as studied by El Maangar *et al.*, it can be deduced that the hydrotrope is not soluble in the organic phase [22]. However, a monophasic domain was found, which is enclosed by a liquid/liquid and a solid/liquid two-phasic system (see Figure 1). The monophasic area was examined using density excess, X-ray, and neutron scattering techniques, and they evidenced three major facts. First, in an ethyl acetate saturated aqueous solution, the hydrotrope NaSal can indeed form aggregates which are reminiscent of micelles. Second, the critical point was determined to be close to the EA-rich corner of the phase diagram, surrounded by asymmetrical tie lines, and around the critical point neither a pre-Ouzo structuring nor a spontaneous Ouzo effect could be evidenced. This suggests that there is only a “normal” critical point in this phase diagram. Finally, in a domain near the liquid/solid phase boundary, X-ray, light, and neutron scattering combined with a density excess determination proved the presence of dynamic aggregates reminiscent of pre-nucleation clusters (PNC) [23]. These aggregates are stabilised without any surfactants but by selective solvation of ethyl acetate. These findings are intriguing and triggered the detailed examination of the nanostructuring occurring in the monophasic region as well as the evolution of the solubilisation capacity of charged trivalent electrolytes—lanthanide salts—by this ternary system in the single-phase region.

Our goal is to establish a structure–function relationship and to determine to what extent the microstructure influences the solubilisation of solutes

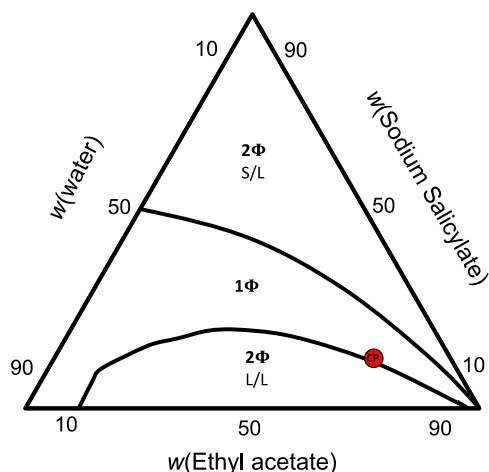


Figure 1. Ternary phase diagram of water, sodium salicylate, and ethyl acetate, showing the single phase-region present is separated by a binodal line from the 2-phase region and a S/L region with an excess precipitate that is rich in sodium salicylate. The red dot indicates the critical point. The figure is adapted from [22].

and how this will be different for electrolytes and non-electrolytes.

2. Experimental section

2.1. Materials

Ethyl acetate (EA) (purity > 99.9%) was purchased from Merck. Sodium salicylate (NaSal) (purity > 99.5%) was purchased from Sigma Aldrich. All samples were prepared with deionised water using a Millipore Milli-Q purification system (Merck Millipore, Billerica, MA). All other chemicals were purchased from Sigma Aldrich: lanthanum (III) nitrate hexahydrate $\text{La}(\text{NO}_3)_3 \cdot 6\text{H}_2\text{O}$ (purity > 99.99%), neodymium (III) nitrate hexahydrate $\text{Nd}(\text{NO}_3)_3 \cdot 6\text{H}_2\text{O}$ (purity > 99.9%), europium (III) nitrate hexahydrate $\text{Eu}(\text{NO}_3)_3 \cdot 6\text{H}_2\text{O}$ (purity > 99.9%), dysprosium (III) nitrate hexahydrate $\text{Dy}(\text{NO}_3)_3 \cdot 6\text{H}_2\text{O}$ (purity > 99.9%), and ytterbium (III) nitrate hexahydrate $\text{Yb}(\text{NO}_3)_3 \cdot 6\text{H}_2\text{O}$ (purity 99.9%). All chemicals were used without further purification.

2.2. Phase diagrams

All phase diagrams were determined with the cloud point method [24], by initially mixing sodium

salicylate with one of the other two solvents, then adding the third one dropwise to the solutions, until a visible change in the phase behaviour occurred. The initial phase diagrams were determined in mass fractions w_i . To obtain the phase diagrams in molar fractions x_i , the molar masses of the pure solvents were used. All phase diagrams were determined at 25 °C, and the phase transitions were determined with the naked eye and through two cross-polarised filters to check the presence of liquid crystals.

We define compositions in the monophasic region based on a mass fraction relative to binary fluids: α is the mass fraction of EA in the water/EA binary mixture, not taking into account the amount of hydrotrope present in the sample for the determination of α . All additions were measured by weight with a laboratory scale. Solutions were prepared at room temperature.

2.3. Density measurement and tie-line determination in the miscibility gap

Solution densities were determined using a vibrating tube density meter (DMA 5000 M, Anton Paar, Austria) at (25 ± 0.005) °C with a nominal precision of $\pm 5 \times 10^{-6}$ g/mL. Calibration was performed using air and pure water at 25 °C. Calibration was checked using pure water and between each measurement against air (allowed deviation: $\pm 5 \times 10^{-5}$ g/ml).

The determination of the density allows determining the two extremities of the tie-lines in the biphasic liquid/liquid region very precisely, i.e., the phase boundary actually corresponds to the binodal (compositions of phases in contact at equilibrium). To this purpose, a mapping of more than a hundred samples was used after interpolation of the measured densities as explained in the work of El Maangar *et al.* [22], and thus the compositions of the two phases at equilibrium are obtained.

2.4. Conductivity measurements

Conductivity measurements were carried out in a thermostatic measurement cell (25.0 °C) under permanent stirring and if necessary, manual mixing using a low-frequency WTW inoLab Cond 730 conductivity meter connected with a WTW TetraCon 325 electrode (Weilheim, Germany). 20 g of initial sample were placed in the measurement cell and

successively diluted either with pure water or ethyl acetate. The electrode was calibrated with potassium chloride, and a cell constant of $R = 0.472 \text{ cm}^{-1}$ was determined.

2.5. Diffusion-ordered NMR(DOSY) experiments

Diffusion-ordered NMR spectroscopy experiments were performed on a Bruker Avance III HD 600 MHz spectrometer, equipped with a 5 mm CPPBBO BB- $^1\text{H}/^{19}\text{F}$ probe. All measurements were performed at 298 K, and the temperature was controlled by a BVT 3000 and a BVTE 3900 temperature unit. NMR data were processed, evaluated, and plotted with the TopSpin 3.2 software.

Deuterated solvents were not employed, and no field-frequency lock was established. Due to the rather short measurement times, no drift of the chemical shifts was observed due to a missing field-frequency lock. To establish magnetic field homogeneity, shimming was performed on the ^1H NMR signals (either on the singlet of H_2O or ethyl acetate). ^1H NMR signals were not referenced.

Measurements were performed in the monophasic region (depicted in Figure 3). To this purpose 5 g samples were prepared and centrifuged at 4300 g for 10 min. Then the solutions were transferred to standard NMR tubes.

The DOSY measurements were performed with the convection-suppressing DSTE (double stimulated echo) pulse sequence developed by Jerschow and Müller in a pseudo 2D mode [25]. The diffusion time delay was set to 45 ms. Smoothed square (SMSQ10.100) gradient shapes and a linear gradient ramp with 20 increments between 5% and 95% of the maximum gradient strength (5.35 G/mm) were used. For the homospoil gradient strengths, values of 100, -13.17, 20, and -17.13% were used. For each compound in the sample, gradient pulse lengths were first optimised to obtain a sigmoidal signal decay for increasing gradient strength, with gradient pulse lengths ranging from 0.75 to 3.3 ms. NMR spectra were processed with Bruker TopSpin 3.2 (T1/T2 relaxation package), and diffusion coefficients were derived according to Jerschow and Müller [25].

2.6. X-ray fluorescence (XRF) measurements

For ternary systems containing organic compounds, X-ray fluorescence (XRF) is a precise and suitable

method to quantify the elements present in the solution. The commercial XRF spectrometer used to analyse the samples after solubilising lanthanides is a SPECTRO XEPOS (AMETEK) model. It is commercially equipped with an energy dispersive X-ray analyser (ED-XRF) that uses the energy loss of the X photon in a silicon material to determine the spectrum by suitable signal processing. Secondary targets reduce background noise compared to the output signal from the tube and improve fluorescence detection. Liquid samples were placed in 6 mm diameter cups, the bases of which consisted of a 4 mm-thick proline film. The XRF spectrometer was used to analyse a series of eleven cups in sequence, using a rotating carousel that positions the samples to be measured above the inverted optical part. A volume of 200 μL of each of the samples was placed in the microcups for analysis for a duration of 40 min. The X-ray tube generator was set at 40 kV and an intensity of 0.160 mA. The zirconium secondary target was monitored between 15 and 17 keV to visualise the fluorescence of all lanthanides and between 4 keV and 10 keV for iron.

In order to quantify the elements from the raw spectra, we used a calibration procedure described and further detailed in the Supporting Information. In other words, one XRF spectrum yields a concentration value after processing with the calibration. Calibration was carried out using commercial ICP-OES standard solutions.

2.7. Small- and wide-angle X-ray scattering (SWAXS) experiments

Small- and wide-angle X-ray scattering experiments were carried out on a bench, built by Xenocs using X-ray radiation from a molybdenum source ($\lambda = 0.71 \text{ \AA}$), delivering a 1 mm-large circular beam of 17.4 keV. The scattered beam was recorded by a large on-line scanner detector (MAR Research 345) which was located 750 mm from the sample stage. Off-center detection was used to cover a large q range simultaneously ($0.2 \text{ nm}^{-1} < q < 30 \text{ nm}^{-1}$, $q = (4\pi/\lambda) \sin(\theta/2)$).

Collimation was applied using a $12:\infty$ multilayer Xenocs mirror (for Mo radiation), coupled to two sets of Forvis scatterless slits, which provides a $0.8 \text{ mm} \times 0.8 \text{ mm}$ X-ray beam at the sample position. A high-density polyethylene sample (from Goodfellow) as

a calibration standard was used to obtain absolute intensities. Silver behenate in a sealed capillary was used as scattering vector calibration standard. Integration of the two-dimensional spectra was performed, using the FIT2D software. Data were normalised considering the electronic background of the detector, transmission measurements, and empty cell subtraction. The acquisition time was 1800 s per sample.

Fitting of the spectra was done with the SasView package [26], assuming two different models. On the one hand, an Ornstein–Zernike formula was used for composition fluctuations which gives information about the pseudo-phase domain size [27], on the other hand, a simple sphere model was used to fit mainly the spectra near the EA-rich region where little aggregates are observed. More detailed information can be found in the manual [26].

3. Results and discussion

3.1. Conductivity experiments

In order to investigate the structuring of the ternary mixtures H₂O/NaSal/EA, conductivity measurements were performed first. Conductivity measurements provide detailed information on the mobility of charge carriers and yield insight into the local structuring of a system [6,28–31]. Conductivity measurements in the domain of microemulsions are a common and very well-known method to distinguish between regions of w/o, o/w and bicontinuous microemulsions [24,32]. In order to obtain meaningful and conclusive results, the conductivity must be measured by diluting with water but also by diluting with the solvent (EA). In both cases, the polar fraction contains all the charge carriers.

Two different dilution lines (see the phase diagram on Figure 2a) as a function of α are depicted in Figure 2a. α is calculated in the investigated samples using the following equations:

$$\alpha = \frac{w_{EA}}{w_{EA} + w_{water}} \quad (1)$$

where w_i is the weight fraction of molecule i in the ternary mixture.

It should be noted that the same alpha value can be obtained for two samples with different compositions (see Figure 2a). So, the reader is kindly invited to refer both to the alpha value but also to the color

code of the graphs and dilution lines. The water dilution line is shown in blue and the solvent dilution line is shown in red.

In Figure 2a, the red curve shows a decrease in conductivity when α increases. At α values above 0.9, the polar volume fraction is too small to obtain significant conductivity values (a few $\mu\text{S}\cdot\text{cm}^{-1}$) but a flat rise in the conductivity with decreasing α values is observed (at low water content). Below 0.9, the charge carriers are released (increase in the polar fraction), and a linear increase in conductivity is observed. A strong linear increase in conductivity with increasing water content is observed followed by a change in slope at $\alpha = 0.4$. It should be noted that this slope change at ($\alpha = 0.4$) corresponds to the prenucleation cluster (PNC) region [22].

In order to determine the origin of the sharp increase in conductivity as well as for a better understanding of the curve shape, conductivity was normalised to the reduced equivalent conductivity. It should be noted that the conductivity depends on two critical factors:

- the concentration of charge carriers present in the solution
- the volume in which these charge carriers can move.

Thus, we normalised the experimentally determined specific conductivity σ and translated it to the reduced equivalent conductivity Λ^* , according to:

$$\Lambda^* = \frac{\sigma}{c(\text{NaSal}) \cdot \phi_{\text{polar}}^*} \quad (2)$$

where ϕ_{polar}^* is an estimation of the polar volume fraction taking into account the distribution coefficient of the three components. The polar volume fractions were calculated in the investigated samples using the following equation:

$$\phi_{\text{polar}} = 0.1 \cdot \nu_{EA} + 0.96 \cdot \nu_{\text{water}} + 0.9 \cdot \nu_{\text{NaSal}} \quad (3)$$

where ν_i is the volume fraction of molecule i in the ternary mixture.

We call Λ^* the “reduced conductivity” or “reduced equivalent conductivity” of the system, in order to avoid confusion with notations of the equivalent conductivity Λ . This normalisation is based on the conductivity introduced in the charge-fluctuation model presented by Eicke et al. [33], where the specific conductivity is normalised by the volume

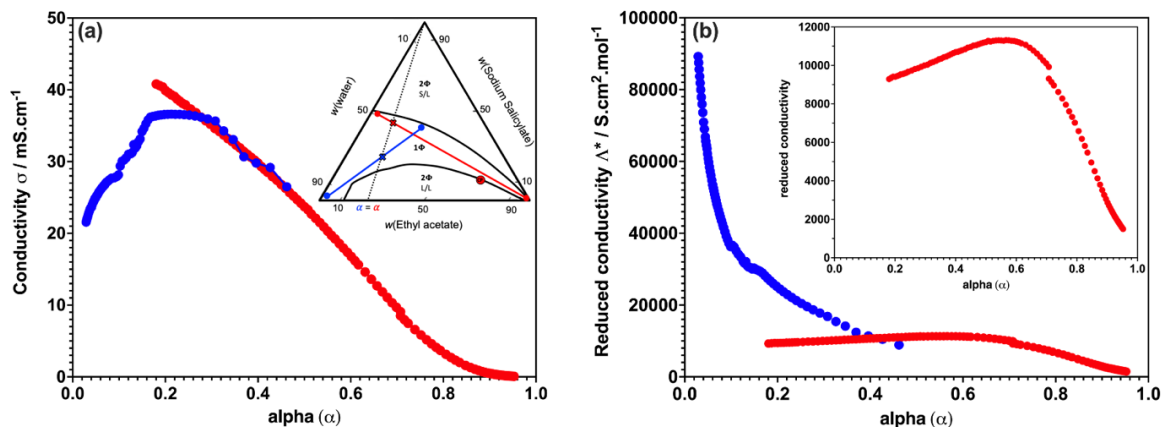


Figure 2. (a) Conductivity, (b) reduced conductivity measured along the two dilution lines represented in the phase diagram as a function of α that is the mass fraction of water versus ethyl acetate, not taking into account the mass of hydrotrope. The insert is a scaled-up graph of the reduced conductivity of the dilution line with ethyl acetate. The black dashed line on the phase diagram shows that two samples with different compositions (red and blue crosses) can have the same α value.

fraction of water. Further, the background to normalise the conductivity by the NaSal concentration stems from the classical aqueous model, which has also been adapted in one of Eicke's earlier works [28]. This reduced conductivity is thus the contribution of a single charge carrier to the total conductivity.

Figure 2b shows the reduced conductivity Λ^* as a function of α for the same two dilution lines depicted in the phase diagram. For α below 0.6, the reduced conductivity depends weakly on the amount of solvent present, i.e. the majority of mobile ions are free to move. The maximum of reduced conductivity occurs when charged PNCs are detected by their scattering pattern.

The conductivity of the dilution line towards water is shown in Figure 2a in blue. The curve is bell-shaped, characteristic of pre-Ouzo aggregates showing an increase towards low water contents [7]. With an increasing water content, a maximum is reached before the conductivity decreases again due to excessive dilution of the present charge carriers ($0 < \alpha < 0.2$). For the reduced conductivity, a slope change is observed below $\alpha = 0.1$, demonstrating the dissociation of the pre-Ouzo aggregates present near the phase boundary.

For $\alpha > 0.9$, the slope of reduced conductivity is smaller than in the water corner: charge carriers could be aggregates.

3.2. NMR experiments

Figure 3 shows the self-diffusion coefficients of the three molecules composing the ternary system: NaSal, EA, and water as a function of α . These self-diffusion coefficients allow us to see the interactions of each molecule with the others. The self-diffusion coefficients were measured along the two dilution lines (the numbered samples on the phase diagram, see Figure 3a).

Figure 3a shows the self-diffusion coefficient of NaSal along the two dilution lines. Starting from the EA-rich corner (red curve, $\alpha = 0.93$), we can see that in an organic medium, the NaSal molecule cannot move freely compared to the water-rich corner (blue curve, $\alpha \approx 0$), where NaSal is more mobile with a 50-fold increase in diffusion coefficient. This value decreases with the decrease in α (from sample 11 to 20 on the phase diagram, Figure 3a) passing through the PNC region, already discussed in a previous paper [1], and then towards the solid/liquid region where the value of D is minimal. For the water dilution line, the difference in diffusion coefficients between the two extremities of the curve (between sample 1 and 9) is more pronounced compared to the red dilution line (between sample 11 and 20) with a minimum reached near the PNC region ($\alpha = 0.4$). This indicates that the NaSal molecules (or their ions) are distributed between water and EA with a preference for

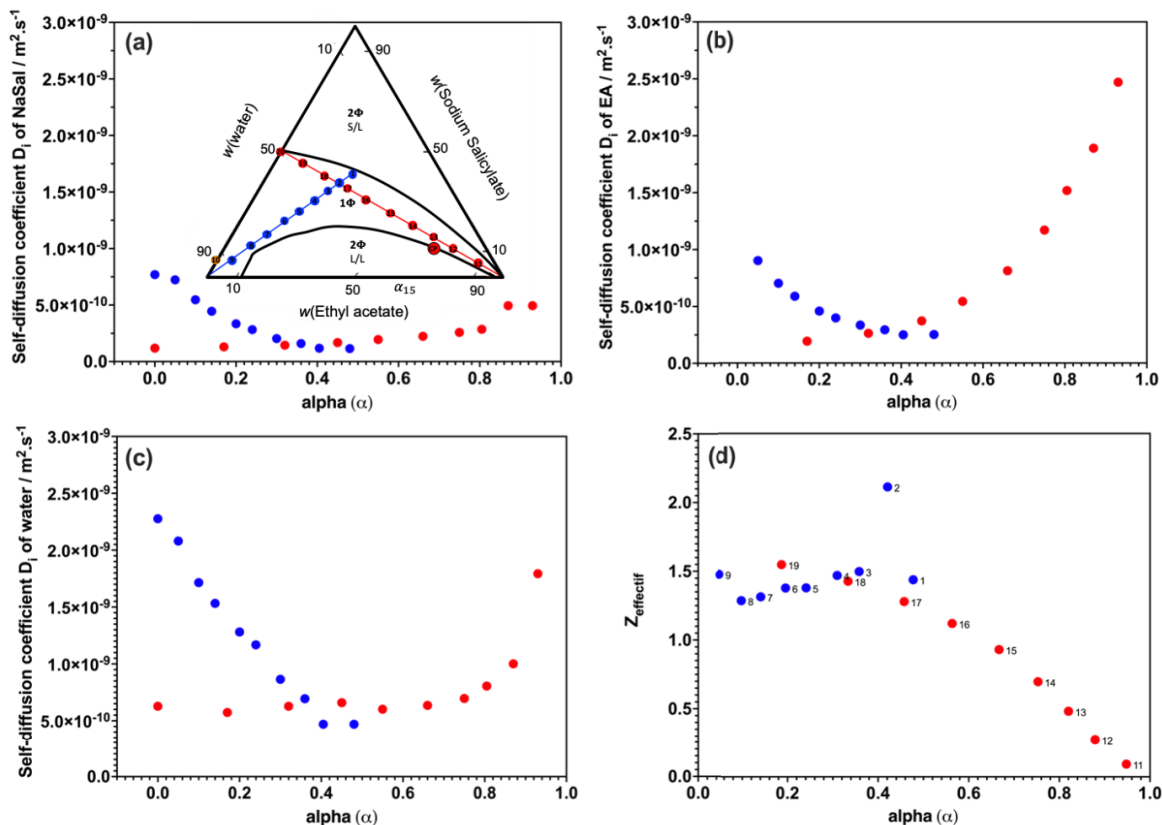


Figure 3. Self-diffusion coefficients as a function of the water/EA mass ratio α of (a) sodium salicylate, (b) ethyl acetate, (c) water, as well as (d) the effective charge derived from the ratio of conductivity to self-diffusion along the water (blue) and EA (red) dilution lines at the positions shown in the phase diagram.

water. This is consistent with the slope of tie-lines observed in the biphasic region and with the fact that ethyl acetate acts as a weak antisolvent. This is also in agreement with the results obtained in a previous publication concerning the same ternary system, where using optical density we noticed that in EA-saturated water (20 wt%), sodium salicylate micellises like a medium-chain classical surfactant [22].

Figure 3b and c represent the self-diffusion coefficients of EA and water, respectively. The trends are quite similar. In the EA-rich corner, the EA curve reaches its maximum (red curve, $\alpha = 0.93$) and then decreases exponentially with decreasing α passing by the PNC region and approaching the solid/liquid phase separation limit. In the blue dilution line, the D value of EA decreases with increasing α (from sample 9 to 1 on the phase diagram) and remains constant for $\alpha < 0.4$. For water and in the water-rich corner, the D values decrease considerably with in-

creasing α until it reaches a constant value at $\alpha = 0.4$. Concerning the red curve, the D of water decreases from sample 20 to 11, but this decrease is not pronounced compared to the decrease of D of EA. It should be pointed out that in the PNC region, where the two dilution curves cross, we notice that NaSal and EA have approximately the same value of D . This is not the case for water, which confirms that the EA and NaSal molecules are confined in the same small aggregates and that water is the main component of the “external” solvent as already reported [22].

Figure 3d shows the effective charge as a function of α for each point where self-diffusion coefficients were measured. The effective charge Z was calculated assuming that NaSal is the only charge carrier according to the equation:

$$Z = \sqrt{\frac{kT\sigma}{e^2 DC}} \quad (4)$$

where k (joules per Kelvin) is the Boltzmann constant, T (Kelvin) is the temperature, σ (milliSiemens per centimetre) is the conductivity, e (coulombs) is the elementary charge, D is the self-diffusion coefficient in cm^2/s and C is the solute concentration in molecules per m^3 .

In Figure 3d, we can see that the effective charge of the main charge carrier near the PNC as well as the pre-Ouzo region is above 1. Near the EA corner, NaSal is only partially dissociated or forms neutral clusters. The calculation of the effective charge gave us the approximate average charge in the pre-Ouzo region as well as in the PNC region. As these PNCs are negatively charged aggregates with a charge ranging from 1.5 to 2, we wondered what would happen if we added a trivalent ion (for example a lanthanum) to a ternary mixture of a given composition in the monophasic region.

3.3. Solubilisation map

Figure 4 shows the saturation concentration of lanthanum—converted to solubilisation efficiency ($E\%$)—in the monophasic region as a function of the location in the phase diagram. The solubilisation experiments were performed in vials by adding lanthanum salt to a given ternary mixture. Different compositions of the ternary mixtures in the monophasic region were tested to obtain a mapping of solubilisation efficiency as shown in Figure 4. A stirring bar was added to the solution, and the lanthanum was added gradually to the solution until a solid/liquid separation occurred, i.e., the solution was saturated with lanthanum. The vials were then closed with a sealed lid. The mixtures were stirred for 15 h at room temperature. Afterwards, the vials were centrifuged for 10 min at 5300 rpm. The concentrations were obtained after filtration of the solid residue and measurement of the remaining liquid by XRF. The solubilisation efficiency ($E\%$) is defined as:

$$E\% = \frac{\text{Amount of metal in the solution}}{\text{Total amount of metal in the solution and residue}} \quad (5)$$

As shown in Figure 4, we can distinguish four regions where the solubilisation of lanthanum, and consequently the saturation concentration are high.

- (1) The region near the critical point, which is a classical critical point. No pre-transition effect due to heterophase fluctuation was

observed. It is known that critical fluctuations can lead to a remarkable enhancement of the solubility [1,34,35]. The solubilisation regime in this region is governed by critical fluctuations and thus by entropy linked to concentration fluctuations of NaSal [36].

- (2) The second region is the region previously called “pre-Ouzo” region which was observed first by conductivity measurements (and confirmed later by SAXS). These are dynamic aggregates in the water-rich region at the phase separation boundary.
- (3) The third region with high solubilisation is the region where prenucleation clusters (PNC) are formed. As mentioned before, these PNCs with inter-aggregate distance of 2.5 nm possess an effective charge of 2. Thus, solubilisation in this case is mainly governed by electrostatic interactions between the charged aggregates and the trivalent lanthanum.
- (4) And finally, a region close to the oil-rich corner. In this region, reverse aggregates coexist in equilibrium with monomers, and a more detailed study of this region will be the focus of the following part of this paper.

It has been shown in several studies that salicylate and lanthanides form stable complexes of different stoichiometry [37–41]. Aoyagi *et al.* reported a stability constant only for the 1:1 complex [38]. Hasegawa *et al.* determined the stability constants of complexes with 1:1 and 1:2 metal-to-ligand ratios and also thermodynamic data (but only the reaction enthalpy) of these two complexes in the case of europium only [42,43]. Irving and Sinha reported additionally the thermodynamic data of the neutral 1:3 complex $\text{Eu}(\text{Sal})_3$, detected with solvent extraction [39]. A crystal structure of the 1:3 complex was published by Kuke *et al.* [37]. However, in solution they assume the existence of only the 1:1 and 1:2 complexes. Also, a theoretical study concerning possible structures of the 1:1 complex in an aqueous phase has been published [40]. Wujuan *et al.* have studied a series of rare earth complexes using different spectroscopy techniques. They demonstrate that the lanthanide ions coordinate with salicylate via the carboxyl group. They also showed that energy transfer between the salicylate and the rare-earth ions is the primary process and that the heavier the rare

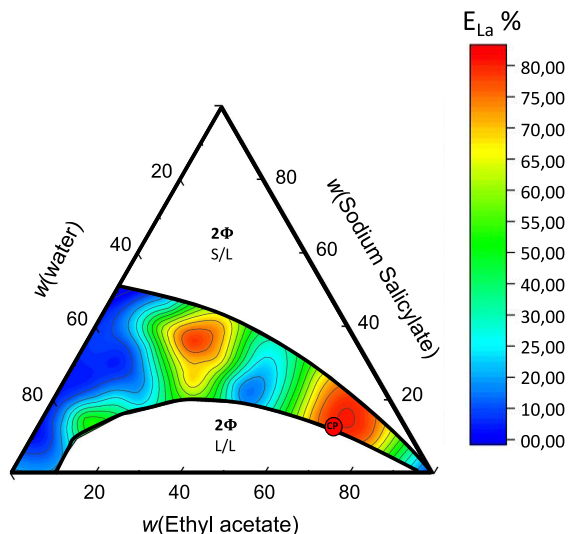


Figure 4. Solubilisation map of lanthanum in the water/NaSal/EA ternary system. The colour scale relates to a relative value of solubilised lanthanum nitrate observed in the presence of a small excess of solute.

earth, the higher the efficiency of intermolecular energy transfer [44].

However, these four solubilisation regimes cannot be explained with only a complexation mechanism between lanthanum and salicylate. If this was the case, there should be a correlation between the solubilisation efficiency and the amount of NaSal in the ternary solution. In other words, a better solubilisation with high quantities of NaSal could be expected since there will be more free sites to complex the lanthanum. On the other hand, a sharp decrease should occur when the ternary mixture contains less NaSal, i.e., less complexing sites. This correlation between the amount of NaSal and solubilisation is not observed and we can reach $E\%$ values higher than 50% even with small amounts of NaSal in the region called pre-Ouzo and the EA-rich region (see Figure 4). To understand the origin of these solubilisation regimes, we investigated the structuring of these ternary systems using scattering techniques. The aim was to see if there is a solubilisation–structure relationship that can explain these observed regimes.

It should be noted that these solubilisation regimes were not found in the case of curcumin solubilisation, which is effective only near the

critical point [45]. This is maybe due to the fact that curcumin is a large uncharged molecule and thus difficult to solubilise compared to rare-earth salts which are electrolytes involving a first layer of highly bound solvating water molecules ($V_{\text{curcumin}} = 4.701 \times 10^2 \text{ \AA}^3 > V_{\text{lanthanum}} = 3.757 \times 10^1 \text{ \AA}^3$).

The solubilisation of lanthanum salts was investigated in the monophasic region above the liquid/liquid miscibility gap of the ternary system. Whenever solubilisation is efficient near a liquid/liquid miscibility gap, separation and purification processes in the biphasic region can be performed via liquid/liquid equilibria, which will be the focus of a next paper.

3.4. Small-angle X-ray scattering (SAXS) of ternary mixtures and microstructures inferred from them

To better understand the link between solubilisation and microstructure, SWAXS experiments were carried out on the different regions where lanthanum solubility was at its maximum.

The primary subject of this study was a detailed characterisation of the microstructures in the monophasic region of the water/NaSal/EA system. X-ray techniques are among the few suited methods for probing structure transitions. SWAXS is particularly appropriate, as it gives multiscale information from atomic scale up to colloidal scale. In previous work, investigations of microstructures in ternary mixtures of the considered water/NaSal/EA system focused only on the so-called “Pre-Nucleation Cluster” region near the solid/liquid boundary. The current work aims to cover the entire monophasic region of the phase diagram in order to understand the relationship between the solubilisation of trivalent ions and the microstructure. The samples chosen are illustrated in Figure 5 with the corresponding SWAXS spectra.

In order to determine the correlation length and the radii of the aggregates, an Ornstein–Zernike (OZ) formalism was used for data fitting in the low- q range ($0.2\text{--}4 \text{ nm}^{-1}$). The OZ function can be converted into an effective radius of gyration R_G of the aggregates by:

$$I(q) = \frac{I_0}{1 + \xi^2 q^2} = \frac{I_0}{1 + \frac{R_G^2 q^2}{3}} \quad (6)$$

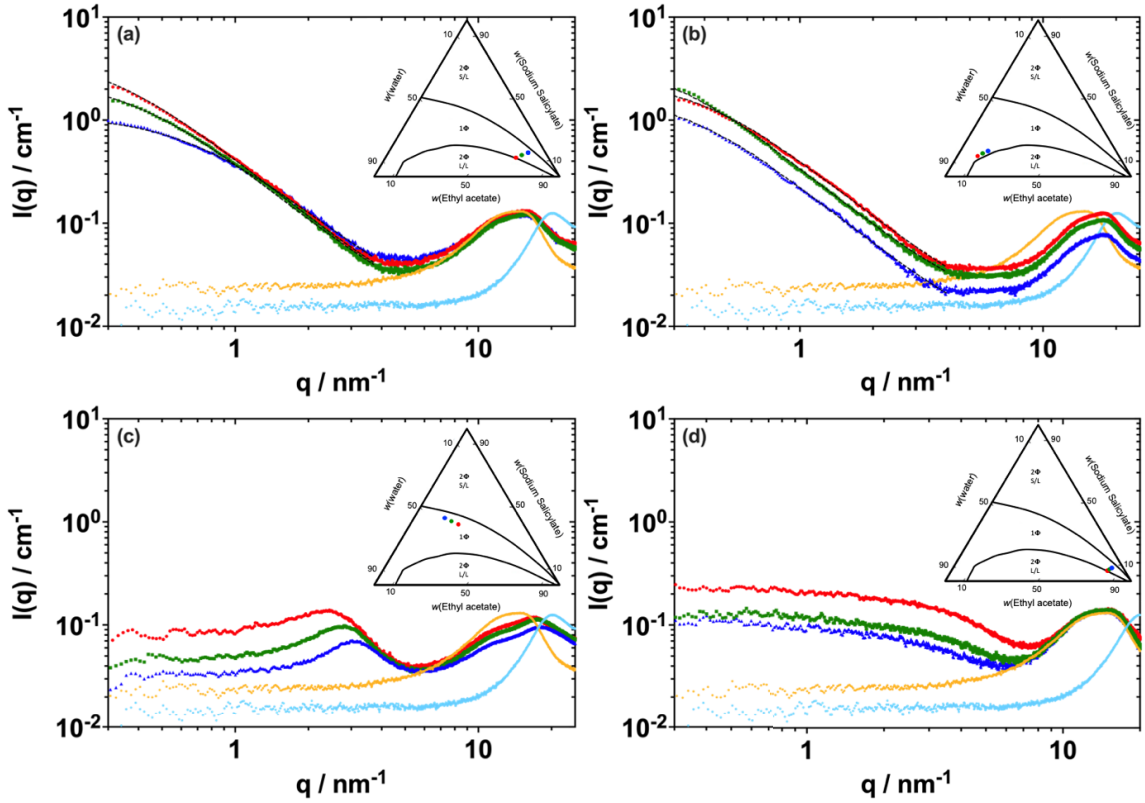


Figure 5. Experimental small and wide angle X-ray scattering (SWAXS° curves and their corresponding location on the phase diagram for: (a) the region near the critical point, (b) the region of pre-Ouzo aggregates, (c) the region of pre-nucleation clusters (PNC), i.e., ternary aggregates involving typically 6 to 20 EA molecules associated with NaSal and water, and (d) the region of weak reverse w/o aggregates. In the four figures, the light blue spectrum corresponds to pure water, while the orange one corresponds to pure EA for comparison. Figure (a) is dominated by critical scattering, Figure (b) by OZ behaviour far from the critical point corresponding to polydisperse surfactant-free microemulsions (SFME), while Figure (d) is typical scattering from supramolecular stoichiometric complexes.

where ξ is the correlation length and I_0 the intensity for $q = 0$. The spherical radius R_S of all identical compact spherical aggregates stands as:

$$R_G^2 = \frac{3}{5} R_S^2. \quad (7)$$

In this case, the link between correlation length and the spherical radius of the aggregate is valid:

$$R_S = 2.24 \cdot \xi. \quad (8)$$

In Figure 5a, different SWAXS experimental spectra are shown in log-log scale for the critical point as well as for pure water and pure EA. The colour of each of the spectra corresponds to the colour of the sample presented in the associated phase diagram.

In the WAXS regime, above 7 nm^{-1} , the curves converge and a peak is visible. This broad peak is linked to different packings of aliphatic chains. We have not observed any peak linked to crystallinity [46]. In the small-angle regime below 7 nm^{-1} , all spectra show an intense OZ signal ($I_0 > 1 \text{ cm}^{-1}$) which weakens with the distance from the critical point. Table 1 shows the values of the correlation length (ξ) as well as the radius of the aggregates (R_S), which effectively decreases from $\xi = 32 \text{ Å}$ to $\xi = 14.5 \text{ Å}$. This means that critical fluctuations persist even far from the critical point (dark blue sample on Figure 5a). This confirms that critical fluctuations, driven by entropy, govern the solubilisation

Table 1. Structural parameters obtained from fitting the spectra near the critical point as well as those in the pre-Ouzo region

	Critical point region			Pre-Ouzo region		
	Red sample	Green sample	Blue sample	Red sample	Green sample	Blue sample
Forward scattering I_0 (cm^{-1})	4.53	2.65	1.13	2.6	4.2	1.88
Correlation length (\AA)	32	25	14.5	25	35	29
Background (cm^{-1})	0.01	0.01	0.01	0.015	0.014	0.01
R_S	71.68	56	32.48	56	78.4	64.96

regime in this region as already mentioned (see Figure 4).

In Figure 5b, SWAXS experiments are performed in the second region, where solubilisation of lanthanum is maximal, called “pre-Ouzo region”. As in Figure 5a, the curves converge in the WAXS regime above 7 nm^{-1} . While the WAXS local correlation peak of ethyl acetate can be found around 14 nm^{-1} , the signature peak of water is located at 20 nm^{-1} (the spectra of the pure solvents are plotted in each case of Figure 5 (the light blue spectrum is for water and the orange one is for ethyl acetate)). The position of the peaks in Figure 5b are slightly shifted towards higher q values ($q = 17.9 \text{ nm}^{-1}$), due to higher water content compared to the samples of Figure 5a, where the opposite was found. Indeed, the peak remains at $q = 14 \text{ nm}^{-1}$ due to the low amount of water in the ternary solution. Diat *et al.* have shown that the WAXS signal for mixtures of three solvents can be approximately estimated by superposition of the pure solvent spectra [10]. At low q values ($q < 7 \text{ nm}^{-1}$), a strong OZ behaviour is also observed even far from the critical point, as it is expected in the case of heterophase fluctuation due to pre-transition effects called pre-Ouzo effect previously [47]. These signals indicate the formation of dynamic aggregates at the nanometre scale. To estimate the size of these aggregates, the Ornstein–Zernike equation was applied (see Equation (6)). We obtained a value I_0 between 1.88 and 4.2 cm^{-1} for the zero-angle intensity, and a value of ξ between 25 and 35 \AA for the correlation length, which is a measure for the size of the aggregates. These results prove the presence of mesoscopic objects, which are larger than in the case of the well-studied water/ethanol/1-octanol system [3,48,49]. This difference in correla-

tion lengths is related to the miscibility of water in ethyl acetate that is larger than in 1-octanol [50].

In Figure 5c, SWAXS spectra are shown for the third solubilisation region, which is the pre-nucleation clusters (PNC) region. The spectra in this region show a particular forward scattering behaviour: a broad peak corresponding to a distance in real space derived from the peak position of 2 nm is detected. This result is in good agreement with reports in the previous work of El Maangar *et al.* which was devoted to this PNC region [22]. Using SWAXS and small angle neutron scattering (SANS) measurements, the presence of aggregates was confirmed, with an inter-aggregate distance of 2 nm in a region where density anomalies were observed. These PNC aggregates contain 12 NaSal molecules and a mole ratio of 1 NaSal to 2 EA inside the aggregates [22]. Their effective average charge is 2 (see Figure 3d) corresponding to a dissociation of approximately 16% of the sodium salt included in a PNC, which is consistent with the dressed model of micelles [51]. Thus, it can be concluded that solubilisation in this domain is dominated by electrostatic interactions between negatively charged aggregates with a surface charge of 0.15 e/nm^2 and trivalent cations.

Figure 5d shows the SWAXS spectra of the fourth solubilisation domain in the EA-rich region. In the WAXS regime, the curves converge, and a peak is visible at $q = 14 \text{ nm}^{-1}$, which corresponds to the peak of pure EA. This is due to the low amount of water in this region and already observed in the case of the critical fluctuation region (cf. Figure 5a). At low q values, a signal close to what is observed for the well-described weak w/o aggregates is measured [52]. The scattering intensity at low q values increases only slightly ($I_0 = 0.2$) when approaching

the phase boundary. The intensity values at low q are within the range of a ternary solution that contains weak aggregates.

These spectra show an organisation of NaSal molecules in EA. Indeed, with the addition of water to the “blue” sample, an increase at small angles appears which is more marked for the “red” sample than for the “green” sample. The increase in intensity indicates that the aggregation of salicylates is favoured by the addition of water, which favours the organisation of small inverse aggregates of salicylate molecules. These aggregates are therefore either more numerous or larger with the addition of water. The effect of water on the size of the aggregates’ polar core has already been studied in the case of aggregates of extractants like DMDOHEMA for example [53]. It has been shown that the amount of water co-extracted in the polar core of the w/o reverse aggregates of extractants influences their size and thus the extraction performances, since more ions in the core require a higher dilution in order to reach a stable form. The water extraction and its influence on stabilisation of the aggregate core are often reported in the literature [54–57]. These results prove the presence of small w/o inverse aggregates in the EA-rich side, which are more stable with the addition of water. These results are in perfect agreement with the previous work of El Maangar *et al.* where they found by using optical density measurements of added DR-13 dye that NaSal already starts to “micellise” in the presence of water saturated with ethyl acetate much as a medium-chain classical surfactant. This confirms the antisolvent effect of ethyl acetate for NaSal [22].

In this case, form factors, modified by a Baxter interaction term if necessary, are more suited than an OZ fit in absolute scale. The form factor $P(q)$ was taken as a simple sphere without attraction, since there is no hard sphere effect when aggregates are produced by fluctuation. Details of equation are given in the Supplementary Material. $P(q)$ depends on the aggregates’ radii and their scattering length density. The latter was estimated by taking into account the “lowest aggregation concentration” (LAC) of NaSal, which corresponds to the concentration of monomers in equilibrium with the aggregates as well as the solubility of water in EA. Details of calculation and estimated values are also shown in the Supplementary Material.

Overall, all the quantities are fixed thanks to the sample composition already determined, and the only variable is the aggregation number N_{agg} .

Figure 6 shows the experimental spectrum (same as the red one in Figure 5d) as well as the calculated spectra for different aggregation numbers $2 < N_{\text{agg}} < 10$. Imposing a priori histograms of aggregates size would require too many parameters [3]. In binary systems, an approximation is usually made: an aggregate of N molecules produces a form factor with N times the molecular volume. We have extended this approximation to ternary systems with the known water-to-NaSal ratio for each sample. The multiple-equilibria model requires that aggregates of N_{agg} molecules must coexist with aggregates of $N_{\text{agg}} - 1$ and $N_{\text{agg}} + 1$ [58]. The size distribution function depends on the exact form of the free energy linked to stacking or packing and cannot be derived quantitatively. Figure 6 shows the calculated spectra for monodisperse aggregates from $N_{\text{agg}} = 2$ to $N_{\text{agg}} = 10$ as well as the spectrum that best fits the experimental result. This spectrum I_{cal} is obtained by minimising the following equation:

$$I_{\text{cal}} - I_{\text{exp}} = 0 \quad (9)$$

with:

$$I_{\text{cal}}(q) = \sum_{N_{\text{agg}}=2}^{N_{\text{agg}}=10} x_{N_{\text{agg}}} \cdot I_{N_{\text{agg}}}(q) \quad (10)$$

$x_{N_{\text{agg}}}$ is the proportion of aggregates with N_{agg} NaSal molecules in the sample, and $I_{N_{\text{agg}}}(q)$ is the calculated spectrum for monodisperse aggregates with an aggregation number of N_{agg} .

The result of this equation shows that the sample contains mainly aggregates with $N_{\text{agg}} < 5$, and the tetramers (i.e., aggregates of four NaSal molecules) are the dominant species. So they are indeed small w/o aggregates with an aggregation number below 5.

To conclude the first part of this work, the experimental analysis allowed us to confirm that four solubilisation regimes exist in the monophasic region. Furthermore, SWAXS measurements give proof that these four regimes correspond to four different microstructures: pre-nucleation clusters (PNC), critical fluctuations (CF), direct pre-Ouzo aggregates (PO), and reverse aggregates (RA). This allows us to define a mapping of the monophasic domain as depicted in Figure 7. Note that, in addition to the data shown here, other compositions were investigated with the

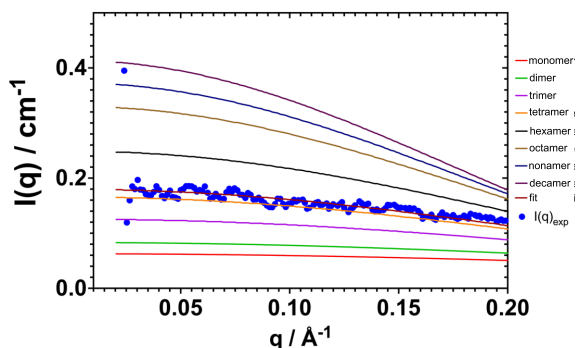


Figure 6. Experimental and theoretical Small Angle X-ray Scattering (SAXS) curves for the complexes formed in the EA-rich region represented in logarithmic scale.

help of SWAXS experiments. The results and discussion of these data are given in Figures S1 and S2.

3.5. Effect of lanthanum salt on miscibility gap and tie-lines

A striking observation is the shift in the liquid/liquid phase boundary of the miscibility gap and a variation of the slope of tie-lines when adding lanthanum salt to water. A similar effect was initially observed by Tobias and coworkers when adding sulfuric acid to the water/ethanol/1-octanol ternary system [48].

As shown in Figure 8, the monophasic region is growing slightly on the water-rich side of the phase diagram with increasing concentration of lanthanum salt, ranging from 0 to 100 mM. By contrast, the biphasic region grows in the EA-rich side. There is a crossing of the binodals reflecting the change in partition of the hydrotrope (NaSal). The critical point is experimentally identical to the point marked in red for low concentrations of lanthanum.

The maximum amount of added NaSal is reduced from 20 wt% for pure water to 16 wt% for aqueous solutions containing 30 mM of lanthanum salt. The increase seems to be proportional to lanthanum salt concentration.

Considering the different types of mesoscale structuring introduced in the first part of this work, the lanthanum salt stabilises the pre-Ouzo aggregates, while it reduces the region where critical fluctuations and w/o tetramers are observed. Addition of electrolytes reduce the stability of w/o aggregates

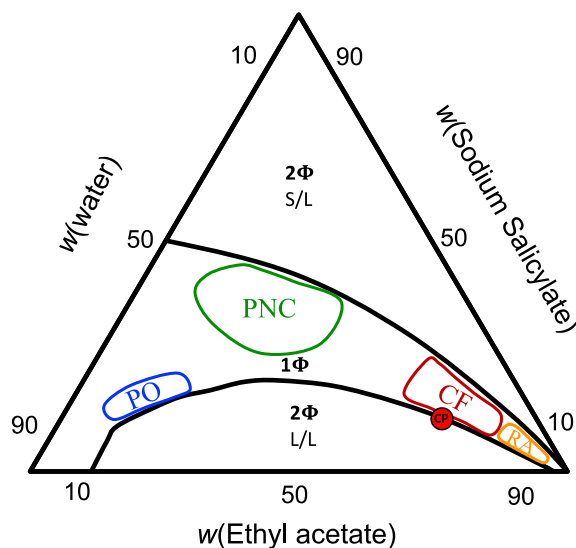


Figure 7. Schematic view of the mesoscopic structuring in the ternary phase diagram water/NaSal/EA. The region around the liquid/liquid phase transition border is dominated by three different regimes: the regime where pre-Ouzo aggregates are dominant (PO), critical fluctuations (CF) and supramolecular complexes (RA) are close to the L/L miscibility gap while pre-nucleation clusters (PNC) are close to the solid/liquid phase separation boundary, while one further regime exists near the solid/liquid phase boundary. The white monophasic region corresponds to a simple molecular solution.

regardless of the electrolyte considered. This is due to the Born energy of the electrolyte in EA [59].

The displacement to the right of the binodal lines is thus the result of two opposing features: the additional stabilisation (salting in) in the water-rich region and the salting out of water out of ethyl acetate in the EA-rich region. The partition of NaSal is significantly shifted towards a higher NaSal concentration in the aqueous phase. This can be seen by the change in the slope of the tie-lines, as represented in Figure 9.

To check whether the four different regimes are still present after addition of lanthanum salt or if they experience serious structural rearrangements, SWAXS spectra have been recorded in each of the four regimes. The compositions corresponding to

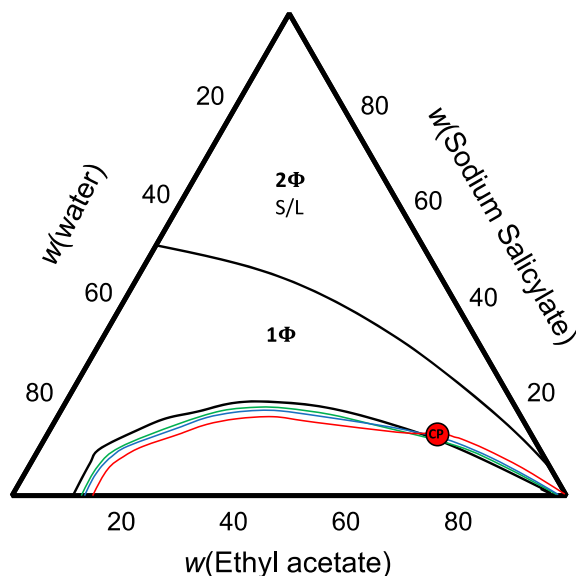


Figure 8. Phase diagram of EA/NaSal/aqueous solution of lanthanum. The phase diagrams are plotted in weight fractions wt%. The boundary in black is without lanthanum nitrate; 0.01, 0.05 and 0.1 mol·L⁻¹ are shown in green, blue and red respectively. Rare-earth salts produce salting-in on the water-rich side and salting out on the EA-rich side of the phase boundary while the critical point remains indifferent to the addition of rare-earth nitrate.

the investigated samples are shown in the phase diagrams depicted in Figure 10, where the amount of water (in wt%) is replaced by the same amount of an aqueous solution of lanthanum (also in wt%). It should be noted that the significant amount of salt slightly changes the sample density, which would lead to different points in diagrams based on volume or mole fractions. As depicted in Figure 10, the shape of the spectra remains roughly the same and thus confirms that the aggregates are still present up to 30 mM of lanthanum salt. All spectra have a higher intensity in the low-angle scattering regime, except in the critical fluctuation regime, compared to the ternary systems without lanthanum salt. The introduction of an electron-dense component enhances the scattering contrast, which leads to an increase in intensity.

Figure 10a shows the SAXS spectra obtained near the critical point with and without lanthanum salt.

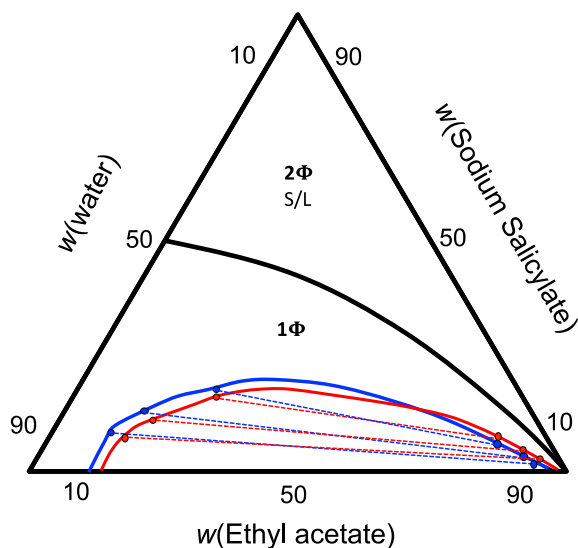


Figure 9. Pseudo-ternary phase diagram of lanthanum aqueous phase/NaSal/EA in wt%. The phase transition is given in blue for pure water, in red for 0.1 mol/L of lanthanum salt. Three tie-lines are given for each case: tie-lines rotate counterclockwise around the critical point that remains invariant in position.

The darkest red indicates the spectrum without lanthanum salt and the lighter shades the spectra at growing lanthanum concentrations in the aqueous phase. The addition of 0.1 M of lanthanum salt corresponds to an average distance between trivalent cations of 4 Å. Any fluctuation of more than 4 Å is quenched, because it implies modification of the distance between highly repulsive charged ions (0.105 nm). The location of the critical point is not noticeably changed, since it corresponds to the fluctuation concentration of NaSal.

Figure 10b shows that the main dominant aggregates are tetramers with or without lanthanum salt. The presence of trivalent salts increases the number of aggregates and reduces the critical micelle concentration (CMC). Attraction between the aggregates' cores is responsible for the smaller domain of stability [52].

Figure 10c shows that adding lanthanides in the PNC region (1 trivalent cation per cluster) produces an increase in cluster volume since the composition is the same. In the absence of lanthanum, the cluster contains 12 NaSal molecule, and the average

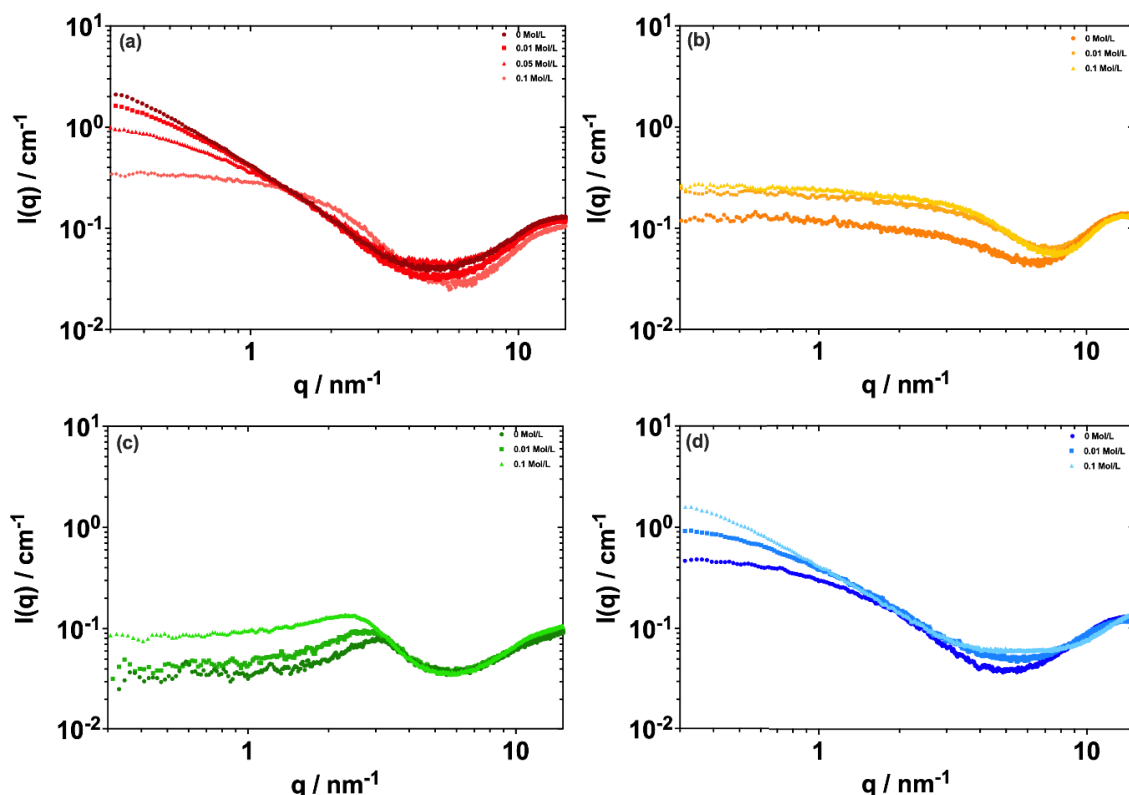


Figure 10. SWAXS spectra in the presence of lanthanum salt in the four solubilisation regimes: (a) critical fluctuations, (b) w/o reverse aggregates, (c) pre-nucleation clusters (PNCs) and (d) pre-Ouzo aggregates dominant in the scattering patterns.

distance between clusters is 2 nm. The addition of lanthanum produces a shift of the peak to the left and a corresponding distance of 2.5 nm between the clusters. Therefore, the average aggregation number increases from 12 to 24. The electrostatic interaction between the trivalent cation and monovalent salicylate favours larger PNC aggregates. This explains the high efficiency of solubility in this region.

Figure 10d shows that in the pre-Ouzo region, the correlation length increases when adding lanthanum salt. Lanthanum salts favour large pre-Ouzo aggregates. Values of correlation length are shown in the Supplementary Material. As in the case of the PNCs, this is a molecular mechanism responsible for the higher solubility in this domain. In between the PNC and pre-Ouzo domain, there is no local structuring that can be stabilised by lanthanide salts: this is the origin of the minimum of solubilisation observed between the pre-Ouzo and PNC region in Figure 4.

So far, we have only focused on lanthanum as a trivalent ion. However, for a future application, selectivity is a key parameter to implement a separation process. The solubilisation of four other rare-earths salts in addition to lanthanum nitrate was investigated in the two regions where solubilisation is maximal (see Figure 4), i.e., in the PNC and CF region. The results are summarised in Table 2. It can be seen that this ionic hydrotrope-based system can solubilise both light and heavy rare earths. A very slight selectivity is observed in the case of solubilisation in the region close to the critical point. This selectivity increases significantly in the PNC region. This is related to the solubilisation mechanism. In contrast to PNCs, the critical fluctuations do not induce differences between the solubility of ions, because the solubilisation mechanism is governed by entropy, which is not the case in the PNC region, where interactions between molecules are involved.

Table 2. Solubilisation efficiency of rare-earths elements

Sample	Solubilisation efficiency				
	% E_{La}	% E_{Nd}	% E_{Eu}	% E_{Dy}	% E_{Yb}
PNC	73.6	80.9	91.4	95.2	97.1
CF	80.1	81.9	80.3	84.1	86.7

These results strengthen the interest of this eco-compatible system which can solubilise rare earths and in addition induce selectivity as well.

4. Conclusion

The solubilisation–structuring relationship in the monophasic region of the water/NaSal/EA ternary system was investigated. By performing conductivity, DOSY, SWAXS, and XRF measurements on different monophasic mixtures, we revealed fundamental changes in the nanostructuring of the system considered.

Four differently structured regions were detected and could be related to increased solubilisation regimes:

- Region CF is a region dominated by critical fluctuations, where entropy is the dominant driving force. In this region, the presence of trivalent ions quenches critical fluctuations.
- Region PNC containing pre-nucleation clusters, where charged aggregates of typically 12 EA molecules exist. In this case, solubilisation of rare-earth salts is enhanced by surface electrostatics of the prenucleation clusters and lanthanides increase their aggregation number.
- Region PO far from the critical point where small dynamic pre-Ouzo aggregates are present on the water-rich phase separation boundary. The aggregates in this region increase in volume upon solubilisation of rare-earth salts facilitated by the PO aggregates (also known as SFME or even UFME for ultra-flexible microemulsions). This mechanism is also known as mesoscale solubilisation.
- The diluted region on the EA-rich side, where reverse aggregates consisting mainly of tetramers coexist with monomers. The presence of lanthanides in this case increases the

number of aggregates present, transforming them in supramolecular complexes. This is the only region for which the standard theory, taking only into account the complexation Gibbs energy difference combined with the mass action law, applies quantitatively. This complexation was the only theory for liquid/liquid extraction before the availability of the *ienaics* theory.

These different structure–solubilisation regimes and their modifications in the presence of electrolytes may have significant consequences on various applications [60]. The selectivity induced by this system may lead to a potential application in the field of rare-earth recovery, but this will be the topic of future research.

Declaration of interests

The authors do not work for, advise, own shares in, or receive funds from any organization that could benefit from this article, and have declared no affiliations other than their research organizations.

Acknowledgements

We thankfully acknowledge the CNRS for financial support through the International Research Project “NISI” program. JG thanks the Fonds der Chemischen Industrie for funding. We thank M.-H. Hengé for critical proof-reading of the manuscript.

Supplementary data

Supporting information for this article is available on the journal's website under <https://doi.org/10.5802/crchim.310> or from the author.

References

- [1] M. L. Klosek, D. Touraud, T. Zemb and W. Kunz, “Structure and solubility in surfactant-free microemulsions”, *ChemPhysChem*. **13** (2012), pp. 4116–4119.
- [2] V. Fischer, J. Marcus, D. Touraud, O. Diat and W. Kunz, “Toward surfactant-free and water-free microemulsions”, *J. Colloid Interface Sci.* **453** (2015), pp. 186–193.
- [3] S. Schöttl, J. Marcus, O. Diat, D. Touraud, W. Kunz, T. Zemb and D. Horinek, “Emergence of surfactant-free micelles from ternary solutions”, *Chem. Sci.* **5** (2014), pp. 2949–2954.

- [4] W. Kunz, K. Holmberg and T. Zemb, "Hydrotropes", *Curr. Opin. Colloid Interface Sci.* **22** (2016), pp. 99–107.
- [5] K. Holmberg, D. O. Shah and M. J. Schuuger (eds.), *Handbook of Applied Surface and Colloid Chemistry*, Wiley: Chichester, England; New York, 2002.
- [6] P. Bošković, V. Sokol, T. Zemb, D. Touraud and W. Kunz, "Weak micelle-like aggregation in ternary liquid mixtures as revealed by conductivity, surface tension, and light scattering", *J. Phys. Chem. B* **119** (2015), pp. 9933–9939.
- [7] T. Buchecker, S. Krickl, R. Winkler, I. Grillo, P. Bauduin, D. Touraud, A. Pfizner and W. Kunz, "The impact of the structuring of hydrotropes in water on the mesoscale solubilisation of a third hydrophobic component", *Phys. Chem. Chem. Phys.* **19** (2017), pp. 1806–1816.
- [8] C. Neuberg, "Hydrotropische Erscheinungen", *Biochem. Z.* **76** (1916), pp. 107–158.
- [9] J. Mehringer and W. Kunz, "Carl Neuberg's hydrotropic appearances (1916)", *Adv. Colloid Interface Sci.* **294** (2021), article no. 102476.
- [10] O. Diat, M. L. Klossek, D. Touraud, B. Deme, I. Grillo, W. Kunz and T. Zemb, "Octanol-rich and water-rich domains in dynamic equilibrium in the pre-ouzo region of ternary systems containing a hydrotrope", *J. Appl. Crystallogr.* **46** (2013), pp. 1665–1669.
- [11] P. Bauduin, A. Renoncourt, A. Kopf, D. Touraud and W. Kunz, "Unified concept of solubilization in water by hydrotropes and cosolvents", *Langmuir* **21** (2005), pp. 6769–6775.
- [12] T. Zemb and W. Kunz, "Weak aggregation: State of the art, expectations and open questions", *Curr. Opin. Colloid Interface Sci.* **22** (2016), pp. 113–119.
- [13] J. J. Booth, S. Abbott and S. Shimizu, "Mechanism of hydrophobic drug solubilization by small molecule hydrotropes", *J. Phys. Chem. B* **116** (2012), pp. 14915–14921.
- [14] J. J. Booth, M. Omar, S. Abbott and S. Shimizu, "Hydrotrope accumulation around the drug: the driving force for solubilization and minimum hydrotrope concentration for nicotinamide and urea", *Phys. Chem. Chem. Phys.* **17** (2015), pp. 8028–8037.
- [15] M. Spadina, K. Bohinc, T. Zemb and J.-F. Dufrêche, "Synergistic solvent extraction is driven by entropy", *ACS Nano* **13** (2019), pp. 13745–13758.
- [16] S. T. Kumar, D. G. Prakash and N. Nagendra Gandhi, "Effect of hydrotropes on solubility and mass transfer coefficient of lauric acid", *Korean J. Chem. Eng.* **26** (2009), pp. 1328–1333.
- [17] Y. P. Koparkar and V. G. Gaikar, "Solubility of o-/p-hydroxyacetophenones in aqueous solutions of sodium alkyl benzene sulfonate hydrotropes", *J. Chem. Eng. Data* **49** (2004), pp. 800–803.
- [18] S. Theneshkumar, D. Gnanaprakash and N. Nagendra Gandhi, "Enhancement of solubility and mass transfer coefficient of salicylic acid through hydrotropy", *J. Zhejiang Univ. Sci. A* **10** (2009), pp. 739–745.
- [19] R. Revathi, T. Ethiraj, V. S. Saravanan, V. Ganeshan, V. Saranya and T. Sengottuvel, "New spectroscopic determination of nifedipine using hydrotropic solubilization", *Int. J. Pharm. Pharm. Sci.* **2** (2010), pp. 74–76.
- [20] K. Nidhi, S. Indrajeet, M. Khushboo, K. Gauri and D. J. Sen, "Hydrotropy: A promising tool for solubility enhancement: A review", *Int. J. Drug Dev. Res.* **3** (2011), pp. 26–33.
- [21] E. Merinville, A. J. Byrne, A. V. Rawlings, A. J. Muggleton and A. C. Laloef, "Original contribution: Three clinical studies showing the anti-aging benefits of sodium salicylate in human skin", *J. Cosmet. Dermatol.* **9** (2010), pp. 174–184.
- [22] A. El Maangar, P. Degot, V. Huber, J. Causse, P. Berthault, D. Touraud, W. Kunz and T. Zemb, "Pre-nucleation cluster formation upon ethyl acetate addition to an aqueous solution of an anionic hydrotrope", *J. Mol. Liq.* **310** (2020), article no. 113240.
- [23] D. Gebauer, M. Kellermeier, J. D. Gale, L. Bergström and H. Cölfen, "Pre-nucleation clusters as solute precursors in crystallisation", *Chem. Soc. Rev.* **43** (2014), pp. 2348–2371.
- [24] M. Clausse, L. Nicolas-Morgantini, A. Zradba and D. Touraud, *Microemulsion Systems* (H. Rosano and M. Clausse, eds.), Surfactant series, vol 24, CRC Press: Boca Raton, 1987.
- [25] A. Jerschow and N. Müller, "Suppression of convection artifacts in stimulated-echo diffusion experiments. Double-stimulated-echo experiments", *J. Magnet. Res.* **125** (1997), pp. 372–375.
- [26] M. Doucet, J. H. Cho, G. Alina, et al., *SasView version 4.1*, *Zenodo*, 2017. Online at <http://www.sasview.org> (accessed on May 20, 2019).
- [27] S. Prevost, T. Lopian, M. Pleines, O. Diat and T. Zemb, "Small-angle scattering and morphologies of ultra-flexible microemulsions", *J. Appl. Crystallogr.* **49** (2016), pp. 2063–2072.
- [28] H. F. Eicke, H. Hammerich and G. Vasta, "A thermodynamic analysis of the molar conductivity of the ternary system: Water-aerosol OT-isooctane", *J. Colloid Interface Sci.* **93** (1983), pp. 593–595.
- [29] J. Schmidt, R. Prignitz, D. Peschka, A. Münch, B. Wagner, E. Bansch and W. Peukert, "Conductivity in nonpolar media: Experimental and numerical studies on sodium AOT-hexadecane, lecithin-hexadecane and aluminum(III)-3,5-diisopropyl salicylate-hexadecane systems", *J. Colloid Interface Sci.* **386** (2012), pp. 240–251.
- [30] B. Lagourette, J. Peyrelasse, C. Boned and M. Clausse, "Percolative conduction in microemulsion type systems", *Nature* **281** (1979), pp. 60–62.
- [31] M. Clausse, J. Peyrelasse, J. Heil, C. Boned and B. Lagourette, "Bicontinuous structure zones in microemulsions", *Nature* **293** (1981), pp. 636–638.
- [32] A. Bumajdad and J. Eastoe, "Conductivity of mixed surfactant water-in-oil microemulsions", *Phys. Chem. Chem. Phys.* **6** (2004), pp. 1597–1602.
- [33] H. F. Eicke, M. Borkovec and B. Das-Gupta, "Conductivity of water-in-oil microemulsions: a quantitative charge fluctuation model", *J. Phys. Chem.* **93** (1989), pp. 314–317.
- [34] R. Fernández-Prini, "Solubility in fluids close to their critical points", *Pure Appl. Chem.* **67** (1995), pp. 519–526.
- [35] K. I. Gutkowski, R. Fernández-Prini and M. L. Japas, "Solubility of solids in near-critical conditions: Effect of a third component", *J. Phys. Chem. B* **112** (2008), pp. 5671–5679.

- [36] J. Frenkel, "A general theory of heterophase fluctuations and pretransition phenomena", *J. Chem. Phys.* **7** (1939), pp. 538–547.
- [37] S. Kuke, B. Marmodée, S. Eidner, U. Schilde and M. U. Kumke, "Intramolecular deactivation processes in complexes of salicylic acid or glycolic acid with Eu(III)", *Spectrochim. Acta A: Mol. Biomol. Spectrosc.* **75** (2010), pp. 1333–1340.
- [38] N. Aoyagi, T. Toraishi, G. Geipel, H. Hotokezaka, S. Nagasaki and S. Tanaka, "Fluorescence characteristics of complex formation of europium(III)-salicylate", *Radiochim. Acta* **92** (2004), pp. 589–593.
- [39] H. M. N. H. Irving and S. P. Sinha, "The formation constants of europium(III)-salicylate complexes and their extraction into isoamyl alcohol", *Anal. Chim. Acta* **49** (1970), pp. 449–454.
- [40] T. Toraishi, S. Nagasaki and S. Tanaka, "A theoretical study on molecular structure of Eu(III)-salicylate complexes in aqueous system", *J. Mol. Struct. Theochem.* **757** (2005), pp. 87–97.
- [41] Z. L. Ernst and P. J. Newman, "Spectrophotometric determination of association constant of lanthanum salicylate", *Trans. Faraday Soc.* **64** (1968), pp. 1052–1058.
- [42] Y. Hasegawa, N. Yamazaki, S. Usui and G. R. Choppin, "Effects of phenyl groups on thermodynamic parameters of lanthanoid(III) complexation with aromatic carboxylic acids", *Bull. Chem. Soc. Japan* **63** (1990), pp. 2169–2172.
- [43] Y. Hasegawa, Y. Morita, M. Hase and M. Nagata, "Complexation of lanthanoid (III) with substituted benzoic or phenylacetic acids and extraction of these acids", *Bull. Chem. Soc. Japan* **62** (1989), pp. 1486–1491.
- [44] S. W. X. H. L. Shengli, "Spectra of rare earth complexes with salicylate", *Acta Photonica Sinica* **35** (2006), pp. 1593–1596.
- [45] P. Degot, V. Huber, A. El Maangar, et al., "Triple role of sodium salicylate in solubilization, extraction, and stabilization of curcumin from *Curcuma longa*", *J. Mol. Liq.* **329** (2021), article no. 115538.
- [46] G. Förster, A. Meister and A. Blume, "Chain packing modes in crystalline surfactant and lipid bilayers", *Curr. Opin. Colloid Interface Sci.* **6** (2001), pp. 294–302.
- [47] T. N. Zemb, M. Klossek, T. Lopian, et al., "How to explain microemulsions formed by solvent mixtures without conventional surfactants", *Proc. Natl. Acad. Sci. USA* **113** (2016), pp. 4260–4265.
- [48] T. Lopian, S. Schöttl, S. Prévost, S. Pellet-Rostaing, D. Horinek, W. Kunz and T. Zemb, "Morphologies observed in ultraflexible microemulsions with and without the presence of a strong acid", *ACS Central Sci.* **2** (2016), pp. 467–475.
- [49] M. L. Klossek, D. Touraud, T. Zemb and W. Kunz, "Structure and solubility in surfactant-free microemulsions", *ChemPhysChem.* **13** (2012), pp. 4116–4119.
- [50] D. Subramanian and M. A. Anisimov, "Phase behavior and mesoscale solubilization in aqueous solutions of hydrotropes", *Fluid Phase Equilib.* **362** (2014), pp. 170–176.
- [51] J. B. Hayter, "A self-consistent theory of dressed micelles", *Langmuir* **8** (1992), pp. 2873–2876.
- [52] C. Erlinger, L. Belloni, T. Zemb and C. Madic, "Attractive interactions between reverse aggregates and phase separation in concentrated malonamide extractant solutions", *Langmuir* **15** (1999), pp. 2290–2300.
- [53] M. Špadina, K. Bohinc, T. Zemb and J.-F. Dufrêche, "Multicomponent model for the prediction of nuclear waste/rare-earth extraction processes", *Langmuir* **34** (2018), pp. 10434–10447.
- [54] B. J. Gullekson, A. T. Breshears, M. A. Brown, J. B. Essner, G. A. Baker, J. R. Walensky, A. Paulenova and A. V. Gelis, "Extraction of water and speciation of trivalent lanthanides and americium in organophosphorus extractants", *Inorg. Chem.* **55** (2016), pp. 12675–12685.
- [55] B. Gannaz, M. R. Antonio, R. Chiarizia, C. Hill and G. Cote, "Structural study of trivalent lanthanide and actinide complexes formed upon solvent extraction", *Dalton Trans.* **38** (2006), pp. 4553–4562.
- [56] W. Bu, H. Yu, G. Luo, et al., "Observation of a rare earth ion-extractant complex arrested at the oil–water interface during solvent extraction", *J. Phys. Chem. B* **118** (2014), pp. 10662–10674.
- [57] D. Darvishi, D. F. Haghshenas, S. Etemadi, E. K. Alamdari and S. K. Sadrnezhaad, "Water adsorption in the organic phase for the D2EHPA–kerosene/water and aqueous Zn²⁺, Co²⁺, Ni²⁺ sulphate systems", *Hydrometallurgy* **88** (2007), pp. 92–97.
- [58] H. Wennerström, "Micelles. Physical chemistry of surfactant association", *Phys. Rep.* **52** (1979), pp. 1–86.
- [59] H. F. Eicke, M. Borkovec and B. Das-Gupta, "Conductivity of water-in-oil microemulsions: a quantitative charge fluctuation model", *J. Phys. Chem.* **93** (1989), pp. 314–317.
- [60] T. Zemb, C. Bauer, P. Bauduin, et al., "Recycling metals by controlled transfer of ionic species between complex fluids: en route to "ienacs"", *Colloid. Polym. Sci.* **293** (2015), pp. 1–22.



Research article

GDR Prométhée – French Research Network on *Hydrometallurgical Processes for Primary and Secondary Resources*

Propylene glycol-based deep eutectic solvent as an alternative to Ethaline for electrometallurgy

Calogera Bertoloni^{✉,a}, Vitalys Mba Ekomo^b, Benoît Villemejeanne^c, Charly Lemoine^c, Romain Duwald^{✉,c}, Emmanuel Billy^{✉,c}, Hakima Mendil-Jakani^{✉,b} and Sophie Legeai^{✉,*,a}

^a Institut Jean Lamour, Groupe Chimie et Electrochimie des Matériaux, UMR CNRS 7198—Université de Lorraine, 1 Boulevard Arago, BP 95823, 57078 Metz Cedex 3, France

^b Laboratoire Systèmes Moléculaires et nanoMatériaux pour l'Énergie et la Santé (SyMMES), Commissariat à l'énergie atomique site de Grenoble, France

^c Laboratoire des technologies de Valorisation des procédés et Matériaux pour les EnR (LVME), Commissariat à l'énergie atomique site de Grenoble, France

E-mail: sophie.legeai@univ-lorraine.fr (S. Legeai)

Abstract. Deep eutectic solvents (DESs) are of particular interest for electrometallurgy processes, since intrinsically conductive and electrochemically stable in a wide range of potentials. Cheaper and greener than conventional ionic liquids, DESs are often bio-sourced and exhibit a higher biodegradability. Ethaline, a DES composed of choline chloride (ChCl) as hydrogen bond acceptor and ethylene glycol (EG) as hydrogen bond donor in 1:2 molar proportions (Et 1:2), is commonly used in electrometallurgy thanks to its good transport properties. However, if ChCl can be considered as a “green” reactant, this is not the case for EG. A DES with a lower toxicity can be obtained by replacing EG by propylene glycol (PG), widely used in cosmetics and pharmacology, yielding a DES called Propeline. The present paper explores the potential of this lesser-known DES in the electrometallurgy of precious metals. Because changing the hydrogen bond donor leads to a modification in the DES bulk properties, the first part of this work deals with the determination of PG-based DESs' density, viscosity, and conductivity, which are properties of interest for electrochemical processes. The influence of water and PG content is presented and values are compared to those of Ethaline. It appears that ChCl:PG in a molar ratio 1:3 (Pr 1:3) presents the best transport properties. The potentiality of this solvent for the electrometallurgy of precious metals is then discussed: electrochemical stability and electrochemical systems of Ag, Pd, and Au are compared in Pr 1:3 and Et 1:2. Finally, diffusion coefficients of the metallic species and the DES components are given, determined by electrochemical and NMR techniques, respectively.

Keywords. Electrometallurgy, Deep eutectic solvent, Precious metals, Propeline, Transport properties.

Funding. Agence Nationale de la Recherche (EE4Precious project, ANR-20-CE08-0035-01).

Manuscript received 29 September 2023, revised 15 December 2023 and 30 January 2024, accepted 2 February 2024.

*Corresponding author

1. Introduction

The discovery of ionic liquids in 1914 by Paul Walden [1] with beneficial properties (vapor pressure, flammability, modulation, viscosity, density, refractive index, electrical conductivity, and thermal stability) led to applications such as electrochemistry, extraction, synthesis, analytical chemistry discussed by Kaur *et al.* [2]. These ionic liquids have also been used as additives in cosmetic products or as corrosion inhibitors [2,3]. An ongoing need to improve existing properties has led to the emergence of new so-called deep eutectic solvents (DES) based on the mixture of a proton acceptor (HBA) and a proton donor (HBD), first presented by Abbott *et al.* [4]. The first DES studied was a mixture of choline chloride as HBA and urea as HBD, and the resulting solvent was named Reline. Reline has properties similar to ionic liquids, which intended it for the same applications, but with a better control over the properties mentioned above and a reduced cost due to easier synthesis and composition modulation. As for ionic liquids, the conductivity of DESs and their complexing properties intend them for applications in electrochemical processes of metals. In the field of metal recycling, electrometallurgy in DES can be an alternative to toxic aqueous electrolytes (cyanides) for the recovery of precious metals for example, by consecutive electrochemical leaching and electrodeposition. The most popular DES for electrometallurgy applications is Ethaline which is based on the eutectic mixture of choline chloride (ChCl) and ethylene glycol (EG), *i.e.*, in the 1:2 molar proportion [5–8]. Ethaline has more suitable properties for electrometallurgy (for example, low viscosity, better conductivity) than other DESs, even Reline. Most of the studies on DESs have thus been devoted to Ethaline. To date, a more ecological approach and a need to associate it with a reduction in costs guide research towards DESs that are more respectful of the environment and less expensive. Although the toxicity of eutectic mixtures is weakly investigated, databases are full of information on the toxicity of HBD. Several studies were published that call into question the harmlessness of some DESs considered as natural, thus showing that natural is not synonymous with green for environment [9]. The conclusion of such studies ultimately shows a certain unexpected toxicity of some DESs [10]. These studies also highlight the *in-vivo*

toxicity of DESs compared to the individual elements (HBA and HBD) and the influence of their molar ratio [10,11]. In summary, studies have shown that DESs based on choline chloride as HBA have rather low toxicity [12,13] but that their toxicity increases with the toxicity of the HBD and thus with its molar ratio [10,11,14]. It is then reasonable to expect that the less toxic a HBD is, the less toxic the resulting DES will be.

In this work, to look for a DES with a lower toxic profile than Ethaline, ethylene glycol was switched by propylene glycol as HBD. The choice fell on propylene glycol because it shows the advantage of being a lot less toxic than ethylene glycol, known to be lethal for humans as well as terrestrial and aquatic animals by drinking water contamination. The structure of propylene glycol derives from ethylene glycol based on substitution of a proton by a methyl functional group. In addition, the use of propylene glycol instead of ethylene glycol is still economically viable, as the price of both solvents is similar (78 €/L, December 2023)¹ to propylene glycol price (50 €/L, December 2023)² according to Sigma Aldrich for a same *reagent grade* (>99%). Aware that the change of HBD leads to a modification of DES properties, and that these properties condition the applications of DESs, the first part of this work will deal with the investigation of relevant transport properties such as density, viscosity, and conductivity depending on the HBD choice, either ethylene glycol or propylene glycol. In addition, the possibility of using the prepared PG-based DESs for electrometallurgy applications will be presented by comparing their electrochemical properties to those of Ethaline and studying the electrochemical behavior of precious metals (Pd, Au, Ag) in these two DESs.

2. Experimental section

2.1. Chemicals and materials

The choline chloride (ChCl, 98%), ethylene glycol (EG, 99%), propylene glycol (PG, 99%) used for DES preparation, as well as ferrocene ($\text{Fe}[\text{C}_5\text{H}_5]_2 \cdot 6\text{H}_2\text{O}$,

¹<https://www.sigmaaldrich.com/FR/fr/product/sigald/102466>.

²<https://www.sigmaaldrich.com/FR/fr/substance/760957556>.

98%), gold chloride (AuCl_3 , >99.99%) and silver chloride (AgCl , >99%) were purchased from Sigma-Aldrich, France. Ethanol (EtOH , 96%) and palladium chloride (PdCl_2 , 59%) were purchased from Merck France. Gold wire (99.99%), silver wire (99.99%) and palladium wire (99.95%) were purchased at Métalor Technologies France.

2.2. DES preparation

$\text{ChCl}:\text{EG}$ (Et) and $\text{ChCl}:\text{PG}$ (Pr) DESs were prepared respectively by mixing ChCl with EG, and ChCl with PG at 60 °C in a closed container under stirring. DESs were prepared at different molar ratios written down: HBA:HBD. When the influence of water content is studied, a third molar ratio is added in the name of the sample: HBA:HBD: H_2O . This ratio is expressed relative to HBA set at 1.

2.3. Physico-chemical properties measurements

All experiments were performed without any atmosphere control. The water content was measured by Karl Fischer coulometric titration using a Metrohm Karl Fischer 899 Coulometer with a HYDRANAL Coulomat E solution. Density was measured in a temperature range from 25 to 65 °C with 5 °C intervals, using an Anton Paar DMA 4100 M density meter, with a measurement accuracy of $10^{-4} \text{ g}\cdot\text{cm}^{-3}$. Viscosity was determined using an Anton Paar AMVn viscometer with a repeatability of 0.1%. Conductivity was evaluated by potentiostatic electrochemical impedance spectroscopy (PEIS) using a Biologic Lab Potentiostat VSP 300. The conductivity cell was constituted of two parallel platinum plates, and the cell constant was determined using calibration samples (1.413 ; 5.0 and $12.8 \text{ mS}\cdot\text{cm}^{-1}$ at 25 °C). The sine wave amplitude was 10 mV, the studied frequency range extends from 1 MHz to 100 mHz with 6 measuring points per decade. The viscosity and the conductivity were measured in a temperature range of 25–60 °C with a step of 5 °C.

2.4. Electrochemical characterizations

All experiments were performed at 40 °C without any atmosphere control, using a Biologic Lab Potentiostat VSP 300. Au, Pd, and Ag were dissolved by anodic leaching of metallic wires, applying $1 \text{ mA}\cdot\text{cm}^{-2}$ in galvanostatic mode at 313 K in Et 1:2 and 333 K in

Pr 1:3. The coulombic charge was adapted to the targeted concentration. Final concentrations were determined by the weight loss of the anode. Counter electrode (CE) was separated from the bulk electrolyte by a fritted glass to avoid electrodeposition of leached metals on the CE. Resulting electrochemical systems were studied by cyclic voltammetry. Electrochemical stability and electrochemical systems of metallic species were studied by cyclic voltammetry (CV) at a scan rate of $20 \text{ mV}\cdot\text{s}^{-1}$. For CV experiments, the working electrode (WE) was a Pt disk of 2 mm in diameter. The CE and the reference electrode (RE) used in all electrochemical experiments were respectively a glassy carbon rod and an Ag^+/Ag electrode (Ag wire immersed in the studied DES containing 10 mM AgCl). The RE was calibrated against Fc^+/Fc ($E^0(\text{Fc}^+/\text{Fc}) = 0.63 \text{ V}/\text{SHE}$). All potential values measured in this study are therefore relative to SHE (standard hydrogen electrode).

2.5. NMR measurements

All NMR spectra were recorded with a Bruker Neo 400 MHz NMR spectrometer, equipped with a BBFO smartprobe. DOSY experiments were performed with Bipolar Pulsed Pair Stimulated Echo (BPSTE) pulse sequence. Each DOSY-NMR was based on 16 BPSTE-recorded spectra with 8 K data points. The diffusion time was 750 ms. The duration of the pulse field gradient was adjusted in a 600–2000 ms range in order to obtain 2–5% residual signal with the maximum gradient strength. The gradient strength was incremented in 16 steps from 5 to 95% of its maximum value in a linear ramp. Data processing was performed using Topspin 4.0.9 software.

3. Results and discussion

3.1. Density

Density (ρ) and its temperature dependence are important physical properties, which are useful for designing industrial processes. Densities of $\text{ChCl}:\text{EG}$ and $\text{ChCl}:\text{PG}$ DESs with HBA:HBD molar ratio 1:2 and 1:3 were measured in a 293–333 K temperature range at low and similar water content. The results are reported in Figure 1. The density of both DESs decreases with increasing temperature. This phenomenon is due to thermal expansion associated

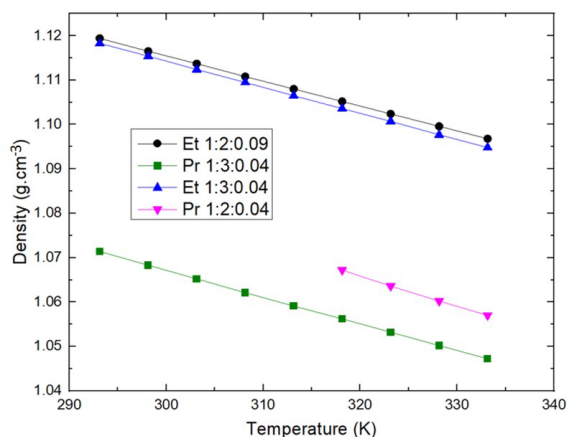


Figure 1. Density comparison of ChCl:EG and ChCl:PG DESs at different HBA:HBD ratios as a function of temperature.

with hydrogen bonding, and follows a linear temperature dependence.

Values were not measured under 318 K for Pr 1:2 (Propylene) because it is solid at lower temperatures. Moreover, there is a decrease in DES density with increasing HBD molar ratios, with much more impact on ChCl:EG than on ChCl:PG DESs given the difference observed. In the cases where only density matters, this would mean that the properties of ChCl:PG DESs would be more easily modulated than the properties of ChCl:EG DESs. The density of ChCl:PG DESs is lower than the density of ChCl:EG DESs whatever the HBA:HBD ratio. The values measured in this study are in accordance with existing literature [15,16]. Knowing that the density of ethylene glycol is higher than that of propylene glycol, it can be concluded that the density of the resulting DES is directly related to the density of the HBD. Wang et al. had already made the same observation by comparing the density of a larger number of DESs and concluded that the molar mass as well as the density of the HBD had a very large impact on the density of the resulting DES [17]. The density partially reflects the interaction strength between HBA and HBD components, which is ascribed to the strong hydrogen bond ability. This notable difference of density might be attributed to a different molecular organization or packing of the DES, changing the size of the HBA/HBD association spheres and leading to more free volume in ChCl:PG than in ChCl:EG DESs [18].

The extra methyl group of propylene glycol could be responsible for this by steric hindrance.

3.2. Viscosity

Viscosity is a very important information to relate the macroscopic properties linked to matter transport and hydrodynamic flow to the microscopic phenomena from which these macroscopic properties most often find their explanation.

The impact of temperature (Figure 2a) on ChCl:EG and ChCl:PG DESs' viscosity has been measured for 1:2 and 1:3 ratio. Increasing the HBD fraction clearly makes viscosity decrease for both DESs. Besides, viscosity of Pr 1:3 is higher than that of Et 1:3. This seems logical as propylene glycol alone is more viscous than ethylene glycol (56 and 21 mPa·s at 293 K, respectively). Several studies in the literature have already corroborated this observation: the decrease can be related to the formation or strengthening of hydrogen bonds, resulting in loss of molecular mobility as it closes free volume, on which the viscosity depends [15,16,19]. As for all liquids, the viscosity of ChCl:EG and ChCl:PG DESs decreases when temperature increases, due to thermal dilatation. The higher viscosity of ChCl:PG DESs suggests that they would be less interesting than ChCl:EG DESs, however it has to be noticed that both viscosities tend to get closer as temperature increases. Giving the fact that Pr 1:2 (Propylene) is solid under 318 K, and that it is very viscous compared to Et 1:2 (Ethylene) and Pr 1:3, further characterizations reported in this work will only concern Pr 1:3 in comparison to Et 1:2.

The influence of water content was studied by adding variable amounts of water from 600 to 47,000 ppm, which corresponds to ChCl:PG:H₂O molar ratios from 1:3:0.01 to 1:3:0.818. Viscosity measurements of Et 1:2 at similar water contents were added for comparison purpose (Figure 2b).

The increase in water content leads to a decrease in viscosity of both Et 1:2 and Pr 1:3. Water content therefore seems to be another interesting way to modulate the transport properties of Pr 1:3 [20]. Tuning temperature and water content of Pr 1:3 could then allow this DES to remain in the range of viscosity considered for ionometallurgical recycling applications, however keeping in mind that a high water content could destabilize the chloro-metallic

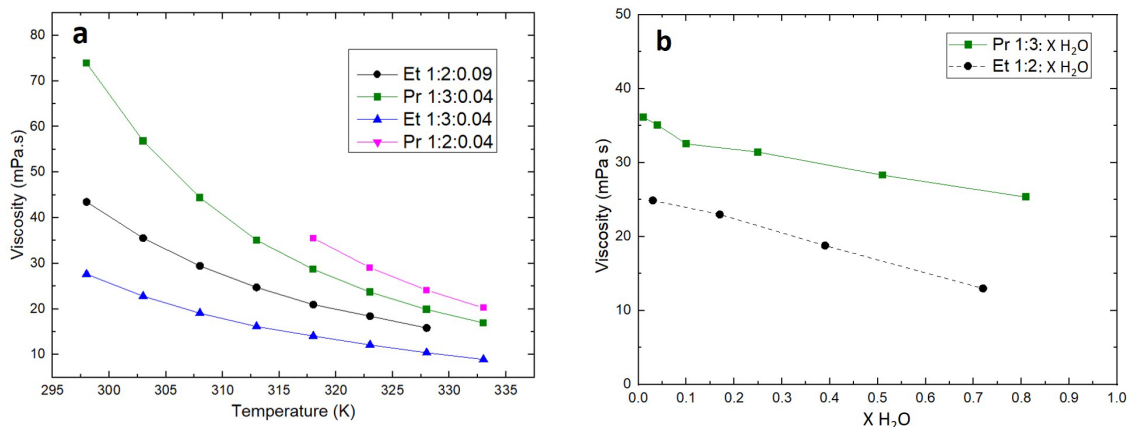


Figure 2. Viscosity of the DESs depending on (a) temperature and (b) water content at 313 K.

complexes or even lead to the formation of insoluble metallic species.

3.3. Conductivity

Figures 3a and 3b show the conductivity values of Et 1:2 and Pr 1:3 normalized by the ChCl molar ratio, as a function of temperature and water content, respectively. Ch^+ and Cl^- being the conductive species of the DESs, this representation allows to free oneself from the difference in ChCl proportion between the two considered DESs.

The conductivity of both DESs increases with temperature (Figure 3a). This is linked to the decrease in viscosity allowing faster ion diffusion. Indeed, the Walden plot ($\log(\Lambda)$ vs $\log(1/\eta)$) based on the Walden equation ($\Lambda \cdot \eta^\alpha = C$, Λ being the molar conductivity, η the viscosity and α and C constant parameters) presented in SI as Figure SI1 clearly shows that a linear fit can be obtained, meaning that only the viscosity impacts the molar conductivity.

The high viscosity of Pr 1:3 compared to Et 1:2 reflects a slower flow rate related to van der Waals and hydrogen interactions in the network, more important in Pr 1:3 than in Et 1:2. As well as the higher viscosity, hydrogen interactions in Pr 1:3 also help to explain the observed lower conductivity compared to Ethaline. Besides, Abbott *et al.* [21,22] put forward the theory of holes, which explains the viscosity of DESs. In DESs, not only molecular interactions tend to oppose the transport of ionic species, but also the holes generated by these interactions which leave inter- or intramolecular spaces. The size of these

holes depends on hydrogen bond strength, temperature, and water content. Smaller holes will increase the viscosity, while larger holes will decrease it, and so hinder or enhance ion mobility, respectively.

Figure 3b shows that the conductivity of Ethaline remains higher than that of Pr 1:3 regardless of the water content. The review article published by Bryant *et al.* [23] on the interfacial nanostructure and the properties of ChCl:glycerol DES shows that water can be considered as a co-HBD for molar content higher than 5%, as a structural modification of DES was observed above this value. Below 25%, only the alignment of the liquid structure was modified. Alfurayj *et al.* [20] demonstrated that modest amounts of water addition (1–10%) to Ethaline are of little concern for practical use and can even lead to performance improvements, such as accelerated solvation and higher conductivity.

Knowing this behavior, Pr 1:3 therefore remains an interesting electrolyte as an alternative to Et 1:2 with reduced cost and environmental impact. Its similar physico-chemical properties can be easily modulated by temperature and water addition.

3.4. Electrochemical stability

Electrochemical stability, commonly called electrochemical window (EW), is one of the parameters of interest sought in DESs and ionic liquids, because they often show at least similar or even higher stability compared to common aqueous electrolytes [24–27]. For electrometallurgy applications, this characteristic is of primary importance, especially to avoid

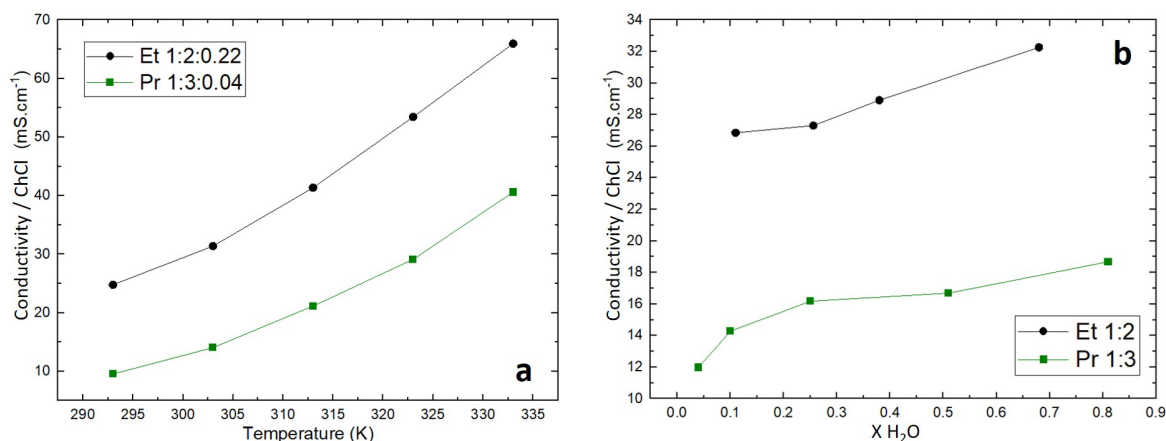


Figure 3. Conductivity of the DESs depending on (a) temperature and (b) water molar ratio at 298 K.

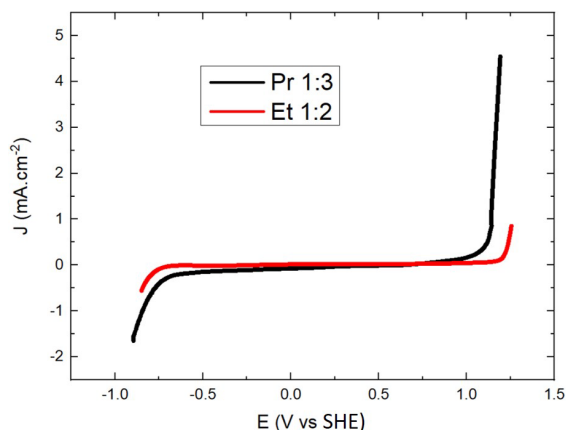


Figure 4. Electrochemical window of Et 1:2 and Pr 1:3 recorded by linear sweep voltammetry on a Pt working electrode at 20 mV.s⁻¹ and 313 K.

DES degradation, which is more critical than water electrolysis using aqueous electrolytes, for cost and environmental reasons. The EW of Pr 1:3 was determined at a temperature of 313 K and compared to the EW of Et 1:2, widely used by the Abbott *et al.* group for electrometallurgy applications [28,29]. Figure 4 shows that the EW of Pr 1:3 ranges from -0.8 to 1.1 V vs SHE, very similar to the one of Et 1:2, as already observed by Costa *et al.* in the case of Pr 1:2 [30]. The oxidation signal recorded above 1.1 V vs SHE is usually attributed to EG/PG or chloride oxidation, whereas the reduction signal around -0.8 V vs SHE is associated to cholinium cation reduction [31].

The low difference in stability between the two DESs suggests that Pr 1:3 could replace Ethaline in electrometallurgical recycling processes. In addition, the potential ranges determined are comparable to those defined in the literature and frame the redox potentials of numerous electroactive metals of interest (gold, silver, palladium, etc.) [8,32]. The electrochemical stability of DESs can be somewhat limited by the amount of water. Valverde *et al.* [33] showed that the electrochemical window of Ethaline can vary by around 0.2 V with varying water amount from 1 to 15%.

3.5. Electrochemical characterizations of precious metals

In electrometallurgy, the oxidation and reduction potentials of metallic species are an indicator of their ability to be reduced (i.e., electrodeposited) or oxidized (i.e., electrochemically leached) in a specific electrolyte. Corresponding potential values must be included in the EW of the electrolyte. For that, Au, Pd, and Ag were dissolved by anodic leaching of metallic wires in Et 1:2 and Pr 1:3, and resulting electrochemical systems were studied by cyclic voltammetry. The superposition of the voltammograms in Figures 5a (Pr 1:3) and 5b (Et 1:2) allowed to compare the redox potentials of the chloro-metallic complexes formed in the two DESs, but also to define the possibility to leach, deposit, and so electrochemically recycle corresponding metals in both DESs.

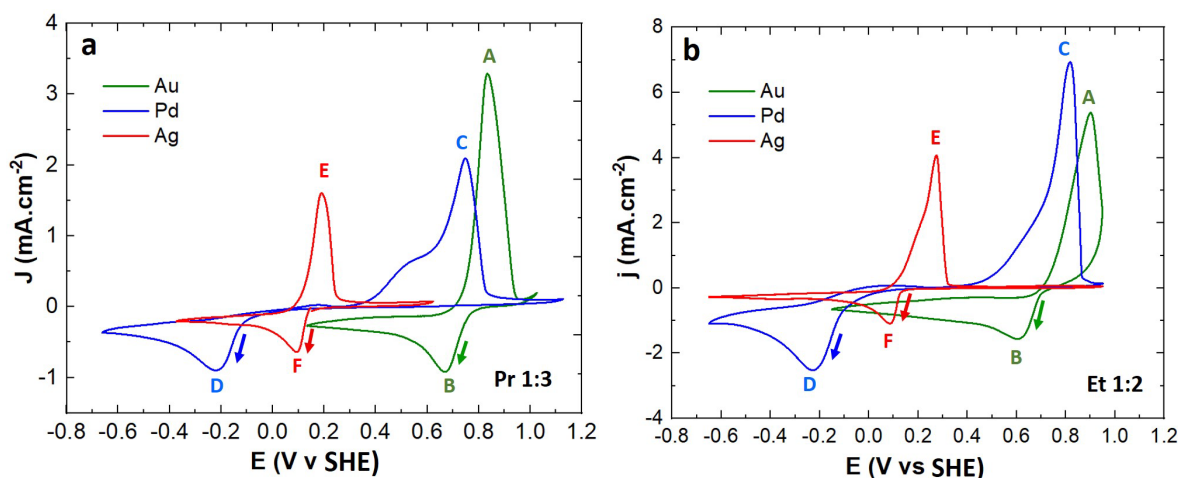


Figure 5. Cyclic voltammograms of Au(I), Pd(II) and Ag(I) monometallic leachates in (a) Pr 1:3 ([Au(I)] = 50 mM, [Ag(I)] = 16 mM, [Pd(II)] = 50 mM) and (b) Et 1:2 ([Au(I)] = 25 mM, [Ag(I)] = 25 mM, [Pd(II)] = 25 mM) recorded on Pt at 313 K at a scan rate of 20 mV.s⁻¹.

Obviously, Pd(II)/Pd(0) is a non-reversible system with a slow charge transfer kinetics, as reduction and oxidation signals are separated by almost 0.9 V. As can be observed on the figures SI2 and SI3, the peak potential of Ag(I) and Au(I) reduction varies with the scan rate, meaning that these systems are not fully reversible. Here the redox system attribution is based on our previous work (Villemejeanne 2022) and literature data [34,35] in Et 1:2.

Table 1 and Figure 6 summarize the formal redox potential E_{app} (V vs SHE) determined from cyclic voltammograms according to Abbott et al. [36,37] using the average of onset potentials of the oxidation and reduction waves for each redox couple. The values obtained are compared to those published by Abbott et al. in 2011 using Et 1:2 [36,37].

It appears that all the redox potentials are included in the EW of Pr 1:3 determined in 3.4. The formal redox potential values are offset by approximately 150–210 mV compared to Abbott et al. values, despite Abbott values being corrected to SHE reference electrode. Nevertheless, the oxidation and reduction peaks of metals determined in this work, are very close for Et 1:2 and Pr 1:3. The difference for a same metal does not exceed 100 mV. The distinct potentials for the reduction or oxidation of considered metallic species show a possibility for some to be leached and/or recovered. Depending on the targeted application, values extracted from the voltam-

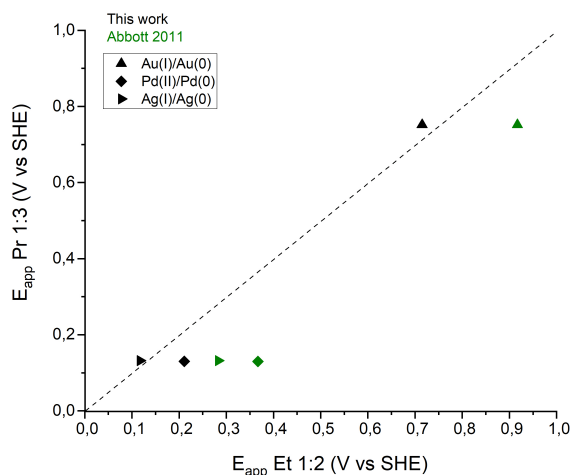


Figure 6. E_{app} of Au(I)/Au(0), Pd(II)/Pd(0) and Ag(I)/Ag(0) in Pr 1:3 vs E_{app} of Au(I)/Au(0), Pd(II)/Pd(0) and Ag(I)/Ag(0) in Et 1:2. Black labels: this work, green labels: Et1:2 values extracted from Abbott et al.

mograms are useful to determine the range of potential to apply. Indeed, to leach a metal, the applied potential has to be on the ascending part of the oxidation peak or superior to it, while for electrodeposition, the applied potential has to be on the descending part of the reduction peak or inferior to it. However, in case of a mix of metallic species, it would be possible to leach or deposit some but not

Table 1. Formal redox potentials of Au(I)/Au(0), Pd(II)/Pd(0) and Ag(I)/Ag(0) in Et 1:2 and Pr 1:3

Peaks	Redox couple	E_{app} (V vs SHE)	
		<i>In italics: Abbott 2011</i>	
		Pr 1:3	Et 1:2
A/B	Au(I)/Au(0)	0.752	0.715 <i>0.917</i>
C/D	Pd(II)/Pd(0)	0.130	0.211 <i>0.367</i>
E/F	Ag(I)/Ag(0)	0.132	0.117 <i>0.283</i>

all. Considering increasing oxidation potentials, Ag would be leached first, then Pd, and finally Au. In opposition, considering decreasing reduction potentials, the deposition would happen first with Au, then Ag, and finally Pd. It would not be possible to leach and recover Pd alone for example.

The CVs presented above also allow to calculate the diffusion coefficient of each metallic species leached in the DESs. The diffusion coefficient is a key parameter in electrometallurgy, contributing to the process efficiency. The deposition diffusion coefficients were calculated using the Berzins–Delahay Equation (Equation (1)) which takes into account the changes at the surface of the working electrode due to the metal deposition process.

$$I_{\text{BD}} = 0.6105AC(nF)^{3/2}\sqrt{D\nu/RT}. \quad (1)$$

I_{BD} is the current intensity of the cathodic peak, A is the electrode area, C the concentration of the metallic ion, n the number of electrons transferred in the reduction reaction, F the Faraday constant, D the diffusion coefficient of the metallic ion, ν the scan rate, R the gas constant and T the temperature. In order to verify that the diffusion of species is the driving force at this scan rate value, scan rate ν was varied between 5 and 100 mV/s in the case of the Ag electrochemical system. Figure S14 shows that the Ag(I) reduction peak current i_{peak} is proportional to $\nu^{1/2}$ in the whole scan rate range tested for Pr 1:3 and Et 1:2. The diffusion laws can then be applied to calculate the diffusion coefficient from CV runs at 20 mV/s for all metallic species. The diffusion coefficients calculated at 313 K, for a concentration of 50 mM of salts in Pr 1:3 and 25 mM in Et 1:2, are displayed in Table 2.

Table 2. Diffusion coefficients of metallic species in Et 1:2 and Pr 1:3

	Ag(I)	Pd(II)	Au(I)
$D_{\text{Pr1:3}}$ ($\text{m}^2\cdot\text{s}^{-1}$)	2.5×10^{-11}	6.3×10^{-12}	5.2×10^{-11}
$D_{\text{Et1:2}}$ ($\text{m}^2\cdot\text{s}^{-1}$)	1.9×10^{-10}	1.2×10^{-11}	3.9×10^{-11}

The diffusion coefficients of the considered metallic species in Pr 1:3 are almost the same or at most one order of magnitude lower than in Ethaline. Au(I) shows the fastest diffusion and Pd(II) the lowest for both DESs. These values are comparable to those previously published in Et 1:2 (Ag [38,39], Au [39,40], Pd [36,37,41]) and are higher than those determined in Reline [41–43], a DES often used in electrometallurgy.

3.6. NMR characterization of Pr 1:3/metal salts solutions

3.6.1. Identification of DES solution structure

The solution structure of Pr 1:3 was investigated by ^1H NMR, and compared to the solution structure of Et 1:2 as a reference. DESs were characterized as pure solvents, without the use of a deuterated diluent. Regarding the Pr 1:3 spectrum, the ^1H NMR signals corresponding to ChCl are observed at 5.02, 3.68, 3.31, and 2.98 ppm. The signals corresponding to PG are seen at 4.57, 3.45, 3.09, and 0.78 ppm (Figure 7, top). The NMR spectra of Et 1:2 exhibit signals at 5.24, 3.99, 3.61, and 3.30 ppm for ChCl, and 4.78 and 3.58 ppm for EG. In both DESs, the most unshielded signals correspond to labile protons a of ChCl and e and h protons of PG or f protons of EG for Pr 1:3 or Et 1:2, respectively.

The influence of metallic species was studied by addition of metallic salts (AgCl, PdCl₂, AuCl₃). Interestingly, upon addition of previously listed metals in Pr 1:3 (Figure 8), it appears that interactions between DESs and metallic species are not systematically the same. In fact, no differences can be seen between Pr 1:3 with and without PdCl₂ or AgCl. Nevertheless, in presence of AuCl₃, it appears that all labile protons from OH groups are fused (Figure 8, green). The fusion of those signals is explained by a fast exchange of the protons from the hydroxyl groups.

As well as for Pr 1:3, there is no observable effect of PdCl₂ in the solution structure of Et 1:2 in ^1H NMR

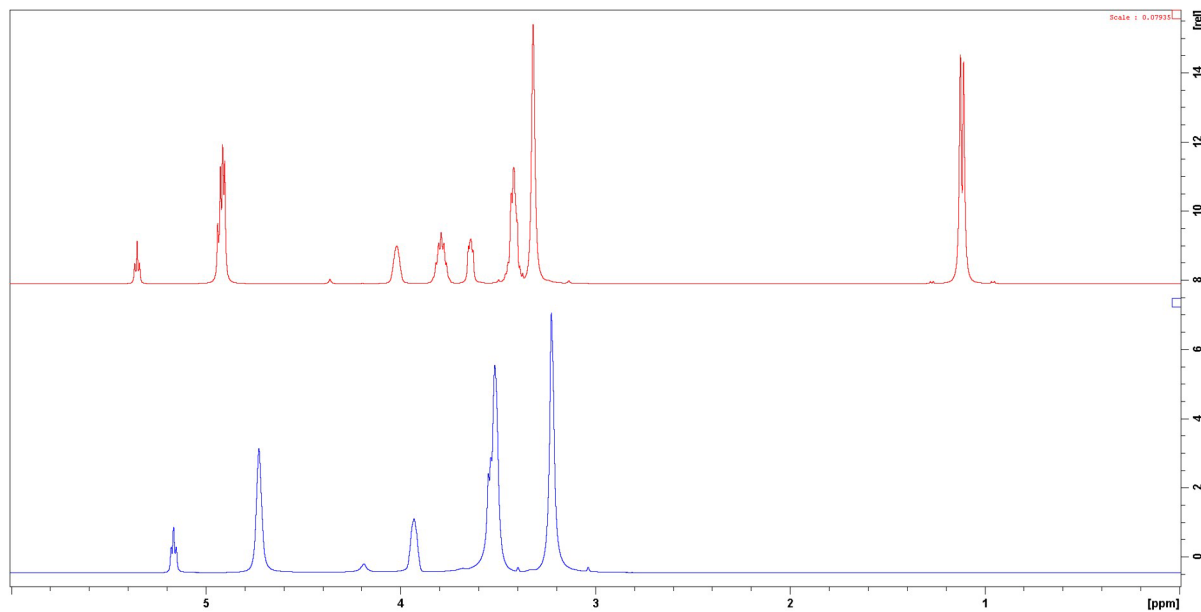


Figure 7. ^1H NMR spectra of Pr 1:3 (top) and Et 1:2 (bottom).

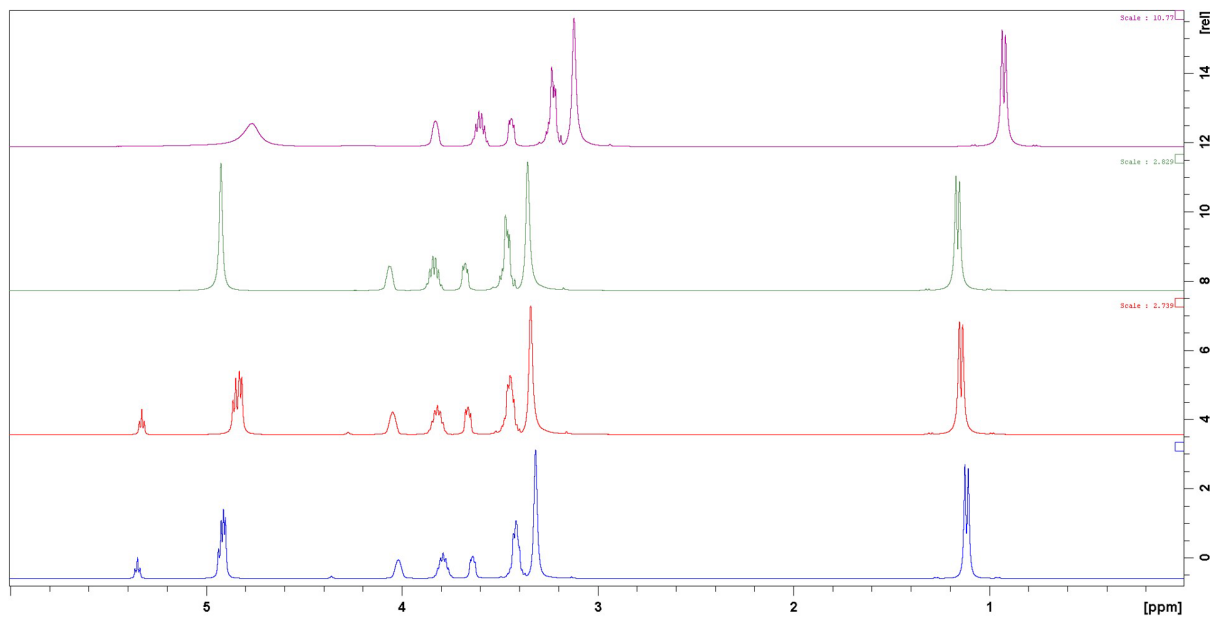


Figure 8. ^1H NMR spectra of Pr 1:3 (blue), and Pr1:3 + PdCl₂ (red), Pr 1:3 + AuCl₃ (green) and Pr 1:3 + AgCl (purple).

(Figure 9). Nevertheless, a broadening of OH signals corresponding to a fast exchange is observed in the presence of AuCl₃ and AgCl salts.

3.6.2. PFG-NMR analyses

Diffusion experiments carried by NMR allows an in-depth comprehension of solvent/metals interac-

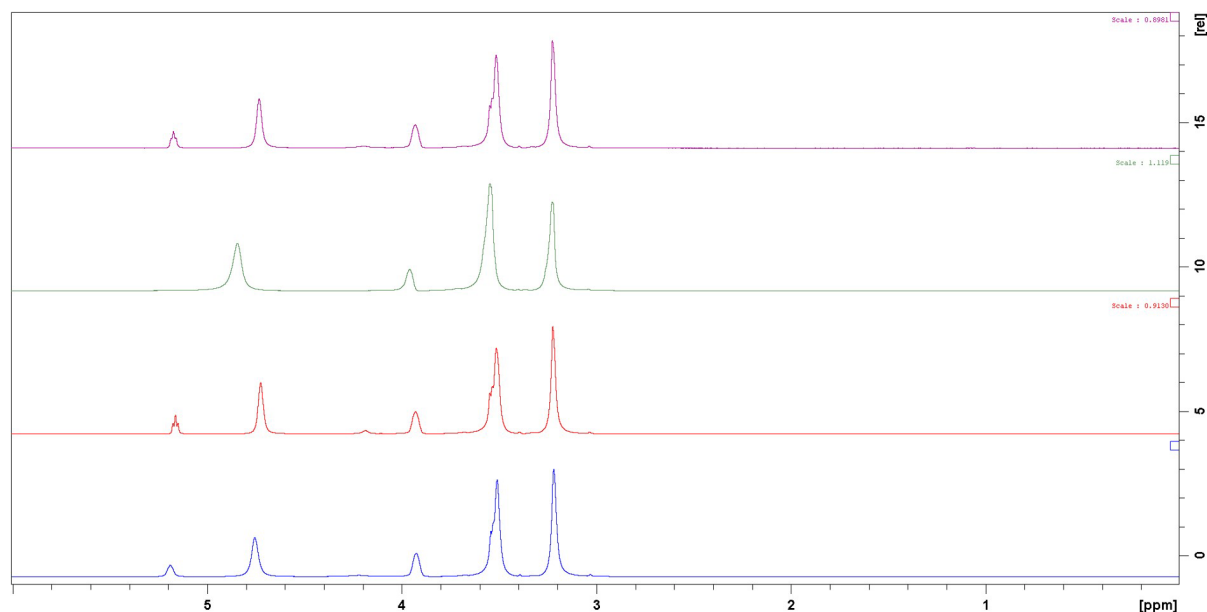


Figure 9. ^1H NMR spectra of Et 1:2 (blue), and Et 1:2 + PdCl_2 (red), Et 1:2 + AuCl_3 (green) and Et 1:2 + AgCl (purple).

tions. Diffusion-ordered spectroscopy (DOSY) with a decreasing magnetic field gradient from 95 to 5% were run at 313 K. The diffusion coefficient D of each species in solution is determined according to Debye–Einstein Equation (2), where the molecule is approximated as a spherical particle of hydrodynamic radius r_H , η is the viscosity of the solvent (mPa·s), k_B the Boltzmann constant, and T the temperature (K).

$$D = \frac{k_B T}{6\pi\eta r_H}. \quad (2)$$

The diffusion coefficients for choline chloride HBA and ethylene glycol or propylene glycol HBD are listed in Tables 3 and 4 for Et 1:2 and Pr 1:3, respectively. The diffusivity of aliphatic (D_{Ch^+}) and hydroxyl ($D_{\text{OH–Ch}^+}$) protons in the choline chloride moiety of Et 1:2 are slightly different (Table 3, entry 1). This is due to a fast exchange between hydroxyl protons of ChCl and water. Furthermore, the diffusivity of choline cations is lower than the diffusivity of HBD. This is due to the higher molecular weight and molecular size of the cation compared to those of the corresponding HDB. The diffusivity of aliphatic protons of ChCl (D_{Ch^+}) and ethylene glycol (D_{EG}) in Et 1:2 are slightly decreased after dissolution of Pd(II) , Au(III) or Ag(I) metal ions (Table 3,

entries 2–4). Despite the increase in water fraction in the DES after metal salts dilution, which must be responsible for an increase in diffusivity, the decreasing diffusivity of both HBA and HBD species tends to indicate a strong interaction between the metal ions and the DES. These observations are in agreement with the study of Abbott *et al.* [44]. The diffusivity difference between aliphatic (D_{EG}) and acidic protons ($D_{\text{OH–EG}}$) of ethylene glycol indicates that the acidic protons are in fast exchange with some other species. This observation is reinforced by the disappearance of the OH–Ch^+ protons in the case of Au and Ag salts (Table 3, entry 3–4). The high water content of these solutions explains the rapid exchange between the labile protons of all the components of the solutions.

On the contrary, the metal salts dissolution has no marked influence on the diffusion coefficients of Ch^+ cation (D_{Ch^+}) and propylene glycol (D_{PG} , $D_{\text{OH–PG}}$) in Pr 1:3 (Table 4). Two possibilities have to be considered (i) the third equivalent of HBD in the DES composition interacts preferentially with the metal ions rather than with the HBA/HBD association and (ii) the metal salts are not dissociated in Pr 1:3 and keep a neutral form instead of an ionic form. Indeed, as it was observed in the case of Et 1:2, the

Table 3. Diffusion coefficients for Et 1:2 solutions

	Ethaline	Composition HBA/HBD/H ₂ O	$10^{-11} D_{\text{Ch}^+}$ (m ² ·s ⁻¹)	$10^{-11} D_{\text{OH-CH}^+}$ (m ² ·s ⁻¹)	$10^{-11} D_{\text{EG}}$ (m ² ·s ⁻¹)	$10^{-11} D_{\text{OH-EG}}$ (m ² ·s ⁻¹)
1	Et 1:2	1/2/0.09	4.18	7.69	7.55	7.92
2	Et 1:2 + Pd	1/2/0.18	3.17	5.65	5.39	6.78
3	Et 1:2 + Au	1/2/0.09	2.84	-	5.89	6.44
4	Et 1:2 + Ag	1/2/0.18	2.41	-	4.66	5.47

Table 4. Diffusion coefficients for Pr 1:3 solutions

	Pr 1:3	Composition HBA/HBD/H ₂ O	$10^{-11} D_{\text{Ch}^+}$ (m ² ·s ⁻¹)	$10^{-11} D_{\text{OH-CH}^+}$ (m ² ·s ⁻¹)	$10^{-11} D_{\text{PG}}$ (m ² ·s ⁻¹)	$10^{-11} D_{\text{OH-PG}}$ (m ² ·s ⁻¹)
1	Pr 1:3	1/3/0.01	1.69	1.91	2.50	2.41
2	Pr 1:3 + Pd	1/3/0.01	1.72	2.17	2.55	2.65
3	Pr 1:3 + Au	1/3/0.09	3.32	-	5.17	5.06
4	Pr 1:3 + Ag	1/3/0.04	1.86	-	2.72	3.30

formation of a strong ionic pair between DES and metal ion lead to a decrease in diffusivity of both HBA and HBD species, even if the water ratio of the solution increases. The increase in diffusivity of HBA and HBD species in the case of Au dissolution is attributed to the increase in water content in the solvent (Table 4, entry 3).

4. Conclusions

From this work, it can be concluded that it is possible to consider Pr 1:3 as an alternative system to Ethaline for electroleaching/deposition applications, with the advantage of much lower toxicity. The electrochemical properties of Pr 1:3 and of precious metals studied here as examples, are similar to Ethaline. The slightly lower transport properties of ChCl-PG DESs could be circumvented by the modulation of HBD molar ratio and a moderate increase in working temperature or water content. Diffusion experiments carried by NMR showed that strong interactions exists between Ethaline and metallic species, whereas the dissolution of the same metals in Pr 1:3 had no influence on diffusion coefficients, indicating a different state of solvation in this solvent. The lower interaction between Pr 1:3 and metal ions should be a strength in the durability of the solvent during cycling. This will be a part of a future work.

Declaration of interests

The authors do not work for, advise, own shares in, or receive funds from any organization that could benefit from this article, and have declared no affiliations other than their research organizations.

Funding

This work has been supported by the Agence Nationale de la Recherche (EE4Precious project, ANR-20-CE08-0035-01).

Raw data

Raw data corresponding to this research work are available in open access at: <https://doi.org/10.12763/EGL57A>.

Supplementary data

Supporting information for this article is available on the journal's website under <https://doi.org/10.5802/crchim.297> or from the author.

References

- [1] P. Walden, *Bull. Acad. Imper. Sci.*, 1914, **8**, 405-422.
- [2] G. Kaur, H. Kumar, M. Singla, *J. Mol. Liquids*, 2022, **351**, article no. 118556.

- [3] M. Yadav, D. Behera, S. Kumar, R. R. Sinha, *Ind. Eng. Chem. Res.*, 2013, **52**, 6318-6328.
- [4] A. P. Abbott, G. Capper, D. L. Davies, R. K. Rasheed, V. Tambyrajah, *Chem. Commun.*, 2003, **1**, 70-71.
- [5] S. Ghosh, S. Roy, *Surf. Coat. Technol.*, 2014, **238**, 165-173.
- [6] N. G. Sousa, C. P. Sousa, O. S. Campos, P. de Lima-Neto, A. N. Correia, *J. Mol. Liquids*, 2019, **288**, article no. 111091.
- [7] N. Peeters, K. Janssens, D. de Vos, K. Binnemans, S. Riaño, *Green Chem.*, 2022, **24**, 6685-6695.
- [8] A. P. Abbott, R. C. Harris, F. Holyoak, G. Frisch, J. Hartley, G. R. T. Jenkin, *Green Chem.*, 2015, **17**, 2172-2179.
- [9] M. Hayyan, Y. P. Mbous, C. Y. Looi, W. F. Wong, A. Hayyan, Z. Salleh, O. Mohd-Ali, *SpringerPlus*, 2016, **5**, article no. 913.
- [10] M. Hayyan, C. Y. Looi, A. Hayyan, W. F. Wong, M. A. Hashim, *PLoS One*, 2015, **10**, article no. e0117934.
- [11] L. Lomba, M. P. Ribate, E. Sangüesa, J. Concha, M. P. Garalaga, D. Errazquin, C. B. García, B. Giner, *Appl. Sci.*, 2021, **11**, article no. 10061.
- [12] K. Radošević, M. Cvjetko Bubalo, V. Gaurina Srček, D. Grgas, T. Landeka Dragičević, I. Radojčić Redovniković, *Ecotoxicol. Environ. Safety*, 2015, **112**, 46-53.
- [13] K. Radošević, N. Čurko, V. Gaurina Srček, M. Cvjetko Bubalo, M. Tomašević, K. Kovačević Ganić, I. Radojčić Redovniković, *LWT*, 2016, **73**, 45-51.
- [14] R. Ahmadi, B. Hemmateenejad, A. Safavi, Z. Shojaeifard, M. Mohabbati, O. Firuzi, *Chemosphere*, 2018, **209**, 831-838.
- [15] N. F. Gajardo-Parra, V. P. Cotroneo-Figueroa, P. Aravena, V. Vesovic, R. I. Canales, *J. Chem. Eng. Data*, 2020, **65**, 5581-5592.
- [16] E. S. C. Ferreira, I. V. Voroshylova, N. M. Figueiredo, C. M. Pereira, M. N. D. S. Cordeiro, *J. Mol. Liquids*, 2020, **298**, article no. 111978.
- [17] Y. Wang, W. Chen, Q. Zhao, G. Jin, Z. Xue, Y. Wang, T. Mu, *Phys. Chem. Chem. Phys.*, 2020, **22**, 25760-25768.
- [18] Q. Zhang, K. De Oliveira Vigier, S. Royer, F. Jérôme, *Chem. Soc. Rev.*, 2012, **41**, 7108-7146.
- [19] A. P. Abbott, S. Nandhra, S. Postlethwaite, E. L. Smith, K. S. Ryder, *Phys. Chem. Chem. Phys.*, 2007, **9**, 3735-3743.
- [20] I. Alfurayj, C. C. Fraenza, Y. Zhang *et al.*, *J. Phys. Chem. B*, 2021, **125**, 8888-8901.
- [21] A. P. Abbott, *ChemPhysChem*, 2004, **5**, 1242-1246.
- [22] A. P. Abbott, G. Capper, D. L. Davies, R. Rasheed, *Inorg. Chem.*, 2004, **43**, 3447-3452.
- [23] S. J. Bryant, A. J. Christofferson, T. L. Greaves, C. F. McConville, G. Bryant, A. Elbourne, *J. Colloid Interface Sci.*, 2022, **608**, 2430-2454.
- [24] N. Sinclair, X. Shen, J. S. Wainright, *Meet. Abstr.*, 2021, **MA2021-01**, 25.
- [25] M. H. Chakrabarti, F. S. Mjalli, I. M. AlNashef, M. A. Hashim, M. A. Hussain, L. Bahadori, C. T. J. Low, *Renew. Sustain. Energy Rev.*, 2014, **30**, 254-270.
- [26] D. Lloyd, T. Vainikka, L. Murtomäki, K. Kontturi, E. Ahlberg, *Electrochim. Acta*, 2011, **56**, 4942-4948.
- [27] R. Cheng, J. Xu, X. Wang, Q. Ma, H. Su, W. Yang, Q. Xu, *Front. Chem.*, 2020, **8**, article no. 619.
- [28] A. P. Abbott, K. E. Ttaib, G. Frisch, K. J. McKenzie, K. S. Ryder, *Phys. Chem. Chem. Phys.*, 2009, **11**, 4269-4277.
- [29] B. Villemejeanne, S. Legeai, E. Meux, S. Dourdain, H. Mendil-Jakani, E. Billy, *J. Environ. Chem. Eng.*, 2022, **10**, article no. 108004.
- [30] R. Costa, M. Figueiredo, C. M. Pereira, F. Silva, *Electrochim. Acta*, 2010, **55**, 8916-8920.
- [31] K. Haerens, E. Matthijs, K. Binnemans, B. Van der Bruggen, *Green Chem.*, 2009, **11**, 1357-1365.
- [32] W. Sánchez-Ortiz, J. Aldana-González, T. Le Manh *et al.*, *J. Electrochem. Soc.*, 2021, **168**, article no. 016508.
- [33] P. E. Valverde, T. A. Green, S. Roy, *J. Appl. Electrochem.*, 2020, **50**, 699-712.
- [34] A. P. Abbott, G. Frisch, J. Hartley, W. O. Karim, K. S. Ryder, *Prog. Nat. Sci.: Mater. Int.*, 2015, **25**, 595-602.
- [35] S. Datta, J. Mahin, E. Liberti, I. Manasi, K. J. Edler, L. Torrente-Murciano, *ACS Sustain. Chem. Eng.*, 2023, **11**, 10242-10251.
- [36] C. D'Agostino, R. C. Harris, A. P. Abbott, L. F. Gladden, M. D. Mantle, *Phys. Chem. Chem. Phys.*, 2011, **13**, 21383-21391.
- [37] A. P. Abbott, G. Frisch, S. J. Gurman, A. R. Hillman, J. Hartley, F. Holyoak, K. S. Ryder, *Chem. Commun.*, 2011, **47**, 10031-10033.
- [38] F. Bohrn, M. Leitzenberger, S. Schwab, P. Kuegler, L. Brunnbauer, S. Jordan, H. Hutter, *ECS J. Solid State Sci. Technol.*, 2022, **11**, article no. 024006.
- [39] S. Rahali, R. Zarrougui, M. Marzouki, O. Ghodbane, *J. Electroanal. Chem.*, 2020, **871**, article no. 114289.
- [40] L. Aldous, D. S. Silvester, C. Villagrán, W. R. Pitner, R. G. Compton, M. Cristina Lagunas, C. Hardacre, *New J. Chem.*, 2006, **30**, 1576-1583.
- [41] G. Lanzinger, R. Böck, R. Freudenberger, T. Mehner, I. Scharf, T. Lampke, *Trans. IMF*, 2013, **91**, 133-140.
- [42] Y. Katayama, Y. Bando, T. Miura, *Trans. IMF*, 2008, **86**, 205-210.
- [43] F. Soma, Q. Rayée, M. Bougouma, C. Baustert, C. Buess-Herman, T. Doneux, *Electrochim. Acta*, 2020, **345**, article no. 136165.
- [44] A. P. Abbott, R. C. Harris, K. S. Ryder, *J. Phys. Chem. B*, 2007, **111**, 4910-4913.

Comptes Rendus

Chimie

Objectif de la revue

Les *Comptes Rendus Chimie* sont une revue électronique évaluée par les pairs de niveau international, qui couvre l'ensemble des domaines des sciences chimiques.

Ils publient des numéros thématiques, des articles originaux de recherche, des articles de synthèse, des mises au point, des mises en perspective historiques, des textes à visée pédagogique, ou encore des actes de colloque, en anglais ou en français, sans limite de longueur et dans un format aussi souple que possible (figures, données associées, etc.).

Depuis 2020, les *Comptes Rendus Chimie* sont publiés avec le centre Mersenne pour l'édition scientifique ouverte, selon une politique vertueuse de libre accès diamant, gratuit pour les auteurs (pas de frais de publication) comme pour les lecteurs (accès libre, immédiat et pérenne).

Directeur de la publication : Antoine Triller.

Rédacteur en chef : Pierre Braunstein.

Éditeurs associés : Azzedine Bousseksou, Janine Cossy.

Comité scientifique : Rick D. Adams, Didier Astruc, Guy Bertrand, Bruno Chaudret, Avelino Corma, Patrick Couvreur, Stefanie Dehnen, Paul J. Dyson, Odile Eisenstein, Marc Fontecave, Pierre Grandclaude, Robert Guillaumont, Paul Knochel, Daniel Mansuy, Bernard Meunier, Armando J. L. Pombeiro, Michel Pouchard, Didier Roux, João Rocha, Clément Sanchez, Philippe Sautet, Jean-Pierre Sauvage, Patrice Simon, Pierre Sinaÿ.

Secrétaire scientifique : Julien Desmarets.

À propos de la revue

Les *Comptes Rendus Chimie* sont exclusivement publiés au format électronique.

Toutes les informations sur la revue, ainsi que le texte intégral de l'ensemble des articles, sont disponibles sur son site internet, à l'adresse <https://comptes-rendus.academie-sciences.fr/chimie/>.

Informations pour les auteurs

Pour toute question relative à la soumission d'un manuscrit, merci de consulter le site internet de la revue : <https://comptes-rendus.academie-sciences.fr/chimie/>.

Contact

Académie des sciences

23 quai de Conti

75006 Paris (France)

cr-chimie@academie-sciences.fr



Les articles de cette revue sont mis à disposition sous la licence
Creative Commons Attribution 4.0 International (CC-BY 4.0)
<https://creativecommons.org/licenses/by/4.0/deed.fr>

COMPTES RENDUS DE L'ACADÉMIE DES SCIENCES

Chimie

Volume 27, n° S4, 2024

Special issue / Numéro spécial

GDR Prométhée – French Research Network on *Hydrometallurgical Processes for Primary and Secondary Resources* / GDR Prométhée – Groupement de Recherche sur les Procédés Hydrométallurgiques pour la Gestion Intégrée des Ressources Primaires et Secondaires

Guest editors / Rédacteurs en chef invités

Laurent Cassayre (CNRS-Université de Toulouse, Laboratoire de Génie Chimique, France) and Hervé Muhr (CNRS-Université de Lorraine, Laboratoire Réactions et Génie des Procédés, France)

Cover illustration / Illustration de couverture

Cover illustration (clockwise from left): Fig. 2 from article Jacob et al., Fig. 7 from Laskar et al., Fig. 4 from El Maangar et al.

Contents / Sommaire

Guest Editors	1-1	Christian Manfoumbi, Kevin Roger, Martine Meireles	
Laurent Cassayre, Hervé Muhr		Filtering the unfilterable: tuning the mesostructure of precipitating silica gels to improve the filterability of acidic lixiviation slurries	111-122
Special issue on hydrometallurgical processes for the integrated management of primary and secondary resources: Foreword	3-4	Virginie Nachbaur, Firas Ayadi, Béatrice Foulon, Malick Jean, Valérie Pralong, Samuel Jouen	
Nicolas M. Charpentier, Dong Xia, Jean-Christophe P. Gabriel		A sustainable solvothermal process extracting critical elements from Li-ion batteries	123-132
Printed circuit board recycling: a focus on a novel, efficient and sustainable process for spent critical metals recovery	5-15	Lorena E. Ramirez Velazquez, Hervé Muhr	
Agathe Hubau, Kathy Bru, Safiatou Idrissa Oumarou, Cécile Leycuras		Lithium recovery from secondary sources: A review in battery recycling with emphasis on chemical precipitation	133-141
Lessons learned from the upscaling of an iron bio-oxidation process to improve uranium recovery	17-35	Julie Réaux-Durain, Boushra Mortada, Murielle Bertrand, Jérôme Maynadié, Michaël Carboni, Daniel Meyer, Damien Bourgeois	
Clément Laskar, Amine Dakkoune, Carine Julcour, Florent Bourgeois, Béatrice Biscans, Laurent Cassayre		Back-extraction of major actinides from organic phase through precipitation	143-152
Case-based analysis of mechanically-assisted leaching for hydrometallurgical extraction of critical metals from ores and wastes: application in chalcopyrite, ferronickel slag, and Ni-MH black mass	37-52	Fabrice Giusti, Elise Guerinoni, David Lemire, Marine Thimotée, Guilhem Arrachart, Sandrine Dourdain, Stéphane Pellet-Rostaing	
Emilie Régnier, Agathe Hubau, Solène Touzé, Sylvain Guignot, Daniel Meyer, Olivier Diat, Damien Bourgeois		Solvent extraction of uranium from an acidic medium for the front-end of nuclear fuel cycle: from mechanisms understanding to innovative process design	153-183
Copper leaching with aqueous foams for the processing of electronic waste	53-61	Asmae El Maangar, Johannes Gramüeller, Verena Huber, Pierre Degot, Didier Touraud, Ruth Gschwind, Werner Kunz, Thomas Zemb	
Jérôme Jacob, Douglas Pino-Herrera, Catherine Greffié, Guillaume Wille, Emmanuelle Plat		Solubilisation-microstructure relationship of trivalent salts in hydrotropic ternary systems	185-202
Reprocessing of waste produced during acid mine drainage lime treatment by selective leaching	63-80	Calogera Bertoloni, Vitalys Mba Ekomo, Benoît Villemejeanne, Charly Lemoine, Romain Duwald, Emmanuel Billy, Hakima Mendil-Jakani, Sophie Legeai	
Mateus De Souza Buriti, Pierre Cézac, Lidia Casás		Propylene glycol-based deep eutectic solvent as an alternative to Ethaline for electrometallurgy	203-214
Dissolution and precipitation of jarosite-type compounds: state of the art and future perspectives	81-109		

1878-1543 (electronic)

COMPTES RENDUS
DE L'ACADEMIE DES SCIENCES

Gazette

Volume 27, no 34, 2024